Collection of Solved Nonlinear Problems for Remote Shaping and Patterning of Liquid Structures on Flat and Curved Substrates by Electric and Thermal Fields

Thesis by
Chengzhe Zhou

In Partial Fulfillment of the Requirements for the
Degree of
Doctor of Philosophy

CALIFORNIA INSTITUTE OF TECHNOLOGY
Pasadena, California

2020
Defended August 29, 2019

Chengzhe Zhou
ORCID: 0000-0002-4577-5278

ACKNOWLEDGEMENTS

Firstly, I would like to express my sincere gratitude to my advisor Prof. Troian for supporting my Ph.D study and related research, for her patience, motivation and confidence in me, as well for her penetrating questions and immense knowledge. Under her guidance, I was trained to think critically and granted freedom to explore scientific problems with nonstandard approaches which is really what this thesis is all about. I could not have imagined having a better mentor for my Ph.D study.

Besides my advisor, I would like to thank the rest of my thesis committee, Prof. Bruno, Prof. Porter and Prof. Politzer as well as Prof. Hou and Prof. Cross who have guided me before, for their inspiring conversations and insightful comments, which widened my research from different perspectives.

I also thank my fellow labmates, Kelvin, Teddy and Daniel, for the interesting discussions, for the sleepless nights we pulled before the APS talks and for all the fun we have had in the last five years. With a special mention to Nick, several projects presented in this dissertation were inspired by numerous stimulating conversions between us. I'm indebted to the system administrator of our lab, Dr. Thompson, who volunteered his time to ensure that computer hardware and software were always up to date, for his quick fixes to all IT issues and his assistance to expedite simulations on the computing cluster.

Outside of academics, I am truly grateful to my parents Xianzhu and Fengmei, who have provided me with unconditional moral, emotional and financial support throughout the entire journey. It would not be possible to conduct this Ph.D research without their precious support. I'm also in debt to many other family members not mentioned here.

Also I thank my dearest friends Chenglu from University of Iowa, Jingxing from the Case Western Reserve University, Yuan from the University of Utah, Kuan from Michigan State University, Caltech colleagues Cong, Cheng, Junlong and Yuchen as well as Yuanhao, Zhihong, Yifan and Lei back home in Shanghai who always treated me with extreme hospitality every time I visited home.

To Xuan, despite the hardship I will always memorize the encouraging words you have said to me throughout this journey about holding onto my dream and never giving up.

To Lining, I couldn't possibly finish the writing of this dissertation without your unlimited patience, encouragement and faith in me. I'm lucky to have you by my side.

Last, but by no means the least, in the loving memory of grandpa Zhaopei and grandma Jianhua who passed away when I was only six, this work is the result of your dedication to education on honesty, morality, aesthetics and science in my early childhood.

ABSTRACT

There has been significant interest during the past decade in developing methods for remote manipulation and shaping of soft matter such as polymer melts or liquid metals to pattern films at the micro- and nanoscale. The appeal of low-cost fabrication of micro-optical devices for beam shaping or metallic films to produce high order cuspidal arrays for antireflective or self-cleaning coatings has driven considerable interest in the fundamentals associated with film shaping and liquid curvature. Physicists and applied mathematicians have uncovered new rich ground in examining the complex behavior of high order, nonlinear partial differential equations describing the motion and response of liquid structures driven to redistribute and reorganize by externally applied thermal and electric fields. For the problems relevant to this thesis, which focuses on liquid structures at small scales, the applied fields induce surface forces which act only at the moving interface. Because the surface-to-volume ratios tend to be very large however, the corresponding forces are considerable in magnitude and dominate the formation and growth processes described. In all cases examined, once the driving forces are removed and the operating temperatures dropped below the melting point, the patterned films and liquid shapes rapidly solidify in place, leaving behind structures with molecularly smooth surfaces, an especially advantageous feature for micro-optical applications.

The first part of this thesis examines the nonlinear dynamics of free surface films in the long wavelength limit coating either a flat or curved substrate. We examine the long wavelength limit in which inertial forces are suppressed in comparison to viscous forces such that the system reacts instantaneously to interfacial forces acting in the direction normal to the moving interface, such as capillary and Maxwell forces, or in the direction parallel to the moving interface, such as thermocapillary forces. In the first example, we demonstrate by analytic and numerical means how a system designed to incur large runaway thermocapillary forces can pattern films with conic cusps whose tips undergo self-focused sharpening through a novel self-similar process. This finding expands the known categories of flows that can generate cusp-like shapes and introduces a new lithographic method for remote, one-step fabrication of cuspidal microarrays. We next examine a lithographic technique known as Electrohydrodynamic Lithography in which remote patterned electric field distributions projected onto the surface of a dielectric film generate Maxwell stresses which cause growth and accumulation toward regions of highest field gradients. Here we solve the inverse problem associated with the governing fourth-order nonlinear interface equation by appealing to a control-theoretical approach. This approach reveals the optimal electrode topography required to generate precise complex liquid patterns within a given time interval. Numerical implementation of this algorithm yields high fidelity pattern replication by essentially incorporating proximity

corrections which quench undesirable interference effects of material waves. We then extend the long wavelength analysis to a liquid layer coating a curved manifold and demonstrate how a desired film shape can be obtained by novel application of the Helmholtz minimum dissipation principle. We illustrate this solution method by deriving the nonlocal tensorial partial differential equation for the evolution of a slender, perfectly conducting or insulating liquid film supported on a curved electrode. Finite element simulations demonstrate the complex shapes which can result, including formation of liquid accumulation sites and flow instabilities not accessible to films supported on a planar substrate.

The second part of this thesis focuses exclusively on geometric singularities which result from nonlinear effects caused by the coupling of capillary and Maxwell forces in perfectly conducting liquids. Here, we do not restrict ourselves to the long wavelength approximation but instead examine systems with comparable lateral and transverse dimensions. We probe the energy stability of such systems using a convective Lagrangian approach. The exact variational characterization of equilibrium shapes and their stability is derived in the most general form without restriction to coordinate system or shape deformations. This formulation unmasks several terms, typically not evident in calculations restricted to normal deformations of an electrified spherical drop. Our result provides new insights into the energy stability of equilibrium shapes that do not necessarily have constant interface curvature or uniform surface charge distribution. We then turn attention to the classical problem of a conical meniscus produced in an electrified liquid body. The analysis by G. I. Taylor (1963) first determined that the hydrostatic equilibrium shape for a liquid body subject only to capillary and Maxwell forces is given by a cone with an opening angle of 98.6°. However, the fact that such a cone represents an unsteady configuration is often ignored. We revisit the inviscid analysis by Zubarev (2001) who proposed that conic cusps in perfectly conductive liquid evolve through a time-dependent self-similar process. Using the unsteady Bernoulli's equation, he analyzed the force balance at the moving interface and obtained an asymptotically correct self-similar solution dominated by a sink flow far from the evolving apex whose streamlines orient nearly parallel to the moving surface. In addition to the sink flow our analysis, supported by accurate, high resolution numerical solutions of the boundary integral equations, independently reveals a two-parameter family of non-spherically symmetric self-similar solutions whose velocity streamlines intercept the conic surface at an angle. This new family of solutions not only properly account for the interplay between capillary, Maxwell and inertial forces but generate advancing and recoiling type interface shapes, which substantially alter current understanding of the formation and acceleration of dynamic cones.

PUBLISHED CONTENT AND CONTRIBUTIONS

S. W. D. Lim, K. R. Fiedler, C. Zhou, and S. M. Troian. "Fabrication of single and tiered microlens arrays by projection of patterned thermocapillary forces". In preparation for *Nature Nanotechnology* (Mar. 2020).

Contribution: To complement experimental work by S.W.D.L. and S.M.T demonstrating a new lithographic technique based on thermocapillary patterning, C.Z. conducted finite element simulations of the governing thin film model to illustrate the evolution in film shapes as a function of time in response to specified external thermal field distributions. Time stamped images by C.Z. showing the evolution of the thin film in response to a patterned mask will be included in the manuscript for submission.

C. Zhou and S. M. Troian. "Electrohydrodynamic patterning of thin films on curved manifolds: theory and simulation". To be submitted to *Physical Review Fluids* (Feb. 2020).

Basis: Article for future journal submission is based on the material in Chapter 4.

Contribution: The thin film patterning technique known as Electrohydrodynamic Lithography (EHL) has so far been only applied to the shaping of liquid films supported on a flat and planar substrate. In this work, C.Z. has extended the conventional governing thin film equation to substrates represented by curved manifolds by invoking the Helmholtz minimum dissipation principle. This principle helps identify the unique resulting flow state responsive to the Maxwell stresses and inherent capillary forces in a coordinate-free fashion. C.Z. also conducted finite element simulations to demonstrate how Maxwell forces, capillary forces and substrate curvature combine to influence the film distribution process on a spherical substrate. The work to be submitted, for which C.Z. has provided the original figures, is being jointly drafted by C.Z. and S.M.T. In addition, C.Z. will assist S.M.T. in drafting responses to referee reports.

C. Zhou and S. M. Troian. "Electrohydrodynamic lithography: Solution of the inverse problem". To be submitted to *Physical Review Letters* (Jan. 2020).

Basis: Article for future journal submission is based on the material in Chapter 3.

Contribution: Fabrication of micro/nanostructures of specific shape and size using photolithographic techniques requires proximity correction principles and algorithms to quench undesirable optical wave interference effects. In this work, C.Z. has developed the equivalent of proximity correction principles and algorithm for the emerging thin film lithographic tool known as Electrohydrodynamic Lithography (EHL). This thin film patterning technique relies on projection of Maxwell forces from a nearby patterned counter electrode onto the surface of a liquefied dielectric film to self-organize the flow into a desired three-dimensional shape. Using optimal control theory, C.Z. has reformulated the computational principle of electrode design in EHL as a constrained inverse problem, which is then solved by the adjoint method with high efficiency. C.Z. is responsible for writing source code to simulate the EHL system and to implement the optimization algorithm. This approach, demonstrated by a number of simulations performed by C.Z., yields the optimal counter electrode topography required to mold a flowing film into the desired three-dimensional shape within a specified time interval.

The work to be submitted, for which C.Z. has provided the original figures, is being jointly drafted by C.Z. and S.M.T. In addition, C.Z. will assist S.M.T. in drafting responses to referee reports.

C. Zhou and S. M. Troian. "Conic cusp growth in perfectly conducting ideal liquids: Unmasking of novel self-similar modes". To be submitted to *Journal of Fluid Mechanics Rapids* (Dec. 2019).

Basis: Article for future journal submission is based on the material in Chapter 6.

Contribution: C.Z. solved the influential model for self-similar conic cusp growth in ideal perfectly conducting electrified liquids first developed by Zubarev (2001), based on the time-dependent Bernoulli's equation evaluated at the accelerating boundary. Zubarev originally proposed an asymptotic solution dominated by a far-field sink flow which was believed to underlie the cone growth. C.Z. independently performed asymptotic expansion of far-field liquid interface, velocity and electric field potentials and uncovered a more general family of similarity solutions dominated by an asymptotic "lifting" flow. More importantly, C.Z. developed and implemented a novel boundary-integral method posed on truncated semi-infinite domains to solve for the exact form of these self-similar conic shapes. The resulting two-parameter family of solutions manifest non-spherically symmetric velocity fields whose streamlines orient at an angle to the conic surface. The complete family of solutions capture both advancing and recoiling interface shapes, configurations were known to exist experimentally but never predicted theoretically before, due to the time-reversal symmetry recognized by C.Z.. The work to be submitted, for which C.Z. has provided the original figures, is being jointly drafted by C.Z. and S.M.T. In addition, C.Z. will assist S.M.T. in drafting responses to referee reports.

C. Zhou and S. M. Troian. "Self-similar cuspidal formation by runaway thermocapillary forces in thin liquid films". *New Journal of Physics* **21** (1) (Jan. 2019), p. 013018.

Basis: Published article is based on the material in Chapter 2.

Contribution: Dietzel and Troian (2009-10) originally proposed a linear instability mechanism based on thermocapillary stress as the underlying source for spontaneous formation of pillar arrays in molten nanofilms. C.Z. extended that investigation by examining (a) the global stability of volume-conserving stationary solutions by appealing to an analogy to gradient flow structure and (b) the asymptotic self-similar growth and stability of conic cusp formation during the final stage of evolution. This analysis expands the field of conic cusp growth in liquids by identifying a system that can sustain tangentially oriented surface forces and provides a analytic relation for the conic angle. C.Z. also conducted finite element simulations to extract the self–similar growth exponents associated with conic cusp formation and showed these were in excellent agreement with the theoretical analysis. The published work, for which C.Z. provided the original figures and tables, was jointly drafted by C.Z. and S.M.T. C.Z. also assisted S.M.T. in drafting responses to all referee reports.
DOI: 10.1088/1367-2630/aaf51d.

TABLE OF CONTENTS

LIST OF ILLUSTRATIONS

Number *Page*

LIST OF TABLES

Chapter 1

INTRODUCTION: PATTERNING LIQUID FLOW BY INTERFACIAL FORCES

The need for patterning materials with high resolution and high fidelity levels at micro- and nano-length scales continues to grow as new technological applications emerge. As a result, lithography is constantly under active development and has yield many advanced technologies. Typically, small-scale patterns are constructed with conventional lithographic techniques such as photolithography and electron beam lithography. The intended reader can consult on reviews (Ito and Okazaki, 2000; Quake and Scherer, 2000; del Campo and Arzt, 2008) for more information. Typically, these methods involve exposing target material (resist) under patterned radiation of photons or electrons followed by material removal in a developer where the solubility of the resist is significantly altered upon exposure to radiation. Although these traditional tools have been extensively studied and optimized in the past few decades, on a fundamental level there still exists known drawbacks, such as the optical diffraction limit in the case of photolithography (Wong, 2001), proximity effects in the case of e-beam lithography (T. H. P. Chang, 1975) and the issue of high cost and complicated pre- and post-processing procedures in general.

Recently, self-organization and self-assembly of soft materials have been reported to overcome some of the drawbacks of conventional lithographic methods by exploring the intrigue coupling between intrinsic material properties and externally applied fields. In many of these "soft" lithographic methods, the use of liquefied materials prevails because, unlike elastic solids which are often constrained by restoring fores proportional to its relative displacement to the initial configuration, liquids do not resist deformation: a liquid parcel immediately accelerates under exerted driving forces and sometimes decelerates due to viscous forces sensitive to the rate at which it's being deformed (not deformation magnitude). Due to the fluidity of the target material, soft lithography in general is not necessarily additive or subtractive as the case with conventional techniques. Instead materials are spontaneously redistributed in accordance with the transport process enforced by externally imposed forces.

One distinguishing feature about lithographic systems operating at micro- and nanoscale is that, the volume-to-area ratio scales down drastically with the characteristic size of the system. As a result, surface forces at liquid interface become dominant over or at least as important as volumetric forces in the bulk. Shaping of liquid masses becomes possible, sometimes even more effectively, with careful manipulation of interfacial forces. A notable example is capillary stress induced by surface tension which is ubiquitous at any liquid/air interface. Liquid shapes are regularized by capillary stresses acting

in the direction normal to the interface with a magnitude proportional to the local mean curvature (Plateau, 1873). Mechanically speaking, whenever the shape of a liquid undergoes infinitesimal deformations, capillary stresses always act to penalize excessive surface energy, which is proportional to the total area of the interface. Hence, droplets and bubbles of spherical or near-spherical shapes are the most ubiquitous geometric configurations of a liquid mass in nature.

However, the stabilizing effect of capillarity against small-scale geometric variations also becomes an obstacle in developing sharp features at a liquid interface below a certain characteristic capillary length scale for micro- and nanosize systems (recall curvature scales as inverse of characteristic length). In order to achieve diverse patterns with liquefied materials, aside side from capillarity researchers have uncovered a zoo of physical mechanisms that can generate significant surface forces at the interface between two phases. Many of these ongoing developments in this thriving area of fluid mechanics and related applications are highlighted in the comprehensive reviews (Oron, S. H. Davis, and Bankoff, 1997; Craster and Matar, 2009). It is worth noting that because virtually all materials respond to electric and thermal fields to some degree and the interactions with these fields are often non-contact, Maxwell forces induced by electric field (Chou and Zhuang, 1999; Schäffer et al., 2001) and thermocapillary forces by thermal field (Dietzel and Troian, 2009b; McLeod, Y. Liu, and Troian, 2011) have shown promising results and potential. It is the subject of this dissertation that, illustrated through five hydrodynamic problems concerning controlled deformation of liquid, electrically and thermally induced interfacial forces, if deliberately engineered, can be used to oppose or collaborate with the repressive capillary stresses and eventually lead to formation of non-spherical liquid shapes.

Aside from practical application in lithography, another underlying theme of this thesis is the theoretical and computational treatment of geometric nonlinearity in hydrodynamics. Nonlinearity, being the most prominent character of the conservation laws underlying fluid mechanics, is not a new concept. For inertia-dominant phenomena of fluids at large scales, the source of nonlinearity is commonly attributed to the convective acceleration. The most well known example is turbulent flow for which kinetic energy cascades into a spectrum of velocity fluctuations due to the nonlinear processes of energy transfer between small- and large-scale flow structures (Kolmogorov, 1991). Another example is the nonlinearity in the thermodynamic equation of state which plays a central role in the formation of shock waves in a compressible fluid medium due to the nonlinear steepening of ordinary acoustic waves (White, 2006). There is also the material nonlinearity in the stress-strain-rate relation of non-Newtonian fluids (Bird, 1976) which exhibit curious rheological behaviors such as shear thinning/thickening and plastic-like responses to applied forces.

That being said, a common "misconception" about the behavior of fluids at smaller length scales is that the dynamics must be almost linear since the governing equation—Stokes equation—is a linearized version of the incompressible Navier-Stokes equation in the limit of vanishing Reynolds number. However benefits of such linearity expire when the interface and domain that define a liquid body continuously undergo large deformations. This type of nonlinearity stems from the fact that, a liquid reacts to the current deformation rate rather than its displacement to the initial configuration. The resulting kinematics is globally nonlinear in the current geometric quantities (domain, boundary, coordinates, etc.) of the evolving liquid volume, regardless of the magnitude of the Reynolds number. In such cases, a different source of nonlinearity, namely the geometric nonlinearity, arises even though the incremental dynamics may be perfectly linear. For this reason, the methodology to achieve precision control of liquid shapes is not straightforward and sometimes can be counter-intuitive. For the systems examined in this thesis, a suitable language describing the evolving geometry of liquid bodies is developed to provide analytic insight into the nonlinear aspect of the problem before resorting to direct numerical simulation.

1.1 Contributions of this thesis

This thesis is divided into two parts, namely Chapter 2, 3, 4, and Chapter 5, 6, 7, and the principal contributions of this thesis are summarized as follows. The first half deals with interfacial flows in a special limit so-called the "lubrication" regime where the streamwise dimension of the liquid volume is much longer than the transverse dimensions. The potential energy of the liquid body (or a liquid film to be more precise) is completely lost to the internal viscous dissipation due to the rate of shear deformation against the supporting substrate, and therefore not transferred into kinetic energy. In the lubrication limit, geometric noninearity of the thin viscous fluid is captured by the Reynolds equation of liquid film thickness (Reynolds, 1886).

In Chapter 2, we demonstrate, by analytic and numerical means, spontaneous formation of cuspidal cones in a thin liquid film exposed to large thermocapillary stresses, a shearing type of interfacial force due to the heterogeneous temperature distribution along the interface. On a fundamental level, this finding broadens our understanding of known categories of flows that can generate cuspidal forms. More practically, the mechanism discovered here introduces a potentially novel lithographic method for one-step non-contact fabrication of cuspidal microarrays.

In Chapter 3, a control protocol is devised for Electrohydrodynamic Lithography (EHL), a simple yet effective electrostatic technique which deforms slender dielectric liquid films on a flat substrate through interfacial Maxwell stresses projected by a structured electrode in close proximity. The control methodology developed in this chapter provides a computational cure to the current bottleneck of EHL, the fidelity of film pattern repli-

cated from electrode topography. The optimal design of electrode topography generated by our algorithm, illustrated through finite element simulations, is capable of guiding dielectric liquid films into complex three-dimensional structures such as the nearly uniform leveling of a heart-like pattern.

In Chapter 4, we generalize the classical lubrication theory originally derived for lubrication flows on a flat plane to flows on curved substrates. Unlike previous approaches which rely on asymptotic expansions of the Stokes equation, our formulation is established upon the Helmholtz minimum dissipation theorem in the lubrication regime, which naturally conforms to the energy-dissipation law of fluidic systems. In particular, we develop a novel nonlocal model in the form of a tensorial partial differential equation describing the evolution of the local volume density of a thin dielectric liquid coating an arbitrarily curved conductor in the presence of an external electrode, accompanied by the usual capillary and gravitational forces.

The second half of this thesis revisits the minimal mechanical model of a perfectly conductive liquid body, first studied by Rayleigh (1882), for which only electrostatic energy stored in the surrounding vacuum and surface energy of the liquid/vacuum interface are considered. The focus here is on the strong interface distortion due to the nonlinear interplay between capillary and Maxwell stresses as well as inertia forces if dynamics is involved. We show that the classical problem of an electrified liquid, when equipped with modern mathematical tools, yields some interesting surprises.

In Chapter 5, we systematically derive the first and second shape variations for the total potential energy (i.e. electrostatic plus surface energy) of an arbitrarily shaped conductive liquid body subject to exact mass conservation. The second order stability criterion is identified for any liquid shapes that satisfy the first order equilibrium condition. Our work is fundamentally different than previous approaches in the sense that the convective Lagrangian methodology developed here is neither restricted to a specific geometry nor limited to normal-only deformations. Several contributions to the energy stability, previously obscured by the assumption of a spherical geometry, are uncovered for equilibrium shapes with nonuniform surface charge distribution or mean curvature. We expect this result to shed light on the existence and stability of the hydrostatic Taylor cone, a conic equilibrium shape on which capillary and Maxwell stresses are everywhere equal and opposite (except at the conic vertex).

In Chapter 6, the apical behavior of an ideal, perfectly conductive incompressible fluid surrounded by vacuum is examined under circumstances where the capillary, Maxwell and inertial forces contribute to dynamical formation of a liquid cone. A previous inviscid model (Zubarev, 2001) showed that dynamic formation of a conic cusp in a perfectly conductive liquid evolves by a dynamic self-similar process. At the time, Zubarev didn't provide actual solutions to the model and the fluid motion near a self-sharpening apex

predicted by his asymptotic analysis orients parallel to the moving surface. By carefully matching asymptotic velocity and electric potential to the far-field conditions dictated by a stationary Taylor cone, our theoretical analysis, supported by accurate numerical solutions to an equivalent reformulation of the self-similar dynamics as coupled boundary integral equations, reveals a two-parameter family of non-spherically symmetric, self-similar solutions whose streamlines intercept the conic surface at an angle. These solutions also unmask the existence of field-driven advancing and recoiling interface dynamics for the first time. Our finding expands the understanding of cusp formation and introduces a new twist to many existing theories based on Taylor's static cone.

In Chapter 7, we expound on some technical details concerning the discretization of boundary integrals and numerical approximations to the integral equations. The iterative procedure for solving the exact similarity solutions on a semi-infinite domain is outlined in depth.

Chapter 2

CUSPIDAL FORMATION IN THERMOCAPILLARY THIN LIQUID FILMS

Note: Significant content of this chapter is taken from the work of C. Zhou and Troian (2019).

2.1 Cusp Formation in Physical Systems

Despite that capillary forces always act to repress regions of high curvature, nature nonetheless finds clever ways of forming and sustaining cusps in many physical systems. In fact, cusps are rather ubiquitous and occur in such diverse phenomena as thermal grooving at grain boundaries (Mullins, 1957), surface diffusion and pinchoff in annealed or sintered systems (Bernoff, Bertozzi, and Witelski, 1998), complex plasma formations (Schwabe et al., 2009), wavefront propagation in systems described by the linear (Z.-H. Yang, Maitra, and Burke, 2012) or nonlinear Schrödinger equation (Amiranashvili, Bandelow, and Akhmediev, 2011), critically charged droplets (Burton and Taborek, 2011), microbranching instabilities in fast moving cracks (Kolvin, G. Cohen, and Fineberg, 2015), line attractor states in neural computation models (Xiao et al., 2017), evaporative dryout in liquid films (Burelbach, Bankoff, and S. H. Davis, 1988) and many more. A recent delightful book by Eggers and Fontelos (2015) describes as well the complex dynamics governing cusp formation in many liquid systems including thread and droplet breakup, Hele-Shaw sink flow and thin film rupture caused by a negative disjoining pressure (Bernoff, Bertozzi, and Witelski, 1998; Zhang and Lister, 1999; Thete et al., 2015). The latter system sketched in figure 2.1(a) and (b) shows that the receding air/liquid interface traces a cusp.

In these and other systems (Eggers, 1993; Eggers, 2001; Zhang, 2004; Blanchette and Zhang, 2009; Karpitschka et al., 2017), the apical region of the evolving cusp exhibits self-similar behavior characterized by universal exponents, some of which have been confirmed experimentally (Pont and Eggers, 2006; I. Cohen and Nagel, 2002; Peters et al., 2009; Marin et al., 2014; Villermaux and Almarcha, 2016). The resulting power laws stem from scaling symmetries that are invariant in time up to a change of scale. In almost all cases reported in the literature, however, the moving interface is assumed to be *shear-free* and the operable surface forces orient exclusively in the direction normal to the advancing boundary. The interface therefore experiences no shear force and therefore plays no active role in corralling fluid into a sharpened tip. Krechetnikov (2010) has recently conducted elegant analyses of chemically driven tip streaming emanating from conical singularities in self-driven Marangoni systems; however, those studies have had to assume steady state (i.e. time independent) flows since the dynamics of cusp formation

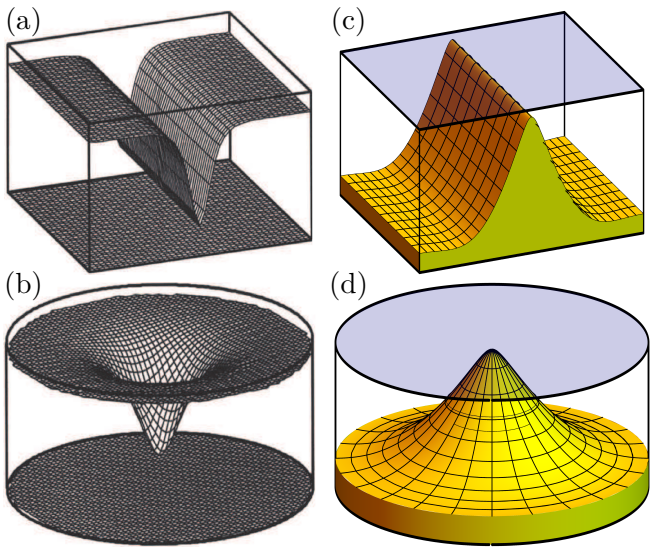

Figure 2.1: Liquid (a) line type and (b) point type cusp formation in a thin film subject to a negative disjoining pressure from van der Waals forces that promote dewetting of the film from the bottom substrate. Reprinted from Witelski and Bernoff (2000) with permission from Elsevier. Liquid (c) line type and (d) point type conical cusp formation caused by thermocapillary forces which draw fluid away from the lower warm substrate toward the top colder substrate, as described in the text.

there remains an unsolved problem (Krechetnikov, 2012; Krechetnikov, 2015).

To explore further the possibility of cuspidal formation driven by shear forces at a free interface, we here focus on nanoscale liquid films confined by a geometry designed to elicit self-reinforcing thermocapillary stresses at the air/liquid interface. We analyze the dynamics by which the ensuant self-similar process gives rise to fluid elongations resembling cuspidal shapes whose conical tips promote self-focusing. Shown in figure 2.1(c) and (d) are examples of thermocapillary driven line and point cuspidal formations caused by runaway thermocapillary forces. While figures 2.1(a) and (b) depict cusp formation arising from forces exclusively oriented normal to the free interface (disjoining pressure counterbalanced by capillary pressure), figures 2.1(c) and (d) depict formation of cuspidial shapes from thermocapillary (shear) forces which orient parallel to the moving interface. An additional challenging feature of the thermocapillary problem is that the apical region exhibits multiscale dynamics which considerably complicates the stability analysis.

Aside from such fundamental considerations, there is a practical motivation for this study as well. We are interested in exploring thermocapillary based techniques for patterning nanoscale films which can be rapidly solidified in situ. The system geometry examined in this work offers a potentially novel lithographic method for one-step non-contact fabrication of cuspidal microarrays. This development can facilitate design and man-

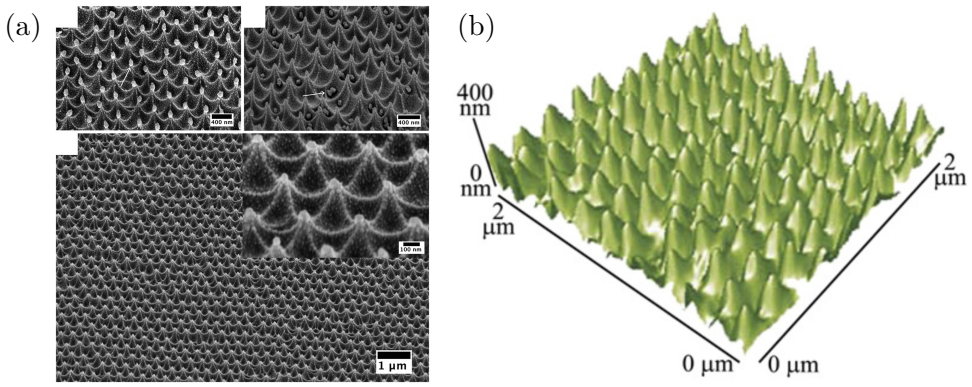

Figure 2.2: Cuspidal arrays: (a) SEM micrograph of plasma etched substrate for super antireflective coatings, adapted from Nowlin and LaJeunesse (2017) with permission from the Royal Society of Chemistry, and (b) AFM image of cicada wing, reprinted from Wisdom et al. (2013) with permission from PNAS.

ufacture of specialty microarrays such as biomimetic cuspidal substrates. Two recent important examples of such desirable substrates include infrared (IR) antireflective moth eye surfaces patterned with quintic cusps for eliminating Fresnel reflections in the mid-IR (Southwell, 1991; Weiblen et al., 2016; Nowlin and LaJeunesse, 2017) as in figure 2.2(a) and superhydrophobic, self-cleaning antimicrobial surfaces mimicking the surface of a cicada wing (Wisdom et al., 2013) as in figure 2.2(b). Such substrates can likely be architected using thermocapillary forces to pattern thin films in which form follows function, i.e. imprinted cuspidal shapes relating directly to their intended function.

Our group has previously demonstrated experimentally how large patterned thermocapillary forces can be used to sculpt nanofilms into liquid microlens arrays, which are then solidified rapidly in situ (McLeod, Y. Liu, and Troian, 2011). The resulting ultrasmooth surfaces are ideally suited to micro-optical applications such as beam shaping. The analysis presented in this work suggests that if the microlens configurations are allowed to evolve further in time before solidification is imposed, the system will transition to a microcuspidal array. The local analysis presented in this work indicates how initial protrusions of any sort, whether triggered by the linear instability (Dietzel and Troian, 2009b; Dietzel and Troian, 2010) or triggered by large amplitude perturbations (Dietzel and Troian, 2009a; McLeod and Troian, 2011), are expected to evolve into individual or array-like cuspidal patterns.

The outline of this chapter is as follows. In Section 2.2 we sketch the derivation of the fourth-order nonlinear diffusion equation which governs the evolution of the liquid film interface driven by interfacial traction forces in general. In Section 2.3 we present the evolution equation for an ultrathin Newtonian liquid layer subject to very large thermocapillary forces induced by thermal conduction across a slender quiescent gas

film. Nominal estimates (Dietzel and Troian, 2010) extracted from experiment for the spanwise temperature gradient across the gas/liquid bilayer reveal values in the range $10^5 - 10^8$ °C/cm. This slender geometry is known to give rise to an initial linear instability (Dietzel and Troian, 2009b; Dietzel and Troian, 2010) which generates spontaneous periodic arrays of slender domes. The array pitch, given by the wavelength characterizing the fastest growing mode is subsequently used to rescale the original equation. Further rescaling to parameter-free dimensionless form yields an equation belonging to the general class of gradient flows. In Section 2.4, it is shown that this evolution equation does not support stable stationary states because the dynamics incurred by the confined geometry involve *runaway* thermocapillary forces whereby the nanofilm can reduce its free energy by advancing ever closer to the top colder substrate. In Section 2.5, 2D and 3D numerical solutions of the nonlinear interface equation reveal formation of a stable cuspidal shape which terminates in a cone with a rounded tip that undergoes continuous sharpening. The numerical simulations reveal the self-similar process underlying the power law growth behavior characterizing the tip speed and tip curvature. In Section 2.6 we present an asymptotic analysis of the conical region which reveals the presence of a stable fundamental mode acting as an attractor state. Various measures characterizing this fundamental mode are shown to be in excellent quantitative agreement with the numerical simulations. The asymptotic analysis also provides an analytic relation for the slope of the conical tip which should prove useful in designing arrays with specific tip textures. In Section 2.7, we conclude with some final thoughts on how these findings may help advance a novel lithographic method for fabrication of specialty cuspidal microarrays.

2.2 Thin Film Equation on a Flat Substrate

In this section we briefly review the standard derivation of the classical lubrication approximation to an incompressible Newtonian fluid of constant density and viscosity bounded by a surface that's free to move and deform. Lubrication theory applies when the evolution of the thickness of a slender liquid layer is of greater interest than the velocity or pressure field within the bulk of fluid. The foundations of the theoretical treatment of lubrication flows have been well established since the pioneering work of Reynolds (1886) on the hydrodynamic lubrication of journal bearing. Assuming that the viscosity is constant and using the slenderness of the liquid film as a small parameter, an asymptotic approximation in the limit of vanishing slenderness, namely the well-known Reynolds equation expressed solely in terms of the film height, can be derived for the evolution of the film thickness in place of the governing Navier-Stokes equation coupled to a moving free surface which is analytically intractable.

As the use of lubrication approximation for the fluid mechanics of thin liquid films becomes pervasive in the field of physics, engineering and mathematics, there have been

many excellent review articles on the derivation, modeling and analysis of thin liquid films. The standard procedure of deriving the thin film equation on a flat substrate, which we closely follow in this thesis to obtain the thermocapillary and electrohydrodynamic lubrication models in Chapter 2 and 3, is largely based on the comprehensive survey by Oron, S. H. Davis, and Bankoff (1997), in which the modeling of various physical situations are discussed in great details. An overview of the mathematical results and techniques on the resultant lubrication equations describing surface-tension-driven thin film flows subject to a number of physical processes can be found in the review article by Myers (1998). Rigorous mathematical and numerical details of moving contact line and undercompressive shock formation in the context of thin liquid film are examined the lecture series published by Bertozzi and Bowen, 2002. The introductory article by O'Brien and L. Schwartz (2002) demonstrates numerical simulations of a collection of thin film models from a more practical perspective oriented towards industrial applications. For fluid flowing down an inclined plane, the pedagogical paper by Kondic (2003) presents theoretical, computational and experimental aspects of the instability development in the gravity driven flow of thin fluid films. The (relatively) recent review by Craster and Matar (2009) on the dynamics and stability of thin liquid films structures the discussion into how the liquid films are driven by external forcing, thermal effects and inter-molecular forces. The article highlights the most prominent developments and technological advances in the area of thin film flows since the work of Oron, S. H. Davis, and Bankoff (1997) in the 90s. Aside from deterministic hydrodynamic equations, analytic and numerical studies of stochastic thin-film equations derived from first principles, which play a crucial role in thermally activated process such as film rupture and droplet formation during dewetting, are expounded in the pioneer work of Grün, Mecke, and Rauscher (2006) for uncorrelated thermal noise and in a follow-up article (Durán-Olivencia et al., 2019) for perfectly correlated noise.

Continuum equations of fluids

The standard derivation of the lubrication equation begins with the Navier-Stokes equation of incompressible fluids. Here the basic formulation of fluid mechanics follows the presentation in the widely used textbook (Leal, 2007) on transport phenomena. The dimensional Navier-Stokes equation describes the motion of viscous fluid in the convective form

$$\left.\begin{aligned} \rho\frac{\mathrm{D}\boldsymbol{u}}{\mathrm{D}t} &= -\nabla p + \mu\nabla^2\boldsymbol{u}, \\ 0 &= \nabla\cdot\boldsymbol{u}, \end{aligned}\right\} \text{(Navier-Stokes equation)} \tag{2.1}$$

where ρ is the density of the fluid , μ is the dynamic viscosity, $\boldsymbol{u} = [u, v, w]^\top$ is the velocity field defined in the three-dimensional Euclidean space and $\mathrm{D}/\mathrm{D}t = \partial/\partial t + \boldsymbol{u}\cdot\nabla$ is the material derivative. The total pressure field

$$p = p_{\mathrm{liq}} + \rho g z \tag{2.2}$$

is the sum of the true liquid pressure p_{liq} and the hydrostatic pressure (g is the gravitation acceleration). The Navier-Stokes equation (2.1) is known to be a particular form of the Cauchy momentum equation (Leal, 2007). Under the incompressible condition, the equivalent convective form of the Cauchy momentum equation is given by

$$\left.\begin{aligned} \rho\frac{\mathrm{D}\boldsymbol{u}}{\mathrm{D}t} &= \nabla\cdot\boldsymbol{\sigma}, \\ 0 &= \nabla\cdot\boldsymbol{u}, \end{aligned}\right\} \text{(Cauchy momentum equation)} \tag{2.3}$$

where the linear constitutive equation of the stress tensor

$$\boldsymbol{\sigma} = -p\mathbb{I} + 2\mu\boldsymbol{e} \tag{2.4}$$

subject to incompressibility can be decomposed into an isotropic pressure ($\mathbb{I}$ is the identity tensor), also known as the confining stress, and a viscous stress proportional to the strain rate tensor $2\boldsymbol{e} = \nabla\boldsymbol{u} + \nabla\boldsymbol{u}^{\top}$ with tensor components given by

$$2e_{ij} = \begin{bmatrix} 2\partial u/\partial x & \partial u/\partial y + \partial v/\partial x & \partial u/\partial z + \partial w/\partial x \\ \partial v/\partial x + \partial u/\partial y & 2\partial v/\partial y & \partial v/\partial z + \partial w/\partial y \\ \partial w/\partial x + \partial u/\partial z & \partial w/\partial y + \partial v/\partial z & 2\partial w/\partial z \end{bmatrix}. \tag{2.5}$$

In this chapter we will not be dealing with the Cauchy momentum equation (2.3) directly since the Navier-Stokes equation (2.1) has proven to be more useful for modeling lubrication flow on a flat substrate. However, at an interface γ where a liquid meeting another fluid (e.g., air), integrating the Cauchy momentum equation (2.3) over an infinitesimally thin Gaussian pillbox enclosing the surface γ yields the stress balance equation

$$(\boldsymbol{\sigma}_{\text{air}} - \boldsymbol{\sigma}_{\text{liq}})\boldsymbol{n} + \boldsymbol{f} = \boldsymbol{0} \quad \text{on} \quad \gamma, \tag{2.6}$$

where $\boldsymbol{n}$ is the unit normal pointing toward the air and $\boldsymbol{f}$ is the surface traction attached to the liquid/air interface. In fluid mechanics, stress balance equation (2.6) serves as a boundary condition for interfacial flows, complementing the Navier–Stokes equations.

Traction forces $\boldsymbol{f}$ acting on a capillary surface usually have two components,

$$\boldsymbol{f} = -\sigma(\nabla_s\cdot\boldsymbol{n})\boldsymbol{n} + \nabla_s\sigma \quad \text{on} \quad \gamma. \tag{2.7}$$

Here ∇_s is the surface gradient (behaves like a vector with contravariant components) along the curved interface γ. The first term on the right hand side of traction equation (2.7) is called the capillary stress with σ being the surface tension coefficient at a liquid/air interface, which is also commonly referred to as the Young-Laplace pressure since it acts exclusively normal to the interface. Microscopically speaking, capillary stress arises from the stronger cohesion bonding between liquid molecules than the adhesion attraction between liquid and air molecules. In continuum limit, the effect of capillary stress is captured by the quantity $-\nabla_s\cdot\boldsymbol{n}$, which is twice the mean curvature $\hbar$ of the

surface. The second term $\nabla_s \sigma$, known as the Marangoni stress, accounts for the presence of interfacial shear tractions due to the variation of surface tension coefficient with respect to a distribution of additional interfacial quantities. There are three common interfacial phenomena attributed to the Marangoni stress, the electrocapillary convection due to surface excess charge density (Choo and Toguri, 1992; J. Lee and Kim, 2000; L. Wang and J. Liu, 2016), the surfactant spreading caused by the significant change in surface tension due to contamination of specific immiscible solutes (Gennes, 1985; O. E. Jensen and Grotberg, 1993; Wit, Gallez, and Christov, 1994; Matar and Troian, 1999; Warner, Craster, and Matar, 2004) and thermocapillary motion driven by the thermal fluctuation of interfacial tension (Williams and S. H. Davis, 1982; Burelbach, Bankoff, and S. H. Davis, 1988; Oron and Rosenau, 1994; Vanhook et al., 1997; Bestehorn, Pototsky, and Thiele, 2003).

When the interface of a fluid body is a material surface, it does not allow flow through it. Let $\boldsymbol{x}_\gamma$ be a material point attached to the fluid interface γ. Then the difference of the velocity at which $\boldsymbol{x}_\gamma$ moves and velocity field $\boldsymbol{u}$ evaluated at fluid interface in the direction normal to the surface should be zero. This observation translates into the kinematic boundary condition which states

$$\boldsymbol{n} \cdot \frac{\mathrm{d}\boldsymbol{x}_\gamma}{\mathrm{d}t} = \boldsymbol{n} \cdot \boldsymbol{u} \quad \text{on} \quad \gamma. \tag{2.8}$$

An alternative way to specify a fluid interface is to invoke a level function $l(x, y, z, t)$ for which the zero set

$$\gamma = \{(x, y, z) \mid l(x, y, z, t) = 0\} \tag{2.9}$$

coincides with the fluid interface. Then kinematic boundary condition (2.8) can be alternatively expressed as the statement that the zero set of the level function $l(x, y, z, 0)$ stays as the zero set of $l(x, y, z, t)$ at all times, which is equivalent to

$$\frac{\mathrm{D}l}{\mathrm{D}t} = 0 \quad \text{on} \quad \gamma. \tag{2.10}$$

A fluid interface which is both free to move and free of traction forces, therefore satisfying kinematic boundary condition (2.8) and stress balance condition (2.6), is called a free surface.

Classical lubrication theory

Lubrication theory applies when the evolution of the thickness of a slender liquid layer is of greater interest than the actual velocity or pressure field within the bulk of fluid. In the limit of vanishing slenderness, lubrication approximations allow us to replace the governing Navier-Stokes and the free surface conditions of a thin liquid film deposited on a flat substrate with a time-dependent partial differential equation expressed solely in terms of the film height. Following the development of classical lubrication theory

outlined in the comprehensive review article (Oron, S. H. Davis, and Bankoff, 1997), we start the derivation by first non-dimensionalizing the governing fluid equations (2.1) using $[L]$ for the lateral length scale in x- and y-coordinates, $[H]$ for the vertical length scale in z, $[T]$ for the time scale, $[U] = [L]/[T]$ and $[W] = [H]/[T]$ for the in-plane and out-of-plane reference velocities and $[P]$ for reference pressure. The first assumption of the theory is the slender (or long-wavelength) limit, which is equivalent to assume a small vertical-to-lateral aspect ratio ϵ defined as

$$\epsilon = \frac{[H]}{[L]} = \frac{[W]}{[U]} \ll 1. \quad \text{(assumption I)} \tag{2.11}$$

The mass and momentum conservation laws within the thin liquid film described by the Navier-Stokes equation (2.1) are recast into the dimensionless form

$$\left.\begin{aligned}
\mathrm{Re}\frac{\mathrm{D}U}{\mathrm{D}\tau} &= -\frac{[P][L]}{[U]\mu}\frac{\partial P}{\partial X} + \frac{\partial^2 U}{\partial X^2} + \frac{\partial^2 U}{\partial Y^2} + \frac{1}{\epsilon^2}\frac{\partial^2 U}{\partial Z^2}, \\
\mathrm{Re}\frac{\mathrm{D}V}{\mathrm{D}\tau} &= -\frac{[P][L]}{[U]\mu}\frac{\partial P}{\partial Y} + \frac{\partial^2 V}{\partial X^2} + \frac{\partial^2 V}{\partial Y^2} + \frac{1}{\epsilon^2}\frac{\partial^2 V}{\partial Z^2}, \\
\epsilon\mathrm{Re}\frac{\mathrm{D}W}{\mathrm{D}\tau} &= -\frac{[P][L]}{[U]\mu}\frac{1}{\epsilon}\frac{\partial P}{\partial Z} + \epsilon\frac{\partial^2 W}{\partial X^2} + \epsilon\frac{\partial^2 W}{\partial Y^2} + \frac{1}{\epsilon}\frac{\partial^2 W}{\partial Z^2}, \\
0 &= \frac{\partial U}{\partial X} + \frac{\partial V}{\partial Y} + \frac{\partial W}{\partial Z},
\end{aligned}\right\} \quad \text{in} \quad \Omega_{\mathrm{liq}} \tag{2.12}$$

where the Reynolds number is defined as

$$\mathrm{Re} = \frac{\rho[U][L]}{\mu} \tag{2.13}$$

and the dimensionless total pressure field

$$P = P_{\mathrm{liq}} + \frac{\rho g[L]}{[P]}\epsilon Z \tag{2.14}$$

with the non-dimensional liquid pressure P_{liq}. The key idea behind the slender approximation (2.11) is that, the terms modified by the inverse powers of ϵ in the non-dimensional Navier-Stokes equation (2.12) are significantly amplified as $\epsilon \to 0$ so that these leading order terms alone could mostly determine the behavior of the fluid in this asymptotic limit. Note the incompressibility condition (i.e. mass conservation) is not compromised in the slender limit.

The second assumption of the lubrication theory is the scaling balance between pressure and viscous forces:

$$\frac{[P][L]}{[U]\mu} = \frac{1}{\epsilon^2}. \quad \text{(assumption II)} \tag{2.15}$$

Enforcing scaling (2.15) is equivalent to choosing the slow time scale $[T] = \epsilon^{-2}\mu/[P]$. This a common feature shared by all lubrication systems: the lubrication flows operate

on a much slower time scale as the overall geometry becomes slenderer and slenderer. With lubrication scaling (2.11) and (2.15), the momentum equations in (2.12) can be rearranged into

$$\left.\begin{aligned}
\epsilon^2 \mathrm{Re}\frac{\mathrm{D}U}{\mathrm{D}\tau} &= \epsilon^2\frac{\partial^2 U}{\partial X^2} + \epsilon^2\frac{\partial^2 U}{\partial Y^2} - \frac{\partial P}{\partial X} + \frac{\partial^2 U}{\partial Z^2},\\
\epsilon^2 \mathrm{Re}\frac{\mathrm{D}V}{\mathrm{D}\tau} &= \epsilon^2\frac{\partial^2 V}{\partial X^2} + \epsilon^2\frac{\partial^2 V}{\partial Y^2} - \frac{\partial P}{\partial Y} + \frac{\partial^2 V}{\partial Z^2},\\
\epsilon^3 \mathrm{Re}\frac{\mathrm{D}W}{\mathrm{D}\tau} &= \epsilon^4\frac{\partial^2 W}{\partial X^2} + \epsilon^4\frac{\partial^2 W}{\partial Y^2} + \epsilon^2\frac{\partial^2 W}{\partial Z^2}. - \frac{\partial P}{\partial Z}.
\end{aligned}\right\} \tag{2.16}$$

If all the higher order terms proportional to or higher than ϵ^2 in the momentum equations (2.16) were truncated, we would then arrive at the classical lubrication equation first derived by Reynolds (1886). In order to do so, we would need the third assumption:

$$\mathrm{Re} = O(1). \quad \text{(assumption III)} \tag{2.17}$$

For flows in many micro/nanoscale systems (Oron, S. H. Davis, and Bankoff, 1997; Craster and Matar, 2009), assumption (2.17) can be easily satisfied due to the presence of length and velocity scales in Re. Under the assumption of vanishing Reynolds number, we arrive at the Reynolds lubrication equation in the bulk of the thin liquid film,

$$\left.\begin{aligned}
-\frac{\partial P}{\partial X} + \frac{\partial^2 U}{\partial Z^2} &= 0,\\
-\frac{\partial P}{\partial Y} + \frac{\partial^2 V}{\partial Z^2} &= 0,\\
-\frac{\partial P}{\partial Z} &= 0.
\end{aligned}\right\} \quad \text{in} \quad \Omega_{\mathrm{liq}} \tag{2.18}$$

It is worthwhile to mention that, in the opposite regime where Reynolds number is large (e.g., $\mathrm{Re} \sim \epsilon^{-2} \gg 1$), we recover Prandtl's boundary layer equations at the leading order.

The liquid volume Ω_{liq} occupied by the thin film is bounded between the flat support substrate at $Z = 0$ and the evolving interface described by a height field function $H(X, Y, \tau)$,

$$\Omega_{\mathrm{liq}} = \{(X, Y, Z) \mid 0 \le Z \le H(X, Y, \tau)\}. \tag{2.19}$$

Kinematic boundary condition of a free surface

$$\frac{\mathrm{D}}{\mathrm{D}\tau}\Big|_{Z=H}[Z - H(X, Y, \tau)] = 0 \tag{2.20}$$

states that fluid particles on the free surface always remain part of the free surface. For surfaces specified by a height field $Z = H(X, Y, \tau)$, kinematic boundary condition (2.20) becomes

$$\frac{\partial H}{\partial \tau} + \frac{\partial H}{\partial X}U(X, Y, H) + \frac{\partial H}{\partial Y}V(X, Y, H) = W(X, Y, H). \tag{2.21}$$

Equation (2.21) can be further simplified if we derive the following identity by integrating incompressibility condition in (2.12) along the out-of-plane Z-direction,

$$\begin{aligned} 0 &= \int_0^H \frac{\partial U}{\partial X} + \frac{\partial V}{\partial Y} + \frac{\partial W}{\partial Z}\,\mathrm{d}Z = \int_0^H \frac{\partial U}{\partial X} + \frac{\partial V}{\partial Y}\,\mathrm{d}Z + W\Big|_0^H \\ &= \frac{\partial}{\partial X}\int_0^H U\,\mathrm{d}Z - \frac{\partial H}{\partial X}U(X,Y,H) \\ &+ \frac{\partial}{\partial Y}\int_0^H V\,\mathrm{d}Z - \frac{\partial H}{\partial Y}V(X,Y,H) + W(X,Y,H), \end{aligned} \tag{2.22}$$

where in the last equality Leibniz integral rule is used to move in-plane differentiations out of the integral. If we further introduce the in-plane velocity field $\boldsymbol{U}_\parallel$ and the volumetric flux $\boldsymbol{Q}$ as

$$\boldsymbol{U}_\parallel = \begin{bmatrix} U \\ V \\ 0 \end{bmatrix}, \quad \boldsymbol{Q}(X,Y,\tau) = \int_0^H \boldsymbol{U}_\parallel\,\mathrm{d}Z, \tag{2.23}$$

and apply identity (2.22) to the free surface condition (2.21), then the evolution of film thickness $H(X,Y,\tau)$ can be written as a continuity equation

$$\frac{\partial H}{\partial \tau} + \nabla_\parallel \cdot \boldsymbol{Q} = 0, \tag{2.24}$$

where $\nabla_\parallel = (\partial/\partial X, \partial/\partial Y)$ is the in-plane differential operator with the usual rules of gradient $\nabla_\parallel$, divergence $\nabla_\parallel\cdot$ and Laplacian $\nabla_\parallel^2$. From (2.23) we see that volumetric flux $\boldsymbol{Q}(X,Y)$ is fully determined by integrating out the Z-dependence in the in-plane velocity field $\boldsymbol{U}_\parallel$. In other words, in the lubrication limit mass conservation due to incompressibility is integrated to an in-plane conservative form instead of satisfied pointwisely in the three-dimensional fluid volume.

The solution to the velocity components U, V and W (hence $\boldsymbol{U}_\parallel$) can be found by solving the Reynolds lubrication equation (2.18) subject to appropriate boundary conditions, for instance, the no-slip condition between the liquid and the support substrate,

$$U = V = 0 \quad \text{at} \quad Z = 0, \tag{2.25}$$

which is appropriate for continuous films considered throughout the thesis. At the free surface $Z = H(X,Y,T)$, the stress-free condition at air-liquid interface states that, any surface traction $\boldsymbol{F}$ would result in a jump in the total stresses acting on the interface from both sides of the dividing interface,

$$(\boldsymbol{\Sigma}_{\text{air}} - \boldsymbol{\Sigma}_{\text{liq}})\boldsymbol{N} + \boldsymbol{F} = \boldsymbol{0} \quad \text{at} \quad Z = H, \tag{2.26}$$

where $\boldsymbol{N}$ is the unit normal vector pointing from liquid into air. The dimensionless stress tensor $\boldsymbol{\Sigma}$ of an isotropic Newtonian fluid under the lubrication scaling (2.15) takes the form,

$$\boldsymbol{\Sigma} = -P\mathbb{I} + 2\epsilon^2\boldsymbol{E}. \tag{2.27}$$

In order to identify various stress components at the liquid/air interface, it is convenient to set up a local coordinate system adapted to the interface. In addition to the normal vector $\boldsymbol{N}$, we introduce two unit tangent vectors, designated as $\boldsymbol{S}_{\alpha=1,2}$, such that the interfacial traction $\boldsymbol{F}$ can be decomposed into its normal and tangent components,

$$\boldsymbol{F} = \boldsymbol{F}_S + F_N \boldsymbol{N}, \quad \boldsymbol{F}_S = F_1 \boldsymbol{S}_1 + F_2 \boldsymbol{S}_2 \ . \tag{2.28}$$

We further assume air flow is almost inviscid, i.e. $O(\mu_{\text{air}}) \ll O(\mu_{\text{liq}})$, and hence drop the viscous stress contribution from air. Then the projection of stress balance (2.26) into local surface coordinates yields

$$\left.\begin{aligned} P_{\text{liq}} - \epsilon^2 \boldsymbol{N} \cdot (2\boldsymbol{E}) \boldsymbol{N} &= P_{\text{air}} - F_N, \\ \epsilon^2 \boldsymbol{S}_1 \cdot (2\boldsymbol{E}) \boldsymbol{N} &= F_1, \\ \epsilon^2 \boldsymbol{S}_2 \cdot (2\boldsymbol{E}) \boldsymbol{N} &= F_2. \end{aligned}\right\} \text{ at } Z = H \tag{2.29}$$

In the event when interface shape is specified by a height field (2.19), these surface unit vectors can be parametrized using the rescaled coordinates (X, Y, Z),

$$\left.\begin{aligned} \boldsymbol{N} &\propto \left(\nabla_{\parallel} + \frac{1}{\epsilon}\frac{\partial}{\partial Z}\right)\left[\epsilon Z - \epsilon H(X, Y, \tau)\right], \\ \boldsymbol{S}_1 &\propto \frac{\partial}{\partial X}\begin{bmatrix} X \\ Y \\ \epsilon H(X, Y, \tau) \end{bmatrix}, \\ \boldsymbol{S}_2 &\propto \frac{\partial}{\partial Y}\begin{bmatrix} X \\ Y \\ \epsilon H(X, Y, \tau) \end{bmatrix}. \end{aligned}\right\} \tag{2.30}$$

In the limit of small aspect ratio $\epsilon \ll 1$, we can expand the normalized expressions from (2.30) in orders of ϵ and obtain the leading order approximations to surface unit vectors $\boldsymbol{N}$ and $\boldsymbol{S}_\alpha$,

$$\left.\begin{aligned} \boldsymbol{N} &= \begin{bmatrix} 0 \\ 0 \\ 1 \end{bmatrix} - \epsilon \begin{bmatrix} \partial H/\partial X \\ \partial H/\partial Y \\ 0 \end{bmatrix} + O(\epsilon^2), \\ \boldsymbol{S}_1 &= \begin{bmatrix} 1 \\ 0 \\ 0 \end{bmatrix} + \epsilon \begin{bmatrix} 0 \\ 0 \\ \partial H/\partial X \end{bmatrix} + O(\epsilon^2), \\ \boldsymbol{S}_2 &= \begin{bmatrix} 0 \\ 1 \\ 0 \end{bmatrix} + \epsilon \begin{bmatrix} 0 \\ 0 \\ \partial H/\partial Y \end{bmatrix} + O(\epsilon^2). \end{aligned}\right\} \tag{2.31}$$

Similarly the strain rate tensor $2\boldsymbol{E} = \nabla \boldsymbol{U} + \nabla \boldsymbol{U}^\top$ is rescaled by powers of ϵ,

$$2\boldsymbol{E} = \begin{bmatrix} 2\partial U/\partial X & \partial U/\partial Y + \partial V/\partial X & \epsilon^{-1}\partial U/\partial Z + \epsilon \partial W/\partial X \\ \partial V/\partial X + \partial U/\partial Y & 2\partial V/\partial Y & \epsilon^{-1}\partial V/\partial Z + \epsilon \partial W/\partial Y \\ \epsilon \partial W/\partial X + \epsilon^{-1}\partial U/\partial Z & \epsilon \partial W/\partial Y + \epsilon^{-1}\partial V/\partial Z & 2\partial W/\partial Z \end{bmatrix}. \tag{2.32}$$

Substituting components of the strain rate tensor $\boldsymbol{E}$ from (2.32) and surface unit vectors $\boldsymbol{N}$ and $\boldsymbol{S}_\alpha$ from (2.31) into the stress balance (2.29) and collecting leading order terms produce three boundary conditions at the interface,

$$\left.\begin{aligned} P - \frac{\rho g[L]}{[P]}\epsilon Z + O(\epsilon^2) &= P_{\text{air}} - F_N, \\ \frac{\partial U}{\partial Z} + O(\epsilon^2) &= \frac{1}{\epsilon}F_1, \\ \frac{\partial V}{\partial Z} + O(\epsilon^2) &= \frac{1}{\epsilon}F_2. \end{aligned}\right\} \text{ at } Z = H \tag{2.33}$$

We see that the slender assumption (2.11) and pressure scaling (2.15) of the lubrication theory significantly simplify the stress balance equation at the interface. The solution to the Reynolds lubrication equation (2.18) is found to be polynomials in Z where the in-plane velocity field $\boldsymbol{U}_\parallel$, out-of-plane component W and pressure field P are given by

$$\left.\begin{aligned} \boldsymbol{U}_\parallel &= \Big(\frac{1}{2}Z^2 - HZ\Big)\nabla_\parallel P + Z\boldsymbol{F}_\parallel, \\ W &= \Big(\frac{1}{2}HZ^2 - \frac{1}{6}Z^3\Big)\nabla_\parallel^2 P + \frac{1}{2}Z(\nabla_\parallel P \cdot \nabla_\parallel H - \nabla_\parallel \cdot \boldsymbol{F}_\parallel), \\ P &= P_{\text{air}} - F_N(X, Y, H(X, Y, T)) + \frac{\rho g[L]}{[P]}\epsilon H, \end{aligned}\right\} \tag{2.34}$$

where

$$\overline{\boldsymbol{F}}_\parallel = \frac{1}{\epsilon}\begin{bmatrix} F_1(X, Y, H) \\ F_2(X, Y, H) \\ 0 \end{bmatrix} \tag{2.35}$$

is introduced as a rescaled in-plane approximation to the true tangential traction $\boldsymbol{F}_S$. Note the true tangential traction $\boldsymbol{F}_S$ is described by the surface unit vectors (2.28) and is different from the Cartesian definition of $\overline{\boldsymbol{F}}_\parallel$ in (2.35). We shall make this subtle point clear when dealing with a particular form of the tangential traction, for example, the thermocapillary stress.

Finally the volumetric flux $\boldsymbol{Q}$ is found by integrating (2.23) with the in-plane velocity profile $\boldsymbol{U}_\parallel$ substituted from (2.34),

$$\boldsymbol{Q} = -\frac{1}{3}H^3\nabla_\parallel P + \frac{1}{2}H^2\overline{\boldsymbol{F}}_\parallel. \tag{2.36}$$

Together with the conservation law (2.24) we derive the general form of the evolution equation for the thickness of a thin liquid film on a flat substrate,

$$\frac{\partial H}{\partial \tau} + \nabla_\parallel \cdot \left(-\frac{1}{3}H^3\nabla_\parallel P + \frac{1}{2}H^2\overline{\boldsymbol{F}}_\parallel\right) = 0. \tag{2.37}$$

The thin film equation (2.37) is mostly driven by two mechanisms: in-plane gradient of interfacial pressure P and tangential traction approximation $\overline{\boldsymbol{F}}_{\parallel}$. The nonlinear mobility coefficients, H^3 and H^2, convert interfacial pressure gradient and tangential traction into volumetric fluxes which now scale with the local film thickness $H(X, Y, \tau)$.

Capillary and Marangoni stresses in lubrication limit

Let σ be the surface tension coefficient between the liquid and air. The dimensionless surface traction $\boldsymbol{F}$ in the lubrication limit is rescaled as

$$\boldsymbol{F} = \frac{\epsilon^2}{[U]\mu}\left[\sigma(-\nabla_S \cdot \boldsymbol{N})\boldsymbol{N} + \nabla_S \sigma\right], \tag{2.38}$$

where ∇_S is the dimensionless surface gradient and the surface divergence of the unit normal vector is twice the dimensionless mean curvature $\mathscr{H}$ of a surface specified by the height field H,

$$-\nabla_S \cdot \boldsymbol{N} = 2\mathscr{H} = \nabla_{\parallel} \cdot \left(\frac{\epsilon \nabla_{\parallel} H}{\sqrt{1 + |\epsilon \nabla_{\parallel} H|^2}}\right). \tag{2.39}$$

We further assume surface tension coefficient $\sigma(c)$ is a function of some interfacial quantity c. Let σ_o be the reference surface tension coefficient evaluated at the reference interfacial quantity c_o. The functional form of $\sigma(c)$ is called the equation of state. In a simple model where variation of c is relatively weak, we approximate the equation of state by a linear relation,

$$\sigma(\Theta) = \begin{cases} \sigma_o + \Delta c\, \sigma_c\, \Theta & \text{if} \quad \mathrm{d}\sigma/\mathrm{d}c|_{c=c_0} > 0, \\ \sigma_o - \Delta c\, \sigma_c\, \Theta & \text{if} \quad \mathrm{d}\sigma/\mathrm{d}c|_{c=c_0} < 0, \end{cases} \tag{2.40}$$

where $\sigma_c = |\mathrm{d}\sigma/\mathrm{d}c|$ is the absolute magnitude of the local slope evaluated at $c = c_o$ and Θ is some dimensionless variable such that $\sigma(0) = \sigma_o$ and $\sigma(1) = \sigma_o \pm \Delta c \times \sigma_c$.

With capillary number $\overline{\mathrm{Ca}}$, Bond number Bo and Marangoni number $\overline{\mathrm{Ma}}$ defined as

$$\overline{\mathrm{Ca}} = \frac{\mu[U]}{\epsilon^3 \sigma_o}, \quad \mathrm{Bo} = \frac{\rho g [L]^2}{\sigma_o}, \quad \overline{\mathrm{Ma}} = \epsilon \frac{\sigma_c \Delta c}{\mu[U]} = \frac{1}{\overline{\mathrm{Ca}}} \frac{\sigma_c \Delta c}{\epsilon^2 \sigma_o}, \tag{2.41}$$

the pressure expression (2.34) becomes

$$P = P_{\mathrm{air}} - \left(\frac{1}{\overline{\mathrm{Ca}}} \pm \epsilon^2 \overline{\mathrm{Ma}}\right) \nabla_{\parallel} \cdot \left(\frac{\nabla_{\parallel} H}{\sqrt{1 + |\epsilon \nabla_{\parallel} H|^2}}\right) + \frac{\mathrm{Bo}}{\overline{\mathrm{Ca}}} H \tag{2.42}$$

and the dimensionless Marangoni stress in (2.38) is proportional to the surface gradient of the interfacial quantity $\Theta(X, Y, H)$,

$$\boldsymbol{F}_S = \begin{cases} +\epsilon \overline{\mathrm{Ma}}\, \nabla_S \Theta & \text{if} \quad \mathrm{d}\sigma/\mathrm{d}c|_{c=c_o} > 0, \\ -\epsilon \overline{\mathrm{Ma}}\, \nabla_S \Theta & \text{if} \quad \mathrm{d}\sigma/\mathrm{d}c|_{c=c_o} < 0, \end{cases} \tag{2.43}$$

where the surface gradient $\nabla_S \Theta$ can be parametrized with the in-plane coordinates (X, Y) using the height field specification (2.19),

$$\nabla_S \Theta = \frac{\boldsymbol{S}_1}{\sqrt{1+(\epsilon \partial H/\partial X)^2}} \frac{\partial \Theta}{\partial X} + \frac{\boldsymbol{S}_2}{\sqrt{1+(\epsilon \partial H/\partial Y)^2}} \frac{\partial \Theta}{\partial Y}. \tag{2.44}$$

The dimensionless numbers $\overline{\mathrm{Ca}}$ and $\overline{\mathrm{Ma}}$ differ from the standard definitions by factors of the small aspect ratio parameter ϵ. This is one of the distinct features of the lubrication theory: interfacial forces scale differently in the slender limit.

Assuming $\overline{\mathrm{Ca}}$ and $\overline{\mathrm{Ma}}$ are both $O(1)$, the leading order slender approximation to the pressure expression (2.42) is given by

$$P = P_{\mathrm{air}} - \frac{1}{\overline{\mathrm{Ca}}} \nabla_{\parallel}^2 H + \frac{\mathrm{Bo}}{\overline{\mathrm{Ca}}} H + O(\epsilon). \tag{2.45}$$

In practice, material properties such as liquid density ρ, gravitational acceleration g and surface tension coefficient σ generally don't exhibit order-of-magnitude variations. It then follows from the definition of Bond number (2.41) that, at micro/nanoscale the effect of gravity soon becomes negligible as Bo rapidly scales down with characteristic length $[L]^2$. On the other hand, substitution of the component-wise projection $F_\alpha = \boldsymbol{F}_S \cdot \boldsymbol{S}_\alpha$ into the in-plane approximation $\overline{\boldsymbol{F}}_{\parallel}$ yields of the slender approximation of the Marangoni stresses used in the thin film equation (2.37),

$$\overline{\boldsymbol{F}}_{\parallel} = \pm \overline{\mathrm{Ma}}\, \nabla_{\parallel} \Theta + O(\epsilon^2), \tag{2.46}$$

where Θ is determined by solving additional physical systems related to the interfacial quantity c.

2.3 Thermocapillary Growth of Ultrathin Viscous Film

A theoretical model has previously been derived (Dietzel and Troian, 2009b; Dietzel and Troian, 2010) to describe the evolution and stability of a confined slender gas layer overlaying a nanoscale molten film as sketched in figure 2.3. The molten nanofilm of initial uniform or average thickness h_o is confined to a very narrow gap width d_o by two impenetrable solid substrates maintained at a uniform temperature difference $\Delta T = T_{\mathrm{hot}} - T_{\mathrm{cold}} > 0$. The nanofilm is assumed to comprise a single-component, non-volatile, incompressible liquid. The model is based on a long wavelength approximation (also called the lubrication or slender gap limit) for which the thickness of the molten film is much smaller than any characteristic lateral scale $[L]$ such that $\epsilon^2 = (h_o/[L])^2 < (d_o/[L])^2 \ll 1$, inertial forces are negligible such that $\mathrm{Re} \ll 1$ where Re is the Reynolds number, and thermal conduction is the dominant mode of heat transfer such that $\mathrm{RePr} \ll 1$ where Pr is the Prandtl number. Estimates (Dietzel and Troian, 2010) based on experimental values have shown that hydrostatic forces are much smaller than viscous forces by at least order 10^{-7} (quantified by the ratio of Bond

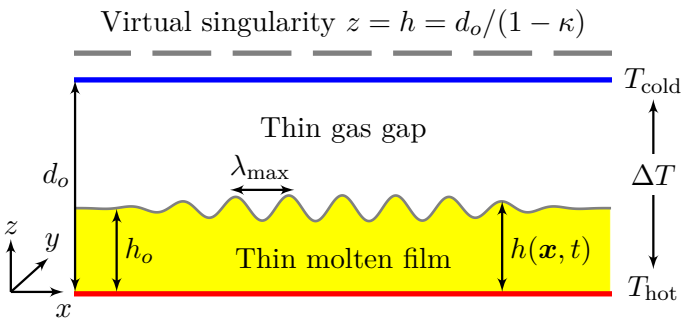

Figure 2.3: Sketch of a linearly unstable thin molten film overlay by a gas layer. The gas/liquid bilayer is subject to a very large vertical temperature gradient enforced by the uniform temperature difference $\Delta T = T_{\text{hot}} - T_{\text{cold}}$ maintained across the very small gap width d_o, typically less than a couple microns. Nominal vertical temperature gradients, $\Delta T/d_o$, are estimated (Dietzel and Troian, 2010) to be extremely large and range from about $10^5 - 10^8$ $^{\circ}\text{C/cm}$. As discussed in the text, the governing interface contains a virtual singularity designated by the dashed line at $h(\boldsymbol{x},t) = d_o/(1-\kappa)$ where $\kappa < 1$. This singularity is never accessible to the evolving film because it lies beyond the top cold substrate situated at $z = d_o$.

number to capillary number) and therefore gravitational effects are also negligible. The viscosity of the film $\mu = \mu(T_{\text{hot}})$ is also assumed relatively constant given the ultra-small gap dimension d_o. The model also disallows any contact with the bottom or top substrate such that $0 < h(\boldsymbol{x},t) < d_o$ where $\boldsymbol{x} = (x,y)$.

Since for single component fluids the variation in surface tension σ with temperature T given by $\mathrm{d}\sigma/\mathrm{d}T$ is a negative quantity, any fluctuation giving rise to a local protrusion generates a local segment of the interface with relatively cooler surface temperature and therefore higher surface tension. Such variations in surface temperature generate thermocapillary stresses $\nabla_S\sigma = (\mathrm{d}\sigma/\mathrm{d}T)\nabla_S T$, which act to pull liquid from warmer to cooler regions of the film. As we discussed in the last section, within the slender approximation the operator ∇_S denoting the surface gradient reduces to the in-plane gradient $\nabla_{\|}$. Therefore the dominant interfacial shear stresses caused by thermocapillarity are mostly oriented in-plane and give rise to large lateral fluxes that push liquid into protruding regions of the film, which grow further in height and become cooler in temperature, thereby establishing a feedback mechanism.

In terms of non-dimensionalization, we choose the average film thickness h_o to be the vertical length scale $[H]$ and the characteristic fluid speed based on in-plane thermocapillary flow (Dietzel and Troian, 2010) to be the reference speed $[U]$. Following the procedure outlined in the last section for deriving the lubrication equation, we introduce the dimensionless variables

$$\boldsymbol{X} = \frac{\boldsymbol{x}}{[L]}, \quad H(\boldsymbol{X},\tau) = \frac{h(\boldsymbol{x},t)}{h_o}, \quad D = \frac{d_o}{h_o}, \quad \tau = \frac{[U]}{[L]}t, \tag{2.47}$$

which eventually lead to the evolution equation of the thin liquid film,

$$\frac{\partial H}{\partial \tau} + \nabla_{\parallel} \cdot \left(\frac{H^3}{3\overline{\mathrm{Ca}}} \nabla_{\parallel} \nabla_{\parallel}^2 H - \frac{\overline{\mathrm{Ma}}}{2} H^2 \nabla_{\parallel} \Theta \right) = 0, \tag{2.48}$$

where Θ is the dimensionless temperature evaluated at the interface to be determined. The dynamics of film thickness $H(X, Y, T)$ in equation (2.48) is controlled by two dimensionless numbers, namely a modified capillary number $\overline{\mathrm{Ca}} = \mu[U]/\epsilon^3 \sigma_o$ and a modified Marangoni number $\overline{\mathrm{Ma}} = \epsilon \sigma_T \Delta T / \mu[U]$ with the reference surface tension coefficient $\sigma_o = \sigma(T_{\mathrm{hot}})$ and slope $\sigma_T = |\mathrm{d}\sigma/\mathrm{d}T|_{T_{\mathrm{hot}}}$.

Heat transfer within a slender gap

Assuming no heat source or sink in the system, the general form of heat transfer for a fluid of density ρ involves both advection and conduction (Leal, 2007),

$$\rho c_p \frac{\mathrm{D}T}{\mathrm{D}t} = k \nabla^2 T, \tag{2.49}$$

where k is the thermal conductivity and c_p is the specific heat. The conservation of energy requires continuity of temperature and heat flux across a material surface,

$$\left.\begin{aligned} T_{\mathrm{air}} &= T_{\mathrm{liq}}, \\ \boldsymbol{n} \cdot k_{\mathrm{air}} \nabla T_{\mathrm{air}} &= \boldsymbol{n} \cdot k_{\mathrm{liq}} \nabla T_{\mathrm{liq}}, \end{aligned}\right\} \quad \text{at} \quad z = h \tag{2.50}$$

Under the previous nondimensionlization used in the slender approximation, the heat transfer equation (2.49) takes the dimensionless form,

$$\epsilon^2 \mathrm{RePr} \frac{\mathrm{D}\Theta}{\mathrm{D}\tau} = \epsilon^2 \frac{\partial^2 \Theta}{\partial X^2} + \epsilon^2 \frac{\partial^2 \Theta}{\partial Y^2} + \frac{\partial^2 \Theta}{\partial Z^2}, \tag{2.51}$$

where Θ is the non-dimensional temperature,

$$\Theta = \frac{T - T_{\mathrm{cold}}}{T_{\mathrm{hot}} - T_{\mathrm{cold}}}, \tag{2.52}$$

and RePr is the product of Reynolds number and Prandtl number,

$$\mathrm{RePr} = \frac{c_p \rho [L][U]}{k}, \quad \mathrm{Pr} = c_p \mu / k \ . \tag{2.53}$$

The typical ranges (Dietzel and Troian, 2010) of material parameters for polymer material are $c_p \sim O(10^3\ \mathrm{J/K/kg})$, $k \sim O(1\ \mathrm{W/m/K})$, $\rho \sim O(10^3\ \mathrm{kg/m^3})$. In mircro/nanoscale systems where $[L] = O(10^{-6}\ \mathrm{m})$ and $[U] = O(10^{-6}\ \mathrm{m/s})$, the product $\mathrm{RePr} \ll 1$ implies the effect of heat advection is negligible and thermal conduction along the vertical direction, $\partial^2 \Theta / \partial Z^2$, is mostly responsible for heat transfer in the slender geometry. Similarly, the continuity of the heat flux in (2.50) is dominated by the matching of vertical flux,

$$\frac{k_{\mathrm{air}}}{k_{\mathrm{liq}}} \left(\frac{\partial \Theta_{\mathrm{air}}}{\partial Z} + O(\epsilon^2) \right) = \frac{\partial \Theta_{\mathrm{liq}}}{\partial Z} + O(\epsilon^2), \tag{2.54}$$

where we have used the slender expansion of the normal vector $\boldsymbol{N}$ from (2.31).

The above analysis conveniently reduces the heat transfer problem to an one-dimensional thermal conduction across a liquid/air bilayer,

$$\left.\begin{aligned} \frac{\partial^2 \Theta_{\rm air}}{\partial Z^2} &= 0 \quad \text{in} \quad \Omega_{\rm air}, \\ \frac{\partial^2 \Theta_{\rm liq}}{\partial Z^2} &= 0 \quad \text{in} \quad \Omega_{\rm liq}, \end{aligned}\right\} \tag{2.55}$$

subject to isothermal boundary conditions at $Z = 0$ and $Z = D$ plus two continuity conditions at the interface,

$$\left.\begin{aligned} \Theta_{\rm air} &= 1 \qquad\quad \text{at} \quad Z = D, \\ \Theta_{\rm air} &= \Theta_{\rm liq} \quad \text{at} \quad Z = H, \\ \kappa \frac{\partial \Theta_{\rm air}}{\partial Z} &= \frac{\partial \Theta_{\rm liq}}{\partial Z} \quad \text{at} \quad Z = H, \\ \Theta_{\rm liq} &= 0 \qquad\quad \text{at} \quad Z = 0. \end{aligned}\right\} \tag{2.56}$$

The material parameter $\kappa = k_{\rm air}/k_{\rm liq}$ denotes the ratio of gas to liquid thermal conductivity evaluated at the temperatures of the respective adjacent substrates. Since the gas layer is always more thermally insulating than the liquid layer, κ is restricted to the range $0 < \kappa < 1$. Depending on the materials of choice, however, the magnitude of κ can range anywhere from about $1/4$ or higher for molten polymer films overlay by an air film (Dietzel and Troian, 2010) to 10^{-4} or smaller for liquid metal films (Peralta-Martinez and Wakeham, 2001) overlay by a xenon gas layer (Haynes, 2011). The solution to equation (2.55) is straightforward:

$$\Theta = \begin{cases} \dfrac{Z - (1-\kappa)H}{D - (1-\kappa)H} & \text{if} \quad H \le Z \le D, \\[2ex] \dfrac{\kappa Z}{D - (1-\kappa)H} & \text{if} \quad 0 \le Z \le H. \end{cases} \tag{2.57}$$

The dimensionless temperature distribution at leading order along the liquid interface is found to be

$$\Theta(X, Y, H) = \frac{\kappa H}{D - (1-\kappa)H}\,. \tag{2.58}$$

Governing equation of thermocapillary thin film

Substituting Θ from (2.58) into thin film equation (2.48) yields the evolution equation describing the long-wavelength thermocapillary model,

$$\frac{\partial H}{\partial \hat{\tau}} + \nabla_{\!\parallel} \cdot \left\{ \frac{H^3}{3\overline{\rm Ca}} \nabla_{\!\parallel} \nabla_{\!\parallel}^2 H + \frac{\kappa D \overline{\rm Ma} H^2}{2\big[D + (\kappa - 1)H\big]^2} \nabla_{\!\parallel} H \right\} = 0\,. \tag{2.59}$$

The system described is known to undergo a linear instability (Dietzel and Troian, 2009b; Dietzel and Troian, 2010) which occurs irrespective of the magnitude of ΔT. Physically,

the confined geometry generates self-reinforcing runaway thermocapillary stresses, which promote growth of elongations toward the colder substrate. This process is mitigated only by capillary forces which tend to suppress regions of high curvature. At early times, infinitesimal disturbances generate periodic undulations in film thickness which undergo exponential growth. The wavelength of the fastest growing mode is given by

$$\lambda_{\max} = 2\pi h_o \left(\frac{4\sigma_o h_o}{3\kappa d_o \sigma_T \Delta T} \right)^{1/2} \left(\frac{d_o}{h_o} + \kappa - 1 \right). \tag{2.60}$$

All else equal, a larger difference in temperature ΔT causes undulations of smaller wavelength. Recent (McLeod, Y. Liu, and Troian, 2011; Fiedler and Troian, 2016; Fiedler, McLeod, and Troian, 2019) and ongoing experiments to confirm the mechanism leading to instability so far indicate good agreement with predictions for the fastest growing mode and its growth rate. In what follows, $\lambda_{\max}$ is selected as the characteristic lateral scale $[L]$ used to non-dimensionalize lateral scales in the governing equation of motion. (This parameter should not be confused with the small parameter ε pertaining to temporal behavior introduced in Section 2.6.) As evident, equation (2.59) exhibits a virtual singularity at

$$H_s = \frac{D}{1-\kappa} \tag{2.61}$$

(or $h = d_o/(1-\kappa)$ in dimensional variables). This singularity lies outside the physical domain beyond the top cold substrate since $\kappa < 1$. For purposes of this current study, it proves convenient to recast equation (2.59) into parameter-free form via the transformation

$$H_* = \frac{H}{[H_*]}, \quad \boldsymbol{X}_* = \frac{\boldsymbol{X}}{[X_*]}, \quad \tau_* = \frac{\tau}{[\tau_*]}, \tag{2.62}$$

where the scalings are given by

$$[H_*] = H_s, \quad [X_*] = \sqrt{\frac{2DH_s}{3\kappa \overline{\mathrm{Ma}}\,\overline{\mathrm{Ca}}}}, \quad [\tau_*] = \frac{4D^2}{3\kappa^2 H_s \overline{\mathrm{Ma}}^2\,\overline{\mathrm{Ca}}}. \tag{2.63}$$

We then drop $()_*$ subscription of H_*, $\boldsymbol{X}_*$ and τ_* in the transformed equation and obtain the final form:

$$\frac{\partial H}{\partial \tau} + \nabla_{\parallel} \cdot \left[H^3 \nabla_{\parallel} \nabla_{\parallel}^2 H + \frac{H^2}{(1-H)^2} \nabla_{\parallel} H \right] = 0. \tag{2.64}$$

It suffices to study the behavior of equation (2.64) alone rather than equation (2.59) parametrized by an arbitrary combination of $\overline{\mathrm{Ca}}$, $\overline{\mathrm{Ma}}$ and κ. In these new variables, the top cold substrate is located at $H = 1-\kappa$ while the virtual singularity occurs at $H = 1$. In this work, we establish that the conical tip at the apex of the evolving cuspidal shape undergoes self-similar sharpening characterized by distinct power law exponents. Extraction of robust exponents, however, requires growth over several decades in time. We therefore focus on systems such that $\kappa \simeq 2 \times 10^{-4}$ (e.g., liquid metal films overlaid by a highly insulating gas film) in order to allow longer evolution times.

Some elementary properties of equation (2.64) can be examined in the linear limit. Consider an initially uniform film of thickness H_0 (i.e. base state) subject to a periodic perturbation $H = H_0 + \delta H_0 \exp(\beta\tau) \exp(i\boldsymbol{K}\cdot\boldsymbol{X})$ where $|\delta H_0| \ll 1$ is the infinitesimally small amplitude and $\boldsymbol{K}$ is the two-dimensional wave vector. The resulting expression for the growth rate β as a function of wave number $K = |\boldsymbol{K}|$ is

$$\beta(K) = -H_0^3 K^4 + \frac{H_0^2}{(1-H_0)^2} K^2. \tag{2.65}$$

The critical wave number, designated as K_{crit} for which $\beta(K_{\text{crit}}) = 0$, sits at the boundary between the band of growing wave numbers $0 < K \leq K_{\text{crit}}$ and the decaying band $0 < K \leq K_{\text{crit}}$. In other words, there always exist exponentially growing disturbances of wavelength $\Lambda > \Lambda_{\text{crit}}$ for an initially flat film of thickness H_0 (disturbances of $0 < \Lambda < \Lambda_{\text{crit}}$ decay instead), among which the fastest growing (or the most unstable) wavelength $\Lambda_{\max}$ corresponds to the maximum of $\beta(K)$ in equation (2.65),

$$\Lambda_{\max} = \sqrt{2}\Lambda_{\text{crit}}, \quad \Lambda_{\text{crit}} = 2\pi\sqrt{H_0}(1-H_0). \tag{2.66}$$

If we convert $\Lambda_{\max}$ back to dimensional form, we recover $\lambda_{\max}$ in (2.60), which is the lateral length scale eventually used to scale the system.

2.4 Stability Considerations by Analogy to Gradient Flows

In previous work (Dietzel and Troian, 2009b; Dietzel and Troian, 2010), the classical linear stability analysis of equation (2.59) was examined, which exclusively focused on early time behavior of infinitesimal fluctuations in interfacial temperature or film thickness. That analysis showed that the instability is of Type II (Cross and Greenside, 2009) where all modal fluctuations of wavelength $\lambda > \lambda_{\max}/\sqrt{2}$ are linearly unstable irrespective of the magnitude of temperature difference ΔT. The authors also investigated nonlinear growth in late stages by deriving the exact from of the free energy (Lyapunov) functional $\mathcal{F}[H]$ of the thermocapillary system. Through a series of numerical experiments, they showed that a flat film, not mass-limited, is likely to be driven to touch the opposing cold substrate whereas a mass-limited film tends to saturate to a configuration in which interstitial portions between primary film pillars thin to zero thickness. In this section, we elicit the stability characteristics of stationary states of the full nonlinear equation (2.64) through a different analytic approach based on the system free energy $\mathcal{F}[H]$. By exploiting an analogy to general gradient flows, we show next that equation (2.64) does not admit any stable stationary states on periodic or infinite (lateral) domains so long as $H > 0$.

Free energy functional

Mitlin (1993) has previously shown that the interface equation describing thin film dewetting by van der Waals forces, the process depicted in figure 2.1(a) and (b), can

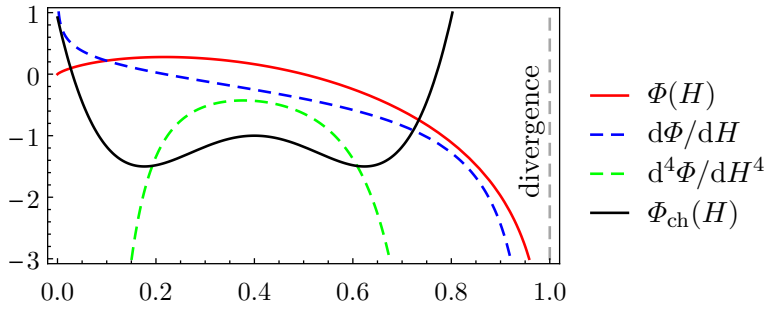

Figure 2.4: Plots of $\Phi(H)$, $0.2\times \mathrm{d}\Phi/\mathrm{d}H$ and $0.005\times \mathrm{d}^4\Phi/\mathrm{d}H^4$ for the thermocapillary equation. Magnitudes have been rescaled to accommodate all curves on a common scale. $\Phi_{\mathrm{ch}}(H) = 200((H-0.4)^2 - 0.05)^2 - 1.5$ is an example of the double-well potential in Cahn-Hilliard theory of phase separation.

be rewritten in Cahn-Hilliard form described by

$$\frac{\partial H}{\partial \tau} = \nabla_{\parallel} \cdot \left\{ \mathcal{M}(H) \nabla_{\parallel} \frac{\delta \mathcal{F}[H]}{\delta H} \right\}, \tag{2.67}$$

known more generally as gradient flow (Giacomelli and F. Otto, 2003). The thermocapillary model described by equation (2.64) posed on the in-plane domain Ω can also be written in this form where the free energy functional is given by

$$\mathcal{F}[H] = \int_{\Omega} \frac{1}{2} \left| \nabla_{\parallel} H \right|^2 + \Phi(H) \, \mathrm{d}\Omega \tag{2.68}$$

with mobility coefficient

$$\mathcal{M}(H) = H^3 \tag{2.69}$$

and potential function

$$\Phi(H) = H \left[\ln(1-H) - \ln H \right], \tag{2.70}$$

such that evaluating the (unconstrained) variational derivative of the free energy

$$\frac{\delta \mathcal{F}}{\delta H} = -\nabla_{\parallel}^2 H + \frac{\mathrm{d}\Phi}{\mathrm{d}H} \tag{2.71}$$

recovers the original governing equation (2.64). The curves in figure 2.4 show that, in contrast to the conventional double-well potential $\Phi_{\mathrm{ch}}(H)$ in the Cahn–Hilliard theory of binary phase separation (J. E. Taylor and Cahn, 1994), $\Phi(H)$ has no global minimum (and that $\Phi(H)$, $\mathrm{d}\Phi/\mathrm{d}H$ and $\mathrm{d}^4\Phi/\mathrm{d}H^4$ all diverge at the virtual singularity $H = 1$), mimicking an infinitely sharp potential well at virtual singularity $H = 1$.

We first show that for any periodic domain Ω, functional $\mathcal{F}[H]$ is indeed a free energy, i.e., $\mathrm{d}\mathcal{F}/\mathrm{d}\tau \leq 0$. We evaluate the quantity $\mathrm{d}\mathcal{F}[H]/\mathrm{d}\tau$ for the free energy $\mathcal{F}[H]$ defined in equation (2.68) by applying Leibnitz's rule for differentiation over a fixed periodic domain Ω:

$$\frac{\mathrm{d}\mathcal{F}[H]}{\mathrm{d}\tau} = \frac{\mathrm{d}}{\mathrm{d}\tau} \int_{\Omega} \frac{1}{2} \left| \nabla_{\parallel} H \right|^2 + \Phi(H) \, \mathrm{d}\Omega = \int_{\Omega} \nabla_{\parallel} H \cdot \frac{\partial \nabla_{\parallel} H}{\partial \tau} + \frac{\mathrm{d}\Phi}{\mathrm{d}H} \frac{\partial H}{\partial \tau} \, \mathrm{d}\Omega. \tag{2.72}$$

Interchanging the order of operators $\nabla_\parallel$ and $\partial/\partial\tau$ followed by application of the Green's first identity to the first integral in equation (2.72) gives

$$\frac{\mathrm{d}\mathcal{F}[H]}{\mathrm{d}\tau} = \int_\Omega \left(-\nabla_\parallel^2 H + \frac{\mathrm{d}\Phi}{\mathrm{d}H}\right)\frac{\partial H}{\partial \tau}\,\mathrm{d}\Omega, \tag{2.73}$$

where continuity of H and higher order derivatives ensures that the boundary term proportional to $\nabla_\parallel H$ vanishes identically. Substitution of the term $\partial H/\partial\tau$ in equation (2.73) by the relations given in equation (2.67) and (2.68) yields

$$\frac{\mathrm{d}\mathcal{F}[H]}{\mathrm{d}\tau} = \int_\Omega \left(-\nabla_\parallel^2 H + \frac{\mathrm{d}\Phi}{\mathrm{d}H}\right)\nabla_\parallel \cdot \left[\mathcal{M}(H)\nabla_\parallel\left(-\nabla_\parallel^2 H + \frac{\mathrm{d}\Phi}{\mathrm{d}H}\right)\right]\mathrm{d}\Omega. \tag{2.74}$$

Application of Green's first identity subject to the vanishing boundary term yields the desired inequality

$$\frac{\mathrm{d}\mathcal{F}[H]}{\mathrm{d}\tau} = -\int_\Omega \mathcal{M}(H)\left|\nabla_\parallel\left(-\nabla_\parallel^2 H + \frac{\mathrm{d}\Phi}{\mathrm{d}H}\right)\right|^2 \mathrm{d}\Omega \leq 0. \tag{2.75}$$

The proof for infinite (lateral) domain simply requires that the integrand in equation (2.68) be augmented by the term $\Phi[H(\boldsymbol{X}\to\infty,\tau)]$, but otherwise proceeds similarly.

First and second variations of free energy

Due to the conservative (divergence) form of the evolution equation, the total volume of the liquid film over a periodic domain is a conserved quantity. The energy analysis is only instructive to the dynamics if it is carried out for film states of identical total volume. However the form of the free energy (2.68) of the thin film system depends on the total liquid volume. We can enforce the constrain on the total volume by augmenting the free energy $\mathcal{F}[H]$ with the Lagrange multiplier constant P,

$$\mathcal{F}[H,P] = \int_\Omega \frac{1}{2}\left|\nabla_\parallel H\right|^2 + \Phi(H)\,\mathrm{d}\Omega - P\left(\int_\Omega H\,\mathrm{d}\Omega - \mathrm{Vol}\right), \tag{2.76}$$

where the total volume

$$\mathrm{Vol} = \int_\Omega H\,\mathrm{d}\Omega\,. \tag{2.77}$$

For $\overline{H}$ to represent an extrema of the free energy (2.76) with some fixed total volume, the infinitesimal change $\delta\mathcal{F}$ in the free energy $\mathcal{F}[\overline{H}+\delta H, \overline{P}+\delta P]$ must vanish against all infinitesimal variations δH and δP. Evaluating the first variations of free energy (2.76) results in two expressions,

$$\delta\mathcal{F}[\overline{H},\overline{P};\delta H] = \int_\Omega \left(-\nabla_\parallel^2\overline{H} + \left.\frac{\mathrm{d}\Phi}{\mathrm{d}H}\right|_{\overline{H}} - \overline{P}\right)\delta H\,\mathrm{d}\Omega, \tag{2.78}$$

$$\delta\mathcal{F}[\overline{H},\overline{P};\delta P] = -\left(\int_\Omega \overline{H}\,\mathrm{d}\Omega - \mathrm{Vol}\right)\delta P, \tag{2.79}$$

where we have used the Green's identity $\int_\Omega \nabla_\parallel\delta H\cdot\nabla_\parallel\overline{H}\,\mathrm{d}\Omega = -\int_\Omega \delta H\,\nabla_\parallel^2\overline{H}\,\mathrm{d}\Omega$ for a periodic domain Ω. This yields the value of the Lagrange multiplier

$$\overline{P} = -\nabla_\parallel^2\overline{H} + \left.\frac{\mathrm{d}\Phi}{\mathrm{d}H}\right|_{\overline{H}} \text{ such that } \int_\Omega \overline{H}\,\mathrm{d}\Omega = \mathrm{Vol}, \tag{2.80}$$

which defines the effective surface pressure required for maintaining stationary states of constant volume. It's straightforward to verity that the film profile $\overline{H}$ satisfying equilibrium condition (2.80) is a steady state solution to the evolution equation (2.67).

To conclude the nature (e.g., local minimum, maximum or saddle point) of these stationary solutions $\overline{H}$ obtained by solving equation (2.80), we must proceed to the second variation of the free energy around $\overline{H}$,

$$\delta^2\mathcal{F}[\overline{H},\overline{P};\delta H] = \int_\Omega |\nabla_\parallel \delta H|^2 + \frac{\mathrm{d}^2\Phi}{\mathrm{d}H^2}\Big|_{\overline{H}} \delta H^2 \,\mathrm{d}\Omega, \tag{2.81}$$

$$\delta^2\mathcal{F}[\overline{H},\overline{P};\delta P] = 0, \tag{2.82}$$

$$\delta^2\mathcal{F}[\overline{H},\overline{P};\delta H,\delta P] = -\delta P \int_\Omega \delta H \,\mathrm{d}\Omega = 0, \tag{2.83}$$

where in equation (2.83) we invoke the volume constraint $\int_\Omega \overline{H} + \delta H \,\mathrm{d}\Omega = \mathrm{Vol}$ on an admissible variation δH. Usually one needs to first numerically solve for the stationary solution $\overline{H}$ and then examines the convexity of the quadratic forms (2.81), (2.82) and (2.83) that appear under the integral of the second variation. Fortunately we can do better for the thin film equations. It has previously been shown that for a general class of thin film equations (Laugesen and Pugh, 2002) which include the form of equation (2.80), there always exist some small perturbations to the periodic stationary states $\overline{H}$ which lead to strictly negative values of the second variation whenever the potential function satisfies the relation the relation $\mathrm{d}^4\Phi/\mathrm{d}H^4 < 0$ over the entire range of $\overline{H}$.

To prove this claim, let's consider the free energy associated with a small deviation about a stationary solution $\overline{H}$ of equation (2.76) for admissible (i.e., periodic and zero total volume) perturbations δH:

$$\mathcal{F}[\overline{H}+\delta H,\overline{P}+\delta P] = \mathcal{F}[\overline{H},\overline{P}]+\delta\mathcal{F}[\overline{H},\overline{P};\delta H,\delta P]+\frac{1}{2}\delta^2\mathcal{F}[\overline{H},\overline{P};\delta H,\delta P]+O(\delta H,\delta P)^3. \tag{2.84}$$

By definition, the first variation of the energy $\delta\mathcal{F}[\overline{H},\overline{P};\delta H,\delta P]$ must vanish identically for any such stationary solution $\overline{H}$. Application of Green's first identity reduces the second variation to the form

$$\delta^2\mathcal{F}[\overline{H},\overline{P};\delta H,\delta P] = \delta^2\mathcal{F}[\overline{H},\overline{P};\delta H] = \int_\Omega \delta H \left(-\nabla_\parallel^2 \delta H + \frac{\mathrm{d}^2\Phi}{\mathrm{d}H^2}\Big|_{\overline{H}}\delta H\right) \mathrm{d}\Omega, \tag{2.85}$$

where the additional boundary integral vanishes for any periodic perturbation δH. It is now a straightforward exercise to show that there always exist admissible arbitrary perturbations δH such that $\delta^2\mathcal{F}[\overline{H},\overline{P};\delta H,\delta P]$ is always strictly negative. We differentiate equilibrium condition (2.80) twice with respect to X and obtain the relation

$$-\nabla_\parallel^2 \frac{\partial^2\overline{H}}{\partial X^2} + \frac{\mathrm{d}^2\Phi}{\mathrm{d}H^2}\Big|_{\overline{H}} \frac{\partial^2\overline{H}}{\partial X^2} = -\frac{\mathrm{d}^3\Phi}{\mathrm{d}H^3}\Big|_{\overline{H}} \Big(\frac{\partial\overline{H}}{\partial X}\Big)^2. \tag{2.86}$$

Substituting equation (2.86) into equation (2.85) for a perturbation of the form

$$\delta H = \frac{\partial^2 \overline{H}}{\partial X^2} \tag{2.87}$$

(note $\int_\Omega \delta H \, \mathrm{d}\Omega = 0$ is admissible) yields

$$\begin{aligned}
\delta^2 \mathcal{I}[\overline{H}, \overline{P}; \delta H, \delta P] &= -\int_\Omega \Big(\frac{\partial^2 \overline{H}}{\partial X^2}\Big) \frac{\mathrm{d}^3 \Phi}{\mathrm{d}H^3}\Big|_{\overline{H}} \Big(\frac{\partial \overline{H}}{\partial X}\Big)^2 \mathrm{d}\Omega \\
&= -\int_\Omega \frac{\mathrm{d}^3 \Phi}{\mathrm{d}H^3}\Big|_{\overline{H}} \frac{1}{3} \frac{\partial}{\partial X} \Big(\frac{\partial \overline{H}}{\partial X}\Big)^3 \mathrm{d}\Omega \\
&= \frac{1}{3} \int_\Omega \Big(\frac{\mathrm{d}^4 \Phi}{\mathrm{d}H^4}\Big|_{\overline{H}} \frac{\partial \overline{H}}{\partial X}\Big) \Big(\frac{\partial \overline{H}}{\partial X}\Big)^3 \mathrm{d}\Omega = \frac{1}{3} \int_\Omega \Big(\frac{\partial \overline{H}}{\partial X}\Big)^4 \frac{\mathrm{d}^4 \Phi}{\mathrm{d}H^4}\Big|_{\overline{H}} \mathrm{d}\Omega.
\end{aligned} \tag{2.88}$$

All boundary terms from integrations by parts vanish due to periodic boundary conditions. For the thermocapillary model described by the potential function (2.70), its fourth derivative (as plotted in figure 2.4)

$$\frac{\mathrm{d}^4 \Phi}{\mathrm{d}H^4} = -\frac{2(1-2H)^2 + 4H^2}{H^3(1-H)^4} < 0 \quad \text{for} \quad 0 < H < 1 \tag{2.89}$$

is always negative. When substituted into equation (2.88), this yields the relation $\delta^2 \mathcal{I}[\overline{H}, \overline{P}; \delta H, \delta P] < 0$. This inequality assures that for every (if exists) nonuniform stationary state $\overline{H}$ such that $\partial H / \partial X$ is not identically zero everywhere, there always exists a neighboring state $\overline{H} + \delta H$ with same periodicity as $\overline{H}$ but of strictly lower free energy. Therefore we conclude that equation (2.80) cannot therefore support any energetically stable stationary periodic states, at least not any classical smooth solutions such that $\overline{H} > 0$ everywhere. This analysis is quite general and can be modified and applied to many other thin film systems (even volume non-conserving systems) so long as the governing interface equation can be cast into the gradient flow equation (2.67).

2.5 Numerical Solution of Nonlinear Thermocapillary Equation

In this section we perform direct numerical simulations for the thermocapillary equation (2.64) on a rectilinear, axsymmetric and a full two-dimensional domain. In order not to divert us from the physics, technical details of the finite element formulation and time step integration scheme employed are postponed to Section 3.2 in Chapter 3.

One-dimensional rectilinear and cylindrical simulations

To gain further insight into the behavior of equation (2.64) for growth in the nonlinear regime, we examine details of the dynamical shapes obtained from numerical solutions for rectilinear $H(X, \tau)$ and cylindrical $H(R, \tau)$ geometry. By virtue of the fact that vertical dimensions cannot exceed the substrate separation distance and that lateral dimensions continue to scale with the dominant wavelength of the initial instability, the results below rigorously satisfy the lubrication approximation throughout the cuspidal

formation process (in contrast with other thin film problems which involve asymptotic matching to regions described by a Stokes flow (Krechetnikov, 2010)). A mixed Lagrange finite element method (COMSOL Multiphysics, Inc. V5.3, 2017) was used to evolve the solutions, subject to no-flux conditions at the boundaries of the lateral domain $[0, \Lambda_{\max}/2]$ and initial condition

$$H(X, \tau = 0) = \frac{1}{3}\left(1 + 0.1\cos\frac{2\pi X}{\Lambda_{\max}}\right) \tag{2.90}$$

(with X replaced by R for cylindrical geometry). The restriction to a domain size $\Lambda_{\max}/2$ ensured that the dynamics of an individual cuspidal shape could be examined with high resolution without interference from similar adjacent shapes arising from the native linear instability (2.66). Quadratic elements numbering about 20000 and of minimum size 4×10^{-8} ensured sufficient spatial resolution of the emerging cuspidal region. The mesh sizes were everywhere much smaller than $|\nabla_{\|}^2 H|^{-1}$ at all times. Integration in time relied on a second order backward difference scheme with small adaptive time stepping. Typically, full evolution toward the asymptotic shapes required about 11000 integration steps. Simulations were terminated when the (dimensionless) distance between the virtual singularity at $H = 1$ and the liquid cusp apex $H_{\rm apex}(\tau) = H(0, \tau)$ reached a value of about 10^{-4}.

Shown in figure 2.5 are far-field (a) and magnified views (b) of an evolving cusp capped by a conical tip. As expected from consideration of volume accumulation, the rectilinear geometry leads to a slightly thinner cusp for the same time interval. Inspection of the shape of the fluid tip reveals a conical protrusion with constant slope whose tip radius decreases rapidly in time. Plotted in figure 2.5(c) are the tip speed $\partial H/\partial\tau|_{\rm apex}$ and magnitude of the tip curvature $|\nabla_{\|}^2 H|_{\rm apex}$ as a function of the decreasing distance $1 - H_{\rm apex}(\tau)$. The power law behavior observed persists for almost four decades in time indicating robust self-similar growth. The indicated asymptotic values for the slope and intercept values (in parentheses) of the lines shown were obtained from least square fits over the shaded (yellow) portion shown. This self-similar behavior confirms the relations

$$\frac{\partial H_{\rm apex}}{\partial \tau} \sim \frac{1}{(1 - H_{\rm apex})^3}, \quad \nabla_{\|}^2 H_{\rm apex} \sim \frac{1}{1 - H_{\rm apex}} \ . \tag{2.91}$$

Introducing the singular time τ_s where the local film apex $H_{\rm apex}$ reaches $H = 1$—the singular point of equation (2.64)—yields the scaling relations governing the conical tip region, namely $(1-H_{\rm apex}/(\tau_s-\tau) \sim (1-H_{\rm apex})^{-3}$ and $(1-H_{\rm apex})/X^2 \sim (1-H_{\rm apex})^{-1}$. These reveal the self-similar variables characterizing this asymptotic regime, namely

$$X \sim 1 - H_{\rm apex} \sim (\tau_s - \tau)^{1/4}, \tag{2.92}$$

which reflect the lack of an intrinsic spatial or temporal scale in the conical region. As evident in figure 2.5(d), the shape of the conical tip undergoes collapse onto a

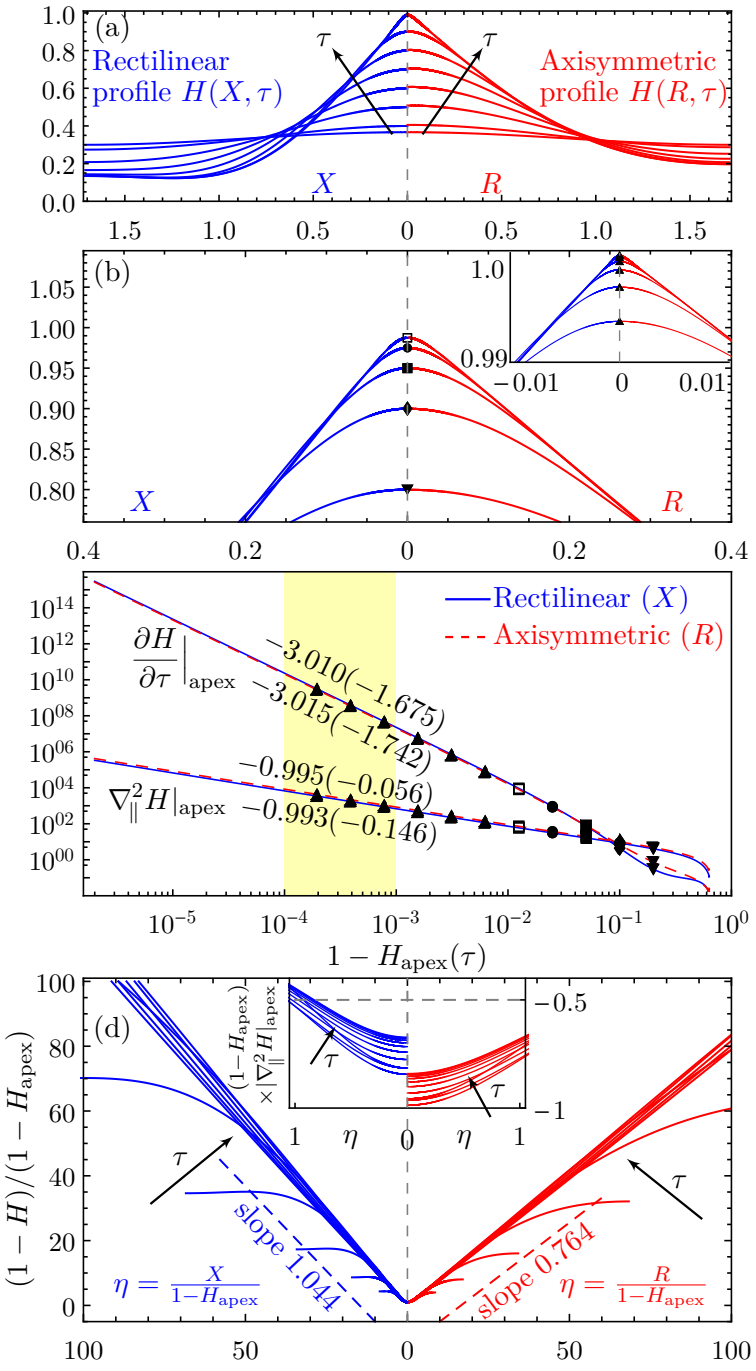

Figure 2.5: Self-similar formation of conical cusp from numerical solution of equation (2.64) for rectilinear (X) and axisymmetric (R) geometry. Arrows indicate increasing time τ. (a) Far field view of cuspidal formation for $H_{\rm apex}(\tau) = 0.367,\ 0.4,\ 0.5,\ \ldots\ ,\ 0.8,\ 0.9,\ 0.9875$. (b) Magnified view of conical tip for $H_{\rm apex}(\tau) = 1 - 0.2/2^n$ showing $n = 0$ (▼), $n = 1$ (♦), $n = 2$ (■), $n = 3$ (●) and $n = 4$ (□). Inset: Magnified view of conical tip for $H_{\rm apex}(\tau) = 1 - 0.2/2^n$ showing $n = 5 - 10$ (▲). (The last two curves $n = 9,\ 10$ are indistinguishable.) (c) Power law behavior of $\partial H/\partial\tau|_{\rm apex}$ and $|\nabla^2_{\parallel} H|_{\rm apex}$ versus $1 - H_{\rm apex}(\tau)$. Slopes and intercept values (in parentheses) were obtained from least squares fits over the shaded (yellow) region. (d) Rescaled solutions $(1-H)/(1-H_{\rm apex})$ showing self-similar collapse of the conical tip for $H_{\rm apex}(\tau) = 1 - 0.2/2^n$ where $n = 0 - 10$. Inset: Rescaled apex curvature $(1 - H_{\rm apex})(\nabla^2_{\parallel} H)_{\rm apex}$ versus η.

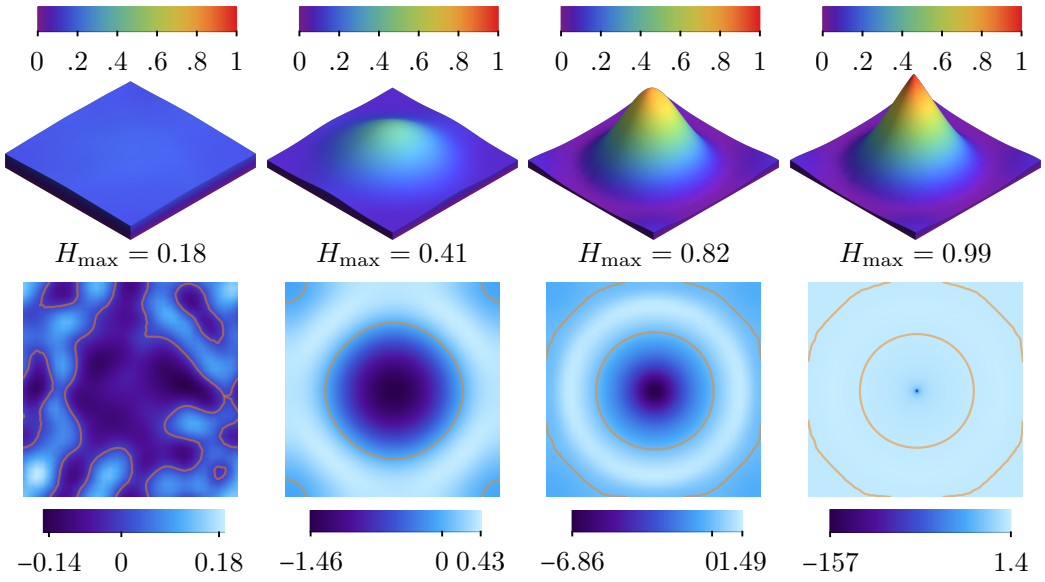

Figure 2.6: Four images of the film thickness $H(\boldsymbol{X}, \tau)$ (top panel) and interface curvature $\nabla_{\parallel}^2 H$ (bottom panel) from numerical simulation of equation (2.64) on a square periodic domain with edge length $\Lambda_{\max} \approx 3.02$. The initial condition was $H(\boldsymbol{X}, 0) = \{1 - 0.05[\cos(2\pi X/\Lambda_{\max}) + \cos(2\pi Y/\Lambda_{\max})] + \mathrm{rand}(\boldsymbol{X})\}/6$, where $\mathrm{rand}(\boldsymbol{X})$ denotes a uniformly distributed random variable between -0.2 and 0.2. The maximum film thickness is denoted $H_{\max}$. The orange lines are the boundaries between regions of positive and negative curvature. The evolution times depicted are $\tau = 0.0$, 30.0, 50.5 and 50.84552722.

common curve when both the vertical and lateral dimensions are normalized by the factor $(1 - H_{\mathrm{apex}})$. The extent of the collapsed region is observed to increase in time. Shown in the inset of figure 2.5(d) is the rescaled apical curvature $(1 - H_{\mathrm{apex}})(\nabla_{\parallel}^2 H)_{\mathrm{apex}}$ versus $\eta = X/(1 - H_{\mathrm{apex}})$ or $R/(1 - H_{\mathrm{apex}})$, which also exhibits self-similar collapse. The virtual singularity $H_{\mathrm{apex}} = 1$ appears therefore to act as an attractor state for formation of the conical tip.

Two-dimensional periodic square domain

We also performed a full two-dimensional direct numerical simulation of equation (2.64) to demonstrate the robustness of cuspidal formation in a thermocapillary-driven thin film. The top panel shown in figure 2.6 represents 3D views of an evolving cusp with a conical tip at the four times designated, as obtained from finite element simulation of the full nonlinear equation (2.64). The square domain was discretized into 15872 triangular elements of quadratic order with 63746 degrees of freedom in total. Since the evolving cusp was centered about the origin of the domain, the nested mesh shown in figure 2.7 was implemented in order to resolve details of the apical region with sufficient resolution. The edge size ΔX of the smallest mesh element in the central was about 0.0004,

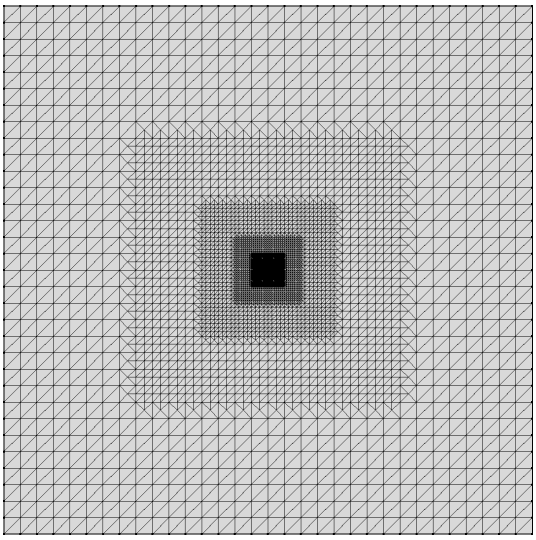

Figure 2.7: Image of progressively refined mesh used to resolve details in the apical region.

intentionally chosen to be smaller than the minimum value of $|\nabla_{\|} H|^{-1} \sim O(10^{-2})$. The finite element simulation was run until the cusp apex height reached a maximum value $H_{\max}$ that just exceeded 0.99.

The bottom panel displays the value of the curvature of the gas/liquid interface at every point within the computational domain. The orange curves delineate concave from convex regions. The last image in the bottom panel clearly reveals that the interface evolves into a cuspidal shape capped by a conical tip with shrinking radius flanked by a broader convex surface.

We verified that these results, i.e. rectilinear, axisymmetric and full two-dimensional simulations, converged upon mesh refinement and that the minimum mesh size chosen was sufficient to capture the dynamics of the evolving tip with high resolution. In particular, the scaling relations (2.92) noted above establish constraints on the minimum mesh size $\Delta X \sim 1 - H_{\text{apex}} \sim 1/|\nabla_{\|}^2 H|_{\text{apex}}$ required to resolve the curvature in the apical region. For the results shown in figure 2.5, the simulations were terminated when $1 - H_{\text{apex}} \sim O(10^{-4})$. The minimum element size used of 4×10^{-8} ensured that $O(\Delta X) \ll O(1 - H_{\text{apex}})$. Therefore, the overall local error in was sufficiently small in our simulations to capture with high resolution the self-similar dynamics in the apical region before the simulations were terminated to prevent contact with the top colder substrate. Similar argument applies to the two-dimensional simulation on the square domain.

2.6 Asymptotic Analysis of Self-Similar Cusp Formation

The exponents obtained from these numerical simulations were also confirmed by analysis of equation (2.64) by considering a Taylor expansion about the virtual singular point $H = 1$, which yields the asymptotic evolution equation

$$\frac{\partial H}{\partial \tau} + \nabla_{\|} \cdot \left[\nabla_{\|} \nabla_{\|}^2 H + \frac{1}{(1-H)^2} \nabla_{\|} H \right] + O(1-H)^{-1} = 0. \tag{2.93}$$

Balancing the first and second term with the second and third term yields the same asymptotic relation (2.92) obtained previously. These scalings suggest introduction of the stretched variables

$$\eta = \frac{X}{\varepsilon} \quad \text{or} \quad \frac{R}{\varepsilon}, \quad 1 - H = \sum_{n=0}^{\infty} \varepsilon^n \mathcal{W}_n(\eta) \quad \text{where} \quad \varepsilon = (\tau - \tau_s)^{1/4} \tag{2.94}$$

(recall τ_s is the singular time where film apex $H_{\text{apex}} \to 1$). We note here that if equation (2.64) were truly scale-invariant, and not just asymptotically so as $H_{\text{apex}} \to 1$, the expansion in equation (2.94) would terminate at $n = 1$. The appearance of the $1-H$ term in the denominator of equation (2.64), however, precludes such global scaling and instead leads to multiscale expansions of the form:

$$\frac{\partial H}{\partial \tau} = \frac{1}{\varepsilon^4} \sum_{n=1}^{\infty} \varepsilon^n \mathcal{T}_n(\mathcal{W}_1, \ldots, \mathcal{W}_n), \tag{2.95}$$

$$\nabla_{\|} \cdot \left(H^3 \nabla_{\|} \nabla_{\|}^2 H \right) = \frac{1}{\varepsilon^4} \sum_{n=1}^{\infty} \varepsilon^n \mathcal{S}_n(\mathcal{W}_1, \ldots, \mathcal{W}_n), \tag{2.96}$$

$$\nabla_{\|} \cdot \left[\frac{H^2}{(1-H)^2} \nabla_{\|} H \right] = \frac{1}{\varepsilon^4} \sum_{n=1}^{\infty} \varepsilon^n \mathcal{M}_n(\mathcal{W}_1, \ldots, \mathcal{W}_n), \tag{2.97}$$

where the symbols $\nabla_{\|}$, $\nabla_{\|} \cdot$ and $\nabla_{\|}^2$ represent the appropriate forms of the gradient, divergence and Laplacian operators for rectilinear (X) or cylindrical (R) geometry. To leading order $n = 1$, equation (2.93) then reduces to the nonlinear, fourth order equation given by

$$\mathcal{T}_1(\mathcal{W}_1) + \mathcal{S}_1(\mathcal{W}_1) + \mathcal{M}_1(\mathcal{W}_1) = 0, \tag{2.98}$$

where the operators $\mathcal{T}_1$, $\mathcal{S}_1$ and $\mathcal{M}_1$ are defined as

$$\mathcal{T}_1(\mathcal{W}_1) = \frac{1}{4} \left(\mathcal{W}_1 - \eta \frac{\mathrm{d}\mathcal{W}_1}{\mathrm{d}\eta} \right), \tag{2.99}$$

$$\mathcal{S}_1(\mathcal{W}_1) = -\nabla_\eta^2 \nabla_\eta^2 \mathcal{W}_1, \tag{2.100}$$

$$\mathcal{M}_1(\mathcal{W}_1) = \nabla_\eta^2 \left(\frac{1}{\mathcal{W}_1} \right). \tag{2.101}$$

Here and in what follows, operator subscripts ∇_η denote differentiation with respect to the self-similar variable η for rectilinear or cylindrical form. These self-similar solutions

can be used to derive some characteristics of the local touch-up process,

$$1 - H_{\text{apex}}(\tau) = \sum_{n=1}^{\infty} \varepsilon^n \mathcal{W}_n(0) = \varepsilon \mathcal{W}_1(0) + O(\varepsilon^2), \tag{2.102}$$

$$\nabla_{\parallel}^2 H|_{\text{apex}}(\tau) = -\sum_{n=1}^{\infty} \varepsilon^{n-2} \nabla_\eta^2 \mathcal{W}_n(0) = -\frac{1}{\varepsilon} \nabla_\eta^2 \mathcal{W}_1(0) + O(\varepsilon^0), \tag{2.103}$$

$$\frac{\mathrm{d}H_{\text{apex}}}{\mathrm{d}\tau} = \sum_{n=1}^{\infty} \frac{n}{4} \varepsilon^{n-4} \mathcal{W}_n(0) = \frac{1}{4\varepsilon^3} \mathcal{W}_1(0) + O(\varepsilon^{-2}). \tag{2.104}$$

Required symmetry about the axis of origin yields two boundary conditions, namely

$$\left.\frac{\mathrm{d}\mathcal{W}_1}{\mathrm{d}\eta}\right|_{\eta=0} = \left.\frac{\mathrm{d}^3\mathcal{W}_1}{\mathrm{d}\eta^3}\right|_{\eta=0} = 0. \tag{2.105}$$

It is argued (Bernoff, Bertozzi, and Witelski, 1998) that in order to describe localized self-similar behavior, the solution profile away from a localized singularity must not rely on the rapidly evolving singularity as the singular time τ_s is approached. This means equation (2.98) must also conform to far-field boundary conditions allowing asymptotic matching to the slow dynamics away from the apical region. In other words, at any fixed distance away from the cusp point, film height must stay bounded. In the dynamically stretched variables (2.94), it translates into the requirement that equation (2.99) remains bounded as $\varepsilon \to 0$, or equivalently $\eta \to \infty$, which requires the leading term $\mathcal{T}_1(\mathcal{W}_1)$ to vanish. This then leads to the additional Robin boundary condition at far field

$$\mathcal{T}_1(\mathcal{W}_1)|_{\eta\to\infty} = 0, \quad \text{or equivalently} \quad \mathcal{W}_1 \sim \eta \text{ as } \eta \to \infty. \tag{2.106}$$

To leading order then, the asymptotic solution to equation (2.98) is satisfied by the Laurent series

$$\mathcal{W}_1^{\infty} = \sum_{k=0}^{\infty} a_{k+1} \eta^{1-4k} = a_1\eta + \frac{a_2}{\eta^3} + \frac{a_3}{\eta^7} + \ldots \quad \text{as} \quad |\eta| \to \infty, \tag{2.107}$$

where the higher order coefficients $a_{k>1}$, for instance,

$$a_2 = \begin{cases} -\dfrac{2}{a_1} & \text{(rectilinear)} \\ a_1 - \dfrac{1}{a_1} & \text{(axisymmetric)} \end{cases}, \quad a_3 = \begin{cases} -30\left(\dfrac{12}{a_1} + \dfrac{1}{a_1^3}\right) & \text{(rectilinear)} \\ \dfrac{25}{2}\left(9a_1 - \dfrac{8}{a_1} - \dfrac{1}{a_1^3}\right) & \text{(axisymmetric)} \end{cases}, \tag{2.108}$$

are all uniquely determined by the leading order linear slope a_1 alone, which in general can only be obtained numerically.

Long-wavelength transformation

The asymptotic slope a_1 is a free parameter and cannot be determined from far-field expansion at $\eta \to \infty$ alone. Nevertheless in the limit of small slope $|a_1| \ll 1$, it is

possible to extract information about the structure of $\mathcal{W}_1$ through the long-wavelength transformation,

$$\mathcal{W}_1 = \sqrt{a_1}\,\tilde{\mathcal{W}}_1(\tilde{\eta}), \quad \tilde{\eta} = \sqrt{a_1}\eta. \tag{2.109}$$

We rewrite equation (2.98) in terms of the long-wavelength variables $\tilde{\eta}$ and $\tilde{\mathcal{W}}_1$,

$$\mathcal{T}_1(\tilde{\mathcal{W}}_1) + \mathcal{M}_1(\tilde{\mathcal{W}}_1) + a_1^2\mathcal{S}_1(\tilde{\mathcal{W}}_1) = 0. \tag{2.110}$$

The highest derivative $\nabla_\eta^2\nabla_\eta^2$ in the transformed equation (2.110) is multiplied by a small parameter a_1^2 which makes it a singular perturbation. The solution to the unperturbed part of equation (2.110),

$$\mathcal{T}_1(\tilde{\mathcal{W}}_1) + \mathcal{M}_1(\tilde{\mathcal{W}}_1) = \frac{1}{4}\left(\tilde{\mathcal{W}}_1 - \tilde{\eta}\frac{\mathrm{d}\tilde{\mathcal{W}}_1}{\mathrm{d}\tilde{\eta}}\right) + \nabla_{\tilde{\eta}}^2\left(\frac{1}{\tilde{\mathcal{W}}_1}\right) = 0, \tag{2.111}$$

serves as an excellent approximation to the full problem except for the near-field region which would require a different rescaling of η and $\mathcal{W}_1$ other than (2.109).

It's standard to recast a second order inhomogeneous ordinary differential equation into a three-dimensional autonomous dynamical system. For example, with $\mathbb{X} = \mathrm{d}\tilde{\mathcal{W}}_1/\mathrm{d}\tilde{\eta}$, $\mathbb{Y} = \tilde{\mathcal{W}}_1$, $\mathbb{Z} = \tilde{\eta}$ and $\mathbb{T} = \tilde{\eta}$ introduced, it's straightforward to show that the corresponding autonomous system $\mathrm{d}[\mathbb{X},\mathbb{Y},\mathbb{Z}]^\top/\mathrm{d}\mathbb{T} = \mathbb{F}(\mathbb{X},\mathbb{Y},\mathbb{Z}) = [\mathrm{function}(\mathbb{X},\mathbb{Y},\mathbb{Z}),\mathbb{X},1]^\top$. However, the invariance of equation (2.111) under long-wavelength transformation (2.109) immediately suggests a symmetry reduction in the dimension of the resulting dynamical system. If instead we define

$$\mathbb{X} = \frac{1}{\tilde{\mathcal{W}}_1^2}\frac{\mathrm{d}\tilde{\mathcal{W}}_1}{\mathrm{d}\tilde{\eta}}, \quad \mathbb{Y} = \frac{\tilde{\eta}}{\tilde{\mathcal{W}}_1}\frac{\mathrm{d}\tilde{\mathcal{W}}_1}{\mathrm{d}\tilde{\eta}}, \quad \mathbb{T} = \ln|\tilde{\eta}|, \tag{2.112}$$

then the second order ODE (2.111) is mapped onto a first order autonomous dynamical system of only two dimensions,

$$\frac{\mathrm{d}}{\mathrm{d}\mathbb{T}}\begin{bmatrix}\mathbb{X}\\ \mathbb{Y}\end{bmatrix} = \mathbb{F}(\mathbb{X},\mathbb{Y}) = \begin{cases} \begin{bmatrix} \mathbb{Y}(1-\mathbb{Y})/(4\mathbb{X}) \\ \mathbb{Y}^2(1-\mathbb{Y})/(4\mathbb{X}^2) + \mathbb{Y}(1+\mathbb{Y}) \end{bmatrix}, & (\mathrm{rectilinear}) \\ \begin{bmatrix} \mathbb{Y}(1-\mathbb{Y})/(4\mathbb{X}) - \mathbb{X} \\ \mathbb{Y}^2(1-\mathbb{Y})/(4\mathbb{X}^2) + \mathbb{Y}^2 \end{bmatrix}. & (\mathrm{axisymmetric}) \end{cases} \tag{2.113}$$

It's easy to verify that the solution of $\tilde{\mathcal{W}}_1$ at $\tilde{\eta} = 0$ is mapped to the origin $(0,0)$ in the $(\mathbb{X},\mathbb{Y})$-phase plane while the far-field linear asymptope of $\tilde{\mathcal{W}}_1$ is mapped to the point $(0,1)$. The phase portrait of vector field $\mathbb{F}(\mathbb{X},\mathbb{Y})$ shown in figure 2.8 was created with the symbolic mathematical computation program (Wolfram Research, 2019). We immediately observe that there are infinitely many trajectories connecting the two singularities, a hyperbolic point at $(0,0)$ and a sink point at $(0,1)$. Although all of these trajectories have a linear asymptope, there is only one unique trajectory such that the derivatives of the solution $\tilde{\mathcal{W}}_1$ that corresponds to this trajectory is bounded near

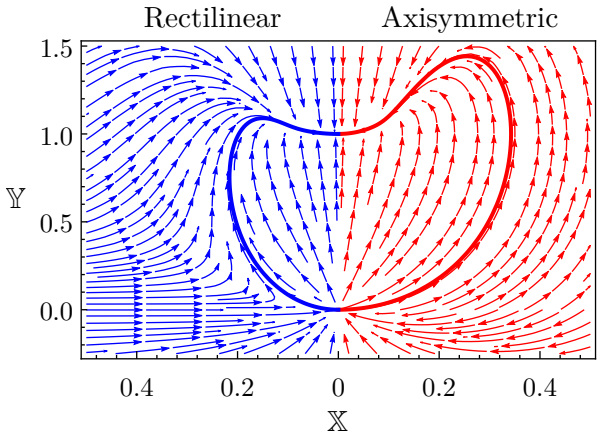

Figure 2.8: Phase portrait (arrow) of dynamical system (2.113): a hyperbolic fixed point at $(0,0)$, a saddle point $(0,1)$ and the two unique trajectories (solid line) that are continuous at all orders.

$\tilde{\eta}=0$. Note each trajectory shooting out of $(0,0)$ can be characterized by its exiting slope $\mathrm{d}\mathbb{Y}/\mathrm{d}\mathbb{X}$ in the neighborhood of $(0,0)$. The local behavior of the vector field near $(\mathbb{X},\mathbb{Y})=(0,0)$ can be mapped back to the corresponding local structure of $\tilde{\mathcal{W}}_1$ near $\tilde{\eta}=0$,

$$\left.\begin{aligned}\mathbb{Y}\approx c\,\mathbb{X}^2+\ldots \Longleftrightarrow \tilde{\mathcal{W}}_1\approx \tilde{\mathcal{W}}_1(0)+\frac{\tilde{\eta}^2}{2}\frac{\mathrm{d}^2\tilde{\mathcal{W}}_1}{\mathrm{d}\tilde{\eta}^2}\Big|_{\tilde{\eta}=0}+\ldots,\\ \mathbb{Y}\approx c\,\mathbb{X}+\ldots \Longleftrightarrow \tilde{\mathcal{W}}_1\approx \frac{\text{const.}}{\tilde{\eta}}+\ldots.\end{aligned}\right\} \tag{2.114}$$

For $\tilde{\mathcal{W}}_1$ to well behave near $\tilde{\eta}=0$, the corresponding trajectory near the origin of $(\mathbb{X},\mathbb{Y})$-phase plane must be locally parabolic instead of linear. We plot the two such unique trajectories (thick lines) in figure 2.8 for both rectilinear and axisymmetric cases. This exercise implies that if we ignore the small scale details induced by the singularly perturbed capillary term $a_1^2\mathcal{S}_1$ near $\eta=0$, the solutions $\mathcal{W}_1(\eta)$ to the similarity equation (2.98) shall all collapse onto a single unique trajectory in the long-wavelength phase space.

WKBJ approximation

As we discussed in the last section, all solutions $\mathcal{W}_1(\eta)$ to ODE (2.98) are expected to converge to a linear asymptote, presumably of different slopes. The algebraic expansion (2.107) only captures perturbative corrections to the linear far-field asymptope. Instead of seeking a power series approximation (2.107), we pursue a WKBJ-type approximation (Bender and Orszag, 1999) in the form

$$\mathcal{W}_1(\eta)=a_1\eta+\Delta\mathcal{W}(\eta), \tag{2.115}$$

where the WKBJ ansatz

$$\Delta\mathcal{W}(\eta) = \exp\left[\frac{1}{\delta}\sum_{k=0}^{\infty}\delta^k S_k(\xi)\right], \quad \delta = \nu^{4/3}, \quad \xi = \nu\eta \tag{2.116}$$

measures deviations from the linear asymptote with the asymptotic scaling δ and slow-varying coordinate ξ for some small parameter $\nu \ll 1$. Substituting ansatz (2.115) into the original ODE (2.98) and setting coefficients of the leading order terms to zero yield

$$\left.\begin{aligned} O(\delta^{-1}): \quad & \frac{1}{4}\xi\frac{\mathrm{d}S_0}{\mathrm{d}\xi} + \Big(\frac{\mathrm{d}S_0}{\mathrm{d}\xi}\Big)^4 = 0, \\ O(\delta^{0}): \quad & \Big[\frac{1}{4}\xi + 4\Big(\frac{\mathrm{d}S_0}{\mathrm{d}\xi}\Big)^3\Big]\frac{\mathrm{d}S_1}{\mathrm{d}\xi} = \frac{1}{4} - 6\Big(\frac{\mathrm{d}S_0}{\mathrm{d}\xi}\Big)^2\frac{\mathrm{d}^2S_0}{\mathrm{d}\xi^2} - \underbrace{\frac{2}{\xi}\Big(\frac{\mathrm{d}S_0}{\mathrm{d}\xi}\Big)^3}_{\text{if axisymmetric}}. \end{aligned}\right\} \tag{2.117}$$

The solution to equation (2.117) is straightforward. The fact that $\mathrm{d}S_0/\mathrm{d}\xi$ belongs to the four roots (two real and two complex) of the fourth degree polynomial $\xi(\xi^3 + \xi/4) = 0$ leads to four possible modes of the far-field behavior,

$$\Delta\mathcal{W} \approx \beta_0\eta + \sum_{k=0}^{3}\frac{\beta_k}{\eta^\alpha}\exp\Big[-\frac{3}{4^{4/3}}e^{i2\pi k/3}\eta^{4/3}\Big] + O(\eta^{-3}), \tag{2.118}$$

where $\alpha = 1$ for rectilinear geometry and $= 5/3$ for axisymmetric. WKBJ approximation (2.118) sometimes is referred to as a non-perturbative method because the Taylor expansion of $\Delta\mathcal{W}$ (excluding the β_0 term) in the small parameter η^{-1} is zero at every order. Such contribution is not visible in any order of the perturbative approximation (2.107).

From equation (2.118), we see that the β_1- and β_2- modes in the summation undergo divergent oscillatory growth whereas the two remaining non-vanishing modes proportional β_0 and β_3 simply reflect an infinitesimal shift in the far-field slope a_1 and a super-exponential decay, respectively. In order to satisfy the far-field condition (i.e. convergence to $a_1\eta$), we must require $\beta_0 = \beta_1 = \beta_2 = 0$. However, combined with the two symmetry conditions (2.105) at $\eta = 0$ which $\mathcal{W}_1$ must satisfy, this gives a total of five constraints on the solution of a fourth order differential equation—the problem (2.98) with boundary conditions (2.105) and (2.106) is in fact over determined. This overdeterminancy is a classic sign of a beyond-all-orders eigenvalue problem: the solutions to equation (2.98), if exist, can only be expected to exist for specific values of a_1, i.e. must be discrete and locally unique in the far-field asymptotic slope a_1 (we think of the solution family $\mathcal{W}_1$ as being parameterized by a_1). The discrete selection mechanism is made clear by using exponential asymptotics which has been successfully applied to the self-similar solutions of thin film equation during the process of van der Waals-driven rupture (Chapman, Trinh, and Witelski, 2013).

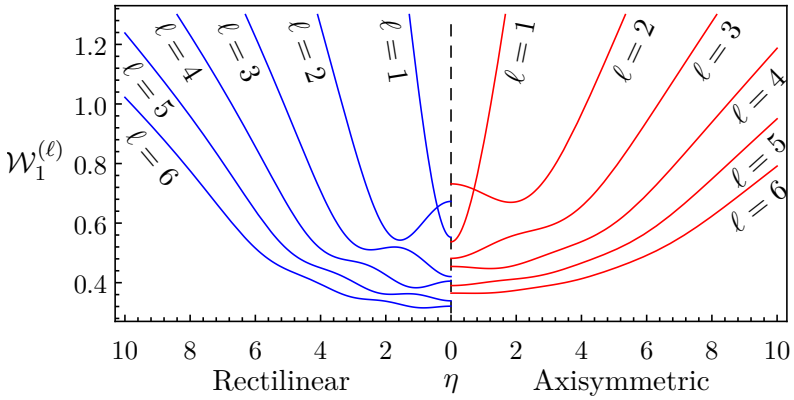

Figure 2.9: Leading order self-similar solutions $\mathcal{W}_1^{(\ell)}(\eta)$ of equation (2.98). Only the first six convergent solutions are shown.

Numerical solution

In order to compute the self-similar solutions, we truncate the semi-infinite domain at a sufficiently large distance L and then project equation (2.98) into the finite element space over interval $[0, L]$. We impose $\mathrm{d}\mathcal{W}_1/\mathrm{d}\eta = \mathrm{d}^3\mathcal{W}_1/\mathrm{d}\eta^3 = 0$ at $\eta = 0$ to enforce symmetry condition and a constraint $\mathcal{T}_1(\mathcal{W}_1) = 0$ at $\eta = L$ to eliminate the two growing modes predicted by (2.118). The resulting discretized system of equations is solved by Newton iteration. The initial guess of each iteration is in the form of a hyperbola $(a^2 + b^2\eta^2)^{1/2}$ with b being an adjustable parameter for asymptotic linear slope. Given a range of b-values swept, the solver (COMSOL Multiphysics, Inc. V5.3, 2017) only converges to a discrete family of solutions. The numerical solutions to equation (2.98) are computed on a finite domain of sufficiently long sizes, i.e. $L = 50$, 100 and 200, to preclude finite distance effects. The results also converge upon progressive mesh refinement as the finite domain $[0, L]$ is discretized into 10^3, 10^4 and 10^5 elements. Shown in figure 2.9 are the first six similarity solutions with corresponding numerical values listed in table 2.1. The asymptotic interface slopes of the conical tip for axisymmetric geometry are always smaller than the slopes for rectilinear geometry, as expected. The axisymmetric solutions also display weaker oscillatory behavior, likely due to suppression by the capillary pressure associated with the additional term in the interface curvature. The fundamental mode $\ell = 1$ exhibits no oscillatory behavior unlike the higher order solutions $\ell \geq 2$.

Next we compare the fitting coefficients from the asymptotic self-similar analysis of equation (2.98) with those obtained from direct numerical simulations of equation (2.64), which are plotted in figure 2.5. To the leading order, if we assume $1 - H_{\mathrm{apex}} \approx \varepsilon\mathcal{W}_1^{(\ell)}(0)$ then it can be shown that the intercept values for the log-log plot in figure 2.5(b) are

ℓ	$\lim_{\eta\to\infty} \mathrm{d}\mathcal{W}_1^{(\ell)}/\mathrm{d}\eta$		$\mathcal{W}_1^{(\ell)}(0)$		$\nabla_\eta^2 \mathcal{W}_1^{(\ell)}$	
	X	R	X	R	X	R
1	1.0437	0.7639	0.5526	0.5372	1.2082	1.5563
2	0.3430	0.2474	0.6728	0.7317	-0.2316	-0.1624
3	0.2145	0.1610	0.4204	0.4816	0.2021	0.1669
4	0.1580	0.1196	0.4052	0.4544	-0.0884	-0.0438
5	0.1257	0.0962	0.3390	0.3902	0.0792	0.0526
6	0.1046	0.0806	0.3211	0.3649	-0.0364	-0.0087

Table 2.1: Asymptotic values of the interface slope, apex height and apex curvature for the leading order solution $\mathcal{W}_1$ to equation (2.98). The columns with headers X and R denote values of the first six solutions $\mathcal{W}_1^{(\ell)}$ found for rectilinear and axisymmetric geometry, respectively.

approximately given by

$$\log_{10} \frac{\partial H}{\partial \tau}\Big|_{\text{apex}} \approx -3\log_{10}(1-H_{\text{apex}}) + 4\log_{10}\left(\mathcal{W}_1^{(\ell)}(0)\right) - \log_{10} 4, \tag{2.119}$$

$$\log_{10} \nabla_\parallel H^2\Big|_{\text{apex}} \approx -\log_{10}(1-H_{\text{apex}}) + \log_{10}\left(\mathcal{W}_1^{(p)}(0)\nabla_\parallel \mathcal{W}_1^{(\ell)}|_{\eta=0}\right) . \tag{2.120}$$

Substitution of the values for $\ell = 1$ from table 2.1 into these expressions yields intercept values for $\partial H/\partial\tau|_{\text{apex}}$ equal to -1.632 (rectilinear) and -1.681 (axisymmetric). Likewise, the intercept values for $\nabla_\parallel^2 H|_{\text{apex}}$ equal -0.175 (rectilinear) and -0.078 (axisymmetric). These predicted values are in excellent agreement with the numerical intercept values (shown in parentheses) in figure 2.5(c). Additionally, the asymptotic values of the interface slope $\lim_{\eta\to\infty} \mathrm{d}\mathcal{W}_1^{(1)}/\mathrm{d}\eta$ given in table 2.1 show good agreement when superimposed on the profiles in figure 2.5(d). The asymptotic values from the self-similar theory are predicted to be 1.0437 (rectilinear) and 0.7639 (axisymmetric) while the numerical results of the time-dependent simulations yielded 1.044 and 0.764. Converting back to dimensional form, the value of conical tip slope is given by the relation

$$\text{Conical tip slope} = \sqrt{\frac{\sigma_T \Delta T}{\sigma_o}\frac{3\kappa}{2(1-\kappa)}} \times \lim_{\eta\to\infty} \frac{\mathrm{d}\mathcal{W}_1^{(1)}}{\mathrm{d}\eta} . \tag{2.121}$$

Modal stability of the self-similar solution

In Section 2.5, it is shown that the numerical solution to the full nonlinear equation given by equation (2.64) asymptotes to a fluid elongation resembling a cuspidal shape capped by a conical tip. The asymptotic analysis in this section reveals that the numerical solution for this shape corresponds identically to the fundamental solution $\mathcal{W}^{(1)}$. A general analytic proof of why the time-dependent numerical solution always converges to this fundamental solution and not other solutions $\mathcal{W}^{(\ell\geq 2)}$ is beyond the scope of this work. Further examination of this finding by implementing a conventional linear stability analysis of equation (2.64) about evolving self-similar solution $\mathcal{W}_1(\eta)$ is a non-trivial

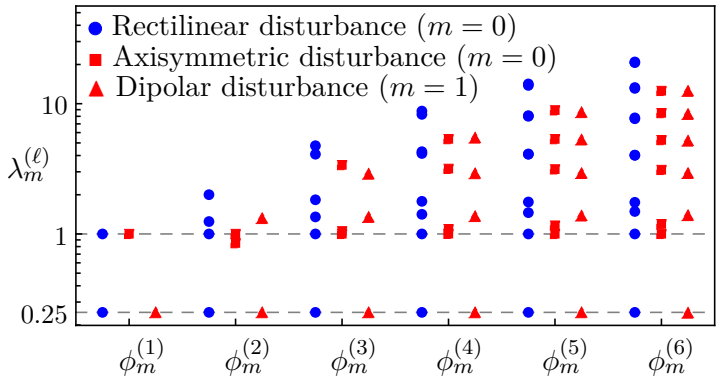

Figure 2.10: Discrete eigenvalue spectrum $\lambda_m^{(\ell)}$ of equation (2.123) for perturbations $\phi_m^{(\ell)}$ to the $\mathcal{W}_1^{(\ell)}$ $(\ell = 1 - 6)$ base state solutions of equation (2.98) for rectilinear $(m = 0)$, axisymmetric $(m = 0)$ and dipolar $(m = 1)$ disturbances.

exercise because of the multiscale nature (2.94) of the self-similar base state solutions, which evolve on multiple time scales $\{\varepsilon^n\}_{n=1}^{\infty}$. However, since both the numerical and analytic solutions suggest that the late stage dynamics of equation (2.64) towards the conic singularity is dominated by the term $\mathcal{W}^{(1)}$ described by the locally truncated PDE (2.93), it suffices then to consider infinitesimal perturbations described by

$$1 - H = \varepsilon \mathcal{W}_1^{(\ell)}(\eta) + \varepsilon^{1-4\lambda} \sum_{m=0}^{\infty} e^{im\theta} \phi_m^{(\ell)}(\eta), \tag{2.122}$$

where $|\phi_m^{(\ell)}(\eta)| \ll 1$ denotes an infinitesimal modal perturbation to $\mathcal{W}_1^{(\ell)}(\eta)$, θ is the polar angle in cylindrical coordinates and ε is time-to-singularity variable defined in equation (2.94). Substituting ansatz (2.122) into the truncated PDE (2.93) and collecting terms that are linear in $\phi_m^{(\ell)}(\eta)$ result in an eigenvalue problem:

$$\mathcal{T}_1(\phi_m^{(\ell)}) + \mathcal{S}_1(\phi_m^{(\ell)}) + \delta \mathcal{M}_1(\mathcal{W}_1^{(\ell)}; \phi_m^{(\ell)}) = \lambda_m^{(\ell)} \phi_m^{(\ell)} \ , \tag{2.123}$$

where the linearized operator

$$\delta \mathcal{M}_1(\mathcal{W}_1^{(\ell)}; \phi_m^{(\ell)}) = -\nabla_{(\eta,\theta)}^2 \left[\frac{\phi_m^{(\ell)}}{(\mathcal{W}_1^{(\ell)})^2} \right] \tag{2.124}$$

is formally the Fréchet derivative of operator $\mathcal{M}_1(\mathcal{W}_1^{(\ell)})$ and

$$\nabla_{(\eta,\theta)}^2 = \nabla_\eta^2 + \frac{1}{\eta^2} \frac{\partial^2}{\partial \theta^2} \tag{2.125}$$

is the full Laplacian operator in terms of both radial coordinate η and angular coordinate θ. In the same vein, differential operators of $\mathcal{S}_1$ defined in (2.100) must also be expanded to include the angular dependence on θ. We only consider localized disturbances to the

base state $\mathcal{W}_1^{(\ell)}$ such that the disturbed state given by (2.122) still preserves the same linear asymptote of $\mathcal{W}_1^{(\ell)}$ in the far field. It is then required that

$$\mathcal{T}_1(\phi_m^{(\ell)}) - \lambda_m^{(\ell)}\phi_m^{(\ell)} \to 0 \quad \text{as} \quad \eta \to \infty, \tag{2.126}$$

which yields the far-field solution $\phi_m^{(\ell)} \propto \eta^{1-4\lambda_m^{(\ell)}}$. Here, positive eigenvalues $\lambda_m^{(\ell)}$ reflect modal perturbations $\phi_m^{(\ell)}$ with algebraic growth $\varepsilon^{1-4\lambda_m^{(\ell)}}$, which is faster than the growth $\varepsilon = (\tau_s - \tau)^{1/4}$ of the ℓ-th base state solution $\mathcal{W}_1^{(\ell)}$, therefore considered unstable. We also note that, since the leading order PDE (2.93) is translationally invariant in both space and time, for each value of ℓ there must exist at least two eigenvalues (and eigenfunctions) reflecting these symmetries. The actions of these invariant symmetries lead to the exact eigenvalues and eigenfunctions,

$$\left.\begin{aligned} \text{Temporal shift}: \quad \tau_s \to \tau_s + \delta, \qquad & \lambda_0^{(\ell)} = 1, \quad \phi_0^{(\ell)} = \mathcal{T}_1(\mathcal{W}_1^{(\ell)}), \\ \text{Spatial shift (rectilinear)}: \quad X_s \to X_s + \delta, \qquad & \lambda_1^{(\ell)} = \frac{1}{4}, \quad \phi_1^{(\ell)} = \frac{\mathrm{d}\mathcal{W}_1^{(\ell)}}{\mathrm{d}\eta}, \\ \text{Spatial shift (axisymmetric)}: \boldsymbol{X}_s \to \boldsymbol{X}_s + \begin{bmatrix}\delta \\ 0\end{bmatrix}, \quad & \lambda_1^{(\ell)} = \frac{1}{4}, \quad \phi_1^{(\ell)} = \frac{\mathrm{d}\mathcal{W}_1^{(\ell)}}{\mathrm{d}\eta}\cos\theta. \end{aligned}\right\} \tag{2.127}$$

These exact eigenmodes correspond to infinitesimal shifts in the singular time τ_s with eigenvalue $\lambda_0^{(\ell)} = 1$ and in the singular point $\boldsymbol{X}_s$ (we set $\boldsymbol{X}_s = (0,0)$ for simplicity) along the X-axis with eigenvalue $\lambda_1^{(\ell)} = 1/4$.

Plotted in figure 2.10 is the eigenvalue spectrum $\lambda_m^{(\ell)}$ for infinitesimal modal perturbations $\phi_m^{(\ell)}$ for the first six self-similar base state solutions $\mathcal{W}_1^{(\ell)}$ where $\ell = 1 - 6$. Each solution contains 2ℓ eigenvalues. Irrespective of the geometry, the fundamental solution $\mathcal{W}_1^{(1)}$ is the only solution with no positive eigenvalues aside from $1/4$ and 1. The solution $\mathcal{W}_1^{(1)}$ is therefore the only solution that is linearly stable to perturbations. The remaining positive eigenvalues increase in magnitude with increasing ℓ, indicating more rapid growth and instability associated with the coefficient $\varepsilon^{1-4\lambda}$ multiplying the last term in equation (2.122). The numerical simulations described in Section 2.5 and plotted in figure 2.5 and 2.6 are always found to locally asymptote to the fundamental solution $\mathcal{W}_1^{(1)}$. Similar strong convergence to the stable fundamental solution has previously been reported for the thin film equation describing van der Waals rupture (Witelski and Bernoff, 1999) shown in figure 2.1. In that example, initialization of the thin film equation by the corresponding solution $\mathcal{W}_1^{(\ell\geq 2)}$ for that problem leads to a different global liquid film configuration—however, the local behavior in the vicinity of the line or point rupture converges to the fundamental mode $\mathcal{W}_1^{(1)}$. A full investigation of the local scaling behavior leading to self-similar cuspidal formation in the thermocapillary system for initial conditions resembling higher order ($\ell \geq 2$) base solutions is left for further study. It is anticipated that irrespective of the initial condition, simulation of

the full nonlinear evolution equation given by equation (2.64) will still yield film shapes dominated by $\mathcal{W}_1^{(1)}$ in the region of the conical tip since $\mathcal{W}_1^{(1)}$ is the only self-similar solution found to be linearly stable.

2.7 Conclusion

The analysis and simulations presented in this work reveal how surface shear forces due to runaway thermocapillary stresses generate fluid protrusions resembling cuspidal shapes capped by a conical tip. This finding expands the category of hydrodynamic flows known to form stable cuspidal shapes to include thin film systems subject to interfacial shear, where the driving force is oriented parallel to the moving interface. The asymptotic analysis reveals how the conical tip undergoes self-focusing toward a virtual attractor state characterized by a line (rectilinear case) or point (axisymmetric case) singularity via a robust self-similar process. The asymptotic derivation also yields an analytic relation for the slope of the conical tip which should prove useful to experimentalists who wish to design microarrays with specified tip slopes for beam shaping, antireflective coatings, or other textured substrates.

The original system described, based on a thin uniform molten film confined by parallel solid boundaries maintained at different uniform temperature, is known to support a linear instability that forms arrays of rounded protrusions resembling microlenses. These protrusions are expected to evolve into arrays of cuspidal shapes with conical tips by the nonlinear dynamical process described since the thermal gradient across the gas layer just above the fluid tip progressively increases in time, leading to a runaway process. We anticipate that any initial film configuration that contains local maxima in film thickness, whether or not periodically arranged and however initially seeded, will also trigger cusp formation at such locations given the local, self-similar nature of the underlying growth process. We also anticipate that evaporative effects (Grigoriev and Qin, 2018) in nanofilms containing volatile components which require that the temperature of the warmer substrate exceed the vapor saturation temperature, an effect not considered in this work, may preclude self-similarity in the apical region.

We have previously shown (McLeod, Y. Liu, and Troian, 2011; McLeod and Troian, 2011; Fiedler and Troian, 2016; Fiedler, McLeod, and Troian, 2019) that the evolution process leading to rounded lenslet microarrays can be terminated on demand and the liquid shapes affixed in place by dropping the temperature of both substrates below the solidification point. Rapid solidification of these liquid structures is made possible by two advantageous features: the large surface to volume ratios intrinsic to microscale or nanoscale films which facilitates rapid cooling and digital control over the temperature of the confining substrates. We fully expect that similar rapid solidification can be achieved once the desired conical protrusions have formed in order to solidify and affix their shape on demand. Perhaps alternative methods of flow control by laser manipulation,

previously applied to thin film thermocapillary spreading along a solid substrate, can also be used (Garnier, Grigoriev, and Schatz, 2003). In summary, we hope the theoretical analysis provided here helps guide development of a novel lithographic method for direct, non-contact fabrication of cuspidal microarrays, whose shapes would be more difficult, costly, or even impossible to fabricate by other means.

Chapter 3

COMPUTATIONAL ELECTROHYDRODYNAMIC LITHOGRAPHY OF DIELECTRIC FILMS

3.1 Electrically Induced Structure Formation in Thin Dielectric Film

Micro- and nano-fabrication techniques free of ultraviolet curing, chemical development and wet etching are attractive for a number of advantages such as simplifying fabrication procedures, enhancing product yield and cost-effectiveness. Chou, Zhuang, and Guo (1999) and Chou and Zhuang (1999) discovered for the first time that, by creating a heterogeneous distribution of polarization charges on the surface of dielectric liquids via a patterned top electrode, they were able to induce self-assembled microstructures of arbitrary shapes in in thin molten polymer films. Because the polymer melt thickness is ultrathin $\sim O(100\,\mathrm{nm})$, the observed lithographically induced self-assembly is not due to the instabilities from conventional mechanism such as the Rayleigh-Benárd thermal convection. They proposed an electrohydrodynamic (EHD) model based on the interplay between the interfacial Maxwell stress arsing from the surface charge in the polymer melt induced by the top electrode and hydrodynamic force in the thin polymer film. The method, later termed Electrohydrodynamic Lithography (EHL), has potential for important applications in the fabrication of polymer electronic and optoelectronic devices due to its fast dynamics and low cost.

Shortly after Chou's initial discovery, Schäffer et al. (2000) reported a similar technique based on the electrostatic forces experienced by a dielectric media exposed to an electric field gradient. They demonstrated self-assembled polymer film patterns replicated from the lateral structures of a topographically patterned electrode on a sub-micron length scale. In a subsequent work, Schäffer et al. (2001) refined Chou's electrohydrodynamic model and derived an expression of the characteristic wavelength $\lambda_{\max}$ of the fastest growing fluctuation for a uniform dielectric thin film subject to only two competing surface forces, i.e. the stabilizing capillary stress and the destabilizing Maxwell (electrostatic) stress. They also performed measurements on the correlation between the most unstable wavelength $\lambda_{\max}$ and the applied electric field strength using an unpatterned flat electrode. Their experimental data quantitatively agrees with the prediction from the theoretical EHD model without any adjustable parameters.

In fluid mechanics, EHL is considered as a branch of electrohydrodynamics, the theoretical development and mathematical modeling of which have a long history in literature. Many classical results, built on the early work of G. I. Taylor and McEwan (1965) and Melcher and Smith (1969), are summarized in a review paper by Saville (1997) on the effect of electric fields in the emerging instability of electrohydrodynamic systems featuring

two-phase interfaces. Typically a critical voltage is required to destabilize perturbations of intermediate wave number, the value of which depends whether the fluid is "perfect" or "leaky" dielectrics, that is, whether lateral transport of free charge on the interface is possible, whereas long and short wavelength disturbances are often stabilized by gravity and capillarity, respectively. The instability of conductive liquids, for example the case of liquid metal examined by Miskovsky et al. (1991), can be viewed as a perfect dielectrics of an infinite dielectric constant. The recent development of EHL is motivated by the intention of manipulating electrified liquid interfaces (e.g., films and droplets) on a much smaller scale where inertia and gravity are less important and lubrication approximation naturally applies. The linear stability of thin films in lubrication regime was thoroughly investigated for various situations including perfectly conductive media (Herminghaus, 1999; Schäffer et al., 2001), two-layer polymeric systems (Z. Lin et al., 2001), leaky dielectric fluids (Pease and Russel, 2002; Pease and Russel, 2003; Shankar and Sharma, 2004; Craster and Matar, 2005) and applied AC electric fields (S. A. Roberts and Kumar, 2009). Numerical simulations have elucidated the interfacial evolution and induced patterns of electrified thin films in late nonlinear stage when subject to nonlocal contribution of electric stress (Tseluiko and Papageorgiou, 2007), over substrate topography (Tseluiko, Blyth, Papageorgiou, and Vanden-broeck, 2008; Ramkrishnan and Kumar, 2014), driven by abruptly applied or removed electric fields (Corson et al., 2016) and under structured electrodes directly modeled by the two-dimensional Navier-Stokes equation (Tian, Shao, Ding, X. Li, X. Li, et al., 2011; Q. Yang, B. Q. Li, and Ding, 2013; H. Li et al., 2014) or reduced three-dimensional lubrication approximation (Wu, Pease, and Russel, 2005; Verma et al., 2005; Berendsen et al., 2013; Nazaripoor et al., 2016).

On experimental side, there have been substantial developments over the past decade in EHL aiming for a promising non-contact soft lithographic method due to its simple process, cost-effectiveness and high-resolution patterning. In a typical setup of EHL shown in figure 3.2, a thin layer of liquid polymer is first spin-coated on a flat substrate and then positioned below a patterned top electrode with protrusions of different shapes. An electric potential difference usually about $10 \sim 100$ volts is applied across the air gap maintained by spacers on the order of micrometers. The entire electrode-polymer-substrate system is heated above the glass transition temperature of the polymer and then maintained for a time period ranging from a few minutes to a few days. On some length scales, the polymer melt is unstable under the influence of the electric field imposed by the patterned electrode and self-assembles into array of pillars. The whole system is then cooled back to room temperature quickly to freeze the microstructures that have formed. The idea of shaping liquid with electrohydrodynamic forces has given birth to fruitful innovations in micro/nanotechnologies including electric field tweezers for surface characterization of liquid interface (Sakai and Yamamoto, 2006), surface-

charge writing of liquid film on dielectric substrates (Berendsen et al., 2013), bifocal microlenses via electrohydrodynamic reflow of prepatterned polymer (Tian, Shao, Ding, X. Li, and Hu, 2014; Hu et al., 2014) and patterning of ceramic TiO_2 micro/nanostructures (Voicu et al., 2007), low-viscosity polymer (Goldberg-Oppenheimer and Steiner, 2010), crystalline organic materials (Goldberg-Oppenheimer, Kohn, et al., 2012) and various inorganic functional materials (S. Lee et al., 2016).

As promising as it looks, EHL intended for a high-resolution lithographic method currently still suffers from a significant bottleneck, i.e. pattern fidelity. Generally speaking, the ultimate goal of any lithographic method at small scales is to manufacture certain user-specified micron- and submicron-size structures in faithful details. However, what most existing literature on the applications of EHL has demonstrated are large film areas packed with isolated micropillars (cylindrical protrusions) and parallel strips. As we will see in Section 3.2, this is due to the strong nonlinearity and unstable nature of electrohydrodyamic thin film. There are several factors contributing to the fidelity of replicated patterns in EHL. For example, pattern resolution is fundamentally constrained by the instability wavelength set by material and operating parameters of the system. Schäffer et al. (2001) derived the expression of the most unstable wavelength $\lambda_{\max}$ when a uniform film of dielectric constant ε_{liq} and thickness h_o overlaid by an air layer of dielectric constant ε_{air} destabilizes under a flat electrode of height d_o (see figure 3.2),

$$\lambda_{\max} = \frac{2\pi}{\varepsilon_{\text{liq}} - \varepsilon_{\text{air}}} \sqrt{\frac{\sigma \Delta\Psi}{\varepsilon_0 \varepsilon_{\text{air}} \varepsilon_{\text{liq}}}} \left(\frac{\Delta\Psi}{\varepsilon_{\text{liq}} d_o - (\varepsilon_{\text{liq}} - 1) h_o} \right)^{-3/2}, \tag{3.1}$$

where ε_0 is the vacuum permittivity, σ is the surface tension coefficient and $\Delta\Psi$ is the applied voltage difference. Expression (3.1) indicates that pattern resolution is limited by the ability to create a strong electric field strength $\sim \Delta\Psi/\varepsilon_{\text{liq}} d_o$ within a slender gap of width d_o against liquid surface tension. Another contributing factor is the proximity effect of electrode topography. In EHL, a structured electrode acts as a trigger to the onset of localized electrohydrodynamic instability concentrated under the region where electric field gradient is the strongest, e.g., below sharp edges of the electrode. The subsequent growth of patterns in dielectric liquid films is not only guided by the top electrode but also heavily influenced by the nonlinear propagation and interaction of these localized instabilities, which often result in isolated protrusions interleaved by unintended secondary structures between. There is also the temporal factor since EHL is a dynamic process after all. The fine details of electrode geometry, initially projected onto the liquid film through electric field, are lost overtime to the dissipative hydrodynamics within the viscous thin film unless electrode topography is properly engineered to account for pattern formation at late stages. Hence, achieving a faithful pattern transfer from an electrode with designated topography onto the surface of polymer melt is a nontrivial task on account of all these factors.

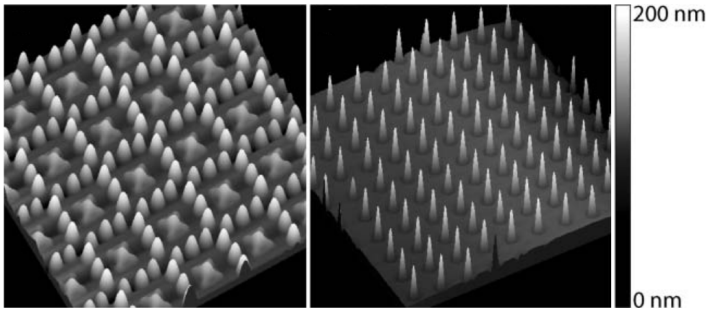

Figure 3.1: Atomic force microscopy images reveal formation of unintended structures when replicating design patterns in TiO_2 films. Electrode pattern used for the image on the left was a square lattice with three cylindrical protrusions on each side of the square and a simple square pattern for the image on the right. Adapted from Voicu et al. (2007) with permission from The Royal Society of Chemistry.

The problem of pattern fidelity is best illustrated in the experimental work of Voicu et al. (2007) on ceramic TiO_2 film patterning. The atomic force microscopy images shown in figure 3.1 are direct evidence of how pattern replications in dielectric liquid films can be plagued by intuitive designs of structured electrode. The measured film structures shown in the left figure formed under an electrode topography of a square lattice bordered by twelve cylindrical protrusions. During replication process, the film was locally depleted only next to the twelve columns which in turn led to unintended contraction of the material towards the center, leaving behind a pyramid-like film patch in the center of each square. The electrode pattern corresponding to the image on the right is a simple square block at the center of a larger square. However due to high-intensity electric field gradient near sharp edges and corners of the electrode, instead of a uniformly leveled film surface, isolated pillars were attracted to corners of each square. Note these pillars are not perfect cylinders as well, usually accompanied with oscillatory over- and undershooting at the bottom edge.

On the other hand, numerical simulations of the thin film model for perfect dielectric liquids are found to be in close agreement with the experimental results in the literature (Wu, Pease, and Russel, 2005; Nazaripoor et al., 2016). The predictive power of the EHD thin film model provides invaluable insights into the pattern formation driven by electrodes of specific geometries. For instance, using finite difference method Verma et al. (2005) demonstrated that, through fine-tuning the mean film thickness, applied voltage drop and the geometric parameters of an electrode decorated with deep grooves, it is possible to adjust the number density of the electric field induced micropillars as well as to suppress the formation of secondary structures in between. Wu, Pease, and Russel (2005) performed a weakly nonlinear analysis on the second and third order nonlinearities near the onset of nonlinear growth in EHD thin film, which indicates growth of hexagonal patterns is favored under a featureless (flat) electrode. Their numerical

simulations based on the fully nonlinear model suggests some "smart" electrode designs (e.g., replacing large flat protrusions with interconnected ridges) to achieve large areas of ordered patterns.

While these previous works all exhibited improvements of pattern fidelity to a certain degree, none of them managed to achieve precise replications of customized patterns even as simple as a triangle or a square. This is because their approaches were based on trials and errors over a finite set of material and geometry parameters (e.g., spacing between electrode features and average film thickness) while there are infinitely many possibilities in the design space of electrode topography not being fully explored yet. Furthermore, EHL is a dynamic process that relies on the strongly nonlinear transient evolution of liquid film driven by the structured electrode. The pattern transferring process from mask (electrode) to the target (liquid film) can be counter-intuitive and very different from other conventional lithographic processes that are usually steady and linear. For instance, the conventional optical proximity correction (O. W. Otto et al., 1994; Cobb and Zakhor, 1995; Ea and A. D. Brown, 2001; Granik, 2005), commonly employed by semiconductor industry during the process of photolithography, compensates for pattern errors due to diffraction effect of linear superposition of steady light fields by directly manipulating the geometric elements of optical mask. However for soft lithography methods such as EHL, the issue of nonlinearity and transient evolution must be properly addressed. A systematic treatment on the design of electrode topography beyond human intuition is required to improve pattern fidelity during the replication process.

Given input of a model predicting its outcome is called the "forward problem". The inverse of a forward problem, or simply the "inverse problem", is to deduce input based on an observed or desired outcome of the model (Vogel, 2002). In the context of EHL, observing final film shapes after hand-tuning electrode topography is precisely forward modeling. However for lithographic purposes, it is the inverse problem that needs to be addressed: given a user-specified target film profile, what is the optimal design of the top electrode topography guiding an initially flat dielectric liquid film towards the target shape as close as possible? In the theory of optimal control, a powerful computational framework, namely the adjoint method, has already been fully developed to tackle the inverse problem. In brief, the ajdoint method in general involves construction of an objective function with relevant (possibly nonlinear) constraints identified and efficient evaluation of constrained derivatives with respect to feasible design parameters. In modern design process of microelectromechanical systems (MEMS), the adjoint method is extensively used to improve fabrication quality and performance goals of MEMS devices, examples of which include, but not limited to, full wave optimization of microwave circuits (Alessandri, Mongiardo, and Sorrentino, 1993), systematic design of phononic band–gap materials and structures (Sigmund and J. S. Jensen, 2003), sensitiv-

ity analysis and topology optimization of photonic crystal devices (Veronis, Dutton, and Fan, 2004; J. S. Jensen and Sigmund, 2010), mask design for optical microlithography (Poonawala and Milanfar, 2007), geometrical shape optimization of complex electromagnetic components (Lalau-Keraly et al., 2013) and inverse design of nanophotonics subject to fabrication constraints (Piggott et al., 2017). Recently the adjoint method has even found its application in a tumor growth model to assist the optimization of spatiotemporal radiotherapy (Fujarewicz and Łakomiec, 2016). As a side note, the type of inverse problem we consider here belongs to a larger class of optimization problem, i.e. the shape optimization, which was originally examined for mechanical problems in continuum mechanics and is still an active research area currently. The adjoint method for shape optimization has yielded fruitful results in hydrodynamics including minimum drag hydrofoil profile in a viscous fluid (Pironneau, 1974), optimum plane diffuser of maximum static pressure rise (Çlabuk and Modi, 1992), design of fluid paths allowing minimum power dissipation (Borrvall and Petersson, 2002), full control of free surface liquids in physics-based animation (McNamara et al., 2004), optimal shape of capillary barriers between micro-channels and reservoirs on microfluidic biochips (Antil et al., 2010), control of fingering instability in gravity-driven lubrication flow by optimal substrate curvature (Balestra, Badaoui, et al., 2019), etc.

The outline of this chapter is as follows. In Section 3.2 we derive the governing evolution equation for a thin dielectric or conductive liquid layer subject to large Maxwell forces induced by a proximate electrode on top of a slender quiescent gas film. The slender geometry is known to give rise to an electrohydrodynamic instability (Schäffer et al., 2001). In additional to the nonexistence of energetically stable equilibrium film shapes, the self-similar analysis reveals a severe runaway process, i.e. self-reinforced formation of a genuine cusp in EHD thin film. The finite element method employed for the numerical simulation of the thin film equation is also discussed in details. We then illustrate the problem of pattern fidelity by finite element simulations of localized pillar growth under a top electrode patterned with a heart-like protrusion. In Section 3.3, we reformulate the ultimate goal of Electrohydrodynamic Lithography as a constrained inverse problem. Using elements of control theory, we analytically identify the optimality conditions that the optimal electrode topography must satisfy in order to eliminate the discrepancy between the desired structure and the evolving film profile. In Section 3.4, we present the discrete control algorithm using the adjoint method and provide implementation details particularly tailored for the finite element model developed in Section 3.2. In Section 3.5, we outline the procedure of nonlinear optimization. Our implementation of the control protocol is verified against a test problem. In the end, we demonstrate the optimal design of electrode topography that is able to produce a nearly perfect heart-like protrusion from an initially flat dielectric film.

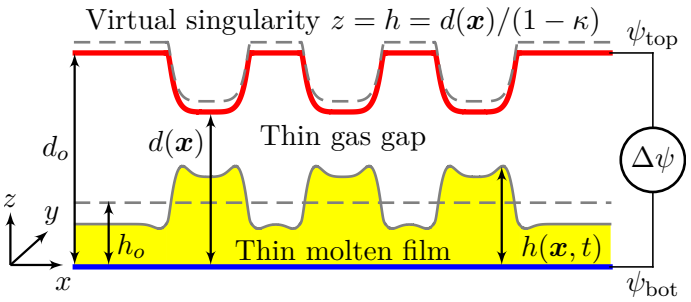

Figure 3.2: Sketch of a linearly unstable thin molten film overlaid by a gas layer. The gas/liquid bilayer is subject to a very large vertical electric field enforced by the uniform voltage difference $\Delta\psi = \psi_{\text{top}} - \psi_{\text{bot}}$ across the very small gap with characteristic width d_o, typically of a few microns, applied through a patterned electrode (red curve). Nominal vertical electric field strength, $\Delta\psi/d_o$, are estimated to be extremely large and range from about $10^7 - 10^8$ V/m (Schäffer et al., 2001). The governing interface equation contains a virtual singularity designated by the dashed line at $h(\boldsymbol{x},t) = d(\boldsymbol{x})/(1-\kappa)$ where $0 \leq \kappa < 1$. This singularity is not accessible to the dielectric film because it lies beyond the top electrode situated at $z = d(\boldsymbol{x})$. For perfectly conducting film ($\varepsilon_{\text{liq}} = \infty$ therefore $\kappa = 0$), the virtual singularity actually coincides with the top electrode.

3.2 Thin Film Model of Electrohydrodynamic Lithography (EHL)

The molten polymer layer is modeled as an incompressible Newtonian fluid. Electrohydrodynamic flow within the melt is driven by the jump in Maxwell stress across the gas/liquid interface due to the contrast of dielectric constant in each medium. In this chapter, we exclusively focus on the dynamics of perfect dielectric liquid films. The slender geometry of lithographic system allows us to directly apply the thin film equation (2.37) in its most general form derived from the classical lubrication theory in Section 2.2. In this section we provide a brief review on the derivation of the interfacial pressure P and tangential traction (if any) $\overline{\boldsymbol{F}}_{\parallel}$ present in the thin film equation (2.37). The formalism of interfacial Maxwell stresses adopts the approach oulined in the review article by Saville (1997) on electrohydynamics which however does not include the lubrication limit. Although as mentioned in Section 3.1 there are articles on the linear stability analysis of electrohydrodynamic thin film, to the best of author's knowledge, the first appearance of the full nonlinear evolution equation for perfect dielectric films under a flat electrode is due to Schäffer et al. (2001). Shortly after, Pease and Russel (2003) and Pease and Russel (2004) generalized the lubrication model to describe the effect of charge transport in leaky dielectric films. The equation was then immediately extended to the case of patterned electrodes (Wu and Russel, 2005; Wu, Pease, and Russel, 2005; Verma et al., 2005). The interested reader should consult these references for detailed discussions on the scaling argument used in lubrication approximation.

Electrohydrodynamic thin film equation

Assuming a perfect dielectric medium with no bulk free charges , the Maxwell equations simplify to the electrostatic (Laplace) equation in free space,

$$\nabla \cdot \varepsilon_0 \varepsilon \nabla \psi = 0, \tag{3.2}$$

where ε is the homogeneous isotropic dielectric constant of the medium and ε_0 is the vacuum permitivity. Interface conditions for electromagnetic fields (Jackson, 1999) require continuity of electric potential ψ and displacement field $-\varepsilon_0 \varepsilon \nabla \psi$ in the direction normal to the interface,

$$\left.\begin{aligned} \psi_{\text{air}} &= \psi_{\text{liq}}, \\ \boldsymbol{n} \cdot \varepsilon_0 \varepsilon_{\text{air}} \nabla \psi &= \boldsymbol{n} \cdot \varepsilon_0 \varepsilon_{\text{liq}} \nabla \psi, \end{aligned}\right\} \quad \text{at} \quad z = h. \tag{3.3}$$

We introduce the nondimensional electric potential,

$$\Psi = \frac{\psi - \psi_{\text{bot}}}{\Delta \psi}, \quad \Delta \psi = \psi_{\text{top}} - \psi_{\text{bot}}, \tag{3.4}$$

where $\Delta \psi$ is the voltage difference between the top electrode (ψ_{top}) and ground substrate (ψ_{top}) at the bottom. Under our previous choice of nondimensionlization employed in the slender limit, the electrostatic equation (3.2) subject to interface boundary condition (3.3) is identical to the heat transfer problem (2.49) within a slender gap in the thermocapillary model. As a result, the electrostatics problem is dominated by electric conduction along the vertical direction, $\partial^2 \Psi / \partial Z^2$, which yields a similar solution to the heat problem,

$$\Psi = \begin{cases} \dfrac{Z - (1-\kappa)H}{D - (1-\kappa)H} & \text{if} \quad H \le Z \le D(X,Y), \\ \dfrac{\kappa H}{D - (1-\kappa)H} & \text{if} \quad 0 \le Z \le H, \end{cases} \tag{3.5}$$

where the permittivity contrast parameter $\kappa = \varepsilon_{\text{air}}/\varepsilon_{\text{liq}}$ is defined alike. Note in the limit $\kappa \to 0$, the solution (3.5) to electric potential corresponds to a perfectly conducting material, e.g., a liquid metal film.

The new complication in electrohydrodynamic thin film is the additional interfacial traction $\boldsymbol{f}$ which arises when the (dimensional) Maxwell stress tensor

$$\boldsymbol{t} = \varepsilon \Big(\boldsymbol{e} \otimes \boldsymbol{e} - \frac{1}{2} |\boldsymbol{e}|^2 \mathbb{I} \Big) \tag{3.6}$$

suffers a discontinuity across the liquid/air interface (Saville, 1997),

$$\boldsymbol{f} = (\boldsymbol{t}_{\text{air}} - \boldsymbol{t}_{\text{liq}}) \boldsymbol{n}, \tag{3.7}$$

where $\boldsymbol{e}$ is the dimensional electric field. For an electrostatics system, the jump in Maxwell stress gives rise to normal traction forces only. To see this claim, let's consider the tangential traction expressed in terms of electric field components,

$$\boldsymbol{s}_\alpha \boldsymbol{t} \boldsymbol{n} = \boldsymbol{s}_\alpha \varepsilon \Big(\boldsymbol{e} \otimes \boldsymbol{e} - \frac{1}{2} |\boldsymbol{e}|^2 \mathbb{I} \Big) \boldsymbol{n} = \varepsilon (\boldsymbol{s}_\alpha \cdot \boldsymbol{e})(\boldsymbol{n} \cdot \boldsymbol{e}), \tag{3.8}$$

where ε and $\boldsymbol{e}$ can be the dielectric constant and electric field in the medium on either side of the interface ($\boldsymbol{s}_{\alpha=1,2}$ is the unit tangent vector of the interface). But we know displacement field is continuous across the interface, i.e. $-\boldsymbol{n}\cdot\varepsilon_{\text{air}}\boldsymbol{e}_{\text{air}} = -\boldsymbol{n}\cdot\varepsilon_{\text{liq}}\boldsymbol{e}_{\text{liq}}$, as well as the tangential components of electric field $\boldsymbol{e}$. Hence tangential stress (3.8) evaluated on either side of the interface immediately suggests $\boldsymbol{s}_\alpha\boldsymbol{t}_{\text{air}}\boldsymbol{n} = \boldsymbol{s}_\alpha\boldsymbol{t}_{\text{liq}}\boldsymbol{n}$ and therefore zero tangential traction. This leaves us with normal jump of the Maxwell stress only,

$$\boldsymbol{n}(\boldsymbol{t}_{\text{air}}-\boldsymbol{t}_{\text{liq}})\boldsymbol{n} = \frac{\varepsilon_{\text{air}}}{2}\Big[(\boldsymbol{n}\cdot\boldsymbol{e}_{\text{air}})^2-\sum_{\alpha=1}^{2}(\boldsymbol{s}_\alpha\cdot\boldsymbol{e}_{\text{air}})^2\Big]-\frac{\varepsilon_{\text{liq}}}{2}\Big[(\boldsymbol{n}\cdot\boldsymbol{e}_{\text{liq}})^2-\sum_{\alpha=1}^{2}(\boldsymbol{s}_\alpha\cdot\boldsymbol{e}_{\text{liq}})^2\Big]. \tag{3.9}$$

Nondimensionlizing the normal traction (3.9) with the lubrication scales and the expanding electric field $\boldsymbol{E}$, normal vector $\boldsymbol{N}$ and tangent vectors $\boldsymbol{S}_\alpha$ as usual yield

$$\boldsymbol{N}(\boldsymbol{T}_{\text{air}}-\boldsymbol{T}_{\text{liq}})\boldsymbol{N} = \frac{\varepsilon_0\Delta\Psi^2}{2[L]^2[P]}\left[\varepsilon_{\text{air}}\Big(\frac{1}{\epsilon}\frac{\partial\Psi_{\text{air}}}{\partial Z}\Big)^2-\varepsilon_{\text{liq}}\Big(\frac{1}{\epsilon}\frac{\partial\Psi_{\text{liq}}}{\partial Z}\Big)^2\right]+O(1). \tag{3.10}$$

Substituting the leading order solution to Ψ found in (3.5) leads to the leading order approximation to the normal traction $\boldsymbol{F} = F_N\boldsymbol{N}$ produced by Maxwell stress in terms of reference pressure $[P]$ and length scale $[L]$ defined previously,

$$F_N = \frac{1}{\epsilon^2}\frac{\varepsilon_{\text{air}}\varepsilon_0\Delta\Psi^2}{[L]^2[P]}\frac{1-\kappa}{2[D(X,Y)-(1-\kappa)H]^2}. \tag{3.11}$$

To gain more insights into the normal traction (3.11), we define $[E]$ to be the characteristic electric field strength between the top electrode and the bottom substrate,

$$[E] = \frac{\Delta\Psi}{[H]}, \quad \overline{\text{Ec}} = \frac{1}{\epsilon}\frac{\varepsilon_0\varepsilon_{\text{air}}[E]^2}{\sigma/[L]}, \tag{3.12}$$

where $\overline{\text{Ec}}$ is the (rescaled) electric-capillary number. The total pressure P at film interface is then given by

$$P = -\frac{1}{\overline{\text{Ca}}}\nabla_\parallel^2 H+\frac{\text{Bo}}{\overline{\text{Ca}}}\nabla_\parallel^2 H-\frac{\overline{\text{Ec}}}{\overline{\text{Ca}}}\frac{1-\kappa}{2[D-(1-\kappa)H]^2}. \tag{3.13}$$

In micro- and nanofabrications where electrohydrodynamic thin film model is meant to apply, the lateral length scale $[L]\sim O(\text{micron})$ or even smaller and the effect of gravity soon becomes negligible compared to other interfacial forces. Substituting interfacial pressure P from (3.13) into the conservative form (2.37) of the thin film equation with gravity term dropped yields the electrohydrodynamics of a viscous thin liquid film,

$$\frac{\partial H}{\partial\tau}+\nabla_\parallel\cdot\left\{\frac{1}{3\overline{\text{Ca}}}H^3\nabla_\parallel\left[\nabla_\parallel^2 H+\overline{\text{Ec}}\,\frac{1-\kappa}{2}\frac{1}{[D-(1-\kappa)H]^2}\right]\right\}=0. \tag{3.14}$$

Partial differential equation (3.14) is identical to the previously derived equation for perfect dielectric films (Schäffer et al., 2001; Pease and Russel, 2004; Wu and Russel, 2005; Verma et al., 2005; Nazaripoor et al., 2016). We further apply transformations,

$$H_* = \frac{H}{[H_*]}, \quad D_* = \frac{D}{[H_*]}, \quad \boldsymbol{X}_* = \frac{\boldsymbol{X}}{[X_*]}, \quad \tau_* = \frac{\tau}{[\tau_*]}, \tag{3.15}$$

similar to the ones for the thermocapillary equation (2.62), where the scalings are given by

$$[H_*] = \frac{D_{\rm ref}}{1-\kappa}, \quad [X_*] = \frac{1}{1-\kappa}\sqrt{\frac{2}{\overline{\rm Ec}}}D_{\rm ref}^{3/2}, \quad [\tau_*] = \frac{12}{1-\kappa}\frac{\overline{\rm Ca}}{\overline{\rm Ec}^2}D_{\rm ref}^3. \tag{3.16}$$

Here $D_{\rm ref}$ represents some reference height of the electrode topography $D(X,Y)$, for instance, the spatial average or the maximum/minimum height of $D(X,Y)$ over a periodic domain in the (X,Y)-plane. In what follows we drop the $(\cdot)_*$ subscription on all the transformed variables and recast equation (3.14) into a parameter-free form of gradient flow,

$$\frac{\partial H}{\partial \tau} = \nabla_{\parallel}\cdot\left\{\mathcal{M}(H)\nabla_{\parallel}\left[-\nabla_{\parallel}^2 H - \Pi(H,D)\right]\right\} \tag{3.17}$$

with the usual mobility coefficient $\mathcal{M} = H^3$ and the effective electrostatic pressure

$$\Pi(H,D) = \frac{1}{(D-H)^2} \tag{3.18}$$

which is inversely proportional to the distance squared between the local height of the electrode topography $D(X,Y)$ and the local thickness of the instantaneous film profile $H(X,Y,\tau)$. Although in the rescaled model (3.17), the physical electrode is now positioned at $Z = D(X,Y)/(1-\kappa)$, we still refer to the virtual singularity $D(X,Y)$ as the electrode topography. This is motivated by the consideration that, unlike the thermocapillary problem in Chapter 2, we are less concerned with making a distinction between the virtual singularity and the physical electrode as the goal is to achieve controlled pattern growth in the early and intermediate stages of the evolution rather than to rely on the runaway process of localized cusp-like pillar growth attracted by the virtual singularity.

As for boundary conditions, in this work we restrict ourselves to periodic boundary condition on both H and D for a periodic domain Ω in the (X,Y)-plane. This is justified by the practical purpose of soft lithography which is to achieve efficient fabrication of massive arrays of identical structures at micro- and nanoscales. Though other types of boundary conditions such as flux injection rate of liquid material through the boundaries of a non-periodic domain are certainly possible and left for future studies.

Some rough estimates on the regime where the electrostatic-hydrodynamics thin film equation (3.17) is expected to operate can be obtained from the electric-capillary number $\overline{\rm Ec}$ defined in (3.12). For a length scale $[L] \sim O(10\,\mathrm{micron})$, surface tension $\sigma \sim 0.078$ $\mathrm{N/m}$ (e.g., water-air interface) and a relative permittivity $\varepsilon_{\rm air} \sim 1$, we have $\overline{\rm Ec} \sim 10^{-5}\epsilon^{-3}(\Delta\Psi/\mathrm{volts})^2$. The electrohydrodynamics thin film equation (3.14) is only an accurate description of liquid motion if $\overline{\rm Ec}$ is $O(1)$. For aspect ratios ϵ ranging from 0.05 to 0.25, the required voltage difference between the ground substrate and the proximate electrode, separated by a few microns, is roughly between 3.5 to 40 volts, which is experimentally feasible (Schäffer et al., 2000).

Unstable film growth under flat electrode

In previous work (Schäffer et al., 2001), the classical linear stability analysis of equation (3.14) is examined for the early time behavior of sinusoidal perturbations to a polymer film of uniform thickness. The result described by the electrohydrodynamics model quantitatively agrees with experimental data without any adjustable parameter. Here we present the same result only with the dimensionless equation (3.17). Adopting the linear stability analysis in the thermocapillary model for a flat film of thickness H_0 and a flat electrode of height D_0, the resulting expression for growth rate is a function of wave number K,

$$\beta(K) = -H_0^3 K^4 + \frac{2H_0^3}{(D_0 - H_0)^2} K^2, \tag{3.19}$$

where the critical wavelength and the most unstable wavelength are given by

$$\Lambda_{\max} = \sqrt{2}\Lambda_{\text{crit}}, \quad \Lambda_{\text{crit}} = \sqrt{2}\pi(D_0 - H_0)^{3/2}. \tag{3.20}$$

If $\Lambda_{\max}$ is transformed back to its dimensional form $\lambda_{\max}$ (not shown), we indeed recover expression (3.1). It is clear from (3.20) that the wavelength $\Lambda_{\max}$ of the fastest growing perturbation rapidly decreases as the gap width $D_0 - H_0$ diminishes. This is reflected in free energy functional $\mathcal{F}[H, D]$ of the electrohydrodynamic thin film equation (3.17) as well. Consider the free energy functional

$$\mathcal{F}[H, D] = \int_\Omega \frac{1}{2}\nabla_\parallel H \cdot \nabla_\parallel H + \Phi(H, D(X, Y))\,\mathrm{d}\Omega, \tag{3.21}$$

where the potential function

$$\Phi = \int -\Pi(D, H)\,\mathrm{d}H = -\frac{1}{D(X, Y) - H} \tag{3.22}$$

is inversely proportional to the local separation between patterned electrode and local film thickness. Note $\mathrm{d}\mathcal{F}[H, D]/\mathrm{d}\tau \leq 0$ irrespective of whether electrode $D(\boldsymbol{X})$ is uniform or patterned. For a flat electrode such that $D_0 = 1$ after transformation (3.15), the fourth-derivative test (2.88) reveals a similar unstable nature as in the thermocapillary film: no stable equilibrium film profile can be reached under the balance between capillary and Maxwell stresses.

In fact the situation is even worse. If we perform self-similar analysis near the virtual singularity $D = 1$, to the leading order we arrive at the truncated PDE

$$\frac{\partial H}{\partial \tau} + \nabla_\parallel^2 \left[\nabla_\parallel^2 H + \frac{1}{(1 - H)^2}\right] + O((1 - H)^{-1}) = 0, \tag{3.23}$$

which implies the local scaling balance

$$1 - H_{\text{apex}} \sim X^{2/3} \sim (\tau_s - \tau)^{1/6} \tag{3.24}$$

as the film apex H_{apex} approaches the virtual singularity. The leading order self-similar solution $\mathcal{W}_1 = (1 - H)/(\tau_s - \tau)^{1/6}$ has an asymptotic behavior $\sim \eta^{2/3}$ as $\eta \to \infty$ where

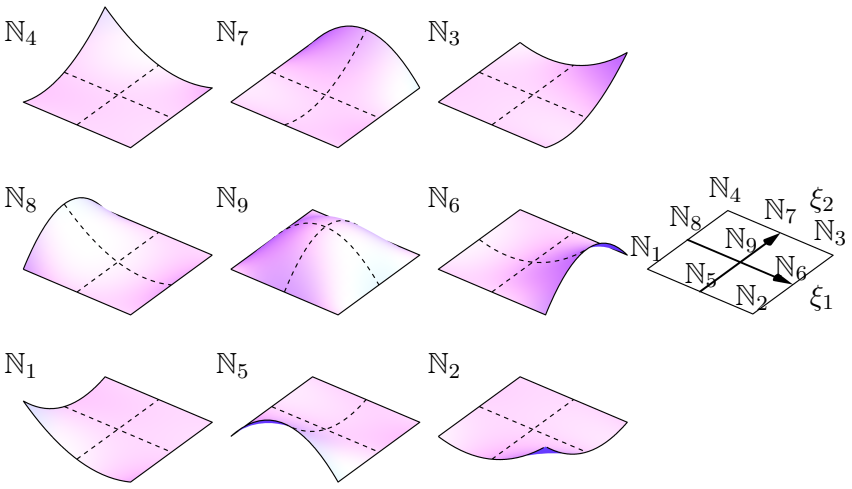

Figure 3.3: Lagrange polynomial basis $\{\mathbb{N}_1(\xi_1,\xi_2),\dots,\mathbb{N}_9(\xi_1,\xi_2)\}$ and nine corresponding nodes for bi-quadratic interpolation in the canonical domain $[-1,1]\times[-1,1]$.

$\eta = X/(\tau_s-\tau)^{1/4}$ is the self-similar coordinate. However unlike the conic cusp found in the thermocapillary system, spatial derivative $\mathrm{d}(\cdot)/\mathrm{d}X$ of $\eta^{2/3}$ becomes singular as $\eta\to 0$. Therefore near the singular point $\boldsymbol{X}_s$, local film profile is expected to converge to a genuine cuspidal shape $|1-H|\propto|\boldsymbol{X}-\boldsymbol{X}_s|^{2/3}$ as $H_{\mathrm{apex}}\to 1$. In contrast to the thermocapillary system where the slope of film profile remains finite even in the late stage of the self-similar runaway process, surface slope in the apical region blows up indefinitely for electrohydrodynamic thin film, which is a clear violation of the slender assumption that lubrication models all rely on. These peculiar features of electrohydrodynamic thin films, if not properly controlled, would lead to multiple sites of localized cuspidal blow-up.

Finite element discretization

In this section we outline the numerical scheme for simulating the thin film equation. There are many classical references on the general theory and practice of finite element method such as treatments on elliptic problems (Ciarlet, 2002), parabolic problems (Thomée, 2006), implementation details (Zienkiewicz, R. L. Taylor, and Zhu, 2013) and Navier-Stokes equation (Girault and Raviart, 1986). Owing to the vast literature, here we do not aim to give a comprehensive review of the finite element method. Interested readers should consult the aforementioned references. The presentation on the finite element approximation follows the exposition in the review article (Becker et al., 2002) on the numerical method for fourth order nonlinear degenerate diffusion problems.

We clarify here all finite element computations in this chapter are implemented in C++ from scratch with the help of high performance linear algebra library EIGEN (Guen-

nebaud, Jacob, et al., 2010). The reason for a bottom-up implementation is that, applying adjoint method to solve the inverse problem in EHL requires a highly customized matrix assembly procedure that is not readily available in most closed-source commercial software. The tutorial of finite element method presented in this section aims to prepare for a correct implementation of the adjoint method. Accuracy of our finite element code is discussed at the end of this section.

Let $\mathcal{Q}_\mathrm{h}$ be the quadrilateralization of a periodic rectangular domain Ω. The grid size h is the maximal edge length over all elements. Let O be the canonical element $[-1,1]\times[-1,1]$ with canonical coordinates $\boldsymbol{\xi}=(\xi_1,\xi_2)$. In this work, we restrict ourselves to straight elements $Q_e\in\mathcal{Q}_\mathrm{h}$ obtained only by translating and rescaling of the canonical element O,

$$\boldsymbol{X}\in Q_e \underset{\varphi_e}{\overset{\varphi_e^{-1}}{\rightleftharpoons}} \boldsymbol{\xi}\in O, \tag{3.25}$$

where φ_e is some bijectively affine map between element $Q_e\in\mathcal{Q}_\mathrm{h}$ in the (X,Y)-plane and the canonical square element O in the (ξ_1,ξ_2)-plane.

The set of all bi-quadratic functions in the canonical space is spanned by any linear-independent combination of the polynomial basis $\{1,\xi_1,\xi_1^2\}\otimes\{1,\xi_2,\xi_2^2\}$. In finite element method, it's standard to use the Lagrange polynomial basis $\{\mathbb{N}_i\}_{i=1}^9$,

$$\left.\begin{aligned}
\mathbb{N}_1(\boldsymbol{\xi})&=\frac{1}{4}(\xi_1^2-\xi_1)(\xi_2^2-\xi_2), & \mathbb{N}_2(\boldsymbol{\xi})&=\frac{1}{4}(\xi_1^2+\xi_1)(\xi_2^2-\xi_2),\\
\mathbb{N}_3(\boldsymbol{\xi})&=\frac{1}{4}(\xi_1^2+\xi_1)(\xi_2^2+\xi_2), & \mathbb{N}_4(\boldsymbol{\xi})&=\frac{1}{4}(\xi_1^2-\xi_1)(\xi_2^2+\xi_2),\\
\mathbb{N}_5(\boldsymbol{\xi})&=\frac{1}{2}(1-\xi_1^2)(\xi_2^2-\xi_2), & \mathbb{N}_6(\boldsymbol{\xi})&=\frac{1}{2}(\xi_1^2+\xi_1)(1-\xi_2^2),\\
\mathbb{N}_7(\boldsymbol{\xi})&=\frac{1}{2}(1-\xi_1^2)(\xi_2^2+\xi_2), & \mathbb{N}_8(\boldsymbol{\xi})&=\frac{1}{2}(\xi_1^2-\xi_1)(1-\xi_2^2),\\
\mathbb{N}_9(\boldsymbol{\xi})&=(1-\xi_1^2)(1-\xi_2^2),
\end{aligned}\right\} \tag{3.26}$$

so that any bi-quadratic function can be represented by its value at the nine local nodes shown in figure 3.3. There are nine nodes in the canonical square element with indices $\{1,2,3,4\}$ for the ones at four corners, $\{5,6,7,8\}$ for the mid points of four edges and 9 for the central interior point, hence the name "Q9" element. As shown in figure 3.3, the Lagrange basis is designed in such way that, $\mathbb{N}_i(\boldsymbol{\xi})=1$ at the i-th local node and $=0$ at all other nodes. Since only translation and scaling are involved in the mapping φ_e for each element Q_e, any Lagrange basis function after being mapped to the physical space,

$$\mathbb{N}_i^e(\boldsymbol{X})=\mathbb{N}_i(\varphi_e^{-1}(\boldsymbol{X})), \tag{3.27}$$

is also a bi-quadratic function in the (X,Y)-plane.

Let $\mathbb{V}^\mathrm{h}$ be the space consisting of continuous functions which are piecewise bi-quadratic on each element $Q_e\in\mathcal{Q}_\mathrm{h}$. A function in $\mathbb{V}^\mathrm{h}$ is uniquely defined by its values on the set

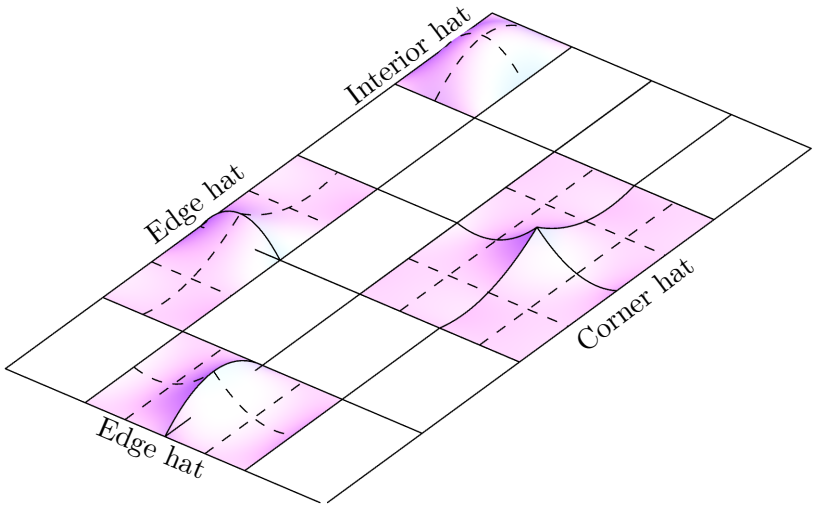

Figure 3.4: Global hat functions $\mathbb{V}_i$ at corner node of local indices $\{1,2,3,4\}$, at edge node of local indices $\{5,6,7,8\}$ and at interior (central) node of local index 9.

of nodes $\{\boldsymbol{X}_j\}_{j\in\mathbb{J}}$ of quadrilateralized domain $\mathcal{Q}_\mathrm{h}$ where $\mathbb{J}$ is the index set of all nodes. For each nodal point $\boldsymbol{X}_j$, we associate a compactly supported hat function $\mathbb{V}_j \in \mathbb{V}^h$ such that

$$\mathbb{V}_j(\boldsymbol{X}_i) = \begin{cases} 1 & \text{if} \quad i = j, \\ 0 & \text{if} \quad i \neq j. \end{cases} \tag{3.28}$$

The set of hat functions over all the nodal points spans the finite-dimensional vector space $\mathbb{V}^h$. In figure 3.4 we show a typical quadrilateral mesh where each rectangle is a Q9 Lagrange element. Depending on the type of each individual node (e.g., corner, edge or interior), the corresponding hat function may span one, two or four elements. The projection $H_\mathrm{h}(\boldsymbol{X})$ of a continuous function $H(\boldsymbol{X})$ into the finite element space $\mathbb{V}^\mathrm{h}$ is accomplished by the nodal interpolation operator $\mathscr{P}_\mathrm{h}$,

$$H_\mathrm{h} = \mathscr{P}_\mathrm{h}[H] \equiv \sum_i H(\boldsymbol{X}_i)\mathbb{V}_i \ . \tag{3.29}$$

In what follows, we identify the projected function $H_\mathrm{h} \in \mathbb{V}^\mathrm{h}$ with its nodal vector representation $\boldsymbol{H}$ in boldface character,

$$\boldsymbol{H} = [H_1, H_2, ...]^\top \longleftrightarrow H_\mathrm{h}(\boldsymbol{X}) = \sum_i H_i \mathbb{V}_i(\boldsymbol{X}). \tag{3.30}$$

Composition of continuous functions can be projected into $\mathbb{V}^\mathrm{h}$ in a similar fashion. For example let $\mathit{\Pi}(A(\boldsymbol{X}), B(\boldsymbol{X}), ...)$ be some elementary function (possibly nonlinear) of its arguments. We then associated a nodal vector $\boldsymbol{\mathit{\Pi}}$ with $\mathit{\Pi}(A(\boldsymbol{X}), B(\boldsymbol{X}), ...)$,

$$\boldsymbol{\mathit{\Pi}}(\boldsymbol{A}, \boldsymbol{B}, ...) = [\mathit{\Pi}_1, \mathit{\Pi}_2, ...]^\top \longleftrightarrow \mathscr{P}_\mathrm{h}[\mathit{\Pi}(A, B, ...)] = \sum_i \mathit{\Pi}(A_i, B_i, ...)\mathbb{V}_i(\boldsymbol{X}). \tag{3.31}$$

The inner product of the finite-dimensional vector space $\in \mathbb{V}^{\mathrm{h}}$ between two continuous functions $A \in \mathbb{V}^{\mathrm{h}}$ and $B \in \mathbb{V}^{\mathrm{h}}$ is defined as

$$\langle A, B \rangle \equiv \int_{\Omega} AB \, \mathrm{d}\Omega. \tag{3.32}$$

An equivalent formulation in the nodal vector representation (3.30) yields

$$\langle A, B \rangle = \boldsymbol{A}^{\top} \boldsymbol{M} \boldsymbol{B}, \quad M_{ij} = \langle \mathbb{V}_i, \mathbb{V}_j \rangle, \tag{3.33}$$

where $\boldsymbol{M}$ is the mass matrix. The entries of mass matrix $\boldsymbol{M}$ are precisely the inner product of all possible pairs of basis hat functions. It's evident that $\boldsymbol{M}$ is positive definite and symmetric, however not diagonal due to the overlaps of hat functions which share one identical element in the physical domain Ω (see figure 3.4). In practice, the solution of many transient problems become more efficient if the mass matrices can be diagonalized and hence inverted trivially. The process of replacing the true (consistent) mass matrix by a diagonal approximation without drastic degradation in overall accuracy is called mass lumping (Thomée, 2006; Zienkiewicz, R. L. Taylor, and Zhu, 2013). The essential idea is to approximate the inner product $\langle \cdot, \cdot \rangle$ in (3.32) with the lumped mass product $\langle \cdot, \cdot \rangle_{\mathrm{h}}$ such that

$$\langle A, B \rangle_{\mathrm{h}} \equiv \int_{\Omega} \mathscr{P}_{\mathrm{h}}[AB] \, \mathrm{d}\Omega \tag{3.34}$$

which yields the lumped mass matrix $\boldsymbol{M}_{\mathrm{h}}$ for which

$$\langle A, B \rangle_{\mathrm{h}} = \boldsymbol{A}^{\top} \boldsymbol{M}_{\mathrm{h}} \boldsymbol{B}, \quad (M_{\mathrm{h}})_{ii} = \langle 1, \mathbb{V}_i \rangle. \tag{3.35}$$

Recall the partition of the unity function, $1 = \sum_j \mathbb{V}_j(\boldsymbol{X})$. The name "lumped mass matrix" comes from the observation that, every row (column) of the true mass matrix $\boldsymbol{M}$ is lumped into a sum of its entries through the lumped mass product (3.35),

$$(M_{\mathrm{h}})_{ii} = \langle 1, \mathbb{V}_i \rangle = \langle \sum_j \mathbb{V}_j, \mathbb{V}_i \rangle = \sum_j \langle \mathbb{V}_j, \mathbb{V}_i \rangle = \sum_j M_{ji}.$$

In this work throughout, we use the lumped mass matrix $\boldsymbol{M}_{\mathrm{h}}$ for its computational efficiency when dealing with transient problems. With a slight abuse of notation, from now on we redefine $\boldsymbol{M}$ as the lumped mass matrix $\boldsymbol{M}_{\mathrm{h}}$ unless stated otherwise. The standard definition of the stiffness matrix $\boldsymbol{K}$ is given by

$$K_{ij} = \langle \nabla_{\parallel} \mathbb{V}_i, \nabla_{\parallel} \mathbb{V}_j \rangle \equiv \int_{\Omega} (\nabla_{\parallel} \mathbb{V}_i) \cdot (\nabla_{\parallel} \mathbb{V}_j) \, \mathrm{d}\Omega, \tag{3.36}$$

where the inner product is understood to be the sum of component-wise scalar products. Definition (3.36) is motivated by the finite element projection of the Laplacian operator $\nabla_{\parallel}^2$ since

$$\langle A, \nabla_{\parallel}^2 B \rangle = \int_{\Omega} A \nabla_{\parallel}^2 B \, \mathrm{d}\Omega = \int_{\partial\Omega} A \, \boldsymbol{N}_{\partial\Omega} \cdot \nabla_{\parallel} B \, \mathrm{d}S - \int_{\Omega} (\nabla_{\parallel} A) \cdot (\nabla_{\parallel} B) \, \mathrm{d}\Omega = -\boldsymbol{A}^{\top} \boldsymbol{K} \boldsymbol{B} \tag{3.37}$$

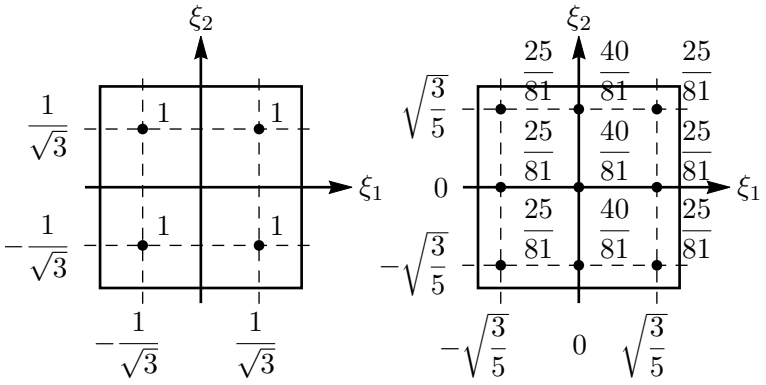

Figure 3.5: 2-point (left) and 3-point (right) Gauss quadrature rules for two-dimensional integration: quadrature weights are shown next to the nodes (dots).

where the boundary integral ($\boldsymbol{N}_{\partial\Omega}$ is the in-plane normal of domain boundary $\partial\Omega$) vanishes under periodic or no-flux boundary conditions. In the same spirit we introduce the weighted stiffness matrix $\boldsymbol{W}(\boldsymbol{H})$ for the mobility function $\mathcal{M}(\cdot)$ acting on some function $H \in \mathbb{V}^{\mathrm{h}}$,

$$W(H)_{ij} = \langle \nabla_{\parallel}\mathbb{V}_i, \mathscr{P}_{\mathrm{h}}[\mathcal{M}(H)]\nabla_{\parallel}\mathbb{V}_j\rangle. \tag{3.38}$$

Integrals arising from the finite element method are often approximated by n_{qd}-point Gauss quadrature rules. For the Q9 element used in this work, the 2- and 3-point quadrature rules are recommended (Cook et al., 2007) for approximating integral of a sufficiently continuous function $A(\boldsymbol{\xi})$ over the canonical square element,

$$\int_{-1}^{1}\int_{-1}^{1} A(\boldsymbol{\xi})\,\mathrm{d}\xi_1\mathrm{d}\xi_2 \approx \sum_{k=1}^{{n_{\mathrm{qd}}}^2} w_k A(\boldsymbol{\xi}_k) \tag{3.39}$$

where $\boldsymbol{\xi}_k$ and w_k are the n_{qd}-point quadrature nodes and weights for the canonical square element O as illustrated in figure 3.5.

Following Becker et al. (2002), we employ a semi-implicit discretization for time integration which leads to the variational (weak) form of the thin film equation (3.17): given a known time series of film profiles $H_0, H_1, \ldots, H_k \in \mathbb{V}^{\mathrm{h}}$, find two functions $H_{k+1} \in \mathbb{V}^{\mathrm{h}}$ and $P_{k+1} \in \mathbb{V}^{\mathrm{h}}$ such that,

$$\left.\begin{aligned} \langle A, \mathfrak{D}_\tau[H_{k+1}]\rangle_{\mathrm{h}} + \langle \nabla_{\parallel}A, \mathscr{P}_{\mathrm{h}}[\mathcal{M}(H_k)]\nabla_{\parallel}P_{k+1}\rangle = 0,\\ \langle B, P_{k+1}\rangle_{\mathrm{h}} - \langle \nabla_{\parallel}B, \nabla_{\parallel}H_{k+1}\rangle = -\langle B, \Pi(H_{k+1}, D)\rangle_{\mathrm{h}},\end{aligned}\right\} \tag{3.40}$$

for all $A, B \in \mathbb{V}^{\mathrm{h}}$. To avoid confusion in subscripts, H_k and similar objects always refer to the function in finite element space $\mathbb{V}^{\mathrm{h}}$ at the k-th time step whereas $(H_k)_i$ refers to the i-th nodal value of the film profile H_k. The discrete time derivative operator $\mathfrak{D}_\tau[\cdot]$ in variational formulation (3.40) is treated with either the first or second order backward

Scheme	α_k^+	α_k^0	α_k^-
BDF1	1	1	0
VS-BDF2	$\dfrac{1+\Delta_k}{1+2\Delta_k}$	$\dfrac{(1+\Delta_k)^2}{1+2\Delta_k}$	$-\dfrac{\Delta_k^2}{1+2\Delta_k}$
BDF2	$\dfrac{2}{3}$	$\dfrac{4}{3}$	$-\dfrac{1}{3}$

Table 3.1: Coefficients of the backward differentiation formula (BDF) family. $\Delta_k = \Delta\tau_k/\Delta\tau_{k-1}$ is the ratio between adjacent time steps.

differentiation formula (BDF) scheme (Crouzeix and Lisbona, 1984),

$$\mathfrak{D}_\tau[H_{k+1}] = \begin{cases} \dfrac{1}{\Delta\tau_k}(H_{k+1}-H_k), & \text{(BDF1)} \\ \dfrac{1}{\Delta\tau_k}\left[\dfrac{1+2\Delta_k}{1+\Delta_k}H_{k+1} - (1+\Delta_k)H_k + \dfrac{\Delta_k^2}{1+\Delta_k}H_{k-1}\right], & \text{(VS-BDF2)} \\ \dfrac{1}{\Delta\tau}\left(\dfrac{3}{2}H_{k+1} - 2H_k + \dfrac{1}{2}H_{k-1}\right), & \text{(BDF2)} \end{cases} \tag{3.41}$$

where $\Delta\tau_k$ is the incremental time step. Note BDF1 is identical to the first order implicit Euler scheme. For BDF2 with a constant time step, we set $\Delta\tau_k = \Delta\tau$ for all k. The variable step BDF (VS-BDF2) requires the ratio between current and previous time stepS, designated as $\Delta_k = \Delta\tau_k/\Delta\tau_{k-1}$.

Using nodal vector representation, we recast variation formulation (3.40) into a nonlinear system of equations at each time step. The discrete form of variation formulation (3.40) reads: given a known time series of nodal vectors $\boldsymbol{H}_0, \boldsymbol{H}_1, \dots, \boldsymbol{H}_k$, find two nodal vectors $\boldsymbol{H}_{k+1}$ and $\boldsymbol{P}_{k+1}$ such that

$$\left.\begin{aligned} \boldsymbol{M}\boldsymbol{H}_{k+1} + \Delta\tau_k\alpha_k^+\boldsymbol{W}(\boldsymbol{H}_k)\boldsymbol{P}_{k+1} &= \boldsymbol{M}(\alpha_k^0\boldsymbol{H}_k + \alpha_k^-\boldsymbol{H}_{k-1}), \\ -\boldsymbol{K}\boldsymbol{H}_{k+1} + \boldsymbol{M}\boldsymbol{P}_{k+1} &= -\boldsymbol{M}\boldsymbol{\Pi}(\boldsymbol{H}_{k+1}, \boldsymbol{D}), \end{aligned}\right\} \tag{3.42}$$

where coefficients α_k^+, α_k^0 and α_k^- at time stamp τ_k are defined in table 3.1. Since the mass matrix $\boldsymbol{M}$ for Lagrange Q9 element is positive definite, we can eliminate effective pressure vector $\boldsymbol{P}_{k+1}$ in (3.42) which yields a nonlinear system of equations with $\boldsymbol{H}_{k+1}$ being the only unknown,

$$\boldsymbol{F}_{k+1}(\boldsymbol{H}_{k-1}, \boldsymbol{H}_k, \boldsymbol{H}_{k+1}, \boldsymbol{D}) = \boldsymbol{0}, \tag{3.43}$$

where the nonlinear function

$$\boldsymbol{F}_{k+1} = \boldsymbol{M}(\boldsymbol{H}_{k+1} - \alpha_k^0\boldsymbol{H}_k - \alpha_k^-\boldsymbol{H}_{k-1}) + \Delta\tau_k\alpha_k^+\boldsymbol{R}_{k+1}(\boldsymbol{H}_k, \boldsymbol{H}_{k+1}, \boldsymbol{D}) \tag{3.44}$$

contains a linear component and a nonlinear function

$$\boldsymbol{R}_{k+1}(\boldsymbol{H}_k, \boldsymbol{H}_{k+1}, \boldsymbol{D}) = \boldsymbol{W}(\boldsymbol{H}_k)[\boldsymbol{M}^{-1}\boldsymbol{K}\boldsymbol{H}_{k+1} - \boldsymbol{\Pi}(\boldsymbol{H}_{k+1}, \boldsymbol{D})]. \tag{3.45}$$

The nonlinear system of equations (3.43) can be efficiently solved via the Newton's Method. Starting from a "good" initial guess $\boldsymbol{H}_{k+1}^{(0)}$, for example $\boldsymbol{H}_{k+1}^{(0)} = \boldsymbol{H}_k$ from previous time step, Newton's iteration scheme

$$\boldsymbol{H}_{k+1}^{(i+1)} = \boldsymbol{H}_{k+1}^{(i)} - [\boldsymbol{J}^{(i)}]^{-1}\boldsymbol{F}_{k+1}(\boldsymbol{H}_{k-1}, \boldsymbol{H}_k, \boldsymbol{H}_{k+1}^{(i)}, \boldsymbol{D}) \tag{3.46}$$

produces successively better approximations $\boldsymbol{H}_{k+1}^{(i)}$ to the roots of equation (3.44) where the Jacobian matrix in (3.46)

$$\boldsymbol{J}^{(i)} = \boldsymbol{M} + \Delta\tau_k\alpha_k^+\boldsymbol{W}(\boldsymbol{H}_k)\left[\boldsymbol{M}^{-1}\boldsymbol{K} - \frac{\partial\boldsymbol{\Pi}(\boldsymbol{H}_{k+1}^{(i)}, \boldsymbol{D})}{\partial\boldsymbol{H}_{k+1}}\right] \tag{3.47}$$

is the linearization of $\boldsymbol{F}_{k+1}$ about $\boldsymbol{H}_{k+1}^{(i)}$.

In practice, direct inversion of the Jacobian matrix $\boldsymbol{J}^{(i)}$ is strictly forbidden due to its large dimensions. Instead we can take advantage of the sparse pattern in $\boldsymbol{J}^{(i)}$ which can be seen from the following two observations: first of all, $\boldsymbol{W}$ and $\boldsymbol{M}^{-1}\boldsymbol{K}$ are assembled element-wisely (this is explained in Section 3.4) with identical locations of non-zero entries, which means if the one-ring element neighbors of the element which the i-th node belongs to and that of the j-th node are disjoint, it must be that $[\boldsymbol{W}\boldsymbol{M}^{-1}\boldsymbol{K}]_{ij} = 0$, hence sparse; secondly, recall from (3.30) that the action of $\boldsymbol{\Pi}$ on $\boldsymbol{H}_{k+1}$ is an entry-wise operation, which implies $\partial\boldsymbol{\Pi}/\partial\boldsymbol{H}_{k+1}$ must be diagonal. Therefore it is more favorable to implement the Newton's method (3.46) with an iterative solver (Saad, 2003) such as bi-conjugate gradient stabilized method (BiCGSTAB),

$$\left.\begin{aligned}\boldsymbol{J}^{(i)}\delta\boldsymbol{H}^{(i)} &= -\boldsymbol{F}_{k+1}(\boldsymbol{H}_{k-1}, \boldsymbol{H}_k, \boldsymbol{H}_{k+1}^{(i)}, \boldsymbol{D}),\\ \boldsymbol{H}_{k+1}^{(i+1)} &= \boldsymbol{H}_{k+1}^{(i)} + \delta\boldsymbol{H}^{(i)}.\end{aligned}\right\} \tag{3.48}$$

Another advantage of employing an iterative method to solve the linear system (3.48) is the control over accuracy. The ultimate goal is to drive the residue in $\boldsymbol{F}_{k+1}$ below certain tolerance threshold. A perfectly accurate solution to $\delta\boldsymbol{H}^{(i)}$ in (3.48) is not necessary as long as the iterative increment $\delta\boldsymbol{H}^{(i)}$ helps guide $\boldsymbol{F}_{k+1}$ to $\boldsymbol{0}$. Likewise it is not necessary to update $\boldsymbol{J}^{(i)}$ at each Newton step which can be potentially time consuming as well. For sufficiently small time step $\Delta\tau_k$, we only need to reassemble $\boldsymbol{J}^{(i)}$ every a few Newton steps.

The finite element formulation outlined in this section is very general and can be applied to all sorts of thin film models including the thermocapillary equation (2.64). Calculations of the mass and stiffness matrices are only slight different for the one-dimensional line mesh and the triangular mesh used in the simulation reported in Section 2.5 due to different forms of Lagrange basis functions on a line and triangle element.

Film evolution under an electrode of a heart-like topography

Figure 3.7 represents 3D views of the discrete film profile $\boldsymbol{H}_k$ of an evolving elctrostatic-driven thin film at designated time stamps respectively, obtained from finite element

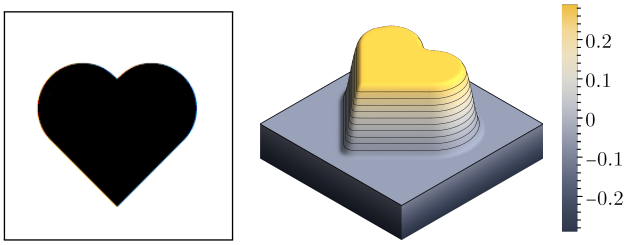

Figure 3.6: Electrode topography (right) on a periodic square domain $[0, 4.5] \times [0, 4.5]$ reconstructed from a grayscale bitmap (left). For visual purpose, $1 - D(\boldsymbol{X})$ is plotted instead.

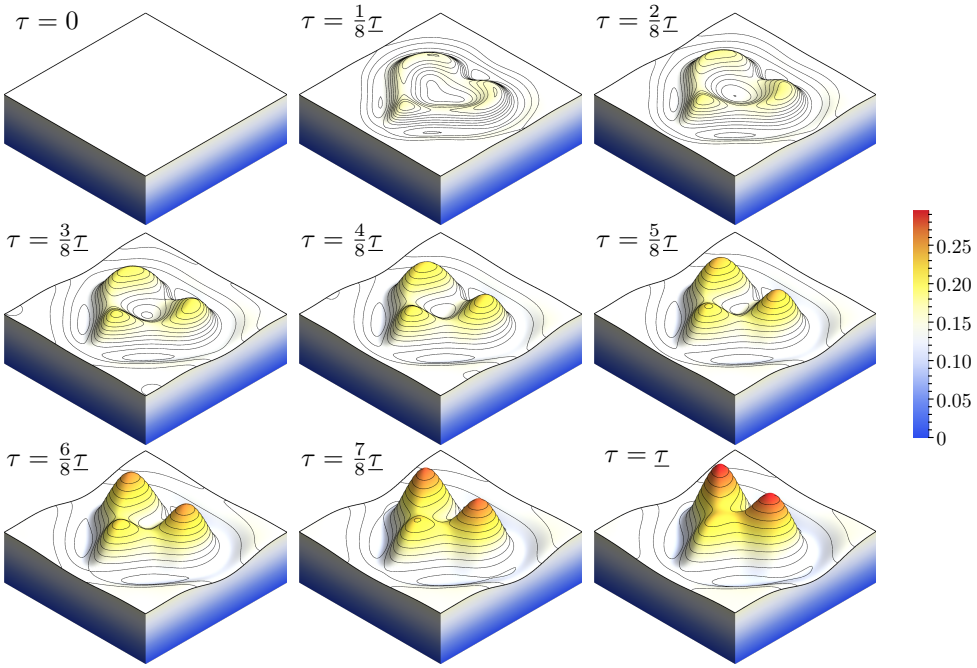

Figure 3.7: Finite element simulation of film thickness $H(\boldsymbol{X}, \tau)$ on a periodic computational domain $[0, 4.5] \times [0, 4.5]$ driven by a heart-like electrode shown in figure 3.6. Snapshots with elevation contours (black line) are taken at time stamps $\tau = 0, \underline{\tau}/9, ..., \underline{\tau}$ where $\underline{\tau} = 4.2$ is the final time.

simulation of the nonlinear EHL equation (3.17). The simulation is performed on a periodic square domain $[0, 4.5] \times [0, 4.5]$ consist of 100^2 Lagrange Q9 elements with 40000 degrees of freedom in total for an initially flat film of uniform thickness $H_0 = 0.15$. Time span of the simulation ranges from $\tau = 0$ to the final time $\underline{\tau} = 4.2$. We evenly divide the time interval $[0, \underline{\tau}]$ into 400 intermediate steps with constant increment $\Delta\tau = 0.0105$ between the steps and integrate the resulting discrete evolution equation with semi-implicit BDF2.

Discretized electrode topography $\boldsymbol{D}$ is reconstructed from the grayscale bitmap of a heart-shape pattern shown in figure 3.6 and shifted by a constant according to equation (3.117) to ensure that the spatial average of electrode topography is unity. Here we briefly outline the reconstruction procedure. Any grayscale bitmap can be regarded as a function $\phi(i, j)$ defined on a square domain (up to a rescaling) with its function value at each pixel coordinate (i, j) equal to the rescaled gray level between zero (black) and unity (white). The heart-shaped bitmap in figure 3.6 would yield a step-like function which is discontinuous and not suitable for higher order PDEs such as the EHL equation (3.17). There are many filter-based image smoothing techniques capable of producing gentle transitions between black and white pixels (Gonzalez and Woods, 2017). In order to preserve the step-like feature of the original bitmap, we implement a reconstruction process based on the level-set method (Sethian, 1999) by advancing a time-dependent Eikonal-like equation $\partial\phi/\partial t + (\phi - 0.5)(\sqrt{c_1 + |\nabla_{(i,j)}\phi|^2} - 1) = c_2\nabla^2_{(i,j)}\phi$ till a stopping time t_s with the original gray level being the initial condition of ϕ. Here $\nabla_{(i,j)}$ and $\nabla^2_{(i,j)}$ are the discrete gradient and Laplacian operator defined with respect to the pixel grid of the bitmap. Two positive constants $c_0 \ll 1$ and $c_2 \ll 1$ control the final smoothness of ϕ. The topography function on the right hand side of figure 3.6 is the result of applying this reconstruct algorithm to the 200×200 bitmap on the left where $t_s = 0.15$, $c_1 = 0.05$ and $c_2 = 0.02$.

In figure 3.8 we demonstrate the convergence behavior of the discrete film states $\boldsymbol{H}_k$ as the mesh and time steps are progressively refined while the initial condition $H_0 = 0.15$, domain size $[0, 4.5] \times [0, 4.5]$ and final time $\underline{\tau}$ are fixed. The discrepancies in maximum and minimum film thickness are virtually indistinguishable between various configurations of element size and time steps. Although the absolute error in free energy appears to be discernible due to the integral nature of $\mathcal{F}[H]$, the relative error is still less than 0.5%.

Similar to what have been reported in literature, we observe rapid growth of multiple localized pillars triggered by large electric field gradient near the sharp edges and corner of the heart-like electrode, which eventually would turn into cusp-like structures through the runaway self-similar process discussed in Section 3.2 if we let the simulation run longer. The blow-up tendency in film growth is reflected in the time-dependent data of the total free energy $\mathcal{F}[H]$ plotted in figure 3.8. Towards the final time $\underline{\tau} = 4.2$,

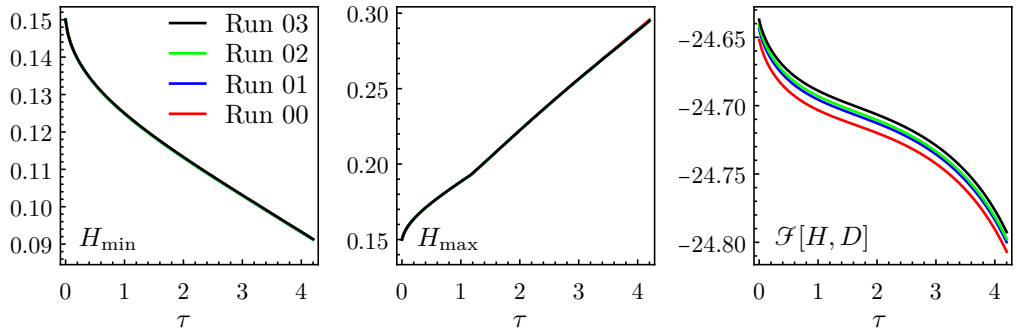

Figure 3.8: Time-dependent data of maximum thickness $H_{\max}$, minimum thickness $H_{\min}$ and the total free energy $\mathcal{F}[H]$ of the evolving film state. Each colored line represents a different combination of mesh size and time steps used: run 00 (40^2 elements and 100 time steps), run 01 (60^2 elements and 200 time steps), run 02 (80^2 elements and 300 time steps) and run 03 (100^2 elements and 400 time steps) which corresponds to the simulation shown in figure 3.7.

the free energy of the system begins to decrease in an accelerating fashion, which can be peculiar because the free energy (3.21) of the EHL system is neither convex nor globally bounded below. As the film apexes approach the bottom of the electrode, the underlying pillars become slenderer while growing taller accompanied with a rapid reduction in the total free energy by forming cusp-like shapes. In addition, we notice the undershooting of film surface at the bottom circumference of the pillars which forms a "trench" bordering these pillars due to drainage caused by the accelerating growth. This is the repercussion of mass conservation for incompressible liquids: local aggregation of liquid material inevitably leads to removal of nearby material.

3.3 EHL as a Constrained Inverse Problem and Its Optimal Control

Having given an overview of the physical principle, mathematical modeling and numerical simulation of EHL, we are now in the position to discuss electrostatic control of pattern formation in dielectric viscous thin liquid film, which essentially reduces to optimization, a well established subject in the field of mathematics and engineering. Nevertheless an immediate solution to the inverse problem of EHL is not quite readily available. The challenge we face here is threefold: first, liquid films are not parameterized by a discrete set of parameters but a continuous distribution of interface height; secondly, electrostatic shaping of liquid films is a not static but evolving process; thirdly, the evolution equation is nonlinear in both film profile and electrode topography. The relevant tools to overcome these difficulties are scattered in different context of optimization. The textbook by Tröltzsch (2010) discusses how adjoint equations arise during parameter identification of coefficients in differential equations describing steady continuum systems. A one-dimensional tutorial is illustrated in the monograph by Vogel

(2002) which highlights ill-posedness of these inverse problems with a strong focus on various regularization methods. Although the adjoint formalism presented is applicable to time-dependent systems, the author admits the numerical implementation can be much more problematic than in the steady-state case. The first volume of the book series by Bertsekas (2005) on dynamic programming elaborates on the continuous-time optimal control of deterministic discrete systems over a finite horizon (i.e. a finite span of time), which we extend to continuum fluid systems such as EHL. Finally, identifying the optimal electrode topography under the adjoint formalism reduces to a large-scale unconstrained nonlinear optimization problem, various solution methods of which are explained in the comprehensive book by Nocedal and Wright (2006) on numerical optimization. We refer the interested readers to the monograph by Isakov (2006) for rigorous mathematical treatment and latest development on the theory of inverse problem for partial differential equations. We shall see how a combination of these tools adopted from different perspectives of optimization yields a drastic improvement of EHL pattern fidelity on a computational level.

State, control, constraint and objective

In this subsection we layout the computational methodology of finding the optimal counter electrode pattern $\underline{D}(\boldsymbol{X})$. By optimal what we mean is that, under certain constraint (should there be any) the electrode pattern $\underline{D}(\boldsymbol{X})$ is expected to drive an evolving film state $H(\boldsymbol{X},\tau)$ from an initially uniform film of average thickness H_0 towards a desired target shape $\underline{H}(\boldsymbol{X})$ at a user-specified termination time $\tau = \underline{\tau}$ as close as possible.

On an abstract level, the optimization task of EHL can be reformulated as a special case of the finite horizon problem in dynamic programming (Bertsekas, 2005) which was popularized in the 50's through the pioneer work of Bellman (1957) and has been widely applied to problems of optimal control (see Hocking (1991) for numerous applications). In this framework, an admissible control $D(\boldsymbol{X})$ is sought over a finite horizon $[0,\underline{\tau}]$, which, together with its corresponding state trajectory $\{H(\boldsymbol{X},\tau) \mid \tau \in [0,\underline{\tau}]\}$, minimizes a terminal objective (or cost) functional of the form $\mathcal{J}[H(\boldsymbol{X},\underline{\tau}), D(\boldsymbol{X})]$. Mathematically we encode the two primary goals of Electrohydrodynamic Lithography, namely the fidelity of final interface shape $H(\boldsymbol{X},\underline{\tau})$ to the target profile $\underline{H}(\boldsymbol{X})$ and the physical plausibility of the electrode topography $\underline{D}(\boldsymbol{X})$, into the objective functional

$$\mathcal{J}[H(\boldsymbol{X},\underline{\tau}), D(\boldsymbol{X})] = \int_\Omega \frac{1}{2}\left[H(\boldsymbol{X},\underline{\tau}) - \underline{H}(\boldsymbol{X})\right]^2 \mathrm{d}\Omega + \mathcal{R}[D(\boldsymbol{X})], \tag{3.49}$$

where functional $\mathcal{R}[D]$ is a regularization that penalizes nonphysical geometric features of the electrode pattern. For example, the H^1-regularization (Heinkenschloss, 1998; Vogel, 2002)

$$\mathcal{R}[D(\boldsymbol{X})] = \gamma \int_\Omega \frac{1}{2}|\nabla_\parallel D|^2 \,\mathrm{d}\Omega \tag{3.50}$$

would suppress excessive amount of high-frequency spatial oscillations and ensure certain level of smoothness in $D(\boldsymbol{X})$ depending the numerical value of penalty parameter $\gamma > 0$.

Our goal is to minimize the objective functional $\mathcal{J}$ defined in (3.49) as much as possible. Obviously this is not a free minimization: the final film shape $H(\boldsymbol{X}, \tau = \underline{\tau})$ is the last snapshot of the evolution equation (3.17) which is directly influenced by the electrode topography $D(\boldsymbol{X})$. The optimization problem we are dealing with here is constrained and most likely non-convex: given an initial film thickness H_0, a termination time $\underline{\tau}$, dimensions of the periodic domain Ω and the desired target film profile $\underline{H}(\boldsymbol{X})$, find the optimal electrode topography

$$\begin{aligned} \underline{D}(\boldsymbol{X}) &= \underset{D}{\operatorname{argmin}}\, \mathcal{J}[H(\boldsymbol{X}, \underline{\tau}), D(\boldsymbol{X})] \\ \text{subject to} \quad & \frac{\partial H}{\partial \tau} + \mathcal{N}(H, D) = 0 \quad \text{for} \quad 0 \leq \tau \leq \underline{\tau}, \end{aligned} \tag{3.51}$$

where $\mathcal{N}(H, D)$ stands for the negative of the nonlinear operator on the right hand side of equation (3.17) in shorthand. Most optimization algorithms are gradient-based methods which search for local minima of the objective. Unlike the explicit gradient in the context of multi-variable calculus, the gradient in optimization problem (3.51) is rather abstract, which can be interpreted as the infinitesimal total variation of the objective $\mathcal{J}[H(\boldsymbol{X}, \tau), D(\boldsymbol{X})]$ with respect to infinitesimal changes in the control variable $D(\boldsymbol{X})$ along the hypersurface implicitly given by the constraint between the control $D(\boldsymbol{X})$ and the state $H(\boldsymbol{X}, \tau)$.

The type of control studied in this work falls into the open-loop category (Kirk, 2004): once the optimal topography is computed, the control action exerted by the electrode pattern $\underline{D}(\boldsymbol{X})$ is independent of the evolving film state $H(\boldsymbol{X}, \tau)$. As the film deforms, modifying the electrode topography concurrently, i.e. $D(\boldsymbol{X}) \to D(\boldsymbol{X}, \tau)$, would be difficult at the scale of micro- and nano-lithography. Although it is experimentally feasible to alter the overall amplitude of voltage difference across the thin gap in time. It is mathematically equivalent to replace the effective electrostatic pressure $\Pi(D, H)$ with $A(\tau)\Pi(D, H)$ where $A(\tau)$ is a function of time. This type of control is called feedback or closed-loop (Kirk, 2004; Bertsekas, 2005), which is particularly useful when stochasticity in EHL is taken into account and is left for future study.

Optimal electrode topography acting on an initially flat film

Let electrode topography $\underline{D}(\boldsymbol{X})$ be one of the optimal designs which at least locally minimizes the constrained objective functional $\mathcal{J}[H, D]$ defined in (3.49) and $\underline{H}(\boldsymbol{X}, \tau)$ be the spatial-temporal film profile generated by $\underline{D}(\boldsymbol{X})$. In this subsection we derive a set of necessary conditions which the optimal topography $\underline{D}(\boldsymbol{X})$ and the optimal evolution trajectory of film profile $\underline{H}(\boldsymbol{X}, \tau)$ must satisfy.

The derivation of optimality condition here closely follows the variational formalism in Tröltzsch (2010) which treats adjoint state as a Lagrange multiplier. In order to enforce the dynamic evolution (3.17) on film state $H(\boldsymbol{X},\tau)$, it is convenient to employ the method of augmented Lagrangian with the Lagrangian functional

$$\mathcal{L}[H(\boldsymbol{X},\tau),D(\boldsymbol{X}),\Lambda(\boldsymbol{X},\tau)]=\mathcal{J}[H,D]-\int_0^{\tau}\int_{\Omega}\Lambda\Big[\frac{\partial H}{\partial\tau}+\mathcal{N}(H,D)\Big]\,\mathrm{d}\Omega\,\mathrm{d}\tau, \quad (3.52)$$

where $\Lambda(\boldsymbol{X},\tau)$ is the spatial-temporal Lagrange multiplier which implicitly imposes the dynamic constraint between the time-varying film profile $H(\boldsymbol{X},\tau)$ and the electrode topography $D(\boldsymbol{X})$. By definition the augmented Lagrangian $\mathcal{L}[H,D,\Lambda]$ is unconstrained in all of its arguments, the critical points of which coincide with the ones of the constrained objective $\mathcal{J}[H,D]$. One way to characterize the optimal evolution trajectory $\underline{H}(\boldsymbol{X},\tau)$, the optimal topography $\underline{D}(\boldsymbol{X})$ and the optimal multiplier $\underline{\Lambda}(\boldsymbol{X},\tau)$ of the Lagrangian is to identify conditions under which the first variations $\delta\mathcal{L}$ of Lagrangian $\mathcal{L}[\underline{H},\underline{D},\underline{\Lambda}]$ evaluated at optimal solutions vanish against all infinitesimal perturbations in its arguments.

Let $\delta H(\boldsymbol{X},\tau)$, $\delta D(\boldsymbol{X})$, $\delta\Lambda(\boldsymbol{X},\tau)$ be some admissible infinitesimal variations to the optimal solutions. Then the first variations of Lagrangian $\mathcal{L}[H,D,\Lambda]$ are given by the Fréchet derivative in the directions of these prescribed variations,

$$\delta\mathcal{L}[\underline{H},\underline{D},\underline{\Lambda};\delta\Lambda]=\int_0^{\tau}\int_{\Omega}\delta\Lambda\Big[\frac{\partial\underline{H}}{\partial\tau}+\mathcal{N}(\underline{H},\underline{D})\Big]\mathrm{d}\Omega\,\mathrm{d}\tau, \quad (3.53)$$

$$\delta\mathcal{L}[\underline{H},\underline{D},\underline{\Lambda};\delta H]=\delta\mathcal{J}[\underline{H},\underline{D};\delta H]-\int_0^{\tau}\int_{\Omega}\underline{\Lambda}\Big[\frac{\partial\delta H}{\partial\tau}+\mathfrak{L}_H(\underline{H},\underline{D})\delta H\Big]\mathrm{d}\Omega\,\mathrm{d}\tau, \quad (3.54)$$

$$\delta\mathcal{L}[\underline{H},\underline{D},\underline{\Lambda};\delta D]=\delta\mathcal{J}[\underline{H},\underline{D};\delta D]-\int_0^{\tau}\int_{\Omega}\underline{\Lambda}\mathfrak{L}_D(\underline{H},\underline{D})\delta D\,\mathrm{d}\Omega\,\mathrm{d}\tau, \quad (3.55)$$

where $\delta\mathcal{J}[\underline{H},\underline{D};\delta H]$ and $\delta\mathcal{J}[\underline{H},\underline{D};\delta D]$ are the unconstrained (free) variations of the objective functional $\mathcal{J}$ with respect to its arguments. The two operators $\mathfrak{L}_H$ and $\mathfrak{L}_D$ in (3.54) and (3.55) are the linearizations of the nonlinear operator $\mathcal{N}(H,D)$ about the optimal solutions $\underline{H}$ and $\underline{D}$, respectively,

$$\begin{aligned}\mathfrak{L}_H(\underline{H},\underline{D})\delta H=\nabla_{\!\parallel}\cdot\Big\{\mathcal{M}(\underline{H})\nabla_{\!\parallel}\Big[\nabla_{\!\parallel}^2\delta H+\frac{\partial\Pi}{\partial H}\Big|_{\underline{H},\underline{D}}\delta H\Big]\Big\}\\ +\nabla_{\!\parallel}\cdot\Big\{\frac{\mathrm{d}\mathcal{M}}{\mathrm{d}H}\Big|_{\underline{H}}\delta H\,\nabla_{\!\parallel}\Big[\nabla_{\!\parallel}^2\underline{H}+\Pi(\underline{H},\underline{D})\Big]\Big\},\end{aligned} \quad (3.56)$$

$$\mathfrak{L}_D(\underline{H},\underline{D})\delta D=\nabla_{\!\parallel}\cdot\Big\{\mathcal{M}(\underline{H})\nabla_{\!\parallel}\Big[\frac{\partial\Pi(\underline{H},\underline{D})}{\partial D}\delta D\Big]\Big\}. \quad (3.57)$$

The condition that the first variation $\delta\mathcal{L}$ in (3.53) vanishes for any spatial-temporal variation $\delta\Lambda$ of the optimal multiplier $\underline{\Lambda}$ simply recovers the nonlinear constraint, i.e. the optimal trajectory $\underline{H}$ and topography $\underline{D}$ must fulfill the electrohydrodynamic thin film equation (3.17),

$$\left.\begin{aligned}\frac{\partial\underline{H}}{\partial\tau}+\mathcal{N}(\underline{H},\underline{D})=0 \quad \text{for} \quad 0\le\tau\le\underline{\tau},\\ \underline{H}(\boldsymbol{X},0)=H_0 \quad \text{at} \quad \tau=0.\end{aligned}\right\} \quad (3.58)$$

Equation (3.58) is called the state (forward) PDE.

The condition that $\delta\mathcal{L}$ in (3.54) vanishes for any spatial-temporal variation δH of the optimal evolution trajectory $\underline{H}$ is not yet explicit because the operators under the spatiotemporal integrals in (3.54) are still acting on the variation δH. We need to rearrange the integrals into equivalent forms such as $\int_0^{\underline{\tau}}\int_\Omega \delta H \times (...)\,\mathrm{d}\tau\,\mathrm{d}\Omega$ so that the response to the variation δH can be explicitly identified. Performing integration by parts on (3.54) yields

$$\begin{aligned}
&\int_0^{\underline{\tau}}\int_\Omega \underline{\Lambda}\Big[\frac{\partial \delta H}{\partial \tau} + \mathfrak{L}_H(\underline{H},\underline{D})\delta H\Big]\,\mathrm{d}\Omega\,\mathrm{d}\tau \\
&= \int_\Omega\int_0^{\underline{\tau}} \underline{\Lambda}\frac{\partial \delta H}{\partial \tau}\,\mathrm{d}\tau\,\mathrm{d}\Omega + \int_0^{\underline{\tau}}\int_\Omega \mathfrak{L}_H(\underline{H},\underline{D})\delta H\,\mathrm{d}\Omega\,\mathrm{d}\tau \\
&= \int_\Omega \delta H(\boldsymbol{X},\underline{\tau})\underline{\Lambda}(\boldsymbol{X},\underline{\tau})\,\mathrm{d}\Omega - \int_\Omega \delta H(\boldsymbol{X},0)\underline{\Lambda}(\boldsymbol{X},0)\,\mathrm{d}\Omega \\
&\quad - \int_\Omega\int_0^{\underline{\tau}} \delta H\frac{\partial \underline{\Lambda}}{\partial \tau}\,\mathrm{d}\tau\,\mathrm{d}\Omega + \int_0^{\underline{\tau}}\int_\Omega \delta H\mathfrak{L}_H^\dagger(\underline{H},\underline{D})\underline{\Lambda}\,\mathrm{d}\Omega\,\mathrm{d}\tau \\
&= \int_\Omega \delta H(\boldsymbol{X},\underline{\tau})\underline{\Lambda}(\boldsymbol{X},\underline{\tau})\,\mathrm{d}\Omega + \int_0^{\underline{\tau}}\int_\Omega \delta H\left\{-\frac{\partial \underline{\Lambda}}{\partial \tau} + \mathfrak{L}_H^\dagger(\underline{H},\underline{D})\Lambda^*\right\}\mathrm{d}\Omega\,\mathrm{d}\tau,
\end{aligned} \tag{3.59}$$

where we drop the integral at $\tau = 0$ because the initial condition is meant to be fixed for which $\delta H(\boldsymbol{X},0) = 0$. The linear operator $\mathfrak{L}_H^\dagger(\underline{H},\underline{D})$ is the adjoint of $\mathfrak{L}_H(\underline{H},\underline{D})$ defined in (3.57), the closed-form expression of which can be derived thanks to the Green's identity. We begin with the definition of adjoint operator,

$$\begin{aligned}
\int_\Omega A\mathfrak{L}_H(\underline{H},\underline{D})B\,\mathrm{d}\Omega &= \int_\Omega B\mathfrak{L}_H^\dagger(\underline{H},\underline{D})A\,\mathrm{d}\Omega \\
&= \int_\Omega B\left\{\Big[\nabla_\parallel^2 + \frac{\partial \Pi}{\partial H}\Big|_{\underline{H},\underline{D}}\Big]\nabla_\parallel\cdot\Big[\mathcal{M}(\underline{H})\nabla_\parallel A\Big]\right\}\mathrm{d}\Omega \\
&\quad - \int_\Omega B\left\{\frac{\mathrm{d}\mathcal{M}}{\mathrm{d}H}\Big|_{\underline{H}}\nabla_\parallel\Big[\nabla_\parallel^2\underline{H} + \Pi(\underline{H},\underline{D})\Big]\cdot\nabla_\parallel A\right\}\mathrm{d}\Omega,
\end{aligned} \tag{3.60}$$

where periodic boundary conditions on A, B, $\underline{H}$ and $\underline{D}$ eliminate all boundary terms arsing from Green's identity. This concludes the form of the adjoint operator

$$\mathfrak{L}_H^\dagger(\underline{H},\underline{D})A = \Big[\nabla_\parallel^2 + \frac{\partial \Pi}{\partial H}\Big|_{\underline{H},\underline{D}}\Big]\nabla_\parallel\cdot\Big[\mathcal{M}(\underline{H})\nabla_\parallel A\Big] - \frac{\mathrm{d}\mathcal{M}}{\mathrm{d}H}\Big|_{\underline{H}}\nabla_\parallel\Big[\nabla_\parallel^2\underline{H} + \Pi(\underline{H},\underline{D})\Big]\cdot\nabla_\parallel A. \tag{3.61}$$

Recall from definition (3.49) of the objective functional $\mathcal{J}$ that its first unconstrained variation in the direction of δH is given by

$$\delta\mathcal{J}[\underline{H},\underline{D};\delta H] = \int_\Omega \delta H(\boldsymbol{X},\underline{\tau})\Big[\underline{H}(\boldsymbol{X},\underline{\tau}) - \underline{H}(\boldsymbol{X})\Big]\,\mathrm{d}\Omega. \tag{3.62}$$

With (3.59) and (3.62) in mind, the condition that $\delta\mathcal{L}$ vanishes for any spatial-temporal variation δH to the optimal trajectory $\underline{H}$ is equivalent to impose another transient partial differential equation on the optimal multiplier $\underline{\Lambda}$,

$$\left.\begin{aligned}
-\frac{\partial \underline{\Lambda}}{\partial \tau} + \mathfrak{L}_H^\dagger(\underline{H},\underline{D})\underline{\Lambda} = 0 \qquad &\text{for} \quad 0 \le \tau \le \underline{\tau}, \\
\underline{\Lambda}(\boldsymbol{X},\underline{\tau}) = \underline{H}(\boldsymbol{X}) - \underline{H}(\boldsymbol{X}) \quad &\text{at} \quad \tau = \underline{\tau}.
\end{aligned}\right\} \tag{3.63}$$

Equation (3.63) is called the adjoint (backward) PDE. The issue of ill-posedness and severe instability in backward parabolic PDEs is discussed in Isakov (2006). For instance, in the case where forward model is simply a linear diffusion PDE, the operators $\mathcal{N} = \mathfrak{L}_H = \mathfrak{L}_H^\dagger = -\nabla_\parallel^2$ all become the Laplacian and the adjoint PDE (3.63) is now the backwards diffusion equation which is peculiarly unstable at all high spatial frequencies. In general it is advised to integrate the unstable adjoint PDE backwards in time (Giles and Pierce, 2000; Stoll and Wathen, 2013) by relabeling the temporal variable $\overline{\tau} = \underline{\tau} - \tau$ so that the final time condition at $\tau = \underline{\tau}$ becomes an initial condition at $\overline{\tau} = 0$.

Likewise, the condition for which variation $\delta\mathcal{L}$ in (3.55) vanishes in all directions of δD would require us to first compute the adjoint operator of $\mathfrak{L}_D(\underline{H}, \underline{D})$ which has the analytic form

$$\begin{aligned}\int_\Omega A\mathfrak{L}_D(\underline{H}, \underline{D})B\,\mathrm{d}\Omega &= \int_\Omega B\,\mathfrak{L}_D^\dagger(\underline{H}, \underline{D})A\,\mathrm{d}\Omega \\ &= \int_\Omega B\left\{\frac{\partial \Pi}{\partial D}\Big|_{\underline{H},\underline{D}}\nabla_\parallel \cdot \Big[\mathcal{M}(\underline{H})\nabla_\parallel A\Big]\right\}\mathrm{d}\Omega, \\ \mathfrak{L}_D^\dagger(\underline{H}, \underline{D})A &= \frac{\partial \Pi}{\partial D}\Big|_{\underline{H},\underline{D}}\nabla_\parallel \cdot \Big[\mathcal{M}(\underline{H})\nabla_\parallel A\Big]. \end{aligned} \tag{3.64}$$

The free variation of the objective functional $\mathcal{J}$ with respect to δD usually comes from the regularization $\mathcal{R}[D]$ alone. For instance, the H^1 regularization (3.50) leads to,

$$\delta\mathcal{J}[\underline{H}, \underline{D}; \delta D] = \delta\mathcal{R}[\underline{D}; \delta D] = \int_\Omega \gamma\nabla_\parallel\delta D \cdot \nabla_\parallel \underline{D}\,\mathrm{d}\Omega = \int_\Omega \delta D(-\gamma\nabla_\parallel^2\underline{D})\,\mathrm{d}\Omega. \tag{3.65}$$

With (3.65) and (3.64) substituted into (3.55), the variation of Lagrangian $\mathcal{L}[\underline{H}, \underline{D}, \underline{\Lambda}]$ in the directions of all δD is evaluated to be

$$\begin{aligned}\delta\mathcal{L}[\underline{H}, \underline{D}, \underline{\Lambda}; \delta D] &= \int_\Omega \delta D(-\gamma\nabla_\parallel^2\underline{D})\,\mathrm{d}\Omega - \int_0^{\underline{\tau}}\int_\Omega \delta D\,\mathfrak{L}_D^\dagger(\underline{H}, \underline{D})\underline{\Lambda}\,\mathrm{d}\Omega\,\mathrm{d}\tau \\ &= \int_\Omega \delta D\Big\{-\gamma\nabla_\parallel^2\underline{D} - \int_0^{\underline{\tau}}\mathfrak{L}_D^\dagger(\underline{H}, \underline{D})\underline{\Lambda}\,\mathrm{d}\tau\Big\}\mathrm{d}\Omega, \end{aligned} \tag{3.66}$$

where we have exploited the fact that $\delta D(\boldsymbol{X})$ is only a spatial variation to the optimal topography $\underline{D}(\boldsymbol{X})$ and must commute with the time integral. The condition for $\delta\mathcal{L}$ to vanish for all variations $\delta D(\boldsymbol{X})$ is now straightforward:

$$\frac{\delta\mathcal{L}}{\delta D}\Big|_{\underline{H},\underline{D},\underline{\Lambda}} = -\gamma\nabla_\parallel^2\underline{D} - \int_0^{\underline{\tau}}\mathfrak{L}_D^\dagger(\underline{H}, \underline{D})\underline{\Lambda}\,\mathrm{d}\tau = 0. \tag{3.67}$$

Equation (3.67) is called the control PDE. We observe that, the effect of H^1-regularization, i.e. the term multiplied by γ, is equivalent to the Laplacian smoothing introduced through a small amount of artificial diffusion controlled by the size of γ into the system so that the optimal topography $\underline{D}(\boldsymbol{X})$ is regularized at high spatial frequencies to ensure physical plausibility in the optimal design of the electrode pattern.

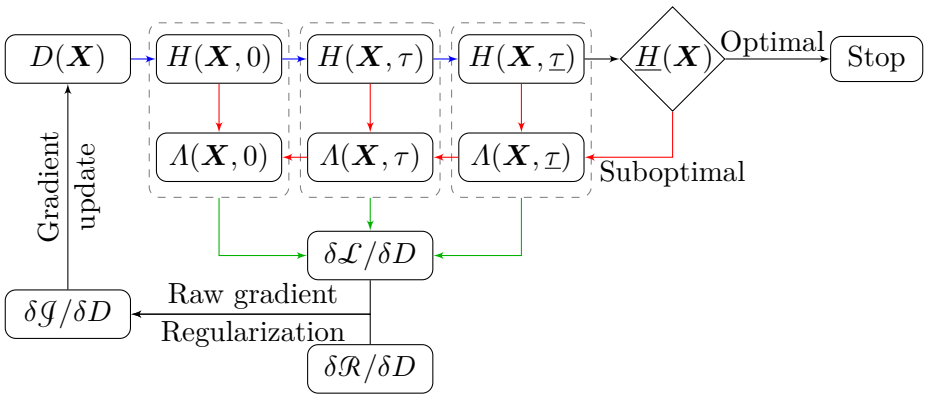

Figure 3.9: Flow chart of computing constrained variational derivative in electrode topography $D(\boldsymbol{X})$: state PDE (blue) for $H(\boldsymbol{X},\tau)$, adjoint PDE (red) for $\Lambda(\boldsymbol{X},\tau)$ and control equation (green) for $D(\boldsymbol{X})$.

In order to obtain the optimal topography $\underline{D}(\boldsymbol{X})$, one must simultaneously solve all three equations for the optimal solutions $\underline{H}(\boldsymbol{X},\tau)$, $\underline{D}(\boldsymbol{X})$ and $\underline{\Lambda}(\boldsymbol{X},\tau)$ which is a non-trivial task. In practice, the solutions to (3.58), (3.63) and (3.67) are usually acquired incrementally (Nocedal and Wright, 2006). In a typical iterative framework, we would start with a good initial guess of the topography function $D(\boldsymbol{X})$. The control equation (3.67) is relaxed whereas the state equation (3.58) and the adjoint equation (3.63) are solved exactly for $H(\boldsymbol{X},\tau)$ and $\Lambda(\boldsymbol{X},\tau)$. We then compute the residue of the control equation (3.67) and use the gradient information $\delta\mathcal{L}/\delta D$ to help the objective functional $\mathcal{J}[H,D]$ descend. Once $\mathcal{J}$ almost reaches its (local) minimum $\underline{\mathcal{J}}$, we expect $H \to \underline{H}$, $\Lambda \to \underline{\Lambda}$ and $D \to \underline{D}$ converging to their (local) optimal solutions as well. This entire process is illustrated in the flow chart shown in figure 3.9.

3.4 Adjoint-Based Discrete Optimal Control of EHL

There are two schools of numerical approach that can be taken to solve PDE-constrained optimization problems (Hinze et al., 2009): optimize-then-discretize (OTD) and discretize-then-optimize (DTO). In OTD, optimality conditions are first derived from the infinite-dimensional (continuum) partial differential equations, which often result in a set of additional PDEs as we have already encountered in Section 3.3. These equations are then discretized and solved by numerical means for the optimal solutions. In DTO, state, control and objective are first discretized into finite-dimensional objects, for example, nodal vectors in finite element space. The control solution to the resulting finite-dimensional optimization problem can be directly constructed from the underlying discrete dynamic system using techniques from dynamic programming. As discussed in Hinze et al. (2009), there is no general recipe which approach should be preferred. Ideally upon resolution refinement, OTD and DTO shall converge to the identical optimal solution. In this work we proceed with DTO since a thorough understanding of

the discrete evolution system by means of finite element approximation is already established in Section 3.2. We shall see that the DTO approach taken in this section to some extent reflects and preserves the structure inherent in the infinite-dimensional optimization problem solved in Section 3.3.

Adjoint method as duality in linear programming

Adjoint method essentially is just a way of regrouping operations which could potentially lead to a much faster way of computing infinitesimal responses of the objective to all available controls in the system. The key idea behind the adjoint method can be explained with the concept of duality in linear programming (Giles and Pierce, 2000; McNamara et al., 2004; Nocedal and Wright, 2006; Johnson, 2012).

Suppose matrices $\boldsymbol{A}$ and $\boldsymbol{B}$ are known. In many practical applications, it is of great interest to compute the matrix product between some matrix $\boldsymbol{S}$ and another yet unknown matrix $\boldsymbol{X}$ determined from the matrix equation $\boldsymbol{AX} = \boldsymbol{B}$. We call this the primal problem:

$$\text{compute} \quad \boldsymbol{S}^\top \boldsymbol{X} \quad \text{such that} \quad \boldsymbol{AX} = \boldsymbol{B}. \qquad \text{(primal)} \tag{3.68}$$

Of course the dimensions of matrices $\boldsymbol{A}$, $\boldsymbol{B}$, $\boldsymbol{X}$ and $\boldsymbol{S}$ have to be compatible,

$$\boldsymbol{A}_{p\times q}, \quad \boldsymbol{X}_{q\times r}, \quad \boldsymbol{B}_{p\times r}, \quad \boldsymbol{S}_{q\times s}, \tag{3.69}$$

where p, q, r and s are positive integers. The most straightforward method is to first solve $\boldsymbol{AX} = \boldsymbol{B}$ either by direct or iterative methods and then perform matrix multiplication between $\boldsymbol{S}^\top$ and $\boldsymbol{X}$. Alternatively, we can consider the dual of the primal problem (3.68) by introducing an adjoint matrix $\boldsymbol{Y}_{p\times s}$ such that matrix product in (3.68) is equivalent to the solution of the dual problem:

$$\text{compute} \quad \boldsymbol{Y}^\top \boldsymbol{B} \quad \text{such that} \quad \boldsymbol{A}^\top \boldsymbol{Y} = \boldsymbol{S}. \qquad \text{(dual)} \tag{3.70}$$

Using basic rules of matrix operation we can easily prove the equivalence between the primal problem (3.68) and its dual (3.70),

$$\boldsymbol{S}^\top \boldsymbol{X} = (\boldsymbol{X}^\top \boldsymbol{S})^\top = (\boldsymbol{X}^\top \boldsymbol{A}^\top \boldsymbol{Y})^\top = \boldsymbol{Y}^\top \boldsymbol{AX} = \boldsymbol{Y}^\top \boldsymbol{B}. \tag{3.71}$$

The name "adjoint method" stems from the adjoint matrix $\boldsymbol{A}^\top$ instead of $\boldsymbol{A}$ in the linear system (3.70).

Despite the equivalence between their final outcomes, the operational cost of solving the primal problem versus its dual can be drastically different. Computational complexity of the primal (3.68) and the dual (3.70) are tightly related to the matrix dimension r and s. If we only restrict ourselves to very basic algorithms of numerical linear algebra, then computational cost of the primal formulation (3.68) is equivalent to

$$\text{solve } p \times q \text{ linear system } r \text{ times} + O(rsq) \text{ matrix multiplication.} \tag{3.72}$$

For the dual formulation (3.70), we have another estimation,

$$\text{solve } q \times p \text{ linear system } s \text{ times} + O(rsp) \text{ matrix multiplication.} \tag{3.73}$$

In numerical analysis of physical problems, it is common to have dimensions $O(p) \sim O(q)$. For example in PDE-constrained optimization, $\boldsymbol{A}$ can be taken as the discrete form of some differential operator and is almost always a square matrix. Then it immediately follows that the primal formulation (3.68) would be more efficient if $s \gg r$ whereas the dual formulation is more advantageous if $r \gg s$. We shall see in the next section that, the control problem (3.51) of Electrohydrodynamic Lithography, after discretization, greatly benefits from the adjoint (dual) formulation.

In the context of control theory, dimension r in $\boldsymbol{B}$ is often connected to the available degrees of freedom in the control of the system and the dimension s of $\boldsymbol{S}$ is related to the dimension of the objective of interest. For example, a natural strategy for designing a multi-dimensional space curve on a computer screen with mouse as the only navigation tool is to modify the curve progressively in a trial-and-error fashion. Such procedure corresponds to the primal formulation (3.68) since the control (mouse movement on a screen) is low-dimensional whereas the objective (multi-dimensional coordinates of the space curve) has a much higher degrees of freedom. It's therefore much easier and more efficient for us to first map out the responses of the space curve to mouse movement. However it is not the case in modern airfoil shape optimization where the objective is usually to maximize the lift coefficient or to minimize the drag coefficient using hundreds of design parameters from the geometry parameterization. Adjoint method (Jameson, 1988) complemented with advances in Newton-based optimization scheme and the relentless increases in CPU speed and memory capacity, has largely removed the limitation on the number of design parameters and allows the "truly optimal" designs to be computed.

Discretize-then-optimize

The finite element procedure outlined in Section 3.2 propagates a discretized initial film state $\boldsymbol{H}_0$ into n_τ subsequent states $\boldsymbol{H}_1, \dots, \boldsymbol{H}_{n_\tau}$. Let integer n_H be the degrees of freedom in any discrete film state $\boldsymbol{H}_k$. For notation simplicity, we concatenate the entire sequence of film states $\boldsymbol{H}_1, \dots, \boldsymbol{H}_{n_\tau}$ into a master state vector

$$\boldsymbol{H}^\top = [\boldsymbol{H}_1^\top, \dots, \boldsymbol{H}_{n_\tau}^\top]. \tag{3.74}$$

Given a sequence of film states $\boldsymbol{H}_0, \dots, \boldsymbol{H}_k$ up to the k-th time step, the film state $\boldsymbol{H}_{k+1}$ at the next time step is the solution to the discrete dynamics (3.43) of the nonlinear state PDE,

$$\boldsymbol{F}_{k+1}(\boldsymbol{H}_{k-1}, \boldsymbol{H}_k, \boldsymbol{H}_{k+1}, \boldsymbol{D}) = \boldsymbol{0} \quad \text{for} \quad k = 1, \dots, n_\tau - 1, \tag{3.75}$$

where $\boldsymbol{F}_{k+1} \in \mathbb{R}^{n_H}$ is a nonlinear function of its arguments arsing from the particular discretization method used in the numerical simulation. In the fully discretized finite element formulation of electrohydrodynamic thin film equation, $\boldsymbol{F}_{k+1}$ takes the form in equation (3.44). In the same spirit of master state vector (3.74), we introduce a master nonlinear function $\boldsymbol{F}(\boldsymbol{H}, \boldsymbol{D})$ whose action on the master vector $\boldsymbol{H}$ is given by

$$\begin{aligned}\boldsymbol{F}(\boldsymbol{H}, \boldsymbol{D})^\top = [\boldsymbol{F}_1(\boldsymbol{H}_0, \boldsymbol{H}_1, \boldsymbol{D})^\top, \boldsymbol{F}_2(\boldsymbol{H}_0, \boldsymbol{H}_1, \boldsymbol{H}_2, \boldsymbol{D})^\top, \\ \dots, \boldsymbol{F}_{n_\tau}(\boldsymbol{H}_{n_\tau-2}, \boldsymbol{H}_{n_\tau-1}, \boldsymbol{H}_{n_\tau}, \boldsymbol{D})^\top].\end{aligned} \tag{3.76}$$

With the master notation introduced, we can express the discrete version of the optimization problem (3.51) in a concise matrix form: given initial film thickness H_0, termination time $\underline{\tau}$, dimensions of the periodic domain Ω and the desired discrete target film profile $\underline{\boldsymbol{H}}$, find the optimal discrete electrode topography

$$\underline{\boldsymbol{D}} = \underset{\boldsymbol{D}}{\operatorname{argmin}}\ J(\boldsymbol{H}, \boldsymbol{D}) \quad \text{subject to} \quad \boldsymbol{F}(\boldsymbol{H}, \boldsymbol{D})^\top = [\boldsymbol{0}^\top, \dots, \boldsymbol{0}^\top], \tag{3.77}$$

where

$$J(\boldsymbol{H}, \boldsymbol{D}) = \frac{1}{2}(\boldsymbol{H}_{n_\tau} - \underline{\boldsymbol{H}})^\top \boldsymbol{M}(\boldsymbol{H}_{n_\tau} - \underline{\boldsymbol{H}}) + \frac{\gamma}{2}\boldsymbol{D}^\top \boldsymbol{K}\boldsymbol{D} \tag{3.78}$$

is the discrete version of the continuous objective functional $\mathcal{J}(H(\boldsymbol{X}, \underline{\tau}), D(\boldsymbol{X}))$ defined in equation (3.49). The evaluation of the discrete objective $J(\boldsymbol{H}, \boldsymbol{D})$ is constrained to a finite-dimensional (since discretized) hypersurface implicitly specified by $\boldsymbol{F}(\boldsymbol{H}, \boldsymbol{D}) = [\boldsymbol{0}^\top, \dots, \boldsymbol{0}^\top]^\top$.

Now suppose we have a discretized electrode pattern $\boldsymbol{D}$ and have solved the evolution equation for the master vector $\boldsymbol{H}$ via some numerical method, for instance the finite element method. In order to proceed with any kind of local optimization algorithm, we must acquire the total derivative (or the gradient) of objective J with respect to $\boldsymbol{D}$,

$$\frac{\mathrm{d}J}{\mathrm{d}\boldsymbol{D}} = \frac{\partial J}{\partial \boldsymbol{H}}\frac{\mathrm{d}\boldsymbol{H}}{\mathrm{d}\boldsymbol{D}} + \frac{\partial J}{\partial \boldsymbol{D}}, \tag{3.79}$$

where the numerator layout convention (Minka, 1997) is assumed throughout. The second quantity on the right hand side of equation (3.79), i.e. partial derivative $\partial J/\partial \boldsymbol{D}$, is easy to compute since it usually comes from the regularization term exclusively which only involves $\boldsymbol{D}$ in case of (3.78). The real challenge lies in the matrix differentiation term $\mathrm{d}\boldsymbol{H}/\mathrm{d}\boldsymbol{D}$: any change in the discrete form of electrode pattern $\boldsymbol{D}$ would affect the entire sequence of film states $\boldsymbol{H}_1, \boldsymbol{H}_2, \dots, \boldsymbol{H}_{n_\tau}$. There is always a brutal-force approach, namely the finite difference approximation: first slightly modify the current design of electrode $\boldsymbol{D}$ by some perturbation $\delta\boldsymbol{D}$, run the simulation again with the perturbed electrode $\boldsymbol{D}+\epsilon\delta\boldsymbol{D}$ for some small parameter $\epsilon \ll 1$ and check for the resulting variations in film states. For example a central difference method would provide a second-order accuracy in ϵ (Nocedal and Wright, 2006):

$$\frac{\mathrm{d}\boldsymbol{H}}{\mathrm{d}\boldsymbol{D}}\delta\boldsymbol{D} \approx \frac{\boldsymbol{H}(\boldsymbol{D} + \epsilon\delta\boldsymbol{D}) - \boldsymbol{H}(\boldsymbol{D} - \epsilon\delta\boldsymbol{D})}{2\epsilon} + O(\epsilon^2). \tag{3.80}$$

However in order to obtain the full gradient, it would require a complete set of perturbations $\{\delta_0\boldsymbol{D}, \delta_1\boldsymbol{D}, ...\}$ which span all degrees of freedom available in the design space of the electrode topography $\boldsymbol{D}$. The finite difference approximation (3.80) must be computed for every single perturbation $\delta_i\boldsymbol{D}$ in that set. In Electrohydrodynamic Lithography, the electrode pattern, just like the interface shape of the liquid film, is expected to have a continuous geometry. Thus the discrete electrode pattern $\boldsymbol{D}$ may contain as many degrees of freedom as the discrete film state $\boldsymbol{H}_i$. In finite element method where the continuous film state $H(\boldsymbol{X}, \tau)$ is discretized into a large number of elements easily exceeding $O(10^4)$, the finite difference approach (3.80) is clearly not viable. An even bigger issue is the error of the inexact gradient approximated by the finite difference approach. Such approximate gradient may work for any first order optimization method but is not suitable for second order methods. For example, the quasi-Newton methods approximate the second order information (i.e. Hessian matrix) to speed up optimization process by accumulating the first order gradients of the objective. The error in the inexact gradient would propagate and eventually destroy the accuracy in the approximate Hessian which virtually all quasi-Newton methods heavily rely on.

A more efficient and reliable approach is to implicitly extract $\mathrm{d}\boldsymbol{H}/\mathrm{d}\boldsymbol{D}$ from $\boldsymbol{F}(\boldsymbol{H}, \boldsymbol{D})$ by differentiating with respect to $\boldsymbol{D}$ on both sides of the constraint equation in (3.77),

$$\frac{\partial \boldsymbol{F}}{\partial \boldsymbol{H}}\frac{\mathrm{d}\boldsymbol{H}}{\mathrm{d}\boldsymbol{D}} + \frac{\partial \boldsymbol{F}}{\partial \boldsymbol{D}} = \boldsymbol{0}. \tag{3.81}$$

According to the exact gradient expression (3.79) of $\mathrm{d}J/\mathrm{d}\boldsymbol{D}$, the matrix quantity $\mathrm{d}\boldsymbol{H}/\mathrm{d}\boldsymbol{D}$ alone, whose dimension can be potentially very large, is not of interest but rather its matrix product with $\partial J/\partial \boldsymbol{H}$. A simple rearrangement of (3.81) yields the computational problem needed to be solved:

$$\text{compute} \quad \frac{\partial J}{\partial \boldsymbol{H}}\frac{\mathrm{d}\boldsymbol{H}}{\mathrm{d}\boldsymbol{D}} \quad \text{such that} \quad \frac{\partial \boldsymbol{F}}{\partial \boldsymbol{H}}\frac{\mathrm{d}\boldsymbol{H}}{\mathrm{d}\boldsymbol{D}} = -\frac{\partial \boldsymbol{F}}{\partial \boldsymbol{D}}. \tag{3.82}$$

Problem (3.82) is precisely the primal formulation (3.68) discussed in the last section. If we count the dimensions of the matrices involved,

$$\left[\frac{\partial J}{\partial \boldsymbol{H}}\right]_{1\times n_\tau n_H}, \left[\frac{\mathrm{d}\boldsymbol{H}}{\mathrm{d}\boldsymbol{D}}\right]_{n_\tau n_H \times n_D}, \left[\frac{\partial \boldsymbol{F}}{\partial \boldsymbol{H}}\right]_{n_\tau n_H \times n_\tau n_H}, \left[\frac{\partial \boldsymbol{F}}{\partial \boldsymbol{D}}\right]_{n_\tau n_H \times n_D}, \tag{3.83}$$

it's evident that the dual formulation of problem (3.82) is much more efficient. Let $\boldsymbol{\Lambda}_{n_\tau n_H \times 1}$ be the master adjoint matrix (in fact $\boldsymbol{\Lambda}$ and $[\partial J/\partial \boldsymbol{H}]^\top$ in this problem are both column vectors). Then the dual formulation of the primal problem (3.82) reads,

$$\text{compute} \quad -\boldsymbol{\Lambda}^\top\frac{\partial \boldsymbol{F}}{\partial \boldsymbol{D}} \quad \text{such that} \quad \frac{\partial \boldsymbol{F}}{\partial \boldsymbol{H}}^\top \boldsymbol{\Lambda} = \frac{\partial J}{\partial \boldsymbol{H}}^\top. \tag{3.84}$$

To obtain the exact gradient of objective function $J(\boldsymbol{H}, \boldsymbol{D})$, we only need to solve the linear system defined in the dual problem (3.84) for adjoint vector $\boldsymbol{\Lambda}$ once regardless of the total degree of freedom in the control vector $\boldsymbol{D}$.

Let's now delve more specifically into the details of calculating the adjoint system (3.84). The vector on the right hand side of the matrix equation has a simple structure,

$$\frac{\partial J}{\partial \boldsymbol{H}} = [\boldsymbol{0}^\top, \dots, \boldsymbol{0}^\top, (\boldsymbol{H}_{n_\tau} - \underline{\boldsymbol{H}})^\top \boldsymbol{M}]. \tag{3.85}$$

Most entries of $\partial J/\partial \boldsymbol{H}$ are zero because our objective J only concerns the difference between final film state $\boldsymbol{H}_{n_\tau}$ and target state $\underline{\boldsymbol{H}}$. These zero entries would be non-zero if our objective is affected by the intermediate evolution as well. We next make an important observation that, despite its deceivingly large dimensions, $\partial \boldsymbol{F}/\partial \boldsymbol{H}$ is a sparse block matrix because the time integration scheme (BDF) only relates up to three states adjacent in time. This argument becomes clear if we write out the block-matrix representation of $\partial \boldsymbol{F}/\partial \boldsymbol{H}$ explicitly,

$$\frac{\partial \boldsymbol{F}}{\partial \boldsymbol{H}} = \begin{bmatrix} \frac{\partial \boldsymbol{F}_1}{\partial \boldsymbol{H}_1} & & & \cdots & \boldsymbol{0} \\ \frac{\partial \boldsymbol{F}_2}{\partial \boldsymbol{H}_1} & \frac{\partial \boldsymbol{F}_2}{\partial \boldsymbol{H}_2} & & & \vdots \\ \frac{\partial \boldsymbol{F}_3}{\partial \boldsymbol{H}_1} & \frac{\partial \boldsymbol{F}_3}{\partial \boldsymbol{H}_2} & \frac{\partial \boldsymbol{F}_3}{\partial \boldsymbol{H}_3} & & \\ & \frac{\partial \boldsymbol{F}_4}{\partial \boldsymbol{H}_2} & \frac{\partial \boldsymbol{F}_4}{\partial \boldsymbol{H}_3} & \frac{\partial \boldsymbol{F}_4}{\partial \boldsymbol{H}_4} & \\ \vdots & & \ddots & \ddots & \ddots \\ \boldsymbol{0} & \cdots & & \frac{\partial \boldsymbol{F}_{-1}}{\partial \boldsymbol{H}_{-3}} & \frac{\partial \boldsymbol{F}_{-1}}{\partial \boldsymbol{H}_{-2}} & \frac{\partial \boldsymbol{F}_{-1}}{\partial \boldsymbol{H}_{-1}} \end{bmatrix}. \tag{3.86}$$

Note the block matrix (3.86) is not only sparse but also lower-triangular ($[\partial \boldsymbol{F}/\partial \boldsymbol{H}]^\top$ is upper-triangular). The master adjoint vector $\boldsymbol{\Lambda}$ given by the adjoint linear system (3.84) can be efficiently computed through backward substitution without the constructing and storing the entire matrix $[\partial \boldsymbol{F}/\partial \boldsymbol{H}]^\top$. If we break the master adjoint vector

$$\boldsymbol{\Lambda}^\top = [\boldsymbol{\Lambda}_1^\top, \dots, \boldsymbol{\Lambda}_{n_\tau}^\top] \tag{3.87}$$

into a concatenated sequence of adjoint states $\boldsymbol{\Lambda}_k$ (similar to how the master state vector $\boldsymbol{H}$ is formed), then the ensemble of all matrix equations needed to be solved according to the adjoint system (3.84) forms a discrete dynamical system for the subsequent adjoint

states $\boldsymbol{\Lambda}_k$,

$$\left.\begin{aligned}
\left[\frac{\partial \boldsymbol{F}_{n_\tau}}{\partial \boldsymbol{H}_{n_\tau}}\right]^\top \boldsymbol{\Lambda}_{n_\tau} &= \left[\frac{\partial J}{\partial \boldsymbol{H}_{n_\tau}}\right]^\top, \\
\left[\frac{\partial \boldsymbol{F}_{n_\tau-1}}{\partial \boldsymbol{H}_{n_\tau-1}}\right]^\top \boldsymbol{\Lambda}_{n_\tau-1} &= -\left[\frac{\partial \boldsymbol{F}_{n_\tau}}{\partial \boldsymbol{H}_{n_\tau-1}}\right]^\top \boldsymbol{\Lambda}_{n_\tau}, \\
&\vdots \\
\left[\frac{\partial \boldsymbol{F}_{k}}{\partial \boldsymbol{H}_{k}}\right]^\top \boldsymbol{\Lambda}_{k} &= -\left[\frac{\partial \boldsymbol{F}_{k+1}}{\partial \boldsymbol{H}_{k}}\right]^\top \boldsymbol{\Lambda}_{k+1} - \left[\frac{\partial \boldsymbol{F}_{k+2}}{\partial \boldsymbol{H}_{k}}\right]^\top \boldsymbol{\Lambda}_{k+2}, \\
&\vdots \\
\left[\frac{\partial \boldsymbol{F}_{1}}{\partial \boldsymbol{H}_{1}}\right]^\top \boldsymbol{\Lambda}_{1} &= -\left[\frac{\partial \boldsymbol{F}_{2}}{\partial \boldsymbol{H}_{1}}\right]^\top \boldsymbol{\Lambda}_{2} - \left[\frac{\partial \boldsymbol{F}_{3}}{\partial \boldsymbol{H}_{1}}\right]^\top \boldsymbol{\Lambda}_{3},
\end{aligned}\right\} \tag{3.88}$$

where $\partial J/\partial \boldsymbol{H}_{n_\tau} = \boldsymbol{M}(\boldsymbol{H}_{n_\tau} - \underline{\boldsymbol{H}})$. In the adjoint dynamical system (3.88), the final adjoint state $\boldsymbol{\Lambda}_{n_\tau}$ propagates the discrepancy between the final film state $\boldsymbol{H}_{n_\tau}$ and the target film profile $\underline{\boldsymbol{H}}$ to the preceding adjoint states backwards in time.

Once we have obtained the whole sequence of adjoint states $\boldsymbol{\Lambda}_1, \dots, \boldsymbol{\Lambda}_{n_\tau}$, we are left with the contraction between master adjoint vector $\boldsymbol{\Lambda}$ and $\partial \boldsymbol{F}/\partial \boldsymbol{D}$ according to the dual formulation (3.84). The fact that $\partial \boldsymbol{F}/\partial \boldsymbol{D}$ is block-diagonal significantly simplifies the vector-matrix contraction,

$$-\boldsymbol{\Lambda}^\top \frac{\partial \boldsymbol{F}}{\partial \boldsymbol{D}} = \sum_{k=1}^{n_\tau} \boldsymbol{C}_k, \quad \boldsymbol{C}_k = -\boldsymbol{\Lambda}_k^\top \frac{\partial \boldsymbol{F}_k}{\partial \boldsymbol{D}}, \tag{3.89}$$

where the vectors $\boldsymbol{C}_k$ are interpreted as the generalized constraint forces (as in classical Lagrangian mechanics) required to enforce the temporal trajectory of film states $\boldsymbol{H}_k$ staying on the abstract manifold described by the PDE constraint (3.75) at all times.

By the definition of $\boldsymbol{F}_{k+1}(\boldsymbol{H}_{k-1}, \boldsymbol{H}_k, \boldsymbol{H}_{k+1}, \boldsymbol{D})$ in equation (3.44), we can write down the analytic expression of the partial differentiation of $\boldsymbol{F}_{k+1}$ with respective to its arguments,

$$\frac{\partial \boldsymbol{F}_{k+1}}{\partial \boldsymbol{H}_{k-1}} = -\alpha_k^- \boldsymbol{M}, \tag{3.90}$$

$$\frac{\partial \boldsymbol{F}_{k+1}}{\partial \boldsymbol{H}_{k}} = -\alpha_k^0 \boldsymbol{M} + \Delta\tau_k \alpha_k^+ \frac{\partial \boldsymbol{R}_{k+1}}{\partial \boldsymbol{H}_k}, \tag{3.91}$$

$$\frac{\partial \boldsymbol{F}_{k+1}}{\partial \boldsymbol{H}_{k+1}} = \boldsymbol{M} + \Delta\tau_k \alpha_k^+ \frac{\partial \boldsymbol{R}_{k+1}}{\partial \boldsymbol{H}_{k+1}}, \tag{3.92}$$

$$\frac{\partial \boldsymbol{F}_{k+1}}{\partial \boldsymbol{D}} = \Delta\tau_k \alpha_k^+ \frac{\partial \boldsymbol{R}_{k+1}}{\partial \boldsymbol{D}}. \tag{3.93}$$

Substituting these partial derivatives into the discrete adjoint dynamical system (3.88)

yields the adjoint system for the electrohydrodynamic thin film equation,

$$\left.\begin{aligned}
\left\{\boldsymbol{M}+\Delta\tau_{n_\tau-1}\alpha^+_{n_\tau-1}\left[\frac{\partial \boldsymbol{R}_{n_\tau}}{\partial \boldsymbol{H}_{n_\tau}}\right]^\top\right\}\boldsymbol{\Lambda}_{n_\tau} &= \boldsymbol{M}(\boldsymbol{H}_{n_\tau}-\underline{\boldsymbol{H}}),\\
\left\{\boldsymbol{M}+\Delta\tau_{n_\tau-2}\alpha^+_{n_\tau-2}\left[\frac{\partial \boldsymbol{R}_{n_\tau-1}}{\partial \boldsymbol{H}_{n_\tau-1}}\right]^\top\right\}\boldsymbol{\Lambda}_{n_\tau-1} &= \boldsymbol{M}\alpha^0_{n_\tau-1}\boldsymbol{\Lambda}_{n_\tau},\\
&\quad -\Delta\tau_{n_\tau-1}\alpha^+_{n_\tau-1}\left[\frac{\partial \boldsymbol{R}_{n_\tau}}{\partial \boldsymbol{H}_{n_\tau-1}}\right]^\top\boldsymbol{\Lambda}_{n_\tau},\\
&\vdots\\
\left\{\boldsymbol{M}+\Delta\tau_{k-1}\alpha^+_{k-1}\left[\frac{\partial \boldsymbol{R}_{k}}{\partial \boldsymbol{H}_{k}}\right]^\top\right\}\boldsymbol{\Lambda}_{k} &= \boldsymbol{M}(\alpha^0_k\boldsymbol{\Lambda}_{k+1}+\alpha^-_{k+1}\boldsymbol{\Lambda}_{k+2})\\
&\quad -\Delta\tau_k\alpha^+_k\left[\frac{\partial \boldsymbol{R}_{k+1}}{\partial \boldsymbol{H}_{k}}\right]^\top\boldsymbol{\Lambda}_{k+1},\\
&\vdots\\
\left\{\boldsymbol{M}+\Delta\tau_0\alpha^+_0\left[\frac{\partial \boldsymbol{R}_{1}}{\partial \boldsymbol{H}_{1}}\right]^\top\right\}\boldsymbol{\Lambda}_{1} &= \boldsymbol{M}(\alpha^0_1\boldsymbol{\Lambda}_{2}+\alpha^-_2\boldsymbol{\Lambda}_{3})\\
&\quad -\Delta\tau_1\alpha^+_1\left[\frac{\partial \boldsymbol{R}_{2}}{\partial \boldsymbol{H}_{1}}\right]^\top\boldsymbol{\Lambda}_{2}.
\end{aligned}\right\} \tag{3.94}$$

Discrete dynamical system (3.94) resembles a semi-implicit time integration scheme applied backwards since the solution to $\boldsymbol{\Lambda}_k$ requires $\boldsymbol{\Lambda}_{k+1}$ and $\boldsymbol{\Lambda}_{k+2}$ as well as $\boldsymbol{\Lambda}_k$ itself. This is one of the reasons we choose a semi-implicit scheme for the (forward) time integration of the film state $\boldsymbol{H}_k$ as opposed to the fully implicit used by Becker et al., 2002. If the forward time stepping was fully implicit, then the time integration of the discrete adjoint dynamics would be fully explicit and hence may be subject to certain stability criterion. The discrete control equation (3.89) is essentially a Riemann sum in time, i.e. approximating the time integral in the continuous control equation (3.67) by a series of rectangular "boxes" in time. We also note that the summation in (3.89) can be accumulated concurrently with the backwards propagating adjoint vector $\boldsymbol{\Lambda}_k$. The procedure of computing discrete optimal control is illustrated in the flow chart 3.10.

In order to implement the discrete dynamical system (3.94) for adjoint states, we need to compute the analytic expressions of differentiating $\boldsymbol{R}_{k+1}(\boldsymbol{H}_k, \boldsymbol{H}_{k+1}, \boldsymbol{D})$ with respect to its arguments. We recall the definition of $\boldsymbol{R}_{k+1}$ from (3.44) and derive,

$$\frac{\partial \boldsymbol{R}_{k+1}}{\partial \boldsymbol{H}_{k+1}} = \boldsymbol{W}(\boldsymbol{H}_k)\Big[\boldsymbol{M}^{-1}\boldsymbol{K}-\frac{\partial \boldsymbol{\Pi}(\boldsymbol{H}_{k+1},\boldsymbol{D})}{\partial \boldsymbol{H}_{k+1}}\Big], \tag{3.95}$$

$$\frac{\partial \boldsymbol{R}_{k+1}}{\partial \boldsymbol{H}_{k}} = \frac{\partial \boldsymbol{W}(\boldsymbol{H}_k)\boldsymbol{P}_{k+1}}{\partial \boldsymbol{H}_{k}}, \quad \boldsymbol{P}_{k+1} = \boldsymbol{M}^{-1}\boldsymbol{K}\boldsymbol{H}_{k+1}-\boldsymbol{\Pi}(\boldsymbol{H}_{k+1},\boldsymbol{D}), \tag{3.96}$$

$$\frac{\partial \boldsymbol{R}_{k+1}}{\partial \boldsymbol{D}} = -\boldsymbol{W}(\boldsymbol{H}_k)\frac{\partial \boldsymbol{\Pi}(\boldsymbol{H}_{k+1},\boldsymbol{D})}{\partial \boldsymbol{D}}. \tag{3.97}$$

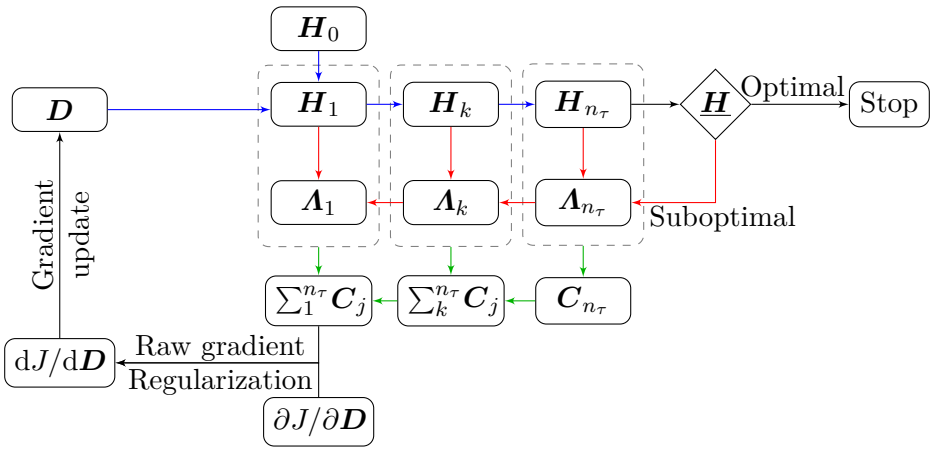

Figure 3.10: Flow chart: discrete state equation (blue) for $\boldsymbol{H}_k$, discrete adjoint equation (red) for $\boldsymbol{\Lambda}_k$ and discrete control equation (green) for $\boldsymbol{C}_k$.

The assembly of matrices $\partial \boldsymbol{R}_{k+1}/\partial \boldsymbol{H}_{k+1}$ and $\partial \boldsymbol{R}_{k+1}/\partial \boldsymbol{D}$ is straightforward, the former of which we have already encountered in the forward time integration of film state $\boldsymbol{H}_k$. To the contrary, we must be careful about the calculation of $\partial \boldsymbol{R}_{k+1}/\partial \boldsymbol{H}_k$ which seems to be deceptively simple. Technically we could have directly evaluated the expression of $\partial \boldsymbol{W}(\boldsymbol{H}_k)/\partial \boldsymbol{H}_k$ first and then contract it with $\boldsymbol{P}_{k+1}$ since $\boldsymbol{P}_{k+1}$ doesn't depend on $\boldsymbol{H}_k$ at all. However, $\boldsymbol{W}(\boldsymbol{H}_k)$ is a matrix whose entries are assembled from the state vector $\boldsymbol{H}_k$. A naive differentiation of $\boldsymbol{W}$ with respect to $\boldsymbol{H}_k$ would promote $\partial \boldsymbol{W}(\boldsymbol{H}_k)/\partial \boldsymbol{H}_k$ to a rank-3 tensor whose the storage and contraction with other tensorial objects can be computationally challenging. Fortunately, the sparsity in matrix $\boldsymbol{W}$ allows us to compute the exact expression of $\partial \boldsymbol{R}_{k+1}/\partial \boldsymbol{H}_k$ in a much more efficient way.

Differentiation of weighted stiffness matrix

Before digging into details of differentiating weighted stiffness matrix $\boldsymbol{W}(\boldsymbol{H}_k)$, we need to first analyze the assembly pattern for the stiffness matrix $\boldsymbol{K}$. Let's introduce the operator

$$[i] : \text{global nodal indices} \to \text{sets of elemental indices} \tag{3.98}$$

to denote the index set of all elements which contain the i-th node. We also define the surjective map

$$i|e : \text{global nodal indices} \to \text{local nodal indices of element } Q_e, \tag{3.99}$$

which maps a global index i to its local nodal index $i|e$ in element Q_e. A first glance at the definition (3.36) of stiffness matrix $\boldsymbol{K}$ suggests a nodal-index-based strategy for assembling each of its entry K_{ij}. In practice, it's more convenient to perform an assembling procedure that loops over elemental indices instead. To see this, we define

the elemental (local) stiffness matrix $\boldsymbol{K}^e$ with its entries

$$K_{ij}^e = \begin{cases} \langle \nabla_{\parallel} \mathbb{N}_{i|e}^e, \nabla_{\parallel} \mathbb{N}_{j|e}^e \rangle & \text{if } \boldsymbol{X}_i \text{ and } \boldsymbol{X}_j \in Q_e, \\ 0 & \text{otherwise.} \end{cases} \tag{3.100}$$

According to definition (3.36), the ij-entry of the global stiffness matrix $\boldsymbol{K}$ can be expressed as

$$K_{ij} = \sum_{e \in [i] \cap [j]} K_{ij}^e. \tag{3.101}$$

The restriction on the summation $e \in [i] \cap [j]$ is fact redundant. To see this argument, let's consider an element $Q_{e'}$ such that $e' \notin [i] \cap [j]$. Then by definition (3.100) of local stiffness matrix $\boldsymbol{K}^{e'}$, its ij-entry $K_{ij}^{e'}$ must be zero otherwise e' would belong to $e \in [i] \cap [j]$. Thus the global stiffness matrix $\boldsymbol{K}$ is the sum of all elemental stiffness matrices $\boldsymbol{K}^e$,

$$\boldsymbol{K} = \sum_e \boldsymbol{K}^e. \tag{3.102}$$

Inspired by the element-wise assembling strategy of the global stiffness matrix $\boldsymbol{K}$, we reformulate the formidable matrix-vector multiplication in (3.96) by breaking the node-wise definition (3.38) of weighted stiffness matrix $\boldsymbol{W}$ into a sum of local weighted stiffness matrices $\boldsymbol{W}^e$ which are assembled locally in each element Q_e,

$$W(A)_{ij} = \begin{cases} \langle \nabla_{\parallel} \mathbb{N}_{i|e}^e, \mathscr{P}_{\mathrm{h}}[\mathcal{M}(A)] \nabla_{\parallel} \mathbb{N}_{j|e}^e \rangle & \text{if } \boldsymbol{X}_i \text{ and } \boldsymbol{X}_j \in Q_e, \\ 0 & \text{otherwise.} \end{cases} \tag{3.103}$$

Then the contraction between the global weighted stiffness matrix $\boldsymbol{W}(\boldsymbol{A})$ and some nodal vector $\boldsymbol{B}$ is the sum of the individual contraction between each local weighted stiffness matrices $\boldsymbol{W}^e$ and $\boldsymbol{B}$,

$$\boldsymbol{W}(\boldsymbol{A})\boldsymbol{B} = \sum_e \boldsymbol{W}^e(\boldsymbol{A})\boldsymbol{B}, \tag{3.104}$$

which then can be further reduced to the interactions between nodal basis functions $\mathbb{N}_{i|e}^e$,

$$\begin{aligned} [\boldsymbol{W}^e(\boldsymbol{A})\boldsymbol{B}]_i &= \sum_k W_{ik}^e B_k \\ &= \sum_{\boldsymbol{X}_k \in Q_e} B_k \int_{Q_e} \Big(\sum_{\boldsymbol{X}_j \in Q_e} \mathcal{M}(A_j) \mathbb{N}_{j|e}^e \Big) (\nabla_{\parallel} \mathbb{N}_{i|e}^e) \cdot (\nabla_{\parallel} \mathbb{N}_{k|e}^e) \, \mathrm{d}\Omega \\ &= \sum_{\boldsymbol{X}_k \in Q_e} \sum_{\boldsymbol{X}_j \in Q_e} \mathcal{M}(A_j) B_k \int_{Q_e} \mathbb{N}_{j|e}^e (\nabla_{\parallel} \mathbb{N}_{i|e}^e) \cdot (\nabla_{\parallel} \mathbb{N}_{k|e}^e) \, \mathrm{d}\Omega \\ &= 0 \quad \text{if} \quad \boldsymbol{X}_i \notin Q_e. \end{aligned} \tag{3.105}$$

Differentiating the local matrix-vector product $\boldsymbol{W}^e(\boldsymbol{A})\boldsymbol{B}$ defined in (3.105) with respect to $\boldsymbol{B}$ now becomes straightforward,

$$\begin{aligned}\Big[\frac{\partial \boldsymbol{W}^e(\boldsymbol{A})\boldsymbol{B}}{\partial \boldsymbol{A}}\Big]_{ij} &= \frac{\partial [\boldsymbol{W}^e(\boldsymbol{A})\boldsymbol{B}]_i}{\partial A_j} \\ &= \frac{\mathrm{d}\mathcal{M}(A_j)}{\mathrm{d}A_j} \sum_{\boldsymbol{X}_k \in Q_e} B_k \int_{Q_e} \mathbb{N}^e_{j|e}(\nabla_{\|}\mathbb{N}^e_{i|e}) \cdot (\nabla_{\|}\mathbb{N}^e_{k|e})\,\mathrm{d}\Omega \\ &= 0 \quad \text{if} \quad \boldsymbol{X}_i \text{ or } \boldsymbol{X}_j \notin Q_e.\end{aligned} \tag{3.106}$$

Just like the stiffness and the mass matrix, $\partial \boldsymbol{W}^e(\boldsymbol{A})\boldsymbol{B}/\partial \boldsymbol{A}$ is a local matrix of element Q_e as well. The global matrix $\partial \boldsymbol{W}(\boldsymbol{A})\boldsymbol{B}/\partial \boldsymbol{A}$ can be assembled in a similar element-by-element fashion instead,

$$\frac{\partial \boldsymbol{W}(\boldsymbol{A})\boldsymbol{B}}{\partial \boldsymbol{A}} = \frac{\partial}{\partial \boldsymbol{A}} \sum_e \boldsymbol{W}^e(\boldsymbol{A})\boldsymbol{B} = \sum_e \frac{\partial \boldsymbol{W}^e(\boldsymbol{A})\boldsymbol{B}}{\partial \boldsymbol{A}}. \tag{3.107}$$

It turns out that in equation (3.106) we do need to compute a rank-3 tensor $\boldsymbol{N}^e$ only much smaller, constructed from the Lagrange basis of each individual element,

$$N^e_{ijk} = \int_{Q_e} \mathbb{N}^e_{j|e}(\nabla_{\|}\mathbb{N}^e_{i|e}) \cdot (\nabla_{\|}\mathbb{N}^e_{k|e})\,\mathrm{d}\Omega. \tag{3.108}$$

In analogy to the local stiffness matrix $\boldsymbol{K}^e$, integral (3.108) depends purely on the geometry of each element and only needs to be assembled once for a given fixed mesh. The storage of all local tensors $\boldsymbol{N}^e$ is affordable since it's only linearly proportional to the total number of elements. We remark that, while analytic evaluation of integral (3.108) is certainly possible, it is suffice to use Gauss quadrature rule (3.39) since error in finite element simulation is usually dominated by mesh size and time step instead of the approximation error in numerical integration. In fact the integrand of N^e_{ijk} is at most a sixth order polynomial which can be integrated exactly by the 4-point Gauss quadrature rule.

We consider the simplest scenario where the mapping from the canonical square element O to any element Q_e of size $\Delta X \times \Delta Y$ in (X, Y)-plane is just an affine transformation involving only translation and scaling,

$$\boldsymbol{X} \in Q_e = \varphi_e(\boldsymbol{\xi}) = \begin{bmatrix} X^e_o \\ Y^e_o \end{bmatrix} + \frac{1}{2}\begin{bmatrix} \Delta X & 0 \\ 0 & \Delta Y \end{bmatrix}\begin{bmatrix} \xi_1 \\ \xi_2 \end{bmatrix}, \tag{3.109}$$

where $[X^e_o, Y^e_o]^\top$ is the geometric center of the straight quad element Q_e. The components of the 9-by-9 local mass matrix $\boldsymbol{M}^e$ before lumping are given by

$$M^e_{ij} = \langle \mathbb{N}^e_i(\boldsymbol{X}), \mathbb{N}^e_j(\boldsymbol{X}) \rangle = \int_O \mathbb{N}_i(\boldsymbol{\xi})\mathbb{N}_j(\boldsymbol{\xi}) \frac{\Delta X \Delta Y}{4}\,\mathrm{d}\xi_1\,\mathrm{d}\xi_2. \tag{3.110}$$

We analytically integrate (3.110) according to the polynomial expression of $\mathbb{N}_i$ in (3.26) and obtain

$$\boldsymbol{M}^e = \Delta X \Delta Y \begin{bmatrix} \frac{4}{225} & \frac{1}{225} & \frac{1}{900} & \frac{1}{225} & \frac{2}{225} & \frac{1}{450} & \frac{1}{450} & \frac{2}{225} & \frac{1}{225} \\ \frac{1}{225} & \frac{4}{225} & \frac{1}{225} & \frac{1}{900} & \frac{2}{225} & \frac{2}{225} & \frac{1}{450} & \frac{1}{450} & \frac{1}{225} \\ \frac{1}{900} & \frac{1}{225} & \frac{4}{225} & \frac{1}{225} & \frac{1}{450} & \frac{2}{225} & \frac{2}{225} & \frac{1}{450} & \frac{1}{225} \\ \frac{1}{225} & \frac{1}{900} & \frac{1}{225} & \frac{4}{225} & \frac{1}{450} & \frac{1}{450} & \frac{2}{225} & \frac{2}{225} & \frac{1}{225} \\ \frac{2}{225} & \frac{2}{225} & \frac{1}{450} & \frac{1}{450} & \frac{16}{225} & \frac{1}{225} & \frac{4}{225} & \frac{1}{225} & \frac{8}{225} \\ \frac{1}{450} & \frac{2}{225} & \frac{2}{225} & \frac{1}{450} & \frac{1}{225} & \frac{16}{225} & \frac{1}{225} & \frac{4}{225} & \frac{8}{225} \\ \frac{1}{450} & \frac{1}{450} & \frac{2}{225} & \frac{2}{225} & \frac{4}{225} & \frac{1}{225} & \frac{16}{225} & \frac{1}{225} & \frac{8}{225} \\ \frac{2}{225} & \frac{1}{450} & \frac{1}{450} & \frac{2}{225} & \frac{1}{225} & \frac{4}{225} & \frac{1}{225} & \frac{16}{225} & \frac{8}{225} \\ \frac{1}{225} & \frac{1}{225} & \frac{1}{225} & \frac{1}{225} & \frac{8}{225} & \frac{8}{225} & \frac{8}{225} & \frac{8}{225} & \frac{64}{225} \end{bmatrix}. \tag{3.111}$$

On the other hand, the evaluation of the local stiffness matrix $\boldsymbol{K}^e$ must be split into two 9-by-9 matrices $\boldsymbol{K}_1^e$ and $\boldsymbol{K}_2^e$ since the quad element Q_e may be stretched differently in the X and Y directions,

$$K_{ij}^e = \langle \nabla_{\parallel} \mathbb{N}_i^e(\boldsymbol{X}), \nabla_{\parallel} \mathbb{N}_j^e(\boldsymbol{X}) \rangle = \int_O \Bigg[\underbrace{\frac{\Delta Y}{\Delta X} \frac{\partial \mathbb{N}_i}{\partial \xi_1} \frac{\partial \mathbb{N}_j}{\partial \xi_1}}_{(K_1^e)_{ij}} + \underbrace{\frac{\Delta X}{\Delta Y} \frac{\partial \mathbb{N}_i}{\partial \xi_2} \frac{\partial \mathbb{N}_j}{\partial \xi_2}}_{(K_2^e)_{ij}} \Bigg] \mathrm{d}\xi_1 \, \mathrm{d}\xi_2. \tag{3.112}$$

Analytic integration yields $\boldsymbol{K}^e = \boldsymbol{K}_1^e + \boldsymbol{K}_2^e$ where

$$\boldsymbol{K}_1^e = \frac{\Delta Y}{\Delta X} \begin{bmatrix} \frac{14}{45} & \frac{2}{45} & -\frac{1}{90} & -\frac{7}{90} & -\frac{16}{45} & \frac{1}{45} & \frac{4}{45} & \frac{7}{45} & -\frac{8}{45} \\ \frac{2}{45} & \frac{14}{45} & -\frac{7}{90} & -\frac{1}{90} & -\frac{16}{45} & \frac{7}{45} & \frac{4}{45} & \frac{1}{45} & -\frac{8}{45} \\ -\frac{1}{90} & -\frac{7}{90} & \frac{14}{45} & \frac{2}{45} & \frac{4}{45} & \frac{7}{45} & -\frac{16}{45} & \frac{1}{45} & -\frac{8}{45} \\ -\frac{7}{90} & -\frac{1}{90} & \frac{2}{45} & \frac{14}{45} & \frac{4}{45} & \frac{1}{45} & -\frac{16}{45} & \frac{7}{45} & -\frac{8}{45} \\ -\frac{16}{45} & -\frac{16}{45} & \frac{4}{45} & \frac{4}{45} & \frac{32}{45} & -\frac{8}{45} & -\frac{8}{45} & -\frac{8}{45} & \frac{16}{45} \\ \frac{1}{45} & \frac{7}{45} & \frac{7}{45} & \frac{1}{45} & -\frac{8}{45} & \frac{56}{45} & -\frac{8}{45} & \frac{8}{45} & -\frac{64}{45} \\ \frac{4}{45} & \frac{4}{45} & -\frac{16}{45} & -\frac{16}{45} & -\frac{8}{45} & -\frac{8}{45} & \frac{32}{45} & -\frac{8}{45} & \frac{16}{45} \\ \frac{7}{45} & \frac{1}{45} & \frac{1}{45} & \frac{7}{45} & -\frac{8}{45} & \frac{8}{45} & -\frac{8}{45} & \frac{56}{45} & -\frac{64}{45} \\ -\frac{8}{45} & -\frac{8}{45} & -\frac{8}{45} & -\frac{8}{45} & \frac{16}{45} & -\frac{64}{45} & \frac{16}{45} & -\frac{64}{45} & \frac{128}{45} \end{bmatrix}, \quad \boldsymbol{K}_2^e = \frac{\Delta X}{\Delta Y} \begin{bmatrix} \frac{14}{45} & -\frac{7}{90} & -\frac{1}{90} & \frac{2}{45} & \frac{7}{45} & \frac{4}{45} & \frac{1}{45} & -\frac{16}{45} & -\frac{8}{45} \\ -\frac{7}{90} & \frac{14}{45} & \frac{2}{45} & -\frac{1}{90} & \frac{7}{45} & -\frac{16}{45} & \frac{1}{45} & \frac{4}{45} & -\frac{8}{45} \\ -\frac{1}{90} & \frac{2}{45} & \frac{14}{45} & -\frac{7}{90} & \frac{1}{45} & -\frac{16}{45} & \frac{7}{45} & \frac{4}{45} & -\frac{8}{45} \\ \frac{2}{45} & -\frac{1}{90} & -\frac{7}{90} & \frac{14}{45} & \frac{1}{45} & \frac{4}{45} & \frac{7}{45} & -\frac{16}{45} & -\frac{8}{45} \\ \frac{7}{45} & \frac{7}{45} & \frac{1}{45} & \frac{1}{45} & \frac{56}{45} & -\frac{8}{45} & \frac{8}{45} & -\frac{8}{45} & -\frac{64}{45} \\ \frac{4}{45} & -\frac{16}{45} & -\frac{16}{45} & \frac{4}{45} & -\frac{8}{45} & \frac{32}{45} & -\frac{8}{45} & -\frac{8}{45} & \frac{16}{45} \\ \frac{1}{45} & \frac{1}{45} & \frac{7}{45} & \frac{7}{45} & \frac{8}{45} & -\frac{8}{45} & \frac{56}{45} & -\frac{8}{45} & -\frac{64}{45} \\ -\frac{16}{45} & \frac{4}{45} & \frac{4}{45} & -\frac{16}{45} & -\frac{8}{45} & -\frac{8}{45} & -\frac{8}{45} & \frac{32}{45} & \frac{16}{45} \\ -\frac{8}{45} & -\frac{8}{45} & -\frac{8}{45} & -\frac{8}{45} & -\frac{64}{45} & \frac{16}{45} & -\frac{64}{45} & \frac{16}{45} & \frac{128}{45} \end{bmatrix}. \tag{3.113}$$

In our simple example of a rectangular element, the local matrix $\boldsymbol{K}_2^e$ of every element Q_e is merely a permutation of $\boldsymbol{K}_1^e$. Similarly, the local weighted stiffness matrix

$$N_{ijk}^e = \int_O \Bigg[\underbrace{\frac{\Delta Y}{\Delta X} \mathbb{N}_j \frac{\partial \mathbb{N}_i}{\partial \xi_1} \frac{\partial \mathbb{N}_k}{\partial \xi_1}}_{(N_1^e)_{ijk}} + \underbrace{\frac{\Delta X}{\Delta Y} \mathbb{N}_j \frac{\partial \mathbb{N}_i}{\partial \xi_2} \frac{\partial \mathbb{N}_k}{\partial \xi_2}}_{(N_2^e)_{ijk}} \Bigg] \mathrm{d}\xi_1 \, \mathrm{d}\xi_2 \tag{3.114}$$

is the sum of two 9-by-9-by-9 tensors $\boldsymbol{N}_1^e$ and $\boldsymbol{N}_2^e$. Here we do not explicitly list in total 2×729 entries of $(N_1^e)_{ijk}$ and $(N_2^e)_{ijk}$.

3.5 Nonlinear Optimization and Results

In the last section, we have provided a recipe to the exact computation of objective gradient with respect to the electrode topography pattern $\boldsymbol{D}$. We now proceed with nonlinear optimization of the objective $J(\boldsymbol{D})$ through a suitable choice of gradient-based method.

Broyden–Fletcher–Goldfarb–Shanno algorithm

In numerical optimization, the Broyden–Fletcher–Goldfarb–Shanno (BFGS) algorithm is one of the most popular quasi-Newton methods in the class of hill-climbing techniques which seek a stationary point of a function by iteratively making incremental changes to the current solution (Nocedal and Wright, 2006). A necessary condition of achieving optimality is that the gradient must be is zero in every direction of the parameter space. In quasi-Newton methods, the second derivatives of the objective function represented by the Hessian matrix $\mathrm{d}^2 J/\mathrm{d}\boldsymbol{D}^2$, are not computed exactly but rather approximated based on a selective history of the past gradient evaluations. Quasi-Newton methods can be thought of as generalizations of the one-dimensional root-finding algorithm, i.e. secant method, to multivariate calculus. In multi-dimensional problems such as the PDE-constrained control problem of electrohydodynamic lithography, quasi-Newton schemes differ in the way they constrain the iterative updates. The BFGS method introduces a rank-2 correction to the approximate Hessian matrix at each update such that the approximate Hessian is always symmetric and behaves like the true Hessian at least locally for every incremental change.

For models numerically discretized by finite element method, we must be cautious about the precise meaning of “gradient". The finite-dimensional vector space in finite element method is equipped with a non-trivial inner product/norm (3.33), namely the mass matrix $\boldsymbol{M}$ which is positive and symmetric but not necessarily uniform nor scale-invariant. The gradient computation

$$\nabla_{\boldsymbol{D}} J = \frac{\mathrm{d}J}{\mathrm{d}\boldsymbol{D}} \boldsymbol{M}^{-1} \tag{3.115}$$

must respect the inner product of the underling vector space so that $\delta J = \nabla_{\boldsymbol{D}} J \boldsymbol{M} \delta \boldsymbol{D} = (\partial J/\partial \boldsymbol{D})\delta \boldsymbol{D}$. In the context of tensor analysis, $\nabla_{\boldsymbol{D}} J$ and $\mathrm{d}J/\mathrm{d}\boldsymbol{D}$ are the contravariant and covariant components of the same gradient. Following the Riemannian BFGS method presented in Qi, Gallivan, and Absil (2010), in algorithm 1 we modify the standard version of the BFGS algorithm and introduce mass matrix $\boldsymbol{M}$ at step 11 of the inverse Hessian update to account for the discrete inner product of the finite element space. In the standard form of BFGS algorithm, $\boldsymbol{M}$ is simply the identity matrix $\mathbb{I}$.

In addition we must also ensure the feasibility of target film profile $\underline{\boldsymbol{H}}$. Just like the continuum equation (3.17) of the EHL model, finite element formulation (3.40) also conserves the discrete total mass at all time steps which means for an initially flat film

Algorithm 1 Broyden–Fletcher–Goldfarb–Shanno algorithm

procedure BFGS
  Compute and storage $\nabla_{\boldsymbol{D}} J|_{(0)}$ ▷ initialize BFGS
  Line search to find $\alpha = \operatorname{argmin} J(\boldsymbol{D}_{(0)} + \alpha \boldsymbol{G})$
  Storage $\boldsymbol{S}_{(1)} = \alpha \boldsymbol{G}$
  Update $\boldsymbol{D}_{(1)} = \boldsymbol{D}_{(0)} + \boldsymbol{S}_{(0)}$
  Initialize $\boldsymbol{B}^{-1}_{(0)} = \mathbb{I}$
  Initialize $k = 1$
  while objective $J(\boldsymbol{D}_{(k)}) >$ tolerance **do** ▷ BFGS iteration loop
    Compute and storage $\nabla_{\boldsymbol{D}} J|_{(k)}$
    Compute $\boldsymbol{Y} = \nabla_{\boldsymbol{D}} J|_{(k)} - \nabla_{\boldsymbol{D}} J|_{(k-1)}$
    Rank-2 symmetric update on the inverse of approximated Hessian $\boldsymbol{B}^{-1}$

$$\boldsymbol{B}^{-1}_{(k)} = \boldsymbol{B}^{-1}_{(k-1)} + \frac{\boldsymbol{S}^{\top}_{(k-1)}\boldsymbol{M}\boldsymbol{Y} + \boldsymbol{Y}^{\top}\boldsymbol{M}\boldsymbol{B}^{-1}_{(k-1)}\boldsymbol{Y}}{(\boldsymbol{S}^{\top}_{(k-1)}\boldsymbol{M}\boldsymbol{Y})^2}\boldsymbol{S}_{(k-1)}\boldsymbol{S}^{\top}_{(k-1)}\boldsymbol{M} - \frac{1}{\boldsymbol{S}^{\top}_{(k-1)}\boldsymbol{M}\boldsymbol{Y}}\Big[\boldsymbol{B}^{-1}_{(k-1)}\boldsymbol{Y}\boldsymbol{S}^{\top}_{(k-1)}\boldsymbol{M} + \boldsymbol{S}_{(k-1)}\boldsymbol{Y}^{\top}\boldsymbol{M}\boldsymbol{B}^{-1}_{(k-1)}\Big]$$

    Compute $\boldsymbol{G} = \boldsymbol{B}^{-1}_{(k)}[-\nabla_{\boldsymbol{D}} J|_{(k)}]^{\top}$
    Line search to find $\alpha = \operatorname{argmin} J(\boldsymbol{D}_{(k)} + \alpha \boldsymbol{G})$
    Storage $\boldsymbol{S}_{(k)} = \alpha \boldsymbol{G}$
    Update $\boldsymbol{D}_{(k+1)} = \boldsymbol{D}_{(k)} + \boldsymbol{S}_{(k)}$
    Shift $\boldsymbol{D}_{(k+1)}$
    $k \to k + 1$

of thickness H_0, the equality

$$\mathbf{1}^{\top}\boldsymbol{M}\boldsymbol{H}_k = \mathbf{1}^{\top}\boldsymbol{M}(H_0\mathbf{1}) \tag{3.116}$$

holds for all subsequent film states. If total mass of the desired target film profile $\underline{\boldsymbol{H}}$ over the periodic domain is different from the initially flat state $H_0\mathbf{1}$, then it is impossible for any film state $\boldsymbol{H}_k$ to converge to target $\underline{\boldsymbol{H}}$ no matter how we update the electrode topography $\boldsymbol{D}$, i.e. target $\underline{\boldsymbol{H}}$ is unfeasible according to the constraint. In practice, the discrete values of target film profile is generated by a user-specified input $\underline{\boldsymbol{H}}_{\text{in}}$, for example, the heart-like protrusion reconstructed from the raster height map shown in figure 3.6, is likely not to have an identical total mass with $H_0\mathbf{1}$. Preprocessing on these user-generated inputs is required to ensure feasibility of the target film profile $\underline{\boldsymbol{H}}$ used in the optimization procedure. There are infinitely many ways to correct $\underline{\boldsymbol{H}}_{\text{in}}$. We prefer shifting $\underline{\boldsymbol{H}}_{\text{in}}$ by a constant value everywhere,

$$\underline{\boldsymbol{H}} = \underline{\boldsymbol{H}}_{\text{in}} + \Big(H_0 - \frac{\mathbf{1}^{\top}\boldsymbol{M}\underline{\boldsymbol{H}}_{\text{input}}}{\mathbf{1}^{\top}\boldsymbol{M}\mathbf{1}}\Big)\mathbf{1}, \tag{3.117}$$

so that the geometric details of user input $\underline{\boldsymbol{H}}_{\text{in}}$ is not compromised too much.

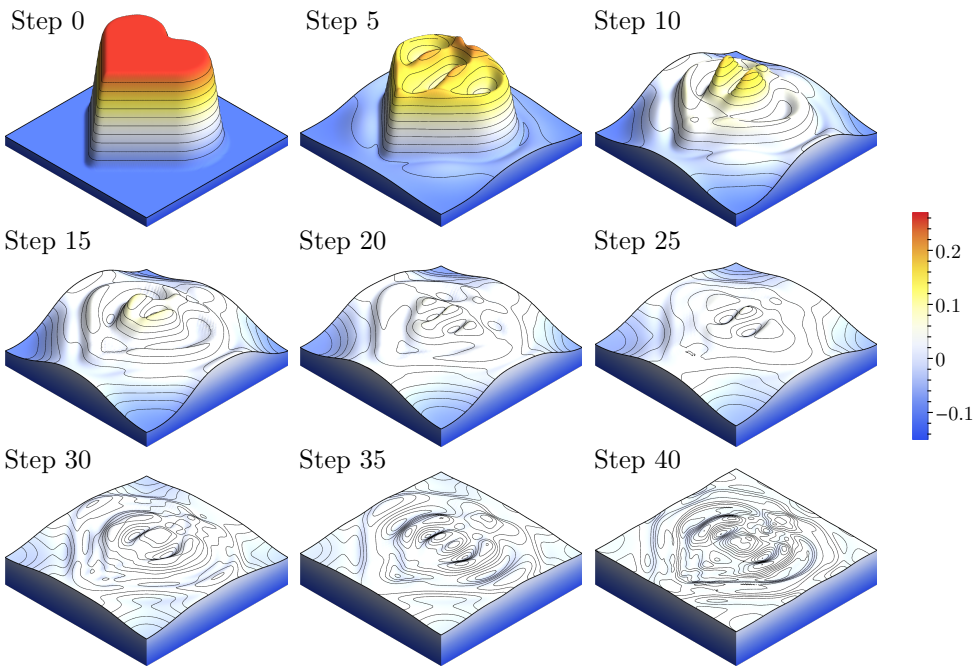

Figure 3.11: Sequence of electrode topography profiles $1 - D$ on a periodic square domain $[0, 4.5] \times [0, 4.5]$ at iteration step 0, 5, ... , 40 of the BFGS optimization process; the nonlinear EHL evolution equation is discretized with 60^2 elements and 200 evenly spaced time steps till the final time $\underline{\tau} = 4.2$.

We also apply the shifting transformation (3.117) to the discrete electrode topography $\boldsymbol{D}$ after the BFGS update in step 15 for a different reason. The purpose of such shift is to maintain a fixed reference height (e.g., average height) on the electrode topography throughout the entire optimization process and to prevent pathological scenario where electrode topography $\boldsymbol{D}$ being optimized may drift infinitely far away from the film.

Validation on a target film shape of uniform thickness

We verify our implement of the optimization algorithm against the follwing test problem: find the optimal electrode topography $\underline{D}(\boldsymbol{X})$ for a target film profile of uniform thickness, which happens to be identical to the initial condition $\underline{\boldsymbol{H}} = H_0\mathbf{1}$ due to volume conservation. It is one of the few cases for which exact analytic solution of the optimal electrode topography, i.e. a flat electrode $\underline{\boldsymbol{D}} = \mathbf{1}$, is known. Recall from (3.21) that the free energy $\mathcal{F}[H, D]$ of the EHL system is always non increasing. Any nonflat electrode would necessarily deform an initially flat film and hence cannot produce another flat state of the same volume at a later time $\underline{\tau} > 0$. If we take the constraint on the spatial average of electrode topography into account, then the optimal pattern must be the unique "do-nothing" flat electrode $\underline{\boldsymbol{D}} = \mathbf{1}$.

The convergence to a flat electrode is shown in figure 3.11. The test problem is posed

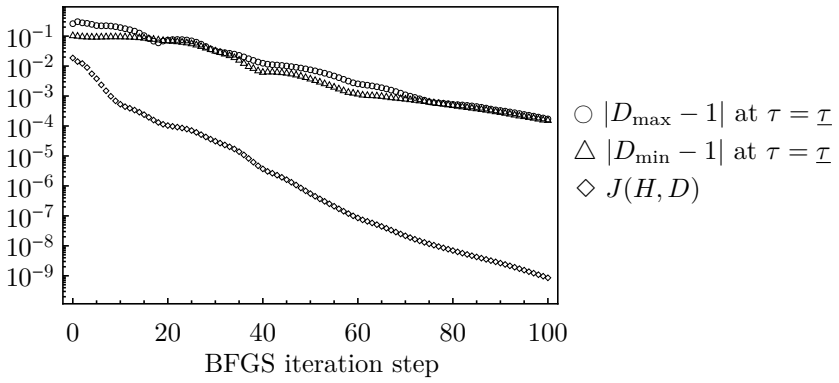

Figure 3.12: The BFGS optimization underlying figure 3.11: the minimum and maximum signed deviation to the analytic solution $\underline{D} = 1$ and objective functional $J(\boldsymbol{H}, \boldsymbol{D})$ at final time $\underline{\tau}$ are plotted for the electrode being optimized at each BFGS step.

on a periodic square domain $[0, 4.5] \times [0, 4.5]$ and for a time interval $0 \leq \tau \leq 4.2$. The initial film thickness $H_0 = 0.15$ is uniform over the entire domain. The H^1-regularization parameter $\gamma = 5 \times 10^{-4}$ is used in the discrete objective functional (3.78). We choose the heart-like electrode plotted in figure 3.6 as the initial guess. In the early stage of optimization, features of high spatial frequency such as edges and corners are rapidly damped. We observe that the optimization process picks up large scale spatial variations in the background after the initial damping. This is due to the inherent nonlinearity of the problem being optimized: different spatial modes of electrode pattern $D(\boldsymbol{X})$ are coupled through the nonlinear constraint, i.e. the EHL evolution equation. In figure 3.12 we plot the maximum and minimum signed deviation to the optimal electrode topography $\underline{D} = 1$ and discrete objective J over 100 BFGS iteration steps on a log scale. Deviation from the analytic solution of the optimal flat electrode $\underline{\boldsymbol{D}} = \mathbf{1}$ decreases towards zero as the objective J is minimized. At iteration step 40 shown in figure 3.11, the maximum spatial error of the optimal topography is already driven below 0.01. Th overall linear trend suggests an exponential convergence rate which is typical for optimization methods based on gradient descent (Nocedal and Wright, 2006).

The discrete cosine transform of $1 - D(\boldsymbol{X})$ are shown in figure 3.13 as the electrode topography is being optimized at each iteration step. Each block at a grid number (i, j) represents the absolute (real) amplitude of the (i, j)-th spatial harmonics $\cos(K_i^X X) \cos(K_j^Y Y)$ where K_i^X and K_j^Y are the i-th and j-th spatial frequencies of in X and Y directions, respectively. Unlike a purely diffusive process for which features of higher frequency always receive faster damping, during late stage of the optimization the $(0, 2)$-, $(0, 1)$-, $(2, 0)$-, $(2, 2)$-modes seem to persist as a group. This indicates that, the diffusive effect introduced from the regularization functional $\mathcal{R}[D]$ is not the main driving force behind the optimization. Instead, the approximate Hessian matrix

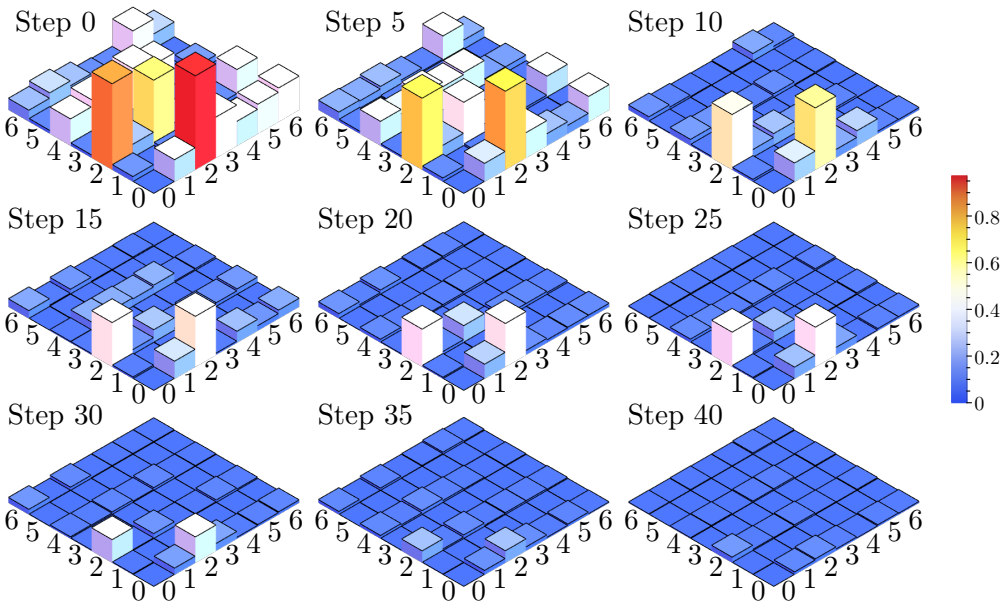

Figure 3.13: Discrete Fourier (cosine) transform of the electrode topography $1-D(\boldsymbol{X})$ at iteration steps shown in figure 3.11. The color and height of a block at grid number (i,j) correspond to the absolute (real) amplitude A_{ij} of the (i,j)-th cosine harmonics $\cos(K_i X)\cos(K_j Y)$ where K_k is the k-th spatial frequency of interval $[0, 4.5]$. For visual purpose, $\log_{10}(1+|A_{ij}|)$ is plotted instead.

of the objective (excluding the regularization) may chose to amplify a selection of its eigenvectors which result in the persisting pattern in the Fourier space we see in figure 3.13.

To gain more insights and intuitions into the control algorithm, we plot the discrete solutions to the film state $H(\boldsymbol{X},\tau)$, adjoint variable $\Lambda(\boldsymbol{X},\tau)$ and the constraint force $C(\boldsymbol{X},\tau)$ at the zeroth step of the nonlinear optimization in figure 3.14 side by side. Film states $H(\boldsymbol{X},\tau)$ in the left-most column are identical to the ones shown in figure 3.7 subject to the top electrode with a heart-like protrusion (see figure 3.6). The adjoint variable $\boldsymbol{\Lambda}_k$ in the middle column propagates the discrepancy between the final film profile $H(\boldsymbol{X},\underline{\tau})$ and target profile $\underline{H}$ as the final time condition backwards in time. The dynamics of the adjoint variable $\Lambda(\boldsymbol{X},\tau)$ mimics a reverse-diffusion process where sharp features become blurry while being transported backwards in time. Recall from the control equations (3.67) and (3.89) that the objective gradient $\nabla_{\boldsymbol{D}} J$ at the zeroth iteration step is given by the time integration of all the constraint forces $\boldsymbol{C}_k$ shown in the right-most column at each discrete time step. We observe that the constraint forces closer to the final time $\underline{\tau}$ are orders of magnitude larger than the ones from the early stage and hence dominate the time integration of all constraint forces. In other words, the behavior of film states in the later stage has significantly more impact on the discrepancy

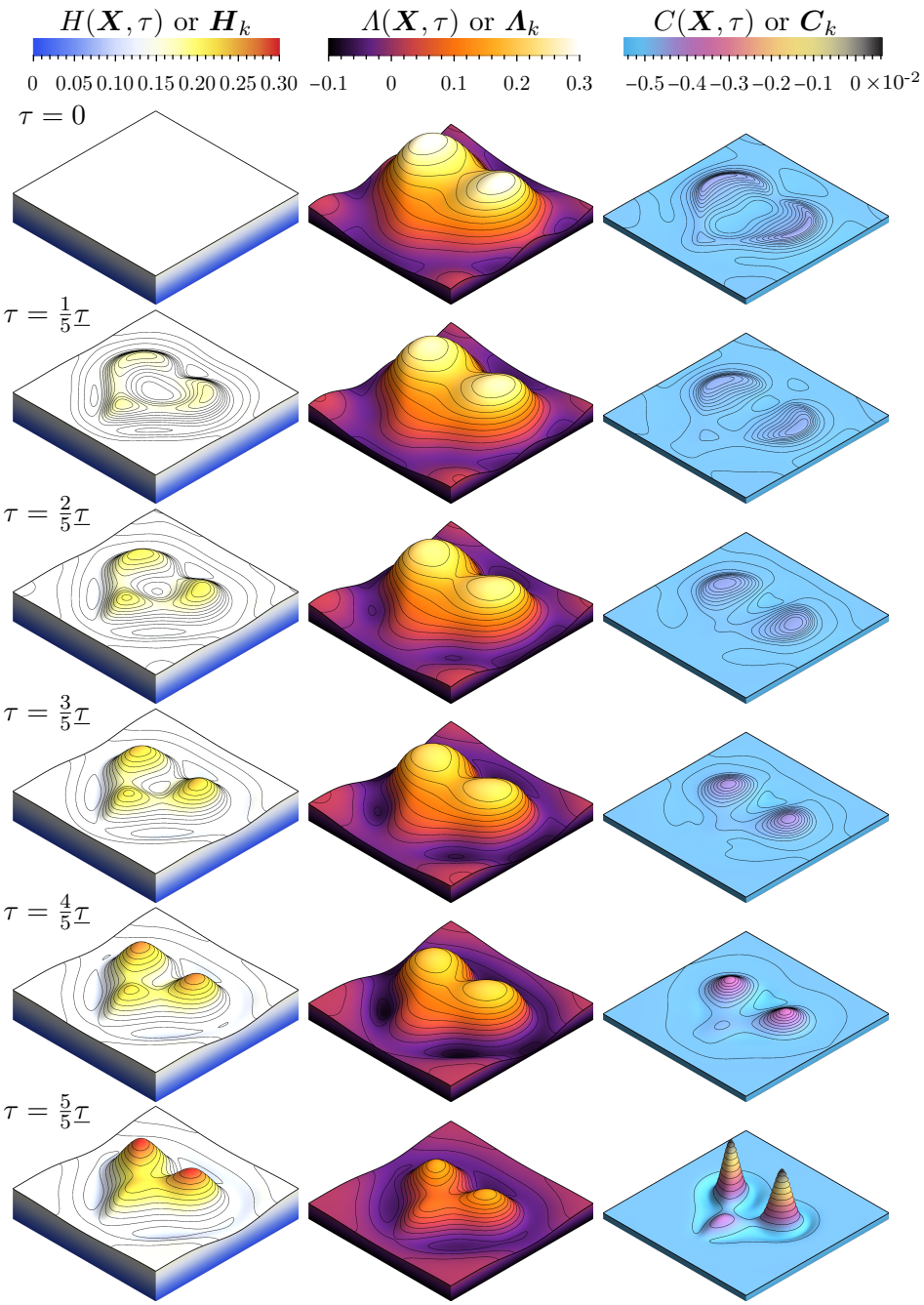

Figure 3.14: Solutions to the film state $H(\boldsymbol{X},\tau)$ (left column), the adjoint $\Lambda(\boldsymbol{X},\tau)$ (middle column) and the negative constraint force $-C(\boldsymbol{X},\tau)$ (right column) on a periodic computational domain $[0,4.5]\times[0,4.5]$ computed from the discrete state, adjoint and control equations (3.75), (3.94) and (3.89). Target film profile $\underline{H}(\boldsymbol{X}) = H_0$ is identical to the initial flat state. Snapshots with elevation contour (black line) are taken at time stamps $\tau = 0, \underline{\tau}/5, ..., \underline{\tau}$ (from top to bottom) where final time $\underline{\tau} = 4.2$.

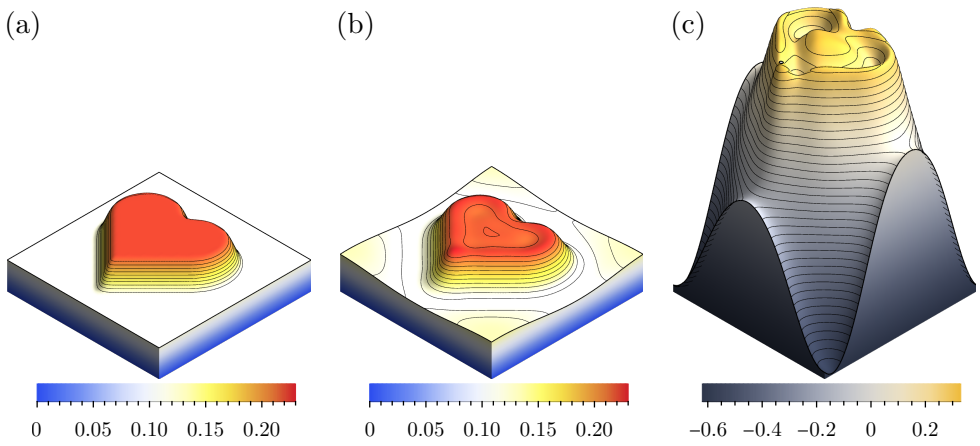

Figure 3.15: (a) Target film profile $\underline{H}(\boldsymbol{X})$ compared to (b) the final film state $H(\boldsymbol{X}, \underline{\tau})$ obtained under (c) the optimal electrode topography $1 - D(\boldsymbol{X})$ found by nonlinear optimization on a square domain $[0, 4.5] \times [0, 4.5]$.

between the final film profile $H(\boldsymbol{X}, \underline{\tau})$ and target shape $\underline{H}$. This is expected because the evolution equation of the EHL system is dissipative under a time-independent electrode with a static geometry and a constant applied voltage. The memory of previous film states beyond certain time period is eventually lost due to dissipation in the system. Unless time-dependency is restored in the electrode (voltage distribution, topography, etc.) which would result in extra terms in the control equations, the best strategy to guide the evolving film profile $H(\boldsymbol{X}, \tau)$ into the target shape $\underline{H}(\boldsymbol{X})$, suggested by our control algorithm, is to promote the desired convergence right before the final time $\underline{\tau}$ rather than to achieve it earlier.

Optimal electrode design for achieving a heart-like film pattern

We apply the control algorithm to obtain the optimal electrode design for a specific film pattern, i.e. the uniform elevation of a filled heart-like shape at the center of a square. The simulation and nonlinear optimization are performed on a square domain of edge length 4.5, discretized by 50^2 Q9 Lagrange finite elements. The heart-like target film profile $\overline{H}(\boldsymbol{X})$ is shown in figure 3.15(a). The goal is to look for an optimal electrode topography function $D(\boldsymbol{X})$ under which the evolving film state $H(\boldsymbol{X}, \tau)$ converges to the target $\overline{H}(\boldsymbol{X})$ at final time $\underline{\tau} = 4.2$. We start the search of the optimal design with an initial guess of a uniform electrode $\boldsymbol{D} = \boldsymbol{1}$. The H^1-regularization parameter $\gamma = 7.5 \times 10^{-4}$ is used to preserve certain level of smoothness in $\boldsymbol{D}$ throughout the entire process. After about 100 BFGS iteration steps, the objective J reduces to about 6.5% of its original value produced by the initial guess and the search therefore terminates. The resulting optimal electrode pattern and the corresponding film profile at the final time $\underline{\tau}$ are plotted in figure 3.15. Snapshots of intermediate film evolution, backward

adjoint propagation and discrete cosine transform (DCT) of film states are shown in the left, middle and right columns of figure 3.16, respectively.

The optimal design solved by the control algorithm seems to suggest an interesting design principle in favor of separating spatial scales. Small-scale features of the optimal electrode shown in figure 3.15(c), e.g., ridges and horns, as usual immediately trigger localized growth resembling the boundary of the heart pattern. However unlike the case of naive electrode designs such as the one in figure 3.6, these structures do not reinforce themselves into narrower pillars. Instead, the subsequent growths are arrested by interface deformations induced by the large-scale sinusoidal oscillations in the optimal electrode topography. As shown in the left column of figure 3.16, while the central void enclosed by the narrow ridges are being filled, four weak bumps also start to appear at corners of the square domain. Due to conservation of mass, if the dielectric film is thickening at the center and corners, it must drain liquid from the region in between, exactly where the prior development of narrow ridges occurs. The competition between the growth of large and small features is made manifest by the discrete cosine transform of $H(\boldsymbol{X}, \tau)$ in the right column of figure 3.16. The rapid development of high frequency modes (e.g., blocks in white) is suddenly choked by the emergence of low frequency oscillations (e.g., blocks in yellow, orange and red) during the time interval between $4\underline{\tau}/5$ and the final time $\underline{\tau}$. Hence a smart combination of sharp and blunt features in the optimal electrode topography computed by our optimization algorithm not only trigger pattern formations in dielectric film at multiple resolutions but also regulate the growth rate of of spatial modulations at both large and small scales as well as the temporal order at which these modulations emerge in order to achieve a complex pattern such as the heart-like pillar.

Lastly, we briefly discuss the role of regularization, particularly the H^1-regularization (3.50). In our specific example of optimizing for a heart-like film pattern, the choice of regularization parameter γ seems to have minor effects on the nonlinear search. Although from the final film states $H(\boldsymbol{X}, \underline{\tau})$ plotted in the the first row of figure 3.17, it is slightly more difficult to reproduce corners and edges of the heart-like pattern with a higher regularization value. This is expected because a stronger H^1-regularization would penalize sharp electrode features: the initial growth of film patterns triggered by these sharp features can only be corrected later by interface modulations emerging on much larger scales due to disspative nature of the EHL system. In future work, it is interesting to explore other choices of objective functional and regularization, for example, the use of l^1-norm instead l^2, i.e. $\mathcal{J} = \int_\Omega |H - \underline{H}| \, \mathrm{d}\Omega$, or distributed ones, i.e. $\mathcal{J}$ and $\mathcal{R}$ are defined independently on disjoint subdomains (Barker, Rees, and Stoll, 2016).

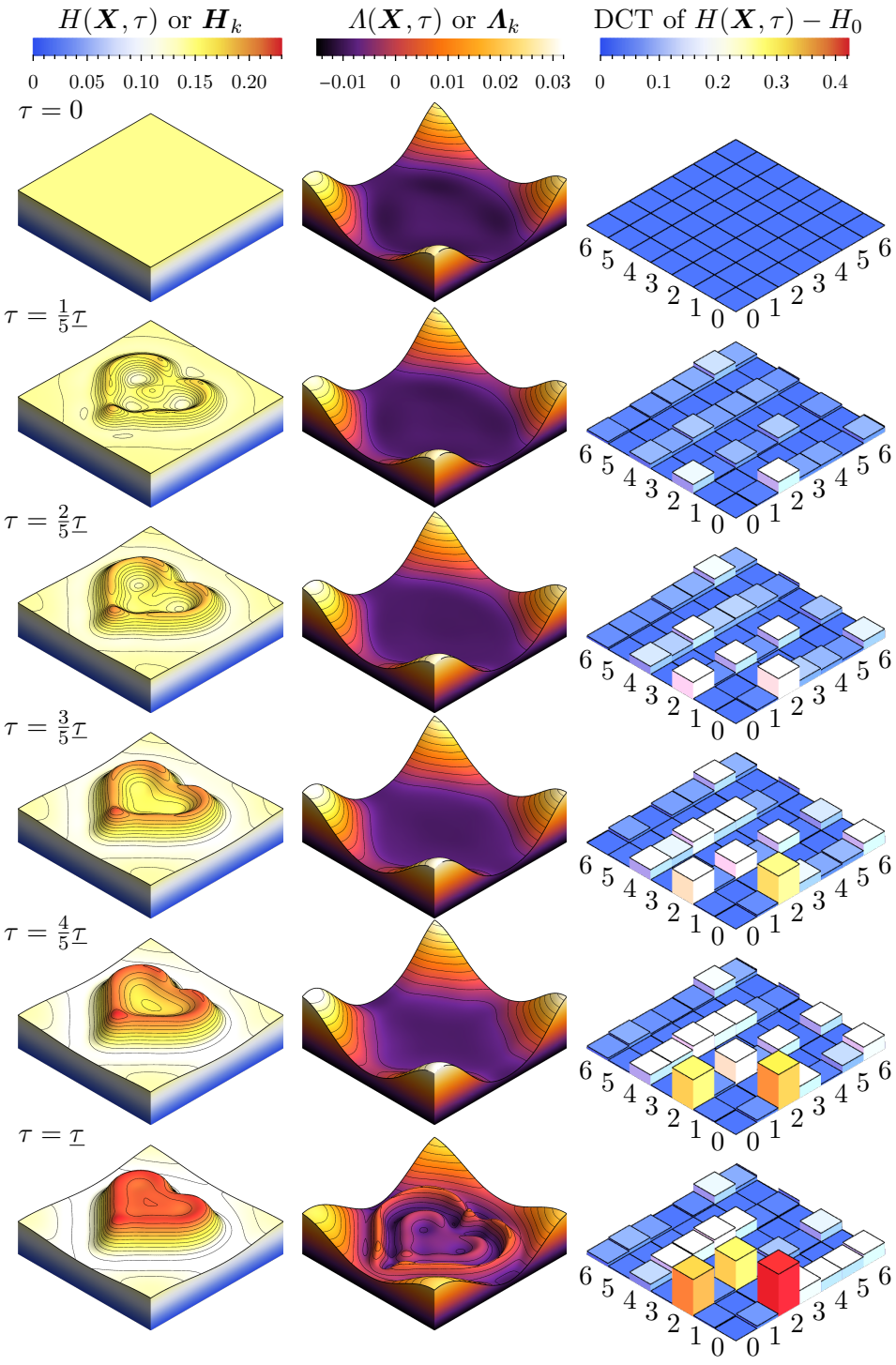

Figure 3.16: Film state $H(\boldsymbol{X},\tau)$ (left column), the adjoint $\Lambda(\boldsymbol{X},\tau)$ (middle column) and the discrete cosine transform (DCT) of $H(\boldsymbol{X},\tau)$ (right column) computed for a heart-like target profile on a periodic square domain $[0, 4.5]^2$. Snapshots are taken at time stamps $\tau = 0, \underline{\tau}/5, \ldots, \underline{\tau}$ (from top to bottom) where final time $\underline{\tau} = 4.2$. Legend setup of DCT is identical to the one in figure 3.13.

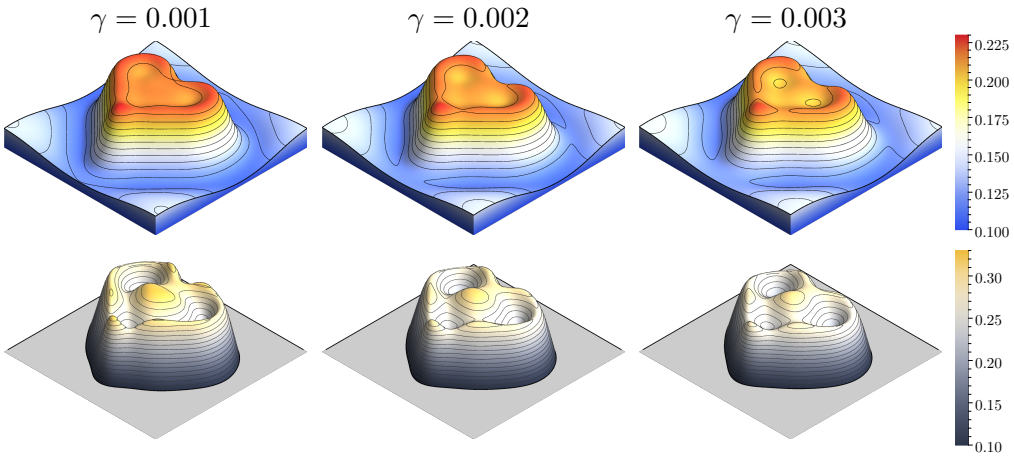

Figure 3.17: Final film state $H(\boldsymbol{X}, \underline{\tau})$ (top row) at $\underline{\tau} = 4.2$ and optimal electrode topography $1 - D(\boldsymbol{X})$ (bottom row) on a periodic square domain $[0, 4.5]^2$ produced by nonlinear optimizations under different H^1-regularization parameters γ.

3.6 Conclusion and Outlook

The control algorithm and simulations presented in this chapter represent a computational resolution to the problem of pattern fidelity in Electrohydrodynamic Lithography (EHL), a simple and promising soft-lithographic method by inducing a heterogeneous distribution of Maxwell stresses on the interface of a dieletric liquid film through a patterned top electrode (Chou, Zhuang, and Guo, 1999; Schäffer et al., 2000). The evolution of film interface is shown to follow a fourth order strongly nonlinear partial differential equation which are discretized based on finite element method.

In order to guide evolving film into a desired target shape in the theoretical framework of EHL, we devise a control protocol using the optimal control theory to optimize the design of electrode topography. Our method fundamentally differs from previous approaches (Verma et al., 2005; Wu, Pease, and Russel, 2005; Nazaripoor et al., 2016) based on trial and error over a finite set of geometry parameters of the electrode: only three PDEs—state, adjoint and control equations—need to be solved regardless of total degrees of freedom in the design space of electrode geometry. We highlight the power of our control algorithm through a nontrivial example of optimal electrode topography achieving a nearly uniform lifting of a heart-like pattern in the center of a periodic square lattice, which cannot be accomplished by conventional design principles of electrode topography due to rapid growth of localized pillars.

The control-theoretical framework established in this work is completely general and can be extended to explore other types of control. For example, it is conceivable that by applying a time-dependent, instead of constant, voltage drop between electrode and bottom substrate (the rate at which voltage signal changes must be slow enough so

that the system is still in the quasi-electrostatic limit), the additional temporal degree of freedom in control may be exploited to improve robustness against random fluctuations in the EHL system or to maintain the interface of a dielectric liquid film at a desired target shape for an exceptionally long period of time. In such cases, signal of the time-varying voltage drop must be determined from a feedback mechanism complementing the current EHL system, for example, surface reconstruction from real-time thin film interferometry (Naughton and Sheplak, 2002). The idea of time-varying control was recently exploited by Boujo and Sellier (2019) who investigated the optimal kinematics of a solid platform on which a solidifying liquid film flows with a temperature-dependent viscosity. Significant improvement in thickness uniformity of the solidifying film was achieved by the use of adjoint method from optimal control theory.

Chapter 4

GENERALIZED LUBRICATION THEORY ON CURVED GEOMETRIES

4.1 Development of Lubrication Theory on Curved Geometries

The lubrication theory was established by Reynolds (1886) to quantify the influence of oil lubricant filled between the cylindrical surfaces of bearing and journal. His idea was later extended to model fluid flow confined in geometries where the transverse dimension is significantly slender than the streamwsie ones. In contrast to the long history and rich studies of thin flows on flat and possibly inclined substrates in literature (Oron, S. H. Davis, and Bankoff, 1997), some of which we have encountered in Chapter 2 and 3, the physics of thin liquid flow on curved geometries has only been developed recently and is still not fully understood. In almost all existing literature on the topic, substrate geometries are limited to simple forms such as spheroid and cylinder, and kinematics being considered is driven exclusively by capillary and gravity forces only.

To study thin liquid flows on nonstandard geometries, L. W. Schwartz and Weidner (1995) proposed a lubrication model for surface tension driven flows on curved surfaces to explain the thinned or "puddled" defects in the coating behavior of liquid paints on highly curved substrates. Their model was subsequently re-examined, corrected and improved by the pioneer work of Roy, A. J. Roberts, and Simpson (2002), who first derived the two-dimensional evolution equation of the film's thickness for the three-dimensional flow of a viscous Newtonian fluid upon an arbitrarily curved substrate using a special curvilinear coordinate system based on orthogonal lines of curvature adapting to curved surfaces. Howell (2003) derived the leading-order lubrication equations for thin viscous films coating a moving curved substrate instead of an immobile surface. He identified three distinguished limits: nearly flat substrate, extremely curved substrate of constant curvature and moderately curved substrate with a radius of curvature comparable to the film length scale. Stocker and Hosoi (2005) presented a lubrication model for the evolution of a thin film covering the an interior corner driven by surface tension and gravity using a hyperbolic coordinate system. Despite singularity in the hyperbolic coordinates at the corner, good agreement with laboratory experiments was found.

On the other hand, thin liquid flow on the surfaces of cylindrical and spherical objects have been studied extensively due to simplicity in the geometry and well developed surface coordinate systems. Takagi and Huppert (2010), by formulating the lubrication theory in spherical coordinates, investigated the spreading dynamics of shallow gravity currents on the exterior surface of cylinders and spheres in the regime where gravity and viscous forces govern the dynamics. The analytic spreading solution they predicted for

the extent of the flow agrees well with their experiments till the advancing front bifurcates into a number of rivulets due to the neglecting of surface tension effect in their model. Braun et al. (2011) reexamined the flow of a tear film on a prolate spheroid shape resembling human cornea, which usually is modeled on a flat substrate. By retaining the next higher order terms of the geometry, they derived a fourth order parabolic PDE for the film dynamics in prolate spheroidal coordinates. Trinh et al. (2014) studied the role of substrate curvature on the gravitationally driven flow of a suspended thin liquid film adhere to the underside of a circular cylinder. Combined with experimental demonstrations, they quantitatively identified the conditions under which the Rayleigh-Taylor stability of a liquid layer can be stabilized by substrate curvature. S. Lee et al. (2016) introduced a simple yet robust mechanism to fabricate hemispherical thin, nearly uniform, elastic shells by the coating, drainage and subsequent curing of polymer solutions on curved molds. Their theoretical model based on lubrication theory, which includes the rheological properties of the curing polymer as well, was able to accurately predict the final thickness of the shell as a function of the material properties and the substrate geometry. Recently, Balestra, Brun, and Gallaire (2016) and Balestra, Badaoui, et al. (2019) considered the optimal topographical perturbations of the substrate geometry for the advancing front of an initially flat thin Newtonian fluid spreading on a horizontal cylinder under action of gravity, which eventually results in the formation of fingers (Troian et al., 1989). They discovered that the most unstable spanwise fingering wavelength induced by substrate topography perturbations was slightly different from the the emerging wavelength on a perfect cylinder and can be deliberately controlled.

The approaches employed above are essentially direct, low-dimensional approximation to the full three-dimensional viscous Stokes equation. An alternative perspective on the formulation of thin film flow was introduced by Rumpf and Vantzos (2013) who reformulated the evolution of thin liquid film as a unique flow state resulting from the interplay between the potential energies (e.g., the surface energy of liquid/gas interface and gravitational energy) and viscous dissipation within the liquid due to tangential frictions against the curved substrate in the thin film limit. The evolution of a viscous thin film on a curved geometry was then approximated based on the underlying gradient flow structure which is faithful to the energy-dissipation law in the fluidic system as opposed to the equations of motion. Their formalism is numerically attractive as well: it leads to the so-called natural time discretization (F. Otto, 2001) under which the incremental time stepping is posed as a transport-equation-constrained optimization problem on a curved manifold.

The outline of this chapter is as follows: In Section 4.2, we develop three curvilinear coordinate systems essential to modeling free surface flow in vicinity of a curved supporting substrate embedded in the three-dimensional ambient space. Section 4.3 begins with two equivalent characterizations of viscous fluid, namely the Stokes equation and the

Helmholtz minimum dissipation principle. Free surface kinematics driven by the viscous dissipation of interfacial free energies is derived based on the curvilinear coordinates developed earlier. In Section 4.4 we construct a truncated minimization problem of the Helmholtz principle in lubrication limit, the solution of which gives rise to a tensorial partial differential equation governing the evolution of thin viscous liquids attached to a gently curved substrate. The derivation here follows the construction of the gradient flow model introduced in Rumpf and Vantzos (2013) with tools of differential geometry developed in the earlier sections in this chapter. We extend their result to cover shear-type tangential interfacial forces in addition to pressure-type normal forces. Examples of common interfacial free energies of local type such as surface and gravitational energies are discussed. At last, in Section 4.5 we present a novel nonlocal model resulting from the total electrostatic energy of a curved conductor in the presence of a thin dielectric liquid coating. Through finite element simulations, we demonstrate the rich interplay between capillary, gravity, Maxwell and viscous forces of a thin liquid film spreading on a spherical conductor. Our model offers key insight into the complex evolution of liquid shapes, mass accumulation sites and flow instabilities not accessible to planar geometries.

4.2 Differential Geometry of Thin Layer Domain

In this section we develop the geometric language suitable for describing the kinematics of a liquid layer. Mathematical concepts and tools from Riemannian geometry are briefly reviewed with an emphasize on embedded surface in $\mathbb{R}^3$. The discussion here roughly follows the exposition of the classical differential geometry textbooks (Kreyszig, 1991; Stoker, 1988). Other books oriented towards applications of curvature in physics such as Frankel (2011) and Sternberg (2012) are also taken as references. We adopt the standard convention (Aris, 1990) of index notation with the Latin indices (e.g., $i = 1, 2, 3$) for the three-dimensional ambient space $\mathbb{R}^3$ and the Greek indices (e.g., $\alpha = 1, 2$) for two-dimensional manifolds.

Supporting substrate: Riemannian 2-manifold

The supporting surface $\hat{\Gamma}$ of the thin liquid layer is assumed to be a sufficiently smooth, closed manifold embedded in the physical space $\mathbb{R}^3$. Let $O \subset \mathbb{R}^2$ be the two-dimensional parameter space. The coordinate chart $\varphi : O \to \mathbb{R}^3$ smoothly maps an open set in O to the supporting surface

$$\hat{\Gamma} = \{\hat{\boldsymbol{x}} = \varphi(\xi^1, \xi^2) \mid (\xi^1, \xi^2) \in O\}, \tag{4.1}$$

where (ξ^1, ξ^2) are the intrinsic coordinates of the surface parametrization. The local tangent plane at each point $\hat{\boldsymbol{x}}$ on surface $\hat{\Gamma}$ is spanned by the surface basis vectors (not

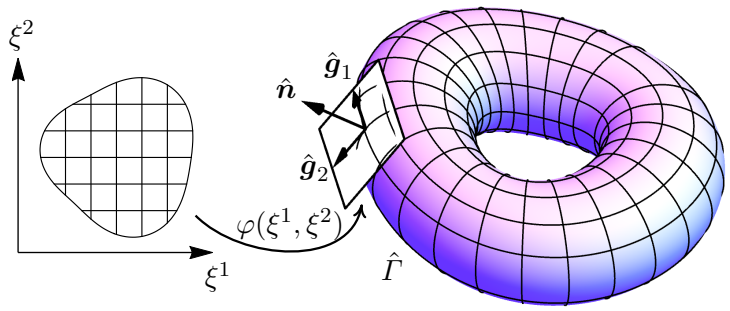

Figure 4.1: Riemannian 2-manifold of an embedded surface $\hat{\Gamma}$ in the ambient Euclidean space $\mathbb{R}^3$ through coordinate chart $\varphi(\xi^1, \xi^2)$, the local tangent plane of which is spanned by the induced basis vectors $\hat{\boldsymbol{g}}_\alpha$.

necessarily normalized)

$$\hat{\boldsymbol{g}}_\alpha = \frac{\partial \varphi}{\partial \xi^\alpha}. \tag{4.2}$$

The induced metric $\hat{\boldsymbol{g}}$ of the embedded surface $\hat{\Gamma}$, also known as the first fundamental form (Stoker, 1988), is a rank-two tensor which assigns an inner product (i.e., symmetric, positive definite, bilinear) at each point $\hat{\boldsymbol{x}} \in \hat{\Gamma}$. The covariant components of metric $\hat{\boldsymbol{g}}$ are induced from the basis vectors,

$$\hat{g}_{\alpha\beta} = \hat{\boldsymbol{g}}_\alpha \cdot \hat{\boldsymbol{g}}_\beta, \quad \hat{g} = \det \hat{g}_{\alpha\beta}, \tag{4.3}$$

where $\hat{g}$ is the metric determinant. Intuitively speaking, metric coefficient $g_{\alpha\beta}$ measures lengths along the embedded surface in the three-dimensional Euclidean space. The first kind Christoffel symbols

$$\hat{\Gamma}^\gamma_{\alpha\beta} = \hat{\boldsymbol{g}}^\gamma \cdot \frac{\partial \hat{\boldsymbol{g}}_\alpha}{\partial \xi^\beta} \tag{4.4}$$

describe the parallel transport of a basis vector $\hat{\boldsymbol{g}}_\alpha$ along another basis vector $\hat{\boldsymbol{g}}_\alpha$ on a curved surface $\hat{\Gamma}$. In differential geometry terms, the Christoffel symbols are the Levi-Cevita connection coefficients induced by the metric $\hat{\boldsymbol{g}}$, for which the covariant derivative of the metric is always zero. See figure 4.1 for a visualization of the coordinate system.

We also assume $\hat{\Gamma}$ is an orientable connected surface equipped with well-defined unit normal vectors everywhere on the surface. Let $\hat{\boldsymbol{n}}$ be the exterior unit normal vector at $\hat{\boldsymbol{x}} \in \hat{\Gamma}$ given by the normalized cross product of the two surface basis vectors,

$$\hat{\boldsymbol{n}} = \frac{\hat{\boldsymbol{g}}_1 \times \hat{\boldsymbol{g}}_2}{|\hat{\boldsymbol{g}}_1 \times \hat{\boldsymbol{g}}_2|}. \tag{4.5}$$

The second fundamental form $\boldsymbol{I\!I}$ of surface $\hat{\Gamma}$ characterizes the rate of change of the normal vector $\boldsymbol{n}$ measured in the local tangent plane spanned by $\hat{\boldsymbol{g}}_\alpha$. The covariant components of the second fundamental form is defined as

$$I\!I_{\alpha\beta} = -\hat{\boldsymbol{g}}_\alpha \cdot \frac{\partial \hat{\boldsymbol{n}}}{\partial \xi^\beta} = \frac{\partial \hat{\boldsymbol{g}}_\alpha}{\partial \xi^\beta} \cdot \hat{\boldsymbol{n}} \tag{4.6}$$

where the second equality is deduced from $\partial(\hat{\boldsymbol{g}}_\alpha \cdot \hat{\boldsymbol{n}})/\partial\xi^\beta = 0$. Two eigenvalues κ_1 and κ_2 of the type-$(1,1)$ tensor $\mathit{I\!I}^\beta_\alpha \hat{\boldsymbol{g}}^\alpha \otimes \hat{\boldsymbol{g}}_\beta$ are called principal curvatures. The mean curvature $\mathcal{H}$ and Gaussian curvature $\mathcal{K}$ are the trace and determinant of $\mathit{I\!I}^\beta_\alpha$, respectively,

$$\left.\begin{aligned} 2\mathcal{H} &= \operatorname{tr} \mathit{I\!I}^\beta_\alpha = \kappa_1 + \kappa_2, \\ \mathcal{K} &= \det \mathit{I\!I}^\beta_\alpha = \kappa_1 \kappa_2. \end{aligned}\right\} \tag{4.7}$$

The second fundamental form $\mathit{I\!I}_{\alpha\beta}$ together with the Christoffel symbols $\hat{\Gamma}^\gamma_{\alpha\beta}$ of the first kind can fully specify how surface tangent vectors $\hat{\boldsymbol{g}}_\alpha$ and exterior normal vector $\hat{\boldsymbol{n}}$ vary with the intrinsic coordinates (ξ^1, ξ^2). These relations are summarized by the formulae of Weingarten and Gauss (Kreyszig, 1991),

$$\frac{\partial \hat{\boldsymbol{n}}}{\partial \xi^\alpha} = -\mathit{I\!I}^\beta_\alpha \hat{\boldsymbol{g}}_\beta, \qquad \text{(Weingarten)} \tag{4.8}$$

$$\frac{\partial \hat{\boldsymbol{g}}_\alpha}{\partial \xi^\beta} = \hat{\Gamma}^\gamma_{\alpha\beta} \hat{\boldsymbol{g}}_\gamma + \mathit{I\!I}_{\alpha\beta} \hat{\boldsymbol{n}}. \qquad \text{(Gauss)} \tag{4.9}$$

Note $\hat{g}_{\alpha\beta}$ and $\mathit{I\!I}_{\alpha\beta}$ contain in total six degrees of freedom at each point on the embedded surface $\hat{\Gamma}$ whereas the three-dimensional ambient Euclidean space $\mathbb{R}^3$ is parametrized by three coordinates at most (only flat ambient space is considered here). In other words, there must be three additional equations for the metric $\hat{\boldsymbol{g}}$ and the second fundamental form $\boldsymbol{\mathit{I\!I}}$ to satisfy. Two of the three constraints are called the Peterson-Codazzi-Mainardi-Gauss equations, also known as the integrability condition on a surface,

$$\hat{\nabla}_\beta \mathit{I\!I}^\gamma_\alpha = \hat{\nabla}_\alpha \mathit{I\!I}^\gamma_\beta, \quad \text{(Peterson-Codazzi-Mainardi-Gauss)} \tag{4.10}$$

where $\hat{\nabla}_\alpha$ denotes the covariant differentiations (Stoker, 1988)

$$\left.\begin{aligned} \hat{\nabla}_\beta v^\alpha &= \frac{\partial v^\alpha}{\partial \xi^\beta} + \hat{\Gamma}^\alpha_{\gamma\beta} v^\gamma, \\ \hat{\nabla}_\beta v_\alpha &= \frac{\partial v_\alpha}{\partial \xi^\beta} + \hat{\Gamma}^\gamma_{\alpha\beta} v_\gamma, \\ \hat{\nabla}_\beta v^\gamma{}_\alpha &= \frac{\partial v^\gamma{}_\alpha}{\partial \xi^\beta} + \hat{\Gamma}^\gamma_{\nu\beta} v^\nu{}_\alpha - \hat{\Gamma}^\mu_{\alpha\beta} v^\gamma{}_\mu, \end{aligned}\right\} \tag{4.11}$$

for various types of tensor field on the curved manifold $\hat{\Gamma}$. The last missing equation is the famous Theorema Egregium by Gauss, which is a statement of the Gaussian curvature $\mathcal{K} = \det \mathit{I\!I}^\alpha_\beta$ being intrinsic, i.e. a quantity depending only on the metric coefficients $\hat{g}_{\alpha\beta}$. In the modern language of Riemannian geometry, Gauss' Theorema Egregium is equivalent to the identity

$$\mathcal{R}_{1212} = \mathcal{K} \hat{g}, \quad \text{(Gauss' Theorema Egregium)} \tag{4.12}$$

where $\mathcal{R}_{1212}$ is the only independent component of the Riemann curvature tensor $\boldsymbol{R}$ in two dimensions. Gauss's Theorema Egregium leads to a simplification of the contraction between two second fundamental forms,

$$\mathit{I\!I}_{\alpha\gamma} \mathit{I\!I}^\gamma_\beta = 2\mathcal{H} \mathit{I\!I}_{\alpha\beta} - \mathcal{K} \hat{g}_{\alpha\beta} = \mathit{I\!I\!I}_{\alpha\beta}. \tag{4.13}$$

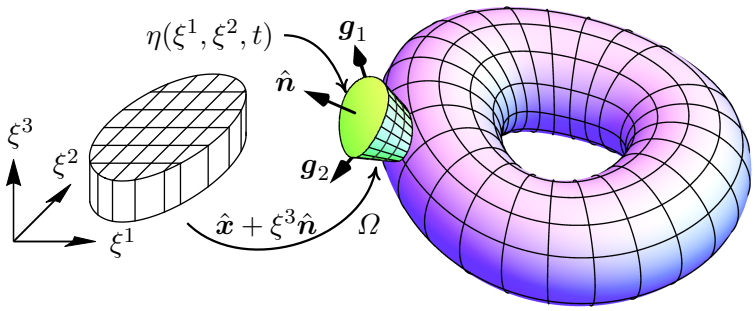

Figure 4.2: Surface-adapted coordinate system (ξ^1,ξ^2,ξ^3) for the thin domain Ω in the neighborhood of the supporting surface $\hat{\Gamma}$ where $\eta(\xi^1,\xi^2,t)$ is the time-dependent height field of the liquid layer.

Tensor $\boldsymbol{\mathit{III}}$ is the third fundamental form which measures the principal linear part of growth of the angle between the normal vector $\hat{\boldsymbol{n}}$ under infinitesimal displacement along the surface basis vectors. However, the third fundamental form is not wildly used in literature since its components $\mathit{III}_{\alpha\beta}$ are completely determined by the first and the second fundamental forms (Stoker, 1988).

Thin liquid layer: surface-adapted coordinates

Let $\Omega \subset \mathbb{R}^3$ be the volume in the three-dimensional ambient space in the vicinity of the embedded surface $\hat{\Gamma}$. Given knowledge of the surface parametrization (4.1), we are now in the position to construct a curvilinear coordinate system (ξ^1,ξ^2,ξ^3). A point $\boldsymbol{x} \in \Omega \subset \mathbb{R}^3$ may be uniquely identified as

$$\boldsymbol{x}(\xi^1,\xi^2,\xi^3) = \hat{\boldsymbol{x}}(\xi^1,\xi^2) + \xi^3\hat{\boldsymbol{n}}(\xi^1,\xi^2), \tag{4.14}$$

where ξ^3 corresponds to coordinate lines normal to the surface Γ. Parametrization (4.14) constructed from coordinates (ξ^1,ξ^2,ξ^3) naturally induces a set of covariant basis,

$$\boldsymbol{g}_\alpha = \frac{\partial \boldsymbol{x}}{\partial \xi^\alpha} = \hat{\boldsymbol{g}}_\alpha - \xi^3 \mathit{II}_\alpha^\beta \hat{\boldsymbol{g}}_\beta, \quad \boldsymbol{g}_3 = \hat{\boldsymbol{n}}, \tag{4.15}$$

where differentiation of the normal vector $\hat{\boldsymbol{n}}$ is resolved by the Weingarten formula (4.8). The 3-by-3 metric tensor $\boldsymbol{g}$ of the coordinate system (4.14) and its determinant g are given by

$$g_{ij} = \boldsymbol{g}_i \cdot \boldsymbol{g}_j, \quad g = \det g_{ij}. \tag{4.16}$$

In general, basis vectors $\boldsymbol{g}_\alpha$ differ from the substrate tangents $\hat{\boldsymbol{g}}_\alpha$ defined in (4.2) except on the supporting surface $\hat{\Gamma}$ where $\xi^3 = 0$. Although $\boldsymbol{g}_\alpha$ is still parallel to $\hat{\boldsymbol{g}}_\alpha$ and is perpendicular to $\hat{\boldsymbol{n}}$ in the thin domain Ω.

The range of ξ^3 is often restricted because the coordinate system (4.14) is not meant to cover the entire ambient space $\mathbb{R}^3$ but only locally near the supporting surface $\hat{\Gamma}$. Normal

ξ^3-coordinate lines emitting from a local surface patch that appears to be locally convex would necessarily collide into each other after moving some normal distance away from the surface. Another possible choice would be to normalize the ξ^3-coordinate for which $\boldsymbol{x} = \hat{\boldsymbol{x}} + \xi^3 \eta(\xi^1, \xi^2)\hat{\boldsymbol{n}}$ for a known layer thickness function $\eta(\xi^1, \xi^2)$ (Storti, D'Elía, and Battaglia, 2011). The coordinate system is well-defined for $\xi \in [0, 1]$, i.e. the region "below" the thickness field $\eta(\xi^1, \xi^2)$. This approach is mathematically equivalent to (4.14) however unwieldy in computations due to additional derivatives acting on the thickness function η. In what follows we proceed with the surface-adapted coordinate system (4.14) and assume it's regular everywhere in the layer domain Ω where it applies. We also assume the liquid layer is sufficiently thin such that the deformation of the liquid layer Ω may be entirely tracked by the graph of a time-dependent height field,

$$\Omega = \{\boldsymbol{x}(\xi^1, \xi^2, \xi^3) \in \mathbb{R}^3 \mid 0 \leq \xi^3 \leq \eta(\xi^1, \xi^2)\}, \tag{4.17}$$

where $\eta(\xi^1, \xi^2) : O \to \mathbb{R}$ is the scalar height field which specifies the local thickness (measured in distance along normal direction) of the liquid layer. Curvilinear coordinate system (4.14) is quite general, not necessarily orthonormal or orthogonal. We also do not limit ourselves to a particular choice of surface parametrization $\varphi(\xi^1, \xi^2)$, for example, the orthonormal coordinate system defined by the lines of curvature (Roy, A. J. Roberts, and Simpson, 2002; Rumpf and Vantzos, 2013). Effect of curvature should naturally appear from the first and second fundamental form of the surface $\hat{\Gamma}$. The surface-adapted coordinate system is illustrated in figure 4.2.

We next compute the metric and connection coefficients for the curvilinear coordinates (4.14). The covariant components of the 3-by-3 metric tensor $\boldsymbol{g}$ are derived from the coordinate basis vectors (4.15),

$$g_{\alpha\beta} = \hat{g}_{\alpha\beta} - 2\xi^3 \mathit{I\!I}_{\alpha\beta} + (\xi^3)^2 \mathit{I\!I}_{\alpha\gamma} \mathit{I\!I}^{\gamma}_{\beta}, \quad g_{i3} = 0, \quad g_{33} = 1. \tag{4.18}$$

Note metric coefficients g_{ij} can be partitioned into exact orders of ξ^3,

$$g_{ij} = \begin{bmatrix} \hat{g}_{\alpha\beta} & 0 \\ 0 & 1 \end{bmatrix} + \xi^3 \begin{bmatrix} -2\mathit{I\!I}_{\alpha\beta} & 0 \\ 0 & 0 \end{bmatrix} + (\xi^3)^2 \begin{bmatrix} \mathit{I\!I\!I}_{\alpha\beta} & 0 \\ 0 & 0 \end{bmatrix}. \tag{4.19}$$

Equation (4.19) implies that the metric determinant $g = \det g_{ij}$, which is required for evaluating volume integrals in the liquid volume Ω, must be an exact fourth order polynomial in ξ^3. Since g_{ij} is only a 3-by-3 matrix with a bordered structure, we directly evaluate its determinant

$$g = \hat{g}\left[1 - 4\mathcal{H}\xi^3 + 4\mathcal{K}(\xi^3)^2 + (4\mathcal{H}^2 - 2\mathcal{K})(\xi^3)^2 - 4\mathcal{H}\mathcal{K}(\xi^3)^3 + \mathcal{K}^2(\xi^3)^4\right]. \tag{4.20}$$

After cleaning up (4.20), the closed-form expression of metric determinant g is surprisingly simple,

$$g = J^2\hat{g}, \quad J = 1 - 2\mathcal{H}\xi^3 + \mathcal{K}(\xi^3)^2. \tag{4.21}$$

The expression (4.21) is exact with no truncated expansion or approximation in ξ^3. We can interpret $J(\xi^1, \xi^2, \xi^3)$ as the Jacobian between area differential $\mathrm{d}\hat{\Gamma}$ at a point $\hat{\boldsymbol{x}} \in \hat{\Gamma}$ and another area differential ξ^3-distance away from the same point. As a result of the metric determinant (4.21), the infinitesimal volume element

$$\mathrm{d}\Omega = J(\xi^1, \xi^2, \xi^3)\, \mathrm{d}\xi^3\, \mathrm{d}\hat{\Gamma} \tag{4.22}$$

of the liquid volume Ω becomes separable in the sense that partial integration along normal direction ξ^3 is decoupled from the in-plane coordinates (ξ^1, ξ^2). When performing volume integration of some function $A(\xi^1, \xi^2, \xi^3)$ over the liquid domain Ω bounded above by the height field (4.17), we can first integrate out the transverse coordinate ξ^3 and lump the result into the remaining area integral on the supporting surface $\hat{\Gamma}$,

$$\int_\Omega A\, \mathrm{d}\Omega = \int_{\hat{\Gamma}} \left(\int_0^{\eta(\xi^1, \xi^2)} AJ\, \mathrm{d}\xi^3 \right) \mathrm{d}\hat{\Gamma}. \tag{4.23}$$

To raise or lower indices of a tensorial object, contracovariant components of the metric tensor $\boldsymbol{g}$ are required. While a closed-form expression of $g^{\alpha\beta}$ is technically possible, the asymptotic behavior of g^{ij} in the limit $|\xi^3| \ll 1$ is more relevant as far as the thin layer domain Ω is concerned. The power series expansion for the inverse of a perturbed matrix $\boldsymbol{A}_\epsilon = \boldsymbol{A} + \dot{\boldsymbol{A}}\,\epsilon + \ddot{\boldsymbol{A}}\,\epsilon^2/2$ in a small parameter $0 < \epsilon \ll 1$ is given by the Neumann series (Golub and Van Loan, 2013)

$$\boldsymbol{A}_\epsilon^{-1} = \boldsymbol{A}^{-1} - \boldsymbol{A}^{-1}\dot{\boldsymbol{A}}\boldsymbol{A}^{-1}\epsilon + \left(\boldsymbol{A}^{-1}\dot{\boldsymbol{A}}\boldsymbol{A}^{-1}\dot{\boldsymbol{A}}\boldsymbol{A}^{-1} - \frac{1}{2}\boldsymbol{A}^{-1}\ddot{\boldsymbol{A}}\boldsymbol{A}^{-1} \right)\epsilon^2 + O(\epsilon^3). \tag{4.24}$$

Applying expansion (4.24) to the covariant coefficients g_{ij} in (4.19) yields the asymptotic expansion of $g^{\alpha\beta}$ in orders of ξ^3,

$$g^{ij} = \begin{bmatrix} \hat{g}^{\alpha\beta} & 0 \\ 0 & 1 \end{bmatrix} + \xi^3 \begin{bmatrix} 2\mathit{I\!I}^{\alpha\beta} & 0 \\ 0 & 0 \end{bmatrix} + (\xi^3)^2 \begin{bmatrix} 3\mathit{I\!I\!I}^{\alpha\beta} & \\ 0 & 0 \end{bmatrix} + O((\xi^3)^3). \tag{4.25}$$

Similar to the covariant matrix g_{ij}, its inverse g^{ij} also has a bordered structure. We point out that coefficients $g^{\alpha 3} = 0$ and $g^{33} = 1$ are exact. The asymptotic expansion (4.25) only affects the 2-by-2 submatrix $g^{\alpha\beta}$. This is one of the nice properties of the surface-adapted coordinate system: we do not need to distinguish between covariance and contracovariance in the ξ^3-component of any tensorial object, i.e. $u^3 = u_3$ and $\boldsymbol{g}^3 = \boldsymbol{g}_3$.

Covariant differentiation ∇_i in the ambient space $\mathbb{R}^3$ requires the first kind Christoffel symbols of the coordinates (ξ^1, ξ^2, ξ^3),

$$\Gamma^k_{ij} = \frac{\partial \boldsymbol{g}_i}{\partial \xi^j} \cdot \boldsymbol{g}^k. \tag{4.26}$$

The fact that ambient coordinate system (4.14) adapts to the surface coordinates $\hat{\boldsymbol{x}}(\xi^1,\xi^2)$ significantly simplifies the calculation of the connection coefficients Γ^k_{ij}. We start with the relatively easy group Γ^3_{ij} of the Christoffel symbols,

$$\left.\begin{aligned}
\Gamma^3_{\alpha\beta} &= \frac{\partial}{\partial\xi^\beta}(\hat{\boldsymbol{g}}_\alpha - \xi^3 I\!I^\gamma_\alpha \hat{\boldsymbol{g}}_\gamma)\cdot\boldsymbol{g}^3 = \Big(\hat{\Gamma}^\gamma_{\alpha\beta}\hat{\boldsymbol{g}}_\gamma + I\!I_{\alpha\beta}\hat{\boldsymbol{n}} - \xi^3\frac{\partial I\!I^\gamma_\alpha \hat{\boldsymbol{g}}_\gamma}{\partial\xi^\beta}\Big)\cdot\hat{\boldsymbol{n}}\\
&= I\!I_{\alpha\beta} - \xi^3 I\!I^\gamma_\alpha \frac{\partial\hat{\boldsymbol{g}}_\gamma}{\partial\xi^\beta}\cdot\hat{\boldsymbol{n}} = I\!I_{\alpha\beta} - \xi^3 I\!I^\gamma_\alpha I\!I_{\gamma\beta}\\
&= I\!I_{\alpha\beta} - \xi^3(2\mathcal{H}I\!I_{\alpha\beta} - \mathcal{K}\hat{g}_{\alpha\beta}),\\
\Gamma^3_{\alpha 3} &= \frac{\partial}{\partial\xi^3}(\hat{\boldsymbol{g}}_\alpha - \xi^3 I\!I^\gamma_\alpha\hat{\boldsymbol{g}}_\gamma)\cdot\boldsymbol{g}^3 = 0,\\
\Gamma^3_{33} &= 0,
\end{aligned}\right\} \tag{4.27}$$

where we have used the Weingarten formula (4.8) and the Gauss formula (4.9). Note expression (4.27) of Γ^3_{ij} derived above is exact without any truncation or approximation. The calculation of Γ^γ_{ij} for $\gamma = 1,2$ is slightly more involved because $\boldsymbol{g}^\gamma = g^{\alpha\gamma}\boldsymbol{g}_\alpha$ is an infinite series expansion thanks to the asymptotic formula (4.25) of $g^{\alpha\gamma}$,

$$\boldsymbol{g}^\gamma = g^{\gamma\alpha}\boldsymbol{g}_\alpha = (\hat{g}^{\gamma\alpha} + 2I\!I^{\gamma\alpha}\xi^3 + O((\xi^3)^2))(\hat{\boldsymbol{g}}_\alpha - \xi^3 I\!I^\beta_\alpha\hat{\boldsymbol{g}}_\beta) = \hat{\boldsymbol{g}}^\gamma + \xi^3 I\!I^\gamma_\alpha\hat{\boldsymbol{g}}^\alpha + O((\xi^3)^2). \tag{4.28}$$

With $\boldsymbol{g}^\gamma$ from (4.28) substituted into $\Gamma^\gamma_{\alpha\beta}$, we then collect the leading order terms and obtain

$$\left.\begin{aligned}
\Gamma^\gamma_{\alpha\beta} &= \Big(\hat{\Gamma}^\nu_{\alpha\beta}\hat{\boldsymbol{g}}_\nu + I\!I_{\alpha\beta}\hat{\boldsymbol{n}} - \xi^3\frac{\partial I\!I^\gamma_\alpha\hat{\boldsymbol{g}}_\nu}{\partial\xi^\beta}\Big)\cdot\boldsymbol{g}^\gamma\\
&= \Big(\hat{\Gamma}^\nu_{\alpha\beta}\hat{\boldsymbol{g}}_\nu + I\!I_{\alpha\beta}\hat{\boldsymbol{n}} - \xi^3\frac{\partial I\!I^\nu_\alpha}{\partial\xi^\beta}\hat{\boldsymbol{g}}_\nu - \xi^3 I\!I^\nu_\alpha\frac{\partial\hat{\boldsymbol{g}}_\nu}{\partial\xi^\beta}\Big)\cdot\Big(\hat{\boldsymbol{g}}^\gamma + \xi^3 I\!I^\gamma_\mu\hat{\boldsymbol{g}}^\mu\Big) + O((\xi^3)^2)\\
&= \hat{\Gamma}^\gamma_{\alpha\beta} + \xi^3\Big(\hat{\Gamma}^\mu_{\alpha\beta}I\!I^\gamma_\mu - \frac{\partial I\!I^\nu_\alpha}{\partial\xi^\beta}\hat{\boldsymbol{g}}_\nu\cdot\hat{\boldsymbol{g}}^\gamma - I\!I^\nu_\alpha\frac{\partial\hat{\boldsymbol{g}}_\nu}{\partial\xi^\beta}\cdot\hat{\boldsymbol{g}}^\gamma\Big) + O((\xi^3)^2)\\
&= \hat{\Gamma}^\gamma_{\alpha\beta} + \xi^3\Big(\hat{\Gamma}^\mu_{\alpha\beta}I\!I^\gamma_\mu - \frac{\partial I\!I^\gamma_\alpha}{\partial\xi^\beta} - \hat{\Gamma}^\gamma_{\nu\beta}I\!I^\nu_\alpha\Big) + O((\xi^3)^2)\\
&= \hat{\Gamma}^\gamma_{\alpha\beta} - \xi^3\hat{\nabla}_\beta I\!I^\gamma_\alpha + O((\xi^3)^2),\\
\Gamma^\gamma_{\alpha 3} &= \frac{\partial}{\partial\xi^3}(\hat{\boldsymbol{g}}_\alpha - \xi^3 I\!I^\gamma_\alpha\hat{\boldsymbol{g}}_\gamma)\cdot\boldsymbol{g}^\gamma\\
&= -I\!I^\nu_\alpha\hat{\boldsymbol{g}}_\nu\cdot(\hat{\boldsymbol{g}}^\gamma + \xi^3 I\!I^\gamma_\mu\hat{\boldsymbol{g}}^\mu) + O((\xi^3)^2) = -I\!I^\gamma_\alpha - \xi^3 I\!I^\gamma_\mu I\!I^\mu_\alpha + O((\xi^3)^2)\\
&= -I\!I^\gamma_\alpha - \xi^3(2\mathcal{H}I\!I^\gamma_\alpha - \mathcal{K}\hat{g}^\gamma_\alpha) + O((\xi^3)^2),\\
\Gamma^\gamma_{33} &= 0.
\end{aligned}\right\} \tag{4.29}$$

The coefficients Γ^γ_{ij} are responsible for parallel transport in the direction tangent to the surface $\hat{\Gamma}$. Note the Levi-Civita connection is defined to have zero torsion. In this basis the connection coefficients are symmetric, i.e. $\Gamma^\gamma_{\alpha\beta} = \Gamma^\gamma_{\beta\alpha}$ must be be symmetric in α and β, which is guaranteed by the integrability conditions (4.10) of the surface $\hat{\Gamma}$.

Free surface of liquid layer: Monge patch

As stated earlier, for a sufficiently slender liquid layer, the local film thickness at point $\hat{\boldsymbol{x}}(\xi^1,\xi^2)$ on the supporting surface $\hat{\Gamma}$ is tracked by the height field $\eta(\xi^1,\xi^2)$. Shallow depth of the thin layer geometry excludes the scenarios where the liquid interface develops overhangs in the normal direction so that height field $\eta(\xi^1,\xi^2)$ becomes multi-valued. This strong assumption allows us to characterize the free surface $\tilde{\Gamma}$ (or the "upper" boundary) of the thin liquid layer Ω using the same set of curvilinear coordinates (ξ^1,ξ^2) of the supporting substrate $\hat{\Gamma}$. For example, a material point $\tilde{\boldsymbol{x}}$ on the free surface $\tilde{\Gamma}$ can be identified as,

$$\tilde{\boldsymbol{x}} = \varphi(\xi^1,\xi^2) + \eta(\xi^1,\xi^2)\hat{\boldsymbol{n}}. \tag{4.30}$$

Coordinate system (4.30) is called the Monge patch (Weatherburn, 2016). From the discussion in Section 2.2 we know that there are two ways to identity $\tilde{\Gamma}$: either explicitly through the parametrization (4.30),

$$\tilde{\Gamma} = \{\hat{\boldsymbol{x}} + \eta(\xi^1,\xi^2)\hat{\boldsymbol{n}} \mid (\xi^1,\xi^2) \subset O\}, \tag{4.31}$$

or implicitly by the zero set of a level function,

$$\tilde{\Gamma} = \{\boldsymbol{x}(\xi^1,\xi^2,\xi^3) \mid \xi^3 - \eta(\xi^1,\xi^2) = 0\}. \tag{4.32}$$

The free surface $\tilde{\Gamma}$ inherits a set of normal and tangent basis vectors from the Monge patch (4.30), which slightly differ from the ones of the supporting surface $\hat{\Gamma}$. The covariant basis vectors $\tilde{\boldsymbol{g}}_\alpha$ are given by

$$\tilde{\boldsymbol{g}}_\alpha = \hat{\boldsymbol{g}}_\alpha + \frac{\partial\eta}{\partial\xi^\alpha}\hat{\boldsymbol{n}} - \eta\mathit{I\!I}^\beta_\alpha\hat{\boldsymbol{g}}_\beta \tag{4.33}$$

with the induced metric tensor

$$\tilde{g}_{\alpha\beta} = \tilde{\boldsymbol{g}}_\alpha\cdot\tilde{\boldsymbol{g}}_\beta = \hat{g}_{\alpha\beta} - 2\eta\mathit{I\!I}_{\alpha\beta} + \frac{\partial\eta}{\partial\xi^\alpha}\frac{\partial\eta}{\partial\xi^\beta} + \eta^2\mathit{I\!I}^\gamma_\alpha\mathit{I\!I}_{\gamma\beta}, \tag{4.34}$$

and the usual definition of metric determinant $\tilde{g} = \det\tilde{g}_{\alpha\beta}$. The unit normal vector $\tilde{\boldsymbol{n}}$ of the free surface $\tilde{\Gamma}$ is proportional to the cross product of the two basis vectors,

$$\begin{aligned}\tilde{\boldsymbol{g}}_1\times\tilde{\boldsymbol{g}}_2 &= (\hat{\boldsymbol{g}}_1 + \frac{\partial\eta}{\partial\xi_1}\boldsymbol{n} - \eta\mathit{I\!I}^\alpha_1\hat{\boldsymbol{g}}_\alpha)\times(\hat{\boldsymbol{g}}_2 + \frac{\partial\eta}{\partial\xi_2}\boldsymbol{n} - \eta\mathit{I\!I}^\beta_2\hat{\boldsymbol{g}}_\beta)\\ &= \hat{\boldsymbol{g}}_1\times\hat{\boldsymbol{g}}_2 + \left(\frac{\partial\eta}{\partial\xi_1}\boldsymbol{n}\times\hat{\boldsymbol{g}}_2 - \frac{\partial\eta}{\partial\xi_2}\boldsymbol{n}\times\hat{\boldsymbol{g}}_1\right) + \left(-\eta\mathit{I\!I}^\alpha_1\hat{\boldsymbol{g}}_\alpha\times\hat{\boldsymbol{g}}_2 + \eta\mathit{I\!I}^\beta_2\hat{\boldsymbol{g}}_\beta\times\hat{\boldsymbol{g}}_1\right)\\ &\quad - \left(\frac{\partial\eta}{\partial\xi_1}\eta\mathit{I\!I}^\beta_2\boldsymbol{n}\times\hat{\boldsymbol{g}}_\beta - \frac{\partial\eta}{\partial\xi_2}\eta\mathit{I\!I}^\alpha_1\boldsymbol{n}\times\hat{\boldsymbol{g}}_\alpha - \eta\mathit{I\!I}^\alpha_1\hat{\boldsymbol{g}}_\alpha\times\eta\mathit{I\!I}^\beta_2\hat{\boldsymbol{g}}_\beta\right).\end{aligned} \tag{4.35}$$

Then by the Lagrange's identity, $(\boldsymbol{a}\times\boldsymbol{b})\cdot(\boldsymbol{c}\times\boldsymbol{d}) = (\boldsymbol{a}\cdot\boldsymbol{c})(\boldsymbol{b}\cdot\boldsymbol{d}) - (\boldsymbol{b}\cdot\boldsymbol{c})(\boldsymbol{a}\cdot\boldsymbol{d})$, metric determinant of the free surface can be expanded in orders of the local height field η,

$$\tilde{g} = |\tilde{\boldsymbol{g}}_1\times\tilde{\boldsymbol{g}}_2|^2 = \hat{g}\left\{1 - 4\mathcal{H}\eta + \hat{g}^{\alpha\beta}\frac{\partial\eta}{\partial\xi^\alpha}\frac{\partial\eta}{\partial\xi^\beta} + (4\mathcal{H}^2 + 2\mathcal{K})\eta^2 + O(\eta^3)\right\}. \tag{4.36}$$

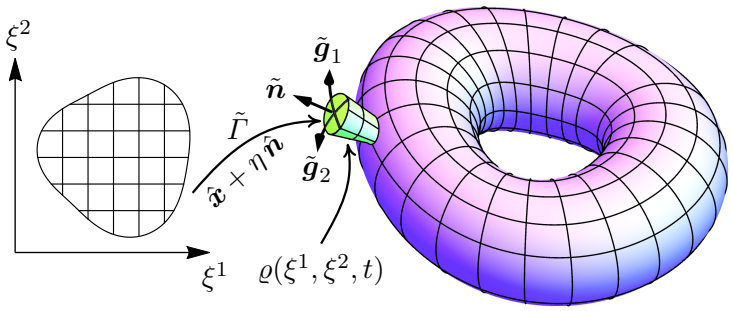

Figure 4.3: Monge parametrization of the free surface $\tilde{\Gamma}$ and columnar volume density ϱ bounded by the local height field η.

Similar to the relative volume Jacobian J, we introduce the relative area Jacobian

$$\mathcal{A} = \sqrt{\frac{\tilde{g}}{\hat{g}}} \tag{4.37}$$

between the supporting surface $\hat{\Gamma}$ and the free surface $\tilde{\Gamma}$. If we retain terms in (4.36) up to second order in η, the area differential of the free surface $\tilde{\Gamma}$ can be pulled back to the supporting surface $\hat{\Gamma}$ with quadratic corrections,

$$\mathrm{d}\tilde{\Gamma} = \mathcal{A}\,\mathrm{d}\hat{\Gamma} = \left\{1 - 2\mathcal{H}\eta + \mathcal{K}\eta^2 + \frac{1}{2}\hat{g}^{\alpha\beta}\frac{\partial\eta}{\partial\xi^\alpha}\frac{\partial\eta}{\partial\xi^\beta} + O(\eta^3)\right\}\mathrm{d}\hat{\Gamma}. \tag{4.38}$$

In order for the free surface surface $\tilde{\Gamma}$ to be validly described by the Monge patch (4.30), its metric determinant $\tilde{g}$ must remain positive and bounded away from zero. The higher order terms in expansion (4.38) immediately suggest a few admissible scaling requirements, i.e. $O(|\kappa_\alpha\eta|) \ll 1$ and $O(|\partial\eta/\partial\xi^\alpha|) \ll 1$, on the height field function η.

The columnar volume density

$$\varrho(\xi^1, \xi^2) = \int_0^{\eta(\xi^1,\xi^2)} J\,\mathrm{d}\xi^3 \tag{4.39}$$

is another important scalar field on the supporting surface $\hat{\Gamma}$. As illustrated in figure 4.3, $\varrho(\xi^1, \xi^2)$ is the volume of an infinitesimal liquid column of local height $\eta(\xi^1, \xi^2)$ centered at $\hat{\boldsymbol{x}}(\xi^1, \xi^2)$, hence the name "columnar volume density". Recall from (4.23) that the total volume of liquid layer Ω enclosed by the height field η is simply the area integral of the columnar volume density ϱ,

$$\int_{\hat{\Gamma}} \varrho(\xi^1, \xi^2)\,\mathrm{d}\hat{\Gamma} = \int_\Omega \mathrm{d}\Omega. \tag{4.40}$$

In light of the Jacobian J in (4.21), the ξ^3-integral (4.39) is decoupled from the surface integral over coordinates (ξ^1, ξ^2) which results in an exact expression for the columnar volume density,

$$\varrho = \int_0^\eta J\,\mathrm{d}\xi^3 = \eta - \mathcal{H}\eta^2 + \frac{1}{3}\mathcal{K}\eta^3. \tag{4.41}$$

As we shall see later, the columnar volume density ϱ is more suitable as the primary dynamic variable enforcing the conservation law of viscous free surface films than the height field η. However, in many situations physical quantities such as electric field or temperature are usually directly related to the local thickness of the free surface $\tilde{\Gamma}$ rather than its areal volume density because the height field η is a geometric quantity. While it's possible to invert the cubic polynomial in (4.41) to obtain an exact solution of $\eta(\varrho)$, it suffices to construct an asymptotic approximation for the height field η in orders of columnar volume density ϱ for hydrodynamics confined within a thin layer,

$$\eta = \varrho + \mathscr{H}\varrho^2 + \frac{1}{3}(6\mathscr{H}^2 - \mathscr{K})\varrho^3 + O(\varrho^4). \tag{4.42}$$

In the limit of slender geometries, the height field η and the volume density ϱ are interchangeable up to higher order corrections depending on the local curvatures.

4.3 Kinematics and Dissipation of Viscous Free Surface Flows

In this section we present a variational (weak) formulation of viscous free surface flows, by consulting the Helmholtz minimum dissipation theorem. We then modify the formulation to incorporate kinematics and traction forces of the liquid free surface. For slender films, it reduces to an energy-dissipation relation.

Helmholtz minimum dissipation theorem

In the limit of vanishing Reynolds, the effect of intertia becomes negligible and the bulk motion of a viscous fluid follows the Stokes equation (Batchelor, 2000; Leal, 2007),

$$\left.\begin{aligned} -\nabla p + \mu\nabla^2\boldsymbol{v} &= \boldsymbol{0}, \\ \nabla\cdot\boldsymbol{v} &= 0. \end{aligned}\right\} \text{ (Stokes equation)} \tag{4.43}$$

As noted earlier in Section 2.2, the Stokes equation (4.43) is only a particular form of the Cauchy momentum equation,

$$\left.\begin{aligned} \boldsymbol{\sigma} &= -p\mathbb{I} + 2\mu\boldsymbol{e}, \\ \nabla\cdot\boldsymbol{\sigma} &= \boldsymbol{0}, \\ \nabla\cdot\boldsymbol{v} &= 0, \end{aligned}\right\} \text{ (Cauchy momentum equation)} \tag{4.44}$$

where the strain rate tensor $\boldsymbol{e} = (\nabla\boldsymbol{v} + \nabla\boldsymbol{v}^\top)/2$ is the symmetrization of velocity gradient $\nabla\boldsymbol{v}$ and $\boldsymbol{\sigma}$ is the Cauchy stress tensor. The equivalence between Stokes equation (4.43) and Cauchy momentum equation (4.44) is straightforward via index manipulation,

$$2\nabla\cdot\boldsymbol{e} = \nabla_i(\nabla_j v^i + \nabla^i v_j) = \nabla_j\nabla_i v^i + \nabla_i\nabla^i v_j \overset{\text{flat}}{=} \nabla_i\nabla^i v_j \overset{\text{div. free}}{=} \nabla^2\boldsymbol{v}, \tag{4.45}$$

where we have used the flatness of the ambient Euclidean space. von Helmholtz (1868) discovered an alternative characterization of viscous flow by introducing the viscous dissipation

$$\mathscr{D}[\boldsymbol{v}] = \int_\Omega 2\mu\,\boldsymbol{e} : \boldsymbol{e}\,\mathrm{d}\Omega, \tag{4.46}$$

a non-negative quadratic functional of velocity field. The Helmholtz minimum dissipation theorem, named after Helmholtz's work, states that the Stokes flow (4.43) is a solution to the following minimization problem,

$$\left.\begin{aligned} \min_{\boldsymbol{v}} \frac{1}{2}\mathscr{D}[\boldsymbol{v}], \\ \text{subject to } \nabla\cdot\boldsymbol{v}=0 \quad \text{in } \Omega, \\ \boldsymbol{v}=\boldsymbol{v}' \text{ on } \hat{\Gamma}. \end{aligned}\right\} \text{(Helmholtz minimum dissipation theorem)} \tag{4.47}$$

In other words, the steady Stokes flow of an incompressible fluid has the smallest rate of viscous dissipation than any other incompressible velocity configurations with the same velocity prescribed on the boundary $\hat{\Gamma}$.

The Helmholtz minimum dissipation theorem (4.47) can be proved from a variational argument. Let $\boldsymbol{v}$ be a solution to the Stokes equation (4.43) and $\delta\boldsymbol{v}$ be an admissible variation to $\boldsymbol{v}$. By admissible we mean that, $\delta\boldsymbol{v}$ is divergence-free and $\delta\boldsymbol{v}=\boldsymbol{0}$ on all boundary because the perturbed velocity field $\boldsymbol{v}+\delta\boldsymbol{v}$ must also be incompressible and agree with the prescribed velocity on the boundary Γ. Since viscous dissipation (4.46) is a quadric form of strain rate, its variation is exactly composed of a linear and a quadratic part in $\delta\boldsymbol{v}$,

$$\frac{1}{2}\mathscr{D}[\boldsymbol{v}+\delta\boldsymbol{v}]=\frac{1}{2}\mathscr{D}[\boldsymbol{v}]+\int_\Omega 2\mu\,\delta\boldsymbol{e}:\boldsymbol{e}\,\mathrm{d}\Omega+\int_\Omega \mu\,\delta\boldsymbol{e}:\delta\boldsymbol{e}\,\mathrm{d}\Omega, \tag{4.48}$$

where $\delta\boldsymbol{e}$ is the strain rate tensor constructed from $\delta\boldsymbol{v}$. The integral linear in $\delta\boldsymbol{e}$ (hence linear in $\delta\boldsymbol{v}$) must vanish for any admissible velocity variation $\delta\boldsymbol{v}$,

$$\begin{aligned}
\int_\Omega 2\mu\,\delta\boldsymbol{e}:\boldsymbol{e}\,\mathrm{d}\Omega &= \int_\Omega 2\mu\,\frac{1}{2}(\nabla\delta\boldsymbol{v}+\nabla\delta\boldsymbol{v}^\top):\boldsymbol{e}\,\mathrm{d}\Omega \\
&= \int_\Omega 2\mu\,\nabla\delta\boldsymbol{v}:\boldsymbol{e}\,\mathrm{d}\Omega=\int_\Omega 2\mu\,(\nabla_i\delta v^j)e^i{}_j\,\mathrm{d}\Omega \qquad \boldsymbol{e} \text{ is symmetric} \\
&= -\int_\Omega 2\mu\,\delta v^j(\nabla_i e^i{}_j)\,\mathrm{d}\Omega+\int_{\hat{\Gamma}} 2\mu\,\delta v^j e^i{}_j n_i\,\mathrm{d}\Gamma \\
&= -\int_\Omega \mu\,\delta\boldsymbol{v}\cdot(2\nabla\cdot\boldsymbol{e})\,\mathrm{d}\Omega+\int_{\hat{\Gamma}} 2\mu\,\delta\boldsymbol{v}\,\boldsymbol{e}\,\boldsymbol{n}\,\mathrm{d}\hat{\Gamma} \\
&= -\int_\Omega \delta\boldsymbol{v}\cdot(\mu\nabla^2\boldsymbol{v})\,\mathrm{d}\Omega+\int_{\hat{\Gamma}} 2\mu\,\delta\boldsymbol{v}\,\boldsymbol{e}\,\boldsymbol{n}\,\mathrm{d}\hat{\Gamma} \quad \text{Identity (4.45)} \\
&= -\int_\Omega \delta\boldsymbol{v}\cdot\nabla p\,\mathrm{d}\Omega+\int_{\hat{\Gamma}} 2\mu\,\delta\boldsymbol{v}\,\boldsymbol{e}\,\boldsymbol{n}\,\mathrm{d}\hat{\Gamma} \quad \text{Stokes equation (4.43)} \\
&= \int_\Omega p\nabla\cdot\delta\boldsymbol{v}\,\mathrm{d}\Omega+\int_{\hat{\Gamma}} \delta\boldsymbol{v}\cdot(-p\boldsymbol{n}+2\mu\,\boldsymbol{e}\,\boldsymbol{n})\,\mathrm{d}\hat{\Gamma} \\
&= 0, \quad \text{Constraint on velocity variation } \delta\boldsymbol{v}
\end{aligned} \tag{4.49}$$

where $\boldsymbol{n}$ is understood to be the outward normal vector of liquid domain Ω. Now it's a straightforward exercise to show that any incompressible flow other than the Stokes solution $\boldsymbol{v}$ with the same velocity prescribed on the boundary can only increase

dissipation rate because

$$\frac{1}{2}\mathscr{D}[\boldsymbol{e}+\delta\boldsymbol{e}]-\frac{1}{2}\mathscr{D}[\boldsymbol{e}]=\int_{\Omega}\mu\,\delta\boldsymbol{e}:\delta\boldsymbol{e}\,\mathrm{d}\Omega\geq 0. \tag{4.50}$$

The Stokes flow (4.43) is indeed an optimal solution to the Helmholtz minimization problem (4.47). It certainly would be desirable if the solution to the Helmholtz minimization problem exists and is unique. Under such a condition the Stokes equation and Helmholtz minimization theorem would be two equivalent formulations of viscous flow,

$$\text{Stokes flow (4.43)} \iff \text{Helmholtz minimum dissipation (4.47)}. \tag{4.51}$$

Statement (4.51) is correct although proving the existence and uniqueness of the solution to Helmholtz minimization problem (4.47) is a highly nontrivial task which requires sophisticated tools from functional analysis that are beyond the scope of this work. See Ern and Guermond (2004) for the technical details and the complete proof. We only briefly sketch the idea. The results follows directly from Lax-Milgram theorem which requires the bilinear form of velocity vector $\boldsymbol{v}$, in this case the viscous dissipation (4.46), to be coercive, i.e. $\mathscr{D}[\boldsymbol{e}]\gtrsim\|\boldsymbol{u}\|_{\mathbb{V}}^2$, for some suitable norm $\|\cdot\|_{\mathbb{V}}$ defined on the functional space $\mathbb{V}$ that velocity field $\boldsymbol{v}$ belongs to. Coercivity of viscous dissipation (4.46) on a Lipschitz domain is guaranteed by the Korn's first and second inequalities.

Energy-dissipation theorem for free surface flows

Now we consider a slightly different scenario where Ω is the domain enclosed between a fixed supporting surface $\hat{\Gamma}$ at the bottom and a free surface $\tilde{\Gamma}$ at the top. In a mixed problem, velocity field (e.g., no slip condition) is prescribed on $\hat{\Gamma}$ whereas the viscous stress must balance traction force $\boldsymbol{f}$ on the free surface $\tilde{\Gamma}$. The resulting Stokes equation,

$$\left.\begin{aligned}-\nabla p+\mu\nabla^2\boldsymbol{v}&=\boldsymbol{0} \quad \text{in} \quad \Omega,\\ \nabla\cdot\boldsymbol{v}&=0 \quad \text{in} \quad \Omega,\\ \boldsymbol{v}&=\boldsymbol{v}' \quad \text{on} \quad \hat{\Gamma},\\ \boldsymbol{\sigma}\tilde{\boldsymbol{n}}&=\boldsymbol{f} \quad \text{on} \quad \tilde{\Gamma},\end{aligned}\right\} \tag{4.52}$$

is called a "mixed" problem in the sense that it has a mixed set of boundary conditions: Dirichlet type on $\hat{\Gamma}$ and Neumann type on $\tilde{\Gamma}$. If we augment the viscous dissipation with an additional surface dissipation, then we can show that the modified minimum dissipation problem,

$$\left.\begin{aligned}&\min_{\boldsymbol{v}}\frac{1}{2}\mathscr{D}[\boldsymbol{v}]-\int_{\tilde{\Gamma}}\boldsymbol{f}\cdot\boldsymbol{v}\,\mathrm{d}\tilde{\Gamma},\\ &\text{subject to } \nabla\cdot\boldsymbol{v}=0 \quad \text{in } \Omega,\\ &\qquad\qquad \boldsymbol{v}=\boldsymbol{v}' \text{ on } \hat{\Gamma},\end{aligned}\right\} \tag{4.53}$$

is an equivalent characterization of the viscous flow described by the Stokes equation (4.52). It's not difficult to show that any fluid motion satisfying Stokes equation under stress boundary condition must be a critical point of the augmented dissipation functional in (4.53) through an expansion procedure similar to (4.48),

$$\begin{aligned}\delta\left\{\frac{1}{2}\mathcal{D}[\boldsymbol{v}]-\int_{\tilde{\Gamma}}\boldsymbol{f}\cdot\boldsymbol{v}\,\mathrm{d}\tilde{\Gamma}\right\}&=\int_{\Omega}2\mu\,\delta\boldsymbol{e}:\boldsymbol{e}\,\mathrm{d}\Omega-\int_{\tilde{\Gamma}}\delta\boldsymbol{v}\cdot\boldsymbol{f}\,\mathrm{d}\Gamma\\&=\int_{\Omega}p\nabla\cdot\delta\boldsymbol{v}\,\mathrm{d}\Omega+\int_{\hat{\Gamma}}\delta\boldsymbol{v}\cdot(\boldsymbol{\sigma}\boldsymbol{n})\,\mathrm{d}\hat{\Gamma}+\int_{\tilde{\Gamma}}\delta\boldsymbol{v}\cdot(\boldsymbol{\sigma}\tilde{\boldsymbol{n}}-\boldsymbol{f})\,\mathrm{d}\tilde{\Gamma}\\&=0.\quad\delta\boldsymbol{v}\text{ is admissible and }\boldsymbol{v}\text{ is traction-free on }\tilde{\Gamma}\end{aligned}\tag{4.54}$$

We again refer to Ern and Guermond (2004) for a detailed proof on the existence and uniqueness of the solution to the augmented minimization (variational) problem (4.58) which eventually yields the equivalence between the Stokes equation (4.52) and the minimum dissipation theorem (4.58) when the fluid is subject to mixed boundary conditions.

In many physical systems, surface traction $\boldsymbol{f}$ arises as a restoring force when the total potential energy $\mathcal{F}[\tilde{\Gamma}]$ available in the mechanical system undergoes infinitesimal variations in its boundary $\tilde{\Gamma}$. For example, capillary stress is equivalent to the variation of surface energy which is proportional to the total surface area. Interfacial Maxwell stress in electrostatic systems can be derived by varying electrostatic energy stored in the medium on both sides of the interface. When the liquid interface is covered by fluid lipid membranes, the variation of Helfrich free energy gives rise to the membrane and bending forces (Helfrich, 1973). When surface tension coefficient is inhomogeneous, surface energy variation produces a force tangent to the free surface, known as the Marangoni stress which we have already encountered in Chapter 2. In these cases, the traction integral becomes the shape variation of the energy functional $\mathcal{F}[\tilde{\Gamma}]$,

$$\int_{\tilde{\Gamma}}\boldsymbol{f}\cdot\boldsymbol{v}\,\mathrm{d}\tilde{\Gamma}=-\delta\mathcal{F}[\tilde{\Gamma};\boldsymbol{v}],\tag{4.55}$$

which measures the amount of (signed) power required in order to deform the free surface $\tilde{\Gamma}$ at a displacement rate $\boldsymbol{v}$. This idea is very similar to the principle of virtual work in the elastic theory of solids (Gurtin, 1973; Washizu, 1982; Marsden and Hughes, 1994). Except for dissipative systems such as viscous fluids, the name "virtual dissipation" or "virtual power" is more appropriate since we are dealing with rate of energy instead of work itself.

Then the modified minimum dissipation formulation (4.53) reads,

$$\left.\begin{aligned}\min_{\boldsymbol{v}}\frac{1}{2}\mathcal{D}[\boldsymbol{v}]+\delta\mathcal{F}[\tilde{\Gamma};\boldsymbol{v}]-\mathcal{I}[\tilde{\Gamma};\boldsymbol{v},\boldsymbol{b}],\\\text{subject to }\nabla\cdot\boldsymbol{v}=0\quad\text{in }\Omega,\\\boldsymbol{v}=\boldsymbol{v}'\text{ on }\hat{\Gamma},\end{aligned}\right\}\tag{4.56}$$

where $\mathscr{T}$ is the virtual power due to the additional external surface tractions $\boldsymbol{b}$,

$$\mathscr{T}[\tilde{\Gamma};\boldsymbol{v},\boldsymbol{b}] = \int_{\tilde{\Gamma}} \boldsymbol{b}\cdot\boldsymbol{v}\,\mathrm{d}\tilde{\Gamma}, \tag{4.57}$$

which do not arise from energy variations, for example, wind shear stress. An important observation due to the energy-dissipation formulation (4.56) is that, the rate at which potential energy $\mathscr{F}[\tilde{\Gamma}]$ is being depleted by the internal viscous frictions exactly equals to the viscous dissipation $\mathscr{D}[\boldsymbol{v}]$ and additional power done by the external surface traction $\boldsymbol{b}$. To see this, we recall from (4.54) that

$$\int_{\Omega} 2\mu\,\delta\boldsymbol{e} : \boldsymbol{e}\,\mathrm{d}\Omega - \int_{\tilde{\Gamma}} \delta\boldsymbol{v}\cdot\boldsymbol{f}\,\mathrm{d}\tilde{\Gamma} = 0 \tag{4.58}$$

for all admissible variation $\delta\boldsymbol{v}$. However the velocity field $\boldsymbol{v}$ of the Stokes flow itself qualifies an admissible variation as well. Replacing $\delta\boldsymbol{v}$ with $\boldsymbol{v}$ in equation (4.58) and substituting the traction force $\boldsymbol{f}$ defined in (4.56),

$$\int_{\Omega} 2\mu\,\boldsymbol{e} : \boldsymbol{e}\,\mathrm{d}\Omega - \int_{\tilde{\Gamma}} \boldsymbol{v}\cdot\boldsymbol{f}\,\mathrm{d}\tilde{\Gamma} = \mathscr{D}[\boldsymbol{v}] + \delta\mathscr{F}[\tilde{\Gamma};\boldsymbol{v}] - \mathscr{T}[\tilde{\Gamma};\boldsymbol{v},\boldsymbol{b}] = 0,$$

lead to the identity

$$\delta\mathscr{F}[\tilde{\Gamma};\boldsymbol{v}] = -\mathscr{D}[\boldsymbol{v}] + \mathscr{T}[\tilde{\Gamma};\boldsymbol{v},\boldsymbol{b}]. \tag{4.59}$$

The following is a physical interpretation of the above equation: the difference between external virtual power $\mathscr{T}$, after being dissipated by the internal viscous frictions $\mathscr{D}[\boldsymbol{v}]$, is equal to the rate at which the total potential energy of the viscous free surface flow varies. Note when the boundary $\tilde{\Gamma}$ is a free surface, it is exactly advected by the instantaneous velocity $\boldsymbol{v}$ evaluated at the free surface, which means $\delta\mathscr{F}[\tilde{\Gamma};\boldsymbol{v}] = \mathrm{d}\mathscr{F}[\tilde{\Gamma}]/\mathrm{d}t$. Therefore in absence of external surface traction $\boldsymbol{b}$, we arrive at the energy-dissipation law for free surface viscous flow,

$$\frac{\mathrm{d}\mathscr{F}[\tilde{\Gamma}]}{\mathrm{d}t} = -\mathscr{D}[\boldsymbol{v}] \leq 0 \quad \text{if} \quad \boldsymbol{b} = \boldsymbol{0}. \tag{4.60}$$

Energy-dissipation law (4.60) states that, if there is no additional power input from external surface traction, the energy of the viscous fluid must always decrease unless it reaches an equilibrium shape.

Kinematic boundary condition

On flat supporting substrates, height field η of the liquid layer is indistinguishable from the columnar volume density ϱ at every point $\hat{\boldsymbol{x}} \in \hat{\Gamma}$. The classical lubrication theory which we use to develop the models for thermocapillary and electrohydrodynamic thin film in Chapter 2 and 3 is established around the height field. However, it's not the case for thin layer flow coating curved substrates. In particular we show that the time-dependent columnar volume density $\varrho(\xi^1,\xi^2,t)$ is more appropriate as a dynamic variable

than the height field η. Let's consider the following integral evaluated via index notation,

$$\begin{aligned}\int_0^\eta (\nabla\cdot\boldsymbol{v})J\,\mathrm{d}\xi^3 &= \int_0^\eta \frac{1}{\sqrt{g}}\frac{\partial\sqrt{g}v^j}{\partial\xi^j}\mathcal{J}\,\mathrm{d}\xi^3 = \int_0^\eta \frac{1}{\sqrt{\hat{g}}}\frac{\partial\sqrt{\hat{g}}v^\alpha J}{\partial\xi^\alpha}+\frac{\partial v^3 J}{\partial\xi^3}\,\mathrm{d}\xi^3\\ &= \frac{1}{\sqrt{\hat{g}}}\int_0^\eta \frac{\partial\sqrt{\hat{g}}v^\alpha J}{\partial\xi^\alpha}\,\mathrm{d}\xi^3 + v^3\mathcal{J}\Big|_{\xi^3=0}^{\xi^3=\eta}\\ &= \frac{1}{\sqrt{\hat{g}}}\frac{\partial}{\partial\xi^\alpha}\left(\sqrt{\hat{g}}\int_0^\eta v^\alpha J\,\mathrm{d}\xi^3\right) - \frac{\partial\eta}{\partial\xi^\alpha}(v^\alpha J)\Big|_{\xi^3=\eta} + v^3 J\Big|_{\xi^3=\eta},\end{aligned} \tag{4.61}$$

where the last line we have used the Leibniz's rule for differentiation under the integral sign. Equation (4.61) must be exactly zero due to incompressibility condition $\nabla\cdot\boldsymbol{v}=0$. We immediately recognize the form of surface divergence on manifold $\hat{\Gamma}$ in (4.61). This motivates the definition of volumetric flux

$$\hat{\boldsymbol{q}} = \hat{\boldsymbol{g}}_\alpha\int_0^\eta v^\alpha J\,\mathrm{d}\xi^3 \tag{4.62}$$

which is a vector field belong to the tangent bundle of the supporting surface $\hat{\Gamma}$. Then equation (4.61) reduces to

$$\hat{\nabla}\cdot\hat{\boldsymbol{q}} + \Big[v^3 - v^\alpha(\xi^1,\xi^2,\eta)\frac{\partial\eta}{\partial\xi^\alpha}\Big]J(\xi^1,\xi^2,\eta) = 0 \tag{4.63}$$

where $\hat{\nabla}$ stands for the covariant differential operators (e.g., divergence and gradient) on the curved surface $\hat{\Gamma}$.

On the other hand, the kinematic boundary condition of a moving free surface $\eta(\xi^1,\xi^2,t)$ states that the material time derivative of the zero contour of level function implicitly defined in (4.32) must remain zero at all times,

$$\Big[\frac{\partial}{\partial t}+\boldsymbol{v}(\xi^1,\xi^2,\eta)\cdot\nabla\Big](\xi^3-\eta) = -\frac{\partial\eta}{\partial t} - v^\alpha(\xi^1,\xi^2,\eta)\frac{\partial\eta}{\partial\xi^\alpha} + v^3(\xi^1,\xi^2,\eta) = 0. \tag{4.64}$$

Substituting kinematic condition (4.64) into the incompressibility identity (4.63) yields

$$J(\xi^1,\xi^2,\eta)\frac{\partial\eta}{\partial t} + \hat{\nabla}\cdot\hat{\boldsymbol{q}} = 0. \tag{4.65}$$

Recall from (4.39) that columnar volume density ϱ is precisely defined as the integral of relative volume Jacobian J along the normal coordinate line ξ^3. Hence equation (4.65) is in fact the exact conservation law for the columnar volume density,

$$\frac{\partial\varrho}{\partial t} + \hat{\nabla}\cdot\hat{\boldsymbol{q}} = 0, \tag{4.66}$$

instead of for the height field η. Volume conservation law (4.66) is no surprise: volumetric flux $\hat{\boldsymbol{q}}(\xi^1,\xi^2)$ has the physical interpretation of total amount velocity vector traversing side walls of the infinitesimal liquid column at $\hat{\boldsymbol{x}}(\xi^1,\xi^2)$, which must be balanced with the rate at which the volume of the liquid column $\varrho(\xi^1,\xi^2,t)$ changes in

time. For a boundary-less manifold $\hat{\Gamma}$, dynamical equation (4.66) conserves the total volume occupied by the thin liquid layer Ω coating a fixed supporting surface $\hat{\Gamma}$ at all times,

$$\frac{\mathrm{d}}{\mathrm{d}t}\int_{\Omega}\mathrm{d}\Omega=\frac{\mathrm{d}}{\mathrm{d}t}\int_{\hat{\Gamma}}\varrho\,\mathrm{d}\hat{\Gamma}=\int_{\hat{\Gamma}}\frac{\partial\varrho}{\partial t}\,\mathrm{d}\hat{\Gamma}=-\int_{\hat{\Gamma}}\hat{\nabla}\cdot\hat{\boldsymbol{q}}\,\mathrm{d}\hat{\Gamma}=0,$$

where the last equality is implied by the (covariant) Stokes theorem on a manifold. As it turns out later, it is convenient to introduce the partial volumetric flux coefficient

$$q^{\alpha}(\xi^1,\xi^2,\xi^3)=\int_0^{\xi^3}v^{\alpha}(\xi^1,\xi^2,\xi^{3\prime})J(\xi^1,\xi^2,\xi^{3\prime})\,\mathrm{d}\xi^{3\prime}\tag{4.67}$$

in analogy to the "full" flux $\hat{\boldsymbol{q}}=q^{\alpha}(\xi^1,\xi^2,\eta)\hat{\boldsymbol{g}}_{\alpha}$. In this sense, the v^{α}-components of the velocity field $\boldsymbol{v}$ are fully specified by the ξ^3-derivative of the partial flux $v^{\alpha}=J^{-1}\partial q^{\alpha}/\partial\xi^3$.

Viscous dissipation in lubrication regime

Let $\boldsymbol{v}$ be the dimensional velocity field within the viscous fluid layer. The essence of Reynolds lubrication theory is encoded in the singularly scaled ansatz for the liquid velocity field,

$$\boldsymbol{v}=v^{\alpha}(\xi^1,\xi^2,\xi^3/\epsilon)\boldsymbol{g}_{\alpha}+v^3(\xi^1,\xi^2,\xi^3/\epsilon)\boldsymbol{g}_3,\quad O(\xi^3)=O(v^3)=O(\epsilon).\tag{4.68}$$

Here $0<\epsilon\ll 1$ is some small parameter (e.g., aspect ratio of the liquid layer) which we will identify later. Partial derivative $\partial\xi^3$ of the velocity field $\boldsymbol{v}$ along the transverse direction is amplified by a factor of $1/\epsilon$ while the scaling of the normal component of velocity field $v^3=O(\epsilon)$ ensures mass conservation still applies for the free surface liquid layer by retaining the full incompressibility condition $O(\nabla_{\alpha}v^{\alpha})=O(\nabla_3 v^3)$. From a mechanical point of view, lubrication scaling (4.68) decouples the "out-of-tangent-plane" components $e^{\alpha}{}_3$ of the strain rate tensor $\boldsymbol{e}$ from the "in-plane" components $e^{\alpha}{}_{\beta}$ owning to the scaling $O(e^{\alpha}{}_3)>O(e^{\alpha}{}_{\beta})$. As a result, the total energy $\mathscr{F}[\tilde{\Gamma}]$ of the liquid layer (assuming no external surface traction) dissipates mostly through tangential shear against the supporting substrate $\hat{\Gamma}$, which is precisely what lubrication theory was invented for.

Such mechanical point of view can be made explicit based on the lubrication ansatz (4.68). Magnitude of the tensor components of the velocity gradient $\nabla\boldsymbol{v}$ in orders of the aspect ratio ϵ can be estimated from the Christoffel symbols (4.29) and (4.27)

derived earlier,

$$\left.\begin{aligned}
\nabla_3 v^3 &= \frac{\partial v^3}{\partial \xi^3} + \Gamma^3_{k3} v^k = \frac{\partial v^3}{\partial \xi^3} = O(1),\\
\nabla_\beta v^\alpha &= \frac{\partial v^\alpha}{\partial \xi^\beta} + \Gamma^\alpha_{k\beta} v^k = O(1),\\
\nabla_3 v^\alpha &= \frac{\partial v^\alpha}{\partial \xi^3} + \Gamma^\alpha_{k3} v^k = \underbrace{\frac{\partial v^\alpha}{\partial \xi^3} - I\!I^\alpha_\beta v^\beta}_{O(\epsilon^{-1})+O(1)} + O(\epsilon),\\
\nabla_\alpha v^3 &= \frac{\partial v^3}{\partial \xi^\alpha} + \Gamma^3_{k\alpha} v^k = \underbrace{I\!I_{\beta\alpha} v^\beta}_{O(1)} + O(\epsilon).
\end{aligned}\right\} \tag{4.69}$$

The integrand of the viscous dissipation (4.46) can be expanded with the use of index notation,

$$2\,\boldsymbol{e} : \boldsymbol{e} = 2\, e^{ij} e_{ij} = (\nabla_j v^i)(\nabla_i v^j) + g^{lm} g_{ij} (\nabla_l v^i)(\nabla_m v^j). \tag{4.70}$$

We look for those leading order terms of the components in (4.70) which couple with $\nabla_3 v^\alpha$,

$$\begin{aligned}
(\nabla_j v^i)(\nabla_i v^j) &= 2(\nabla_3 v^\alpha)(\nabla_\alpha v^3) + O(1)\\
&= 2\Big(\frac{\partial v^\alpha}{\partial \xi^3} - I\!I^\alpha_\beta v^\beta\Big) I\!I_{\gamma\alpha} v^\gamma + O(1)\\
&= \underbrace{2\frac{\partial v^\alpha}{\partial \xi^3} I\!I_{\gamma\alpha} v^\gamma}_{O(\epsilon^{-1})} \underbrace{- 2 I\!I^\alpha_\beta I\!I_{\gamma\alpha} v^\beta v^\gamma}_{O(1)} + O(1)
\end{aligned} \tag{4.71}$$

$$\begin{aligned}
g^{lm} g_{ij} (\nabla_l v^i)(\nabla_m v^j) &= g_{\alpha\beta} (\nabla_3 v^\alpha)(\nabla_3 v^\beta) + O(1)\\
&= \Big(\frac{\partial v^\alpha}{\partial \xi^3} - I\!I^\alpha_\nu v^\nu\Big) g_{\alpha\beta} \Big(\frac{\partial v^\beta}{\partial \xi^3} - I\!I^\beta_\gamma v^\gamma\Big) + O(1)\\
&= \underbrace{g_{\alpha\beta} \frac{\partial v^\alpha}{\partial \xi^3} \frac{\partial v^\beta}{\partial \xi^3}}_{O(\epsilon^{-2})} \underbrace{- 2 I\!I_{\beta\nu} v^\nu \frac{\partial v^\beta}{\partial \xi^3}}_{O(\epsilon^{-1})} + \underbrace{I\!I^\alpha_\nu v^\nu g_{\alpha\beta} I\!I^\beta_\gamma v^\gamma}_{O(1)} + O(1),
\end{aligned} \tag{4.72}$$

where we have used that fact from (4.19) that $g_{\alpha\beta} = \hat{g}_{\alpha\beta} + O(\epsilon) + O(\epsilon^2)$. Summing up (4.71) and (4.72) yields

$$2\boldsymbol{e} : \boldsymbol{e} = \underbrace{g_{\alpha\beta} \frac{\partial v^\alpha}{\partial \xi^3} \frac{\partial v^\beta}{\partial \xi^3}}_{O(\epsilon^{-2})+O(\epsilon^{-1})+O(1)} + O(1), \tag{4.73}$$

where the $O(\epsilon^{-1})$ and $O(1)$ term in (4.73) exclusively come from the coupling with the first and second order corrections in metric coefficients $g_{\alpha\beta}$. We remark that, approximation (4.73) contains $O(1)$ terms, the same order of magnitude of the residue. We made this choice intentionally: by partially retaining some $O(1)$ error, the approximate dissipation (4.73) is symmetrized while still accurate up to some $O(1)$ error.

Next we apply the lubrication scaling (4.68) to the total free energy. In the height field representation, the free energy of the liquid layer Ω coating the supporting substrate $\hat{\Gamma}$ is assumed to be a functional of the height field η,

$$\mathcal{F}[\tilde{\Gamma}] = \mathcal{F}[\xi^1, \xi^2, \eta(\xi^1, \xi^2, t)]. \tag{4.74}$$

Energies which only involve differential operators acting on η are considered local. Local energies are the most common types studied in the literature. For a sufficiently thin liquid layer, an asymptotic series in orders of height field η can be derived. For instance, as stated earlier, capillary stress arises from the variation of the total area of the moving free surface $\tilde{\Gamma}$. Recall the expansion of the area differential $\mathrm{d}\tilde{\Gamma}$ from (4.38). Then the surffface energy of a liquid film with homogeneous surface tension coefficient σ_o can be expanded as

$$\mathcal{F}[\tilde{\Gamma}] = \sigma_o \int_{\tilde{\Gamma}} \mathrm{d}\tilde{\Gamma} = \mathcal{F}[\hat{\Gamma}; \eta] = \sigma_o \int_{\hat{\Gamma}} 1 - 2\mathcal{H}\eta + \mathcal{K}\eta^2 + \frac{1}{2}\hat{g}^{\alpha\beta}\frac{\partial \eta}{\partial \xi^\alpha}\frac{\partial \eta}{\partial \xi^\beta} + O(\eta^3)\,\mathrm{d}\hat{\Gamma}. \tag{4.75}$$

Recall from conservation law (4.66) that the columnar volume density $\varrho(\xi^1, \xi^2, t)$ instead of the height field η serves as the dynamical variable in the governing equation for viscous free surface liquid. By the inversion relations (4.41) and (4.42) between $\varrho(\eta)$ and $\eta(\varrho)$ we can conveniently switch back and forth between $\mathcal{F}[\xi^1, \xi^2, \eta]$ as a functional of the height field or $\mathcal{F}[\xi^1, \xi^2, \varrho]$ of the volume density. The zeroth order term in the free energy usually only concerns the substrate geometry which is treated as a stationary object in the present work. The rate at which free energy $\mathcal{F}$ fluctuates with the moving interface $\tilde{\Gamma}$ is given by

$$\frac{\mathrm{d}\mathcal{F}[\tilde{\Gamma}]}{\mathrm{d}t} = \delta\mathcal{F}[\varrho; \frac{\partial \varrho}{\partial t}] = \int_{\hat{\Gamma}} \frac{\delta \mathcal{F}}{\delta \varrho}\frac{\partial \varrho}{\partial t}\,\mathrm{d}\hat{\Gamma}, \tag{4.76}$$

where $\delta\mathcal{F}/\delta\varrho = O(\varrho)$ is the variational derivative of $\mathcal{F}[\hat{\Gamma}; \varrho]$.

4.4 Truncated Minimum Dissipation Principle for Lubrication Flow

In order to quantify the effects of various competing forces relevant to lubrication layer in terms of the small aspect ratio parameter ϵ, it's convenient to work with a nondimensionalized physical system where reference scales are deliberately chosen to promote the slender geometry.

Nondimesionalization with lubrication scaling

Let $[L]$ be the characteristic radius of curvature of the supporting surface $\tilde{\Gamma}$. The characteristic (normal) thickness $[H] = \epsilon[L]$ of the liquid layer is scaled down by the small aspect ratio parameter ϵ. We assume the viscous flow within the thin liquid layer is characterized by the tangential reference velocity $[V] = [L]/[T]$ where $[T]$ is the characteristic time scale. In the energy-dissipation approach, the total free energy $\mathcal{F}$ in

the system is measured by the reference areal energy density $[\sigma]$ (energy per area) which has the same unit (N/m) as surface tension coefficient. With these scaling in mind, the dimensionless variables indicated by the superscript $(\cdot)^*$ are given by

$$\begin{aligned} \hat{\boldsymbol{x}} &\to [L]\hat{\boldsymbol{x}}^*, & \xi^3 &\to [H]z, & t &\to [T]t^*, \\ v^\alpha &\to [V](v^*)^\alpha, & v^3 &\to \epsilon[V](v^*)^3, & \hat{\boldsymbol{q}} &\to [H][V]\hat{\boldsymbol{q}}^*, \\ \eta &\to [H]\eta^*, & \varrho &\to [H]\varrho^*, & q^\alpha &\to [H][V](q^*)^\alpha \\ \mathcal{F} &\to [\sigma][H][L]\mathcal{F}^*. \end{aligned} \tag{4.77}$$

The appropriate choices for the reference velocity $[V]$ and the time scale $[T]$ would emerge naturally when we balance viscous dissipation with free energy fluctuation rate. In what follows, we drop the superscript $(\cdot)^*$ on all rescaled variables. The relative Jacobian J defined in (4.21) and partial flux coefficient q^α from (4.67) are expressed in the rescaled transverse coordinate z,

$$J(\xi^1, \xi^2, z) = 1 - \epsilon 2\mathcal{H}z + \epsilon^2 \mathcal{K} z^2, \tag{4.78}$$

$$q^\alpha(z) = \int_0^z v^\alpha J \, \mathrm{d}z'. \tag{4.79}$$

Conservation law (4.66) of the columnar volume density ϱ remains invariant after rescaling (4.77), which is expected because mass (volume) conservation is never approximated but enforced exactly in lubrication theory. On the other hand, approximation (4.73) of the viscous dissipation in the rescaled variables leads to the approximate dimensionless dissipation,

$$\frac{1}{2}\mathscr{D}[\boldsymbol{v}] = \frac{\mu[L]^3/(\epsilon[T]^2)}{\epsilon[\sigma][L]^2/[T]} \left\{ \int_{\hat{\Gamma}} \underbrace{\left[\int_0^\eta \frac{1}{2} g_{\alpha\beta} \frac{\partial v^\alpha}{\partial z} \frac{\partial v^\beta}{\partial z} J \, \mathrm{d}z \right]}_{O(1)+O(\epsilon)+O(\epsilon^2)} \mathrm{d}\hat{\Gamma} + O(\epsilon^2) \right\}. \tag{4.80}$$

Likewise the dimensionless rate of energy variation defined in (4.76) becomes

$$\frac{\mathrm{d}\mathcal{F}[\tilde{\Gamma}]}{\mathrm{d}t} = \int_{\hat{\Gamma}} \underbrace{\frac{\delta \mathcal{F}}{\delta \varrho}}_{O(1)} \frac{\partial \varrho}{\partial t} \, \mathrm{d}\hat{\Gamma}, \tag{4.81}$$

where the variational derivative $\delta\mathcal{F}/\delta\varrho$ is an asymptotic series expended in orders of aspect ratio ϵ.

We next consider variation to the virtual power due to external surface traction at the free surface. Let $[B]$ be the charaterstic scale of the external surface traction $\boldsymbol{b}$. Recall

from (4.38) that after dimensionless virtual power can be approximated as,

$$\begin{aligned}\mathcal{T}[\varrho;\boldsymbol{v},\boldsymbol{b}] &= \frac{[B][L]^2[V]}{\epsilon[\sigma][L]^2/[T]}\int_{\hat{\Gamma}}\mathscr{A}\,\boldsymbol{v}\cdot\boldsymbol{b}|_{z=\eta}\,\mathrm{d}\hat{\Gamma}\\ &= \frac{[B][L]}{\epsilon[\sigma]}\int_{\hat{\Gamma}}\mathscr{A}\left(b^\beta v^\alpha g_{\alpha\beta}+\epsilon v^3 b^3\right)|_{z=\eta}\,\mathrm{d}\hat{\Gamma}\\ &= \overline{\mathrm{Ma}}\int_{\hat{\Gamma}}\Big(J+O(\epsilon^2)\Big)\Big(b^\beta v^\alpha g_{\alpha\beta}+O(\epsilon^2)\Big)|_{z=\eta}\,\mathrm{d}\hat{\Gamma}\\ &= \overline{\mathrm{Ma}}\int_{\hat{\Gamma}}\Big(J\,b^\beta v^\alpha g_{\alpha\beta}\Big)|_{z=\eta}\,\mathrm{d}\hat{\Gamma}+O(\epsilon^2),\qquad \overline{\mathrm{Ma}}=\frac{[B][L]}{\epsilon[\sigma]},\end{aligned}\tag{4.82}$$

where we assume ξ^3-component (recall $\boldsymbol{g}^3=\hat{\boldsymbol{n}}$) of traction $\boldsymbol{b}$ is only $O(\epsilon)$. In such cases, Marangoni number $\overline{\mathrm{Ma}}$ in equation (4.82) is appropriate for characterizing the effect of tangential dominant surface traction such as the thermocapillary effect in Chapter 2.

The balance between viscous dissipation (4.80) and free energy fluctuation rate (4.81) immediately suggests the scaling for time and velocity,

$$\frac{\mu[L]^3}{\epsilon[T]^2}=\epsilon\frac{[\sigma][L]^2}{[T]}\Longleftrightarrow[T]=\frac{\mu[L]}{\epsilon^2[\sigma]}\quad\text{or}\quad[V]=\frac{\epsilon^2[\sigma]}{\mu}.\tag{4.83}$$

The singular scaling $1/\epsilon^2$ in $[T]$ is one of the predominant signatures of lubrication flows: the more slender the characteristic film thickness $[H]$ becomes, the slower the thin liquid film redistributes its mass. As suggested by scaling (4.83), such dilemma can be resolved either by reducing the size of the system $[L]\downarrow$ or by increasing the scale of areal energy density $[\sigma]\uparrow$. Although we must be cautious with the rate at which the bulk kinematic energy fluctuates $\sim\rho[V]^2[H][L]^2$. For lubrication theory to be self-consistent, the overall scale of the kinematic energy fluctuation rate must be negligible compared to the leading order terms in the viscous dissipation (4.80) and to the free energy fluctuation rate (4.81) otherwise the conventional lubrication theory doesn't hold under inertial effect. The magnitude of kinematic energy fluctuation rate can be estimated relative to the free energy fluctuation rate (4.81),

$$\frac{\rho[V]^2[H][L]^2/[T]}{\epsilon[\sigma][L]^2/[T]}=\frac{\rho[V][L]}{\mu}\frac{\mu[V]}{[\sigma]}=\epsilon^2\mathrm{Re}=O(\epsilon^2).\quad(\text{lubrication assumption})\tag{4.84}$$

Thanks to the small aspect ratio $\epsilon\ll 1$, the applicability of lubrication theory only requires a moderately small Reynolds number from (4.84) which is more general than the true Stokes limit $\mathrm{Re}=0$. These scaling requirements are quite realistic, for example, when applied to the experiment by Takagi and Huppert (2010) in which $123\,\mathrm{cm}^3$ of golden syrup was released on a beach ball of radius $[L]=23\,\mathrm{cm}$. The experimental parameters are kinematic viscosity $\nu=0.045\,\mathrm{m}^2/\mathrm{s}$, surface tension $[\sigma]=0.078\,\mathrm{N/m}$ and density $\rho=1.4\,\mathrm{kg/m}^3$. For a liquid film of $1\,\mathrm{cm}$ thickness (film thickness was not reported by the authors), the aspect ratio $\epsilon\sim 0.04$. The lubrication scaling (4.83) leads to a characteristic time $[T]\sim 100\,\mathrm{s}$ which agrees with the time scale between

the snapshots of their experiment. In such a case, by equation (4.84) we evaluate the Reynolds number $\mathrm{Re} \sim 0.01 \sim O(\epsilon)$ which is more than sufficient for lubrication theory to apply.

In summary, we replace the original viscous dissipation $\mathscr{D}$, free energy $\mathscr{F}$ and external traction $\mathscr{T}$ by their truncated versions up to $O(\epsilon^2)$ approximation errors,

$$\frac{1}{2}\mathscr{D}[\boldsymbol{v}] = \frac{1}{2}\overline{\mathscr{D}}[\boldsymbol{v}] + O(\epsilon^2), \tag{4.85}$$

$$\delta\mathscr{F}[\tilde{\Gamma}; \boldsymbol{v}] = \delta\overline{\mathscr{F}}[\varrho; \frac{\partial \varrho}{\partial t}] + O(\epsilon^2), \tag{4.86}$$

$$\mathscr{T}[\tilde{\Gamma}; \boldsymbol{v}, \boldsymbol{b}] = \overline{\mathscr{T}}[\varrho; \boldsymbol{v}, \boldsymbol{b}] + O(\epsilon^2), \tag{4.87}$$

where the truncated functionals $\overline{\mathscr{D}}$, $\overline{\mathscr{F}}$ and $\overline{\mathscr{T}}$ are given by,

$$\overline{\mathscr{D}}[\boldsymbol{v}] = \int_{\hat{\Gamma}} \left\{ \int_0^{\eta} g_{\alpha\beta} \frac{\partial v^{\alpha}}{\partial z} \frac{\partial v^{\beta}}{\partial z} J \, \mathrm{d}z \right\} \mathrm{d}\hat{\Gamma}, \tag{4.88}$$

$$\delta\overline{\mathscr{F}}[\varrho; \frac{\partial \varrho}{\partial t}] = \int_{\hat{\Gamma}} \frac{\delta\overline{\mathscr{F}}}{\delta \varrho} \frac{\partial \varrho}{\partial t} \, \mathrm{d}\hat{\Gamma}, \tag{4.89}$$

$$\overline{\mathscr{T}}[\varrho; \boldsymbol{v}, \boldsymbol{b}] = \overline{\mathrm{Ma}} \int_{\hat{\Gamma}} v^{\alpha} J \, g_{\alpha\beta} b^{\beta}|_{z=\eta} \, \mathrm{d}\hat{\Gamma}. \tag{4.90}$$

Truncated minimum dissipation principle

The governing equation of a thin liquid layer driven by dissipation of its free energy and external tangential traction is given by the solution to the truncated minimum dissipation principle in place of the full version (4.56),

$$\left.\begin{aligned} \min_{\boldsymbol{v}} \frac{1}{2}\overline{\mathscr{D}}[\boldsymbol{v}] + \delta\overline{\mathscr{F}}[\varrho; \frac{\partial \varrho}{\partial t}] - \overline{\mathscr{T}}[\varrho; \boldsymbol{v}, \boldsymbol{b}], \\ \text{subject to } \frac{\partial \varrho}{\partial t} + \hat{\nabla} \cdot \hat{\boldsymbol{q}} = 0 \quad \text{on } \hat{\Gamma}, \\ \boldsymbol{v} = \boldsymbol{0} \quad \text{on } \hat{\Gamma}, \end{aligned}\right\} \tag{4.91}$$

where the incompressiblity condition is enforced through the conservation law of columnar volume density ϱ. Since the approximate functionals (4.85)–(4.87) are truncated at $O(\epsilon^2)$, it suffices to look for the necessary conditions for which a unique optimal partial flux $\underline{q}^{\alpha}$ defined in (4.67) must satisfy in order to minimize (4.91) up to some $O(\epsilon^2)$ error only.

Let η be a height field (not necessarily optimal) on the boundary-less surface $\hat{\Gamma}$ and $\underline{\boldsymbol{v}}$ be the optimal velocity field for the liquid volume bounded by η. We consider a flux variation $\delta q^{\alpha}(\xi^1, \xi^2, z)$ be the optimal volumetric flux $\underline{q}^{\alpha}$ associated with the optimal velocity $\underline{\boldsymbol{v}}$. Applying integration by parts in the z-coordinate to the variation of viscous

dissipation yields

$$\begin{aligned}\delta\left\{\frac{1}{2}\overline{\mathcal{D}}[\underline{\boldsymbol{v}};\delta\boldsymbol{v}]\right\} &= \int_{\hat{\Gamma}}\int_0^{\eta} g_{\alpha\beta}\frac{\partial\delta v^{\alpha}}{\partial z}\frac{\partial\underline{v}^{\beta}}{\partial z}J\,\mathrm{d}z\,\mathrm{d}\hat{\Gamma}\\ &= \int_{\hat{\Gamma}}\left\{g_{\alpha\beta}\delta v^{\alpha}\frac{\partial\underline{v}^{\beta}}{\partial z}J\Big|_0^{\eta} - \int_0^{\eta}\delta v^{\alpha}\frac{\partial}{\partial z}\Big(\frac{\partial\underline{v}^{\beta}}{\partial z}g_{\alpha\beta}J\Big)\,\mathrm{d}z\right\}\mathrm{d}\hat{\Gamma}\\ &= \int_{\hat{\Gamma}}\left\{g_{\alpha\beta}\delta v^{\alpha}\frac{\partial\underline{v}^{\beta}}{\partial z}J\Big|_{\eta} - \frac{\delta q^{\alpha}}{\mathcal{G}}\frac{\partial}{\partial z}\Big(\frac{\partial\underline{v}^{\beta}}{\partial z}g_{\alpha\beta}J\Big)\Big|_{\eta}\right.\\ &\quad\left.+\int_0^{\eta}\delta q^{\alpha}\frac{\partial}{\partial z}\left[\frac{1}{\mathcal{G}}\frac{\partial}{\partial z}\Big(\frac{\partial\underline{v}^{\beta}}{\partial z}g_{\alpha\beta}J\Big)\right]\mathrm{d}z\right\}\mathrm{d}\hat{\Gamma}. \end{aligned}\tag{4.92}$$

Note the boundary terms evaluated at $z=0$ vanish due to the integral definition (4.67) of partial flux $\delta q^{\alpha}(\xi^1,\xi^2,z)$ and the no-slip condition $\delta v^{\beta}(\xi^1,\xi^2,0)=0$ at the supporting substrate. For an admissible variation δq^{α} such that $\delta q^{\alpha}|_{z=\eta}=0$, the second term in variation (4.92) drops out. If the free surface were stress-free (zero-traction), the first term should vanish as well. In the presence of tangential interfacial tractions such as Marangoni stresses, the balance between the contribution from viscous dissipation and the external power by tangential traction translates into a boundary condition for $q^{\beta}(z)$ at $z=\eta$,

$$\frac{\partial\underline{v}^{\beta}}{\partial z}J\Big|_{z=\eta} = \overline{\mathrm{Ma}}\,b^{\beta}.\tag{4.93}$$

After dropping out the first and the second term in the integrand of variation (4.92), we are left with a piece which only involves integration in the z-coordinate. A necessary condition for this term to vanish against all variations is that,

$$\frac{\partial}{\partial z}\left\{\frac{1}{J}\frac{\partial}{\partial z}\Big[g_{\alpha\beta}J\frac{\partial}{\partial z}\Big(\frac{1}{J}\frac{\partial\underline{q}^{\beta}}{\partial z}\Big)\Big]\right\}=0.\tag{4.94}$$

Equation (4.94) is a fourth order ODE subject to four boundary conditions derived earlier,

$$\left.\begin{aligned}\underline{q}^{\beta}\Big|_{z=0} &= 0, && \text{(by definition (4.67))}\\ \frac{\partial\underline{q}^{\beta}}{\partial z}\Big|_{z=0} &= 0, && \text{(no-slip condition)}\\ \underline{q}^{\beta}\Big|_{z=\eta} &= \underline{q}^{\beta}(\eta), && \text{(choice of variation)}\\ \frac{\partial}{\partial z}\Big(\frac{1}{J}\frac{\partial\underline{q}^{\beta}}{\partial z}\Big)\Big|_{z=\eta} &= \overline{\mathrm{Ma}}\,b^{\beta}. && \text{(traction-free)}\end{aligned}\right\}\tag{4.95}$$

Equation (4.94) can be solved by elementary integration,

$$\begin{aligned}
\frac{1}{J}\frac{\partial}{\partial z}\Big[g_{\alpha\beta}J\frac{\partial}{\partial z}\Big(\frac{1}{J}\frac{\mathrm{d}\underline{q}^{\beta}}{\mathrm{d}z}\Big)\Big] &= A_{\alpha},\\
g_{\alpha\beta}J\frac{\partial}{\partial z}\Big(\frac{1}{J}\frac{\mathrm{d}\underline{q}^{\beta}}{\mathrm{d}z}\Big) &= B_{\alpha}+A_{\alpha}\int_0^z J\,\mathrm{d}z',\\
\frac{\partial}{\partial z}\Big(\frac{1}{J}\frac{\mathrm{d}\underline{q}^{\beta}}{\mathrm{d}z}\Big) &= \frac{g^{\alpha\beta}}{J}\Big(B_{\alpha}+A_{\alpha}\int_0^z J\,\mathrm{d}z'\Big),\\
\frac{\partial \underline{q}^{\beta}}{\partial z} &= C^{\beta}\mathcal{J}+J\int_0^z\frac{g^{\alpha\beta}}{\mathcal{J}}\Big(B_{\alpha}+A_{\alpha}\int_0^{z'}J\,\mathrm{d}z''\Big)\,\mathrm{d}z',\\
\underline{q}^{\beta} &= D^{\beta}+\int_0^z J\Big[C^{\beta}+\int_0^{z'}\frac{g^{\alpha\beta}}{J}\Big(B_{\alpha}+A_{\alpha}\int_0^{z''}J\,\mathrm{d}z'''\Big)\,\mathrm{d}z''\Big]\,\mathrm{d}z',
\end{aligned} \tag{4.96}$$

where coefficients A_{α}, B_{α}, C^{β} and D^{β} are functions of ξ^1 and ξ^2 only. Applying boundary conditions at $z=0$ eliminates $C^{\beta}=D^{\beta}=0$. Traction condition at free surface imposes a constraint between A_{α} and B_{α},

$$B_{\alpha}+A_{\alpha}\int_0^{\eta}J\,\mathrm{d}z=\overline{\mathrm{Ma}}\,Jg_{\alpha\beta}b^{\beta}|_{z=\eta}. \tag{4.97}$$

The optimal partial flux $\underline{q}^{\beta}$ for a domain bounded by the height field η (or equivalently the columnar volume density ϱ) is found to be

$$\underline{q}^{\beta}(\xi^1,\xi^2,z)=\int_0^z J\Big\{\int_0^{z'}\Big[\overline{\mathrm{Ma}}\,b^{\beta}+\frac{g^{\alpha\beta}A_{\alpha}}{J}\Big(\int_0^{z''}J\,\mathrm{d}z'''-\int_0^{\eta}J\,\mathrm{d}z'''\Big)\Big]\,\mathrm{d}z''\Big\}\,\mathrm{d}z'. \tag{4.98}$$

Any optimal partial flux $\underline{q}^{\beta}$ must be in the form (4.98) otherwise it would necessarily produce $O(\epsilon)$ residues for the truncated minimization problem (4.91) which make $\delta q^{\beta}(\xi^1,\xi^2,z)$ suboptmal.

The only free coefficient $A_{\alpha}(\xi^1,\xi^2)$ left in (4.98) is determined by considering a general variation δq to the optimal flux $\underline{q}^{\beta}$ such that $\delta q^{\beta}(\xi^1,\xi^2,\eta)$ may not be identically zero. Let $\underline{\eta}(\xi^1,\xi^2,t)$ and $\underline{\varrho}(\xi^1,\xi^2,t)$ be the optimal interface shape and volume density respectively and $\delta\hat{q}^{\alpha}$ denote the variation to the total volumetric flux $\hat{\underline{q}}^{\alpha}=\underline{q}^{\alpha}|_{z=\underline{\eta}}$. Substituting optimal partial flux (4.98) into viscous dissipation (4.92) yields the two surviving terms for the truncated variation problem (4.91),

$$\begin{aligned}
&\delta\Big\{\frac{1}{2}\overline{\mathcal{D}}[\boldsymbol{v}]+\delta\overline{\mathcal{F}}[\varrho;\frac{\partial\varrho}{\partial t}]-\overline{\mathcal{F}}[\varrho;\boldsymbol{v},\boldsymbol{b}]\Big\}\\
&=\int_{\hat{\Gamma}}-\frac{\delta q^{\alpha}}{J}\frac{\partial}{\partial z}\Big(\frac{\partial \underline{v}^{\beta}}{\partial z}g_{\alpha\beta}J\Big)\Big|_{\underline{\eta}}\,\mathrm{d}\hat{\Gamma}+\int_{\hat{\Gamma}}\frac{\delta\overline{\mathcal{F}}}{\delta\underline{\varrho}}\Big|_{\underline{\varrho}}\delta\Big\{\frac{\partial\varrho}{\partial t}\Big\}\,\mathrm{d}\hat{\Gamma}\quad\text{First line of 4.96}\\
&=\int_{\hat{\Gamma}}-\delta\hat{q}^{\alpha}A_{\alpha}\,\mathrm{d}\hat{\Gamma}+\int_{\hat{\Gamma}}\frac{\delta\overline{\mathcal{F}}}{\delta\underline{\varrho}}\Big|_{\underline{\varrho}}\delta\Big\{-\hat{\nabla}\cdot\hat{\boldsymbol{q}}\Big\}\,\mathrm{d}\hat{\Gamma}\\
&=\int_{\hat{\Gamma}}-\delta\hat{q}^{\alpha}\hat{g}_{\alpha\beta}A^{\beta}\,\mathrm{d}\hat{\Gamma}-\int_{\hat{\Gamma}}\frac{\delta\overline{\mathcal{F}}}{\delta\underline{\varrho}}\Big|_{\underline{\varrho}}\hat{\nabla}\cdot\delta\hat{\boldsymbol{q}}\,\mathrm{d}\hat{\Gamma}\\
&=\int_{\hat{\Gamma}}\delta\hat{q}^{\alpha}\Big[-\hat{g}_{\alpha\beta}A^{\beta}+\frac{\partial}{\partial\xi^{\alpha}}\Big(\frac{\delta\overline{\mathcal{F}}}{\delta\underline{\varrho}}\Big|_{\underline{\varrho}}\Big)\Big]\,\mathrm{d}\hat{\Gamma}.\quad\text{Boundary-less manifold}
\end{aligned} \tag{4.99}$$

For these terms to vanish, coefficient A^β must satisfy,

$$A^\beta = \hat{g}^{\alpha\beta}\frac{\partial}{\partial \xi^\alpha}\Big(\frac{\delta \overline{\mathcal{F}}}{\delta \varrho}\Big|_{\underline{\varrho}}\Big). \tag{4.100}$$

Substituting A^β into equation (4.98) and evaluating at $z = \underline{\eta}$ shall produce the optimal flux. The truncated minimum dissipation problem (4.91) is essentially a quadratic programming subject to a linear constrain. Since we pursue an approximation to the optimal solution aiming for $O(\epsilon^2)$ errors, it suffices to further expand $\underline{q}^\beta$ with only the $O(1)$ and $O(\epsilon)$ terms retained,

$$\begin{aligned}\underline{\hat{q}}^\beta(\xi^1,\xi^2,\underline{\eta}) = \Big\{ -\frac{\underline{\eta}^3}{3}\hat{g}^{\alpha\beta} + \epsilon\frac{\underline{\eta}^4}{6}(4\mathcal{H}\hat{g}^{\alpha\beta} - \mathit{I\!I}^{\alpha\beta})\Big\}\frac{\partial}{\partial \xi^\alpha}\Big(\frac{\delta \overline{\mathcal{F}}}{\delta \varrho}\Big|_{\underline{\varrho}}\Big) \\ + \overline{\mathrm{Ma}}\Big\{\frac{\underline{\eta}^2}{2}\hat{g}^{\alpha\beta} + \epsilon\underline{\eta}^3\Big(-\frac{2}{3}\mathcal{H}\hat{g}^{\alpha\beta} + \mathit{I\!I}^{\alpha\beta}\Big)\Big\}\hat{b}_\alpha + O(\epsilon^2),\end{aligned} \tag{4.101}$$

where we introduce the tangent vector field

$$\hat{\boldsymbol{b}} = b^\alpha \hat{\boldsymbol{g}}_\alpha \tag{4.102}$$

on the supporting surface $\hat{\Gamma}$ as an alternative approximation to the external tangential traction $\boldsymbol{b}$ on the free surface $\tilde{\Gamma}$. To derive the full evolution equation, we convert height field η to columnar volume density ϱ truncated at $O(\epsilon^2)$ errors,

$$\begin{aligned}\underline{\hat{q}}^\beta(\xi^1,\xi^2,\underline{\varrho}) = -\left\{\frac{\underline{\varrho}^3}{3}\hat{g}^{\alpha\beta} + \epsilon\frac{\underline{\varrho}^4}{6}(2\mathcal{H}\hat{g}^{\alpha\beta} + \mathit{I\!I}^{\alpha\beta})\right\}\frac{\partial}{\partial \xi^\alpha}\Big(\frac{\delta \overline{\mathcal{F}}}{\delta \varrho}\Big|_{\underline{\varrho}}\Big) \\ + \overline{\mathrm{Ma}}\left\{\frac{\underline{\varrho}^2}{2}\hat{g}^{\alpha\beta} + \epsilon\underline{\varrho}^3\Big(\frac{1}{3}\mathcal{H}\hat{g}^{\alpha\beta} + \mathit{I\!I}^{\alpha\beta}\Big)\right\}\hat{b}_\alpha + O(\epsilon^2).\end{aligned} \tag{4.103}$$

Substituting the optimal flux (4.103) back into the conservation law (4.66) with underscores below the optimal variables dropped yields the governing PDE of the optimal columnar volume density in a coordinate-free form,

$$\frac{\partial \varrho}{\partial t} + \hat{\nabla}\cdot\left[-\boldsymbol{D}_F\hat{\nabla}\frac{\delta \overline{\mathcal{F}}}{\delta \varrho} + \overline{\mathrm{Ma}}\,\boldsymbol{D}_T\hat{\boldsymbol{b}}\right] = 0 \quad \text{on} \quad \hat{\Gamma}, \tag{4.104}$$

where the two nonlinear, inhomogeneous mobility tensors, $\boldsymbol{D}_F$ and $\boldsymbol{D}_T$, convert the surface projections of interfacial pressure gradient and external tangential traction to volumetric fluxes in the lubrication limit, respectively,

$$\boldsymbol{D}_F = \frac{\varrho^3}{3}\boldsymbol{I} + \epsilon\frac{\varrho^4}{6}(2\mathcal{H}\boldsymbol{I} + \boldsymbol{I\!I}), \quad \boldsymbol{D}_T = \frac{\varrho^2}{2}\boldsymbol{I} + \epsilon\varrho^3(\frac{1}{3}\mathcal{H}\boldsymbol{I} + \boldsymbol{I\!I}). \tag{4.105}$$

On a flat substrate where the first fundamental form $\boldsymbol{I} = \mathbb{I}$ becomes the identity tensor and the second fundamental form $\boldsymbol{I\!I} = \boldsymbol{0}$ vanishes everywhere, we deduce $\eta = \varrho$ and hence recover the general form of classical lubrication equation (2.37) in Section 2.2. In the absence of external surface traction $\hat{\boldsymbol{b}}$ (or $\overline{\mathrm{Ma}} = 0$), we arrive at an approximate energy-dissipation law similar to (4.60),

$$\frac{\mathrm{d}\overline{\mathcal{F}}[\varrho]}{\mathrm{d}t} = -\int_{\hat{\Gamma}}\left(\hat{\nabla}\frac{\delta \overline{\mathcal{F}}}{\delta \varrho}\right)\boldsymbol{D}_F\left(\hat{\nabla}\frac{\delta \overline{\mathcal{F}}}{\delta \varrho}\right)\mathrm{d}\hat{\Gamma} \leq 0. \tag{4.106}$$

Fluctuations in interfacial energies of local-tpye

In order to put a closure on the evolution PDE (4.104), the free energies must be expanded in the asymptotic orders of slender aspect ratio ϵ. Recall from the scaling (4.81) that all energies associated with the thin liquid film are scaled by the reference energy $\epsilon[\sigma][L]^2$. An interfacial energy is said to be "local" if its areal energy density at a point of the interface only depends on quantities defined at that point. The notion of localness is made clear in the following two example of interfacial energies.

One of the most common energies in physics is the potential energy due to the gravitational force. Let $\mathfrak{g}$ be the unit vector opposite to the direction of gravity. For a medium of uniform density, the total gravitational energy can be expressed as a volume integral of the projection of position vector onto the unit vector $\mathfrak{g}$,

$$\mathcal{G}[\tilde{\Gamma}] = \frac{\rho g[L]^4}{\epsilon[\sigma][L]^2}\int_{\Omega} \boldsymbol{x}\cdot\mathfrak{g}\,\mathrm{d}\Omega = \frac{\mathrm{Bo}}{\epsilon}\int_{\hat{\Gamma}}\epsilon\int_0^{\eta}(\hat{\boldsymbol{x}}+\epsilon z\hat{\boldsymbol{n}})\cdot\mathfrak{g}J\,\mathrm{d}z\,\mathrm{d}\hat{\Gamma},\quad \mathrm{Bo}=\frac{\rho g[L]^2}{[\sigma]}, \tag{4.107}$$

where Bo is the Bond number. For example in the previous example (Takagi and Huppert, 2010) where a golden syrup film of $1\,\mathrm{cm}$ thickness spreads on a beach ball with a radius of $23\,\mathrm{cm}$, $\mathrm{Bo}\sim 9.5$ indicates gravity is the dominant driving force in that system. Although the Bond number diminishes rapidly as size of the system $[L]$ goes down. In terms of columnar volume density ϱ, we have

$$\mathcal{G}[\hat{\Gamma};\varrho] = \mathrm{Bo}\left\{\int_{\hat{\Gamma}}(\hat{\boldsymbol{x}}\cdot\mathfrak{g})\varrho+\epsilon(\hat{\boldsymbol{n}}\cdot\mathfrak{g})\frac{1}{2}\varrho^2\,\mathrm{d}\hat{\Gamma}+O(\epsilon^2)\right\}. \tag{4.108}$$

Variation of the truncated gravitational energy is a simple scalar field

$$\frac{\delta\overline{\mathcal{G}}}{\delta\varrho} = \mathrm{Bo}[\hat{\boldsymbol{x}}\cdot\mathfrak{g}+\epsilon(\hat{\boldsymbol{n}}\cdot\mathfrak{g})\varrho]. \tag{4.109}$$

Note for a supporting surface $\hat{\Gamma}$ almost parallel to the direction of gravity field, it's necessary to retain terms at least up to the first order in the approximate gravitational energy (4.109) because the zeroth order term $\hat{\boldsymbol{x}}\cdot\mathfrak{g}$ completely vanishes and the first order term $(\hat{\boldsymbol{n}}\cdot\mathfrak{g})\varrho$ becomes the dominant driving mechanism underlying the dynamics of the viscous liquid layer layer.

The surface tension coefficient σ_o of the liquid/air interface is selected to be the baseline for various types of interfacial energies per area. When σ_o is homogeneous, i.e. constant everywhere on an uncontaminated free surface, the surface energy after nondimensionalization is simply the total area of the (boundary-less) free surface $\tilde{\Gamma}$,

$$\mathcal{S}[\tilde{\Gamma}] = \int_{\tilde{\Gamma}}\mathrm{d}\tilde{\Gamma} = \frac{1}{\epsilon}\int_{\hat{\Gamma}} 1-2\mathcal{H}\epsilon\eta+\epsilon^2\mathcal{K}\eta^2+\epsilon^2\frac{1}{2}\hat{g}^{\alpha\beta}\frac{\partial\eta}{\partial\xi^{\alpha}}\frac{\partial\eta}{\partial\xi^{\beta}}+O(\epsilon^3)\,\mathrm{d}\hat{\Gamma}. \tag{4.110}$$

In terms of columnar volume density ϱ, the surface energy becomes

$$\mathcal{S}[\hat{\Gamma};\varrho] = \frac{1}{\epsilon}\int_{\hat{\Gamma}}\mathrm{d}\hat{\Gamma}-\int_{\hat{\Gamma}}2\mathcal{H}\varrho+\epsilon\frac{1}{2}\left[(4\mathcal{H}^2-2\mathcal{K})\varrho^2-(\hat{\nabla}\varrho)\cdot(\hat{\nabla}\varrho)\right]\mathrm{d}\hat{\Gamma}+O(\epsilon^2). \tag{4.111}$$

The first integral in (4.111) represents the area of the fixed supporting substrate $\hat{\Gamma}$ covered by the viscous liquid layer which should not contribute to energy variation in time. The second integral contains two scalar pieces similar to the case of gravitational energy plus a gradient-type (Dirichlet) energy. To derive its variation, we perform integration by parts on the boundaryless manifold $\hat{\Gamma}$ which yields

$$\int_{\hat{\Gamma}} -(\hat{\nabla}\varrho)\cdot(\hat{\nabla}\varrho)\,\mathrm{d}\hat{\Gamma} = \int_{\hat{\Gamma}} \varrho\,\hat{\Delta}\varrho\,\mathrm{d}\hat{\Gamma}, \tag{4.112}$$

where the line integral arising from the manifold boundary vanishes and $\hat{\Delta}$ is the Laplace-Beltrami operator (covariant Laplacian) for surface $\hat{\Gamma}$. In the end, we arrive at the expression of the variational derivative of surface energy,

$$\frac{\delta\overline{\mathcal{S}}}{\delta\varrho} = -2\mathscr{H} - \epsilon(4\mathscr{H}^2 - 2\mathscr{K})\varrho - \epsilon\hat{\Delta}\varrho. \tag{4.113}$$

Equation (4.113) is essentially the perturbation expansion of the curvature of the free surface $\tilde{\Gamma}$, expressed with the coordinates of the supporting surface $\hat{\Gamma}$ and the columnar volume density ϱ. Identical expressions were obtained by Roy, A. J. Roberts, and Simpson (2002) and Rumpf and Vantzos (2013). Note the first two terms in the variation (4.113) of the approximate surface energy are entirely due to the curvature of the substrate whereas the Laplace-Beltrami term is the leading approximation to the curvature of the free surface. As we already know from Chapter 2 and Chapter 3, for a flat region of the supporting surface $\hat{\Gamma}$, substrate curvatures completely disappear and the Laplacian of volume density ϱ becomes the sole driving force behind interface deformation of the thin films.

For the classical problem of a thin fluid flowing down an flat plane inclined at an angle α with respect to the (x, y)-plane driven by gravity and capillary stresses, the total free energy $\overline{\mathcal{F}} = \overline{\mathcal{G}} + \overline{\mathcal{S}}$. The resulting governing equation of film thickness agrees with many previous references (Huppert, 1982; Troian et al., 1989; Roy, A. J. Roberts, and Simpson, 2002),

$$\frac{\partial\varrho}{\partial t} + \hat{\nabla}\left\{\frac{\varrho^3}{3}\hat{\nabla}\left[\hat{\Delta}\varrho - \mathrm{Bo}\,(\cos\alpha)\varrho\right] + \mathrm{Bo}\,(\sin\alpha)\frac{\varrho^3}{3}\right\} = 0, \tag{4.114}$$

where differential operators are the usual two-dimensional Euclidean ones defined with respect to the Cartesian coordinates of the inclined plane.

4.5 Perfect Dielectric Films Coating Curved Conductors: Dissipation of a Nonlocal Energy

In this section we derive the total electrostatic energy of a curved conductor coated by a thin dielectric film. The resulting energy variation is nonlocal, i.e. the effective pressure at one location on the conductor boundary not only depends information defined locally

but also anywhere else on the same surface. "Nonlocalness" naturally emerges when a low-dimensional solution (e.g., two-dimensional surface charge density) is obtained from a high-dimensional problem (e.g., three-dimensional electrostatics). In particular for electrified fluid layers wetting a flat solid wall, the effect of nonlocal terms has been examined through a series of analytic and computational investigations for ideal fluid layers of finite depth (Papageorgiou, Petropoulos, and Vanden-Broeck, 2005) or thin viscous lubrication films (Tseluiko and Papageorgiou, 2007) in the presence of wall-normal electric fields, gravity-driven liquid films down a corrugated inclined wall (Tseluiko, Blyth, Papageorgiou, and Vanden-broeck, 2008) or subject to a periodic electrode of arbitrary shape (Tseluiko, Blyth, Papageorgiou, and Vanden-Broeck, 2010) and electrostatically stabilized viscous thin films wetting the underside of a flat wall in the presence of wall-parallel electric fields (Anderson et al., 2017). We refer the interested readers to a recent review article by Papageorgiou (2019) (and references therein), which provides a complete survey on nonlocal terms in the nonlinear theories and models of electrohydrodynamic instabilities in immiscible multi-layer flows for various planar and cylindrical geometries.

On the other hand, previous works on electrohydrodynamic thin films coating substrates of non-planar geometries are very limited and mostly focus on the patterns and waves of dielectric fluids confined in the cylindrical geometries, e.g., annulus between two concentric cylinders (Wray, Papageorgiou, and Matar, 2013; L. Wang and J. Liu, 2016). Nonlocalness of electrostatic pressure that appears in most papers cited in the review article (Papageorgiou, 2019) is derived based on the Hilbert transform technique which only applies to planar problems in a periodic rectangular channel. In this section we derive nonlocal terms in the lubrication model of dielectric thin films residing on a curved conductor of an arbitrary (smooth) shape fixed at a constant potential subject to a far-field electrode by computing the first and second variations of the total electrostatic energy in the film-conductor-electrode system. The overall setup is sketched in figure 4.4(a).

Electrostatic energy of a perfect dielectric film

Let $\Omega_{\rm ext}$ be the exterior region enclosed between the conductor surface $\hat{\Gamma}$ and the electrode surface $\underline{\Gamma}$. It is further divided into the liquid volume Ω and the outer region $\Omega_o = \Omega_{\rm ext} \setminus \Omega$ occupied by the gas. We refer to $\varepsilon_i = \varepsilon_{\rm liq}$ as the inner dielectric constant of the liquid and $\varepsilon_o = \varepsilon_{\rm air}$ as the outer dielectric constant of the air phase. Let $[\psi]$ be the characteristic potential drop between the conductor and the electrode. After the standard procedure of nondimensionalization, we arrive at the electrostatics equations

$$\left.\begin{aligned} \nabla \cdot \varepsilon_o \nabla \psi^{(o)} = 0 \quad \text{in} \quad \Omega_{\rm ext} \setminus \Omega, \\ \nabla \cdot \varepsilon_i \nabla \psi^{(i)} = 0 \quad \text{in} \quad \Omega, \end{aligned}\right\} \tag{4.115}$$

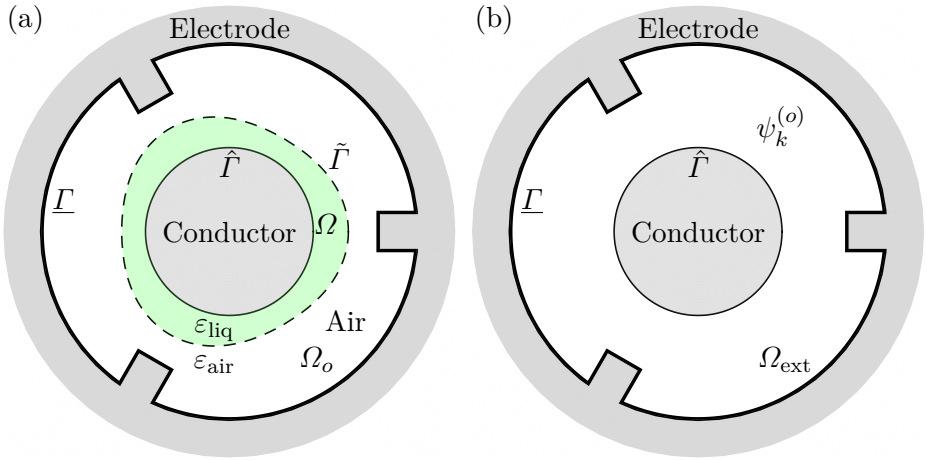

Figure 4.4: (a) Thin dielectric liquid layer (liquid thickness is exaggerated) subject to an electrode with the boundary $\underline{\Gamma}$ (thick solid): $\hat{\Gamma}$ is the conductor surface (thin solid), $\tilde{\Gamma}$ is the liquid free surface (dashed), Ω is the thin liquid volume (green) Ω_o is the gas region exterior to the conductor and the liquid layer. (b) Domain Ω_{ext} for the outer potential correction $\psi_k^{(o)}$, which overlaps with the inner (liquid) domain Ω.

of the inner and outer potentials $\psi^{(i)}$ and $\psi^{(o)}$ subject to a set of boundary conditions due to continuities of electric potential and displacement field,

$$\left.\begin{aligned} \psi &= 0 && \text{on} \quad \hat{\Gamma}, \\ \psi^{(i)} &= \psi^{(o)} && \text{on} \quad \tilde{\Gamma}, \\ \tilde{\boldsymbol{n}} \cdot \varepsilon_i \nabla \psi^{(i)} &= \tilde{\boldsymbol{n}} \cdot \varepsilon_o \nabla \psi^{(o)} && \text{on} \quad \tilde{\Gamma}, \\ \psi &= \underline{\psi} && \text{on} \quad \underline{\Gamma}, \end{aligned}\right\} \tag{4.116}$$

where $\underline{\psi}$ is some potential distribution prescribed on the electrode boundary $\underline{\Gamma}$. The negative gradient of electric potential produces the inner and outer electric fields, $\boldsymbol{E}^{(i)}$ and $\boldsymbol{E}^{(o)}$. Then the total electrostatic energy $\mathcal{E}$ of the electrode-film-conductor system is the sum of the volume integrals of energy density both interior and exterior to the liquid layer,

$$\mathcal{E}[\Omega] = \frac{\mathrm{Ec}}{\epsilon} \left\{ \int_{\Omega_{\text{ext}} \setminus \Omega} \frac{\varepsilon_o}{2} |\boldsymbol{E}^{(o)}|^2 \, \mathrm{d}\Omega + \int_{\Omega} \frac{\varepsilon_i}{2} |\boldsymbol{E}^{(i)}|^2 \, \mathrm{d}\Omega \right\}, \quad \mathrm{Ec} = \frac{\varepsilon_0 [\psi]^2}{[\sigma][L]}, \tag{4.117}$$

where Ec is the electric-capillary number.

In order to identify the leading order effects on the electrostatic energy due to the presence of a dielectric layer, we introduce a consistent base-state electric potential ψ_0 corresponding to the limit of $\epsilon \to 0$, from which the higher order perturbations are constructed. It's not difficult to see that base-state potential ψ_0 solves the bare-bones

electrostatic problem,

$$\left.\begin{aligned} \nabla^2\psi_0 = 0 \quad &\text{in} \quad \Omega_{\text{ext}}, \\ \psi_0 = 0 \quad &\text{on} \quad \hat{\Gamma}, \\ \psi_0 = \underline{\psi} \quad &\text{on} \quad \underline{\Gamma}, \end{aligned}\right\} \tag{4.118}$$

in the absence of a dielectric layer.

Before proceeding with the construction of higher order corrections, we expand differential operators in the close vicinity of the conductor boundary. In such cases, the Laplace operator ∇^2 acting on a three-dimensional scalar can be expressed in terms of the surface-adapted coordinate system (ξ^1, ξ^2, ξ^3),

$$\nabla^2\phi(\xi^1,\xi^2,\xi^3) = \frac{1}{\sqrt{g}}\frac{\partial}{\partial\xi^3}\left(\sqrt{g}\frac{\partial\phi}{\partial\xi^3}\right) + \frac{1}{\sqrt{g}}\frac{\partial}{\partial\xi^\alpha}\left(\sqrt{g}g^{\alpha\beta}\frac{\partial\phi}{\partial\xi^\beta}\right), \tag{4.119}$$

where g^{ij} and g are the metric coefficients and determinant defined in (4.21) and (4.19) respectively. Inspired by exercise 1.1 of Jackson (1999), we make an important observation here: evaluating the Laplace equation on the surface $\hat{\Gamma}$ where $\xi^3 = 0$ leads to a constraint relating the surface Laplacian of potential ϕ to its first and second normal derivatives at the surface,

$$\nabla^2\phi(\xi^1,\xi^2,0) = \frac{\partial^2\phi}{\partial(\xi^3)^2}\Big|_{\xi^3=0} - 2\mathcal{H}\frac{\partial\phi}{\partial(\xi^3)}\Big|_{\xi^3=0} + \hat{\Delta}\phi(\xi^1,\xi^2,0) \tag{4.120}$$

where $\hat{\Delta}$ is the Laplace-Beltrami operator of surface $\hat{\Gamma}$. Relation (4.120) is exact and is very useful in simplifying the electrostatic problem as we will see later. Recall from the metric inverse g^{ij} in (4.25) that in the stretched inner coordinate system (ξ^1, ξ^2, z), the three-dimensional Laplacian and gradient are separated into operators of hierarchical scales,

$$\nabla^2\phi(\xi^1,\xi^2,z) = \frac{1}{\epsilon^2}\frac{\partial^2\phi}{\partial z^2} - \frac{1}{\epsilon}2\mathcal{H}\frac{\partial\phi}{\partial z} + O(1), \tag{4.121}$$

$$\nabla\phi(\xi^1,\xi^2,z) = \frac{1}{\epsilon}\frac{\partial\phi}{\partial z}\hat{\boldsymbol{n}} + \hat{\nabla}\phi + O(\epsilon), \tag{4.122}$$

provided conductor surface $\hat{\Gamma}$ is only gently curved (i.e. $O(\mathcal{H}) = O(1)$) and potential ϕ does not exhibit rapid variations along $\hat{\Gamma}$ (i.e. $O(\hat{\nabla}\phi) = O(1)$).

Inner and outer perturbation solutions

We solve the electrostatic equation interior and exterior to the thin liquid layer by assuming two separate—inner and outer—perturbation expansions of the unknown electric field in terms of the small aspect ratio parameter ϵ. As stated earlier, perturbation series are constructed around the base-state potential ψ_0,

$$\left.\begin{aligned} \psi^{(o)} &= \psi_0 + \epsilon\psi_1^{(o)} + \epsilon^2\psi_2^{(o)} + O(\epsilon^3) \quad \text{in} \quad \Omega_{\text{ext}} \setminus \Omega, \\ \psi^{(i)} &= \psi_0 + \epsilon\psi_1^{(i)} + \epsilon^2\psi_2^{(i)} + O(\epsilon^3) \quad \text{in} \quad \Omega, \end{aligned}\right\} \tag{4.123}$$

where we must emphasize that, the outer corrections $\psi_k^{(o)}$ are defined on the entire exterior domain Ω_{ext} instead of $\Omega \setminus \Omega_{\text{ext}}$ (see figure 4.4(b) for clarification).

At the leading order in ϵ, we find the governing equations of $\psi_1^{(i)}$ and $\psi_1^{(o)}$ to be

$$\left.\begin{aligned} \frac{\partial^2 \psi_1^{(i)}}{\partial z^2} &= 0 \quad \text{in} \quad \Omega, \\ \nabla^2 \psi_1^{(o)} &= 0 \quad \text{in} \quad \Omega_{\text{ext}}, \end{aligned}\right\} \tag{4.124}$$

subject to four boundary conditions, three of which are of Dirichlet-type,

$$\left.\begin{aligned} \psi_1^{(i)} &= 0 \qquad \text{at} \quad z = 0, \\ \psi_1^{(o)} &= \psi_1^{(i)} \quad \text{at} \quad z = \eta, \\ \psi_1^{(o)} &= 0 \qquad \text{on} \quad \underline{\Gamma}. \end{aligned}\right\} \tag{4.125}$$

The last condition comes from the continuity of displacement flux. The leading order balance in the flux jump condition (4.116) is

$$\varepsilon_o \hat{\boldsymbol{n}} \cdot \nabla \psi_0|_{\hat{\Gamma}} = \varepsilon_i \Big[\frac{\partial \psi_1^{(i)}}{\partial z}\Big|_{z=\eta} + \hat{\boldsymbol{n}} \cdot \nabla \psi_0|_{\hat{\Gamma}} \Big], \tag{4.126}$$

which then yields the solution to the leading order equations (4.124)

$$\left.\begin{aligned} \psi_1^{(i)}(\xi^1, \xi^2, z) &= \frac{\varepsilon_o - \varepsilon_i}{\varepsilon_i} (\hat{\boldsymbol{n}} \cdot \nabla \psi_0|_{\hat{\Gamma}}) z, \\ \psi_1^{(o)} &= \frac{\varepsilon_o - \varepsilon_i}{\varepsilon_i} (\hat{\boldsymbol{n}} \cdot \nabla \psi_0|_{\hat{\Gamma}}) \eta \quad \text{on} \quad \hat{\Gamma}, \end{aligned}\right\} \tag{4.127}$$

where $\psi_1^{(o)}$ is the harmonic potential in the exterior domain Ω_{ext} determined indirectly by boundary condition (4.127) on the conductor surface $\hat{\Gamma}$.

The equations governing the inner potential $\psi_2^{(i)}$ and outer potential $\psi_2^{(o)}$ at the next order are found to be

$$\left.\begin{aligned} \frac{\partial^2 \psi_2^{(i)}}{\partial z^2} - 2\mathcal{H} \frac{\partial \psi_1^{(i)}}{\partial z} &= 0 \quad \text{in} \quad \Omega, \\ \nabla^2 \psi_2^{(o)} &= 0 \quad \text{in} \quad \Omega^{\text{ext}}. \end{aligned}\right\} \tag{4.128}$$

The Dirichlet-type boundary conditions at the next order are again straightforward,

$$\left.\begin{aligned} \psi_2^{(i)} &= 0 \qquad \text{at} \quad z = 0, \\ \psi_2^{(o)}|_{\hat{\Gamma}} + (\hat{\boldsymbol{n}} \cdot \nabla \psi_1^{(o)}|_{\hat{\Gamma}}) \eta &= \psi_2^{(i)} \quad \text{at} \quad z = \eta, \\ \psi_2^{(o)} &= 0 \qquad \text{on} \quad \underline{\Gamma}. \end{aligned}\right\} \tag{4.129}$$

The continuity of displacement field flux at the free surface $\tilde{\Gamma}$ deserves careful examinations since it involves the expansion of electric field which is a vector instead of a scalar,

$$\nabla \phi|_{\tilde{\Gamma}} = \nabla \phi|_{\hat{\Gamma}} + \epsilon \nabla (\nabla \phi)|_{\hat{\Gamma}} \, \eta \, \hat{\boldsymbol{n}} + O(\epsilon^2). \tag{4.130}$$

Expansion (4.130) projected to the normal vector $\tilde{\boldsymbol{n}}$ of the free surface $\tilde{\Gamma}$ gives rise to the normal flux at the free surface $\tilde{\Gamma}$ up to the second order,

$$\tilde{\boldsymbol{n}} \cdot \nabla\phi|_{\tilde{\Gamma}} = \hat{\boldsymbol{n}} \cdot \nabla\phi|_{\hat{\Gamma}} + \epsilon\hat{\boldsymbol{n}}_1 \cdot \nabla\phi|_{\hat{\Gamma}} + \epsilon\eta\hat{\boldsymbol{n}}[\nabla(\nabla\phi)|_{\hat{\Gamma}}]\hat{\boldsymbol{n}} + O(\epsilon^2), \tag{4.131}$$

where $\hat{\boldsymbol{n}}_1$ is the first order correction to $\tilde{\boldsymbol{n}}$ so that $\tilde{\boldsymbol{n}} = \hat{\boldsymbol{n}} + \epsilon\hat{\boldsymbol{n}}_1 + O(\epsilon^2)$. However the first order correction $\hat{\boldsymbol{n}}_1$ must be purely tangential (i.e. $\hat{\boldsymbol{n}}_1 \cdot \hat{\boldsymbol{n}} = 0$) since both $\tilde{\boldsymbol{n}}$ and $\hat{\boldsymbol{n}}$ are unit vectors for which $|\tilde{\boldsymbol{n}}| = |\hat{\boldsymbol{n}}| + 2\epsilon\,\hat{\boldsymbol{n}}_1 \cdot \hat{\boldsymbol{n}} + O(\epsilon^2) = 1$ can be fulfilled only if $\hat{\boldsymbol{n}}_1 \cdot \hat{\boldsymbol{n}} = 0$. If we apply expansion (4.131) to the base state ψ_0 which is equipotential on the conductor surface $\hat{\Gamma}$, then

$$\tilde{\boldsymbol{n}} \cdot \nabla\psi_0|_{\tilde{\Gamma}} = \hat{\boldsymbol{n}} \cdot \nabla\psi_0|_{\hat{\Gamma}} + \epsilon\eta\frac{\partial^2\psi_0}{\partial(\xi^3)^2}\Big|_{\xi^3=0} + O(\epsilon^2) \tag{4.132}$$

where we recall in surface-adapted coordinate system (ξ^1, ξ^2, ξ^3), expression $\hat{\boldsymbol{n}}[\nabla(\nabla\phi)|_{\hat{\Gamma}}]\hat{\boldsymbol{n}}$ simplifies to $\partial^2\phi/\partial(\xi^3)^2$ at $\xi^3 = 0$. Then by virtue of relation (4.120), it immediately follows from the harmonicity of potential ψ_0 that,

$$\frac{\partial^2\psi_0}{\partial(\xi^3)^2} = 2\mathcal{H}\frac{\partial\psi_0}{\partial(\xi^3)} \quad \text{at} \quad \xi^3 = 0. \tag{4.133}$$

With identity (4.133) substituted into expansion (4.132), the continuity of displacement flux at next order reads,

$$\varepsilon_o\Big[\hat{\boldsymbol{n}} \cdot \nabla\psi_1^{(o)}|_{\hat{\Gamma}} + 2\mathcal{H}\eta(\hat{\boldsymbol{n}} \cdot \nabla\psi_0|_{\hat{\Gamma}})\Big] = \varepsilon_i\Big[\frac{\partial\psi_2^{(i)}}{\partial z}\Big|_{z=\eta} + 2\mathcal{H}\eta(\hat{\boldsymbol{n}} \cdot \nabla\psi_0|_{\hat{\Gamma}})\Big]. \tag{4.134}$$

The next order corrections to the inner and outer potentials are found by solving equations (4.128) subject to boundary conditions (4.129) and (4.134),

$$\left.\begin{aligned}\psi_2^{(i)} &= \frac{1}{2}2\mathcal{H}\frac{\varepsilon_o - \varepsilon_i}{\varepsilon_i}(\hat{\boldsymbol{n}} \cdot \nabla\psi_0|_{\hat{\Gamma}})z^2 + \frac{\varepsilon_o}{\varepsilon_i}(\hat{\boldsymbol{n}} \cdot \nabla\psi_1^{(o)}|_{\hat{\Gamma}})z,\\ \psi_2^{(o)} &= \frac{1}{2}2\mathcal{H}\frac{\varepsilon_o - \varepsilon_i}{\varepsilon_i}(\hat{\boldsymbol{n}} \cdot \nabla\psi_0|_{\hat{\Gamma}})\eta^2 + \frac{\varepsilon_o - \varepsilon_i}{\varepsilon_i}(\hat{\boldsymbol{n}} \cdot \nabla\psi_1^{(o)}|_{\hat{\Gamma}})\eta,\end{aligned}\right\} \tag{4.135}$$

where $\psi_2^{(o)}$ is the harmonic potential in the exterior domain Ω_{ext} subject to boundary condition (4.135) on conductor surface $\hat{\Gamma}$.

Total electrostatic energy in presence of a dielectric layer

The total electrostatic energy $\mathcal{E}$ defined in (4.117) has two disjoint contributions, the energy confined within in the dielectric layer and the energy stored in the free space exterior to the film. Recall the outer potential corrections $\psi_k^{(o)}$ are defined on the entire exterior region Ω_{ext} instead of the gas volume $\Omega \setminus \Omega_{\text{ext}}$. Therefore we must subtract off the overlapping part to prevent double-counting,

$$\mathcal{E}[\Omega] = \frac{\text{Ec}}{\epsilon}\left\{\varepsilon_o\int_{\Omega_{\text{ext}}}\frac{1}{2}|\nabla\psi^{(o)}|^2\,\mathrm{d}\Omega - \varepsilon_o\int_{\Omega}\frac{1}{2}|\nabla\psi^{(o)}|^2\,\mathrm{d}\Omega + \varepsilon_i\int_{\Omega}\frac{1}{2}|\nabla\psi^{(i)}|^2\,\mathrm{d}\Omega\right\}. \tag{4.136}$$

Applying Green's identity to the first volume integral in (4.136) yields

$$\begin{aligned}
&\int_{\Omega_{\text{ext}}} \frac{1}{2}|\nabla\psi^{(o)}|^2 \,\mathrm{d}\Omega \\
&= \int_{\Omega_{\text{ext}}} \frac{1}{2}|\nabla\psi_0|^2 + \epsilon(\nabla\psi_0)\cdot\nabla\psi_1^{(o)} + \frac{\epsilon^2}{2}|\nabla\psi_1^{(o)}|^2 + \epsilon^2(\nabla\psi_0)\cdot\nabla\psi_2^{(o)} \,\mathrm{d}\Omega + O(\epsilon^3) \\
&= \int_{\Omega_{\text{ext}}} \frac{1}{2}|\nabla\psi_0|^2 \,\mathrm{d}\Omega - \epsilon\int_{\hat{\Gamma}} \psi_1^{(o)}(\hat{\boldsymbol{n}}\cdot\nabla\psi_0)\,\mathrm{d}\hat{\Gamma} \\
&\qquad\qquad - \epsilon^2\int_{\hat{\Gamma}} \frac{1}{2}\psi_1^{(o)}(\hat{\boldsymbol{n}}\cdot\nabla\psi_1^{(o)}) + \psi_2^{(o)}(\hat{\boldsymbol{n}}\cdot\nabla\psi_0)\,\mathrm{d}\hat{\Gamma} + O(\epsilon^3). \quad (4.137)
\end{aligned}$$

The second integral in (4.136) can be separated into orders of ϵ as well. The idea here is to interchange Taylor expansion with integration, i.e. $\int_a^{a+\epsilon} f(x)\,\mathrm{d}x = \int_a^{a+\epsilon} f(a) + f'(a)x + f''(a)x^2/2\,\mathrm{d}x + ...$, for a smooth function $f(x)$. Expanding the integral with index notation leads to,

$$\begin{aligned}
&\int_{\Omega} \frac{1}{2}|\nabla\psi^{(o)}|^2 \,\mathrm{d}\Omega \\
&= \int_{\Omega} \frac{1}{2}\frac{\partial\psi^{(o)}}{\partial\xi^i}\frac{\partial\psi^{(o)}}{\partial\xi^j}g^{ij} \,\mathrm{d}\Omega \\
&= \int_{\hat{\Gamma}}\int_0^{\epsilon\eta} \frac{1}{2}\left[(\hat{g}^{\alpha\beta} + \xi^3 2I\!I^{\alpha\beta})\frac{\partial\psi^{(o)}}{\partial\xi^\alpha}\frac{\partial\psi^{(o)}}{\partial\xi^\beta} + \frac{\partial\psi^{(o)}}{\partial\xi^3}\frac{\partial\psi^{(o)}}{\partial\xi^3} + O((\xi^3)^2)\right] J\,\mathrm{d}\xi^3\,\mathrm{d}\hat{\Gamma} \\
&= \int_{\hat{\Gamma}}\int_0^{\epsilon\eta} \frac{1}{2}\left[\frac{\partial\psi^{(o)}}{\partial\xi^3}\frac{\partial\psi^{(o)}}{\partial\xi^3} + O((\xi^3)^2)\right]\left[1 - 2\mathcal{H}\xi^3 + +O((\xi^3)^2)\right]\,\mathrm{d}\xi^3\,\mathrm{d}\hat{\Gamma} \\
&= \epsilon\int_{\hat{\Gamma}} \frac{\eta}{2}(\hat{\boldsymbol{n}}\cdot\nabla\psi_0)^2\,\mathrm{d}\hat{\Gamma} + \epsilon^2\int_{\hat{\Gamma}} \eta(\hat{\boldsymbol{n}}\cdot\nabla\psi_0)(\hat{\boldsymbol{n}}\cdot\nabla\psi_1^{(o)}) + \frac{\mathcal{H}}{2}\eta^2(\hat{\boldsymbol{n}}\cdot\nabla\psi_0)^2\,\mathrm{d}\hat{\Gamma} + O(\epsilon^3),
\end{aligned} \quad (4.138)$$

where we note $\partial\psi^{(o)}/\partial\xi^\alpha$ must be $O(\epsilon)$ since $\partial\psi_0/\partial\xi^\alpha = 0$ on the equipotential surface $\xi^3 = 0$.

The last volume integral in (4.136) measures the electrostatic energy interior to the dielectric layer due to the interior electric potential $\psi^{(i)}$. In light of the perturbation series from (4.127) and (4.135), we have

$$\begin{aligned}
\int_{\Omega} \frac{1}{2}|\nabla\psi^{(i)}|^2\,\mathrm{d}\Omega &= \epsilon\frac{\varepsilon_o^2}{\varepsilon_i^2}\int_{\hat{\Gamma}} \frac{\eta}{2}(\hat{\boldsymbol{n}}\cdot\nabla\psi_0)^2\,\mathrm{d}\hat{\Gamma} \\
&\quad + \epsilon^2\frac{\varepsilon_o^2}{\varepsilon_i^2}\int_{\hat{\Gamma}} \eta(\hat{\boldsymbol{n}}\cdot\nabla\psi_0)(\hat{\boldsymbol{n}}\cdot\nabla\psi_1^{(o)}) + \frac{\mathcal{H}}{2}\eta^2(\hat{\boldsymbol{n}}\cdot\nabla\psi_0)^2\,\mathrm{d}\hat{\Gamma} + O(\epsilon^3).
\end{aligned} \quad (4.139)$$

Rearranging the expanded integrals from (4.137)–(4.139) into orders of ϵ leads to the first and the second order corrections to the electrostatic energy of the base-state po-

tential (up to a material constant),

$$\begin{aligned}
&\int_{\Omega_{\text{ext}}} \frac{\varepsilon_o}{2}|\nabla\psi^{(o)}|^2\,\mathrm{d}\Omega - \int_{\Omega} \frac{\varepsilon_o}{2}|\nabla\psi^{(o)}|^2\,\mathrm{d}\Omega + \int_{\Omega} \frac{\varepsilon_i}{2}|\nabla\psi^{(i)}|^2\,\mathrm{d}\Omega \\
&= \varepsilon_o \int_{\Omega} \frac{1}{2}|\nabla\psi_0|^2\,\mathrm{d}\Omega + \epsilon\frac{\varepsilon_i-\varepsilon_o}{\varepsilon_i}\varepsilon_o \int_{\hat{\Gamma}} \frac{1}{2}(\hat{\boldsymbol{n}}\cdot\nabla\psi_0)^2\eta\,\mathrm{d}\hat{\Gamma} \\
&\quad +\epsilon^2\frac{\varepsilon_i-\varepsilon_o}{\varepsilon_i}\varepsilon_o \int_{\hat{\Gamma}} \frac{1}{2}\left[\mathscr{H}(\hat{\boldsymbol{n}}\cdot\nabla\psi_0)^2\eta^2 + (\hat{\boldsymbol{n}}\cdot\nabla\psi_0)(\hat{\boldsymbol{n}}\cdot\nabla\psi_1^{(o)})\eta\right]\,\mathrm{d}\hat{\Gamma} + O(\epsilon^3).
\end{aligned} \tag{4.140}$$

To clean up notations, we define the dielectric contrast parameter $\kappa = \varepsilon_{\text{air}}/\varepsilon_{\text{liq}}$ as in the EHL model (3.5) and rewrite potential gradient as electric field $\boldsymbol{E} = -\nabla\psi$. We shall also drop the $(\cdot)^{(o)}$ superscript on the higher order terms since only the outer correction $\psi_1^{(o)}$ is involved. In terms of columnar volume density ϱ, the truncated final form of total electrostatic energy $\overline{\mathcal{E}}$ reduces to the energy of the base state plus two higher order corrections,

$$\begin{aligned}
\overline{\mathcal{E}}[\hat{\Gamma};\varrho] = \mathrm{Ec}\,\varepsilon_{\text{air}}\Bigg\{&\frac{1}{\epsilon}\int_{\Omega_{\text{ext}}} \frac{1}{2}|\boldsymbol{E}_0|^2\,\mathrm{d}\Omega \\
&+ (1-\kappa)\int_{\hat{\Gamma}} \frac{1}{2}(\hat{\boldsymbol{n}}\cdot\boldsymbol{E}_0)^2\varrho\,\mathrm{d}\hat{\Gamma} \\
&+ (1-\kappa)\epsilon\int_{\hat{\Gamma}} \mathscr{H}(\hat{\boldsymbol{n}}\cdot\boldsymbol{E}_0)^2\varrho^2 + \frac{1}{2}(\hat{\boldsymbol{n}}\cdot\boldsymbol{E}_0)(\hat{\boldsymbol{n}}\cdot\boldsymbol{E}_1)\varrho\,\mathrm{d}\hat{\Gamma}\Bigg\}.
\end{aligned} \tag{4.141}$$

The variational derivative immediately follows,

$$\frac{\delta\overline{\mathcal{E}}}{\delta\varrho} = \mathrm{Ec}\,\varepsilon_{\text{air}}(1-\kappa)\left\{\frac{1}{2}(\hat{\boldsymbol{n}}\cdot\boldsymbol{E}_0)^2 + \epsilon 2\mathscr{H}(\hat{\boldsymbol{n}}\cdot\boldsymbol{E}_0)^2\varrho + \epsilon(\hat{\boldsymbol{n}}\cdot\boldsymbol{E}_0)(\hat{\boldsymbol{n}}\cdot\boldsymbol{E}_1)\right\}, \tag{4.142}$$

where the outer field correction $\boldsymbol{E}_1^{(o)}$ is the electric field of the outer potential $\psi_1^{(o)}$ which solves the auxiliary electrostatic problem,

$$\left.\begin{aligned}
\nabla^2\psi_1 &= 0 && \text{in} \quad \Omega_{\text{ext}}, \\
\psi_1 &= 0 && \text{on} \quad \underline{\Gamma}, \\
\psi_1 &= (1-\kappa)\,(\hat{\boldsymbol{n}}\cdot\boldsymbol{E}_0)\varrho && \text{on} \quad \hat{\Gamma}.
\end{aligned}\right\} \tag{4.143}$$

In the lubrication limit, the effective pressure (4.142) is weakened due to the presence of a dielectric layer. For a perfectly conductive liquid (i.e. $\lim_{\varepsilon_{\text{liq}}\to\infty}\kappa = 0$), the familiar electrostatic pressure is recovered at the zeroth order. When liquid material shares the same dielectric property with the gas (i.e. $\lim_{\varepsilon_{\text{liq}}\to\varepsilon_{\text{air}}}\kappa = 1$), the entire effective electrostatic pressure (4.142) disappears. This is expected because in such a limit $\varepsilon_{\text{liq}} = \varepsilon_{\text{air}}$, electric field is no longer discontinuous which means no jump in the Maxwell stresses acting on both sides of the liquid free surface. The first two terms in (4.142) represent the bare-bones electrostatic pressure and a leading order geometric correction due to the dilation of free surface area differential $\mathrm{d}\tilde{\Gamma}$ measured wit respect to $\mathrm{d}\hat{\Gamma}$ of

the conductor surface. The "nonlocalness" in the effective electrostatic pressure $\delta\overline{\mathcal{E}}/\delta\varrho$ attributes to the last term in (4.142), which represents a long-range interaction between the base-state electric field $\boldsymbol{E}_0$ and the correction electric field $\boldsymbol{E}_1$. Such interaction is indeed nonlocal (with respect to the conductor surface $\hat{\Gamma}$) because $\boldsymbol{E}_1 = -\nabla\psi_1$ is deduced from the potential ψ_1 of the auxiliary problem (4.143), the solution of which requires information of the columnar volume density ϱ everywhere on the conductor surface $\hat{\Gamma}$. The nonlocal term becomes dominant when the surface charge distribution induced by the base-state electric field $\hat{\boldsymbol{n}} \cdot \boldsymbol{E}_0$ is uniform (e.g., concentric capacitor of two cylinders or spheres of different radius).

Finite element simulations

We illustrate the generalized lubrication model through finite element simulations of the dynamics of a thin dielectric liquid film coating a grounded spherical conductor. In this case, the total free energy of the system has three components, homogeneous surface energy $\mathcal{S}$ and gravitational energy $\mathcal{G}$ and electrostatic energy $\mathcal{E}$,

$$\mathcal{F} = \mathcal{S} + \mathcal{G} - \mathcal{E}, \tag{4.144}$$

where the minus sign in front of the electrostatic energy $\mathcal{E}$ is due to the fact that for a perfect dielectric film in contact with a conductor at a fixed potential, the external voltage supply is doing work to the liquid film, as opposed to for a charged isolated conductor, surface charges do work to redistribute themselves (Ljepojevic and Forbes, 1995).

Let $\mathbb{V}_{\text{ext}}$ be the finite element interpolation space of the three-dimensional exterior domain Ω_{ext} discretized by quadratic tetrahedral elements and $\hat{\mathbb{V}}$ be the space of the two-dimensional conductor surface $\hat{\Gamma}$ discretized by quadratic triangular elements. $\psi_0^{\text{h}} \in \mathbb{V}_{\text{ext}}$ and $\psi_1^{\text{h}} \in \mathbb{V}_{\text{ext}}$ are the finite element projections of the base-state electric potential ψ_0 and the correction potential ψ_1, respectively. Similarly, we introduce four discretized scalar fields, the columnar volume density $\rho^{\text{h}} \in \hat{\mathbb{V}}$, the effective capillary pressure $(\overline{\mathcal{S}}/\delta\varrho)^{\text{h}} \in \hat{\mathbb{V}}$, the effective hydrostatic (gravitational) pressure $(\overline{\mathcal{G}}/\delta\varrho)^{\text{h}} \in \hat{\mathbb{V}}$ and the effective Maxwell (electrostatic) pressure $(\overline{\mathcal{E}}/\delta\varrho)^{\text{h}} \in \hat{\mathbb{V}}$. Notations $\mathbb{V}_i$ and $\mathbb{X}_i$ are reserved for the i-th hat function and i-th global Lagrange nodal position in a finite element space which can be either $\mathbb{V}_{\text{ext}}$ or $\hat{\mathbb{V}}$. The standard finite element inner product $\langle \cdot, \cdot \rangle$ similar to the one in equation (3.32) is introduced for each discretized domain in terms of volume or surface integrals.

Prior to the time-dependent simulation, we solve the base-state problem only for once,

whose variational formulation reads: find $\psi_0^{\mathrm{h}} \in \mathbb{V}_{\mathrm{ext}}$ such that

$$\left.\begin{aligned} \left\langle \nabla \mathbb{V}_i, \nabla \psi_0^{\mathrm{h}} \right\rangle &= 0 && \text{for all } \mathbb{V}_i \in \mathbb{V}_{\mathrm{ext}}, \\ \text{subject to } \psi_0^{\mathrm{h}}(\mathbb{X}_i) &= 0 && \text{for all } \mathbb{X}_i \in \hat{\Gamma}, \\ \psi_0^{\mathrm{h}}(\mathbb{X}_i) &= \underline{\psi}(\mathbb{X}_i) && \text{for all } \mathbb{X}_i \in \underline{\Gamma}. \end{aligned}\right\} \tag{4.145}$$

Given an initial distribution of film thickness, at each ensuing time step we solve the following semi-discrete variational problem: find $\varrho^{\mathrm{h}} \in \hat{\mathbb{V}}$ such that

$$\left.\begin{aligned} \langle \mathbb{V}_i, \mathfrak{D}_t[\varrho^{\mathrm{h}}] \rangle + \langle \hat{\nabla} \mathbb{V}_i, \boldsymbol{D}_F \hat{\nabla} (\frac{\delta \overline{\mathcal{F}}}{\delta \varrho})^{\mathrm{h}} \rangle &= 0, \\ (\frac{\delta \overline{\mathcal{F}}}{\delta \varrho})^{\mathrm{h}} &= (\frac{\delta \overline{\mathcal{G}}}{\delta \varrho})^{\mathrm{h}} + (\frac{\delta \overline{\mathcal{S}}}{\delta \varrho})^{\mathrm{h}} - (\frac{\delta \overline{\mathcal{E}}}{\delta \varrho})^{\mathrm{h}}, \\ \langle \mathbb{V}_i, (\frac{\delta \overline{\mathcal{G}}}{\delta \varrho})^{\mathrm{h}} \rangle &= \mathrm{Bo} \langle \mathbb{V}_i, \hat{\boldsymbol{x}} \cdot \mathfrak{g} + \epsilon (\hat{\boldsymbol{n}} \cdot \mathfrak{g}) \varrho^{\mathrm{h}} \rangle, \\ \langle \mathbb{V}_i, (\frac{\delta \overline{\mathcal{S}}}{\delta \varrho})^{\mathrm{h}} \rangle + \langle \mathbb{V}_i, 2\mathcal{H} + \epsilon(4\mathcal{H}^2 - 2\mathcal{K}) \varrho^{\mathrm{h}} \rangle &= \epsilon \langle \hat{\nabla} \mathbb{V}_i, \hat{\nabla} \varrho^{\mathrm{h}} \rangle, \\ \frac{\langle \mathbb{V}_i, (\delta \overline{\mathcal{E}} / \delta \varrho)^{\mathrm{h}} \rangle}{\varepsilon_{\mathrm{air}} (1-\kappa) \mathrm{Ec}} - \langle \mathbb{V}_i, \frac{(\hat{\boldsymbol{n}} \cdot \boldsymbol{E}_0^{\mathrm{h}})^2}{2} + \epsilon 2\mathcal{H} (\hat{\boldsymbol{n}} \cdot \boldsymbol{E}_0^{\mathrm{h}})^2 \varrho^{\mathrm{h}} \rangle &= \epsilon \langle \mathbb{V}_i, (\hat{\boldsymbol{n}} \cdot \boldsymbol{E}_0^{\mathrm{h}})(\hat{\boldsymbol{n}} \cdot \boldsymbol{E}_1^{\mathrm{h}}) \rangle, \end{aligned}\right\} \tag{4.146}$$

for all $\mathbb{V}_i \in \hat{\mathbb{V}}$, and $\psi_1^{\mathrm{h}} \in \mathbb{V}_{\mathrm{ext}}$ such that

$$\left.\begin{aligned} \left\langle \nabla \mathbb{V}_i, \nabla \psi_1^{\mathrm{h}} \right\rangle &= 0 && \text{for all } \mathbb{V}_i \in \mathbb{V}_{\mathrm{ext}}, \\ \text{subject to } \psi_1^{\mathrm{h}}(\mathbb{X}_i) &= (1-\kappa)\, (\hat{\boldsymbol{n}} \cdot \boldsymbol{E}_0(\mathbb{X}_i)) \varrho^{\mathrm{h}}(\mathbb{X}_i) && \text{for all } \mathbb{X}_i \in \hat{\Gamma}, \\ \psi_1^{\mathrm{h}}(\mathbb{X}_i) &= 0 && \text{for all } \mathbb{X}_i \in \underline{\Gamma}, \end{aligned}\right\} \tag{4.147}$$

where $\mathfrak{D}_t$ is some discrete time-stepping operator (backward Euler, BDF2, etc.). On the surface of a unit sphere, the second fundamental form $\boldsymbol{I\!I}$ has no preferable principle directions since the principle curvatures $\kappa_1 = \kappa_2 = -1$. The discrete mobility tensor $\boldsymbol{D}_F$ is simply the identity tensor multiplied by a nonlinear mobility coefficient,

$$\boldsymbol{D}_F = \Big[\frac{1}{3} (\rho^{\mathrm{h}})^3 - \frac{\epsilon}{2} (\rho^{\mathrm{h}})^4 \Big] \mathbb{I}. \tag{4.148}$$

The fully discretized finite element system (4.145)–(4.147) is implemented in the commercial software COMSOL Multiphysics, Inc. V5.3 (2017).

Plotted in figure 4.5 is a spherical conductor of unity radius concentric with another spherical electrode of radius $= 5$. A boundary electric potential $\underline{\psi} = 5 Y_3^2(\vartheta, \varphi)$ is prescribed on the electrode surface where Y_m^ℓ is the spherical harmonics of degree ℓ and order m with polar angle ϑ and azimuthal angle φ. The exterior volume Ω_{ext} is discretized by 245957 quadratic tetrahedral elements and the spherical surface $\hat{\Gamma}$ of the conductor by 12550 quadratic triangular elements. Since in equation (4.142) electric-capillary number Ec always comes with the contrast parameter κ and dielectric constant

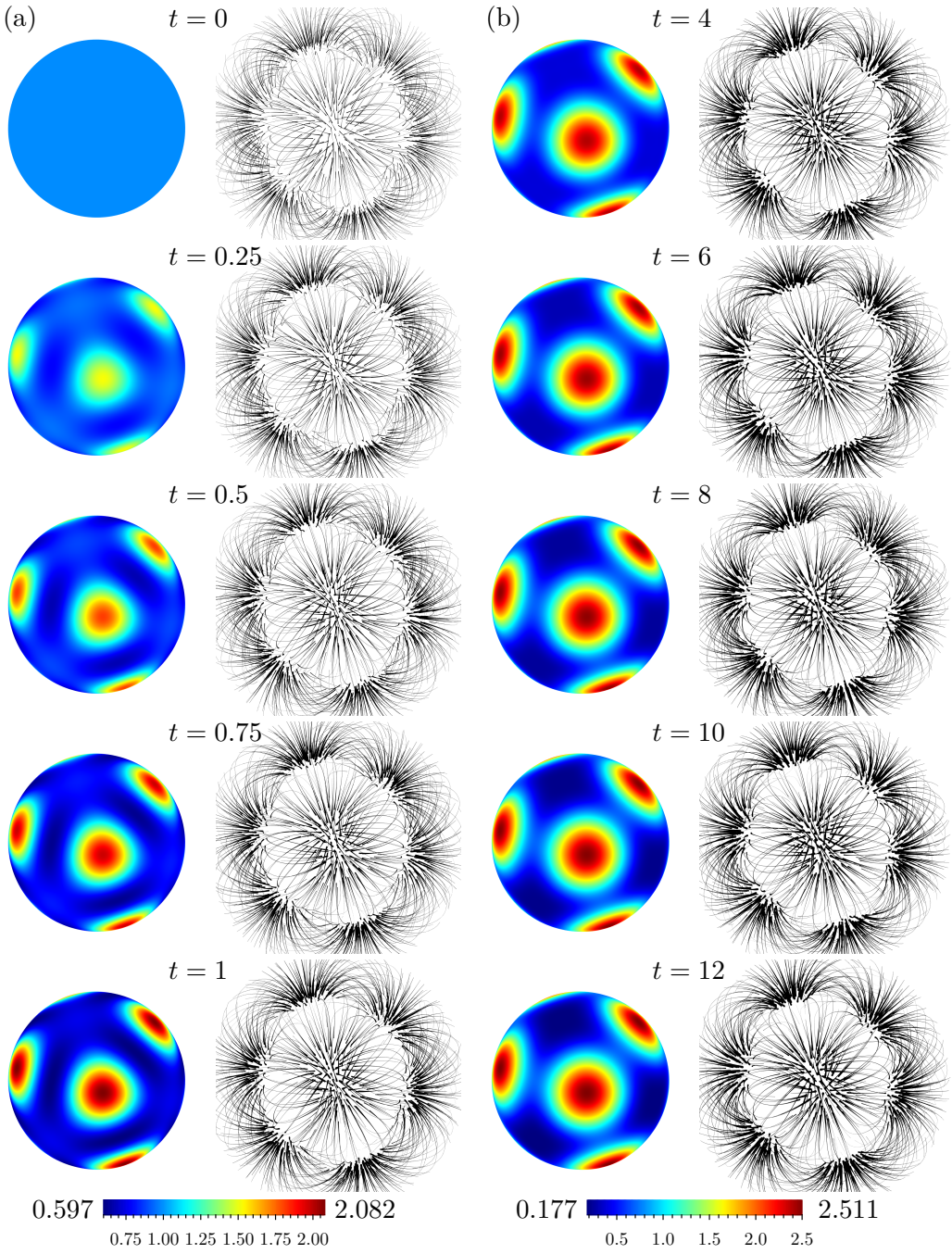

Figure 4.5: Snapshots of (a) early and (b) late stages of the evolution of liquid columnar volume density ϱ (colored) on a conductor of a unit sphere subject to another spherical electrode of radius 5. Black tubes are field lines of the correction potential ψ_1. Tube radius is proportional to field strength $|\boldsymbol{E}_1|$. Parameters used in the simulation: $\kappa = 0$, $\mathrm{Bo} = 0$, $\mathrm{Ec} = 50$ and $\epsilon = 0.005$.

ε_{air}, without loss of generality we set $\kappa = 0$ and $\varepsilon_{\text{air}} = 1$ and vary Ec alone. In this example, gravity is turned off (i.e. $\mathrm{Bo} = 0$) and the pattern formation in the dielectric film with aspect ratio $\epsilon = 0.005$ entirely results from the competition between Maxwell ($\mathrm{Ec} = 50$) and capillary stresses. During the early development $0 \leq t \leq 1$ shown in figure 4.5(a), liquid film immediately responds to the valleys and peaks (eight in total) of the spherical harmonics Y_3^2 in the prescribed potential of the electrode by forming eight charged droplets. The initial growth of triangle-shaped droplets, for example at $t = 0.5$, shows reminiscence of the fine details of the spherical harmonics electrode potential, which however is soon lost to capillary smoothing. Note every charged circular droplet is surrounded by three other droplets of the opposite charge type, as indicated by the connections of electric field lines (black tubes) generated by the correction potential ψ_1. In the late stage of the evolution ($4 \leq t \leq 12$), the positions of these droplets are tightly interlocked by the attractive electric forces between each one and its three neighbors. The surface region between these charged droplets are depleted to about only 18% of the initial film thickness whereas each droplet apex attains more than 2.5 times as tall.

In figure 4.6 is another finite element simulation with the identical setup of the geometry and discretization with the one in figure 4.5 except a different electric potential $\underline{\psi} = x$ is prescribed on the larger spherical electrode of radius 5 in order to mimic a constant electric field parallel to the horizontal plane in the far field. In this simulation, gravity is turned back on ($\mathrm{Bo} = 1$) acting vertically downwards in z-direction on a twice thicker film ($\epsilon = 0.01$) while electrostatic effect is reduced ($\mathrm{Ec} = 1.25$). As shown in figure 4.6(a), a circular pile of liquid four times higher than the background uniform film initially concentrates on the north pole. However, azimuthal symmetry in the system is broken due to the presence of a nearly unidirectional base-state electric field parallel to the horizontal plane. Instead of spreading evenly at every azimuthal angle, the excessive liquid volume is immediately elongated along or against the direction of the electric field $\boldsymbol{E}_0$ depending on the type of charges at the spreading front. In the later stage shown in figure 4.6(b), the thinned liquid pile is split into two separate droplets which gradually slide towards the south pole under the vertical pull of gravity. The two droplets absorb significant amount of liquid volume from the relatively uniform liquid reservoir in the background along with their sliding motion and eventually almost recover the maximum thickness of the initial state. In the end at $t = 0.3$, an equilibrium is about to be reached under the balance between gravitational forces and Maxwell stresses as two circular droplets are suspended at positions between the directions of gravity and base-state electric field. The electric field lines of the correction potential ψ_1 plotted in figure 4.6(b) suggest that the two droplets are also attracted to each other nonlocally due to the induced surface charges they carry.

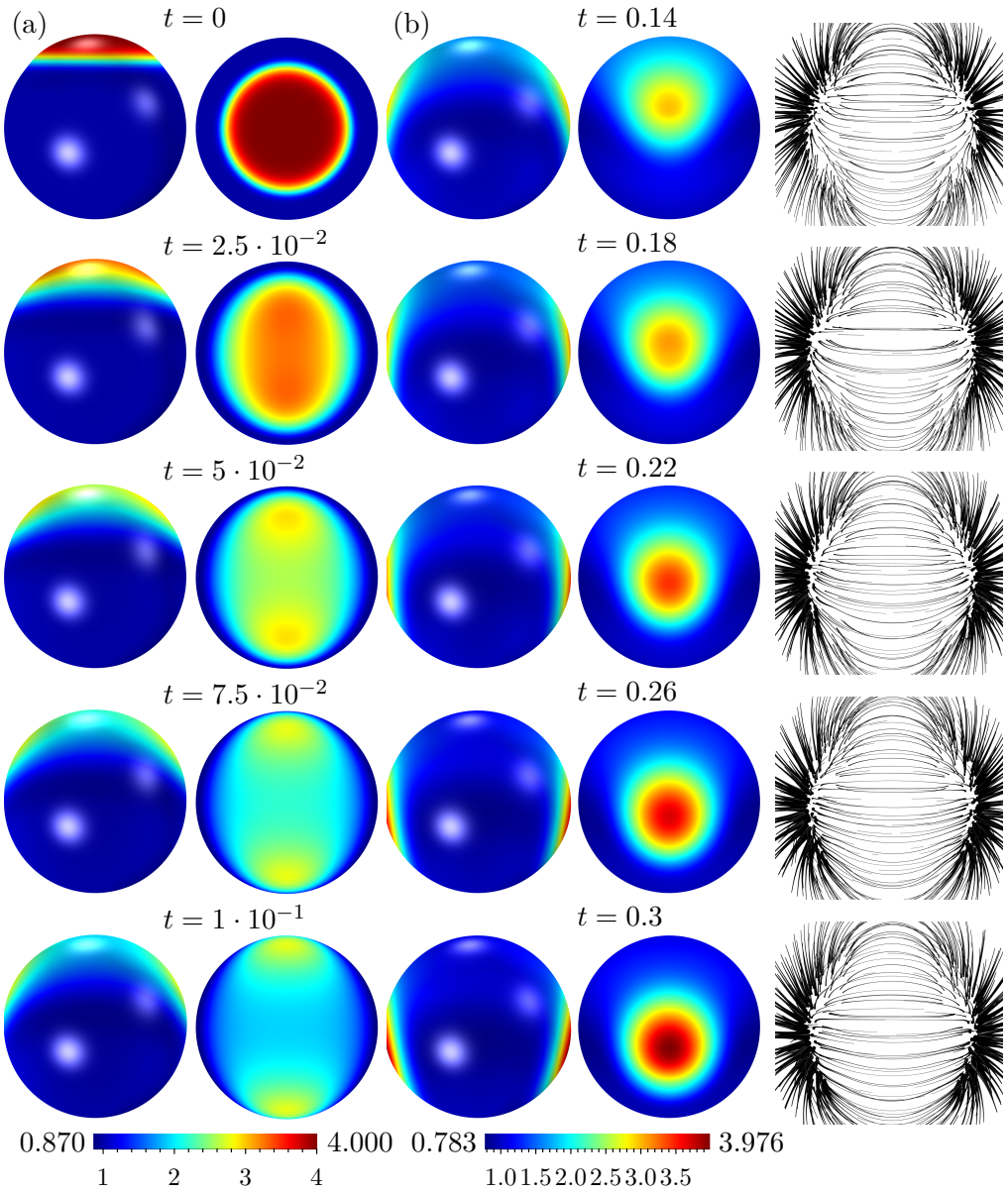

Figure 4.6: Snapshots of (a) early and (b) late stages of the evolution of liquid columnar volume density ϱ (colored) on a conductor of a unit sphere subject to another spherical electrode of radius 5. The second column in each panel is the first column rotated by 90° about one of the axes. Gravity acts vertically downwards whereas the prescribed electrode potential mimics a constant electric field parallel to the horizontal plane. Black tubes are field lines of the correction potential ψ_1. Parameters used in the simulation: $\kappa = 0$, $\mathrm{Bo} = 1$, $\mathrm{Ec} = 1.25$ and $\epsilon = 0.01$.

4.6 Conclusion

In this chapter we have developed the appropriate differential geometry languages to describe the kinematics and dissipation of thin liquid films on curved substrates. The tensorial partial differential equation governing the evolution of local film volume density on curved manifolds is derived based on a novel energy-dissipation formalism of free surface lubrication flow derived from the Helmholtz minimum dissipation theorem in slender limit. It is shown that the dynamics of thin viscous film is uniquely determined by the dissipation of available interfacial free energies in the liquid film due to internal frictions caused by the tangential shear against the curved supporting surface. In particular, we present a novel nonlocal model of a thin dielectric liquid layer coating a gently curved conductor. In addition to interface-normal driving forces (e.g., gravity and capillary) resulting from standard interfacial energies of local type, the local liquid volume at one position on the conductor surface experiences electric forces due to polarization charges carried by the liquid volume at all other positions on the same surface.

The finite element simulation of the nonlocal dielectric model reveals mass accumulation sites on a spherical conductor directly responding to prescribed potential on a larger spherical electrode. Such behavior may inspire new methods of manufacturing artificial compound eye structure on spherical domes, which is currently fabricated through an intricate laser lithography system (Y. Cheng et al., 2019). Based on the selective paths of mass transport in form of droplets observed in the simulation, it is also conceivable that our model can offer some key insight to the development of efficient feeding strategy in liquid metal ion source (LMIS) devices, the performance of which largely relies on transporting material from a liquid metal reservoir to the tungsten needle tip along the surface of a double-coil wire (Jaworek, 2006). In future work, it is straightforward to extend the energy-dissipation framework developed in the current work to incorporate other types of energy, for example, the elastic energy of deformable structures in a dielectric fluid transducer (Acome et al., 2018) which offers high actuation strain and robust muscle-like performance by applying Maxwell stresses on the walls of thin elastic channels filled with dielectric liquids.

Chapter 5

SHAPE ANALYSIS AND ENERGY STABILITY OF CONDUCTIVE LIQUIDS

5.1 Energy Stability of Electrically Charged Conductive Liquid

In 1882, Lord Rayleigh (1882) p resented a concise derivation on the theoretical estimate of the maximum amount of charge a nearly spherical liquid drop could carry while still maintaining stable, which is now known as the Rayleigh charge limit

$$Q_{\mathrm{Ra}} = 8\pi\sqrt{\sigma\varepsilon_0 R_c^3}. \tag{5.1}$$

Here R_c is the characteristic radius, σ is the surface tension coefficient and ε_0 is the vacuum permittivity. Rayleigh's prediction that a droplet reaching this limit would become unstable has been widely quoted since then and confirmed by careful experimental studies for many liquids and droplet sizes (Doyle, Moffett, and Vonnegut, 1964; Taflin, Ward, and E. J. Davis, 1989; Duft et al., 2003). In Rayleigh's original approach, the surface of a near-spherical liquid drop is explicitly parametrized by a series of azimuthally symmetric spherical harmonics multiplied by time-dependent coefficients. Under suitable assumptions, velocity and electric fields are expressed as the gradients of harmonic potentials, which can again be expanded in terms of spherical harmonics multiplied by some radial functions. These harmonic coefficients are then coupled through the kinematic condition at the free surface, exchanging their amplitudes provided the global conservation of kinematic and potential energies. To alleviate the overabundance of the omitted steps in Rayleigh's short communication, Hendricks and Schneider (1963) provided a detailed derivation for an inviscid and incompressible liquid drop, albeit still being ambiguous on the truncation of the first and second order terms. Along similar veins, Rayleigh's theory on the oscillation of electrified liquid drops was later extended to include various effects such as a uniform external electric field (G. I. Taylor, 1964), viscous dissipation (Morrison, Leavitt, and Wortman, 1981), rigid body rotation (Natarajan and R. A. Brown, 1987), the presence of counterions (Deserno, 2001), permittivity of the drop and the surrounding medium (Shrimpton, 2005) and internal inclusion of a highly charged ion (Oh et al., 2017).

All these work mentioned before specialize on spherical coordinate system with spherical harmonics for drop deformations. For drop shapes that are not perfectly spherical, method of spheroidal analysis was popularized by G. I. Taylor (1964). In his analysis, the shape of liquid body was assumed to be a prolate spheroid parametrized by its major radius and minor radius, which were found by satisfying the normal stress condition only at the pole and the equator but not at every point on the surface. Thinking alone the same lines, K. J. Cheng and Chaddock (1984) and K. J. Cheng and Chaddock (1986)

first developed a prototype of variational method from a consideration of the variation of free energy. Although a spheroidal liquid shape was still assumed in their work, instead of pursuing force balance on the surface of the spheroid they determined the deformation and equilibrium/instability criterion of spheroidal drops and bubbles from the extremization of total free energy of the conductive or dielectric liquid body over an eccentricity parameter subject to a constant-volume constraint. They were able to recover Taylor's result and predicted that a minimum energy configuration is always possible for bubbles.

The condition which an arbitrarily shaped conductive liquid body must satisfy in order to be in equilibrium requires a coordinate-free approach such as the variational method. Sujatha et al. (1983) and Chung, Cutler, Feuchtwang, et al. (1984) attempted a variational formalism of the equilibrium configurations of a perfectly conductive fluid kept at a fixed voltage by minimizing the total free energy associated with a volume-conserving liquid body. However, they treated surface charge density as a local variable, i.e. a function of the local geometric quantities described by the first and second derivatives only, rather than a shape functional of the complete surface. Hence their calculations may only be valid for very simple shapes. Later Ljepojevic and Forbes (1995) re-examined the variational problem of an electrified liquid using an Eulerian approach. By carefully tracking the leading order effect of geometric variations on the surface charge density, they managed to recovered the equilibrium condition, which is the familiar pressure balance between capillary and Maxwell stresses. However, due to lack of precise treatments on shape geometry, their first order calculation cannot to be carried out to the second order variation, which is crucial to the stability of charged liquid drop.

It is worth noting that Rayleigh's method is Eulerian: coordinates and potentials do not vary with deformation of the liquid body. The rational for the Eulerian point of view is challenging because functions defined on a reference domain need to be extended onto the deformed domain where these functions were not meant to exist in the first place. Despite the prevailing Eulerian approach in literature of free surface flow, Joseph (1973), inspired by his seminar work on the parametric domain dependence of eigenvalues of elliptic PDE (Joseph, 1967), drew attention to the conceptual and computational difficulties behind the Eulerian formalism commonly used in the derivation of the higher order water wave theory: expansion of the true velocity potential, which is defined for the wavy water domain, into a series of potential functions, which are defined only under the flat water surface, assumes these potentials can be continued analytically into that part of the wavy domain outside the flat domain. He then presented an alternative derivation by mapping the domain of complicated unknown configuration and the potentials defined within onto a relatively simple domain that is readily described by some curvilinear coordinate system. The method of domain variations, the prototype of which is attributed to Hadamard (1908), was developed based on this concept. Inspired

by the work of Joseph (1973), Feng (1997) revisited Rayleigh's result of an electrically charged conductive drop by means of the domain variation technique. However his calculation is limited to perfect spherical and cylindrical geometries only.

In the field of modern control theory, the problem of finding Rayleigh charge limit by extremizing the total potential energy falls into the category of shape optimization, i.e. finding the optimal shape which minimizes a certain cost functional (e.g., potential energy of the liquid drop) subject to constraints (in our case electrostatic equation in vacuum and volume conservation of the liquid) where the method of domain variations plays a central role. For example, H. Wang, L. Liu, and D. Liu (2017) reformulated the problem of determining the equilibrium shape of the bubble in an applied electric field as an energy minimization problem, based on which a fixed mesh level-set gradient method was implemented to simulate equilibrium shapes of wall-contacting bubbles in an electric field. For further references and recent development in the topic of shape optimization, we refer to the comprehensive textbooks (Henrot and Pierre, 2005; Sokolowski and Zolesio, 1992). In this chapter, we adhere to the development laid out in the work of Bandle and Wagner (2015) who computed the first and second domain variations for functionals related to second order elliptic boundary value and eigenvalue problems subject to Robin boundary conditions. Finally, regarding the existence and nonexistence of equilibrium shapes of charged liquid drops with or without constraints, we refer the interested readers to a series of mathematically rigorous works (Goldman, Novaga, and Ruffini, 2014; Goldman and Ruffini, 2017; Muratov, Novaga, and Ruffini, 2018) where the problem is carefully examined in a setting of functional analysis using Riesz potential and Riesz capacity.

In this chapter we would like to address three issues: first of all, we formulate the total potential energy of an isolated, charged, perfectly conductive, arbitrarily shaped liquid body based on the convective Lagrangian coordinates from continuum mechanics which allow systematic and geometrically precise treatments for arbitrary domain deformations. Secondly, in contrast to the usual small amplitude deformations normal to a spherical surface typically considered in the literature, we rigorously derive the constrained first and second order volume-conserving shape variations to the potential energy (electrostatic and surface energies) when liquid boundary undergoes both normal and tangential deformations. The equilibrium condition and stability criterion are also presented. Most importantly we discover that, for an equilibrium shape (if exits) with nonuniform mean curvature or surface charge distribution, there exist additional contributions to the second shape variation of the potential arising from the three-way coupling between normal, tangential deformation and mean curvature, which are entirely overlooked in the existing literature due to inadequate treatment on geometric deformation. Lastly, we recover the classical Rayleigh charge limit by applying the shape variations derived earlier to a perfect sphere. In particular we show that when a spherical liquid drop is charged below

the Rayleigh limit, the second shape variation to its total potential energy is a strictly positive quadratic functional and hence implies local stability in the energy landscape.

5.2 Lagrangian Specification in Continuum Mechanics

When the shape of domain is unknown *a priori*, it is convenient to introduce a coordinate system that follows the domain as it deforms, more commonly known as the convective Lagrangian coordinates which is the basis of continuum mechanics. Convective coordinates are especially important when non-mechanical physics such as electromagnetism occurs in the deformed medium. They are essential to the theory of relativity which does not acknowledge a universal simultaneity (Weile et al., 2013). The exposition of convective Lagrangian coordinates in this section follows the standard approach in continuum mechanics (Wriggers, 2008). Online lecture notes (Kelly, 2013) are found to be very helpful as well. For a more rigorous treatment on the subject, we refer to the classical textbook by Marsden and Hughes (1994) on mathematical elasticity.

Lagrangian description

In the Lagrangian description of continuum mechanics, regions in the three-dimensional ambient space $\mathbb{R}^3$ can be assigned to different configurations of the material body. The position and motion of a continuum body are tracked by a function of the particle position $\boldsymbol{X}$ in some fixed reference domain Ω. Let $\chi(\cdot,\cdot)$ be a smooth one-parameter function which maps some non-negative parameter ϵ and position vector $\boldsymbol{X} \in \Omega$ in the reference domain to another position vector $\boldsymbol{x}$ in the ambient space,

$$\boldsymbol{x} = \chi(\boldsymbol{X}, \epsilon) \quad \text{for} \quad \epsilon \geq 0. \tag{5.2}$$

In literature of continuum mechanics, function $\chi(\cdot,\epsilon)$ is called the configuration map, $\boldsymbol{X}$ is the material (or reference or Lagrangian) configuration and $\boldsymbol{x}$ is the spatial (or Eulerian) configuration. In a mechanical setting, ϵ is often treated as the time variable and $\boldsymbol{x}$ coincides with $\boldsymbol{X}$ in the ambient Euclidean space $\mathbb{R}^3$ initially at $\epsilon = 0$. Physically, if we attach a massless marker particle to position $\boldsymbol{X}$ of the continuum body at $\epsilon = 0$ and let the continuum body undergo transformation $\chi(\cdot,\epsilon)$, then $\boldsymbol{x}$ is the position of the same particle at $\epsilon = t$. The spatial domain

$$\omega = \{\boldsymbol{x} = \chi(\boldsymbol{X}, \epsilon) \mid \boldsymbol{X} \in \Omega, \epsilon \geq 0\} \tag{5.3}$$

represents the ensemble of particle positions evolving from the reference domain. In general ϵ doesn't have to be the time variable. It can represent any continuous parametric dependence of the mapping $\chi(\cdot,\epsilon)$.

We next introduce the material velocity

$$\boldsymbol{V}(\boldsymbol{X}, \epsilon) = \frac{\partial \chi(\boldsymbol{X}, \epsilon)}{\partial \epsilon} \tag{5.4}$$

to be the vectoriol rate at which the position of a particle initially labeled with material coordinate $\boldsymbol{X}$ changes with respect to parameter ϵ. Again if we take $\chi(\boldsymbol{X}, 0) = \boldsymbol{X}$ and ϵ to be time, then $\boldsymbol{V}(\boldsymbol{X}, \epsilon)$ is the velocity of the particle which starts out at the reference position $\boldsymbol{X}$ in Ω. The spatial counterpart of material velocity $\boldsymbol{V}(\boldsymbol{X}, \epsilon)$ is the spatial velocity

$$\boldsymbol{v}(\boldsymbol{x}, \epsilon) = \boldsymbol{V}(\chi^{-1}(\epsilon; \boldsymbol{x}), \epsilon) \tag{5.5}$$

which is the velocity vector of the particular marker particle currently occupying the spatial position $\boldsymbol{x}$. Here $\chi(\epsilon; \cdot) : \Omega \to \omega$ is the invertible configuration map when ϵ is held fixed. In the same spirit, a spatial scalar field $\phi(\boldsymbol{x}, \epsilon)$ in general can be viewed as a material field $\Phi(\boldsymbol{X}, \epsilon)$ if we identify

$$\Phi(\boldsymbol{X}, \epsilon) = \phi(\boldsymbol{x}(\boldsymbol{X}, \epsilon), \epsilon) \tag{5.6}$$

for all $\epsilon \geq 0$ in the valid range.

Convective curvilinear coordinate

Let the vectorial function $\boldsymbol{X}(\xi^1, \xi^2, \xi^3)$ denote the position vector of the material frame constructed out of coordinates (ξ^1, ξ^2, ξ^3) drawn from a subset O in the Euclidean space $\mathbb{E}^3$. Here we differentiate the ambient three-dimensional space $\mathbb{R}^3$ from the Euclidean parameter space $\mathbb{E}^3$ although both of them are flat spaces. The material coordinate curves, i.e. curves of constant ξ^i, form a net in the material configuration. The covariant basis $\boldsymbol{G}_i$ are the tangent vectors to these material coordinate curves ξ^i,

$$\boldsymbol{G}_i = \frac{\partial \boldsymbol{X}}{\partial \xi^i}, \quad \boldsymbol{G}^i \cdot \boldsymbol{G}_j = \delta^i_j, \quad G_{ij} = \boldsymbol{G}_i \cdot \boldsymbol{G}_j, \tag{5.7}$$

where $\boldsymbol{G}^i$ are the contravariant basis vectors and G_{ij} are the metric coefficients (δ^i_j is the Kronecker delta). Given knowledge of the configuration map $\chi(\cdot, \epsilon)$, we can express the spatial coordinates $\boldsymbol{x}$ at $\epsilon \geq 0$ in terms of the same curvilinear coordinates as well,

$$\boldsymbol{x}(\xi^1, \xi^2, \xi^3) = \chi(\boldsymbol{X}(\xi^1, \xi^2, \xi^3), \epsilon). \tag{5.8}$$

The covariant and contravariant basis vectors, $\boldsymbol{g}_i$ and $\boldsymbol{g}^i$ of the spatial curvilinear coordinates are given by

$$\boldsymbol{g}_i = \frac{\partial \boldsymbol{x}}{\partial \xi^i}, \quad \boldsymbol{g}^i \cdot \boldsymbol{g}_j = \delta^i_j, \quad g_{ij} = \boldsymbol{g}_i \cdot \boldsymbol{g}_j, \tag{5.9}$$

where g_{ij} is the spatial metric coefficient. The curvilinear coordinates $\boldsymbol{x}$ are said to be convective if coordinate curves are attached to material particles and deform with the body so that each material particle has the same parameter coordinates (ξ^1, ξ^2, ξ^3) in both the material configuration $\boldsymbol{X}$ and spatial configuration $\boldsymbol{x}$. The mapping triad between parametrization $(\xi^1, \xi^2, \xi^3) \in O \subset \mathbb{E}^3$, material configuration $\boldsymbol{X} \in \Omega \subset \mathbb{R}^3$ and spatial configuration $\boldsymbol{x} \in \omega \subset \mathbb{R}^3$ is illustrated in figure 5.1. A useful fact to have

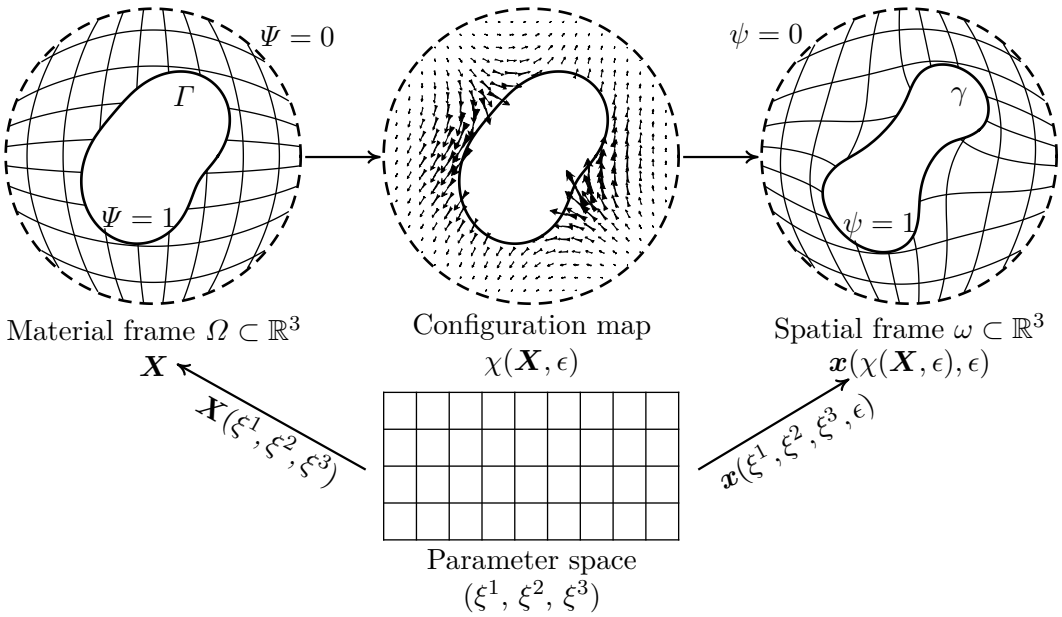

Figure 5.1: Triad of parameter, material and spatial frames: material coordinates $\boldsymbol{X}$ send (ξ^1, ξ^2, ξ^3) from the parameter space $\mathbb{E}^3$ into the material frame Ω in the ambient space $\mathbb{R}^3$ with boundary Γ; Spatial frame ω and its boundary γ in $\mathbb{R}^3$ are convected from the material coordinates $\boldsymbol{X}$ through the configuration map $\chi(\cdot, \epsilon)$; the composition of $\chi(\boldsymbol{X}, \epsilon)$ and $\boldsymbol{X}(\xi^1, \xi^2, \xi^3)$ can be viewed as a set of curvilinear coordinates $\boldsymbol{x}(\xi^1, \xi^2, \xi^3)$ drawn from the parameter space. The thin solid curves are the coordinate lines in each frame while the thick solid curves represent the boundaries Γ and γ of the same conductor (white region) before and after deformation. The material harmonic potential Ψ and its spatial counterpart ψ remain equipotential on these boundaries. The dashed lines are immobile boundaries of the vacuum domain exterior to the conductor.

in mind is that, despite being curvilinear, both $\boldsymbol{x}(\xi^1, \xi^2, \xi^3)$ and $\boldsymbol{X}(\xi^1, \xi^2, \xi^3)$ are a re-parametrization of the ambient three-dimensional space $\mathbb{R}^3$ which is Euclidean, flat and torsion-free.

In what follows, we use operator $\boldsymbol{D}(\cdot)$ to represent the (covariant) gradient vector with respect to material coordinates $\boldsymbol{X}$ and $\boldsymbol{d}(\cdot)$ with respect to spatial coordinates $\boldsymbol{x}$. For example, when $\boldsymbol{D}$ (or $\boldsymbol{d}$) acts on a scalar field Φ (or ϕ) we have

$$\boldsymbol{D}\Phi = \frac{\partial \Phi}{\partial \xi^i}\boldsymbol{G}^i, \quad \boldsymbol{d}\phi = \frac{\partial \phi}{\partial \xi^i}\boldsymbol{g}^i. \tag{5.10}$$

When gradient $\boldsymbol{D}$ (or $\boldsymbol{d}$) acts on a vector field, the resulting object becomes a rank-2 tensor,

$$\boldsymbol{D}\boldsymbol{V} = \frac{\partial \boldsymbol{V}}{\partial \xi^i} \otimes \boldsymbol{G}^i, \quad \boldsymbol{d}\boldsymbol{v} = \frac{\partial \boldsymbol{v}}{\partial \xi^i} \otimes \boldsymbol{g}^i. \tag{5.11}$$

The deformation gradient tensor

$$\boldsymbol{F} = \boldsymbol{D}\boldsymbol{x} = \frac{\partial \boldsymbol{x}}{\partial \xi^i} \otimes \boldsymbol{G}^i \tag{5.12}$$

is defined as the gradient of spatial configuration $\boldsymbol{x}$ with respect to material coordinates $\boldsymbol{X}$. The deformation gradient $\boldsymbol{F}$ is a two-point tensor which maps the tangent space of the material configuration at position $\boldsymbol{X} \in \Omega$ to the tangent space of the spatial configuration at position $\boldsymbol{x} \in \omega$. With convective curvilinear coordinates (ξ^1, ξ^2, ξ^3), it's easy to show that $\boldsymbol{F}$ behaves like a linear operator that transforms the covariant basis vectors $\boldsymbol{G}_i$ at $\boldsymbol{X}$ of the material frame into the covariant basis vectors $\boldsymbol{g}_i$ at $\boldsymbol{x}$ of the spatial frame,

$$\boldsymbol{F} = \boldsymbol{g}_i \otimes \boldsymbol{G}^i, \quad \boldsymbol{F}\boldsymbol{G}_i = \boldsymbol{g}_i. \tag{5.13}$$

In addition to the deformation gradient $\boldsymbol{F}$, its transpose, inverse and inverse-transpose are two-point tensors as well which map a set of basis vectors from one frame onto the other (Kelly, 2013),

$$\left.\begin{aligned} \boldsymbol{F}^{-1} &= \boldsymbol{G}_i \otimes \boldsymbol{g}^i, \quad \boldsymbol{F}^{-1}\boldsymbol{g}_i = \boldsymbol{G}_i, \\ \boldsymbol{F}^{\top} &= \boldsymbol{G}^i \otimes \boldsymbol{g}_i, \quad \boldsymbol{F}^{\top}\boldsymbol{g}^i = \boldsymbol{G}^i, \\ \boldsymbol{F}^{-\top} &= \boldsymbol{g}^i \otimes \boldsymbol{G}_i, \quad \boldsymbol{F}^{-\top}\boldsymbol{G}^i = \boldsymbol{g}^i. \end{aligned}\right\} \tag{5.14}$$

With various two-point tensors introduced in (5.14), the material gradient of a scalar field $\Phi(\boldsymbol{X})$ and the spatial gradient of its spatial counterpart $\phi(\boldsymbol{x})$ can be transformed back and forth through the relations,

$$\boldsymbol{d}\phi = (\boldsymbol{D}\Phi)\boldsymbol{F}^{-1}, \quad \boldsymbol{d}\boldsymbol{v} = (\boldsymbol{D}\boldsymbol{V})\boldsymbol{F}^{-1}. \tag{5.15}$$

It is convenient to introduce the right Cauchy-Green tensor $\boldsymbol{C}$ and its inverse $\boldsymbol{C}^{-1}$,

$$\boldsymbol{C} = \boldsymbol{F}^{\top}\boldsymbol{F}, \quad \boldsymbol{C}^{-1} = \boldsymbol{F}^{-1}\boldsymbol{F}^{-\top}. \tag{5.16}$$

Physically, the Cauchy–Green tensor $\boldsymbol{C}$ measures the squared local change in distances due to body deformation as $\boldsymbol{G}^i\boldsymbol{C}\boldsymbol{G}_i = \boldsymbol{g}^i \cdot \boldsymbol{g}_i$. In the same fashion, we define the velocity gradient as a measure of the rate at which a material is deforming. It's common to use the spatial velocity gradient tensor

$$\boldsymbol{l} = \boldsymbol{d}\boldsymbol{v}. \tag{5.17}$$

The differential volume element of the material configuration $\boldsymbol{X}$ is given by

$$\mathrm{d}\Omega = \sqrt{G}\,\mathrm{d}\xi^1\mathrm{d}\xi^2\mathrm{d}\xi^3, \quad G = \det G_{ij}, \tag{5.18}$$

where G is the determinant of material metric tensor G_{ij}. Similarly, the volume element of the spatial configuration $\boldsymbol{x}$ is given by the determinant g of the spatial metric tensor g_{ij},

$$\mathrm{d}\omega = \sqrt{g}\,\mathrm{d}\xi^1\mathrm{d}\xi^2\mathrm{d}\xi^3. \tag{5.19}$$

Since $\boldsymbol{F}$ is the essentially the Jacobian matrix of $\boldsymbol{x}(\boldsymbol{X}, \epsilon)$, the material volume element $\mathrm{d}\Omega$ and the spatial volume element $\mathrm{d}\omega$ are related through the relation,

$$\mathrm{d}\omega = J\,\mathrm{d}\Omega, \quad J = \det \boldsymbol{F}, \tag{5.20}$$

where J is the coordinate Jacobian. A similar identity exists for the differential area elements. Let Γ (or γ) be the boundary of the material (or spatial) domain Ω (or ω) and $\boldsymbol{N}$ (or $\boldsymbol{n}$) be the unit normal vector of the boundary. The material differential area element $\mathrm{d}\Gamma$ is related to the spatial area element $\mathrm{d}\gamma$ by the Nanson's formula (Wriggers, 2008)

$$\boldsymbol{n}\,\mathrm{d}\gamma = J\boldsymbol{F}^{-\top}\boldsymbol{N}\,\mathrm{d}\Gamma. \tag{5.21}$$

Kinematics: rate of quantities

We next consider how fields transform when material body undergoes deformation. The total change of a scalar field at a spatial coordinate $\boldsymbol{x}$ following a material particle initially labeled with position $\boldsymbol{X}$ is given by the chain rule,

$$\frac{\mathrm{d}\phi(\boldsymbol{x},\epsilon)}{\mathrm{d}\epsilon} = \frac{\mathrm{d}\phi(\boldsymbol{x}(\boldsymbol{X},\epsilon),\epsilon)}{\mathrm{d}\epsilon} = \frac{\partial\phi(\boldsymbol{x},\epsilon)}{\partial\epsilon} + \boldsymbol{v}(\boldsymbol{x},\epsilon)\cdot\boldsymbol{d}\phi\cdot. \tag{5.22}$$

Following the convention in literature of shape analysis, we define

$$\phi'(\boldsymbol{x},\epsilon) = \frac{\partial\phi(\boldsymbol{x},\epsilon)}{\partial\epsilon} \tag{5.23}$$

to be the Eulerian derivative of ϕ and

$$\dot{\phi}(\boldsymbol{x},\epsilon) = \phi'(\boldsymbol{x},\epsilon) + \boldsymbol{v}(\boldsymbol{x},\epsilon)\cdot\boldsymbol{d}\phi(\boldsymbol{x},\epsilon) \tag{5.24}$$

to be the material derivative of ϕ. The name "material derivative" stems from the observation that, alternatively the total derivative (5.22) of spatial field $\phi(\boldsymbol{x},\epsilon)$ is equivalent to the partial derivative of its material counterpart $\Phi(\boldsymbol{X},\epsilon)$,

$$\dot{\phi}(\boldsymbol{x},\epsilon) = \frac{\mathrm{d}\phi(\boldsymbol{x},\epsilon)}{\mathrm{d}\epsilon} = \frac{\mathrm{d}\phi(\boldsymbol{x}(\boldsymbol{X},\epsilon),\epsilon)}{\mathrm{d}\epsilon} = \frac{\partial\Phi(\boldsymbol{X},\epsilon)}{\partial\epsilon}. \tag{5.25}$$

It can be shown that the time derivatives of various forms of deformation gradient tensor $\boldsymbol{F}$ can be expressed in terms of the spatial velocity gradient $\boldsymbol{l}$,

$$\frac{\partial\boldsymbol{F}}{\partial\epsilon} = \boldsymbol{l}\boldsymbol{F},\quad \frac{\partial\boldsymbol{F}^{-1}}{\partial\epsilon} = -\boldsymbol{F}^{-1}\boldsymbol{l},\quad \frac{\partial\boldsymbol{F}^{\top}}{\partial\epsilon} = \boldsymbol{F}^{\top}\boldsymbol{l}^{\top},\quad \frac{\partial\boldsymbol{F}^{-\top}}{\partial\epsilon} = -\boldsymbol{l}^{\top}\boldsymbol{F}^{-\top}. \tag{5.26}$$

The Eulerian derivative of spatial velocity gradient is frequently encountered in this work. If we introduce the material and spatial accelerations,

$$\dot{\boldsymbol{V}} = \frac{\partial^2\chi(\boldsymbol{X},\epsilon)}{\partial\epsilon^2},\quad \dot{\boldsymbol{v}} = \dot{\boldsymbol{V}}(\chi^{-1}(\epsilon;\boldsymbol{x}),\epsilon), \tag{5.27}$$

then $\partial\boldsymbol{l}/\partial\epsilon$ can be computed as

$$\frac{\partial\boldsymbol{l}}{\partial\epsilon} = \frac{\partial\boldsymbol{d}\boldsymbol{v}}{\partial\epsilon} = \frac{\partial(\boldsymbol{D}\boldsymbol{V})\boldsymbol{F}^{-1}}{\partial\epsilon} = \boldsymbol{D}\Big(\frac{\partial\boldsymbol{V}}{\partial\epsilon}\Big)\boldsymbol{F}^{-1} - (\boldsymbol{D}\boldsymbol{V})\boldsymbol{F}^{-1}\boldsymbol{l} = \boldsymbol{d}\dot{\boldsymbol{v}} - \boldsymbol{l}\boldsymbol{l}, \tag{5.28}$$

where we have used (5.26) and (5.15) to simplify. Here $\boldsymbol{d}\dot{\boldsymbol{v}}$, similar to spatial velocity gradient $\boldsymbol{l} = \boldsymbol{d}\boldsymbol{v}$, is the spatial acceleration gradient. A similar expression can be derived for the transposed quantity, i.e. $\partial\boldsymbol{l}^{\top}/\partial\epsilon = (\partial\boldsymbol{l}/\partial\epsilon)^{\top}$.

The rate at which spatial volume element changes is given by the first partial derivative of Jacobian J with respect to ϵ,

$$\frac{\partial J}{\partial \epsilon} = (\det \boldsymbol{F})\mathrm{tr}\left(\frac{\partial \boldsymbol{F}}{\partial \epsilon}\boldsymbol{F}^{-1}\right) = J\mathrm{div}\boldsymbol{v}, \tag{5.29}$$

where the divergence operator div is understood to act on the spatial vector fields (Div acts on material vectors). Differentiating $\partial J/\partial\epsilon$ again yields the second partial derivative of Jacobian J,

$$\begin{aligned}
\frac{\partial^2 J}{\partial \epsilon^2} &= \frac{\partial}{\partial \epsilon}\left[(\det \boldsymbol{F})\mathrm{tr}\left(\frac{\partial \boldsymbol{F}}{\partial \epsilon}\boldsymbol{F}^{-1}\right)\right] \\
&= \frac{\partial J}{\partial \epsilon}\mathrm{tr}(\boldsymbol{I}\boldsymbol{F}\boldsymbol{F}^{-1}) + J\mathrm{tr}\left(\frac{\partial^2 \boldsymbol{F}}{\partial \epsilon^2}\boldsymbol{F}^{-1}\right) + J\mathrm{tr}\left(\frac{\partial \boldsymbol{F}}{\partial \epsilon}\frac{\partial \boldsymbol{F}^{-1}}{\partial \epsilon}\right) \\
&= J\left\{(\mathrm{div}\boldsymbol{v})\mathrm{tr}(\boldsymbol{I}) + \mathrm{tr}\Big[\boldsymbol{D}\Big(\frac{\partial \boldsymbol{x}}{\partial \epsilon^2}\Big)\boldsymbol{F}^{-1}\Big] - \mathrm{tr}(\boldsymbol{I}\boldsymbol{F}\boldsymbol{F}^{-1}\boldsymbol{I})\right\} \\
&= J\left[(\mathrm{div}\boldsymbol{v})^2 + \mathrm{div}(\dot{\boldsymbol{v}}) - \mathrm{tr}(\boldsymbol{I}\boldsymbol{I})\right],
\end{aligned} \tag{5.30}$$

which we will use later.

5.3 Electrostatic Energy and Shape Variations of a Perfect Conductor

In this section, we exclusively focus on the electrostatic energy of a perfect conductor stored in the vacuum and its first and second shape variations when the boundary of the conductor undergoes deformation.

Electrostatic energy and self-capacitance

For a perfect conductor, the total electrostatic energy stored in the free space is the volume integral of electrostatic energy density exterior to the conductor. Let Ω be the volume of surrounding vacuum exterior to the conductor and Γ be the surface of the conductor. Then the electrostatic energy $\mathcal{E}[\Omega]$ of the conductor is given by

$$\mathcal{E}[\Omega] = \int_{\Omega} \frac{1}{2}\varepsilon_0 |\boldsymbol{E}|^2 \,\mathrm{d}\Omega \tag{5.31}$$

where $\boldsymbol{E} = -\boldsymbol{D}\Psi$ is the electric field of a harmonic potential Ψ satisfying the Dirichlet problem,

$$\left.\begin{aligned}
\mathrm{Div}\boldsymbol{D}\Psi &= 0 \quad \text{in} \quad \Omega, \\
\Psi &= \Psi_0 \quad \text{on} \quad \Gamma, \\
\Psi &= 0 \quad \text{everywhere else.}
\end{aligned}\right\} \tag{5.32}$$

We assume electric potential Ψ vanishes at either infinity (e.g., isolated charged drop) or on any other boundary that's not part of the conductor (e.g., external electrode). Potential difference Ψ_0 is a constant and can be either directly prescribed (e.g. a constant potential drop held between conductor and electrode) or indirectly determined (e.g., an appropriate value such that total physical charge on the surface of the conductor

is conserved). Electrostatic energy (5.31), albeit in the form of a volume integral, is completely determined by the shape of the boundary. More explicitly, by Green's identity and the fact Ψ is harmonic in the vacuum phase, electrostatic energy $\mathcal{E}$ can be put into the form of a shape functional of the boundary Γ,

$$\mathcal{E}[\Gamma] = \int_\Gamma \frac{1}{2}\varepsilon_0 \Psi_0 \boldsymbol{E} \cdot (-\boldsymbol{N})\, \mathrm{d}\Gamma, \tag{5.33}$$

where $\boldsymbol{N}$ is defined to be the surface (outward) normal vector pointing from vacuum into the conductor. It's convenient to work with a rescaled version of Dirichlet problem (5.32),

$$\left.\begin{aligned} \mathrm{Div}\boldsymbol{D}\Psi = 0 \quad &\text{in} \quad \Omega, \\ \Psi = 1 \quad &\text{on} \quad \Gamma, \\ \Psi = 0 \quad &\text{everywhere else.} \end{aligned}\right\} \tag{5.34}$$

Now if we introduce the self-capacitance funcitonal

$$\mathcal{C}[\Gamma] = \int_\Gamma \boldsymbol{E} \cdot (-\boldsymbol{N})\, \mathrm{d}\Gamma = \int_\Omega \boldsymbol{D}\Psi \cdot \boldsymbol{D}\Psi \, \mathrm{d}\Omega, \tag{5.35}$$

then the physical self-capacitance C and the total physical charge Q can be expressed as

$$C = \varepsilon_0 \mathcal{C}[\Gamma], \quad Q = \Psi_0 C. \tag{5.36}$$

We therefore recover the classical capacitance-charge-potential relation

$$\mathcal{E}[\Gamma] = \frac{1}{2}\Psi_0^2 C = \frac{1}{2}\Psi_0 Q = \frac{1}{2}\frac{Q^2}{C}. \tag{5.37}$$

Thus to understand variations in the electrostatic energy of a conductor, it suffices to study the properties of the self-capacitance functional $\mathcal{C}[\Gamma]$ defined in equation (5.35) instead of the original unscaled energy $\mathcal{E}[\Gamma]$ in (5.31). An advantage of working with self-capacitance (5.35) is that, we have a single recipe to the variations of electrostatic energy when either potential difference Ψ_0 or total charge Q is held constant,

$$\left.\begin{aligned} \delta\mathcal{E}[\Gamma] &= +\frac{1}{2}\Psi_0^2 C \frac{\delta\mathcal{C}[\Gamma]}{\mathcal{C}[\Gamma]} \qquad \text{for a fixed potential } \Psi_0, \\ \delta\mathcal{E}[\Gamma] &= -\frac{1}{2}\frac{Q^2}{C}\frac{\delta\mathcal{C}[\Gamma]}{\mathcal{C}[\Gamma]} \qquad \text{for a fixed total charge } Q. \end{aligned}\right\} \tag{5.38}$$

Precise notion of the shape variation $\delta\mathcal{C}[\Gamma]$ can be built from concepts of continuum mechanics developed in Section 5.2. Suppose we have a configuration map $\chi(\cdot, \epsilon)$ which transforms the conductor boundary Γ to a new shape γ and the vacuum region Ω to a new volume ω. We identify $\boldsymbol{X} \in \Omega$ as the material (reference) frame and $\boldsymbol{x} \in \omega$ as the spatial (deformed) frame. Aside from regularity requirements (smoothness, boundness, etc.), we do not impose constraints on $\chi(\cdot, \epsilon)$ interior to the vacuum. Later it turns out that it is irrelevant how material coordinates $\boldsymbol{X} \in \Omega$ are mapped to the spatial

region $\boldsymbol{x} \in \omega$ as long as $\chi(\cdot, \epsilon)$ transforms the conductor boundary $\boldsymbol{X} \in \Gamma$ to the new boundary $\boldsymbol{x} \in \gamma$.

The notion of the first shape variation of capacitance functional $\mathcal{C}[\Gamma]$ (formally known as Gateaux derivative) is defined as the infinitesimal change in the capacitance as vacuum domain Ω deforms to ω under a particular choice of configuration mapping $\boldsymbol{x} = \chi(\boldsymbol{X}, \epsilon)$ (Kasumba and Kunisch, 2014),

$$\delta^{(1)}\mathcal{C}[\Omega; \chi] = \frac{\mathrm{d}\mathcal{C}[\omega]}{\mathrm{d}\epsilon}\Big|_{\epsilon=0} = \lim_{\epsilon \downarrow 0^+} \frac{\mathcal{C}[\omega] - \mathcal{C}[\Omega]}{\epsilon}. \tag{5.39}$$

Definition (5.39) can be generalized to higher order shape variations such as the second variation $\delta^{(2)}\mathcal{C}[\Omega; \chi]$ by taking derivative of first shape variation. There are two major obstacles in computing the variations of capacitance $\mathcal{C}[\gamma]$: First of all, it's obvious that changes in geometry would directly affect the volume integral in capacitance functional (5.35). Secondly, the new harmonic electric potential ψ now satisfies the Laplace equation not in the undeformed vacuum region Ω of material frame but the deformed region ω of spatial frame. In addition to pure geometric considerations, calculation of capacitance $\mathcal{C}[\omega]$ must also take the new potential ψ into account instead of Ψ. It's not apparent that how to directly compare the two potentials $\psi(\boldsymbol{x} \in \omega)$ and $\Psi(\boldsymbol{X} \in \Omega)$ defined on two different regions. In the following section, we address these issues using the convective Lagrangian coordinates introduced in Section 5.2.

First shape variation of self-capacitance

Recall ψ is the harmonic potential satisfying the Laplace equation in the deformed vacuum region ω with equipotential boundary condition on the new boundary γ,

$$\left.\begin{aligned} \mathrm{div}\boldsymbol{d}\psi = 0 \quad &\text{in} \quad \omega, \\ \psi = 1 \quad &\text{on} \quad \gamma, \\ \psi = 0 \quad &\text{otherwise.} \end{aligned}\right\} \tag{5.40}$$

In the spatial frame ω, capacitance functional

$$\mathcal{C}[\omega] = \int_{\omega} \boldsymbol{d}\psi \cdot \boldsymbol{d}\psi \, \mathrm{d}\omega \tag{5.41}$$

has the standard form of a Dirichlet energy. We transform capacitance functional back to the reference configuration $\boldsymbol{X} \in \Omega$ where coordinates are fixed but instead the map $\chi(\cdot, \epsilon)$ varies with ϵ. Using gradient transformations between the spatial and material frames introduced in (5.15), we can evaluate capacitance functional using material coordinates,

$$\mathcal{C}[\Omega, \epsilon] = \int_{\Omega} \boldsymbol{D}\Psi \boldsymbol{C}^{-1} \boldsymbol{D}\Psi J \, \mathrm{d}\Omega. \tag{5.42}$$

The total derivative of capacitance $\mathcal{C}[\omega]$ in ϵ now becomes the partial derivative of $\mathcal{C}[\Omega, \epsilon]$ in ϵ. Since material domain Ω is fixed, we can interchange the order of volume

integration and partial differentiation with respect to ϵ,

$$\frac{\mathrm{d}\mathcal{C}[\omega]}{\mathrm{d}\epsilon} = \frac{\partial \mathcal{C}[\Omega,\epsilon]}{\partial \epsilon} = \int_{\Omega} \boldsymbol{D}\Psi \frac{\partial \boldsymbol{C}^{-1}J}{\partial \epsilon}\boldsymbol{D}\Psi + 2\boldsymbol{D}\Psi \boldsymbol{C}^{-1}J\frac{\partial \boldsymbol{D}\Psi}{\partial \epsilon}\,\mathrm{d}\Omega. \tag{5.43}$$

Recall material gradient $\boldsymbol{D}$ and $\partial/\partial\epsilon$ commute. We can simplify the second term that appears in integral (5.43),

$$\begin{aligned}\int_{\Omega} \boldsymbol{D}\Psi \boldsymbol{C}^{-1}J\frac{\partial \boldsymbol{D}\Psi}{\partial \epsilon}\,\mathrm{d}\Omega = \int_{\Omega} \boldsymbol{D}\Psi \boldsymbol{C}^{-1}\boldsymbol{D}\frac{\partial \Psi}{\partial \epsilon}J\,\mathrm{d}\Omega = \int_{\omega} \boldsymbol{d}\psi\cdot\boldsymbol{d}\dot{\psi}\,\mathrm{d}\omega \\ = \int_{\omega} -\dot{\psi}\,\mathrm{div}(\boldsymbol{d}\psi)\,\mathrm{d}\omega + \int_{\gamma}\dot{\psi}\,\boldsymbol{n}\cdot\boldsymbol{d}\psi\,\mathrm{d}\gamma,\end{aligned} \tag{5.44}$$

where the last line we apply Green's identity in spatial frame. Recall from equation (5.40) that ψ is expected to be harmonic everywhere in the spatial frame which immediately eliminates the volume integral in (5.44). Dirichlet boundary condition $\psi(\boldsymbol{x}\in\gamma)=1$ must be enforced in every spatial frame mapped by the configuration $\chi(\boldsymbol{X},\epsilon)$ which means the material time derivative of ψ must vanish on γ for all ϵ. Hence $\psi(\boldsymbol{x})$, being the solution to equation (5.40), completely eliminates the second integral in equation (5.43). As for the first volume integral in equation (5.43), we observe that

$$\frac{\partial \boldsymbol{C}^{-1}J}{\partial \epsilon} = \boldsymbol{C}^{-1}\frac{\partial J}{\partial \epsilon} - \boldsymbol{F}^{-1}(\boldsymbol{I}+\boldsymbol{I}^{\top})\boldsymbol{F}^{-\top}J. \tag{5.45}$$

Substituting expression (5.45) back to the first total derivative (5.43) and converting to spatial frame yield a spatial volume integral,

$$\frac{\mathrm{d}\mathcal{C}[\omega]}{\mathrm{d}\epsilon} = \int_{\omega}\boldsymbol{d}\psi(\mathrm{div}\boldsymbol{v}-\boldsymbol{I}-\boldsymbol{I}^{\top})\boldsymbol{d}\psi\,\mathrm{d}\omega. \tag{5.46}$$

The form of expression (5.46) is not satisfactory due to its volume-integral nature. As we discussed before, the capacitance functional $\mathcal{C}[\omega]$ should be interpreted more precisely as $\mathcal{C}[\gamma]$ since the solution ψ to the Dirichlet problem (5.40) is completely determined by the boundary shape γ alone. Intuitively speaking, how configuration map $\chi(\boldsymbol{X},\epsilon)$ and its derivatives in ϵ behave interior to the domain should have no effect on capacitance except the prescribed deformation on the boundary. We must be able to show that volume integral (5.46) can be recast into a pure surface integral which only involves interfacial information on γ. To see this, we first perform integration by parts on the first term of expression (5.46),

$$\int_{\omega}(\boldsymbol{d}\psi\cdot\boldsymbol{d}\psi)\mathrm{div}\boldsymbol{v}\,\mathrm{d}\omega = \int_{\gamma}\boldsymbol{n}\cdot\boldsymbol{v}(\boldsymbol{d}\psi\cdot\boldsymbol{d}\psi)\,\mathrm{d}\gamma - \int_{\omega}\boldsymbol{v}\cdot\boldsymbol{d}(\boldsymbol{d}\psi\cdot\boldsymbol{d}\psi)\,\mathrm{d}\omega. \tag{5.47}$$

We then note the following identity using index notation,

$$\begin{aligned}2\mathrm{div}((\boldsymbol{v}\cdot\boldsymbol{d}\psi)\boldsymbol{d}\psi) &= 2\nabla_i((v^j\nabla_j\psi)\nabla^i\psi) \\ &= 2(\nabla_i v^j)(\nabla_j\psi)(\nabla^i\psi) + 2v^j(\nabla_i\nabla_j\psi)(\nabla^i\psi) && \text{Harmonic} \\ &= (\nabla_j\psi)(\nabla_i v^j+\nabla_j v^i)(\nabla^i\psi) + 2v^j(\nabla_j\nabla_i\psi)\nabla^i\psi && \text{Torsion free} \\ &= (\nabla_j\psi)(\nabla_i v^j+\nabla_j v^i)(\nabla^i\psi) + v^j\nabla_j((\nabla^i\psi)\nabla_i\psi) \\ &= \boldsymbol{d}\psi(\boldsymbol{I}+\boldsymbol{I}^{\top})\boldsymbol{d}\psi + \boldsymbol{v}\cdot\boldsymbol{d}(\boldsymbol{d}\psi\cdot\boldsymbol{d}\psi).\end{aligned} \tag{5.48}$$

Substitution of identity (5.48) into equation (5.47) cancels out all volume integrals in (5.46) except one in the divergence form $\propto \mathrm{div}(\cdot)$. A straight forward application of divergence theorem in spatial coordinates concludes the first total derivative of capacitance functional

$$\frac{\mathrm{d}\mathcal{C}[\omega]}{\mathrm{d}\epsilon} = \int_\gamma (\boldsymbol{v}\cdot\boldsymbol{n})|\boldsymbol{d}\psi|^2 - 2(\boldsymbol{v}\cdot\boldsymbol{d}\psi)(\boldsymbol{n}\cdot\boldsymbol{d}\psi)\,\mathrm{d}\gamma. \tag{5.49}$$

If the solution $\psi(\boldsymbol{x})$ to the Dirichlet problem (5.40) is known for some configuration $\chi(\cdot,\epsilon)$, we can compute the rate of change in the capacitance $\mathcal{C}[\omega]$ by evaluating the integral defined in the first total derivative (5.49). We would like to point out that, the integrand in (5.49) is in fact the familiar Maxwell stress tensor $\boldsymbol{t}$ (up to a factor of 2),

$$\frac{\mathrm{d}\mathcal{C}[\omega]}{\mathrm{d}\epsilon} = \int_\gamma \boldsymbol{n}\boldsymbol{t}\boldsymbol{v}\,\mathrm{d}\gamma, \quad \boldsymbol{t} = |\boldsymbol{d}\psi|^2\mathbb{I} - 2\boldsymbol{d}\psi\otimes\boldsymbol{d}\psi. \tag{5.50}$$

This is no surprise since we are calculating the variation of electrostatic energy which is precisely the physical interpretation of Maxwell stress tensor in a homogeneous isotropic medium. The first shape derivative (or variation) $\delta^{(1)}\mathcal{C}[\Gamma;\boldsymbol{V}]$ is defined as (Sokolowski and Zolesio, 1992)

$$\delta^{(1)}\mathcal{C}[\Gamma;\boldsymbol{V}] = \int_\Gamma (\boldsymbol{V}\cdot\boldsymbol{N})|\boldsymbol{D}\Psi|^2 - 2(\boldsymbol{V}\cdot\boldsymbol{D}\Psi)(\boldsymbol{N}\cdot\boldsymbol{D}\Psi)\,\mathrm{d}\Gamma, \tag{5.51}$$

where all quantities in (5.51) are understood to be evaluated at $\epsilon = 0$. In fact for a perfect conductor, we know electric field on its boundary is the normal direction only. Hence we recover the usual electrostatic pressure (up to a factor of $1/2$),

$$\delta^{(1)}\mathcal{C}[\Gamma;\boldsymbol{V}] = \int_\Gamma -(\boldsymbol{V}\cdot\boldsymbol{N})(\boldsymbol{N}\cdot\boldsymbol{E})^2\,\mathrm{d}\Gamma, \tag{5.52}$$

which is the result that Ljepojevic and Forbes (1995) arrived at, except our approach is more systematic and rigorous in light of convective Lagrangian coordinates.

Equation for Eulerian derivative ψ'

Although the first total derivative (5.49) of capacitance $\mathcal{C}[\omega]$ doesn't involve any variation in ψ, as we shall see later, the Eulerian derivative ψ' of ψ is required for the second total derivative of $\mathcal{C}[\omega]$ in ϵ. In this section we derive a boundary value problem that ψ' must satisfy. Note we have already encountered the boundary condition for ψ' on γ which comes from the spatial Dirichlet condition on ψ,

$$\dot{\psi} = \psi' + \boldsymbol{v}\cdot\boldsymbol{d}\psi = 0 \quad \text{on} \quad \gamma. \tag{5.53}$$

Deriving the governing equation of $\psi'(\boldsymbol{x})$ in the spatial frame ω is more involved. We begin with transforming the harmonicity of ψ everywhere in the spatial frame back to the material frame,

$$\mathrm{div}\,\boldsymbol{d}\psi = \frac{1}{J}\mathrm{Div}(J\boldsymbol{C}^{-1}\boldsymbol{D}\Psi) = 0 \quad \text{in} \quad \Omega. \tag{5.54}$$

Note the Laplace equation (5.54) must be fulfilled for every configuration $\chi(\cdot,\epsilon)$. Hence differentiating (5.54) with respect to ϵ on both sides yields

$$0=-\frac{\partial J}{\partial\epsilon}\frac{1}{J^2}\mathrm{Div}(J\boldsymbol{C}^{-1}\boldsymbol{D}\Psi)+\frac{1}{J}\mathrm{Div}\Big(J\boldsymbol{C}^{-1}\boldsymbol{D}\frac{\partial\Psi}{\partial\epsilon}\Big)+\frac{1}{J}\mathrm{Div}\Big(\frac{\partial J\boldsymbol{C}^{-1}}{\partial\epsilon}\boldsymbol{D}\Psi\Big). \tag{5.55}$$

With the help of identities (5.54) and (5.45), after some rearrangements we arrive at an equation for ψ' in spatial frame,

$$\mathrm{div}\boldsymbol{d}\psi'=-\mathrm{div}[(\mathrm{div}\boldsymbol{v}-\boldsymbol{I}-\boldsymbol{I}^{\top})\boldsymbol{d}\psi+\boldsymbol{d}(\boldsymbol{v}\cdot\boldsymbol{d}\psi)]. \tag{5.56}$$

We next show that entire right hand side of equation (5.56) is in fact identically zero. To simplify notation, we use $b_k\equiv\nabla_k\psi$ and $b^k\equiv\nabla^k\psi$ to denote the covariant and contracovariant components of $\boldsymbol{d}\psi$ for shorthand. Each term on the right hand side of equation (5.56) can be expanded in index notation of covariant differentiation,

$$\begin{aligned}
\mathrm{div}\boldsymbol{d}(\boldsymbol{v}\cdot\boldsymbol{d}\psi)&=\nabla_i\nabla^i v^k\nabla_k\psi\\
&=\nabla_i g^{ij}\nabla_j(v^k b_k)\\
&=\nabla_i g^{ij}[b_k(\nabla_j v^k)+v^k(\nabla_j b_k)]\\
&=b_k\nabla_i(g^{ij}\nabla_j v^k)+(\nabla^j b_k)(\nabla_j v^k)+(\nabla_j b_k)(\nabla_i g^{ij}v^k)+v^k\nabla_i g^{ij}\nabla_j b_k\\
&=b_k\nabla^i\nabla_i v^k+2(\nabla^j b_k)(\nabla_j v^k)+v^k g^{ij}\nabla_i\nabla_j\nabla_k\psi]\\
&=b_k\nabla^i\nabla_i v^k+2(\nabla^j b_k)(\nabla_j v^k)+v^k g^{ij}\nabla_i\nabla_k\nabla_j\psi] \qquad \text{Torsion free}\\
&=b_k\nabla^i\nabla_i v^k+2(\nabla^j b_k)(\nabla_j v^k)+v^k g^{ij}\nabla_k\nabla_i\nabla_j\psi] \qquad \text{Flat}\\
&=b_k\nabla^i\nabla_i v^k+2(\nabla^j b_k)(\nabla_j v^k)+v^k\nabla_k\nabla_i\nabla^i\psi]\\
&=b_k\nabla^i\nabla_i v^k+2(\nabla^i b_k)(\nabla_i v^k), \qquad \text{Harmonic}
\end{aligned} \tag{5.57}$$

$$\begin{aligned}
\mathrm{div}((\mathrm{div}\boldsymbol{v})\boldsymbol{d}\psi)&=\nabla_i((\nabla_k v^k)\nabla^i\psi)\\
&=b^i\nabla_i\nabla_k v^k+(\nabla_k v^k)\nabla_i\nabla^i\psi\\
&=b^i\nabla_i\nabla_k v^k, \qquad \text{Harmonic}
\end{aligned} \tag{5.58}$$

$$\begin{aligned}
\mathrm{div}(-\boldsymbol{I}\boldsymbol{d}\psi)&=-\nabla_k((\nabla_i v^k)\nabla^i\psi)\\
&=-b^i(\nabla_k\nabla_i v^k)-(\nabla_i v^k)(\nabla_k b^i)\\
&=-b^i(\nabla_i\nabla_k v^k)-(\nabla_i v^k)(\nabla_k b^i) \qquad \text{Flat}\\
&=-b^i(\nabla_i\nabla_k v^k)-(\nabla_i v^k)(g^{ij}\nabla_k\nabla_j\psi)\\
&=-b^i(\nabla_i\nabla_k v^k)-(\nabla_i v^k)(g^{ij}\nabla_j\nabla_k\psi) \qquad \text{Torsion free}\\
&=-b^i(\nabla_i\nabla_k v^k)-(\nabla_i v^k)(\nabla^i b_k), \qquad \text{Torsion free}
\end{aligned} \tag{5.59}$$

$$\begin{aligned}
\mathrm{div}(-\boldsymbol{I}^{\top}\boldsymbol{d}\psi)&=-\nabla_k((\nabla^k v_i)\nabla^i\psi)\\
&=-b^i(\nabla_k\nabla^k v_i)-(\nabla^k v_i)(\nabla_k b^i).
\end{aligned} \tag{5.60}$$

As promised, all terms in the summation of (5.57), (5.58), (5.59) and (5.60) exactly cancel out with each other and in turn eliminate the entire right hand side of equation

(5.56). Therefore the equation for Eulerian derivative ψ' is again the Laplace equation in the spatial frame but this time with a nontrivial Dirichlet boundary condition depending on the interaction between spatial potential ψ and spatial velocity $\boldsymbol{v}$,

$$\left.\begin{aligned} \operatorname{div} \boldsymbol{d}\psi' &= 0 && \text{in} \quad \omega, \\ \psi' &= -\boldsymbol{v}\cdot\boldsymbol{d}\psi && \text{on} \quad \gamma. \end{aligned}\right\} \tag{5.61}$$

Second shape variation of self-capacitance

The second derivative of capacitance functional $\mathcal{C}$ with respect to ϵ is again evaluated in the material frame,

$$\frac{\mathrm{d}^2\mathcal{C}[\omega]}{\mathrm{d}\epsilon^2} = \int_\Omega \boldsymbol{D}\Psi \frac{\partial^2 \boldsymbol{C}^{-1}J}{\partial\epsilon^2}\boldsymbol{D}\Psi + 2\boldsymbol{D}\Psi\frac{\partial \boldsymbol{C}^{-1}J}{\partial\epsilon}\boldsymbol{D}\frac{\partial\Psi}{\partial\epsilon} + \boldsymbol{D}\Psi\boldsymbol{C}^{-1}J\boldsymbol{D}\frac{\partial^2\Psi}{\partial\epsilon^2}\,\mathrm{d}\Omega. \tag{5.62}$$

We note that the last integrand in (5.62) is almost identical to the one we encountered in the first variation (5.43). In spatial frame, $\partial^2\Psi/\partial\epsilon^2$ becomes the second material time derivative $\ddot{\psi}$ which must vanish on γ for the similar reasoning that leads to the boundary condition $\dot{\psi}=0$ on γ for the first derivative $\mathrm{d}\mathcal{C}[\omega]/\mathrm{d}\epsilon$. Therefore it eliminates the last integrand in (5.62).

We next transform the second integral in equation (5.62) into a more symmetric form,

$$\begin{aligned} &\int_\Omega \boldsymbol{D}\Psi\frac{\partial \boldsymbol{C}^{-1}J}{\partial\epsilon}\boldsymbol{D}\frac{\partial\Psi}{\partial\epsilon}\,\mathrm{d}\Omega \\ &= \int_\Gamma \boldsymbol{N}\frac{\partial\Psi}{\partial\epsilon}\frac{\partial \boldsymbol{C}^{-1}J}{\partial\epsilon}\boldsymbol{D}\Psi\,\mathrm{d}\Gamma - \int_\Omega \frac{\partial\Psi}{\partial\epsilon}\operatorname{Div}\frac{\partial \boldsymbol{C}^{-1}J}{\partial\epsilon}\boldsymbol{D}\Psi\,\mathrm{d}\Omega \\ &= \int_\Gamma \boldsymbol{N}\frac{\partial\Psi}{\partial\epsilon}\frac{\partial \boldsymbol{C}^{-1}J}{\partial\epsilon}\boldsymbol{D}\Psi\,\mathrm{d}\Gamma + \int_\Omega \frac{\partial\Psi}{\partial\epsilon}\operatorname{Div}\Big(J\boldsymbol{C}^{-1}\boldsymbol{D}\frac{\partial\Psi}{\partial\epsilon}\Big)\,\mathrm{d}\Omega \\ &= \int_\gamma \dot{\psi}\boldsymbol{n}(\operatorname{div}\boldsymbol{v}-\boldsymbol{I}-\boldsymbol{I}^\top)\boldsymbol{d}\psi\,\mathrm{d}\gamma + \int_\gamma \dot{\psi}(\boldsymbol{n}\cdot\boldsymbol{d}\dot{\psi})\,\mathrm{d}\gamma - \int_\Omega \Big(\boldsymbol{D}\frac{\partial\Psi}{\partial\epsilon}\Big)\boldsymbol{C}^{-1}J\boldsymbol{D}\frac{\partial\Psi}{\partial\epsilon}\,\mathrm{d}\Omega, \end{aligned} \tag{5.63}$$

where in the third line we apply the identity (5.55) derived earlier,

$$\operatorname{Div}\Big(J\boldsymbol{C}^{-1}\boldsymbol{D}\frac{\partial\Psi}{\partial\epsilon}\Big) = -\operatorname{Div}\Big(\frac{\partial J\boldsymbol{C}^{-1}}{\partial\epsilon}\boldsymbol{D}\Psi\Big). \tag{5.64}$$

Applying Dirichlet constraint $\dot{\psi}=0$ on γ to (5.63) yields the second total derivative of capacitance functional $\mathcal{C}[\omega]$ in ϵ,

$$\frac{\mathrm{d}^2\mathcal{C}[\omega]}{\mathrm{d}\epsilon^2} = \int_\Omega \boldsymbol{D}\Psi\frac{\partial^2\boldsymbol{C}^{-1}J}{\partial\epsilon^2}\boldsymbol{D}\Psi - 2\Big(\boldsymbol{D}\frac{\partial\Psi}{\partial\epsilon}\Big)\boldsymbol{C}^{-1}J\boldsymbol{D}\frac{\partial\Psi}{\partial\epsilon}\,\mathrm{d}\Omega. \tag{5.65}$$

In order to proceed from here, we must evaluate the second Eulerian derivative in (5.65). Standard product rule yields

$$\frac{\partial^2\boldsymbol{C}^{-1}J}{\partial\epsilon^2} = \frac{\partial^2\boldsymbol{C}^{-1}}{\partial\epsilon^2}J + 2\frac{\partial\boldsymbol{C}^{-1}}{\partial\epsilon}\frac{\partial J}{\partial\epsilon} + \boldsymbol{C}^{-1}\frac{\partial^2 J}{\partial\epsilon^2}. \tag{5.66}$$

We then lift the second Eulerian derivative of $\boldsymbol{C}^{-1}$ to the spatial frame,

$$\begin{aligned}\frac{\partial^2 \boldsymbol{C}^{-1}}{\partial \epsilon^2} &= \frac{\partial^2 \boldsymbol{F}^{-1}}{\partial \epsilon^2}\boldsymbol{F}^{-\top} + 2\frac{\partial \boldsymbol{F}^{-1}}{\partial \epsilon}\frac{\partial \boldsymbol{F}^{-\top}}{\partial \epsilon} + \boldsymbol{F}^{-1}\frac{\partial^2 \boldsymbol{F}^{-\top}}{\partial \epsilon^2} \\ &= -\frac{\partial \boldsymbol{F}^{-1}\boldsymbol{I}}{\partial \epsilon}\boldsymbol{F}^{-\top} + 2\boldsymbol{F}^{-1}\boldsymbol{I}\boldsymbol{I}^{\top}\boldsymbol{F}^{-\top} - \boldsymbol{F}^{-1}\frac{\partial \boldsymbol{I}^{\top}\boldsymbol{F}^{-\top}}{\partial \epsilon} \\ &= \boldsymbol{F}^{-1}(\boldsymbol{I}\boldsymbol{I} + 2\boldsymbol{I}\boldsymbol{I}^{\top} + \boldsymbol{I}^{\top}\boldsymbol{I}^{\top})\boldsymbol{F}^{-\top} - \boldsymbol{F}^{-1}\frac{\partial \boldsymbol{I} + \boldsymbol{I}^{\top}}{\partial \epsilon}\boldsymbol{F}^{-\top} \\ &= \boldsymbol{F}^{-1}(2\boldsymbol{I}\boldsymbol{I} + 2\boldsymbol{I}\boldsymbol{I}^{\top} + 2\boldsymbol{I}^{\top}\boldsymbol{I}^{\top} - \boldsymbol{d}\dot{\boldsymbol{v}} - \boldsymbol{d}\dot{\boldsymbol{v}}^{\top})\boldsymbol{F}^{-\top}, \end{aligned} \tag{5.67}$$

where the last line we use the identity (5.28) of the material time derivative of $\boldsymbol{v}$. Substituting expressions (5.67) and (5.30) into identity (5.66) transforms the material form (5.62) of the second total derivative of capacitance functional $\mathcal{C}[\omega]$ into a spatial form,

$$\begin{aligned}\frac{\mathrm{d}^2\mathcal{C}[\omega]}{\mathrm{d}\epsilon^2} = \int_{\omega} \boldsymbol{d}\psi\Big\{&2(\boldsymbol{I}\boldsymbol{I} + \boldsymbol{I}\boldsymbol{I}^{\top} + \boldsymbol{I}^{\top}\boldsymbol{I}^{\top}) - \boldsymbol{d}\dot{\boldsymbol{v}} - \boldsymbol{d}\dot{\boldsymbol{v}}^{\top} \\ &+ (\mathrm{div}\boldsymbol{v})^2 - \mathrm{tr}(\boldsymbol{I}\boldsymbol{I}) + \mathrm{div}\dot{\boldsymbol{v}} \\ &- 2(\mathrm{div}\boldsymbol{v})(\boldsymbol{I} + \boldsymbol{I}^{\top})\Big\}\boldsymbol{d}\psi - 2\boldsymbol{d}\dot{\psi}\cdot\boldsymbol{d}\dot{\psi}\,\mathrm{d}\omega. \end{aligned} \tag{5.68}$$

By exploiting symmetries of the quadratic forms in expression (5.68) we rewrite the second total derivative of capacitance functional as the sum of four volume integrals,

$$\frac{\mathrm{d}^2\mathcal{C}[\omega]}{\mathrm{d}\epsilon^2} = \mathcal{I}_1 + \mathcal{I}_2 + \mathcal{I}_3 + \mathcal{I}_4, \tag{5.69}$$

where the integrals $\mathcal{I}_1$, $\mathcal{I}_2$, $\mathcal{I}_3$ and $\mathcal{I}_4$ are given by

$$\mathcal{I}_1 = \int_{\omega} \boldsymbol{d}\psi\big[4\boldsymbol{I}\boldsymbol{I} + 2\boldsymbol{I}\boldsymbol{I}^{\top} - 4\boldsymbol{I}(\mathrm{div}\boldsymbol{v})\big]\boldsymbol{d}\psi\,\mathrm{d}\omega, \tag{5.70}$$

$$\mathcal{I}_2 = \int_{\omega} \Big[(\mathrm{div}\boldsymbol{v})^2 - \mathrm{tr}(\boldsymbol{I}\boldsymbol{I})\Big]\,(\boldsymbol{d}\psi\cdot\boldsymbol{d}\psi)\,\mathrm{d}\omega, \tag{5.71}$$

$$\mathcal{I}_3 = \int_{\omega} -2\boldsymbol{d}\psi'\cdot\boldsymbol{d}\psi' - 4\boldsymbol{d}\psi'\cdot\boldsymbol{d}(\boldsymbol{v}\cdot\boldsymbol{d}\psi) - 2\boldsymbol{d}(\boldsymbol{v}\cdot\boldsymbol{d}\psi)\cdot\boldsymbol{d}(\boldsymbol{v}\cdot\boldsymbol{d}\psi)\,\mathrm{d}\omega, \tag{5.72}$$

$$\mathcal{I}_4 = \int_{\omega} \boldsymbol{d}\psi(\mathrm{div}\dot{\boldsymbol{v}} - \boldsymbol{d}\dot{\boldsymbol{v}} - \boldsymbol{d}\dot{\boldsymbol{v}}^{\top})\boldsymbol{d}\psi\,\mathrm{d}\omega. \tag{5.73}$$

We would like show that the sum of volume integrals (5.70)–(5.73) can be recast into a collection of pure surface integrals because as we discussed before the details of deformation interior to the vacuum region shouldn't matter.

To start we first note the identity

$$\boldsymbol{d}(\boldsymbol{v}\cdot\boldsymbol{d}\psi) = \nabla_i(v^j\nabla_j\psi) = (\nabla_i v^j)\nabla_j\psi + v^j\nabla_i\nabla_j\psi = \boldsymbol{I}^{\top}\boldsymbol{d}\psi + (\boldsymbol{d}^2\psi)\boldsymbol{v}, \tag{5.74}$$

where $\boldsymbol{d}^2\psi = \boldsymbol{d}(\boldsymbol{d}\psi)$ is a rank-2 tensor. Applying the identity (5.74) to integral $\mathcal{I}_1$ yields

$$\begin{aligned}
\mathcal{I}_1 &= 2\int_\omega \boldsymbol{d}\psi\big[2\boldsymbol{II} + \boldsymbol{II}^\top - 2\boldsymbol{I}(\mathrm{div}\boldsymbol{v})\big]\boldsymbol{d}\psi\,\mathrm{d}\omega \\
&= 2\int_\omega \boldsymbol{d}\psi\big[\boldsymbol{II} - \boldsymbol{I}(\mathrm{div}\boldsymbol{v})\big]\boldsymbol{d}\psi\,\mathrm{d}\omega - 2\int_\omega (\boldsymbol{I}^\top\boldsymbol{d}\psi)\cdot\big[(\mathrm{div}\boldsymbol{v}) - \boldsymbol{I} - \boldsymbol{I}^\top\big]\boldsymbol{d}\psi\,\mathrm{d}\omega \\
&= 2\int_\omega \boldsymbol{d}\psi\big[\boldsymbol{II} - \boldsymbol{I}(\mathrm{div}\boldsymbol{v})\big]\boldsymbol{d}\psi\,\mathrm{d}\omega + 2\int_\omega (\boldsymbol{v}\cdot\boldsymbol{d}^2\psi)\cdot\big[(\mathrm{div}\boldsymbol{v}) - \boldsymbol{I} - \boldsymbol{I}^\top\big]\boldsymbol{d}\psi\,\mathrm{d}\omega \\
&+ 2\int_\omega (\boldsymbol{v}\cdot\boldsymbol{d}\psi)\mathrm{div}\big[(\mathrm{div}\boldsymbol{v} - \boldsymbol{I} - \boldsymbol{I}^\top)\boldsymbol{d}\psi\big]\,\mathrm{d}\omega - 2\int_\gamma (\boldsymbol{v}\cdot\boldsymbol{d}\psi)\boldsymbol{n}\cdot\big[(\mathrm{div}\boldsymbol{v} - \boldsymbol{I} - \boldsymbol{I}^\top)\boldsymbol{d}\psi\big]\,\mathrm{d}\gamma \\
&= 2\int_\omega \boldsymbol{d}\psi\big[\boldsymbol{II} - \boldsymbol{I}(\mathrm{div}\boldsymbol{v})\big]\boldsymbol{d}\psi\,\mathrm{d}\omega + 2\int_\omega (\boldsymbol{v}\cdot\boldsymbol{d}^2\psi)\cdot\big[(\mathrm{div}\boldsymbol{v}) - \boldsymbol{I} - \boldsymbol{I}^\top\big]\boldsymbol{d}\psi\,\mathrm{d}\omega \\
&- 2\int_\omega (\boldsymbol{v}\cdot\boldsymbol{d}\psi)\mathrm{div}\boldsymbol{d}(\boldsymbol{v}\cdot\boldsymbol{d}\psi)\,\mathrm{d}\omega - 2\int_\gamma (\boldsymbol{v}\cdot\boldsymbol{d}\psi)\boldsymbol{n}\cdot\big[(\mathrm{div}\boldsymbol{v} - \boldsymbol{I} - \boldsymbol{I}^\top)\boldsymbol{d}\psi\big]\,\mathrm{d}\gamma, \quad (5.75)
\end{aligned}$$

where for the last equality we have used the fact shown earlier that the right hand side of equation (5.56) is zero. We next consider another identity relevant to integral $\mathcal{I}_2$,

$$\begin{aligned}
\mathrm{div}\big\{\big[(\mathrm{div}\boldsymbol{v})\boldsymbol{v} - \boldsymbol{I}\boldsymbol{v}\big]|\boldsymbol{d}\psi|^2\big\} &= \nabla_i\big\{\big[(\nabla_j v^j)v^i - (\nabla_j v^i)v^j\big](\nabla_k\psi)(\nabla^k\psi)\big\} \\
&= \big[(\nabla_j v^j)(\nabla_i v^i) - (\nabla_j v^i)(\nabla_i v^j)\big](\nabla_k\psi)(\nabla^k\psi) \\
&\quad + \big[(\nabla_i\nabla_j v^j)v^i - (\nabla_i\nabla_j v^i)v^j\big](\nabla_k\psi)(\nabla^k\psi) \\
&\quad + \big[(\nabla_j v^j)v^i - (\nabla_j v^i)v^j\big]2(\nabla_k\psi)(\nabla_i\nabla^k\psi) \\
&= \big[(\mathrm{div}\boldsymbol{v})^2 - \mathrm{tr}(\boldsymbol{II})\big]|\boldsymbol{d}\psi|^2 + 2\boldsymbol{v}\big(\mathrm{div}\boldsymbol{v} - \boldsymbol{I}^\top\big)\boldsymbol{d}^2\psi\boldsymbol{d}\psi \quad (5.76)
\end{aligned}$$

Applying the above identity (5.76) to integral $\mathcal{I}_2$, we get

$$\begin{aligned}
\mathcal{I}_2 &= \int_\omega \Big[(\mathrm{div}\boldsymbol{v})^2 - \mathrm{tr}(\boldsymbol{II})\Big]\,(\boldsymbol{d}\psi\cdot\boldsymbol{d}\psi)\,\mathrm{d}\omega \\
&= \int_\omega \mathrm{div}\Big\{\big[(\mathrm{div}\boldsymbol{v})\boldsymbol{v} - \boldsymbol{I}\boldsymbol{v}\big]|\boldsymbol{d}\psi|^2\Big\}\,\mathrm{d}\omega - \int_\omega 2(\mathrm{div}\boldsymbol{v})\boldsymbol{d}\psi(\boldsymbol{d}^2\psi)\boldsymbol{v}\,\mathrm{d}\omega \\
&\quad + \int_\omega 2\boldsymbol{d}\psi(\boldsymbol{d}^2\psi)\boldsymbol{I}\boldsymbol{v}\,\mathrm{d}\omega, \quad (5.77)
\end{aligned}$$

where the symmetry of tensor $\boldsymbol{d}^2\psi$ is evoked to arrive at the last line. As for integral $\mathcal{I}_3$, we apply the Green's identity and integrate by parts,

$$\begin{aligned}
\mathcal{I}_3 &= \int_\omega -2\boldsymbol{d}\psi'\cdot\boldsymbol{d}\psi' - 4\boldsymbol{d}\psi'\cdot\boldsymbol{d}(\boldsymbol{v}\cdot\boldsymbol{d}\psi) - 2\boldsymbol{d}(\boldsymbol{v}\cdot\boldsymbol{d}\psi)\cdot\boldsymbol{d}(\boldsymbol{v}\cdot\boldsymbol{d}\psi)\,\mathrm{d}\omega \\
&= \int_\omega 2(\mathrm{div}\boldsymbol{d}\psi')\psi' + 4(\mathrm{div}\boldsymbol{d}\psi')(\boldsymbol{v}\cdot\boldsymbol{d}\psi) + 2(\mathrm{div}\boldsymbol{d}(\boldsymbol{v}\cdot\boldsymbol{d}\psi))(\boldsymbol{v}\cdot\boldsymbol{d}\psi)\,\mathrm{d}\omega \\
&\quad - \int_\gamma \boldsymbol{n}\cdot\big[2\psi'(\boldsymbol{d}\psi') + 4(\boldsymbol{v}\cdot\boldsymbol{d}\psi)(\boldsymbol{d}\psi') + 2(\boldsymbol{v}\cdot\boldsymbol{d}\psi)(\boldsymbol{d}(\boldsymbol{v}\cdot\boldsymbol{d}\psi))\big]\,\mathrm{d}\gamma. \quad (5.78)
\end{aligned}$$

Recall from equation (5.61) that ψ' must be harmonic which immediately eliminates two integrands in $\mathcal{I}_3$. After summing up contributions from $\mathcal{I}_1$ in (5.75), $\mathcal{I}_2$ in (5.77) and

$\mathcal{J}_3$ in (5.78) altogether, we are left with a combination of volume and surface integrals,

$$\begin{aligned}\mathcal{J}_1+\mathcal{J}_2+\mathcal{J}_3 = 2\int_\omega \boldsymbol{d}\psi\big[\boldsymbol{II}-\boldsymbol{I}(\mathrm{div}\boldsymbol{v})\big]\boldsymbol{d}\psi - \boldsymbol{v}(\boldsymbol{d}^2\psi)(\boldsymbol{I}+\boldsymbol{I}^\top)\boldsymbol{d}\psi + \boldsymbol{d}\psi(\boldsymbol{d}^2\psi)\boldsymbol{I}\boldsymbol{v}\,\mathrm{d}\omega\\ +\int_\gamma \boldsymbol{n}\cdot\big[(\mathrm{div}\boldsymbol{v})\boldsymbol{v}-\boldsymbol{I}\boldsymbol{v}\big]|\boldsymbol{d}\psi|^2\,\mathrm{d}\gamma\\ -2\int_\gamma (\boldsymbol{v}\cdot\boldsymbol{d}\psi)\boldsymbol{n}\cdot\big[(\mathrm{div}\boldsymbol{v}-\boldsymbol{I}-\boldsymbol{I}^\top)\boldsymbol{d}\psi\big]\,\mathrm{d}\gamma\\ -2\int_\gamma \boldsymbol{n}\cdot\big[\psi'(\boldsymbol{d}\psi')+2(\boldsymbol{v}\cdot\boldsymbol{d}\psi)(\boldsymbol{d}\psi')+(\boldsymbol{v}\cdot\boldsymbol{d}\psi)\boldsymbol{d}(\boldsymbol{v}\cdot\boldsymbol{d}\psi)\big]\,\mathrm{d}\gamma.\end{aligned}\tag{5.79}$$

Now it's only a straightforward exercise to convert the volume integrals in $\mathcal{J}_1+\mathcal{J}_2+\mathcal{J}_3$ to pure surface integrals. Consider one of the integrals in equation (5.79),

$$-\int_\omega (\boldsymbol{d}\psi\boldsymbol{I}\boldsymbol{d}\psi)(\mathrm{div}\boldsymbol{v})\,\mathrm{d}\omega = \int_\omega \boldsymbol{v}\cdot\boldsymbol{d}(\boldsymbol{d}\psi\boldsymbol{I}\boldsymbol{d}\psi)\,\mathrm{d}\omega - \int_\gamma (\boldsymbol{n}\cdot\boldsymbol{v})(\boldsymbol{d}\psi\boldsymbol{I}\boldsymbol{d}\psi)\,\mathrm{d}\gamma.\tag{5.80}$$

We observe that the volume integral in (5.80) can be split into two pieces,

$$\begin{aligned}&\boldsymbol{v}\cdot\boldsymbol{d}(\boldsymbol{d}\psi\boldsymbol{I}\boldsymbol{d}\psi)\\ &= v^k\nabla_k((\nabla_j\psi)(\nabla_i v^j)(\nabla^i\psi))\\ &= v^k(\nabla_j\psi)(\nabla_i v^j)(\nabla_k\nabla^i\psi)+v^k(\nabla_k\nabla_j\psi)(\nabla_i v^j)(\nabla^i\psi)+v^k(\nabla_j\psi)(\nabla_k\nabla_i v^j)(\nabla^i\psi)\\ &= v^k(\nabla_k\nabla^i\psi)(\nabla_i v^j)(\nabla_j\psi)+v^k(\nabla_k\nabla_i\psi)(\nabla_j v^i)(\nabla^j\psi)+(\nabla_j\psi)(v^k\nabla_k\nabla_i v^j)(\nabla^i\psi)\\ &= \boldsymbol{v}(\boldsymbol{d}^2\psi)(\boldsymbol{I}+\boldsymbol{I}^\top)\boldsymbol{d}\psi+(\nabla_j\psi)(v^k\nabla_i\nabla_k v^j)(\nabla^i\psi). \qquad \text{Flat}\end{aligned}\tag{5.81}$$

The first term in equation (5.81) exactly cancels out the second integrand in the volume integral (5.79) which leaves us with the only integrand of the volume integral in $\mathcal{J}_1+\mathcal{J}_2+\mathcal{J}_3$,

$$\begin{aligned}&(\nabla_j\psi)(v^k\nabla_i\nabla_k v^j)(\nabla^i\psi)+\boldsymbol{d}\psi\boldsymbol{I}\boldsymbol{I}\boldsymbol{d}\psi+\boldsymbol{d}\psi(\boldsymbol{d}^2\psi)\boldsymbol{I}\boldsymbol{v}\\ &=(\nabla_j\psi)(v^k\nabla_i\nabla_k v^j)(\nabla^i\psi)+(\nabla_j\psi)(\nabla_k v^j)(\nabla_i v^k)(\nabla^i\psi)+(\nabla_i\psi)(\nabla^i\nabla_j\psi)(\nabla_k v^j)v^k\\ &=(\nabla_j\psi)(\nabla^i\psi)(v^k\nabla_i\nabla_k v^j+(\nabla_k v^j)(\nabla_i v^k))+(\nabla_i\psi)(\nabla^i\nabla_j\psi)(v^k\nabla_k v^j)\\ &=(\nabla_j\psi)(\nabla^i\psi)\nabla_i(v^k\nabla_k v^j)+\nabla^i((\nabla_i\psi)(\nabla_j\psi))(v^k\nabla_k v^j)-(\nabla^i\nabla_i\psi)(\nabla_j\psi)(v^k\nabla_k v^j)\\ &=(\nabla_j\psi)(\nabla^i\psi)\nabla_i(v^k\nabla_k v^j)+\nabla_i((\nabla^i\psi)(\nabla_j\psi))(v^k\nabla_k v^j) \qquad \text{Harmonic}\\ &=\nabla_i\Big[v^k(\nabla_k v^j)(\nabla_j\psi)(\nabla^i\psi)\Big]=\mathrm{div}[(\boldsymbol{v}\boldsymbol{I}^\top\boldsymbol{d}\psi)\boldsymbol{d}\psi].\end{aligned}\tag{5.82}$$

After a straightforward use of divergence theorem, the sum of volume integrals $\mathcal{J}_1+\mathcal{J}_2+\mathcal{J}_3$ defined in equation (5.70)–(5.72) simplifies to a collection of pure surface integrals as it must,

$$\begin{aligned}\mathcal{J}_1+\mathcal{J}_2+\mathcal{J}_3 = 2\int_\gamma (\boldsymbol{n}\cdot\boldsymbol{d}\psi)(\boldsymbol{v}\boldsymbol{I}^\top\boldsymbol{d}\psi)-(\boldsymbol{n}\cdot\boldsymbol{v})(\boldsymbol{d}\psi\boldsymbol{I}\boldsymbol{d}\psi)\,\mathrm{d}\gamma\\ +\int_\gamma \boldsymbol{n}\cdot\big[(\mathrm{div}\boldsymbol{v})\boldsymbol{v}-\boldsymbol{I}\boldsymbol{v}\big]|\boldsymbol{d}\psi|^2\,\mathrm{d}\gamma\\ -2\int_\gamma (\boldsymbol{v}\cdot\boldsymbol{d}\psi)\boldsymbol{n}\cdot\big[(\mathrm{div}\boldsymbol{v}-\boldsymbol{I}-\boldsymbol{I}^\top)\boldsymbol{d}\psi\big]\,\mathrm{d}\gamma\\ -2\int_\gamma \boldsymbol{n}\cdot\big[\psi'(\boldsymbol{d}\psi')+2(\boldsymbol{v}\cdot\boldsymbol{d}\psi)(\boldsymbol{d}\psi')+(\boldsymbol{v}\cdot\boldsymbol{d}\psi)\boldsymbol{d}(\boldsymbol{v}\cdot\boldsymbol{d}\psi)\big]\,\mathrm{d}\gamma.\end{aligned}\tag{5.83}$$

We note that the form of integral $\mathcal{J}_4$ is almost identical to the first total derivative (5.46) of the capacitance functional except for spatial velocity vector $\boldsymbol{v}$ replaced by spatial acceleration $\dot{\boldsymbol{v}}$. Hence the surface integral contribution from $\mathcal{J}_4$ shares the same functional form with the first shape variation,

$$\mathcal{J}_4 = \int_\gamma (\dot{\boldsymbol{v}} \cdot \boldsymbol{n})|\boldsymbol{d}\psi|^2 - 2(\dot{\boldsymbol{v}} \cdot \boldsymbol{d}\psi)(\boldsymbol{n} \cdot \boldsymbol{d}\psi)\,\mathrm{d}\gamma. \tag{5.84}$$

After substituting $\mathcal{J}_1 + \mathcal{J}_2 + \mathcal{J}_3$ from (5.83) and $\mathcal{J}_4$ from (5.84) into (5.69), we arrive at the second total derivative of capacitance functional $\mathcal{C}[\omega]$ as a sum of spatial surface integrals only,

$$\begin{aligned}
\frac{\mathrm{d}^2\mathcal{C}[\gamma]}{\mathrm{d}\epsilon^2} = {} & 2\int_\gamma (\boldsymbol{n} \cdot \boldsymbol{d}\psi)(\boldsymbol{v}\boldsymbol{I}^\top \boldsymbol{d}\psi) - (\boldsymbol{n} \cdot \boldsymbol{v})(\boldsymbol{d}\psi \boldsymbol{I} \boldsymbol{d}\psi)\,\mathrm{d}\gamma \\
& + \int_\gamma \left[(\mathrm{div}\boldsymbol{v})(\boldsymbol{n} \cdot \boldsymbol{v}) - \boldsymbol{n}\boldsymbol{I}\boldsymbol{v}\right]|\boldsymbol{d}\psi|^2\,\mathrm{d}\gamma \\
& -2\int_\gamma (\boldsymbol{v} \cdot \boldsymbol{d}\psi)\left[\boldsymbol{n}(\mathrm{div}\boldsymbol{v} - \boldsymbol{I})\boldsymbol{d}\psi\right]\mathrm{d}\gamma \\
& -2\int_\gamma (\boldsymbol{v} \cdot \boldsymbol{d}\psi)\boldsymbol{n}(\boldsymbol{d}^2\psi)\boldsymbol{v}\,\mathrm{d}\gamma \\
& -2\int_\gamma (\boldsymbol{v} \cdot \boldsymbol{d}\psi)(\boldsymbol{n} \cdot \boldsymbol{d}\psi')\,\mathrm{d}\gamma \\
& + \int_\gamma (\dot{\boldsymbol{v}} \cdot \boldsymbol{n})|\boldsymbol{d}\psi|^2 - 2(\dot{\boldsymbol{v}} \cdot \boldsymbol{d}\psi)(\boldsymbol{n} \cdot \boldsymbol{d}\psi)\,\mathrm{d}\gamma,
\end{aligned} \tag{5.85}$$

where shape derivative ψ' is the harmonic potential which solves the Dirichlet problem (5.61) posed on the spatial domain ω. From now on, we officially replace the notation $\mathcal{C}[\omega]$ with $\mathcal{C}[\gamma]$.

Second shape variation in boundary-adapted coordinates

To gain more insight into the surface integrals in the second total derivative (5.85) of capacitance functional $\mathcal{C}[\gamma]$, we introduce an adapted coordinate frame (ξ^1, ξ^2, ξ^3) for vectors and tensors in the neighbourhood of conductor surface γ,

$$\boldsymbol{x}(\xi^1, \xi^2, \xi^3) = \boldsymbol{x}_\gamma(\xi^1, \xi^2) + \xi^3 \boldsymbol{n}. \tag{5.86}$$

The image of map $\boldsymbol{x}_\gamma(\xi^1, \xi^2)$ corresponds to the conductor surface γ and ξ^3 describes the distance away from the in the direction normal to the surface. Under surface-adapted coordinate system, a direct consequence of the equipotential condition defined in the Dirichlet problem (5.40) is $\nabla_3\psi$ being the only non-zero component of $\boldsymbol{d}\psi$ evaluated on the boundary γ,

$$\nabla_i\psi = \delta_3^j \nabla_j\psi \quad \text{on} \quad \gamma, \tag{5.87}$$

which leads to tremendous simplifications in the first three integrals of the second total derivative (5.85). Evaluating the integrands of the first two integrals in (5.85) on the

conductor surface γ in terms of surface-adapted coordinate system yields

$$\begin{aligned}
&2(\boldsymbol{n}\cdot\boldsymbol{d}\psi)(\boldsymbol{v}\boldsymbol{I}^{\top}\boldsymbol{d}\psi)-(\boldsymbol{n}\cdot\boldsymbol{v})(\boldsymbol{d}\psi\boldsymbol{I}\boldsymbol{d}\psi)+\big[(\mathrm{div}\boldsymbol{v})(\boldsymbol{n}\cdot\boldsymbol{v})-\boldsymbol{n}\boldsymbol{I}\boldsymbol{v}\big]|\boldsymbol{d}\psi|^2\\
&=2\nabla_3\psi v^i(\nabla_i v^3)\nabla_3\psi-2v_3\nabla^3\psi(\nabla_3 v^3)\nabla_3\psi+v_3(\nabla_k v^k)(\nabla_3\psi\nabla^3\psi)\\
&\quad-(\nabla_k v^3)v^k(\nabla_3\psi\nabla^3\psi)-2v^3\nabla_3\psi(\nabla_k v^k)\nabla_3\psi+2v^3\nabla_3\psi(\nabla_3 v^3)\nabla_3\psi\\
&=\nabla_3\psi v^i(\nabla_i v^3)\nabla_3\psi-v_3(\nabla_k v^k)(\nabla_3\psi\nabla^3\psi)\\
&=(\psi\nabla_3\psi)^2\big[v^i\nabla_i v^3-(\nabla_k v^k)v_3\big].
\end{aligned}\tag{5.88}$$

Recall the calculation of Christoffel symbols Γ^k_{ij} from (4.27). The last two terms in expression (5.88) can be explicitly expanded in the surface-adapted coordinates (5.86) as

$$v^i\nabla_i v^3=v^\alpha\partial_\alpha v^3+v^\alpha\Gamma^3_{\alpha\beta}v^\beta+v^3\partial_3 v^3,\tag{5.89}$$

$$(\nabla_k v^k)v_3=v^3\mathrm{div}_\gamma(v^\alpha\boldsymbol{g}_\alpha)+v^3\partial_3 v^3-2\hbar v^3,\tag{5.90}$$

where div_γ and $\hbar$ are the surface divergence and mean curvature of boundary γ respectively. We expand the integrand of the fourth integral in the second total derivative (5.85) in a similar fashion,

$$-2(\boldsymbol{v}\cdot\boldsymbol{d}\psi)\boldsymbol{n}(\boldsymbol{d}^2\psi)\boldsymbol{v}=-2v_3\nabla_3\psi(\nabla_3\nabla_3\psi)v_3=-4\hbar(\nabla_3\psi)^2v_3^2,\tag{5.91}$$

where in the second equality we have used the identity (4.133) that $\nabla_3\nabla_3\psi=2\hbar\nabla_3\psi$ on γ for a harmonic potential ψ. Thus if we identify $v_3=v_n$ as a scalar field on manifold γ and $\boldsymbol{v}_\gamma=v^\alpha\boldsymbol{g}_\alpha$ as a surface vector field tangent to γ, we can transform the second total derivative (5.85) of capacitance functional $\mathcal{C}[\gamma]$ back to a coordinate-free form,

$$\begin{aligned}
\frac{\mathrm{d}^2\mathcal{C}[\gamma]}{\mathrm{d}\epsilon^2}=&\int_\gamma\big[\boldsymbol{v}_\gamma\cdot\boldsymbol{d}_\gamma v_n-(\mathrm{div}_\gamma\boldsymbol{v}_\gamma)v_n+\boldsymbol{v}_\gamma\boldsymbol{i}\boldsymbol{i}\boldsymbol{v}_\gamma-\dot{v}_n\big](\boldsymbol{n}\cdot\boldsymbol{d}\psi)^2\,\mathrm{d}\gamma\\
&-\int_\gamma 2v_n(\boldsymbol{n}\cdot\boldsymbol{d}\psi)(\boldsymbol{n}\cdot\boldsymbol{d}\psi')+2\hbar v_n^2(\boldsymbol{n}\cdot\boldsymbol{d}\psi)^2\,\mathrm{d}\gamma,
\end{aligned}\tag{5.92}$$

where $\boldsymbol{d}_\gamma$ is the surface gradient operator and tensor $\boldsymbol{i}\boldsymbol{i}$ is the second fundamental form of conductor surface γ.

We make a few remarks on the observation that both the first (5.49) and second (5.85) total derivative don't involve derivative of spatial velocity $\boldsymbol{v}$ in the direction normal to the boundary γ. In other words, given any two configuration maps $\chi(\boldsymbol{X},\epsilon)$ and $\tilde{\chi}(\boldsymbol{X},\epsilon)$, as long as their prescribed boundary deformations agree, i.e. $\chi(\boldsymbol{X}\in\varGamma,\epsilon)=\tilde{\chi}(\boldsymbol{X}\in\varGamma,\epsilon)$, the resulting derivatives of capacitance functional $\mathcal{C}[\gamma]$ are identical regardless of how interior vacuum region is deformed. This is consistent with the comment we made earlier that the self-capacitance of a conductor is solely determined by the shape of its boundary.

In the end, if we evaluate the second total derivative (5.92) at $\epsilon=0$ (i.e. material frame), then the second shape variation of capacitance functional in direction of the

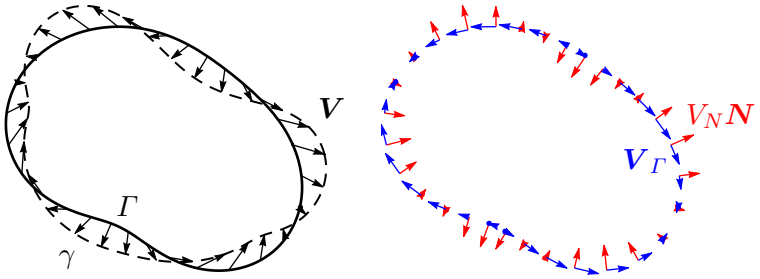

Figure 5.2: Material shape Γ (solid black line) is deformed into the spatial shape γ (dashed black line) under material velocity $\boldsymbol{V}$ (black arrow) with normal (red) components $V_N \boldsymbol{N}$ and tangential (blue) ones $\boldsymbol{V}_\Gamma$.

material velocity $\boldsymbol{V}$ and acceleration $\boldsymbol{A}$ is found to be a combination of contributions from the first order and the second order shape variations,

$$\delta^{(2)}\mathcal{C}[\Gamma;\boldsymbol{V},\boldsymbol{A}] = \delta^{(2)}\mathcal{C}[\Gamma;\boldsymbol{V}] + \delta^{(1)}\mathcal{C}[\Gamma;\boldsymbol{A}], \tag{5.93}$$

where

$$\begin{aligned}\delta^{(2)}\mathcal{C}[\Gamma;\boldsymbol{V}] = &\int_\Gamma [\boldsymbol{V}_\Gamma \cdot \boldsymbol{D}_\Gamma V_N - (\mathrm{Div}_\Gamma \boldsymbol{V}_\Gamma) V_N + \boldsymbol{V}_\Gamma \boldsymbol{I\!I} \boldsymbol{V}_\Gamma](\boldsymbol{N}\cdot\boldsymbol{D}\Psi)^2 \,\mathrm{d}\Gamma \\ &- \int_\gamma 2V_N(\boldsymbol{N}\cdot\boldsymbol{D}\Psi)(\boldsymbol{N}\cdot\boldsymbol{D}\Psi') + 2\mathcal{H}V_N^2(\boldsymbol{N}\cdot\boldsymbol{D}\Psi)^2 \,\mathrm{d}\Gamma\end{aligned} \tag{5.94}$$

accounts for the second order variation induced exclusively by material velocity $\boldsymbol{V}$ ($\boldsymbol{I\!I}$ is the second fundamental form tensor of the material boundary Γ) and $\delta^{(1)}\mathcal{C}[\Gamma;\boldsymbol{A}]$ has the identical functional form with the first shape variation (5.51), except material velocity $\boldsymbol{V}$ is replaced by the acceleration $\boldsymbol{A} = \partial\boldsymbol{V}/\partial\epsilon$ at $\epsilon = 0$. The surface-adapted decomposition of material velocity $\boldsymbol{V}$ into $\boldsymbol{V}_\Gamma$ and $V_N\boldsymbol{N}$ is illustrated in figure 5.2. Note the form of second shape variation (5.93) is exactly what one would obtain for a smooth function $f(x)$ in the context of single-variable calculus,

$$\frac{\mathrm{d}^2 f(x_0 + \epsilon\delta x_1 + \epsilon^2\delta x_2/2 + O(\epsilon^3))}{\mathrm{d}\epsilon^2}\Big|_{\epsilon=0} = f''(x_0)(\delta x_1)^2 + f'(x_0)(\delta x_2). \tag{5.95}$$

It should be emphasized that the second shape variation of self-capacitance has a nonlocal nature because Eulerian derivative Ψ' is the solution to the auxiliary problem (5.61) evaluated at $\epsilon = 0$,

$$\left.\begin{aligned}\mathrm{Div}\,\boldsymbol{D}\Psi' &= 0 && \text{in} \quad \Omega, \\ \Psi' &= -V_N(\boldsymbol{N}\cdot\boldsymbol{D}\Psi) && \text{on} \quad \Gamma,\end{aligned}\right\} \tag{5.96}$$

which requires the information of material velocity field everywhere on the conductor surface Γ.

As a sanity check, we test the second variation of $\mathcal{C}$ on a spherical capacitor occupying the region between two concentric spheres of inner radius r_a and outer radius r_b. The exact solution to the electric field within the capacitor is given by

$$\psi = \frac{r_a}{r_a - r_b}\left(1 - \frac{r_b}{r}\right), \quad \psi(r_a) = 1, \quad \psi(r_b) = 0, \tag{5.97}$$

where r is the radial distance and the outward normal vector $\boldsymbol{n} = -\boldsymbol{g}_r$ on the inner surface. We consider a configuration map $\chi(R, \epsilon)$ such that the inner radius r_a in spatial coordinates is mapped from R_a in material frame,

$$r_a = \chi(R_a, \epsilon) = R_a + \epsilon. \tag{5.98}$$

The rate of spatial deformation vector $\boldsymbol{v} = \boldsymbol{g}_r$ in this case is purely normal to the inner surface. The exact solution to the self-capacitance $\mathcal{C}[r_a]$ and its first two total derivatives in ϵ for any radius r_a can be easily obtained,

$$\mathcal{C}[r_a] = \frac{4\pi r_a r_b}{r_b - r_a}, \quad \frac{\mathrm{d}\mathcal{C}[r_a]}{\mathrm{d}\epsilon} = \frac{4\pi r_b^2}{(r_b - r_a)^2}, \quad \frac{\mathrm{d}^2\mathcal{C}[r_a]}{\mathrm{d}\epsilon^2} = \frac{8\pi r_b^2}{(r_b - r_a)^3}. \tag{5.99}$$

The auxiliary problem of the Eulerian derivative ψ' also admits the analytic solution,

$$\psi' = \frac{r_b}{(r_b - r_a)^2}\left(\frac{r_b}{r} - 1\right), \quad \psi'(r_a) = -\boldsymbol{v} \cdot \boldsymbol{d}\psi = \frac{r_b/r_a}{r_b - r_a}, \quad \psi'(r_b) = 0. \tag{5.100}$$

We also compute the necessary ingredients needed in the integral formula of the first and the second derivatives,

$$\boldsymbol{n} \cdot \boldsymbol{d}\psi|_{r_a} = \frac{r_b/r_a}{r_b - r_a}, \quad \boldsymbol{n} \cdot \boldsymbol{d}\psi'|_{r_a} = \frac{r_b^2/r_a^2}{(r_b - r_a)^2}, \quad \mathscr{H} = \frac{1}{r_a}, \quad v_n = -1. \tag{5.101}$$

It can be easily verified that, with quantities from expression (5.101) substituted, the surface integrals (5.49) and (5.92) are indeed evaluated to the identical results from the exact solution (5.99).

5.4 Geometric Variations of Surface Area and Volume

In this section, we derive the variations in differential elements when geometry undergoes deformation. Such calculations are usually done in a bottom-up approach such as the method employed by Lenz and Lipowsky (2000) where metric variations of surface-adapted coordinate system (ξ^1, ξ^2, ξ^3) are directly computed through index notations which are usually extremely lengthy and error-prone. For example, the first variation of surface metric tensor in equation (19) of Lenz and Lipowsky (2000) is in fact incorrect. Their umbersome index notation and lack of covariant expressions make it impossible to check if it is only a typographical error or the remaining par of their paper is actually wrong (Deserno, 2004). Instead, the use of convective Lagrange coordinates allows a top-down approach: variations are first computed under the general transformation rules of deformation gradient tensor $\boldsymbol{F}$ and then projected to the surface-adapted coordinate frame in the end.

First and second derivatives of area differential

Variational calculations of area element is much easier with convective Lagrangian coordinates. We start with an equivalent expression of a spatial area element $\mathrm{d}\gamma$,

$$\mathrm{d}\gamma = \boldsymbol{n}\cdot\boldsymbol{n}\,\mathrm{d}\gamma. \tag{5.102}$$

Substituting Nanson's relation (5.21) into (5.102) and taking total derivative with respect to ϵ yield

$$\begin{aligned}
\frac{\mathrm{d}\mathrm{d}\gamma}{\mathrm{d}\epsilon} &= \boldsymbol{n}\cdot\frac{\mathrm{d}(\boldsymbol{n}\,\mathrm{d}\gamma)}{\mathrm{d}\epsilon} + \frac{\mathrm{d}\boldsymbol{n}}{\mathrm{d}\epsilon}\cdot\boldsymbol{n}\,\mathrm{d}\gamma \\
&= \boldsymbol{n}\cdot\frac{\partial J\boldsymbol{F}^{-\top}}{\partial\epsilon}\boldsymbol{N}\,\mathrm{d}\Gamma + \frac{1}{2}\frac{\mathrm{d}|\boldsymbol{n}|^2}{\mathrm{d}\epsilon}\,\mathrm{d}\gamma \qquad \text{Note } |\boldsymbol{n}|=1 \\
&= \boldsymbol{n}\cdot\Big[J(\mathrm{div}\boldsymbol{v})\boldsymbol{F}^{-\top} - J\boldsymbol{l}^{\top}\boldsymbol{F}^{-\top}\Big]\boldsymbol{N}\,\mathrm{d}\Gamma \\
&= \boldsymbol{n}\cdot\Big[(\mathrm{div}\boldsymbol{v}) - \boldsymbol{l}^{\top}\Big]\boldsymbol{n}\,\mathrm{d}\gamma = (\mathrm{div}\boldsymbol{v} - \boldsymbol{n}\boldsymbol{l}^{\top}\boldsymbol{n})\,\mathrm{d}\gamma.
\end{aligned} \tag{5.103}$$

Using the adapted curvilinear coordinates for surface γ, we arrive at a convenient expression for the first total derivative (or deformation rate) of spatial area element,

$$\frac{\mathrm{d}(\mathrm{d}\gamma)}{\mathrm{d}\epsilon} = \mathrm{div}_{\gamma}\boldsymbol{v}\,\mathrm{d}\gamma = (\mathrm{div}_{\gamma}\boldsymbol{v}_{\gamma} - 2\hbar v_n)\,\mathrm{d}\gamma. \tag{5.104}$$

Note from the calculation of (5.103) that, the following identity

$$\begin{aligned}
\frac{\mathrm{d}\boldsymbol{n}}{\mathrm{d}\epsilon}\mathrm{d}\gamma &= \frac{\mathrm{d}(\boldsymbol{n}\,\mathrm{d}\gamma)}{\mathrm{d}\epsilon} - \boldsymbol{n}\frac{\mathrm{d}\mathrm{d}\gamma}{\mathrm{d}\epsilon} \\
&= (\mathrm{div}\boldsymbol{v} - \boldsymbol{l}^{\top})\boldsymbol{n}\,\mathrm{d}\gamma - \boldsymbol{n}(\mathrm{div}\boldsymbol{v} - \boldsymbol{n}\boldsymbol{l}^{\top}\boldsymbol{n})\,\mathrm{d}\gamma = \Big[(\boldsymbol{n}\boldsymbol{l}^{\top}\boldsymbol{n})\boldsymbol{n} - \boldsymbol{l}^{\top}\boldsymbol{n}\Big]\,\mathrm{d}\gamma
\end{aligned} \tag{5.105}$$

must hold for all area differentials $\mathrm{d}\gamma$ which is only possible if

$$\frac{\mathrm{d}\boldsymbol{n}}{\mathrm{d}\epsilon} = (\boldsymbol{n}\boldsymbol{l}^{\top}\boldsymbol{n})\boldsymbol{n} - \boldsymbol{l}^{\top}\boldsymbol{n}. \tag{5.106}$$

Equation (5.106) is the first variation of surface normal vector $\boldsymbol{n}$ as boundary γ deforms.

We then apply a similar strategy to derive the second total derivative of spatial area element which yields

$$\begin{aligned}
&\frac{\mathrm{d}^2\boldsymbol{n}\cdot\boldsymbol{n}\mathrm{d}\gamma}{\mathrm{d}\epsilon^2} \\
&= \boldsymbol{n}\cdot\frac{\mathrm{d}^2(\boldsymbol{n}\,\mathrm{d}\gamma)}{\mathrm{d}\epsilon^2} + \frac{\mathrm{d}^2\boldsymbol{n}}{\mathrm{d}\epsilon^2}\cdot\boldsymbol{n}\,\mathrm{d}\gamma + 2\frac{\mathrm{d}\boldsymbol{n}}{\mathrm{d}\epsilon}\cdot\frac{\mathrm{d}(\boldsymbol{n}\,\mathrm{d}\gamma)}{\mathrm{d}\epsilon} \quad \text{note} \quad \frac{\mathrm{d}^2|\boldsymbol{n}|^2}{\mathrm{d}\epsilon^2} = 0 \\
&= \boldsymbol{n}\cdot\frac{\partial^2 J\boldsymbol{F}^{-\top}}{\partial\epsilon^2}\boldsymbol{N}\,\mathrm{d}\Gamma - \frac{\mathrm{d}\boldsymbol{n}}{\mathrm{d}\epsilon}\cdot\frac{\mathrm{d}\boldsymbol{n}}{\mathrm{d}\epsilon}\,\mathrm{d}\gamma + \frac{\mathrm{d}\boldsymbol{n}}{\mathrm{d}\epsilon}\cdot\frac{\mathrm{d}(\boldsymbol{n}\,\mathrm{d}\gamma)}{\mathrm{d}\epsilon} + \frac{\mathrm{d}\boldsymbol{n}}{\mathrm{d}\epsilon}\cdot\frac{\mathrm{d}(\boldsymbol{n}\,\mathrm{d}\gamma)}{\mathrm{d}\epsilon} \\
&= \boldsymbol{n}\cdot\frac{\partial^2 J\boldsymbol{F}^{-\top}}{\partial\epsilon^2}\boldsymbol{N}\,\mathrm{d}\Gamma + \frac{\mathrm{d}\boldsymbol{n}}{\mathrm{d}\epsilon}\cdot\boldsymbol{n}\frac{\mathrm{d}\mathrm{d}\gamma}{\mathrm{d}\epsilon} + [(\boldsymbol{n}\boldsymbol{l}^{\top}\boldsymbol{n})\boldsymbol{n} - \boldsymbol{l}^{\top}\boldsymbol{n}]\cdot[(\mathrm{div}\boldsymbol{v}) - \boldsymbol{l}^{\top}]\boldsymbol{n}\,\mathrm{d}\gamma \\
&= \boldsymbol{n}\cdot\frac{\partial^2 J\boldsymbol{F}^{-\top}}{\partial\epsilon^2}\boldsymbol{N}\,\mathrm{d}\Gamma + \boldsymbol{n}\boldsymbol{l}\boldsymbol{l}^{\top}\boldsymbol{n}\,\mathrm{d}\gamma - (\boldsymbol{n}\boldsymbol{l}^{\top}\boldsymbol{n})^2\,\mathrm{d}\gamma,
\end{aligned} \tag{5.107}$$

where $\partial^2 J\boldsymbol{F}^{-\top}/\partial\epsilon^2$ can be explicitly expanded in aid of (5.28) and (5.30),

$$\begin{aligned}\frac{\partial^2 J\boldsymbol{F}^{-\top}}{\partial\epsilon^2} &= 2\frac{\partial J}{\partial\epsilon}\frac{\partial \boldsymbol{F}^{-\top}}{\partial\epsilon} + \frac{\partial^2 J}{\partial\epsilon^2}\boldsymbol{F}^{-\top} + J\frac{\partial^2 \boldsymbol{F}^{-\top}}{\partial\epsilon^2}\\ &= -2J(\mathrm{div}\boldsymbol{v})\boldsymbol{I}^\top\boldsymbol{F}^{-\top} + J\left[(\mathrm{div}\boldsymbol{v})^2 + \mathrm{div}(\dot{\boldsymbol{v}}) - \mathrm{tr}(\boldsymbol{II})\right]\boldsymbol{F}^{-\top}\\ &\quad + J\boldsymbol{I}^\top\boldsymbol{I}^\top\boldsymbol{F}^{-\top} - J(\boldsymbol{d}\dot{\boldsymbol{v}}^\top - \boldsymbol{I}^\top\boldsymbol{I}^\top)\boldsymbol{F}^{-\top}\\ &= \big[-2(\mathrm{div}\boldsymbol{v})\boldsymbol{I}^\top + (\mathrm{div}\boldsymbol{v})^2 - \mathrm{tr}(\boldsymbol{II}) + 2\boldsymbol{I}^\top\boldsymbol{I}^\top + \mathrm{div}(\dot{\boldsymbol{v}}) - \boldsymbol{d}\dot{\boldsymbol{v}}^\top\big]J\boldsymbol{F}^{-\top}.\end{aligned} \tag{5.108}$$

Applying identity (5.108) to (5.107) finally leads to the spatial form of the second derivative of area differential,

$$\begin{aligned}\frac{\mathrm{d}^2\mathrm{d}\gamma}{\mathrm{d}\epsilon^2} = \big[&-2(\mathrm{div}\boldsymbol{v})\boldsymbol{n}\boldsymbol{I}^\top\boldsymbol{n} + (\mathrm{div}\boldsymbol{v})^2 - \mathrm{tr}(\boldsymbol{II}) + 2\boldsymbol{n}\boldsymbol{I}^\top\boldsymbol{I}^\top\boldsymbol{n}\\ &+ \mathrm{div}\dot{\boldsymbol{v}} - \boldsymbol{n}\boldsymbol{d}\dot{\boldsymbol{v}}^\top\boldsymbol{n} + \boldsymbol{n}\boldsymbol{I}\boldsymbol{I}^\top\boldsymbol{n} - (\boldsymbol{n}\boldsymbol{I}^\top\boldsymbol{n})^2\big]\,\mathrm{d}\gamma.\end{aligned} \tag{5.109}$$

In surface-adapted curvilinear coordinates, equation (5.109) simplifies to

$$\frac{\mathrm{d}^2\mathrm{d}\gamma}{\mathrm{d}\epsilon^2} = \Big[(\mathrm{div}_\gamma\boldsymbol{v})^2 - (\boldsymbol{n}\boldsymbol{I}^\top\boldsymbol{n})^2 - \mathrm{tr}(\boldsymbol{II}) + 2\boldsymbol{n}\boldsymbol{I}^\top\boldsymbol{I}^\top\boldsymbol{n} + \boldsymbol{n}\boldsymbol{I}\boldsymbol{I}^\top\boldsymbol{n} - (\boldsymbol{n}\boldsymbol{I}^\top\boldsymbol{n})^2 + \mathrm{div}_\gamma\dot{\boldsymbol{v}}\Big]\,\mathrm{d}\gamma. \tag{5.110}$$

Using index notation, we can simply various terms in expression (5.110) and group them into contributions intrinsic and extrinsic to the surface γ,

$$\begin{aligned}2\boldsymbol{n}\boldsymbol{I}^\top\boldsymbol{I}^\top\boldsymbol{n} - \mathrm{tr}(\boldsymbol{II}) - (\boldsymbol{n}\boldsymbol{I}^\top\boldsymbol{n})^2 &= 2(\nabla_3 v^i)(\nabla_i v^3) - (\nabla_j v^i)(\nabla_i v^j) - (\nabla_3 v^3)^2\\ &= 2(\nabla_3 v^3)(\nabla_3 v^3) + 2(\nabla_3 v^\alpha)(\nabla_\alpha v^3) - (\nabla_3 v^3)(\nabla_3 v^3)\\ &\quad -(\nabla_\alpha v^3)(\nabla_3 v^\alpha) - (\nabla_\beta v^\alpha)(\nabla_\alpha v^\beta) - (\nabla_3 v^\alpha)(\nabla_\alpha v^3)\\ &\quad -(\nabla_3 v^3)^2\\ &= -(\nabla_\beta v^\alpha)(\nabla_\alpha v^\beta) = -(\hat{\nabla}_\beta v^\alpha - ii^\alpha_\beta v^3)(\hat{\nabla}_\alpha v^\beta - ii^\beta_\alpha v^3)\\ &= -(\hat{\nabla}_\beta v^\alpha)(\hat{\nabla}_\alpha v^\beta) + 2ii^\alpha_\beta v^3(\hat{\nabla}_\alpha v^\beta) - ii^\beta_\alpha ii^\alpha_\beta (v^3)^2,\end{aligned} \tag{5.111}$$

$$\begin{aligned}\boldsymbol{n}\boldsymbol{I}\boldsymbol{I}^\top\boldsymbol{n} - (\boldsymbol{n}\boldsymbol{I}^\top\boldsymbol{n})^2 &= (\nabla_j v^3)(\nabla^j v_3) - (\nabla_3 v^3)^2\\ &= (\nabla_\alpha v^3)g^{\alpha\beta}(\nabla_\beta v_3)\\ &= (\hat{\nabla}_\alpha v^3 + ii_{\alpha\alpha'}v^{\alpha'})g^{\alpha\beta}(\hat{\nabla}_\beta v_3 + ii^{\beta'}_\beta v_{\beta'})\\ &= (\hat{\nabla}_\alpha v^3)(\hat{\nabla}_\beta v_3) + ii^\beta_{\alpha'}v^{\alpha'}(\hat{\nabla}_\beta v_3)\\ &\quad +(\hat{\nabla}_\alpha v^3)ii^{\alpha\beta'}v_{\beta'} + ii^\beta_{\alpha'}ii^{\beta'}_\beta v^{\alpha'}v_{\beta'},\end{aligned} \tag{5.112}$$

$$(\mathrm{div}_\gamma\boldsymbol{v})^2 = (\mathrm{div}_\gamma\boldsymbol{v}_\gamma)^2 - 4\hbar(\mathrm{div}_\gamma\boldsymbol{v}_\gamma)v_n + 4\hbar^2 v_n^2, \tag{5.113}$$

where $\hat{\nabla}_\alpha$ is the low-dimensional covariant derivative restricted to surface γ, for which

$$\nabla_\beta v^\alpha = \hat{\nabla}_\beta v^\alpha - ii^\alpha_\beta \quad \text{on} \quad \gamma \tag{5.114}$$

holds (recall expansions (4.29) of the first kind Christoffel symbol). Substituting expressions (5.111), (5.112) and (5.113) into second total derivative (5.110) of $\mathrm{d}\gamma$ and exploiting properties of the second fundamental form ***ii*** we arrive at

$$\begin{aligned}
\frac{\mathrm{d}^2|\mathrm{d}\gamma|}{\mathrm{d}\epsilon^2} &= \Big[\mathrm{div}_\gamma \dot{\boldsymbol{v}} + (\mathrm{div}_\gamma \boldsymbol{v})^2 - (\nabla_\beta v^\alpha)(\nabla_\alpha v^\beta) + (\nabla_\alpha v^3)(\nabla^\alpha v^3)\Big]\,\mathrm{d}\gamma \\
&= \Big[\mathrm{div}_\gamma \dot{\boldsymbol{v}} + (\mathrm{div}_\gamma \boldsymbol{v}_\gamma)^2 - 4\hbar(\mathrm{div}_\gamma \boldsymbol{v}_\gamma)v_n + 4\hbar^2 v_n^2 \\
&\quad -(\hat{\nabla}_\beta v^\alpha)(\hat{\nabla}_\alpha v^\beta) + 2\mathit{ii}^\alpha_\beta v^3(\hat{\nabla}_\alpha v^\beta) - \mathit{ii}^\beta_\alpha \mathit{ii}^\alpha_\beta (v^3)^2 \\
&\quad +(\hat{\nabla}_\alpha v^3) g^{\alpha\beta}(\hat{\nabla}_\beta v_3) + 2\mathit{ii}^\beta_{\alpha'} v^{\alpha'}(\hat{\nabla}_\beta v_3) + \mathit{ii}^\beta_{\alpha'} \mathit{ii}^{\beta'}_\beta v^{\alpha'} v_{\beta'}\Big]\,\mathrm{d}\gamma \\
&= \Big[\mathrm{div}_\gamma \dot{\boldsymbol{v}} + (\mathrm{div}_\gamma \boldsymbol{v}_\gamma)^2 - 4\hbar(\mathrm{div}_\gamma \boldsymbol{v}_\gamma)v_n + 4\hbar^2 v_n^2 \\
&\quad -(\hat{\nabla}_\beta v^\alpha)(\hat{\nabla}_\alpha v^\beta) + 2\mathit{ii}^\alpha_\beta (v^3 \hat{\nabla}_\alpha v^\beta + v^\beta \hat{\nabla}_\alpha v^3) - (4\hbar^2 - 2\hbar)(v^3)^2 \\
&\quad +(\hat{\nabla}_\alpha v^3)(\hat{\nabla}^\alpha v_3) + \mathit{ii}^\beta_{\alpha'} \mathit{ii}^{\beta'}_\beta v^{\alpha'} v_{\beta'}\Big]\,\mathrm{d}\gamma \\
&= \Big[\mathrm{div}_\gamma \dot{\boldsymbol{v}} + (\mathrm{div}_\gamma \boldsymbol{v}_\gamma)^2 - (\hat{\nabla}_\beta v^\alpha)(\hat{\nabla}_\alpha v^\beta) + (\hat{\nabla}_\alpha v_n)(\hat{\nabla}^\alpha v_n) + 2\hbar v_n^2 \\
&\quad -4\hbar(\mathrm{div}_\gamma \boldsymbol{v}_\gamma)v_n + 2\mathit{ii}^\alpha_\beta \hat{\nabla}_\alpha(v_n v^\beta) + \mathit{ii}^\beta_{\alpha'} \mathit{ii}^{\beta'}_\beta v^{\alpha'} v_{\beta'}\Big]\,\mathrm{d}\gamma
\end{aligned} \tag{5.115}$$

where $\hat{\nabla}_\alpha$ is the low-dimensional covariant differential operation of surface γ. A cleanup of the algebras in expression (5.115) leads to the final result

$$\begin{aligned}
\frac{\mathrm{d}^2\mathrm{d}\gamma}{\mathrm{d}\epsilon^2} = \Big\{&\mathrm{div}_\gamma \dot{\boldsymbol{v}} \\
&+ 2\hbar \boldsymbol{v}_\gamma \mathit{\boldsymbol{ii}} \boldsymbol{v}_\gamma - \hbar \boldsymbol{v}_\gamma \cdot \boldsymbol{v}_\gamma \\
&+ \boldsymbol{d}_\gamma v_n \cdot \boldsymbol{d}_\gamma v_n + 2\hbar v_n^2 \\
&+ (\mathrm{div}_\gamma \boldsymbol{v}_\gamma)^2 - (\hat{\nabla}_\beta v^\alpha)(\hat{\nabla}_\alpha v^\beta) \\
&- 4\hbar(\mathrm{div}_\gamma \boldsymbol{v}_\gamma)v_n + 2\mathit{ii}^\alpha_\beta \hat{\nabla}_\alpha(v_n v^\beta)\Big\}\,\mathrm{d}\gamma.
\end{aligned} \tag{5.116}$$

The first line in (5.116) is due to spatial acceleration $\dot{\boldsymbol{v}}$ which is expected to have the identical form with the first derivative $\mathrm{d}(\mathrm{d}\gamma)/\mathrm{d}\epsilon$ in (5.104) with $\boldsymbol{v}$ replaced by $\dot{\boldsymbol{v}}$. The bilinear form in the second line in (5.116) is known as the third fundamental form tensor $\mathit{iii}_{\alpha\beta} = 2\hbar\, \mathit{ii}_{\alpha\beta} - \hbar g_{\alpha\beta}$. Integrands from the third and the fourth lines are the intrinsic contributions from tangential vector field $\boldsymbol{v}_\gamma$ and from scalar (normal) field v_n, respectively. We interpret the geometric meaning of these intrinsic contributions by recognizing

$$(\mathrm{div}_\gamma \boldsymbol{v}_\gamma)^2 - (\hat{\nabla}_\beta v^\alpha)(\hat{\nabla}_\alpha v^\beta) = (\mathrm{div}_\gamma \boldsymbol{v}_\gamma)^2 - \mathrm{tr}\big((\boldsymbol{d}_\gamma \boldsymbol{v}_\gamma)(\boldsymbol{d}_\gamma \boldsymbol{v}_\gamma)\big) = 2\det(\hat{\nabla}_\beta v^\alpha). \tag{5.117}$$

Expression (5.117) exactly agrees with the second derivative of Jacobian $\partial^2 J/\partial\epsilon^2$ from (5.30) in the case of a flat two-dimensional manifold with tangential deformation $\boldsymbol{v}_\gamma$ only. The last line in (5.116) represents the three-way coupling between $\boldsymbol{v}_\gamma$, v_n and the extrinsic (mean) curvature of surface γ. If the second derivative of $\mathrm{d}\gamma$ in (5.117) is

restricted to normal variations only (i.e. $\boldsymbol{v} = v_n \boldsymbol{n}$), we then arrive at the well known formula in shape analysis,

$$\frac{\mathrm{d}^2 \mathrm{d}\gamma}{\mathrm{d}\epsilon^2} = \left(\mathrm{div}_\gamma \dot{\boldsymbol{v}} + |\boldsymbol{d}_\gamma v_n|^2 + 2k v_n^2 \right) \mathrm{d}\gamma \quad \text{when} \quad \boldsymbol{v}_\gamma = \boldsymbol{0}. \tag{5.118}$$

In the theory of minimal surfaces, integration of expression (5.118) over the entire surface of a critical shape γ leads to a quadratic shape functional whose convexity directly determines whether its total surface area is locally minimal or maximal. The expression of the first area variation (5.104) and the second variation (5.118) restricted to normal displacement can be found in standard textbooks on differential geometry (Stoker, 1988; Kreyszig, 1991). However, the full expression (5.116) of second area variation $\mathrm{d}^2\mathrm{d}\gamma/\mathrm{d}\epsilon^2$ especially including the tangential variations of the surface is less commonly known or documented, at least to the best of the author's knowledge. We find it coincides with the expression derived in Capovilla and Guven (2004).

First and second derivatives of total volume

Variations of volume differential element are straightforward since they mostly deal with the relative Jacobian J. The first derivative of spatial volume differential $\mathrm{d}\omega$ is directly given by $\partial J/\partial\epsilon$ in (5.29),

$$\frac{\mathrm{d}\mathrm{d}\omega}{\mathrm{d}\epsilon} = \frac{\partial J}{\partial \epsilon} \mathrm{d}\Omega = \mathrm{div}\boldsymbol{v} \, \mathrm{d}\omega. \tag{5.119}$$

The first derivative of the total volume can be expressed as a surface integral through divergence theorem,

$$\frac{\mathrm{d}}{\mathrm{d}\epsilon} \int_\omega \mathrm{d}\omega = \int_\Omega \frac{\partial J}{\partial \epsilon} \mathrm{d}\Omega = \int_\gamma \boldsymbol{v} \cdot \boldsymbol{n} \, \mathrm{d}\gamma = \int_\gamma v_n \, \mathrm{d}\gamma. \tag{5.120}$$

The second derivative of spatial volume differential $\mathrm{d}\omega$ is directly given by $\partial^2 J/\partial\epsilon^2$ in (5.30),

$$\frac{\mathrm{d}^2|\mathrm{d}\omega|}{\mathrm{d}\epsilon^2} = \frac{\partial^2 J}{\partial \epsilon^2} \mathrm{d}\Omega = \left[\mathrm{div}\dot{\boldsymbol{v}} + (\mathrm{div}\boldsymbol{v})^2 - \mathrm{tr}(\boldsymbol{II}) \right] \mathrm{d}\omega. \tag{5.121}$$

In order to convert the second derivative of the total volume

$$\frac{\mathrm{d}^2}{\mathrm{d}\epsilon^2} \int_\omega \mathrm{d}\omega = \int_\Omega \frac{\partial^2 J}{\partial \epsilon^2} \mathrm{d}\Omega = \int_\omega \mathrm{div}\dot{\boldsymbol{v}} + (\mathrm{div}\boldsymbol{v})^2 - \mathrm{tr}(\boldsymbol{II}) \, \mathrm{d}\omega \tag{5.122}$$

to a surface integral only, we first recall an identity similar to the one we encounter in (5.76),

$$\begin{aligned} \mathrm{div}\big[(\mathrm{div}\boldsymbol{v})\boldsymbol{v} - \boldsymbol{I}\boldsymbol{v}\big] &= \nabla_i \big[(\nabla_j v^j) v^i - (\nabla_j v^i) v^j \big] \\ &= (\nabla_j v^j)(\nabla_i v^i) - (\nabla_j v^i)(\nabla_i v^j) + (\nabla_i \nabla_j v^j) v^i - (\nabla_i \nabla_j v^i) v^j \\ &= (\mathrm{div}\boldsymbol{v})^2 - \mathrm{tr}(\boldsymbol{II}). \qquad \text{Flat} \end{aligned} \tag{5.123}$$

With identity (5.123) substituted in (5.122), the second derivative of the total volume now becomes a surface integral,

$$\frac{\mathrm{d}^2}{\mathrm{d}\epsilon^2}\int_\omega \mathrm{d}\omega = \int_\gamma \boldsymbol{n}\cdot\dot{\boldsymbol{v}} + (\mathrm{div}\boldsymbol{v})(\boldsymbol{n}\cdot\boldsymbol{v}) - \boldsymbol{n}\boldsymbol{I}\boldsymbol{v}\,\mathrm{d}\gamma. \tag{5.124}$$

We can gain more insights into the second derivative (5.124) by expanding it using index notation of surface-adapted curvilinear coordinates,

$$\begin{aligned}(\mathrm{div}\boldsymbol{v})(\boldsymbol{n}\cdot\boldsymbol{v}) - \boldsymbol{n}\boldsymbol{I}\boldsymbol{v} &= (\nabla_i v^i)v^3 - (\nabla_i v^3)v^i = (\nabla_\alpha v^\alpha)v^3 - (\nabla_\alpha v^3)v^\alpha \\ &= (\hat{\nabla}_\alpha v^\alpha - \mathit{ii}^\alpha_\alpha v^3)v^3 - (\hat{\nabla}_\alpha v^3 + \mathit{ii}_{\alpha\beta}v^\beta)v^\alpha \\ &= v^3\hat{\nabla}_\alpha v^\alpha - v^\alpha\hat{\nabla}_\alpha v^3 - 2\hbar(v^3)^2 - \mathit{ii}_{\alpha\beta}v^\beta v^\alpha. \end{aligned}\tag{5.125}$$

Finally with identity (5.125) we arrive at

$$\frac{\mathrm{d}^2}{\mathrm{d}\epsilon^2}\int_\omega \mathrm{d}\omega = \int_\gamma \dot{v}_n + v_n(\mathrm{div}_\gamma\boldsymbol{v}_\gamma) - \boldsymbol{v}_\gamma\cdot\boldsymbol{d}_\gamma v_n - 2\hbar v_n^2 - \boldsymbol{v}_\gamma\boldsymbol{\mathit{ii}}\boldsymbol{v}_\gamma\,\mathrm{d}\gamma. \tag{5.126}$$

As usual, the first term in the second derivative of the total volume (5.126) is due to spatial acceleration $\dot{\boldsymbol{v}}$. The next two terms are the intrinsic coupling between tangential vector field $\boldsymbol{v}_\gamma$ and scalar normal field v_n, The last two terms represent how vector field $\boldsymbol{v}_\gamma$ and scalar field v_n individually interact with extrinsic curvatures of surface γ.

Both first (5.120) and second (5.126) derivatives of the total volume are surface integral and only involve information of vector field $\boldsymbol{v}$ defined strictly intrinsic to surface γ (e.g., $\boldsymbol{n}\cdot\boldsymbol{dv}$ is considered extrinsic to surface γ). This is expected because the total volume of region ω can be expressed as a surface integral via divergence theorem,

$$\int_\omega \mathrm{d}\omega = \int_\omega \frac{1}{3}\mathrm{div}\,\boldsymbol{x}\,\mathrm{d}\omega = \frac{1}{3}\int_\gamma \boldsymbol{n}\cdot\boldsymbol{x}\,\mathrm{d}\gamma. \tag{5.127}$$

Finally we would like to highlight the necessity of spatial acceleration $\dot{\boldsymbol{v}}$ in volume conservation. Consider a configuration map $\chi(\cdot,\epsilon)$ which is constrained to conserve the total volume for all valid ϵ. The total derivative of $\int_\omega \mathrm{d}\omega$ with respect to ϵ at any order must be zero over the entire range of ϵ as well. As implied by (5.120), a spatial velocity field $\boldsymbol{v} = \boldsymbol{v}_\gamma$ always tangent to surface γ would guarantee that the first derivative of $\int_\omega \mathrm{d}\omega$ vanishes but not necessarily the second derivative! To see this claim, let's consider a unit sphere to be the material frame Ω with $\chi(\boldsymbol{X},\epsilon)$ being a rigid rotation that rotates Ω to a new spatial frame ω about some axis (in this case ϵ is the rotation angle). We expect the total volume of spatial domain ω be conserved for all ϵ. Since $\boldsymbol{v}$ derived from $\chi(\boldsymbol{X},\epsilon)$ is everywhere tangent to the surface γ of the sphere, the first derivative of $\int_\omega \mathrm{d}\omega$ is zero according to formula (5.120). Second fundamental form $\boldsymbol{\mathit{ii}}$ in this case equals to the negative of the identity tensor everywhere on the surface of a unit sphere which renders the second derivative of the total volume

$$\frac{\mathrm{d}^2}{\mathrm{d}\epsilon^2}\int_\omega \mathrm{d}\omega = \int_\gamma \dot{v}_n + \boldsymbol{v}_\gamma\cdot\boldsymbol{v}_\gamma\,\mathrm{d}\gamma \tag{5.128}$$

through the formula (5.126). It's now evident that, integral (5.128) would always be non-negative without the help of spatial acceleration $\dot{\boldsymbol{v}}$ and hence violate volume conservation.

5.5 Energy Variation and Stability of Charged Conductive Liquids

In this section we derive the first and second shape variations of the total potential energy of an isolated charged perfectly conducting liquid body with an arbitrary smooth shape as well the necessary conditions for equilibrium and energy instability. In the end we show that the famous Rayleigh charge limit for a near-spherical shape can be obtained from energy analysis alone. In what follows, we non-dimensionalize length scale with the characteristic radius of curvature R_c of the conductor surface, energy with the characteristic surface energy σR_c^2 (σ is the liquid-vacuum surface tension coefficient) and capacitance with $\varepsilon_0 R_c$. For an isolated conductor, we fix the total physical charge Q residing on its surface for any deformed configuration.

Potential energy of a charged liquid body

Let Γ be the dimensionless boundary of the vacuum region $\Omega_{\rm vac}$ exterior to the undeformed (material) conductive liquid body with γ and $\omega_{\rm vac}$ being the deformed (spatial) counterparts. After the standard procedure of nondimensionalization, the dimensionless total potential energy

$$\mathcal{F}[\gamma] = \mathcal{S}[\gamma] + \mathcal{E}[\gamma] \tag{5.129}$$

of an isolated charged liquid drop is composed of two parts: surface energy

$$\mathcal{S}[\gamma] = \int_\gamma \mathrm{d}\gamma \tag{5.130}$$

which is proportional to the total surface area of the liquid body, and the electrostatic energy $\mathcal{E}[\gamma]$

$$\mathcal{E}[\gamma] = \frac{\mathrm{Ec}}{\mathcal{C}[\gamma]}, \quad \mathrm{Ec} = \frac{Q^2}{2\varepsilon_0 \sigma R_c^3}, \tag{5.131}$$

stored in the surrounding vacuum region $\omega_{\rm vac}$. Here Ec is electric-capillary number and $\mathcal{C}[\gamma]$ is the dimensionless self-capacitance (5.41).

Let $\Omega_{\rm liq}$ and $\omega_{\rm liq}$ be the undeformed (material) and deformed (spatial) liquid volume respectively, with Γ (or γ) being the dividing interface common to both vacuum $\Omega_{\rm vac}$ (or $\omega_{\rm vac}$) and liquid $\Omega_{\rm liq}$ (or $\omega_{\rm liq}$) domains. We assume the variation of drop shape is driven by incompressible motions of the fluid interior to the conductor. Thus mass exchange through the boundary is forbidden here. For a geometry configuration associated with the boundary γ to be dynamically accessible, it must at least conserve the total volume which is equivalent to impose an integral constraint

$$\mathcal{V}[\omega_{\rm liq}] = 0 \tag{5.132}$$

on the potential energy functional of any spatial configuration ω_{liq} where

$$\mathcal{V}[\omega_{\text{liq}}] = 3\Big(\int_{\omega_{\text{liq}}} \mathrm{d}\omega - |\Omega_{\text{liq}}|\Big), \quad |\Omega_{\text{liq}}| = \int_{\Omega_{\text{liq}}} \mathrm{d}\Omega. \tag{5.133}$$

Here $|\Omega_{\text{liq}}|$ is the dimensionless total volume of the undeformed configuration. In other words, only energies of different shapes that share identical liquid volume should be compared. The factor 3 in $\mathcal{V}[\omega_{\text{liq}}]$ arises from the earlier observation (5.127) that volume integral $\mathcal{V}[\omega_{\text{liq}}]$ can be reformed into a shape functional $\mathcal{V}[\gamma]$ through divergence theorem,

$$\mathcal{V}[\omega_{\text{liq}}] = \int_{\gamma} \boldsymbol{x} \cdot \boldsymbol{n}\, \mathrm{d}\gamma - 3|\Omega_{\text{liq}}| = \mathcal{V}[\gamma]. \tag{5.134}$$

In the rest of this chapter, we will adopt one unique global definition of the surface normal vector $\boldsymbol{n}$ (or $\boldsymbol{N}$) pointing from the liquid to the vacuum.

Now let's consider a configuration map $\chi(\boldsymbol{X}, \epsilon)$ which transforms the material domain Ω_{vac} and boundary Γ to their spatial counterparts ω_{vac} and γ. Although the derivatives we developed in the last section hold for arbitrary function χ and value of ϵ as long as the map $\chi(\cdot, \epsilon)$ is well-defined, in energy stability analysis we are mostly interested in the effect of small perturbations to the undeformed geometry of the conductor. We choose to align the material frame with the spatial frame at $\epsilon = 0$, i.e. $\chi(\boldsymbol{X}, 0) = \boldsymbol{X}$ is an identity map. Assuming sufficient continuities in parameter ϵ, then in the spirit of Taylor expansion we can represent any near-identity map $\chi(\cdot, \epsilon)$ in the general form

$$\chi(\boldsymbol{X}, \epsilon) = \boldsymbol{X} + \epsilon \boldsymbol{V} + \frac{1}{2}\epsilon^2 \boldsymbol{A} + O(\epsilon^3) \tag{5.135}$$

for some small ϵ where $\boldsymbol{V}$ and $\boldsymbol{A}$ are the material velocity $\boldsymbol{v}$ and acceleration $\dot{\boldsymbol{v}}$ evaluated at $\epsilon = 0$, respectively. We reemphasize that the terminologies "velocity" and "acceleration" do not refer to physical quantities in time but rather parametric dependence of the map $\chi(\cdot, \epsilon)$ on $0 \leq \epsilon \ll 1$. We also do not specify behaviors of $\chi(\boldsymbol{X} \in \Omega_{\text{liq}}, \epsilon)$ in the liquid volume other than mass conservation and continuity of $\chi(\boldsymbol{X} \in \Gamma, \epsilon)$ on the liquid/vacuum interface.

Constrained first shape variation of potential energy

The boundary Γ is said to be a critical shape of the energy functional $\mathcal{F}[\Gamma]$ if its first shape variation vanishes for all admissible infinitesimal deformations under certain constraint, in our case the conservation of total liquid volume,

$$\frac{\mathrm{d}\mathcal{F}[\gamma]}{\mathrm{d}\epsilon}\Big|_{\epsilon=0} = 0 \quad \text{for all } \chi(\cdot, \epsilon) \quad \text{such that} \quad \mathcal{V}[\gamma] = 0. \tag{5.136}$$

Equation (5.136) is a constrained derivative. If the potential energy and volume constraint in (5.136) were multivariate functions instead of functionals, one could enforce the constraint through the multi-variable chain rule. In an abstract variational problem

of functionals, it's not clear how to apply "chain rule" directly. To overcome this difficulty we instead formulate the Lagrangian functional (not to confuse with Lagrangian coordinates)

$$\mathscr{L}[\gamma,\lambda]=\mathscr{S}[\gamma]+\mathscr{E}[\gamma]-\lambda\mathscr{V}[\gamma], \tag{5.137}$$

where constant λ is the Lagrange multiplier. Then an unconstrained critical point (Γ,Λ) of the Lagrangian (5.137) is also a critical shape of the original constrained potential. The critical condition reads

$$\frac{\mathrm{d}\mathscr{L}[\gamma,\lambda]}{\mathrm{d}\epsilon}\Big|_{\epsilon=0,\lambda=\Lambda}=\frac{\mathrm{d}\mathscr{F}[\gamma]}{\mathrm{d}\epsilon}-\Lambda\frac{\mathrm{d}\mathscr{V}[\gamma]}{\mathrm{d}\epsilon}\Big|_{\epsilon=0}=\delta^{(1)}\mathscr{F}[\Gamma;\boldsymbol{V}]-\Lambda\delta^{(1)}\mathscr{V}[\Gamma;\boldsymbol{V}]=0, \tag{5.138}$$

$$\frac{\mathrm{d}\mathscr{L}[\gamma,\lambda]}{\mathrm{d}\lambda}\Big|_{\epsilon=0,\lambda=\Lambda}=-\frac{\mathrm{d}\mathscr{V}[\gamma]}{\mathrm{d}\epsilon}\Big|_{\epsilon=0}=-\delta^{(1)}\mathscr{V}[\Gamma;\boldsymbol{V}]=0, \tag{5.139}$$

where Λ is the correct constant of multiplier λ to be determined. Using the results (5.51) and (5.104) derived earlier, we arrive at the necessary conditions for Γ to be a critical shape of the constrained potential energy $\mathscr{F}[\gamma]$,

$$\left.\begin{aligned}0&=\int_\Gamma\Big(-\frac{\mathrm{Ec}}{\mathcal{C}[\Gamma]^2}\,|\boldsymbol{D}\Psi|^2-2\mathscr{H}-\Lambda\Big)\boldsymbol{N}\cdot\boldsymbol{V}\,\mathrm{d}\Gamma+\int_\Gamma\mathrm{Div}_\Gamma\boldsymbol{V}_\Gamma\,\mathrm{d}\Gamma,\\0&=\int_{\Omega_{\mathrm{liq}}}\mathrm{d}\Omega-|\Omega_{\mathrm{liq}}|,\end{aligned}\right\} \tag{5.140}$$

where $\int_\Gamma\mathrm{Div}_\Gamma\boldsymbol{V}_\Gamma\,\mathrm{d}\Gamma=0$ on a boundaryless manifold Γ. Note the definition of $\boldsymbol{N}$ in (5.140) is opposite to the normal vector in (5.49). For Γ to be an equilibrium shape, the critical condition (5.140) must hold for all admissible velocity field $\boldsymbol{V}$ which is only possible if

$$-\frac{\mathrm{Ec}}{\mathcal{C}[\Gamma]^2}\,|\boldsymbol{D}\Psi|^2-2\mathscr{H}=\Lambda\quad\text{on}\quad\Gamma, \tag{5.141}$$

where the constant Λ is chosen such that the volume of the liquid equals $|\Omega_{\mathrm{liq}}|$.

In dimensional form, the equilibrium condition (5.141) represents a point-wise balance between the electrostatic and capillary pressure everywhere on the liquid surface only up to a residue pressure that's globally constant over the entire surface. This constant pressure level is implicitly determined by the total volume of the liquid. The potential energy of shape Γ satisfying equilibrium condition (5.141) would have a vanishing first energy variation for all volume-conserving shape deformations. Recall the stability near an equilibrium point of a mechanical system largely attributes to the local convexity of the same point in the energy landscape. We cannot tell if a critical shape Γ (if exist) is a local minimum, maximum or saddle point of the potential energy $\mathscr{F}[\gamma]$ from the first order conditions of the Lagrangian $\mathscr{L}[\gamma,\lambda]$ alone.

Note volume constraint $\mathscr{V}[\gamma]=0$ must hold for every spatial configuration which means its derivatives at all orders of ϵ must vanish,

$$\frac{\mathrm{d}\mathscr{V}[\gamma]}{\mathrm{d}\epsilon}=\frac{\mathrm{d}^2\mathscr{V}[\gamma]}{\mathrm{d}\epsilon^2}=\ldots=\frac{\mathrm{d}^k\mathscr{V}[\gamma]}{\mathrm{d}\epsilon^k}=\ldots=0\quad\text{for}\quad\epsilon\geq0. \tag{5.142}$$

Applying volume variation (5.120) to $\mathrm{d}\mathcal{V}[\gamma]/\mathrm{d}\epsilon$ at $\epsilon = 0$ yields a first order constraint

$$\int_{\Gamma} \boldsymbol{N} \cdot \boldsymbol{V} \, \mathrm{d}\Gamma = 0 \tag{5.143}$$

on the velocity field $\boldsymbol{V}$.

Constrained second shape variation of potential energy

The energy stability of a critical shape Γ is encoded in the functional structure of its second shape variation, which essentially maps out the local energy landscape near the critical shape and thereby allows us to determine the type of local extreme (i.e. maximum, minimum or saddle). The second variation of the total potential energy with respect to ϵ at $\epsilon = 0$ has two contributions from material velocity $\boldsymbol{V}$ and acceleration $\boldsymbol{A}$,

$$\frac{\mathrm{d}^2\mathcal{F}[\gamma]}{\mathrm{d}\epsilon^2}\Big|_{\epsilon=0} = \delta^{(2)}\mathcal{F}[\Gamma; \boldsymbol{V}, \boldsymbol{A}] = \delta^{(2)}\mathcal{F}[\Gamma; \boldsymbol{V}] + \delta^{(1)}\mathcal{F}[\Gamma; \boldsymbol{A}]. \tag{5.144}$$

Note the material acceleration field $\boldsymbol{A}$ cannot be an arbitrary vector field since $\chi(\cdot, \epsilon)$ must conserve total liquid volume. We can eliminate this indirect constraint on $\boldsymbol{A}$ by invoking the first order critical condition (5.138) on Γ,

$$\delta^{(1)}\mathcal{F}[\Gamma; \boldsymbol{V}] = \Lambda \delta^{(1)}\mathcal{V}[\Gamma; \boldsymbol{V}], \tag{5.145}$$

which is expected to hold for any admissible vector field $\boldsymbol{V}$. Now if we replace $\boldsymbol{V}$ in (5.145) by $\boldsymbol{A}$ and then substitute (5.145) back to equation (5.144), we arrive at

$$\frac{\mathrm{d}^2\mathcal{F}[\gamma]}{\mathrm{d}\epsilon^2}\Big|_{\epsilon=0} = \delta^{(2)}\mathcal{F}[\Gamma; \boldsymbol{V}] + \Lambda \delta^{(1)}\mathcal{V}[\Gamma; \boldsymbol{A}]. \tag{5.146}$$

We next evaluate the second order condition in the volume constraint (5.142),

$$0 = \frac{\mathrm{d}^2\mathcal{V}[\gamma]}{\mathrm{d}\epsilon^2}\Big|_{\epsilon=0} = \delta^{(2)}\mathcal{V}[\Gamma; \boldsymbol{V}, \boldsymbol{A}] = \delta^{(2)}\mathcal{V}[\Gamma; \boldsymbol{V}] + \delta^{(1)}\mathcal{V}[\Gamma; \boldsymbol{A}], \tag{5.147}$$

which again has two contributions from $\boldsymbol{V}$ and $\boldsymbol{A}$. It's now evident that the variational contributions in $\mathrm{d}^2\mathcal{F}[\gamma]/\mathrm{d}\epsilon^2$ are functionals of material velocity $\boldsymbol{V}$ alone after substituting identity (5.147) into (5.146). In the end, we arrive at the constrained (i.e. volume conserving) second shape variation of the potential energy $\mathcal{F}[\gamma]$ evaluated at a critical shape Γ provided the material velocity field $\boldsymbol{V}$ of a configuration map $\chi(\cdot, \epsilon)$ satisfies the constraint (5.143),

$$\begin{aligned}
\frac{\mathrm{d}^2\mathcal{F}[\gamma]}{\mathrm{d}\epsilon^2}\Big|_{\epsilon=0} &= \delta^{(2)}\mathcal{F}[\Gamma; \boldsymbol{V}] - \Lambda \delta^{(2)}\mathcal{V}[\Gamma; \boldsymbol{V}] \\
&= -\frac{\mathrm{Ec}}{\mathcal{C}[\Gamma]^2}\left\{\delta^{(2)}\mathcal{C}[\Gamma; \boldsymbol{V}] - 2\frac{(\delta^{(1)}\mathcal{C}[\Gamma; \boldsymbol{V}])^2}{\mathcal{C}[\Gamma]}\right\} \\
&\quad + \delta^{(2)}\mathcal{S}[\Gamma; \boldsymbol{V}] - \Lambda \delta^{(2)}\mathcal{V}[\Gamma; \boldsymbol{V}],
\end{aligned} \tag{5.148}$$

where the Lagrange multiplier constant Λ is determined by the first variation. We make a comment here regarding the elimination of material acceleration $\boldsymbol{A}$: it does not imply $\boldsymbol{A}$ is dispensable. It's merely a consequence of volume conservation under which the contribution of $\boldsymbol{A}$ to the second variation is equivalent to some integral expression involving $\boldsymbol{V}$ only. It is computationally more convenient if we keep $\boldsymbol{V}$ as the only independent variable.

We again employ the surface-adapted curvilinear coordinates (ξ^1, ξ^2, ξ^3) defined in (5.86) and project material velocity $\boldsymbol{V}$ into a surface vector field $\boldsymbol{U}(\xi^1, \xi^2)$ tangent to Γ and a normal component $\Theta(\xi^1, \xi^2)\boldsymbol{N}$,

$$\boldsymbol{V} = \boldsymbol{U} + \Theta \boldsymbol{N}, \quad \boldsymbol{U} = U^\alpha \boldsymbol{G}_\alpha(\xi^1, \xi^2, 0). \tag{5.149}$$

Through the use of the second derivative of area differential (5.116), total volume (5.128) and self-capacitance (5.94) (recall normal vector is flipped in $\mathcal{C}[\gamma]$), we can explicitly write down the expressions for the three functionals in the second shape variations (5.148),

$$\begin{aligned}
\delta^{(2)}\mathcal{C}[\Gamma; \boldsymbol{V}] = &\int_\Gamma 2(\boldsymbol{N}\cdot\boldsymbol{D}\Psi)(\boldsymbol{N}\cdot\boldsymbol{D}\Psi')\Theta + 2\mathcal{H}\Theta^2(\boldsymbol{N}\cdot\boldsymbol{D}\Psi)^2 \,\mathrm{d}\Gamma \\
&- \int_\Gamma \left[\boldsymbol{U}\cdot\boldsymbol{D}_\Gamma\Theta - (\mathrm{Div}_\Gamma \boldsymbol{U})\Theta + \boldsymbol{U}\boldsymbol{I\!I}\boldsymbol{U}\right](\boldsymbol{N}\cdot\boldsymbol{D}\Psi)^2 \,\mathrm{d}\Gamma, \qquad (5.150) \\
\delta^{(2)}\mathcal{S}[\Gamma; \boldsymbol{V}] = &\int_\Gamma \boldsymbol{D}_\Gamma\Theta\cdot\boldsymbol{D}_\Gamma\Theta + 2\mathcal{K}\Theta^2 - \mathcal{K}\boldsymbol{U}\cdot\boldsymbol{U}\,\mathrm{d}\Gamma \\
&+ \int_\Gamma (\mathrm{Div}_\Gamma \boldsymbol{U})^2 - (\hat{\nabla}_\beta U^\alpha)(\hat{\nabla}_\alpha U^\beta) + 2\mathit{I\!I}^\alpha_\beta \hat{\nabla}_\alpha(\Theta U^\beta)\,\mathrm{d}\Gamma \\
&- \int_\Gamma 4\mathcal{H}(\mathrm{Div}_\Gamma \boldsymbol{U})\Theta - 2\mathcal{H}\boldsymbol{U}\boldsymbol{I\!I}\boldsymbol{U}\,\mathrm{d}\Gamma, \qquad (5.151) \\
\delta^{(2)}\mathcal{V}[\Gamma; \boldsymbol{V}] = &\int_\Gamma -2\mathcal{H}\Theta^2 + 2(\mathrm{Div}_\Gamma \boldsymbol{U})\Theta - \boldsymbol{U}\boldsymbol{I\!I}\boldsymbol{U}\,\mathrm{d}\Gamma. \qquad (5.152)
\end{aligned}$$

Here $\mathcal{K}$ is the Gaussian curvature of surface Γ. At first glance, the integrals (5.150), (5.151) and (5.152) appear to be formidable. Fortunately many terms would cancel out each out thanks to Γ being a critical shape. To see this, we first expand the constraint $\Lambda\delta^{(2)}\mathcal{V}[\Gamma; \boldsymbol{V}]$. Note Λ is a constant determined by the critical condition (5.140) which therefore can be moved inside the integral of $\delta^{(2)}\mathcal{V}[\Gamma; \boldsymbol{V}]$,

$$\begin{aligned}
\Lambda\delta^{(2)}\mathcal{V}[\Gamma; \boldsymbol{V}] &= \int_\Gamma \Big(-\frac{\mathrm{Ec}}{\mathcal{C}[\Gamma]^2}|\boldsymbol{D}\Psi|^2 - 2\mathcal{H}\Big)\left[-2\mathcal{H}\Theta^2 + 2(\mathrm{Div}_\Gamma \boldsymbol{U})\Theta - \mathit{I\!I}_{\alpha\beta}U^\alpha U^\beta\right]\,\mathrm{d}\Gamma \\
&= -\frac{\mathrm{Ec}}{\mathcal{C}[\Gamma]^2}\int_\Gamma |\boldsymbol{D}\Psi|^2\left[-2\mathcal{H}\Theta^2 + 2(\mathrm{Div}_\Gamma \boldsymbol{U})\Theta - \mathit{I\!I}_{\alpha\beta}U^\alpha U^\beta\right]\,\mathrm{d}\Gamma \\
&\quad + \int_\Gamma 4\mathcal{H}^2\Theta^2 + 2\mathcal{H}\left[\mathit{I\!I}_{\alpha\beta}U^\alpha U^\beta - 2(\mathrm{Div}_\Gamma \boldsymbol{U})\Theta\right]\,\mathrm{d}\Gamma. \qquad (5.153)
\end{aligned}$$

Substituting equations (5.150), (5.151) and (5.153) into the second shape variation

(5.148) yields a relatively clean expression,

$$\begin{aligned}\frac{\mathrm{d}^2\mathcal{F}[\gamma]}{\mathrm{d}\epsilon^2}\Big|_{\epsilon=0} =& -\frac{\mathrm{Ec}}{\mathcal{C}[\Gamma]^2}\int_\Gamma 2(\boldsymbol{N}\cdot\boldsymbol{D}\Psi)(\boldsymbol{N}\cdot\boldsymbol{D}\Psi')\Theta + 4\mathscr{H}\Theta^2(\boldsymbol{N}\cdot\boldsymbol{D}\Psi)^2\,\mathrm{d}\Gamma\\ &+\int_\Gamma \boldsymbol{D}_\Gamma\Theta\cdot\boldsymbol{D}_\Gamma\Theta + (2\mathcal{K}-4\mathscr{H}^2)\Theta^2\,\mathrm{d}\Gamma\\ &+\frac{\mathrm{Ec}}{\mathcal{C}[\Gamma]^2}\int_\Gamma \mathrm{Div}_\Gamma(\Theta\boldsymbol{U})(\boldsymbol{N}\cdot\boldsymbol{D}\Psi)^2\,\mathrm{d}\Gamma + \int_\Gamma 2I\!I^\alpha_\beta\hat{\nabla}_\alpha(\Theta U^\beta)\,\mathrm{d}\Gamma\\ &+\int_\Gamma(\mathrm{Div}_\Gamma\boldsymbol{U})^2 - (\hat{\nabla}_\beta U^\alpha)(\hat{\nabla}_\alpha U^\beta) - \mathcal{K}\boldsymbol{U}\cdot\boldsymbol{U}\,\mathrm{d}\Gamma\\ &+\frac{2\mathrm{Ec}}{\mathcal{C}[\Gamma]^3}(\delta^{(1)}\mathcal{C}[\Gamma;\boldsymbol{V}])^2,\end{aligned} \tag{5.154}$$

where material velocity $\boldsymbol{V}$ must fulfil $\int_\Gamma \boldsymbol{N}\cdot\boldsymbol{V}\mathrm{d}\Gamma = 0$. The second variation (5.154) contains four parts: a purely normal and extrinsic contribution (line 1 and 2), a cross term (line 3) which couples the tangential vector field $\boldsymbol{U}$ with the normal scalar field Θ of material velocity $\boldsymbol{V}$, a purely intrinsic integral (line 4) plus a contribution from the first order variation (line 5).

We next show that, for an equilibrium shape Γ, the integrals on line 3 and 4 of (5.154) can be significantly simplified. We begin with the second integral on line 3 of (5.154),

$$\begin{aligned}\int_\Gamma 2I\!I^\alpha_\beta\hat{\nabla}_\alpha(\Theta U^\beta)\,\mathrm{d}\Gamma &= \int_\Gamma -2(\hat{\nabla}_\alpha I\!I^\alpha_\beta)\Theta U^\beta\,\mathrm{d}\Gamma = \int_\Gamma -2(\hat{\nabla}_\beta I\!I^\alpha_\alpha)\Theta U^\beta\,\mathrm{d}\Gamma \qquad \text{Codazzi}\\ &= \int_\Gamma -2(\hat{\nabla}_\beta 2\mathscr{H})\Theta U^\beta\,\mathrm{d}\Gamma = \int_\Gamma 4\mathscr{H}\mathrm{Div}_\Gamma(\Theta\boldsymbol{U})\,\mathrm{d}\Gamma.\end{aligned} \tag{5.155}$$

We then substitute identity (5.155) into the integrals on line 3 of (5.154) and compute,

$$\begin{aligned}&\frac{\mathrm{Ec}}{\mathcal{C}[\Gamma]^2}\int_\Gamma \mathrm{Div}_\Gamma(\Theta\boldsymbol{U})(\boldsymbol{N}\cdot\boldsymbol{D}\Psi)^2\,\mathrm{d}\Gamma + \int_\Gamma 2I\!I^\alpha_\beta\hat{\nabla}_\alpha(\Theta U^\beta)\,\mathrm{d}\Gamma\\ =&\int_\Gamma\left\{(\boldsymbol{N}\cdot\boldsymbol{D}\Psi)^2\frac{\mathrm{Ec}}{\mathcal{C}[\Gamma]^2} + 4\mathscr{H}\right\}\mathrm{Div}_\Gamma(\Theta\boldsymbol{U})\,\mathrm{d}\Gamma\\ =&\int_\Gamma(-\Lambda+2\mathscr{H})\mathrm{Div}_\Gamma(\Theta\boldsymbol{U})\,\mathrm{d}\Gamma = \int_\Gamma -2(\boldsymbol{U}\cdot\hat{\nabla}\mathscr{H})\Theta\,\mathrm{d}\Gamma,\end{aligned} \tag{5.156}$$

where in the last line of (5.156) the equilibrium condition (5.140) on Λ is invoked for the critical shape Γ. The integral from line 4 of (5.154) is actually zero,

$$\begin{aligned}&\int_\Gamma(\mathrm{Div}_\Gamma\boldsymbol{U})^2 - (\hat{\nabla}_\alpha U^\beta)(\hat{\nabla}_\beta U^\alpha) - \mathcal{K}\boldsymbol{U}\cdot\boldsymbol{U}\,\mathrm{d}\Gamma\\ =&\int_\Gamma(\mathrm{Div}_\Gamma\boldsymbol{U})^2 + U^\beta\hat{\nabla}_\alpha\hat{\nabla}_\beta U^\alpha - \mathcal{K}\boldsymbol{U}\cdot\boldsymbol{U}\,\mathrm{d}\Gamma\\ =&\int_\Gamma(\mathrm{Div}_\Gamma\boldsymbol{U})^2 + U^\beta\hat{\nabla}_\beta\hat{\nabla}_\alpha U^\alpha + U^\beta\mathcal{R}^\alpha{}_{\nu\alpha\beta}U^\nu - \mathcal{K}U^\alpha G_{\alpha\beta}U^\beta\,\mathrm{d}\Gamma\\ =&\int_\Gamma(\mathrm{Div}_\Gamma\boldsymbol{U})^2 + U^\beta\hat{\nabla}_\beta(\mathrm{Div}_\Gamma\boldsymbol{U}) + U^\alpha(\mathcal{R}ic_{\alpha\beta} - \mathcal{K}G_{\alpha\beta})U^\beta\,\mathrm{d}\Gamma\\ =&\int_\Gamma(\mathrm{Div}_\Gamma\boldsymbol{U})^2 - (\hat{\nabla}_\beta U^\beta)(\mathrm{Div}_\Gamma\boldsymbol{U})\,\mathrm{d}\Gamma = 0,\end{aligned} \tag{5.157}$$

where in the last line of (5.157) we have used the fact that the Ricci tensor of a two-dimensional manifold is intrinsic (Kreyszig, 1991), i.e. $\mathcal{R}ic_{\alpha\beta} = \mathcal{K}G_{\alpha\beta}$. With identities (5.156) and (5.157) substituted into (5.154) we obtain the final form of the second shape variation of the total potential energy $\mathcal{F}[\gamma]$ about an equilibrium shape Γ,

$$\begin{aligned}\frac{\mathrm{d}^2\mathcal{F}[\gamma]}{\mathrm{d}\epsilon^2}\Big|_{\epsilon=0} = &-\frac{\mathrm{Ec}}{\mathcal{C}[\Gamma]^2}\int_\Gamma 2(\boldsymbol{N}\cdot\boldsymbol{D}\Psi)(\boldsymbol{N}\cdot\boldsymbol{D}\Psi')\Theta + 4\mathcal{H}\Theta^2(\boldsymbol{N}\cdot\boldsymbol{D}\Psi)^2\,\mathrm{d}\Gamma \\ &+\int_\Gamma \boldsymbol{D}_\Gamma\Theta\cdot\boldsymbol{D}_\Gamma\Theta + (2\mathcal{K}-4\mathcal{H}^2)\Theta^2\,\mathrm{d}\Gamma \\ &-\int_\Gamma(\boldsymbol{U}\cdot\boldsymbol{D}_\Gamma 2\mathcal{H})\Theta\,\mathrm{d}\Gamma + \frac{2\mathrm{Ec}}{\mathcal{C}[\Gamma]^3}(\delta^{(1)}\mathcal{C}[\Gamma;\boldsymbol{V}])^2 \quad \text{for} \quad \int_\Gamma \Theta\,\mathrm{d}\Gamma = 0,\end{aligned} \tag{5.158}$$

where the Eulerian derivative Ψ' is the harmonic solution to the boundary value problem,

$$\left.\begin{aligned}\operatorname{Div}\boldsymbol{D}\Psi' &= 0 && \text{in} \quad \Omega,\\ \Psi' &= -(\boldsymbol{N}\cdot\boldsymbol{D}\Psi)\Theta && \text{on} \quad \Gamma.\end{aligned}\right\} \tag{5.159}$$

Later we will show that the integrals in the first two lines of the second shape variation (5.158) directly lead to the famous Rayleigh charge limit Q_{Ra}. However, to author's knowledge, the terms in the last line of (5.158) have not been derived before in literature. This is because when a liquid body in equilibrium has both constant mean curvature and constant charge density over its surface, e.g., the shape of a perfect sphere or cylinder considered by most literature, the integrals in the last line of (5.158) are identically zero. However, when the equilibrium shape has a heterogeneous distribution of surface charges, the first variation of capacitance $\delta^{(1)}\mathcal{C}[\Gamma;\boldsymbol{V}]$ from equation (5.52) may not vanish for an arbitrary volume-conserving material velocity $\boldsymbol{V}$. Similarly, if boundary Γ is not a surface of constant curvature then the surface-advection term $\boldsymbol{U}\cdot\boldsymbol{D}_\Gamma 2\mathcal{H}$ is not necessarily zero for every tangential velocity field $\boldsymbol{U}$.

Energy stability of an isolated charged spherical drop

Let Γ be a dimensionless unit sphere (so that the dimensional radius of a physical drop becomes the characteristics length scale R_c). It's natural to use the spherical coordinates $\boldsymbol{X} = (R,\vartheta,\varphi)$ centered at origin of the drop for the material frame Ω. It's easy to verify that a uniformly charged spherical drop is a critical shape of the total potential energy $\mathcal{F}[\gamma]$, the analytic solution of which is given by

$$\Psi(\boldsymbol{X}) = \frac{1}{R}, \quad \boldsymbol{N}\cdot\boldsymbol{D}\Psi|_\Gamma = -1, \quad \mathcal{C}[\Gamma] = 4\pi, \quad \mathcal{H} = -1, \quad \mathcal{K} = 1. \tag{5.160}$$

For a general equilibrium shape, the term $(\delta^{(1)}\mathcal{C}[\Gamma;\boldsymbol{V}])^2$ in the second shape variation (5.158) is nonzero. However in the special case (5.160) of a spherical drop the dimensionless surface charge $\boldsymbol{N}\cdot\boldsymbol{D}\Psi$ is constant on the entire spherical surface which would completely eliminate this term since

$$\delta^{(1)}\mathcal{C}[\Gamma;\boldsymbol{V}] = \int_\Gamma \Theta(\boldsymbol{N}\cdot\boldsymbol{D}\Psi)^2\,\mathrm{d}\Gamma = (\boldsymbol{N}\cdot\boldsymbol{D}\Psi)^2\int_\Gamma \boldsymbol{V}\cdot\boldsymbol{N}\,\mathrm{d}\Gamma = 0 \tag{5.161}$$

where the first order condition of volume constraint is used. The contribution from tangential variation $\boldsymbol{V}_\Gamma$ also drops out due to the constant mean curvature of a spherical surface. Substituting critical solution (5.160) into second shape variation (5.158) yields a surface integral involving normal variation Θ only,

$$\frac{\mathrm{d}^2\mathcal{F}[\gamma]}{\mathrm{d}\epsilon^2}\Big|_{\epsilon=0} = \frac{\mathrm{Ec}}{8\pi^2}\int_\Gamma (\boldsymbol{N}\cdot\boldsymbol{D}\Psi')\Theta + 2\Theta^2\,\mathrm{d}\Gamma - \int_\Gamma \Theta\Delta_\Gamma\Theta + 2\Theta^2\,\mathrm{d}\Gamma, \tag{5.162}$$

where we have replaced the term $\boldsymbol{D}_\Gamma\Theta\cdot\boldsymbol{D}_\Gamma\Theta$ by the Laplace-Beltrami operator $\Delta_\Gamma = \hat{\nabla}^\alpha\hat{\nabla}_\alpha$ via integration by parts on a boundary-less manifold (surface of a sphere). The quadratic forms Θ^2 and $\Theta\Delta_\Gamma\Theta$ are local in the sense that only multiplication and differential operator are involved. On the other hand, the term $\boldsymbol{N}\cdot\boldsymbol{D}\Psi'$ is truly nonlocal: the solution to the boundary value problem (5.159) of the Eulerian derivative Ψ' requires the knowledge of normal variation Θ everywhere on Γ and therefore is considered nonlocal with respect to the intrinsic coordinates of surface Γ. Analytic solution to (5.159) for a general shape Γ is often not possible. However, for the geometry of a unit sphere, it can be treated by the means of spherical harmonics expansion. In what follows, we refer to the elementary treatise by Byerly (1895) for various properties of spherical harmonics functions.

Let $Y_\ell^m(\vartheta,\varphi)$ be the standard notation for spherical harmonics of integer degree $\ell\geq 0$ and integer order $-\ell\leq m\leq\ell$. Normal field Θ on the unit sphere can be expanded in terms of the spherical harmonics Y_ℓ^m,

$$\Theta(\vartheta,\varphi) = \sum_{\ell=0}^{\infty}\sum_{m=-\ell}^{\ell} a_\ell^m Y_\ell^m(\vartheta,\varphi), \tag{5.163}$$

where each complex coefficient

$$a_\ell^m = \langle Y_\ell^m, \Theta\rangle \tag{5.164}$$

is given by the orthonormal projection under inner product integration $\langle\cdot,\cdot\rangle$ over the surface of a unit sphere (or equivalently the solid angle) defined as

$$\langle f, g\rangle = \int_\Gamma f(\vartheta,\varphi)^\dagger g(\vartheta,\varphi)\,\mathrm{d}\Gamma. \tag{5.165}$$

Here $(\cdot)^\dagger$ is the complex conjugate operator. We will suppress the (ϑ,φ)-dependence from now on and only refer to the projected coefficients instead. Note the zeroth degree coefficient must vanish due to the volume constraint,

$$a_0^0 = \langle Y_0^0, \Theta\rangle \propto \int_\Gamma \Theta\,\mathrm{d}\Gamma = \int_\Gamma \boldsymbol{V}\cdot\boldsymbol{N}\,\mathrm{d}\Gamma = 0. \tag{5.166}$$

Any linear combination of spherical harmonics above $\ell = 0$ would have a zero spherical mean which implies the expansion (5.163) of Θ is an admissible variation as long as $a_0^0 = 0$. We then replace boundary condition for the harmonic potential Ψ' in the

auxiliary boundary value problem (5.159) by the expansion (5.163). The solution to the harmonic problem for Eulerian derivative Ψ' exterior to the spherical drop is found to be

$$\Psi' = \sum_{\ell=0}^{\infty} \sum_{m=-\ell}^{\ell} \frac{1}{R^{\ell+1}} a_\ell^m Y_\ell^m \quad \text{in} \quad \Omega_{\text{vac}}. \tag{5.167}$$

Normal vector $\boldsymbol{N}$ on the surface of a unit sphere is simply the unit vector in the radial direction which yields

$$\boldsymbol{N} \cdot \boldsymbol{D}\Psi' = \sum_{\ell=0}^{\infty} \sum_{m=-\ell}^{\ell} -(\ell+1) a_\ell^m Y_\ell^m \quad \text{on} \quad \Gamma. \tag{5.168}$$

On the other hand, the Laplace-Beltrami operator Δ_Γ defined for the surface of a unit sphere is diagonalized by the spherical harmonics Y_ℓ^m with eigenvalue $-\ell(\ell+1)$,

$$\Delta_\Gamma \Theta = \sum_{\ell=0}^{\infty} \sum_{m=-\ell}^{\ell} -\ell(\ell+1) Y_\ell^m. \tag{5.169}$$

Substituting expansions (5.169), (5.168) and (5.163) into the second shape variation (5.162) results in a double summation over two sets of integers $\{\ell, m\}$ and $\{\ell', m'\}$,

$$\frac{\mathrm{d}^2 \mathcal{F}[\gamma]}{\mathrm{d}\epsilon^2}\Big|_{\epsilon=0} = \sum_{\ell,m} \sum_{\ell',m'} \left\{ \frac{\mathrm{Ec}}{8\pi^2}(1-\ell) + \ell(\ell+1) - 2 \right\} a_\ell^m a_{\ell'}^{m'} \int_\Gamma Y_\ell^m Y_{\ell'}^{m'} \, \mathrm{d}\Gamma. \tag{5.170}$$

Orthonormality of spherical harmonics doesn't directly apply yet since Y_ℓ^m under the integral (5.170) is missing the complex conjugate defined in the inner product (5.165). We note that $Y_\ell^{m\dagger}$ can be recovered through manipulation of the spherical harmonics identity $Y_\ell^m = (-1)^m Y_\ell^{-m\dagger}$. We first consider the partial summation in integer m',

$$\begin{aligned}
&\sum_{m'=-\ell'}^{\ell'} a_\ell^m a_{\ell'}^{m'} \int_\Gamma Y_\ell^m Y_{\ell'}^{m'} \, \mathrm{d}\Gamma \\
&= \sum_{m'=-\ell'}^{\ell'} a_\ell^m a_{\ell'}^{m'} \langle Y_\ell^{m\dagger}, Y_{\ell'}^{m'} \rangle = \sum_{m'=-\ell'}^{\ell'} a_\ell^m a_{\ell'}^{m'} (-1)^m \langle Y_\ell^{-m}, Y_{\ell'}^{m'} \rangle \\
&= \sum_{m'=-\ell'}^{\ell'} \langle Y_\ell^m, \Theta \rangle a_{\ell'}^{m'} \frac{1}{(-1)^m} \langle Y_\ell^{-m}, Y_{\ell'}^{m'} \rangle = \sum_{m'=-\ell'}^{\ell'} \langle Y_\ell^{-m\dagger}, \Theta \rangle a_{\ell'}^{m'} \langle Y_\ell^{-m}, Y_{\ell'}^{m'} \rangle \\
&= \sum_{m'=-\ell'}^{\ell'} \langle Y_\ell^{-m}, \Theta \rangle^\dagger a_{\ell'}^{m'} \langle Y_\ell^{-m}, Y_{\ell'}^{m'} \rangle \qquad \text{Note } \Theta \text{ is a real function} \\
&= \sum_{m'=-\ell'}^{\ell'} a_\ell^{-m\dagger} a_{\ell'}^{m'} \delta_{(-m)m'} \delta_{\ell\ell'} = a_\ell^{-m} a_{\ell'}^{-m\dagger} \delta_{\ell\ell'}.
\end{aligned} \tag{5.171}$$

Identity (5.171) reduces the double summation to an infinite sum of real quadratic forms,

$$\frac{\mathrm{d}^2 \mathcal{F}[\gamma]}{\mathrm{d}\epsilon^2}\Big|_{\epsilon=0} = \sum_{\ell=1}^{\infty} \mathcal{F}_\ell \sum_{m=-\ell}^{\ell} a_\ell^m a_\ell^{m\dagger}, \quad \mathcal{F}_\ell = \frac{\mathrm{Ec}}{8\pi^2}(1-\ell) + \ell(\ell+1) - 2, \tag{5.172}$$

where $-m$ in identity (5.171) is relabeled as m provided symmetry in the summation of $m = -\ell, \ldots, \ell$. Since $a_\ell^m a_\ell^{m\dagger} \geq 0$ is always non-negative, the coefficients $\mathscr{F}_\ell$ in the second shape variation (5.172) play a key role in determining the contribution of each spherical harmonics deformation Y_ℓ^m to the total potential energy.

The $\ell = 1$ coefficient $\mathscr{F}_1$ is always zero regardless of the value of the electric-capillary number Ec and hence doesn't contribute to any change in the potential energy $\mathscr{F}[\gamma]$. This is due to the translational symmetry in the electrostatic energy and in the surface energy. The three harmonic modes Y_1^{-1}, Y_1^0 and Y_1^1 correspond to infinitesimal shifts in the direction of three axes of the three-dimensional Euclidean space $\mathbb{R}^3$ which must leave each component of the total potential energy individually invariant.

Rayleigh's charge limit Q_{Ra} controls the sign of $\mathscr{F}_2$ in the $\ell = 2$ modes. These are the modes of prolate and oblate deformations, the combination of which leads to elongation or depression of the spherical drop about an arbitrarily oriented symmetry axis. With some nonzero electric-capillary number $\mathrm{Ec} = Q^2/2\varepsilon_0\sigma R_c^3$, it is possible to set the sign of every $\ell = 2$ quadratic form $a_2^m a_2^{m\dagger}$ to be strictly negative if the following inequality is satisfied,

$$\mathscr{F}_2 = -\frac{\mathrm{Ec}}{8\pi^2} + 4 < 0 \quad \text{if} \quad \mathrm{Ec} > 32\pi^2 \;\Leftrightarrow\; Q > 8\pi\sqrt{\sigma\varepsilon_0 R_c^3} = Q_{\mathrm{Ra}}. \tag{5.173}$$

We can make a more general statement regarding the sign of coefficient $\mathscr{F}_2$: given some integer $\ell' > 1$,

$$\text{if} \quad Q_{\ell'} < Q < Q_{\ell'+1} \quad \text{then} \quad \begin{cases} \mathscr{F}_\ell < 0 & \text{for} \quad 2 \leq \ell \leq \ell', \\ \mathscr{F}_\ell > 0 & \text{for} \quad \ell \geq \ell' + 1, \end{cases} \tag{5.174}$$

where

$$Q_{\ell'} = 4\pi\sqrt{(\ell'+2)\sigma\varepsilon_0 R_c^3} \tag{5.175}$$

is the ℓ'-th Rayleigh charge. If the total charge of a spherical drop falls between Q_ℓ and $Q_{\ell+1}$, then the modes of harmonic deformation $\boldsymbol{V} \propto Y_\ell^m \boldsymbol{N}$ equal to or below degree ℓ' contribute negatively to its potential energy $\mathscr{F}[\gamma]$ while the modes above degree ℓ act to increase the energy. The Rayleigh charge limit $Q_{\mathrm{Ra}} = Q_2$ is the special case where all deformation modes are only allowed to increase the total potential energy. In other words, an isolated perfectly conductive spherical drop, if charged below Q_{Ra}, is forbidden to release any of its potential energy into other forms such as kinematic energy or viscous dissipation.

5.6 Conclusion

Whereas stability of electrically conductive spherical drops has been scrutinized for decades based on Eulerian approaches, a geometrically rigorous treatment on the total potential energy of an arbitrarily shaped liquid body undergoing both normal and

tangential deformations is still lacking. In this work, we apply well developed concepts of convective Lagrangian coordinates from continuum mechanics to the calculation of electrostatic energy and surface energy of an isolated charged liquid drop assigned to a continuously deformed domain. Our methodology allows precise examinations on the effects of deformation arising from both normal and tangential directions of the liquid interface. The overall computational procedure is systematic, free of heuristics in assigning orders of infinitesimal terms and exactly enforces the constraint of constant liquid volume.

For a conductive liquid body in equilibrium (not necessarily a perfect sphere or cylinder), our calculation indicates that tangential deformation does not make a difference in the first shape variation of its total potential energy. However, in the calculation of the second shape variation, which is required for searching stability criterion in energy landscape, we have unmasked two additional contributions for equilibrium shapes which may carry a nonuniform distribution of surface charges and a nonconstant mean curvature over its surface such as the celebrated Taylor cone (G. I. Taylor, 1964). These contributions have been previously obscured by the spherical geometry and omission of tangential deformations usually assumed in literature. The combined effects of these neglected terms on the stability of general equilibrium shapes are left for future studies.

The Lagrangian formalism employed in this work is completely general and systematic. By following the transformation rules of convective Lagrangian coordinates, it is possible, albeit tedious, to carry out shape variation of the potential energy to the third order, similar to the calculation Zhong-can and Helfrich (1989) conducted for the bending energy of vesicle membrane, which would necessarily reveal the directions at which the local energy landscape near an equilibrium shape is tilted. In other words, the third shape variation explains whether an oblate or a prolate ellipsoid is favored when a spherical liquid drop charged just above the Rayleigh limit undergoes deformation. It is also conceivable that the use of convective Lagrangian coordinates allows systematic modifications to the calculation of electrostatic energy and its variations in the presence of a uniform electric field or spatial charges.

Chapter 6

DYNAMIC CONE FORMATION IN CONDUCTIVE LIQUIDS: INVISCID THEORY

6.1 Interfacial Cone Formation in Electrically Conductive Liquids

As already discussed in Chapter 5, if charged beyond a critical level, the interface of an electrically conductive liquid surrounded by an insulator (e.g., air, a vacuum or another dielectric medium) becomes susceptible to the influence of intense electric field. Formation of small conical interfacial features, followed by ejection of liquid filaments or ions in the end, often accompanies the strong distortion of an electrified liquid after its initial loss of stability. This unique electrohydrodynamical phenomenon is often associated with the terminology, Taylor cones, named after G. I. Taylor (1964)'s seminal calculation on the cone opening angle. Although the earliest recorded observation of these conical shapes can be traced back to the 16th century when Gilbert (1600) in his work De Magneto described the deformation of a water drop into a cone in the presence of a charged object and has fascinated scientists in many different disciplines for centuries since then.

It is now commonly accepted that the distinguishing factor which separates many cone-related phenomena into two major categories is liquid electrical conductivity. An infinite conductivity corresponds to the electrostatic limit of a perfect conductor or dielectrics where surface charges are instantaneously distributed on the interface and all the Maxwell forces act normally on the interface. Under such an assumption G. I. Taylor (1964) reported that a perfectly conductive liquid subject only to capillary and electrical forces in hydrostatic equilibrium must adopt the shape of a cone with a vertex angle of 98.6°, known as the Taylor cone angle. On the contrary, for a medium of finite or high conductivity, charge relaxation, i.e. convection-driven departures of the surface charge density away from the value it would have on a perfect conductor, takes a finite amount of time (Saville, 1997). The situation then becomes much complex as tangential Maxwell stresses may be present, leading to shear forces, hence tangential accelerations, on the charged liquid interface that are eventually responsible for jet emission observed in experiments.

Most researches on liquids of finite or high conductivity are oriented around the Taylor cone-jet configuration, a regime where a steady non-breaking jet issues continuously from the cone apex, eventually either breaking into a spray of charged drops, known as electrospray (Fernández de la Mora, 2007), or being drawn further as a continuous fiber (possibly whipping and bending) instead of a charged cloud, known as electrospin (Hohman et al., 2001a; Hohman et al., 2001b). The model of charge transport in

the literature concerning the theory of steady but not static cone-jet modes is largely based on the ohmic conduction (uniform electrical conductivity) and leaky dielectric model (ohmic liquid governed by Stokes equation) introduced and popularized by the reviews (Melcher and G. I. Taylor, 1969; Saville, 1997). The crucial role of charge transport in cone-jet phenomenon has been confirmed in a number of computational studies such as simulated electrohydrodynamic tip streaming of a leaky-dielectric liquid film (Collins, Jones, et al., 2007) and of a conducting drop subject to a uniform external electric field (Collins, Sambath, et al., 2013), progeny formation from critically charged conductive inviscid drops (Burton and Taborek, 2011), micro-jet emission from the tip of low-conductivity pendant drops subject to a step change in the electric field magnitude (Ferrera et al., 2013), first-droplet ejection from a parent capillary meniscus under volumetric relaxation of charge density in the hydrodynamic bulk (Gañán-Calvo, López-Herrera, Rebollo-Muñoz, et al., 2016; Gañán-Calvo, López-Herrera, Herrada, et al., 2018) and the transient electrohydrodynamic response of a liquid drop containing ions, to both small and large values of electric field (Pillai et al., 2016). It's worth noting that the conic base of experimentally observed cone-jet configurations sometimes exhibits substantially smaller opening angles than the Taylor cone due to the presence of space charges carried by the jet which technically violates Taylor's assumption of free-space electrostatics in the region exterior to the cone and inevitable causes repulsion between jet and conic base.

Despite large amount of literature and applications on cone-jet related physics (e.g., electrospray and electrospin), little has been known of the transient process that a round meniscus takes to morph into a conic cusp before any criterion for spontaneous ejection of ion or fluid is met. In particular it is the subject of this chapter to decipher the electrohydrodynamic mechanism underlying the rapid development of conic tips in perfectly conductive liquids. There are many practical reasons that it is important to understand the dynamic process of cone formation in addition to steady cone-jet. For instance, the electrohydrodynamic direct-writing technique (C. Chang, Limkrailassiri, and L. Lin, 2008; Huang et al., 2013), one of the emerging solutions to the increasing demand for micro/nano-scale manufacture, can be used to print nanofibers onto a large-area substrate in a direct, continuous, controllable and free-form fashion. The development of fine and steady jets at cone apex is known from experiments to correlate strongly with electrical conductivity: thread diameter approximately shrinks toward zero in a rate inversely proportional to a power of the electrical conductivity (Fernández de la Mora, 2007). Therefore knowledge of bulk hydrodynamics at the singular limit of infinite conductivity could shed light upon the onset of nano-/micro-sized jet emitted from liquid tips of high but finite electrical conductivity. There is also liquid metal ion source (LMIS) which was originally developed as the charge material of electrostatic droplet sprayers as a heavy charged particle source for electric space micropropulsion

(Bartoli et al., 1984; Rüdenauer, 2007; Tajmar et al., 2009). It was then discovered that LMIS device was a high brightness source of metal ions, capable of being focused to spots of nanometer dimensions. LMIS now becomes a fundamental component of focused ion beam microscopy and micromachining (Orloff, 2017), one of the most precise micro-/nano-fabrication tools at the present time. Once the local intensity of electric field reaches above certain threshold, it causes ions to begin to form through field evaporation and field ionization of the metal atoms in the vapor, a process similar to the mechanism that inspired Fenn (1993) for his Nobel prize winning technology mass spectrometry (Guerrero et al., 2007). The field threshold for common LMIS (e.g., gallium and indium) is on the order of $10^9 \mathrm{V/m}$ (Orloff, Utlaut, and Swanson, 2003). It is crucial to understand the hydrodynamic origin of highly curved cone apex that spontaneously forms in liquid metals which naturally exceeds the requirement for field ion evaporation.

In this chapter, we exclusively focus on the process of dynamic cone formation in perfectly conductive liquids during a small time window long after initial destabilization and but shortly before the onset of other physics on smaller scales (e.g., secondary fluid ejection or field ion evaporation). In practice, the rapid development of conical cusps at liquid interface is notoriously difficult for experimental observations owning to its transcendental nature at small spatial dimensions and explosive fluid/ion ejection that ensues. As technology advances, accurate imaging and measurement of cone formation have only become available in the last few decades since G. I. Taylor (1964)'s original photography of oil/water interfaces. Although it still poses tremendous challenges in high-speed and high-resolution imaging, appearance of the Taylor cone has been recognized in experiments involving a variety of highly conductive liquids including stroboscopic shadow photography of indium-gallium alloy wetting a liquid-metal cathode under high vacuum (Baskin et al., 1995), in situ observation of AuGe liquid alloy and tin liquid metal ion source in a high-voltage transmission electron microscope (Driesel and Dietzsch, 1996; Driesel, Dietzsch, and Mühle, 1996), determination of onset voltage for ionic liquid EMI-BF at tip of a filled capillary tip of a microchined electrospray emitter (Krpoun and Shea, 2008), controlled meniscus evolution of deionized water in microgravity environment over a wide range of fluid properties (Elele et al., 2015) and free surfaces of cryogenic superfluid helium charged from below (Moroshkin et al., 2017).

Direct numerical simulations have also been developed over years to resolve final stages of cone formation that are not accessible to current experiment and imaging techniques. Suvorov and Zubarev (2004) employed standard finite difference discretization of the axisymmetric Navier-Stokes equation for free surface of liquid gallium in vacuum under a flat electrode, where the governing fluid and electrostatic equations were transformed to a set of curvilinear coordinates and numerical grid adaptive to the evolving liquid/vacuum interface. They reported that the formation of a conical singularity seemed to be universal, i.e. irrespective of initial surface shape (in their case a Gaussian

bump). Collins, Jones, et al. (2007) solved the Navier-Stokes equation coupled with surface charge transport modeled by ohmic conduction for a conducting film under a different electrode geometry (a metallic cylindrical rod protruding from upper plate). Their finite element method adaptively remeshed the liquid domain and its interface with elliptic mesh generation. It was confirmed in the paper that when charge transport was turned off, no electrohydrodynamic tip streaming was observed at all and conic cusping singularity occurred instead. Giglio et al. (2008) simulated the spontaneous deformation of an initially critically charged droplet by a spectral method utilizing spherical harmonic functions in a prolate spheroidal coordinate system. The liquid was assumed to be inviscid and incompressible with an irrotational flow. Their simulation (and experiment) suggested the droplet shape right before charge emission was remarkably well fitted by a "lemon" profile with two pointed ends, however, substantially narrower than the Taylor cone. Later, the identical simulation was repeated and refined by Burton and Taborek (2011) via a different yet much more accurate numerical method based on boundary integral formulation of harmonic potential. The ultrahigh resolution of their scheme revealed long-sought convergence to the Taylor cone angle at two conical ends of the droplet as well as decades of power-law behavior of tip electric field and curvature during the last stage of cone formation.

A common theme shared by these researches is that, the apical region of a round meniscus, after initial instability is triggered, continuously undergoes a self-sharpening and accelerating process towards a conic shape while simultaneously accumulating a significant amount of surface charges concentrating near the cone apex. Here is a summary of we have learned from these experiments and numerical simulations. First of all, cone formation in highly conductive liquid is unequivocally a dynamic process. The continuously sharpening and simultaneous enhancement of the electric field near the apex are always accompanied by increasingly large bulk acceleration of the liquid. Secondly, dynamic cone formation appears to be a runaway process that seldom halts on its own. It's usually the non-hydrodynamic causes such as controlled quench-down of electrode potential, ejection of fluid filament/jet due to small-scale charge transport or field ion evaporation into ambient gas, that eventually mitigate the runaway process. Thirdly, since none of the experiments or simulations were set up identical to each other or to pursue an idealization of G. I. Taylor (1964)'s electrostatic solution, formation of conic cusp at liquid/gas interface is very likely to be universal, i.e. not sensitive to geometric details of ambient electrode or initial liquid shape as long as the interface can be destabilized in the first place.

Theoretical understanding of this phenomenon is often credited to G. I. Taylor (1964)'s hydrostatic equilibrium between capillary and electrical forces. Despite simplicity of his static argument, the cone angle Taylor predicted has simulated a large amount of theoretical effort on understanding the steady cone-jet configuration, for instance, the

cone-jet mode of infinitely conductive liquids with a negligibly short jet that opens into the spray infinitesimally close to the cone apex (Fernández de la Mora, 1992), the analytical cone-jet solution of infinitely long and thin, charged liquid jet issuing from the tip of Taylor cone (Gañán-Calvo, 1997), flow structure of the Taylor meniscus and emitted jet examined through singular perturbation methods in the limit of low flow rates (Cherney, 1999), various scaling laws between jet radius, current carried by the jet, liquid dielectric and electrical conductivity (Fernández de la Mora, 2007) and a recent extension of previous theories to account for variations of the cone angles (non-Taylor) by replacing the equipotential assumption of conic base with a finite electric current along the cone surface (Subbotin and Semenov, 2015).

Technically these aforementioned theories are "dynamic" in the sense that surface charges are being steadily transported downstream along the jet. However, the overall interface shape of the cone-jet is still stationary. Besides, none of these existing theories have addressed the spontaneous transition from a round meniscus to a conic cusp. Significant progress has been achieved in the study of non-stationary electrohydrodynamic behavior since Zubarev (2001) pioneered a self-similar theory to capture universality and dynamic nature of conic cusp formation in perfectly conductive inviscid liquid. The novelty of his work lies in the self-similar scaling of an unsteady flow field which results in nontrivial inertia forces contributing to the stress balance at conic surface. The self-similar dynamics that Zubarev developed is also a fully nonlinear theory which is normally obscured if only infinitesimally weak disturbances, as in conventional linear stability analysis, of a Taylor cone under hydrostatic equilibrium, are considered (Sujatha et al., 1983; Chung, Cutler, and Miskovsky, 1989). As correctly pointed out by Zubarev (2001), dynamic cone formation is the result of local balance between capillary, Maxwell (electrostatic) and inertia forces, which in his self-similar framework all blow up at the same rate as the conical singularity is approached. At the time, Zubarev was not able to obtain the exact solutions to his self-similar theory which requires sophisticated numerical techniques. Instead he employed asymptotic expansions of field variables to approximate the true solutions far away from the cone apex. Our work is an extension and an completion of Zubarev (2001)'s initial effort by introducing a more important yet still compatible leading order term in the asymptotic series, based on which a system of boundary integral equations are formulated to numerically compute the exact solutions conforming to the asymptotic behavior analytically derived.

In this chapter we hope to clarify the following: first of all, the classical Taylor cone is merely a geometric condition under which local capillary and Maxwell stresses scale with each other all the way up to the apex. The underlying liquid in the bulk is not necessarily static. Secondly, in inviscid regime formation of conic cusp is a dynamically self-similar process for perfectly conductive liquids, during which capillary, Maxwell and inertia forces all blow up in the vicinity of cone apex. The precise boundary conditions

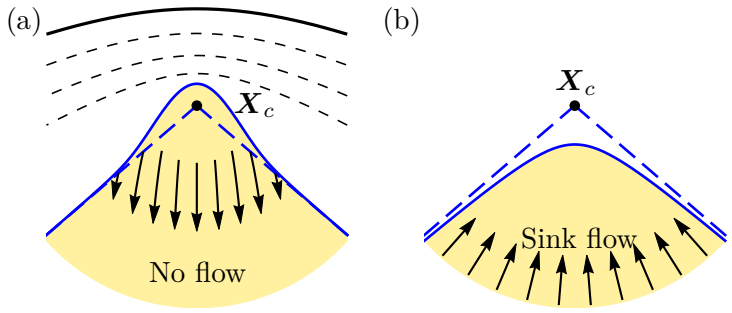

Figure 6.1: Common depictions of a dynamic cone: (a) A pulsating unstable liquid meniscus "glued" onto a far-field Taylor cone (dashed blue) in hydrostatic equilibrium subject to a specific electrode geometry (solid black) which coincides with one of the electric potential contours (dashed black). According to Chung, Cutler, and Miskovsky (1989), no liquid motion can be allowed far away from the conical point $\boldsymbol{X}_c$. The unstable meniscus oscillates up and down due to small vertical shifts of the electrode position. (b) A self-reinforced meniscus converging to the Taylor cone angle due to a spherically symmetric sink flow (arrow) based on Zubarev (2001)'s self-similar mechanism.

(flow or electrostatics) of ambient environment are irrelevant compared to the dominant local scales. Thirdly, we wish to establish the multiplicity of dynamic cone formation. The widespread spherically symmetric sink flow moving tangentially to the conic surface predicted by Zubarev (2001) is one of the many possibilities in the self-similar framework of inviscid cone formation. Our complete asymptomatic analysis independently shows that in addition to sink flow, pressure mismatch between capillary and Maxwell stresses induces a novel uplifting velocity field near cone apex, which we coin the"lifting" flow, with streamlines nearly vertical upward intercepting the conic surface at a finite angle. The exact solution family, uncovered by our use of a patched boundary integral formulation, depends on two parameters reflecting the relative strength between capillary, Maxwell and inertia forces. Novel hydrodynamic patterns in the vicinity of cone apex such as counter flows, stagnation point and oscillatory pressure field during dynamic cone formation are also revealed for the first time.

6.2 Previous Theoretical Developments of Dynamic Cone Formation

In this section we briefly review some previously proposed theoretical analysis on the dynamics of a conic meniscus which seem to prevail in literature.

Conventional hydrostatic stability

Chung, Cutler, and Miskovsky (1989) studied a simplified three-dimensional axially symmetric model for a liquid ion source comprised of a conducting liquid by examining possible leading order shape deformations away from the exact Taylor cone. To author's knowledge their work was the first attempt to introduce a dynamic Taylor cone. They

explored possible deformations in the quasi-hydrostatic limit where deformation is purely caused by hydrostatic forces as well as in the hydrodynamic limit where the inertia forces of the liquid are expected to significantly contribute to interfacial pressure. They treated the exact Taylor cone as the zeroth-order configuration and linearized the Bernoulli's equation to construct the first-order fluid equations. In both limits they made predictions on the evolution of the shape deformation and critical voltage at the onset of instability.

However such linearization excludes strongly nonlinear behavior of conducting liquid. As a result, Chung, Cutler, and Miskovsky (1989) found it was impossible to match inner solutions (near apex) of velocity field to an active flow in the far field (away from apex) and thus concluded their "hydrodynamic" analysis with the claim that there should no fluid motion in the bulk away from the apex (i.e. only hydrostatic), which is contradicting their original intention of a "dynamic" analysis. In addition, as shown in figure 6.1(a) their calculation was deliberately engineered for a very specific electrode geometry introduced in the experiment of G. I. Taylor (1964), the one and only one configuration that a truly hydrostatic Taylor cone must admit. They conjectured that the pulsation of a liquid meniscus "glued" onto a static Taylor cone must be caused by tiny vertical shifts in the exact position of Taylor's electrode. This type of linearized static theory cannot explain the ubiquitous formation of conical features observed in various different scenarios, hence is hardly satisfactory.

Zubarev's self-similar theory

Our work is inspired by Zubarev (2001) who independently examined the nonlinear dynamics of a free surface of an inviscid, irrotional, perfectly conductive liquid subject to strong electric forces. Having retained the full nonlinear form of the Bernoulli's equation, he discovered a self-similar scaling under which surface profile near apex at different stages could all collapse onto a single shape according to a self-reinforced process described by power-law growths in the oppositional interfacial forces and kinetic energy density near the cone apex. He was the first to demonstrate surface curvature and electric field strength at liquid apex could undergo divergence in finite time due to this self-similar process while liquid interface still conforms to the Taylor cone angle far away from the apex. He argued this mechanism is universal in the sense that liquid in a local self-similar frame near the apex "forgets" about boundary conditions of electric and velocity fields in laboratory frame and therefore is driven only by the local scales and forces. Unlike Chung, Cutler, and Miskovsky (1989), Zubarev included a spherically symmetric sink flow in the far field as illustrated in figure 6.1(b) and predicted that the fluid must move to the sink point $\boldsymbol{X}_c$ along the tangent to the surface. He also calculated a leading order shape correction to the exact Taylor cone induced by the sink flow, which rapidly decays $\sim R_{\parallel}^{-5}$ ($R_{\parallel}$ is the axial distance to the liquid apex).

The self-similar scaling underlying the mechanism of dynamic cone formation proposed

by Zubarev (2001) is robust in inertia-dominated regimes and has found its appearance in the Navier-Stokes simulations of a tank of liquid gallium between two plate electrodes (Suvorov and Zubarev, 2004) and the direct numerical simulation of a conductive liquid film under the influence of a protruding electrode (Collins, Jones, et al., 2007). In the inviscid simulation of a charged drop, Burton and Taborek (2011), albeit unaware of Zubarev's work, accurately recovered the universal self-similar scaling. The microgravity experiment (Elele et al., 2015) of self-sharpening meniscus under electric field conducted for a variety of conductive liquids also reported strong evidence of Zubarev's scaling.

Zubarev (2001) was also the first to perform asymptotic expansions of far-field electric potential, velocity field and interface shape to approximate the exact self-similar solutions order by order. We improve his analysis by introducing a crucial leading order term in the asymptotic series of velocity field and therefore make new analytical predictions to flow pattern and interface profile relevant to the existing simulations and experiments. Moreover, while asymptotic analysis does provide a quantitative picture of localized cone formation, important details of physically relevant information such as pressure, velocity field and interface shape near cone apex still remain unknown. On top of extending Zbuarev's asymptotic analysis, we also devise a novel numerical technique based on boundary integral equations which connects our analytically calculated far-field asymptotics to interface profile and velocity/electric fields near the cone apex. Our scheme has successfully uncovered a two-parameter family of the exact solutions (flow pattern, interface shape, electric field) to the self-similar dynamics. Finally we would like to emphasize that, despite the pioneering work of Zubarev in electrohydrodynamics, similar inviscid scaling has been previously exploited in context of capillary pinch-off and recoil of inviscid fluids (Day, Hinch, and Lister, 1998; Leppinen and Lister, 2003; Sierou and Lister, 2004). These theoretical predictions have been found to correlate closely with experimental measurements of a collapsing surface singularity (Zeff et al., 2000).

6.3 Inviscid Theory of Electrohydrodynamics Free Surface Flows

In this section, we derive the governing equations for inviscid motions of a perfectly conductive liquid subject to capillary and Maxwell (electrostatics) stresses acting on its free surface. These electrohydrodynamic equations are by no means new, probably known since the time of Rayleigh (1882)'s work on charged conductive drops. However, the invariance and symmetries hidden in the inviscid model were only recognized a few decades ago by Zubarev (2001) which, as we shall see in this section, lead to the similarity transformation he proposed.

Unsteady Bernoulli's equation

The governing equations will be expressed in dimensionless spatial and time variables, $\boldsymbol{X}$ and T, and non-dimensional velocity $\boldsymbol{U}$, electric field $\boldsymbol{E}$ and pressure P with $[L]$, $[T]$,

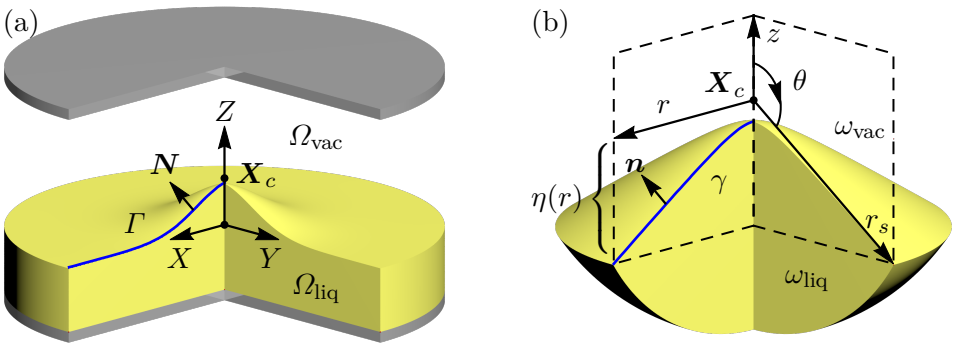

Figure 6.2: Dynamic cone formation of a conducting liquid (yellow) between two plate electrodes viewed in (a) laboratory frame with coordinates $\boldsymbol{X} = (X, Y, Z)$ and (b) axisymmetric self-similar frame $\boldsymbol{\chi} = (r, z)$ or (r_s, θ). At critical time $T = T_c$, liquid interface Γ (blue) would develop a genuine singularity at the conical point $\boldsymbol{X}_c$. Self-similar frame $\boldsymbol{\chi}$ centered at $\boldsymbol{X}_c$ is parametrized either by cylindrical coordinates r (axial radius) and z (height), or by spherical coordinates r_s (spherical radius) and θ (polar angle). In such a frame, liquid interface γ (blue) is expected to be represented by a height field $z = \eta(r)$.

$[U]$, $[E]$ and $[P]$ being the characteristic scales of each variable respectively. Without loss of generality, we further choose time scale $[T] = [L]/[U]$ and pressure scale $[P] = \rho[U]^2$ in favor of inertia effects (ρ is liquid density). In the regime where inertia, capillary and electrostatic forces all contribute, the length, velocity and electric field scaling introduced by Zubarev (2001),

$$[L] = \frac{\sigma^{1/3}}{\rho^{1/3}}[T]^{2/3}, \quad [U] = \frac{\sigma^{1/3}}{\rho^{1/3}}[T]^{-1/3}, \quad [E] = \frac{\sigma^{1/3}\rho^{1/6}}{\varepsilon_0^{1/2}}[T]^{-1/3}, \tag{6.1}$$

represent a balance, $\rho[U]^2 \sim \sigma/[L] \sim \varepsilon_0[E]^2$, between these three interfacial forces where σ is the liquid surface tension coefficient and ε_0 is the vacuum permittivity constant. It's not surprising that scaling (6.1) would completely eliminate all material parameters in the inviscid model as shown later.

We consider the irrotational flow of an incompressible, inviscid, perfectly conductive liquid surrounded by a vacuum. In figure 6.2(a), global coordinate system $\boldsymbol{X} = (X, Y, Z)$ is defined in the lab frame with (X, Y)-plane parallel to the top and bottom plate electrodes. The conducting liquid occupies a time-varying volume Ω_{liq}, separated from the vacuum region Ω_{vac} by a moving free surface Γ implicitly defined by a level function $F(\boldsymbol{X}, T)$ such that the zero set of $F(\boldsymbol{X}, T)$ coincides with the moving free surface Γ at all times,

$$\Gamma = \{\boldsymbol{X} | F(\boldsymbol{X}, T) = 0\}. \tag{6.2}$$

Unit normal $\boldsymbol{N}$ of interface Γ is set to point from the liquid domain Ω_{liq} into the vacuum Ω_{vac}. It then follows from two assumptions of an ideal liquid, irrotationality $\nabla \times \boldsymbol{U} = \boldsymbol{0}$

and incompressibility $\nabla \cdot \boldsymbol{U} = 0$, that the liquid velocity field $\boldsymbol{U} = \nabla \Phi$ can be described by the gradient of a harmonic potential Φ which satisfies the Laplace's equation in the liquid domain,

$$\nabla^2 \Phi = 0 \quad \text{in} \quad \Omega_{\text{liq}}. \tag{6.3}$$

Under these assumptions, the Euler's equation of inviscid fluids simplifies to the unsteady Bernoulli's equation everywhere in the liquid volume (Batchelor, 2000),

$$\frac{\partial \Phi}{\partial T} + \frac{1}{2} \nabla \Phi \cdot \nabla \Phi + P = 0 \quad \text{in} \quad \Omega_{\text{liq}}, \tag{6.4}$$

where the redundant constant of integration in the unsteady Bernoulli's equation (6.4) is set to zero without loss of generality. By evaluating Bernoulli's equation on the moving interface Γ, we find

$$\frac{\mathrm{D}\Phi}{\mathrm{D}T} - \frac{1}{2} \nabla \Phi \cdot \nabla \Phi = -P \quad \text{on} \quad \Gamma, \tag{6.5}$$

where $\mathrm{D}/\mathrm{D}T = \partial/\partial T + \boldsymbol{U} \cdot \nabla$ is the usual material derivative. A combination of the Laplace's equation (6.3) and the unsteady Bernoulli's equation (6.4) specify how pressure forces acting on the free surface are converted into volumetric inertial accelerations. Additionally, the kinematic boundary condition requires the free surface to move with the normal component of the velocity. In the level function representation (6.2), it simply means the level function $F(\boldsymbol{X}, T)$ is advected by the velocity field $\boldsymbol{U}$,

$$\frac{\mathrm{D}F}{\mathrm{D}T} = 0 \quad \text{on} \quad \Gamma. \tag{6.6}$$

It remains to determine the interfacial pressure P. Aside from the capillary stress across a curved interface, induced charges accumulating on the interface result in an interfacial stress due to a discontinuity in the Maxwell stress tensor $\boldsymbol{E}\boldsymbol{E}^{\top} - |\boldsymbol{E}|^2 \mathbb{I}/2$ (in unit of pressure scale $[P]$) in the normal direction $\boldsymbol{N}$ across the liquid/vacuum interface Γ (Saville, 1997). For a perfect conductor, net bulk charge must be zero. All charges in this case reside on the conductor surface, rearranging themselves in a way that the electric potential Ψ is always constant on the surface. Consequently, electric field at the conductor surface only has a normal component, i.e. $\boldsymbol{E} = (\boldsymbol{E} \cdot \boldsymbol{N})\boldsymbol{N}$, which solely depends on the instantaneous shape of the conductor. The jump in Maxwell stresses simplifies to the usual expression of electrostatic pressure $-|\boldsymbol{E}|^2 \boldsymbol{N}/2$. The total pressure just traversing the interface into the liquid (assuming zero pressure in vacuum) is therefore given by

$$P = -2\mathscr{H} - \frac{1}{2}|\boldsymbol{E}|^2 \quad \text{on} \quad \Gamma, \tag{6.7}$$

where $\mathscr{H}$ is the dimensionless mean curvature ($\mathscr{H} < 0$ for a local surface patch curving away from normal $\boldsymbol{N}$). Note the interfacial pressure (6.7) is precisely the first shape variation (5.140) of the combined electrostatic energy and surface energy derived in

Chapter 5. From equation (6.7), we see that the electrostatic pressure is always negative which implies that the Maxwell forces tend to destabilize the conductive liquid by pulling it into the vacuum regardless of surface charge type and convexity of local geometry. For a perfect conductor, electric field $\boldsymbol{E} = -\nabla\Psi$ in the vacuum Ω_{vac} is the negative gradient of the electric potential Ψ which satisfies

$$\nabla^2\Psi = 0 \quad \text{in} \quad \Omega_{\mathrm{vac}}. \tag{6.8}$$

In general the boundary conditions of electric potential depends on the specific problem. Suvorov and Zubarev (2004) and Collins, Jones, et al. (2007) considered a fixed voltage difference between liquid interface Γ and electrode. Their overall system is similar to the setup shown in figure 6.2(a) although their electrode designs differed from each other. Burton and Taborek (2011) performed inviscid simulations for an isolated charged drop, for which a constant surface potential was chosen at every instant to conserved the total surface charge. Despite these differences, the boundary conditions of the liquid or electric field all seem to serve as a trigger of the initial instability which then leads to rapid development of localized conic singularities at the liquid/vacuum interfaces observed in these simulations. The key feature shared by these different scenarios of cone formation in perfectly conductive fluids is that, the liquid interface Γ is always equipotential,

$$\Psi = \text{constant} \quad \text{on} \quad \Gamma. \tag{6.9}$$

Equation (6.9) is the only local electric field condition considered by G. I. Taylor (1964) when he deduced the famous Taylor cone angle.

At last we would like to justify the inviscid-irrotational approach. It's well known that an initially quiescent fluid with zero vorticity cannot produce vorticity from its interior (Batchelor, 2000). Vorticity can only be introduced through the free surface and gets transported/diffused into the bulk. For a perfectly conductive liquid, there is no active interfacial shear stress. The traction-free condition on the free surface is solely responsible for vorticity production. The effect of vorticity and viscous friction is estimated to be confined within a boundary layer of viscous length scale $[L]_{\mathrm{vis}} = \mu^2/\rho\sigma$. If we take the example of liquid gallium in vacuum (Suvorov and Zubarev, 2004), of which $\rho \sim 6\times10^3\,\mathrm{kg/m^3}$, $\mu \sim 2\times10^{-3}\,\mathrm{kg/m\cdot s}$ and $\sigma \sim 0.72\,\mathrm{N/m}$, the resulting scale $[L]_{\mathrm{vis}} \sim O(\mathrm{nm})$ of viscous boundary layer thickness is on the order of only a few nanometers, which is expected to have negligible impact on the inviscid-irrotational flow in the bulk until the late stage when conic singularity has developed sufficiently small radius of curvature at the apex. From a historical perspective, the Bernoulli-based approach has led to a number of theoretical milestones in free surface hydrodynamics including the celebrated crest angle of propagating steep deep-water waves (Stokes, 1847).

Self-similar theory of dynamic cone formation

We assume the conductive liquid described by the inviscid model develops a cuspidal shape with a conical singularity at the conical point $\boldsymbol{X}_c$ as the critical time T_c is approached. Zubarev (2001) proposed a universal mechanism to describe the rapid formation of conical singularities at liquid/vacuum interface. He suggested an axisymmetric coordinate centered at $\boldsymbol{X}_c$ as shown in figure 6.2(b) where the symmetry axis aligns with the cone axis. We note that the scaling (6.1) implies unsteady Bernoulli's equation (6.5) and pressure (6.7) would remain unchanged in time if the local characteristic scales always satisfy the relation $[U]^2 \sim 1/[L] \sim [E]^2$. This observation immediately motivates the self-similar transformation introduced by Zubarev.

To see this, we first define the temporal deviation to the critical time T_c as

$$\tau = \pm(T_c - T) \tag{6.10}$$

where the plus-minus sign ensures τ remains positive (i.e. $\tau = T - T_c$ if $T > T_c$) if the electrohydyrodynamic system is hypothetically allowed to advance beyond T_c. The original transformation by Zubarev is extended to incorporate time-reversal symmetry by introducing the axisymmetric coordinates $\boldsymbol{\chi}(\boldsymbol{X}, T)$ and dilated time $t(T)$,

$$\boldsymbol{\chi}(\boldsymbol{X}, T) = \frac{\boldsymbol{X} - \boldsymbol{X}_c}{\tau^{2/3}}, \quad t(T) = -\ln \tau. \tag{6.11}$$

As illustrated in figure 6.2(b), $\boldsymbol{\chi}$ is the position vector in the similarity frame, parametrized by either spherical (r_s, θ) or cylindrical (r, z) coordinates, and t is the dilated temporal variable which "slows" down the algebraically fast dynamics of cone formation observed in the laboratory frame. The self-similar space is divided by the transformed interface, designated by γ, into a semi-infinite liquid domain ω_{liq} and a semi-infinite vacuum domain ω_{vac}. We then rescale the velocity potential Φ, the electric potential Ψ and the level function F with their self-similar counterparts ϕ, ψ and f,

$$\Phi(\boldsymbol{X}, T) = \pm\tau^{1/3}\phi(\boldsymbol{\chi}, t), \quad \Psi(\boldsymbol{X}, T) = \tau^{1/3}\psi(\boldsymbol{\chi}, t), \quad F(\boldsymbol{X}, T) = \tau^{2/3} f(\boldsymbol{\chi}, t). \tag{6.12}$$

The position of transformed boundary in the self-similar frame, coincides with the zero contour of the transformed level function $f(\boldsymbol{\chi}, t)$,

$$\gamma = \{\boldsymbol{\chi} \mid f(\boldsymbol{\chi}, t) = 0\}. \tag{6.13}$$

A useful form of the level function is the height field representation $f(\boldsymbol{\chi}, t) = z - \eta(r, t)$ which assumes the interface γ doesn't develop overhangs. Here $\eta(r)$ is the height field of γ measured with respect to the ground where $z = 0$. The governing equations (6.3) and (6.8) of velocity potential Φ and electric potential Ψ interior to the liquid and vacuum domains, respectively, remain unchanged when they are expressed in terms of the self-similar coordinates (6.11) and potentials (6.12),

$$\nabla^2\phi = 0 \quad \text{in} \quad \omega_{\text{liq}}, \quad \nabla^2\psi = 0 \quad \text{in} \quad \omega_{\text{vac}}, \tag{6.14}$$

owing to the isotropic rescaling of spatial coordinates, where the differential operator ∇ is understood to act on the self-similar coordinates $\boldsymbol{\chi}$. With these new variables introduced and substituted, we transform the unsteady Bernoulli's equation (6.5), kinematic boundary condition (6.6) and equipotential condition (6.9) into the frame of self-similarity. The two axisymmetric potentials $\phi(\boldsymbol{\chi},t)$ and $\psi(\boldsymbol{\chi},t)$ must satisfy three boundary conditions,

$$\frac{\partial\phi}{\partial t}+\frac{2}{3}\boldsymbol{\chi}\cdot\nabla\phi-\frac{\phi}{3}+\frac{1}{2}\left|\nabla\phi\right|^2=2\hbar+\frac{1}{2}\left|\nabla\psi\right|^2 \quad \text{on} \quad \gamma, \tag{6.15}$$

$$\frac{1}{|\nabla f|}\frac{\partial f}{\partial t}+\frac{2}{3}\boldsymbol{n}\cdot\boldsymbol{\chi}+\boldsymbol{n}\cdot\nabla\phi=0 \quad \text{on} \quad \gamma, \tag{6.16}$$

$$\psi=\text{constant} \quad \text{on} \quad \gamma, \tag{6.17}$$

where $\hbar$ is the mean curvature of boundary γ in the self-similar frame. The identity, $\boldsymbol{n}=\nabla f/|\nabla f|$, is used to simplify the kinematic boundary condition (6.16).

We note that $\pm$ nowhere appears in the self-similar equations (6.15) and (6.16) due to the extra $\pm$ in the transformation (6.12) of the velocity potential Φ. This is a direct consequence of being an ideal fluid with an infinite (perfect) conductivity: zero (or negligible) dissipation in the system means the dynamics is time-reversible. Rewinding backward in time $T\to -T$ is equivalent to reversing the direction of velocity field $\boldsymbol{U}\to-\boldsymbol{U}$. The minus sign in $\tau=-(T-T_c)$ corresponds to post-singularity dynamics of the cone apex beyond the critical time T_c. A pre-singularity ($T<T_c$) convergence to a perfect cone can also be equivalently interpreted as post-singularity ($T>T_c$) onset flow of an initially conical interface. Physical quantities in laboratory frame such as velocity field $\boldsymbol{U}(\boldsymbol{X},T)$, electric field $\boldsymbol{E}(\boldsymbol{X},T)$ and pressure field $P(\boldsymbol{X},T)$ can be recovered in terms of the similarity variables,

$$\boldsymbol{U}(\boldsymbol{X},T)=\pm\frac{\nabla\phi(\boldsymbol{\chi},t)}{\tau^{1/3}},\quad \boldsymbol{E}(\boldsymbol{X},T)=\frac{-\nabla\psi(\boldsymbol{\chi},t)}{\tau^{1/3}},\quad P(\boldsymbol{X},T)=\frac{p(\boldsymbol{\chi},t)}{\tau^{2/3}}, \tag{6.18}$$

where the rescaled pressure $p(\boldsymbol{\chi},t)$ is found by transforming the unsteady Bernoulli's equation (6.4) to the self-similar frame (recall unsteady Bernoulli's equation for potential flows holds throughout the entire liquid domain not just along a streamline if irrotationality of an invsicid liquid is assumed),

$$p(\boldsymbol{\chi},t)=-\frac{\partial\phi}{\partial t}-\frac{2}{3}\boldsymbol{\chi}\cdot\nabla\phi+\frac{\phi}{3}-\frac{1}{2}|\nabla\phi|^2. \tag{6.19}$$

It now becomes clear that the dynamic process of cone formation described by Zubarev (2001) is the "steady" state solution (i.e. t-independent) to the unsteady Bernoulli's system (6.5), (6.6) and (6.7). From a mathematical perspective, we seek two t-independent harmonic potentials, $\phi(\boldsymbol{\chi})$ and $\psi(\boldsymbol{\chi})$, and a "stationary" interface shape γ such that in

the co-moving self-similar frame,

$$\frac{2}{3}\boldsymbol{\chi}\cdot\nabla\phi-\frac{\phi}{3}+\frac{1}{2}\left|\nabla\phi\right|^2=2\hbar+\frac{1}{2}\left|\nabla\psi\right|^2\quad\text{on}\quad\gamma,\tag{6.20}$$

$$\frac{2}{3}\boldsymbol{n}\cdot\boldsymbol{\chi}+\boldsymbol{n}\cdot\nabla\phi=0\qquad\text{on}\quad\gamma,\tag{6.21}$$

$$\psi=\text{constant}\qquad\text{on}\quad\gamma.\tag{6.22}$$

Since the coordinates of self-similar frame extend to infinity, the exact solutions to the above equations closely depend on the far-field behavior of ϕ, ψ and γ at $|\boldsymbol{\chi}|\gg 1$. For a solution to be physical, quantities such as velocity $\nabla\phi$ and electric field $-\nabla\psi$ must be bounded as interface γ matches onto the exact shape of a Taylor cone at $|\boldsymbol{\chi}|\to\infty$. It turns out that, there is not just one but an entire family of self-similar solutions satisfying these constraints, as demonstrated in the next section.

6.4 Family of Asymptotic Solutions to Self-Similar Dynamic Cone Formation

Zubarev (2001) devised valid asymptotic series of the electric field, velocity potential and interface shape to satisfy the self-similar Bernoulli system in the far-field where $|\boldsymbol{\chi}|\gg 1$. His argument was constructed entirely based on a sink-type velocity potential $\phi\sim 1/r_s$. In a subsequent work (Suvorov and Zubarev, 2004), the authors mentioned a previously omitted yet more important leading order velocity potential $\phi\propto\sqrt{r_s}P_{1/2}(-\cos\theta)$, albeit in extreme brevity. In this section, we deliver a thorough analysis on the inclusion of this term by constructing more general asymptotic solutions to the self-similar equations (6.20), (6.21) and (6.22) in the far field where $|\boldsymbol{\chi}|\gg 1$. Physical implications of this new velocity potential and the asymptotic expansions it induces are discussed in great details as well.

Taylor's static cone

G. I. Taylor (1964) examined the static equilibrium between electrostatic and surface tension forces along the surface of a perfectly conductive liquid cone which leads to an opening angle $\approx 98.6^\circ$. Taylor's argument is most easily seen by considering a conical conductor spanning a range of polar angle from θ_0 to π as depicted in figure 6.3. In cylindrical coordinates (r,z), the conical surface γ is given by

$$\gamma=\{(r,z)\mid z=c_0 r\},\tag{6.23}$$

where $c_0=\cot\theta_0$ is the slope of a conic surface at $\theta=\theta_0$. In Taylor's simplified static picture, the self-similar Bernoulli system reduces to

$$0=2\hbar+\frac{1}{2}\left|\nabla\psi\right|^2\quad\text{on}\quad\gamma,\tag{6.24}$$

$$\psi=\text{constant}\qquad\text{on}\quad\gamma.\tag{6.25}$$

Then solution to the electric potential ψ has the general form (Jackson, 1999),

$$\psi=b_0 r_s^{\ell}P_\ell(\cos\theta)\quad\text{with}\quad P_\ell(\cos\theta_0)=0,\tag{6.26}$$

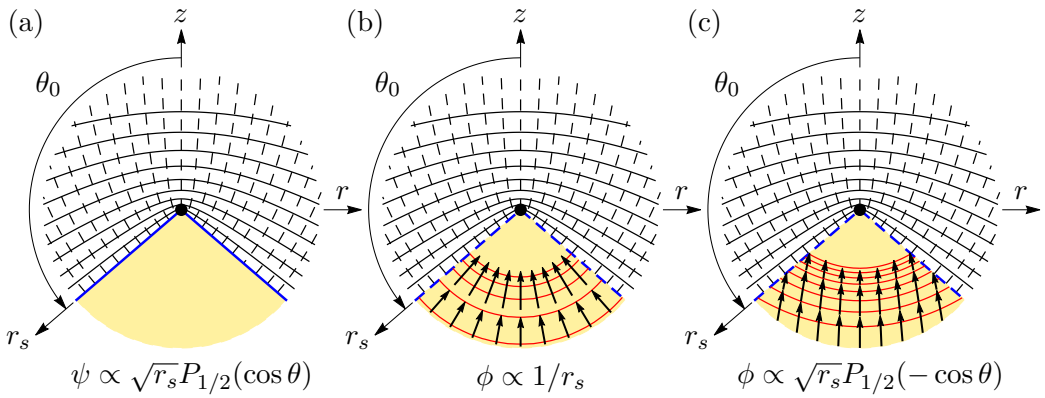

Figure 6.3: (a) Contours (black) and field lines (dashed) of Taylor's conic electric potential. Velocity field (arrow) and pressure contours (red) of (b) Zubarev's sink flow and (c) lifting flow inside liquid (yellow). Taylor cone (blue) is an exact solution (solid blue) in (a) but a leading order approximation (dashed blue) in (b) and (c). Increments between adjacent contours are constant.

where b_0 is an undetermined constant representing the scale of local field strength and $P_\ell(\cdot)$ is the associate Legendre polynomial of order ℓ. It is only possible for ψ to be equipotential along the cone surface $\boldsymbol{\chi} = (r_s, \theta_0)$ if θ_0 is the root of $P_\ell(\cos\theta)$.

On the other hand, the mean curvature $\hbar$ for a surface represented by a height field $\eta(r)$ is given by

$$2\hbar = \frac{1}{[1+(\mathrm{d}\eta/\mathrm{d}r)^2]^{3/2}}\frac{\mathrm{d}^2\eta}{\mathrm{d}r^2} + \frac{1}{r}\frac{1}{\sqrt{1+(\mathrm{d}\eta/\mathrm{d}r)^2}}\frac{\mathrm{d}\eta}{\mathrm{d}r}. \tag{6.27}$$

Applying formula (6.27) to a perfect cone (6.23) for which $\eta(r) = c_0 r$ yields $2\hbar \propto 1/r$. If capillary were to balance with the Maxwell stress $|\boldsymbol{n}\cdot\nabla\psi|^2 \sim r_s^{2\ell-2}$ all the way up to the cone apex, ℓ must equal $1/2$ which immediately yields the Taylor cone angle $2(\pi-\theta_0) \approx 98.6^\circ$ where θ_0 is the unique root of $P_{1/2}(\cos\theta)$. Taylor's solution can be summarized as

$$\phi = \text{constant}, \quad \psi = b_0\sqrt{r_s}P_{1/2}(\cos\theta), \quad \eta = c_0 r, \tag{6.28}$$

where $c_0 = \cot\theta_0 \approx -0.86$ is not a free parameter but the slope locked by the exact Taylor cone angle. In figure 6.3 we plot the electric potential and its field lines. It's evident from the potential contours clustering near the origin that electric field $-\nabla\psi$ locally blows as it moves towards the cone tip.

While Taylor cone is an exact solution to the self-similar equations (6.20)–(6.22) with a trivial (constant) velocity potential, it is not uniformly valid: curvature and electric field are both undefined at the cone apex. As pointed out by Zubarev (2001), in the self-similar framework Taylor cone should be understood as an asymptotic condition away

from the apex. On the other hand, Taylor's static solution (6.28) alone is not sufficient to determine the underlying flow structure that could possibly spawn and sustain such a cone. In fact a truly hydrostatic equilibrium (G. I. Taylor, 1964) must demand exact balance between capillary and Maxwell stresses to achieve a constant pressure distribution everywhere along the liquid/vacuum interface. In our nondimensionalized model, it means the local electric field strength b_0 is not an arbitrary parameter but

$$|b_0| = \frac{\sqrt{-2\cot\theta_0}}{\mathrm{d}P_{1/2}(\cos\theta)/\mathrm{d}\theta|_{\theta=\theta_0}} \approx 1.34593 \tag{6.29}$$

in order to produce a uniform pressure along the cone. In practical situations, condition (6.29) is a very stringent requirement and is unlikely to meet for every spontaneous cone formation observed. Any deviation from the field strength (6.29) immediately results in an $O(1/r_s)$ pressure gradient along the conical surface which must be compensated for by additional physical mechanisms such as inertia forces in the inviscid model.

Taylor' static cone is also problematic in the vicinity of cone apex. Physical quantities such as surface charge density (i.e normal component of electrostatic field) and surface curvature,

$$-\boldsymbol{n}\cdot\nabla\psi = \frac{b_0}{\sqrt{r_s}}\frac{\mathrm{d}P_{1/2}(\cos\theta)}{\mathrm{d}\theta}\Big|_{\theta_0}, \quad 2\mathcal{H} = \frac{c_0}{\sqrt{1+c_0^2}}\frac{1}{r} \quad \text{on} \quad \gamma, \tag{6.30}$$

blow up to infinity as $r \to 0$. In other words, the static conical interface between liquid and vacuum is maintained under the counterbalance between two surface forces becoming singularly large towards the apex, a configuration that's often metastable or unstable in reality. Nevertheless Taylor's theory still unambiguously identifies the unique cone angle θ_0.

Dynamic cone formation

In order to motivate a dynamically formed conic singularity, let's consider material points on a locally conical surface being mapped by the self-similar transformation (6.11), i.e. $\boldsymbol{X} \to \boldsymbol{X}_c + (T_c - T)^{2/3}\boldsymbol{\chi}$. In such a scenario, the material surface formed by these material points remains a "stationary" conical shape (since they all move tangent to the cone surface) while still experiencing large accelerations as $T \to T_c$. This observation suggests possible existence of an inertia-driven Taylor cones, which we term the dynamic cone. It is conceivable that there might exist some special liquid shapes and particular forms of velocity field under the influence of capillary and Maxwell stresses such that the interface geometry maintains a nearly conical shape almost indifferent to the static Taylor cone while liquid in the bulk is being actively advected instead of the hydrostatic "no-flow" situation assumed by previous work (Chung, Cutler, and Miskovsky, 1989).

Mathematically speaking, we seek asymptotic solutions to equations (6.20)–(6.22) of the self-similar Bernoulli system with a nontrivial velocity potential ϕ in the far-field

where $|\boldsymbol{\chi}| \gg 1$. Zubarev (2001) proposed a far-field sink flow at the leading order by placing a fictitious sink $\phi \propto 1/r_s$ at the conical point $\boldsymbol{\chi} = \mathbf{0}$. At first glance, sink flows seem to be a valid candidate accountable for dynamic cone formation as they are tangent to conical surfaces of arbitrary opening angles and thus trivially meet the kinematic boundary condition (6.21). It's also evident from $-\phi/3$ in the self-similar Bernoulli's equation (6.20) that the inertial contribution from a sink flow is comparable to the pressure forces due to capillary and Maxwell stresses. However, we would like to raise an issue with asymptotic sink flows dominating the far field: their streamlines are almost perfectly spherically symmetric about the conical point. It is conceivable that the convergence of a round material surface towards a conical shape under the advection of sink flows must be exceptionally slow unless it is already a conical shape in the first place. For this reason, it is not appropriate to model the dynamic process of cone formation entirely based on sink flows. Although sink flows are widely used in the mathematical description of steady cone-jet configurations (Gañán-Calvo, 1997; Fernández de la Mora, 2007; Subbotin and Semenov, 2015) where a slender cylindrical high-speed jet is matched on to the apex of a stationary conic base.

Following Zubarev's initial effort, we observe that the kinetic energy density $|\nabla\phi|^2/2$ of a velocity potential of the form $\sqrt{r_s}P_{1/2}(\pm\cos\theta)$ in the self-similar frame also scales $O(1/r_s)$ along a conical surface of an arbitrary opening angle. The seemingly unbounded term $\frac{1}{3}\phi$ ($\propto \sqrt{r_s}$) exactly cancels out the growing contribution from $\frac{2}{3}\boldsymbol{\chi}\cdot\nabla\phi$ in Bernoulli's equation (6.20). A similar form of velocity potentials was first employed by Day, Hinch, and Lister (1998) to explain the capillary pinch-off of an inviscid fluid. We choose to discard the unphysical velocity potential $\sqrt{r_s}P_{1/2}(\cos\theta)$ as it's singular along the symmetry axis interior to liquid (recall $\lim_{\theta\to\pi} P_{1/2}(\cos\theta) \to -\infty$). In the end, we propose a larger set of asymptotic ansatzes for velocity potential ϕ, electric potential ψ and height field $\eta(r)$ of interface γ, which are more appropriate for capturing the leading order behavior of the liquid-vacuum system during the self-similar process of dynamic cone formation,

$$\phi(\boldsymbol{\chi}) \sim a_0 r_s^{1/2} P_{1/2}(-\cos\theta) + \frac{a_1}{r_s}, \quad \psi(\boldsymbol{\chi}) \sim b_0 r_s^{1/2} P_{1/2}(\cos\theta), \quad \eta(r) \sim c_0 r. \tag{6.31}$$

Ansatzes (6.31) were briefly mentioned in Suvorov and Zubarev (2004). To illustrate the effect of these leading order solutions, in figure 6.3 we plot the velocity field $\nabla\phi$ and pressure $p(\boldsymbol{\chi})$ field defined in (6.19) for a sink potential $1/r_s$ and a "lifting" potential $\sqrt{r_s}P_{1/2}(-\cos\theta)$, named after its uplifting streamline pattern, along with the electric field $\nabla\psi$ of Taylor's conic potential $\sqrt{r_s}P_{1/2}(\cos\theta)$. The velocity field of a lifting flow is clearly distinct from a sink flow: instead of corralling liquid to a sink point in a spherically symmetric fashion, the resultant forces from the opposing Maxwell and capillary forces lift liquid along streamlines that are nearly vertical, which make the transition from a round menus to a conic cap possible. Another distinct discrepancy between these two

types of flow is that, the local pressure gradient ∇p and velocity $\nabla\phi$ are no longer colinear, which means the inertia force acting on an accelerating infinitesimally small liquid parcel is not in the direction of its motion as opposed to the case of a sink flow. Furthermore, the self-similar Bernoulli's equation (6.20) evaluated at the exact Taylor cone ($z = c_0 r$) can be satisfied at the leading order if coefficients a_0, b_0 and a_1 of the potentials in ansatzes (6.31) fulfil the relation

$$a_1 = \frac{a_0^2}{2}\left\{\left[\frac{P_{1/2}(-\cos\theta_0)}{2}\right]^2 + \left[\frac{\mathrm{d}P_{1/2}(-\cos\theta)}{\mathrm{d}\theta}\bigg|_{\theta_0}\right]^2\right\} - \frac{b_0^2}{2}\left[\frac{\mathrm{d}P_{1/2}(\cos\theta)}{\mathrm{d}\theta}\bigg|_{\theta_0}\right]^2 - c_0, \tag{6.32}$$

or in its numerical form $a_1 \approx 0.144\, a_0^2 - 0.475\, b_0^2 + 0.860$. In a such event, Bernoulli's equation (6.20) would have a residue decaying to zero as $r_s \to \infty$. Likewise, the kinematic boundary condition (6.21) is no longer exactly fulfilled (unless $a_0 = 0$) but evaluated to a diminishing residue $\sim O(1/\sqrt{r_s})$. These asymptotically vanishing residues manifest self-consistency in the ansatzes (6.31) as valid leading order approximations.

In order to formally eliminate the residues of the self-similar Bernoulli system (6.20)–(6.22) at all orders, we construct a set of infinite series expansions ϕ_∞, ψ_∞ and η_∞ for velocity potential ϕ, electric potential ψ and height field η in the far field (Sierou and Lister, 2004),

$$\phi_\infty(\boldsymbol{\chi}) = \sum_{k=0}^{\infty} a_k \phi_k(\boldsymbol{\chi}), \quad \psi_\infty(\boldsymbol{\chi}) = \sum_{k=0}^{\infty} b_k \psi_k(\boldsymbol{\chi}), \quad \eta_\infty(r) = \sum_{k=0}^{\infty} c_k \eta_k(r), \tag{6.33}$$

where the k-th order terms are given by

$$\phi_k(\boldsymbol{\chi}) = r_s^{\frac{1}{2}-\frac{3}{2}k} P_{\frac{3}{2}k-\frac{3}{2}}(-\cos\theta), \quad \psi_k(\boldsymbol{\chi}) = r_s^{\frac{1}{2}-\frac{3}{2}k} P_{\frac{3}{2}k-\frac{3}{2}}(\cos\theta), \quad \eta_k(r) = r^{1-\frac{3}{2}k}. \tag{6.34}$$

The series obtained by Zubarev (2001) is actually a subset of the expansions (6.33), i.e. $\phi_\infty = a_1\phi_1 + a_3\phi_3 + \ldots$, $\psi_\infty = b_0\psi_0 + b_2\psi_2 + \ldots$ and $\eta_\infty = c_0\eta_0 + c_2\eta_2 + \ldots$. Despite there are infinitely many coefficients, all a_k, b_k and c_k for $k > 1$ are in fact uniquely determined by a_0, b_0 and c_0. Since the asymptotic slope c_0 is locked by the Taylor cone angle θ_0, we expect a two-parameter (a_0 and b_0) family of the exact solutions to equations (6.20)–(6.22) of the self-similar Bernoulli system. The order-by-order procedure of determining higher order coefficients, is nontrivial: there are three series of coefficients a_k, b_k and c_k coupled through a set of three nonlinear equations evaluated at the perturbed cone shape $z = c_0 r + \sum_{k=1}^{\infty} c_k \eta_k$—not the exact Taylor cone—in an interleaved fashion. Following the arrows in the flowchart 6.4, we can explicitly calculate higher order coefficients a_k, b_k and c_k up to arbitrary integer order $k > 0$ via the symbolic package MATHEMATICA (Wolfram Research, 2019). The analytic expressions of a_k, b_k and c_k become cumbersome as order k rises. Hence we only list the first few lower order ones here. For instance coefficients $a_0, \ldots, a_2$ are given

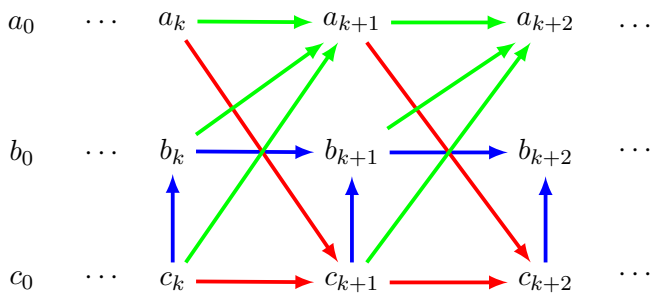

Figure 6.4: Flowchart for the interleaved process of computing coefficients a_k, b_k, c_k. Arrows represent the equations needed to produce a particular coefficient at the next order: equipotential condition (6.22) in blue, kinematic boundary condition (6.21) in red and Bernoulli's equation (6.20) in green.

by the relations

$$\left.\begin{aligned} a_0 &= \text{free parameter},\\ a_1(a_0,b_0,c_0) &= \text{equation (6.32)},\\ a_2(c_0,\dots,c_3,a_1) &= \frac{3}{\sqrt{\sin\theta_0}P'_{3/2}(-\cos\theta_0)}\left(-\frac{a_1c_1}{2}+\frac{c_1^3}{8\sin\theta_0}+\frac{c_3}{\sin^3\theta_0}\right), \end{aligned}\right\} \tag{6.35}$$

where $P'_\ell(\cdot)$ means differentiation with respect to the argument. Coefficients $b_0, ..., b_3$ are found to be

$$\left.\begin{aligned} b_0 &= \text{free parameter},\\ b_1(c_0,c_1,b_0) &= -b_0c_1\sin^{3/2}\theta_0 P'_{1/2}(\cos\theta_0),\\ b_2(c_0,\dots,c_2,b_0) &= -b_0\frac{2c_2P'_{1/2}(\cos\theta_0)+c_1^2\sin^3\theta_0 P''_{1/2}(\cos\theta_0)}{2P_{3/2}(\cos\theta_0)},\\ b_3(c_0,\cdots,c_3,b_0) &= b_0P'_{1/2}(\cos\theta_0)\left[\frac{c_1c_2P'_{3/2}(\cos\theta_0)}{\csc^{3/2}\theta_0 P_{3/2}(\cos\theta_0)P_3(\cos\theta_0)}\right.\\ &\quad\left.-\frac{8c_3\csc^4\theta_0+c_1^3\left(\csc^2\theta_0+1\right)+12c_1c_2\cot\theta_0\csc^2\theta_0}{8\csc^{5/2}\theta_0 P_3(\cos\theta_0)}\right]\\ &\quad+b_0P''_{1/2}(\cos\theta_0)\left[\frac{c_1^3P'_{3/2}(\cos\theta_0)}{2\csc^{9/2}\theta_0 P_{3/2}(\cos\theta_0)P_3(\cos\theta_0)}\right.\\ &\quad\left.-\frac{c_1c_2}{\csc^{3/2}\theta_0 P_3(\cos\theta_0)}\right]\\ &\quad-b_0P'''_{1/2}(\cos\theta_0)\frac{c_1^3}{6\csc^{9/2}\theta_0 P_3(\cos\theta_0)}. \end{aligned}\right\} \tag{6.36}$$

Coefficients $c_0, ..., c_2$ are given by

$$\left.\begin{aligned} c_0 &= \text{slope of Taylor cone angle } \theta_0, \\ c_1(a_0, c_0) &= \frac{P'_{-3/2}(-\cos\theta_0)}{\sqrt{\csc\theta_0}} a_0, \\ c_2(c_0, c_1) &= -\frac{c_1^2}{2P'_{1/2}(-\cos\theta_0)/\sin\theta_0}\Big[2\cos(\theta_0)P'_{1/2}(-\cos\theta_0) \\ &\quad + \sin^2\theta_0 P''_{1/2}(-\cos\theta_0) + 3P_{1/2}(-\cos\theta_0)/4\Big]. \end{aligned}\right\} \tag{6.37}$$

Equation (6.37) indicates that c_1 and a_0 are linearly related by a constant. Therefore the two degrees of freedom in expansion (6.33) can be either (a_0, b_0) or (b_0, c_1). For example, coefficient a_2 after substitutions can be reduced to a function of b_0 and c_1 instead,

$$\begin{aligned} a_2(c_1, b_0) = c_1 &\left[b_0^2 \frac{P_{1/2}(-\cos\theta_0) - 4\cos\theta_0 P'_{1/2}(-\cos\theta_0)}{8\csc^{3/2}\theta_0 P_{3/2}(-\cos\theta_0)P'_{1/2}(-\cos\theta_0)} P'_{1/2}(\cos\theta_0)^2\right. \\ &\left. + \frac{4\cos\theta_0 P_{1/2}(-\cos\theta_0) - (3\cos(2\theta_0)+5)P'_{1/2}(-\cos\theta_0)}{16P_{3/2}(-\cos\theta_0)P'_{1/2}(-\cos\theta_0)} \csc^{3/2}\theta_0\right] \\ &+ c_1^3 \frac{16\cos\theta_0 P'_{1/2}(-\cos\theta_0)^3 + 4P_{1/2}(-\cos\theta_0)P'_{1/2}(-\cos\theta_0)^2 - \csc^2\theta_0 P_{1/2}(-\cos\theta_0)^3}{32\csc^{1/2}\theta_0 P_{3/2}(-\cos\theta_0)P'_{1/2}(-\cos\theta_0)^3}. \end{aligned} \tag{6.38}$$

An important observation from equations (6.37) is that the coefficient c_2 of shape correction η_2 doesn't depend on the sink strength a_1 but instead on c_1 and c_2 from the first two shape corrections. A simple change of variable $-\cos\theta_0 \to x$ reveals c_2 is in fact zero since

$$\begin{aligned} c_2 &\propto 2\cos(\theta_0)P'_{1/2}(-\cos\theta_0) + \sin^2\theta_0 P''_{1/2}(-\cos\theta_0) + \frac{3}{4}P_{1/2}(-\cos\theta_0) \\ &= \frac{\mathrm{d}}{\mathrm{d}x}\left[(1-x^2)\frac{\mathrm{d}P_{1/2}(x)}{\mathrm{d}x}\right] + \frac{1}{2}\left(\frac{1}{2}+1\right)P_{1/2}(x) = 0, \end{aligned} \tag{6.39}$$

where the last line is precisely the definition of associate Legendre polynomials $P_\ell(x)$ as exact solutions to the Legendre's differential equation. Recall the asymptotic corrections to the exact cone shape derived by Zubarev (2001) are only a subset of the expressions (6.33), i.e. $\eta_\infty = c_0 r + c_2/r^2 + c_4/r^5 + O(1/r^8)$. Note $c_2 = 0$ implies the first shape correction to the exact Taylor cone implied by Zubarev's asymptotic sink flow is as negligibly small as $O(1/r^5)$. Once coefficients a_k, b_k and c_k are entirely determined, the asymptotic expansion of liquid pressure p_∞ can be readily computed by collecting terms order by order after substituting expansions (6.33) into self-similar pressure (6.19),

$$\begin{aligned} p_\infty(\boldsymbol{\chi}) = \frac{1}{r_s}&\left\{a_1 - \frac{1}{8}a_0^2\left[4\sin^2\theta P'_{1/2}(-\cos\theta)^2 + P_{1/2}(-\cos\theta)^2\right]\right\} \\ &+ \frac{1}{r_s^{5/2}}\left[\frac{1}{2}a_0 a_1 P_{1/2}(-\cos\theta) + 2a_2 P_{3/2}(-\cos\theta)\right] + O(r_s^{-4}). \end{aligned} \tag{6.40}$$

While the asymptotic pressure $p_\infty(\boldsymbol{\chi})$ still maintains the $O(1/r_s)$ radial scaling of a pure sink flow, its additional angular dependence on θ, as reflected in the pressure contours shown in figure 6.3(c), is due to a nonzero lifting flow strength a_0.

Estimating near-apex behaviors

The exact solutions to the self-similar Bernoulli system can only be determined numerically since one must solve two Laplace's equations posed on semi-infinite liquid and vacuum domains separated by a yet undetermined interface shape. Before delving into details of numerical analysis, we discuss some near-field behaviors of the exact solutions if exist. Recall from the kinematic boundary condition (6.21) that at $r = 0$ we have

$$\frac{2}{3}\eta(0) + \frac{\partial\phi}{\partial z}\Big|_{\boldsymbol{\chi}=(0,\eta(0))} = 0. \tag{6.41}$$

The location of cone apex in the self-similar frame dictates the direction and magnitude of near-field velocity field $\boldsymbol{u} = \nabla\phi$. From relation (6.37) we know that coefficient $c_2 = 0$ which makes the first shape correction $c_1/\sqrt{r}$ to the exact Taylor cone exceptionally relevant. The fact that $c_1 \approx 0.36843\, a_0$ indicates whether $c_1/\sqrt{r}$ leads to a correction beneath or above the exact Taylor cone depends on the sign of a_0, hence the direction of velocity field induced by the lifting potential $a_0\phi_0$. Taking time-reversal symmetry of the inviscid model into account, we illustrate a number of possible shape-velocity configurations in figure 6.5 where self-similar interfaces with $c_1 < 0$ (or $c_1 > 0$) shape corrections in the far field would coverage to (or deviate from) the exact Taylor cone under the influence of lifting (or repressing) flows $\nabla\phi_0$ of strength $a_0 < 0$ (or $a_0 > 0$).

Before resorting to numerical solutions, it is already possible to make several predictions on the self-similar behaviors of the interface. The "super-cone" solutions shown in figure 6.5(a) are the ones whose interfaces are entirely above the exact Taylor cone. Although the "retraction" solution seems to be physically implausible, its time-reversal dynamics can be interpreted as the post-singularity onset growth of a liquid cap. The dynamic cone formation, which indefinitely sharpens the cone apex till the conical point $\boldsymbol{X}_c$ is reached, belongs to the pre-singularity dynamics of the "sub-cone" class shown in figure 6.5(b), of which the interfaces are entirely bounded above by the Taylor cone. Its time-reversal corresponds to a "collapse" situation where an initially sharp conic tip is repressed due to, for instance, a sudden loss of surface charges. We can imagine more sophisticated situations where the interfaces remain above the Taylor cone in the far field but beneath near the apex shown in figure 6.5(c). This is known as the recoil flow (Sierou and Lister, 2004; Hoepffner and Paré, 2013): while liquid in the bulk is still being driven upward to the conical point, the cone apex has already bounced downward.

We next provide some analytic effort on estimating near-apex interface shape. The argument was originally employed by Zubarev (2001) to derive a lower bound on the

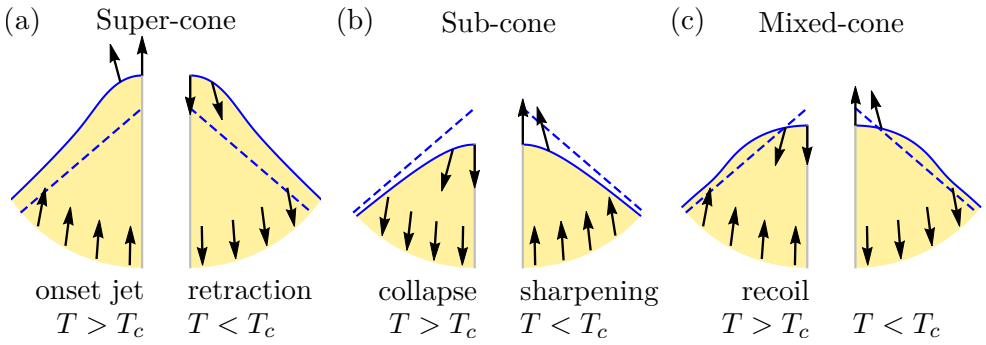

Figure 6.5: Sketches of (a) super-cone, (b) sub-cone and (c) mixed-cone self-similar interfaces γ (solid blue) relative to the exact Taylor cone (dashed blue) and configurations of far-field and near-apex velocity fields $\nabla\phi$ (arrow) in pre-(right) and post-singularity (left) dynamics.

maximum apex depth without actually having the coupled boundary value problems of the self-similar Bernoulli system solved. However, his analysis doesn't directly apply when the deviation of self-similar interface shape from the exact Taylor has a noticeable tail, i.e $(\eta - c_0 r) \sim c_1\sqrt{r} + ...$, caused by the presence of a far-field lifting flow, instead of a rapidly decaying tail $\sim c_4/r^5$ due to a sink flow alone assumed by Zubarev. By making some additional assumptions, we show that it is still possible to arrive at some estimations on the maximum depth near cone apex.

Let $\boldsymbol{\chi}_* = (r_*, z_*)$ be a truncation point on the liquid/vacuum interface γ with $z_* = \eta(r_*)$ for some large axial radius $r_* \gg 1$. We define boundary

$$\gamma_{\mathrm{T}} = \{(r, c_0 r) \mid 0 \le r \le r_*\} \tag{6.42}$$

to be the surface of a perfect Taylor cone and

$$\gamma_* = \{(r, z) \mid z_* \le z \le c_0 r_* \,(\text{or } c_0 r_* \le z \le z_* \text{ if super-cone})\} \tag{6.43}$$

be the vertical strip between Taylor cone γ_{T} and actual interface γ at $r = r_*$. These geometry quantities are illustrated in figure 6.6(a). The total volume ω_{T} enclosed between the exact Taylor cone γ_{T} and liquid/vacuum interface γ is given by the integral

$$\int_{\omega_{\mathrm{T}}} \mathrm{d}\omega = \int_{\omega_{\mathrm{T}}} \frac{1}{3}\nabla\cdot\boldsymbol{\chi}\,\mathrm{d}\omega = \frac{2\pi}{3}\int_{\gamma_{\mathrm{T}}} \boldsymbol{n}_{\mathrm{T}}\cdot\boldsymbol{\chi}\, r\,\mathrm{d}\gamma + \frac{2\pi}{3}\int_{\gamma_*} \boldsymbol{n}_*\cdot\boldsymbol{\chi}\, r\,\mathrm{d}\gamma - \frac{2\pi}{3}\int_{\gamma} \boldsymbol{n}\cdot\boldsymbol{\chi}\, r\,\mathrm{d}\gamma, \tag{6.44}$$

where $\boldsymbol{n}_{\mathrm{T}}$ and $\boldsymbol{n}_*$ are the outward normal vectors of volume ω_{T} whereas $\boldsymbol{n}$ is the globally defined normal of interface γ. Note ω_{T} is a signed volume due to possibilities of super- and sub-cone shapes. The first integral in equation (6.44) is zero since along the surface of a perfect cone $\boldsymbol{n}_{\mathrm{T}}\cdot\boldsymbol{\chi} = 0$. The second integral along strip γ_* is straightforward,

$$\frac{2\pi}{3}\int_{\gamma_*} \boldsymbol{n}_*\cdot\boldsymbol{\chi}\, r\,\mathrm{d}\gamma = \frac{2}{3}\pi r_*^2(c_0 r_* - z_*). \tag{6.45}$$

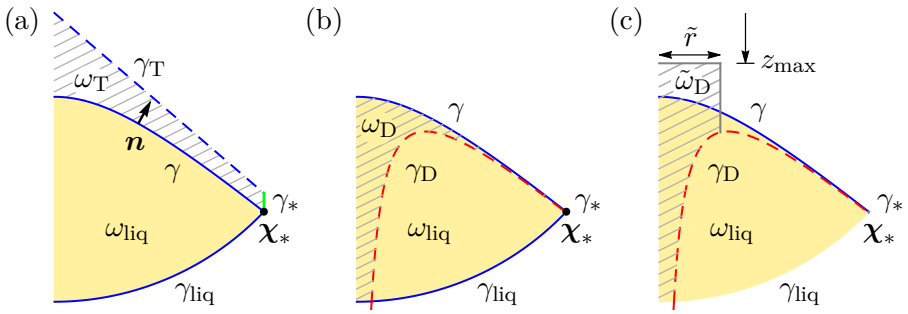

Figure 6.6: (a) Signed volume (hatched) ω_{T}, (b) ω_{D} and (c) $\tilde{\omega}_{\mathrm{D}}$: γ (blue) is the solution to the self-similar Bernoulli system, γ_{T} (dashed blue) is the exact Taylor cone $z = c_0 r$, γ_{D}(dashed red) is the leading order asymptote $z = c_0 r + c_1 r^{-1/2}$, $\boldsymbol{\chi}_* \in \gamma$ is the truncation point, γ_{liq} (blue) is the spherical cap passing through $\boldsymbol{\chi}_*$ and γ_* (green) is the vertical strip bridging γ and γ_{T} (or γ_{D}) at $r = r_*$, $\tilde{r}$ is the turning radius of γ_{D} and depth $z_{\max}$ is related to an estimation on the minimum elevation of interface γ.

Direct evaluation of the third integral in equation (6.44) requires actual geometric information about the interface shape γ which is not available. Fortunately with the use of divergence theorem we can transfer this integral to the spherical cap γ_{liq} which is an arc of radius $|\boldsymbol{\chi}_*|$ spanning from the polar angle θ_* of $\boldsymbol{\chi}_*$ to the south pole $\theta = \pi$ as shown in figure 6.6,

$$
\begin{aligned}
-\int_\gamma \frac{2}{3}\boldsymbol{n}\cdot\boldsymbol{\chi}\,\pi r\,\mathrm{d}\gamma &= \frac{1}{2}\int_\gamma \boldsymbol{n}\cdot\nabla\phi\,2\pi r\,\mathrm{d}\gamma \qquad \text{kinematic B. C. (6.21)} \\
&= \frac{1}{2}\Big(\int_{\gamma\cup\gamma_{\mathrm{liq}}} - \int_{\gamma_{\mathrm{liq}}}\Big)(\boldsymbol{n}\cdot\nabla\phi)\,2\pi r\,\mathrm{d}\gamma \\
&= \frac{1}{2}\int_{\omega_{\mathrm{liq}}} \nabla\cdot\nabla\phi\,\mathrm{d}\omega - \pi\int_{\gamma_{\mathrm{liq}}} (\boldsymbol{n}\cdot\nabla\phi)\,(r_s)_*^2\sin\theta\,\mathrm{d}\theta \quad \text{recall } \nabla^2\phi = 0 \\
&= -\pi\int_{\gamma_{\mathrm{liq}}} (\boldsymbol{n}\cdot\nabla\phi)\,(r_s)_*^2\sin\theta\,\mathrm{d}\theta, \qquad (6.46)
\end{aligned}
$$

where $(r_s)_* = |\boldsymbol{\chi}_*|$ is the spherical radius at the truncation point. Assuming truncation radius r_* is sufficiently large, the unknown velocity potential ϕ is expected to converge to the asymptotic expansion ϕ_∞ on the spherical cap γ_{liq}. Substituting ϕ_k from equation

(6.34) into (6.46) yields

$$
\begin{aligned}
&\int_{\gamma_{\mathrm{liq}}} (\boldsymbol{n}\cdot\nabla\phi)\,(r_s)_*^2\sin\theta\,\mathrm{d}\theta \\
&= \int_{\theta_*}^{\pi} \frac{\partial\phi_\infty}{\partial r_s}\Big|_{\boldsymbol{\chi}=((r_s)_*,\theta)} (r_s)_*^2\sin\theta\,\mathrm{d}\theta \\
&= \sum_{k=0}^{\infty} a_k \int_{\theta_*}^{\pi} \frac{\partial\phi_k}{\partial r_s}\Big|_{\boldsymbol{\chi}=((r_s)_*,\theta)} (r_s)_*^2\sin\theta\,\mathrm{d}\theta \\
&= \sum_{k=0}^{\infty} a_k \int_{\theta_*}^{\pi} \frac{\partial r_s^{\frac{1}{2}-\frac{3}{2}k}}{\partial r_s}\Big|_{r_s=(r_s)_*} P_{\frac{3}{2}k-\frac{3}{2}}(-\cos\theta)(r_s)_*^2\sin\theta\,\mathrm{d}\theta \\
&= \sum_{k=0}^{\infty} a_k \frac{1-3k}{2}(r_s)_*^{\frac{3}{2}-\frac{3}{2}k} \int_{\theta_*}^{\pi} P_{\frac{3}{2}k-\frac{3}{2}}(-\cos\theta)\sin\theta\,\mathrm{d}\theta \\
&= \sum_{k=0}^{\infty} a_k \frac{1-3k}{2}(r_s)_*^{\frac{3}{2}-\frac{3}{2}k} \int_{-\cos\theta_*}^{1} P_{\frac{3}{2}k-\frac{3}{2}}(x)\,\mathrm{d}x \\
&= -a_1(1+\cos\theta_*) + a_0\frac{2}{3}(r_s)_*^{3/2}\sin^2\theta_* P'_{\frac{-3}{2}}(-\cos\theta_*) \\
&\quad + \sum_{k=2}^{\infty} a_k (r_s)_*^{\frac{3-3k}{2}} \frac{2\sin^2\theta_*}{3(1-k)} P'_{\frac{3k-3}{2}}(-\cos\theta_*),
\end{aligned}
\tag{6.47}
$$

where the last line is the result of the integral formula of Legendre polynomial P_ℓ (Byerly, 1895),

$$
\int_x^1 P_\ell(x')\,\mathrm{d}x' = \frac{1-x^2}{\ell(\ell+1)} P'_\ell(x) \quad \text{for} \quad \ell \neq 0. \tag{6.48}
$$

Substituting integrals (6.45) and (6.46) back into in equation (6.44) we obtain

$$
\begin{aligned}
\int_{\omega_{\mathrm{T}}} \mathrm{d}\omega &= a_1\pi(1+\cos\theta_*) - a_0\pi\frac{2\sin^2\theta_*}{3} P'_{1/2}(-\cos\theta_*)(r_s)_*^{3/2} + \ldots + \frac{2}{3}\pi r_*^2(c_0 r_* - z_*) \\
&= a_1\pi(1+\cos\theta_0) + O(r_*^{-3/2}) \\
&\quad -\frac{2}{3}\pi c_1 r_*^{3/2} + a_0^2\pi\frac{P'_{1/2}(-\cos\theta_0)}{3}\left[\frac{c_0 P'_{1/2}(-\cos\theta_0)}{(1+c_0^2)^{3/2}} + \frac{2P''_{1/2}(-\cos\theta_0)}{(1+c_0^2)^2}\right] + O((r_s)_*^{-3/2}) \\
&\quad -\frac{2}{3}\pi(c_1 r_*^{3/2} + c_2) + O(r_*^{-3/2}) \\
&= a_1\pi(1+\cos\theta_0) + a_0^2\pi\frac{P'_{1/2}(-\cos\theta_0)}{3}\left[\frac{c_0 P'_{1/2}(-\cos\theta_0)}{(1+c_0^2)^{3/2}} + \frac{2P''_{1/2}(-\cos\theta_0)}{(1+c_0^2)^2}\right] \\
&\quad -\int_0^{r_*} c_1 r^{-1/2}\,2\pi r\,\mathrm{d}r + O(r_*^{-3/2}), \qquad \text{recall } c_2 = 0
\end{aligned}
\tag{6.49}
$$

where we have replaced z_* by the asymptotic height $z_* = \eta_\infty(r_*)$ in the limit $r_* \gg 1$ and then expanded all terms in powers of $1/r_*$. Since all the residues left in the integral

(6.49) are non-growing, it's now safe to evaluate the limit

$$\lim_{r_*\to\infty}\left\{\int_{\omega_\mathrm{T}}\mathrm{d}\omega+\int_0^{r_*}c_1 r^{-1/2}\,2\pi r\,\mathrm{d}r\right\}$$
$$=a_1\pi(1+\cos\theta_0)+a_0^2\pi\frac{P'_{1/2}(-\cos\theta_0)}{3}\left[\frac{c_0P'_{1/2}(-\cos\theta_0)}{(1+c_0^2)^{3/2}}+\frac{2P''_{1/2}(-\cos\theta_0)}{(1+c_0^2)^2}\right]. \tag{6.50}$$

Note that by setting $a_0=0$ (hence $c_1=0$ as well) we recover the relation derived by Zubarev (2001), which assumes sink flow is the leading order solution. The geometric interpretation of equality (6.50) becomes transparent if we introduce a new asymptotic boundary γ_D of the dynamic cone as

$$\gamma_\mathrm{D}=\{(r,c_0r+c_1r^{-1/2})\mid 0\le r\le r_*\} \tag{6.51}$$

and define another signed volume ω_D enclosed between liquid/vacuum interface γ and the leading order asymptote γ_D (see figure 6.6(b)),

$$\lim_{r_*\to\infty}\omega_\mathrm{D}=\lim_{r_*\to\infty}\int_0^{r_*}\left[c_0r+c_1r^{-1/2}-\eta(r)\right]2\pi r\,\mathrm{d}r$$
$$=a_1\pi(1+\cos\theta_0)+a_0^2\pi\frac{P'_{1/2}(-\cos\theta_0)}{3}\left[\frac{c_0P'_{1/2}(-\cos\theta_0)}{(1+c_0^2)^{3/2}}+\frac{2P''_{1/2}(-\cos\theta_0)}{(1+c_0^2)^2}\right], \tag{6.52}$$

or in its numerical form, $\lim_{r_*\to\infty}\omega_\mathrm{D}\approx 1.093\,a_1-0.118\,a_0^2$.

Equation (6.52) poses a constraint between coefficient a_1 and c_1, or equivalently between b_0 and a_0 due to (6.32) and (6.37), which suggests that arbitrary combinations of the two parameters, a_0 and b_0, might not all be admissible, i.e. there might exist no self-similar solution corresponding to the asymptotic series (6.33) of some particular pairs of a_0 and b_0. For instance, it is impossible for a combination of a strong sink flow ($a_1\gg 0$) and a weak lifting flow ($|a_0|\ll 1$) to produce a self-similar interface shape that's entirely bounded below by the asymptote γ_D for which the signed volume ω_D would have to strictly negative.

An interesting application of constraint (6.52) is estimates on the elevation of interface height $\eta(r)$ near apex. We only consider a special case where $c_1<0$ and liquid/vacuum interface γ is everywhere bounded blow by its asymptote γ_D:

$$c_0r+c_1r^{-1/2}\le\eta(r)\le c_0r\quad\text{for}\quad r\ge 0\text{ and }c_1<0.\quad\text{(assumption)} \tag{6.53}$$

Let $\tilde{r}$ be the axial distance of the turning point where boundary γ_D reaches its maximum height. We can then solve for a height level z_max such that the volume $\tilde{\omega}_\mathrm{D}$, which is bounded between $z=z_\mathrm{max}$ and γ_D till the turning radius $\tilde{r}$, is identical to $\lim_{r_*\to\infty}\omega_\mathrm{D}$ (see figure 6.6 for visualization),

$$\tilde{\omega}_\mathrm{D}=\int_0^{\tilde{r}}\left(c_0r+c_1r^{-1/2}-z_\mathrm{max}\right)2\pi r\,\mathrm{d}r=\lim_{r_*\to\infty}\omega_\mathrm{D}, \tag{6.54}$$

The solution of equation (6.54) is straightforward,

$$\tilde{r} = \left(\frac{c_1}{2c_0}\right)^{2/3}, \quad z_{\max} = \left(\frac{2c_0}{c_1}\right)^{1/3}\left(\frac{5}{3}c_1 - \frac{2c_0}{\pi c_1}\lim_{r_*\to\infty}\omega_{\mathrm{D}}\right). \tag{6.55}$$

It then immediately follows from the assumption (6.53) that the maximum interface elevation of $\eta(r)$ over interval $0 \le r \le \tilde{r}$ must be above the height of γ_{D} at the turning radius $\tilde{r}$ and that the minimum elevation of $\eta(r)$ over the same interval must be below $z_{\max}$:

$$\frac{3}{2^{2/3}}c_1\left(\frac{c_0}{c_1}\right)^{1/3} \le \max_{r\in[0,\tilde{r}]}\eta(r), \quad \min_{r\in[0,\tilde{r}]}\eta(r) \le z_{\max}. \tag{6.56}$$

Inequality (6.56) is different from the estimate in Zubarev (2001). In a simplified sink-flow setting, the liquid interface is assumed to be always bounded above by the exact Taylor cone $z = c_0 r$. However, due to the presence of far-field lifting flows, such assumption can no longer hold and interface profile is more likely to be bounded below by a corrected boundary $z = c_0 r + c_1/\sqrt{r}$.

6.5 Numerical Solutions via Patched Boundary Integral Equation

Asymptotic series (6.33) only converge to the exact solutions of the self-similar equations (6.20)–(6.22) in the far field. To resolve details of the velocity field, electric field and interface profile near cone apex, a patched boundary integral formulation (Leppinen and Lister, 2003) of the Laplace's equation is employed to communicate the near-apex information with analytically derived far-field asymptotic expansions. In figure 6.7(a), the semi-infinite vacuum and liquid domains are truncated by a sphere of a sufficiently large radius $\chi_* \gg 1$. The liquid/vacuum interface γ is intercepted by the same sphere at truncation point $\boldsymbol{\chi}_*$. The resulting vacuum volume ω_{vac} enclosed by γ and a spherical vacuum patch γ_{vac} is finite and closed. Similar truncation applies to the liquid domain γ_{liq}. These conditions allow the use of boundary integral representation of harmonics potentials. For velocity potential ϕ we have

$$\beta(\boldsymbol{\chi}')\phi(\boldsymbol{\chi}') = \int_{\gamma\cup\gamma_{\mathrm{liq}}}\left\{g(\boldsymbol{\chi}';\boldsymbol{\chi})\frac{\partial\phi(\boldsymbol{\chi})}{\partial\boldsymbol{n}} - \phi(\boldsymbol{\chi})\frac{\partial g(\boldsymbol{\chi}';\boldsymbol{\chi})}{\partial\boldsymbol{n}}\right\}2\pi r\,\mathrm{d}\gamma(\boldsymbol{\chi}), \tag{6.57}$$

where $g(\boldsymbol{\chi}';\boldsymbol{\chi})$ is the axisymmetric Green's function (Lennon, P. L.-F. Liu, and Liggett, 1979) of a ring source located at $\boldsymbol{\chi}'$, $\boldsymbol{n}$ is the boundary normal vector pointing from ω_{liq} into ω_{vac} and $\beta(\boldsymbol{\chi}')$ is the interior angle formed by two adjacent boundaries at $\boldsymbol{\chi}'$. The electric potential ψ can be formulated through an almost identical representation as in equation (6.57) only with outward normal $\boldsymbol{n}$ reversed.

Normally for boundary value problems of harmonic potentials exterior to a finite, simply connected body, the integral contribution from these spherical patches are neglected because the integrand from these boundaries tends to decay sufficiently fast in the limit of a infinitely large truncation radius. Unfortunately this is not the case for the problem

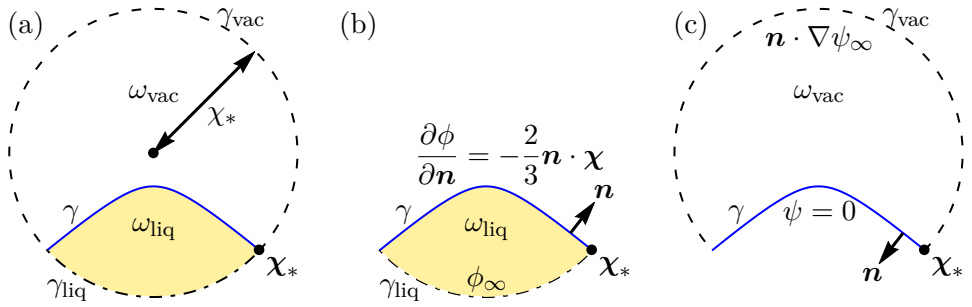

Figure 6.7: (a) Truncated vacuum domain $\omega_{\rm liq}$ with patched vacuum boundary $\gamma_{\rm vac}$ (dashed) and liquid domain $\omega_{\rm liq}$ (dash-dotted), separated by the liquid/vacuum interface γ (solid blue) clamped at the intercept point $\boldsymbol{\chi}_*$. (b) Patched boundary value problem (6.58) for velocity potential ϕ. (c) Patched boundary value problem (6.59) for electric potential ψ.

of self-similar cone formation we consider here. It's not difficult to see that, if velocity potential ϕ converges to its asymptotic expansion ϕ_∞ in (6.33), then the integrand, e.g., $\phi(\boldsymbol{\chi})(\partial g(\boldsymbol{\chi}';\boldsymbol{\chi})/\partial\boldsymbol{n})2\pi r\,\mathrm{d}\gamma$, would grow $\sim\sqrt{r_s}$ as $r_s\to\infty$ instead of decay to zero. Inclusion of the two patched boundaries $\gamma_{\rm liq}$ and $\gamma_{\rm vac}$ is crucial to obtaining accurate solutions to the integral equation (6.57). For the velocity potential ϕ, we impose the kinematic condition (6.21) on γ and a Dirichlet condition on the patched boundary $\gamma_{\rm liq}$ based on the asymptotic expansion (6.33) up to $k=4$,

$$\frac{\partial\phi}{\partial\boldsymbol{n}} = -\frac{2}{3}\boldsymbol{n}\cdot\boldsymbol{\chi} \quad \text{on} \quad \gamma, \quad \phi = \sum_{k=0}^{4} a_k\phi_k \quad \text{on} \quad \gamma_{\rm liq}. \tag{6.58}$$

For the electric potential ψ, equipotential condition (6.22) is imposed on γ and a Neumann condition on $\gamma_{\rm vac}$,

$$\psi = 0 \quad \text{on} \quad \gamma, \quad \frac{\partial\psi}{\partial\boldsymbol{n}} = \sum_{k=0}^{4} b_k\frac{\partial\psi_k}{\partial\boldsymbol{n}} \quad \text{on} \quad \gamma_{\rm vac}. \tag{6.59}$$

We discretize the boundaries γ, $\gamma_{\rm liq}$ and $\gamma_{\rm vac}$ with a set of knots interpolated by quintic splines. Quadratic Lagrange basis functions along the spline arc-length are employed to approximate velocity potential ϕ, normal velocity $\partial\phi/\partial\boldsymbol{n}$ and electric field $\partial\psi/\partial\boldsymbol{n}$ from their Lagrange nodal values on the boundary. Numerical integration in the presence of the Green's function $g(\boldsymbol{\chi}';\boldsymbol{\chi})$ is handled with Gauss-Legendre quadrature rules when the integrand of (6.57) is regular and with the logarithmic-weighted quadrature rules whenever a logarithmic singularity appears. Given a pair of coefficients $(a_0,\ b_0)$, we clamp a trial interface shape γ and its first two derivatives at the truncation point $\boldsymbol{\chi}_*$ (see figure 6.7(a)) according to the analytic expression $\eta_\infty(r)$ from (6.33). The matrix equations arsing from two discretized integral equations of ϕ and ψ subject to

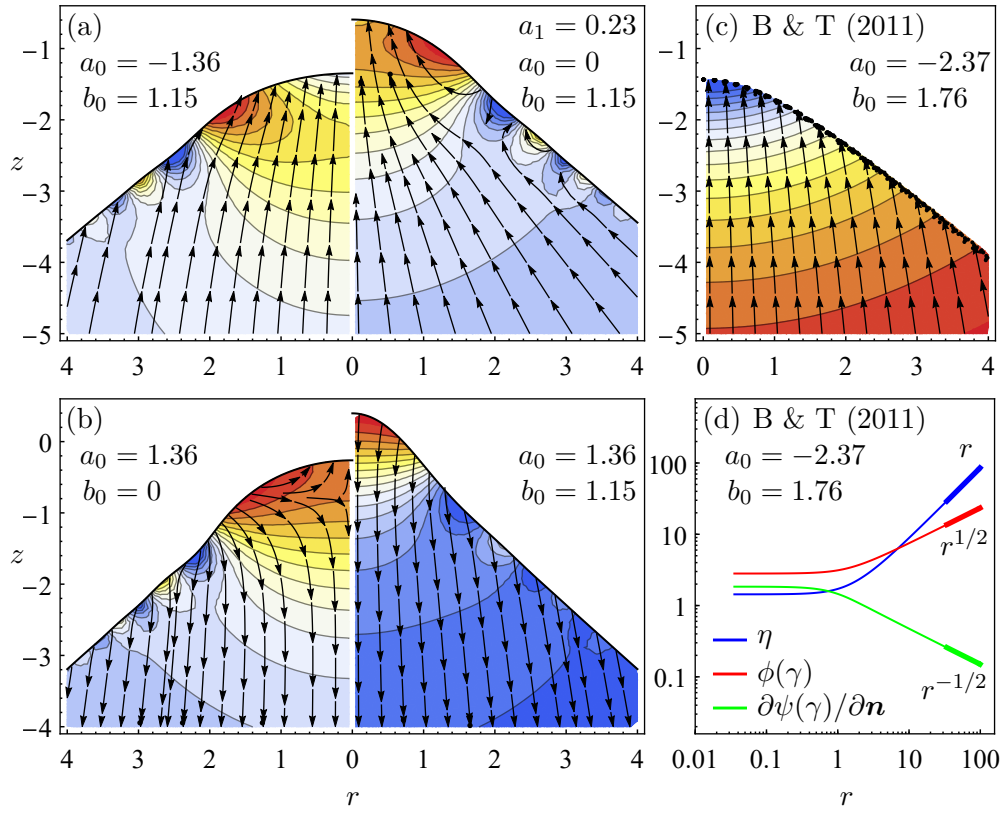

Figure 6.8: Self-similar solutions parametrized by a_0 and b_0: interface shape γ (solid), pressure field p (contours) and velocity field $\nabla\phi$ (arrow). (a) Two sub-cone solutions with $b_0 = 1.15$: $a_0 = 0 \Rightarrow a_1 = 0.23$ (right) and $a_0 = -1.36$ (left). (b)Two super-cone solutions with $a_0 = 1.36$: $b_0 = 1.15$ (right) and $b_0 = 0$ (left). (c) Sub-cone solution $\gamma_{\rm SS}$ corresponding to $a_0 = -2.37$ and $b_0 = 1.76$, overlaid by the rescaled data (dot) from Burton and Taborek (2011). (d) Log-log plot of ϕ (red), $\partial\psi/\partial\boldsymbol{n}$ (green) and η (blue) evaluated along $\gamma_{\rm SS}$ against r. Thick lines are power-law asymptotes $0.989703\,a_0 r^{1/2}$, $0.848582\,b_0 r^{-1/2}$ and $0.860437\,r$ with no adjusting parameters.

mixed boundary conditions (6.58) and (6.59) are solved by QR decomposition to obtain nodal vlaues of ϕ and $\partial\psi/\partial\boldsymbol{n}$ on γ. In the end a Newton-Raphson method is used to iteratively adjust parametrization of the interface γ till the self-similar Bernoulli's equation (6.20) is satisfied up to a sufficiently small residue. The Jacobian at Newton steps is approximated numerically by perturbing interface γ in the normal directions. The details of these numerical methods and approximations are provided in Chapter 7.

In figure 6.8(a) we compare two sub-cone solutions produced by our boundary integral solver under identical far-field electric field strength $b_0 = 1.15$. The solution plotted in the left half is completely beneath the exact Taylor cone which corresponds to a lifting flow $a_0\phi_0$ with $a_0 = -1.36$ dominating the far field. The near-apex surface undulations decay quickly and converge to the leading order correction $\eta \sim c_0 r + c_1/\sqrt{r}$ ($c_1 = -0.5$

by (6.37)). The solution plotted on the right is found by imposing a far-field sink flow $a_1\phi_1$ for which $a_1 = 0.23$ by setting $a_0 = 0$ in (6.32). It's evident from the pressure contour lines that the flow becomes spherically symmetric as it moves away from the apex. Aside from its rapid convergence to the exact Taylor cone (recall sink flow implies $\eta \sim c_0 r + c_4 r^{-5}$), the interface oscillations cross the line of the Taylor cone multiple times leaving behind a series of stagnation points $\boldsymbol{\chi}_s$ in the bulk, i.e. bifurcation points of the streamlines shown in the right half of figure 6.8(a) where $\nabla\phi = \boldsymbol{0}$. Note fluid is only "stagnant" in the co-moving self-similar frame. In the laboratory frame time-dependent trajectories of these points $\boldsymbol{X}_s$ exactly follow the self-similar transformation, $\boldsymbol{X}_s(T) = \boldsymbol{X}_c + \tau^{2/3}\boldsymbol{\chi}_s$. We conjecture these stagnation points may lead to global instabilities as we recall from the unsteady Bernoulli's system (6.5)–(6.6) that self-similar solutions are the steady states in the transformed frame.

In figure 6.8(b) we plot two sub-cone solutions subject to identical far-field flow condition $a_0 = 1.36$. These solutions are computed in a pre-singularity ($T < T_c$) context. However, given time reversal symmetry of the inviscid theory, these solutions could be equivalently interpreted as post-singularity dynamics beyond the critical time T_c. The solution on the left is free of Maxwell stress ($b_0 = 0$) which qualitatively agrees with the capillary recoil of a single conical drop revealed by Sierou and Lister (2004). On the symmetry axis $r = 0$ there exists a stagnation point where the descending flow of the recoil liquid cap meets the uprising bulk. This counter flow results in a parabolic bulge protruding normal to the exact Taylor cone, which in the lab frame turns into a self-similar capillary wave recoiling away from the conical point $\boldsymbol{X}_c$. In the presence of a far-field Maxwell stress ($b_0 = 1.15$), the solution shown in the right half of figure 6.8(b) is now entirely above the Taylor cone with a highly curved apex owning to the upward pulling of electrostatic pressure and a persisting lifting flow ϕ_0 in the far field. Physically this type of solution can be interpreted as early time onset flow of a growing pendent drop or a bursting jet as the liquid cone just transverses the critical time T_c. Contrary to the accelerating apex of pre-singularity sharpening solutions, the cone apexes in these post-singularity dynamics actually decelerate since $\mathrm{d}\boldsymbol{X}/\mathrm{d}T \sim (T - T_c)^{-1/3} \to 0$ as laboratory time T traverses over the critical time T_c.

The self-similar solution dominated by a strong far-field lifting flow instead of a sink flow shows remarkable consistency with the spontaneously sharpening conical ends of an isolated charged drop in the inviscid simulation (Burton and Taborek, 2011). In their work, mean curvature and electric field at the tip of the drop were observed to exhibit decades of robust power-law rates, $|\mathscr{H}| = 0.604\,\tau^{-2/3}$ and $|\boldsymbol{N}\cdot\boldsymbol{E}| = 0.925\,\tau^{-1/3}$. By setting $a_0 = 2.37$ and $b_0 = 1.757$, we successfully identify a self-similar solution γ_{SS} with $\hbar = -0.608$ and $|\boldsymbol{n}\cdot\nabla\psi| = 0.922$ at $r = 0$. The data points of 20 time-dependent interface shapes were extracted from figure 1(b) of Burton and Taborek (2011) and transformed into a local frame where all data points collapse onto a single curve γ_{BT} as

they should. Since tick marks are not included in their figure inset, γ_{BT} is expected to agree with γ_{SS} up to an one-parameter isotropic rescaling which is found by least-square fits. In figure 6.8(c) we overlay the best-rescaled data points from Burton and Taborek (2011) on top of the self-similar solution γ_{SS} produced by our boundary integral solver with $a_0 = 2.37$ and $b_0 = 1.757$ being the input. Almost perfect agreement is achieved between their time-dependent simulation and our self-similar solution. The shape γ_{SS} resembles a clean hyperbola without notable oscillations in the geometry or in the liquid pressure field. In figure 6.8(d) the asymptotic behaviors of of velocity potential ϕ, surface electric field $\partial\psi/\partial\boldsymbol{n}$ and interface shape η evaluated along γ_{SS} computed by the boundary integral solver also agree with the leading order ansatz (6.31) re-parametrized in r,

$$\eta \sim c_0 r, \quad \phi(\gamma) \sim a_0 \frac{P_{1/2}(-\cos\theta_0)}{\sqrt{\sin\theta_0}}\sqrt{r}, \quad \frac{\partial\psi}{\partial\boldsymbol{n}}(\gamma) \sim \frac{b_0}{\sqrt{\sin\theta_0}} \frac{\mathrm{d}P_{1/2}(\cos\theta)}{\mathrm{d}\theta}\Big|_{\theta_0}\sqrt{r}, \tag{6.60}$$

with no adjusting parameters. This result confirms that the local velocity field near apex during a dynamic cone formation is dominated by the lifting flow ϕ_0 as opposed to the sink flow ϕ_1 suggested by Zubarev (2001). Burton and Taborek (2011) also demonstrate robustness of the observed self-similar cone formation against artificial perturbations during the final stage of their time-dependent simulation, which provides strong evidence in favor of the lifting flow being dynamically stable in laboratory frame and hence more likely to be selected during the formation of a conic cusp.

6.6 Discussion and Conclusion

In this work the inviscid mechanism of dynamic cone formation at interface of a perfectly conductive liquid surrounded by vacuum is investigated. In contrast to what's commonly spread in literature, it is not necessary for capillary and Maxwell forces to maintain a perfect balance everywhere along a conic surface. In fact it is the mismatch between these two opposing surface forces giving rise to the inertia forces–which have always been ignored– responsible for the self-reinforced liquid motion and acceleration in the bulk.

After re-examining Zubarev (2001)'s self-similar theory, we have found a family of similarity solutions parametrized by the leading order strength a_0 of a lifting velocity potential $\phi_0 = \sqrt{r_s}P_{1/2}(-\cos\theta)$ and strength b_0 of Taylor's conic electric potential $\psi_0 = \sqrt{r_s}P_{1/2}(\cos\theta)$. Our asymptotic analysis leads to the prediction of a novel flow pattern, i.e. the lifting flow $\nabla\phi_0$, as well as a stronger leading order shape correction $\propto 1/\sqrt{r}$ to the exact Taylor cone. It is shown that Zubarev's asymptotic result is only a subset of the entire solution family. The majority of similarity solutions lift liquid upwards with nearly vertical streamlines intercepting the conic interface at a finite angle, as opposed to the wildly quoted sink motion of nearly spherically symmetric flows (Collins,

Jones, et al., 2007; Moroshkin et al., 2017). These self-similar solutions are exact for inviscid and irrotional liquids, representing dynamic local balances between capillary pressure (curvature) $|2\mathcal{H}|$, Maxwell (electrostatic) pressure $|\boldsymbol{E}|^2/2$ and kinetic energy density $|\boldsymbol{U}|^2/2$ in the vicinity of the conical point $\boldsymbol{X}_c$ during the self-similar process of cone formation. As the critical time T_c is approached, these physical quantities all blow up algebraically $\sim |T_c - T|^{-1/3}$ accompanied by rapidly diminishing length scale of the local frame. In this sense, the self-similar process of cone formation can be regarded universal as boundary conditions away from cone apex become irrelevant compared to the dynamics happening in the local frame. When transformed back to the laboratory frame, velocity potential Φ near the conical point $\boldsymbol{X}_c$ has the local expression near the cone apex,

$$\Phi(\boldsymbol{X}, T) = a_0\sqrt{|\boldsymbol{X} - \boldsymbol{X}_c|}P_{1/2}(-\cos\theta) + a_1\frac{T - T_c}{|\boldsymbol{X} - \boldsymbol{X}_c|} + \dots, \tag{6.61}$$

where the strength of lifting flows is unaffected by the self-similar transformation in contrast to the magnitude of sink flows which actually dwindles linearly in time as $T \to T_c$. Similarly, if we define $H(X, Y)$ to be the height field of interface shape Γ in laboratory frame measured with respect to $Z = Z_c$ (the Z-plane of conical point $\boldsymbol{X}_c$) and $R_\parallel = \sqrt{|\boldsymbol{X}_c - \boldsymbol{X}|^2 - (Z_c - Z)^2}$ as the (cylindrical) axial distance to $\boldsymbol{X}_c$, the asymptotic solution $\eta_\infty(r)$ yields

$$H(R_\parallel, T) = c_0 R_\parallel + c_1\frac{T_c - T}{\sqrt{R_\parallel}} + c_3\frac{(T_c - T)^3}{R_\parallel^{7/2}} + c_4\frac{(T_c - T)^4}{R_\parallel^5} + \dots \tag{6.62}$$

(recall from (6.37) that $c_2 = 0$). Note as the conical singularity is approached, Zubarev's leading order shape correction to the exact Taylor cone, i.e. the c_4 term in equation (6.62), has an extremely rapid convergence in both space and time while the first shape correction uncovered by our analysis has a much more prominent tail with a linear convergence in time.

We have also computed the exact solutions to the self-similar theory for the firs time using a novel boundary integral method which correctly captures the asymptotic behavior derived analytically. Given the time-dependent data of an inviscid, perfectly conductive drop (Burton and Taborek, 2011), we have successfully recovered the similarity solution responsible for the spontaneous development of conical ends with an almost perfect agreement. The result shows that the lifting flow, instead of sink flow, is selected during the last stage of their simulated cone formation. In addition, the solutions computed by the boundary integral method reveal the near-apex flow structure during dynamic cone formation including novel flow patterns such as counter flow, stagnation points and oscillatory pressure distribution which are all not accessible to the far-field asymptotic analysis. Existence of multiple stagnation points in the similarity solution of an asymptotic sink flow shown in figure 6.8(a) leads to localized oscillatory fluctuations

of velocity field in laboratory frame and hence may rise stability concerns. It's also worthy of mentioning that modal stability analysis of the self-similar "steady"-state solutions (Leppinen and Lister, 2003) can be carried out by examining the full self-similar dynamics (6.15)–(6.17) for which the log-time-dependence, $t = -\ln(T_c - T)$, in both velocity potential ϕ and moving interface γ is retained. This analysis is left for future research.

Chapter 7

DYNAMIC CONE FORMATION IN CONDUCTIVE LIQUIDS: BOUNDARY INTEGRAL FORMULATION

7.1 Boundary Integral Method for Interfacial Inviscid Flow

The boundary integral method is a numerical computational technique which approximates the solution to linear partial differential equations (PDEs) by formulating the problem as boundary integral equations of the solution to the same PDE but restricted to the domain boundary. After solving the boundary integral equation, the solution evaluated on the domain boundary is known and then can be further postprocessed to derive solution inside the domain. A boundary integral formulation becomes available typically when the governing PDEs are homogeneous (i.e. do not depend on other spatially varying variables) or only have a finite number of sources or singularity in the domain. In such cases, the governing PDE can be recast to a self-contained integral representation in aid of the Green's functions, for which only information on the boundary is involved.

As a modern technique of numerical analysis, popularity of the boundary integral method has thrived over the last two decades. For state-of-art boundary integral methods in simulating interfacial fluid flows driven by surface tension such as multiphase potential flows and Hele-Shaw flows, we refer to the inspiring review article by Hou, Lowengrub, and Shelley (2001). Theoretical and computational aspects of boundary integral representation for Stokes flows at vanishing Reynolds number are addressed in the survey by Pozrikidis (2001). The two-volume book set (Wrobel, 2002; Aliabadi, 2002) serves as an excellent resource for engineering applications such as heat transfer, acoustic wave scattering, and elastostatics. Mathematically rigorous treatments on the topic of linear integral equations can be found in the classical monograph (Kress, 2014).

Boundary integral representation of the harmonic potential has become an indispensable tool for understanding the formation and dynamics of geometric singularities at the interface of inviscid fluids. Keller and Miksis (1983) developed the self-similar theory of free surface inviscid flows when examining the ensuing capillary-driven motion of an initially wedge-shaped liquid which has just come into contact with a solid. They pioneered the use of integral representation by reformulating the inviscid fluid equations in self-similar frame as an integrodifferential system which led to a family of similarity solutions for receding liquid with different initial wedge angles. Billingham and King (1995) extended the idea of locally self-similar flow in the vicinity of a surface singularity to an interface between two inviscid fluids of different densities advected in an initially uniform flow towards a semi-infinite thin flat plate perpendicular to the interface. They developed an efficient numerical solution method for the full nonlinear boundary value

problem based on Green's integral representation for harmonic potentials. In a three-dimensional setting, Leppinen and Lister (2003) and Sierou and Lister (2004), motivated by the hyperbola-like fluid pinch-off observed in the time-dependent simulations of an inviscid drop (Day, Hinch, and Lister, 1998), recovered a large family of self-similar solutions corresponding to the axisymmetric inviscid pinch-off and recoil of a fluid body immersed in an ambient fluid of a different density over a range of the density ratio and pinch angles. They correctly recognized the necessity of far-field patching in the velocity potentials, which was not present or need in those planar problems studied before, and obtained a family of interface shapes with exotic double-cone structures via a double-layer integral representation of the velocity potential. Burton and Taborek (2007) investigated the two-dimensional pinch-off of an inviscid fluid by numerically solving the boundary integral equations via a method for singularity reduction (Nie and Baker, 1998). Unlike three-dimensional cases, they discovered that the asymptotic collapse of the pinching region exhibits an anomalous similarity exponent which is the signature of self-similarity of the second kind. Padrino and Joseph (2011) extended the numerical simulation of bubble or drop break-up in uniaxial straining flow to study viscous effect in irrotational potential flow. The ultrahigh resolution of their boundary-element method coupled with a time-integration routine uncovered larger break-up times compared to the inviscid case. Burton and Taborek (2011) performed unsteady boundary integral simulations of critically charged inviscid droplets. Their work presented solid numerical evidence on previously predicted power-law behaviors during the formation of conic tips for perfectly conductive liquid as well as new scaling laws for the charge and radius of progeny drops when surface charge transport is limited by a finite electrical conductivity.

In this chapter, we provide technical details of the boundary integral scheme used to solve the system of coupled equations (6.20), (6.21) and (6.22) emerging from the self-similar theory of of dynamic cone formation under the combined effect of capillary and Maxwell stresses. In Section 7.2, numerical techniques such as spline-based curve interpolations and weighted quadrature rules concerning logarithmic singularities in the compete elliptic integrals are discussed. In Section 7.3, we establish the discretization process for the axisymmetric boundary integral equation of harmonic potentials via collocation method with an emphasis on mixed boundary conditions. The accuracy of our C++ implementation of boundary integral solver is verified as well. Finally in Section 7.4 we present the Newton-Raphson algorithm which iteratively modifies the liquid/vacuum interface to guide the convergence to the self-similar solutions of dynamic cone formation shown in Section 6.5.

7.2 Spline Interpolation, Gaussian Quadrature and Elliptic Integral

In this section, we discuss several numerical approximations and techniques that are crucial to achieving accurate solutions to boundary integral equations. In particular, the technical details of quintic spline approximation to curved geometries, weighted Gaussian Quadrature rules for weakly singular integrals and Chebyshev approximations for the complete Elliptic integrals are presented.

Quintic spline interpolation

The accuracy of numerical solutions to equations posed on curved geometries is only as good as the precision and smoothness of the underlying geometric approximation. For 2D problems, we employ the spline approximation of planar curves. A quintic spline is a piecewise-quintic curve defined by a collection of low degree polynomials, which we call the local splines, such that not only it interpolates through a set of knots but also guarantees continuity up to the fourth derivative (Mund, Hallet, and Hennart, 1975). The ability to acquire higher order derivatives with respect to curve parameterization makes higher order spline interpolations especially relevant to continuum mechanics such as modeling of elastic rods and beams, the bending energy of which is proportional to curvature squared (Horn, 1983). The quintic spline algorithm presented in this section closely follows the derivation in the appendix of Padrino Inciarte (2010) with several typos fixed.

Let $\boldsymbol{\chi}_0, \ldots, \boldsymbol{\chi}_N$ be a collection of $N+1$ spline knots and vector $\boldsymbol{\gamma}(s)$ be the global spline that interpolates through these knots with s being the intrinsic coordinate of the curve. Since the spline interpolation is not known *a priori*, a natural choice for the intrinsic coordinate l is to first construct the chords, i.e. the Euclidean distances between adjacent knots $\boldsymbol{x}_j$ and $\boldsymbol{x}_{j+1}$,

$$h_j = \|\boldsymbol{\chi}_{j+1} - \boldsymbol{\chi}_j\| \quad \text{for} \quad j = 0, \ldots, N-1. \tag{7.1}$$

The accumulative sums of these chords yield $N+1$ intrinsic coordinates $s_0, \ldots, s_N$ where

$$s_0 = 0, \quad s_j = \sum_{k=0}^{j-1} h_k \quad \text{for} \quad j = 1, \ldots, N. \tag{7.2}$$

We then construct the global spline $\boldsymbol{\gamma}(s)$ from a set of local splines $\boldsymbol{\gamma}^{(0)}, \ldots, \boldsymbol{\gamma}^{(N-1)}$ where each local spline

$$\boldsymbol{\gamma}^{(j)}(s) = \boldsymbol{\chi}_j + \sum_{k=1}^{5} \boldsymbol{c}_k^{(j)} (s - s_j)^k \quad \text{for} \quad j = 0, \ldots, N-1 \tag{7.3}$$

is a fifth degree polynomial defined within the interval $[s_j, s_{j+1}]$ and $\boldsymbol{c}_k^{(j)}$ are the local vectorial coefficients for each monomial of $\boldsymbol{\gamma}^{(j)}(s)$. Continuities between any neighboring

pairs of local quintic splines is expected to hold up to the fourth derivative,

$$\boldsymbol{\gamma}^{(j)} = \boldsymbol{\gamma}^{(j+1)}, \quad \frac{\mathrm{d}\boldsymbol{\gamma}^{(j)}}{\mathrm{d}s} = \frac{\mathrm{d}\boldsymbol{\gamma}^{(j+1)}}{\mathrm{d}s}, \ldots, \frac{\mathrm{d}^4\boldsymbol{\gamma}^{(j)}}{\mathrm{d}s^4} = \frac{\mathrm{d}^4\boldsymbol{\gamma}^{(j+1)}}{\mathrm{d}s^4}, \quad \text{at} \quad s = s_{j+1} \tag{7.4}$$

which translate into five algebraic equations for the vectorial coefficients $\boldsymbol{c}_k^{(j)}$ of adjacent local splines,

$$\boldsymbol{c}_3^{(j-1)}h_{j-1}^3 + \boldsymbol{c}_4^{(j-1)}h_{j-1}^4 + \boldsymbol{c}_5^{(j-1)}h_{j-1}^5 = \boldsymbol{\chi}_j - \boldsymbol{\chi}_{j-1} - \boldsymbol{c}_1^{(j-1)}h_{j-1} - \boldsymbol{c}_2^{(j-1)}h_{j-1}^2, \tag{7.5}$$

$$3\boldsymbol{c}_3^{(j-1)}h_{j-1}^2 + 4\boldsymbol{c}_4^{(j-1)}h_{j-1}^3 + 5\boldsymbol{c}_5^{(j-1)}h_{j-1}^4 = -\boldsymbol{c}_1^{(j-1)} - 2\boldsymbol{c}_2^{(j-1)}h_{j-1} + \boldsymbol{c}_1^{(j)}, \tag{7.6}$$

$$6\boldsymbol{c}_3^{(j-1)}h_{j-1} + 12\boldsymbol{c}_4^{(j-1)}h_{j-1}^2 + 20\boldsymbol{c}_5^{(j-1)}h_{j-1}^3 = -2\boldsymbol{c}_2^{(j-1)} + 2\boldsymbol{c}_2^{(j)}, \tag{7.7}$$

$$\boldsymbol{c}_3^{(j-1)} + 4h_{j-1}\boldsymbol{c}_4^{(j-1)} + 10h_{j-1}^2\boldsymbol{c}_5^{(j-1)} = \boldsymbol{c}_3^{(j)}, \tag{7.8}$$

$$\boldsymbol{c}_4^{(j-1)} + 5h_{j-1}\boldsymbol{c}_5^{(j-1)} = \boldsymbol{c}_4^{(j)}. \tag{7.9}$$

Many coefficients $\boldsymbol{c}_k^{(j)}$ are redundant which can be eliminated by manipulating the algebraic equations (7.5)–(7.9). In fact the global spline $\boldsymbol{\gamma}(s)$ is fully specified by the first and the second coefficients, $\boldsymbol{c}_1^{(j)}$ and $\boldsymbol{c}_2^{(j)}$, only.

To see this argument, we first eliminate $\boldsymbol{c}_3^{(j-1)}$, $\boldsymbol{c}_4^{(j-1)}$ and $\boldsymbol{c}_5^{(j-1)}$ from equations (7.5)–(7.7) and express them as functions of $\boldsymbol{c}_1^{(j-1)}$, $\boldsymbol{c}_2^{(j-1)}$, $\boldsymbol{c}_1^{(j)}$ and $\boldsymbol{c}_2^{(j)}$ alone,

$$h_{j-1}^3\boldsymbol{c}_3^{(j-1)} = +10(\boldsymbol{\chi}_j - \boldsymbol{\chi}_{j-1}) - 6h_{j-1}\boldsymbol{c}_1^{(j-1)} - 3h_{j-1}^2\boldsymbol{c}_2^{(j-1)} - 4h_{j-1}\boldsymbol{c}_1^{(j)} + h_{j-1}^2\boldsymbol{c}_2^{(j)}, \tag{7.10}$$

$$h_{j-1}^4\boldsymbol{c}_4^{(j-1)} = -15(\boldsymbol{\chi}_j - \boldsymbol{\chi}_{j-1}) + 8h_{j-1}\boldsymbol{c}_1^{(j-1)} + 3h_{j-1}^2\boldsymbol{c}_2^{(j-1)} + 7h_{j-1}\boldsymbol{c}_1^{(j)} - 2h_{j-1}^2\boldsymbol{c}_2^{(j)}, \tag{7.11}$$

$$h_{j-1}^5\boldsymbol{c}_5^{(j-1)} = +6(\boldsymbol{\chi}_j - \boldsymbol{\chi}_{j-1}) - 3h_{j-1}\boldsymbol{c}_1^{(j-1)} - h_{j-1}^2\boldsymbol{c}_2^{(j-1)} - 3h_{j-1}\boldsymbol{c}_1^{(j)} + h_{j-1}^2\boldsymbol{c}_2^{(j)}. \tag{7.12}$$

Once all coefficients $\boldsymbol{c}_1^{(j)}$ and $\boldsymbol{c}_2^{(j)}$ are computed, the rest, i.e. $\boldsymbol{c}_3^{(j)}$, $\boldsymbol{c}_4^{(j)}$ and $\boldsymbol{c}_5^{(j)}$, can be derived from equations (7.10)–(7.12). We next recognize a set of recursive relations between the coefficients $\boldsymbol{c}_1^{(j-1)}$, $\boldsymbol{c}_1^{(j)}$, $\boldsymbol{c}_1^{(j+1)}$, $\boldsymbol{c}_2^{(j-1)}$, $\boldsymbol{c}_2^{(j)}$ and $\boldsymbol{c}_2^{(j+1)}$ based on the observation that expressions of $\boldsymbol{c}_3^{(j)}$ and $\boldsymbol{c}_4^{(j)}$ are basically equivalent to the ones in equations (7.10) and (7.11) only with index j advanced to $j+1$. Together with $\boldsymbol{c}_3^{(j-1)}$, $\boldsymbol{c}_4^{(j-1)}$ and $\boldsymbol{c}_5^{(j-1)}$ substituted from equations (7.10)–(7.12), the last two continuity conditions (7.8) and (7.9) yield a set of $2(N-1)$ coupled linear equations

$$\left.\begin{aligned} 10\left[+\lambda^3\boldsymbol{\chi}_{j-1} - (1+\lambda^3)\boldsymbol{\chi}_j + \boldsymbol{\chi}_{j+1}\right] &= +4h_j\lambda^2\boldsymbol{c}_1^{(j-1)} + 6h_j(\lambda^2-1)\boldsymbol{c}_1^{(j)} - 4h_j\boldsymbol{c}_1^{(j+1)} \\ &\quad + h_j^2\lambda\boldsymbol{c}_2^{(j-1)} - 3h_j^2(1+\lambda)\boldsymbol{c}_2^{(j)} + h_j^2\boldsymbol{c}_2^{(j+1)}, \\ 15\left[-\lambda^4\boldsymbol{\chi}_{j-1} + (\lambda^4-1)\boldsymbol{\chi}_j + \boldsymbol{\chi}_{j+1}\right] &= +7h_j\lambda^3\boldsymbol{c}_1^{(j-1)} + 8h_j(1+\lambda^3)\boldsymbol{c}_1^{(j)} + 7h_j\boldsymbol{c}_1^{(j+1)} \\ &\quad + 2h_j^2\lambda^2\boldsymbol{c}_2^{(j-1)} + 3h_j^2(1-\lambda^2)\boldsymbol{c}_2^{(j)} - 2h_j^2\boldsymbol{c}_2^{(j+1)}, \end{aligned}\right\} \tag{7.13}$$

for $2(N+1)$ unknowns $\boldsymbol{c}_1^{(0)}$, ... , $\boldsymbol{c}_1^{(N)}$ and $\boldsymbol{c}_2^{(0)}$, ... , $\boldsymbol{c}_2^{(N)}$ where $\lambda = h_j/h_{j-1}$ is the ratio between adjacent chords. It is convenient to introduce a ghost local spline $\boldsymbol{\gamma}^{(N)}$ next to $\boldsymbol{\gamma}^{(N-1)}$ which satisfies all continuity conditions as well. The purpose of $\boldsymbol{\gamma}^{(N)}$ is to deal with boundary conditions at the end of the global spline $\boldsymbol{\gamma}(s)$ in a computationally self-consistent manner. Note we have $2(N-1)$ equations from (7.13) but only $2(N+1)$ unknowns. The four additional equations come from constraints on $\boldsymbol{c}_1^{(0)}$, $\boldsymbol{c}_2^{(0)}$, $\boldsymbol{c}_1^{(N)}$ and $\boldsymbol{c}_2^{(N)}$ when we enforce boundary conditions at the begin and the end of the global spline $\boldsymbol{\gamma}(s)$. Here $\boldsymbol{c}_k^{(N)}$ are the vectorial coefficients of the ghost spline $\boldsymbol{\gamma}^{(N)}$.

In general there are three types of boundary condition—even, odd and mixed—that we would like to impose at each end of the global spline. Let χ_j, $\gamma^{(j)}$ and $c^{(j)}$ be one of the scalar components of knots $\boldsymbol{\chi}_j$, local spline $\boldsymbol{\gamma}^{(j)}$ and vectorial coefficient $\boldsymbol{c}^{(j)}$, respectively. Three types of boundary condition evaluated at $s = s_0$ for a quintic spline lead to constraints on the derivatives of the zeroth spline $\boldsymbol{\gamma}^{(0)}$,

$$\frac{\mathrm{d}\gamma^{(0)}}{\mathrm{d}s} = \frac{\mathrm{d}^3\gamma^{(0)}}{\mathrm{d}s^3} = 0, \qquad \text{(even)} \tag{7.14}$$

$$\gamma^{(0)} = \frac{\mathrm{d}^2\gamma^{(0)}}{\mathrm{d}s^2} = \frac{\mathrm{d}^4\gamma^{(0)}}{\mathrm{d}s^4} = 0, \qquad \text{(odd)} \tag{7.15}$$

$$\frac{\mathrm{d}\gamma^{(0)}}{\mathrm{d}s} = \alpha, \quad \frac{\mathrm{d}^2\gamma^{(0)}}{\mathrm{d}s^2} = \beta, \qquad \text{(mixed)} \tag{7.16}$$

which then translate into two linear equations for each type,

$$\left.\begin{aligned} c_1^{(0)} &= 0, \\ 6h_0c_1^{(0)} + 3h_0^2c_2^{(0)} + 4h_0c_1^{(1)} - h_0^2c_2^{(1)} &= -10\chi_0 + 10\chi_1, \end{aligned}\right\} \quad \text{(even)} \tag{7.17}$$

$$\left.\begin{aligned} -8h_0c_1^{(0)} - 3h_0^2c_2^{(0)} - 7h_0c_1^{(1)} + 2h_0^2c_2^{(1)} &= +15\chi_0 - 15\chi_1, \\ c_2^{(0)} &= 0, \end{aligned}\right\} \quad \text{(odd)} \tag{7.18}$$

$$\left.\begin{aligned} c_1^{(0)} &= \alpha, \\ c_2^{(0)} &= \beta/2. \end{aligned}\right\} \quad \text{(mixed)} \tag{7.19}$$

Similarly, boundary conditions evaluated at $s = s_N$,

$$\frac{\mathrm{d}\gamma^{(N-1)}}{\mathrm{d}s} = \frac{\mathrm{d}^3\gamma^{(N-1)}}{\mathrm{d}s^3} = 0, \qquad \text{(even)} \tag{7.20}$$

$$\gamma^{(N-1)} = \frac{\mathrm{d}^2\gamma^{(N-1)}}{\mathrm{d}s^2} = \frac{\mathrm{d}^4\gamma^{(N-1)}}{\mathrm{d}s^4} = 0, \qquad \text{(odd)} \tag{7.21}$$

$$\frac{\mathrm{d}\gamma^{(N-1)}}{\mathrm{d}s} = \alpha, \quad \frac{\mathrm{d}^2\gamma^{(N-1)}}{\mathrm{d}s^2} = \beta, \qquad \text{(mixed)} \tag{7.22}$$

yield another two linear equations for each type of boundary condition,

$$\left.\begin{aligned} c_1^{(N)} &= 0, \\ 4h_{N-1}c_1^{(N-1)} + h_{N-1}^2 c_2^{(N-1)} + 6h_{N-1}c_1^{(N)} - 3h_{N-1}^2 c_2^{(N)} &= 10(\chi_N - \chi_{N-1}), \end{aligned}\right\} \text{(even)} \tag{7.23}$$

$$\left.\begin{aligned} 7h_{N-1}c_1^{(N-1)} + 2h_{N-1}^2 c_2^{(N-1)} + 8h_{N-1}c_1^{(N)} - 3h_{N-1}^2 c_2^{(N)} &= 15(\chi_N - \chi_{N-1}), \\ c_2^{(N)} &= 0, \end{aligned}\right\} \text{(odd)} \tag{7.24}$$

$$\left.\begin{aligned} c_1^{(N)} &= \alpha, \\ c_2^{(N)} &= \beta/2. \end{aligned}\right\} \text{(mixed)} \tag{7.25}$$

Thus a combination of boundary conditions imposed at both ends of the spline interpolation would exactly produce four equations that are needed in order to uniquely determine all coefficients $\boldsymbol{c}_1^{(j)}$ and $\boldsymbol{c}_2^{(j)}$. For a planar curve describing a smooth axisymmetric object in (r, z)-plane (r is the cylindrical radius and z is the axial height), it must begin and end on the symmetry axis with an even condition imposed on its z-component and an odd condition on its r-component at both ends of the curve. On the other hand, for objects with geometric discontinuities, e.g., two boundary segments meeting at a sharp corner, mixed conditions can be employed to prescribe tangential direction and curvature independently for the two curves when approaching from each side of the corner. For computational reasons, if we lump the unknowns $\boldsymbol{c}_1^{(j)}$ and $\boldsymbol{c}_2^{(j)}$ into an one-dimensional array

$$\left[\boldsymbol{c}_1^{(0)}, \boldsymbol{c}_2^{(0)}, \dots, \boldsymbol{c}_1^{(j)}, \boldsymbol{c}_2^{(j)}, \dots, \boldsymbol{c}_1^{(N)}, \boldsymbol{c}_2^{(N)}\right]^\top, \tag{7.26}$$

then the equations in (7.13) complemented by one set of boundary conditions from (7.17)–(7.19) and one set from (7.23)–(7.25) yield a $2(N+1)$-by-$2(N+1)$ system of linear equations. Such system corresponds to a banded diagonal sparse matrix with at most 6 nonzero elements in each row which can be efficiently solved by direct methods such as Thomas algorithm (essentially backward substitution) or iterative methods for sparse matrix (Press et al., 2007). Other spline coefficients, $\boldsymbol{c}_3^{(j)}$, $\boldsymbol{c}_4^{(j)}$ and $\boldsymbol{c}_5^{(j)}$, can be reconstructed through equations (7.10)–(7.12).

For purpose of numerical integration, it is convenient to re-parametrize each local spline $\boldsymbol{\gamma}^{(j)}(s)$ with a local coordinate t of the canonical interval $[0, 1]$ so that

$$\boldsymbol{\gamma}^{(j)}(t) = \boldsymbol{\chi}_j + \sum_{k=1}^{5} \boldsymbol{c}_k^{(j)} t^k \quad \text{for} \quad j = 0, \dots, N-1 \tag{7.27}$$

with $\boldsymbol{c}_k^{(j)}$ redefined as $\boldsymbol{c}_k^{(j)} \to \boldsymbol{c}_k^{(j)} h_j^k$. The total arc-length $\mathfrak{s}^{(j)}$ and arc-length fraction $\xi^{(j)}$ of a local spline $\boldsymbol{\gamma}^{(j)}$ are given by the integrals,

$$\mathfrak{s}^{(j)} = \int_0^1 \|\dot{\boldsymbol{\gamma}}^{(j)}(t')\| \, \mathrm{d}t', \quad \xi^{(j)}(t) = \frac{1}{\mathfrak{s}^{(j)}} \int_0^t \|\dot{\boldsymbol{\gamma}}^{(j)}(t')\| \, \mathrm{d}t', \tag{7.28}$$

where the over-dot notation is used to represent the derivative of a function with respect to its variable. As we will see later, arc-length fraction $\xi^{(j)}$ is essential to the construction of the Lagrange interpolations along the global spline $\boldsymbol{\gamma}(s)$.

The conventions for unit tangent $\boldsymbol{s}$ and unit normal $\boldsymbol{n}$ are chosen such that $\boldsymbol{n}$ equals $\boldsymbol{s}$ rotated 90° counterclockwise,

$$\boldsymbol{s} = \frac{1}{\|\dot{\boldsymbol{\gamma}}\|}\begin{bmatrix}\dot{r}\\ \dot{z}\end{bmatrix}, \quad \boldsymbol{n} = \frac{1}{\|\dot{\boldsymbol{\gamma}}\|}\begin{bmatrix}-\dot{z}\\ \dot{r}\end{bmatrix}. \tag{7.29}$$

If explicit parametrization for each component of an axisymmetric curve $\boldsymbol{\gamma}$ (e.g., a global quintic spline) is known, then total curvature $2\hbar$ of the surface of revolution obtained by rotating curve $\boldsymbol{\gamma}$ about z-axis has the analytic expression

$$2\hbar = \frac{\dot{r}\ddot{z} - \dot{z}\ddot{r}}{(\dot{r}^2 + \dot{z}^2)^{3/2}} + \frac{1}{r}\frac{\dot{z}}{\sqrt{\dot{r}^2 + \dot{z}^2}}, \tag{7.30}$$

where $\hbar \to \ddot{z}/\dot{r}^2$ as $r \to 0$ approaches the symmetry axis, provided the revolving surface is smooth at $r = 0$.

Lastly we remark that, if $\boldsymbol{\gamma}(s)$ were instead a cubic spline, derivative of the mean curvature $\hbar$ would necessarily be discontinuous. Recall from the self-similar theory of dynamic cone formation that mean curvature $\hbar$ is supplied as a boundary condition on the liquid/vacuum interface γ for the velocity potential. The use of cubic splines, which are usually employed in commercial software and libraries, would inevitably degrade rate of convergence.

Gaussian quadrature rule of logarithmic-singular integrals

We briefly review the process of computing quadrature rules for arbitrary weight functions. A Gaussian quadrature rule approximates the definite integral of a function by a weighted sum of function values evaluated at specified points, termed quadrature abassica, within the domain of integration. The quadrature abassica t_k are the roots of polynomials that belong to a class of orthogonal polynomials with respect to a weighted inner product

$$\langle f, g\rangle = \int_0^1 f(t)g(t)w(t)\,\mathrm{d}t \tag{7.31}$$

over the canonical interval $[0, 1]$ with $w(t)$ being the weight function. A set of orthogonal polynomials p_n with respect to the weight $w(t)$ can be bootstrapped from a three-term recurrence relation (Golub and Welsch, 1969)

$$p_{n+1}(t) = \left(t - \frac{\langle t\,p_n, p_n\rangle}{\langle p_n, p_n\rangle}\right)p_n(t) - \underbrace{\frac{\langle t\,p_n, p_{n-1}\rangle}{\langle p_{n-1}, p_{n-1}\rangle}}_{=0 \text{ if } n=0} p_{n-1}(t), \tag{7.32}$$

where the first two polynomials are given by

$$p_{-1}(t) = 0, \quad p_0(t) = 1. \tag{7.33}$$

Abscissae $\mathfrak{t}_k$ of a m-point Gaussian quadrature rule are the roots of the m-th orthogonal polynomial $p_m(t)$ with the corresponding quadrature weights $\mathfrak{w}_k$ given by the integral

$$\mathfrak{w}_k = \frac{1}{\mathrm{d}p_m/\mathrm{d}t|_{t=t_k}} \int_0^1 \frac{p_m(t)}{t - t_k}\,\mathrm{d}t. \tag{7.34}$$

The standard m-point Gauss-Legendre quadrature rule is derived by setting weight $w(t) = 1$ in the inner product (7.31), in which case a regular integral over interval $[0, 1]$ (or more generally $[a, b]$) can be approximated by a discrete summation,

$$\int_a^b f(t)\,\mathrm{d}t \approx \sum_{k=1}^{m} (b-a)\mathfrak{w} f(a + (b-a)\mathfrak{t}_k). \tag{7.35}$$

In the same vein, logarithmic-weighted Gaussian quadrature rules can be derived by selecting weight function $w(t) = -\log(t)$,

$$\left.\begin{aligned} \int_0^1 f(t)\ln t\,\mathrm{d}t &\approx -\sum_{k=1}^{m} \mathfrak{w}_k^{\log} f(\mathfrak{t}_k^{\log}), \\ \int_0^1 f(t)\ln(1-t)\,\mathrm{d}t &\approx -\sum_{k=1}^{m} \mathfrak{w}_k^{\log} f(1-\mathfrak{t}_k^{\log}), \end{aligned}\right\} \tag{7.36}$$

where $\mathfrak{t}_k^{\log}$ and $\mathfrak{w}_k^{\log}$ are the abscissae and weights for a m-point logarithmic-weighted quadrature rule. The symbolic package MATHEMATICA (Wolfram Research, 2019) allows us to compute the abscissae and weights for logarithmic-weighted Gaussian quadrature rules up to an arbitrarily high precision, the first twenty of which are tabulated in table 7.1 and table 7.2.

When integrating functions against alternative logarithmic weights such as $\ln|t - t_*|$ with $t_* \in (0, 1)$ being an interior logarithmic singularity in the canonical interval, we split the integral into a left and a right part separated by the interior singularity t_*,

$$\begin{aligned} \int_0^1 f(t)\ln|t-t_*|\,\mathrm{d}t = t_* \int_0^1 f(t_* t')\ln(1-t')\,\mathrm{d}t' + \bar{t}_* \int_0^1 f(t_* + \bar{t}_* t')\ln t'\,\mathrm{d}t' \\ + t_* \ln t_* \int_0^1 f(t_* t')\,\mathrm{d}t' + \bar{t}_* \ln \bar{t}_* \int_0^1 f(t_* + \bar{t}_* t')\,\mathrm{d}t', \end{aligned} \tag{7.37}$$

where $\bar{t}_* = 1 - t_*$. Applying the Gauss-Legendre and logarithmic-weighted Gaussian quadrature rules derived earlier to the two regular and two logarithmic-singular integrals in (7.37) immediately leads to the quadrature rule when an interior logarithmic singularity $t_* \in (0, 1)$ is present,

$$\begin{aligned} \int_0^1 f(t)\ln|t-t_*|\,\mathrm{d}t \approx t_* \ln t_* \sum_{k=1}^{m} \mathfrak{w}_k f\left[t_* \mathfrak{t}_k\right] + \bar{t}_* \ln \bar{t}_* \sum_{k=1}^{m} \mathfrak{w}_k f\left[t_* + \bar{t}_* \mathfrak{t}_k\right] \\ - t_* \sum_{k=1}^{m} \mathfrak{w}_k^{\log} f\left[t_*(1 - \mathfrak{t}_k^{\log})\right] - \bar{t}_* \sum_{k=1}^{m} \mathfrak{w}_k^{\log} f\left[t_* + \bar{t}_* \mathfrak{t}_k^{\log}\right]. \end{aligned} \tag{7.38}$$

Abscissa $\mathfrak{t}_k$	Weight $\mathfrak{w}_k$
1-point	
2.50000000000000E-1	1.00000000000000
2-point	
1.12008806166976E-1	7.18539319030384E-1
6.02276908118738E-1	2.81460680969616E-1
3-point	
6.38907930873254E-2	5.13404552232363E-1
3.68997063715619E-1	3.91980041201488E-1
7.66880303938941E-1	9.46154065661491E-2
4-point	
4.14484801993832E-2	3.83464068145135E-1
2.45274914320602E-1	3.86875317774763E-1
5.56165453560276E-1	1.90435126950142E-1
8.48982394532985E-1	3.92254871299598E-2
5-point	
2.91344721519721E-2	2.97893471782894E-1
1.73977213320898E-1	3.49776226513224E-1
4.11702520284902E-1	2.34488290044052E-1
6.77314174582820E-1	9.89304595166331E-2
8.94771361031008E-1	1.89115521431958E-2
6-point	
2.16340058441169E-2	2.38763662578548E-1
1.29583391154951E-1	3.08286573273947E-1
3.14020449914766E-1	2.45317426563210E-1
5.38657217351802E-1	1.42008756566477E-1
7.56915337377403E-1	5.54546223248863E-2
9.22668851372120E-1	1.01689586929323E-2
7-point	
1.67193554082585E-2	1.96169389425248E-1
1.00185677915675E-1	2.70302644247273E-1
2.46294246207931E-1	2.39681873007691E-1
4.33463493257033E-1	1.65775774810433E-1
6.32350988047766E-1	8.89432271376580E-2
8.11118626740106E-1	3.31943043565711E-2
9.40848166743348E-1	5.93278701512592E-3
8-point	
1.33202441608925E-2	1.64416604728003E-1
7.97504290138949E-2	2.37525610023306E-1
1.97871029326188E-1	2.26841984431919E-1
3.54153994351909E-1	1.75754079006070E-1
5.29458575234917E-1	1.12924030246759E-1
7.01814529939100E-1	5.78722107177821E-2
8.49379320441107E-1	2.09790737421330E-2
9.53326450056360E-1	3.68640710402762E-3
9-point	
1.08693360841755E-2	1.40068438748135E-1
6.49836663380079E-2	2.09772205201030E-1
1.62229398023883E-1	2.11427149896603E-1
2.93749903971675E-1	1.77156233938080E-1
4.46631881905468E-1	1.27799228033205E-1
6.05481662776129E-1	7.84789026115622E-2
7.54110137157164E-1	3.90225049853991E-2
8.77265828835838E-1	1.38672955495930E-2
9.62250559410282E-1	2.40804103639231E-3
10-point	
9.04263096219965E-3	1.20955131954571E-1
5.39712662225006E-2	1.86363542564072E-1
1.35311824639251E-1	1.95660873277760E-1
2.47052416287160E-1	1.73577142182907E-1
3.80212539609332E-1	1.35695672995484E-1
5.23792317971843E-1	9.36467585381105E-2
6.65775205516425E-1	5.57877273514159E-2
7.94190416011966E-1	2.71598108992333E-2
8.98161091219004E-1	9.51518260284851E-3
9.68847988718634E-1	1.63815763359826E-3

Abscissa $\mathfrak{t}_k$	Weight $\mathfrak{w}_k$
11-point	
7.64394117463771E-3	1.05652256099100E-1
4.55418282565789E-2	1.66571680600629E-1
1.14522297455125E-1	1.80563218287754E-1
2.10378581227034E-1	1.67278736773784E-1
3.26695553221693E-1	1.38697057401631E-1
4.55453246928813E-1	1.03833433365044E-1
5.87648356359084E-1	6.95366978887352E-2
7.13963850012561E-1	4.05416008035963E-2
8.25453217801812E-1	1.94354024762182E-2
9.14193921612543E-1	6.73742934245006E-3
9.73860256275586E-1	1.15248696105748E-3
12-point	
6.54872227908006E-3	9.31926914439313E-2
3.89468095604500E-2	1.49751827576322E-1
9.81502631060066E-2	1.66557454364593E-1
1.81138581590632E-1	1.59633559436988E-1
2.83220067667373E-1	1.38424831864836E-1
3.98434435163437E-1	1.10016570635721E-1
5.19952626792353E-1	7.99618217708290E-2
6.40510916716106E-1	5.24069548246418E-2
7.52865012051831E-1	3.00710888737612E-2
8.50240024162302E-1	1.42492455879983E-2
9.26749683223914E-1	4.89992458232176E-3
9.77756129689997E-1	8.34029038056903E-4
13-point	
5.67476625624267E-3	8.29004967932758E-2
3.36901087990325E-2	1.35368673165745E-1
8.50367544741750E-2	1.53773284392292E-1
1.57497559477889E-1	1.51458158509988E-1
2.47569578876843E-1	1.36040336537283E-1
3.50744312360855E-1	1.13176822881634E-1
4.61773746761610E-1	8.73744304800453E-2
5.74959466525561E-1	6.21602306418049E-2
6.84459880350430E-1	4.00877289341659E-2
7.84602568810347E-1	2.27238449399722E-2
8.70186428407888E-1	1.06712304129684E-2
9.36757829306751E-1	3.64649227597414E-3
9.80843451811591E-1	6.18270034851697E-4
14-point	
4.96600357386854E-3	7.42912250675104E-2
2.94325401188852E-2	1.22988772469323E-1
7.43762922245358E-2	1.42199306562523E-1
1.38138491989186E-1	1.43229297641264E-1
2.18055648498959E-1	1.32345083772085E-1
3.10662083918102E-1	1.14135875736676E-1
4.11872475177750E-1	9.22830380790736E-2
5.17179307398654E-1	6.97536732939376E-2
6.21864859728511E-1	4.88303236005136E-2
7.21220745208109E-1	3.11017960644161E-2
8.10765988071590E-1	1.74628119501961E-2
8.86454038034435E-1	8.14242342987594E-3
9.44859139461819E-1	2.76843641856394E-3
9.83331026485678E-1	4.67935914040560E-4
15-point	
4.38311017547540E-3	6.70099789164937E-2
2.59358981053306E-2	1.12264150286706E-1
6.55960954123162E-2	1.31760177039680E-1
1.22101934073332E-1	1.35217649061935E-1
1.93395262374007E-1	1.27881798645680E-1
2.76772838706102E-1	1.13532907490219E-1
3.69015127139743E-1	9.52052397843587E-2
4.66524328964707E-1	7.53893141673960E-2
5.65473473791817E-1	5.60784244926537E-2
6.61962919012456E-1	3.87682953750182E-2
7.52178883378786E-1	2.44514832687501E-2
8.32548033866190E-1	1.36246301382388E-2
8.99882050120898E-1	6.31644759859076E-3
9.51506188743410E-1	2.13888991594447E-3
9.85364468122132E-1	3.60613818335407E-4

Table 7.1: Abscissae and weights for 1- to 10-point (left panel) and 11- to 15-point (right panel) logarithmic-weighted Gaussian quadrature rules

Abscissa $\mathfrak{t}_k$	Weight $\mathfrak{w}_k$
16-point	
3.89783448711592E-3	6.07917100435912E-2
2.30289456168732E-2	1.02915677517582E-1
5.82803983062404E-2	1.22355662046009E-1
1.08678365091054E-1	1.27569246937016E-1
1.72609454909844E-1	1.23013574600071E-1
2.47937054470578E-1	1.11847244855486E-1
3.32094549129917E-1	9.65963851521243E-2
4.22183910581949E-1	7.93566643514731E-2
5.15082473381463E-1	6.18504945819652E-2
6.07556120447729E-1	4.54352465077267E-2
6.96375653228214E-1	3.10989747515818E-2
7.78432565873265E-1	1.94597659273608E-2
8.50850269715391E-1	1.07762549632055E-2
9.11086857222272E-1	4.97254289008764E-3
9.57025571703542E-1	1.67820111005119E-3
9.87047800247984E-1	2.82353764668436E-4
17-point	
3.48944942809365E-3	5.54350690606789E-2
2.05860406877611E-2	9.47187691894761E-2
5.21217916297223E-2	1.13880141162429E-1
9.73354259275744E-2	1.20355013998229E-1
1.54945857983249E-1	1.17980764446305E-1
2.23243954205450E-1	1.09431257929842E-1
3.00161598873464E-1	9.68312916837090E-2
3.83343519530540E-1	8.19531082099494E-2
4.70225073199601E-1	6.62795971230357E-2
5.58115277026492E-1	5.10192843604564E-2
6.44283151731502E-1	3.71053713203179E-2
7.26044960838813E-1	2.51931143920290E-2
8.00849737279702E-1	1.56624561420511E-2
8.66360460578840E-1	8.62924747911945E-3
9.20528319303556E-1	3.96638761660894E-3
9.61657532071674E-1	1.33491824730003E-3
9.88456918847435E-1	2.24207638462937E-4
18-point	
3.14246513800145E-3	5.07847569150232E-2
1.85133122080843E-2	8.74918217698710E-2
4.68891829953568E-2	1.06231987072427E-1
8.76681791779751E-2	1.13600962803119E-1
1.39821274385391E-1	1.12940421014858E-1
2.01966306570199E-1	1.06540929054561E-1
2.72420255500711E-1	9.62078032569690E-2
3.49252538662625E-1	8.34492524143092E-2
4.30342588559143E-1	6.95422794922013E-2
5.13441600439316E-1	5.55525077526928E-2
5.96237308519533E-1	4.23366797199512E-2
6.76420232632214E-1	3.05405451343943E-2
7.51749655041838E-1	2.05983704127194E-2
8.20117526905824E-1	1.27372513543855E-2
8.79608522893184E-1	6.98775937952583E-3
9.28554528829897E-1	3.20143571140962E-3
9.65581851992832E-1	1.07495526563557E-3
9.89648238497166E-1	1.80281475947801E-4

Abscissa $\mathfrak{t}_k$	Weight $\mathfrak{w}_k$
19-point	
2.84511472758003E-3	4.67193525156959E-2
1.67394868602341E-2	8.10871117350897E-2
4.24062333121213E-2	9.93176888151342E-2
7.93646495242485E-2	1.07306686287853E-1
1.26779524713245E-1	1.07993224036674E-1
1.83521965374816E-1	1.03360703222194E-1
2.48209751538999E-1	9.49578478153139E-2
3.19247560858021E-1	8.40770856575388E-2
3.94870226085803E-1	7.18209287678724E-2
4.73189256050998E-1	5.91249841059563E-2
5.52241966862257E-1	4.67634017963781E-2
6.30042214445635E-1	3.53481401173877E-2
7.04631556024242E-1	2.53276486089719E-2
7.74129598714736E-1	1.69879052239090E-2
8.36782282905287E-1	1.04573449694563E-2
8.91006879458074E-1	5.71638941331142E-3
9.35432532472656E-1	2.61174087234964E-3
9.68935159159729E-1	8.75215444108251E-4
9.90664392788623E-1	1.46600594806024E-4
20-point	
2.58832795592196E-3	4.31427521332081E-2
1.52096623495602E-2	7.53837099085894E-2
3.85365503721653E-2	9.30532674516631E-2
7.21816138158739E-2	1.01456711849830E-1
1.15460526487633E-1	1.03201762056072E-1
1.67442856275330E-1	1.00022549805273E-1
2.26983787260203E-1	9.32597993002977E-2
2.92754960941546E-1	8.40289528719411E-2
3.63277429857859E-1	7.32855891300307E-2
4.36957140090768E-1	6.18503369137303E-2
5.12122594678967E-1	5.04166044383747E-2
5.87064044914410E-1	3.95513700052984E-2
6.60073413314909E-1	2.96940778958128E-2
7.29484083929687E-1	2.11563153554271E-2
7.93709671987086E-1	1.41237329389640E-2
8.51280892789126E-1	8.66097450433550E-3
9.00879680854418E-1	4.71994014620360E-3
9.41369749129092E-1	2.15139740396521E-3
9.71822741075263E-1	7.19728214653203E-4
9.91538081438712E-1	1.20427676330217E-4

Table 7.2: Abscissae and weights for 16- to 18-point (left panel) and 19- to 20-point (right panel) logarithmic-weighted Gaussian quadrature rules

The quadrature rule (7.38) reduces to formula (7.36) for $t_* = 0$. The logarithmic-weighted Gaussian quadrature rules are indispensable to numerical evaluation of the convolutional boundary integrals of the two-dimensional Green's function. A m-point logarithmic-weighted Gaussian quadrature rule converges much faster than a m-point Gauss-Legendre quadrature rule when a logarithmic singularity is present in the integrand or hidden in its higher order derivatives.

Chebyshev approximations of complete elliptic integrals

The complete elliptic integral of the first and the second kind (Abramowitz and Stegun, 1965), designated as $K(m)$ and $E(m)$, frequently appear in the analytic expressions of the Green's function for the axisymmetric Laplace operator and its partial derivatives. The integral forms of $K(m)$ and $E(m)$ are given by

$$K(m) = \int_0^{\pi/2} \frac{\mathrm{d}\theta}{\sqrt{1 - m\sin^2\theta}}, \quad E(m) = \int_0^{\pi/2} \sqrt{1 - m\sin^2\theta}\,\mathrm{d}\theta. \tag{7.39}$$

It's well known that the complete elliptic integral of the first kind $K(m)$ has a logarithmic singularity $\sim \ln(1-m)$ at $m = 1$. Here we present an elementary proof. Consider the following two integrals,

$$\begin{aligned} K(m) &= \int_0^{\pi/2} \frac{\mathrm{d}\theta}{\sqrt{1 - m\sin^2\theta}} = \int_0^{\pi/2} \frac{\mathrm{d}\theta'}{\sqrt{1 - m\cos^2\theta'}} && \theta' = \frac{\pi}{2} - \theta \\ &= \int_{\pi/4}^{\pi/2} \frac{\mathrm{d}\theta'}{\sqrt{1 - m\cos^2\theta'}} + \int_0^{\pi/4} \frac{\mathrm{d}\theta'}{\sqrt{1 - m\cos^2\theta'}}, && (7.40) \\ \int_0^{\pi/4} \frac{\mathrm{d}\theta'}{\sqrt{1 - m\cos^2\theta'}} &= \int_0^{\pi/4} \frac{(\cos^2\theta' + \sin^2\theta')\,\mathrm{d}\theta'}{\sqrt{\cos^2\theta' + \sin^2\theta'}\sqrt{\sin^2\theta' + \delta^2\cos^2\theta'}} && \delta = \sqrt{1-m} \\ &= \int_0^{\pi/4} \frac{1 + \tan^2\theta'}{\sqrt{1 + \tan^2\theta'}\sqrt{\delta^2 + \tan^2\theta'}}\,\mathrm{d}\theta' \\ &= \int_0^1 \frac{\mathrm{d}x}{\sqrt{1 + x^2}\sqrt{\delta^2 + x^2}} && x = \tan\theta' \\ &= \int_0^1 \frac{\mathrm{d}x}{\sqrt{\delta^2 + x^2}} - \int_0^1 \left(1 - \frac{1}{\sqrt{1 + x^2}}\right) \frac{\mathrm{d}x}{\sqrt{\delta^2 + x^2}}. && (7.41) \end{aligned}$$

In the limit $m \to 1$, the integrals from (7.40) and (7.41) in $K(m)$ that remain bounded eventually drop out to finite values since

$$\begin{aligned} \lim_{m\to 1} K(m) = {} & \overbrace{\lim_{m\to 1} \int_{\pi/4}^{\pi/2} \frac{\mathrm{d}\theta'}{\sqrt{1 - m\cos^2\theta'}}}^{\text{finite}} \\ & + \lim_{\delta\to 0} \int_0^1 \frac{\mathrm{d}x}{\sqrt{\delta^2 + x^2}} - \underbrace{\lim_{\delta\to 0} \int_0^1 \frac{x^2}{1 + x^2 + \sqrt{1 + x^2}} \frac{\mathrm{d}x}{\sqrt{\delta^2 + x^2}}}_{\text{finite}} \\ = {} & \lim_{\delta\to 0} \arctan\frac{1}{\sqrt{1 + \delta^2}} = \lim_{\delta\to 0} \left[\ln\frac{2}{\delta} + O(\delta^2)\right] = \lim_{m\to 1} -\frac{1}{2}\ln(1-m), \end{aligned} \tag{7.42}$$

i	K_P^i	K_Q^i
0	1.3862943611989062502E0	4.9999999999999999821E-1
1	9.6573590281169012653 5E-2	1.2499999999870820058E-1
2	3.0885146524671199599 8E-2	7.0312499696395746973 9E-2
3	1.4938044891680525271 8E-2	4.8828034757099823923 2E-2
4	8.7907827395274377225 4E-3	3.7377431417382322896 9E-2
5	6.1890103363768761322 9E-3	3.0120471522760404698 8E-2
6	6.8748968744994987792 5E-3	2.3908960271592489272 7E-2
7	9.8582137902122600871 4E-3	1.5485051664976239933 5E-2
8	7.9740401322041517936 7E-3	5.9405830375316779325 7E-3
9	2.2802572400587556738 5E-3	9.1418472386591722657 1E-4
10	1.3798286460627323715 0E-4	2.9407895504859850751 1E-5

i	E_P^i	E_Q^i
0	1.0000000000000000299E0	0.0
1	4.4314718056099085061 8E-1	2.4999999999888314361E-1
2	5.6805194561786055347 0E-2	9.3749999719764427844 5E-2
3	2.1831799601555725310 3E-2	5.8593663447110105564 2E-2
4	1.1568843681057412731 9E-2	4.2718092651893151171 7E-2
5	7.5839528941351470851 9E-3	3.3483390488822491861 4E-2
6	7.7739549251678709295 1E-3	2.6176974245449365958 3E-2
7	1.0735094905607619340 3E-2	1.6886216399331131730 0E-2
8	8.6878681656588962842 9E-3	6.5060948997692749143 3E-3
9	2.5088849216360206099 0E-3	1.0096279267935671513 3E-3
10	1.5355257730101329336 5E-4	3.2795489857648587265 6E-5

Table 7.3: Coefficients K_P^i, K_Q^i, E_P^i and E_Q^i for Chebyshev approximations (7.44) of the complete elliptic integrals $K(m)$ and $E(m)$

which reveals the logarithmic singularity of $K(m)$ at $m = 1$. To effectively capture the weakly singular behavior of the complete elliptic integrals, Cody (1965) devised logarithmic-weighted Chebyshev approximations of $K(m)$ and $E(m)$ with numerical errors down to machine size $\sim O(10^{-16})$. These approximations share a general polynomial form multiplied by a logarithm function,

$$K(m) \approx K_P(m) - \ln(1-m)K_Q(m), \quad E(m) \approx E_P(m) - \ln(1-m)E_Q(m), \tag{7.43}$$

where K_P, E_P, K_Q, and E_Q are tenth degree polynomials,

$$K_{P(Q)}(m) = \sum_{i=0}^{10} K_{P(Q)}^i (1-m)^i, \quad E_{P(Q)}(m) = \sum_{i=0}^{10} E_{P(Q)}^i (1-m)^i. \tag{7.44}$$

Polynomial coefficients K_P^i, K_Q^i, E_P^i and E_Q^i are listed in table 7.3.

An immediate application of Chebyshev approximation (7.44) is the high precision evaluation of the $1/2$-family of associate Legendre polynomials, which are essential to the far-field asymptotic expansions of the velocity and electric potentials in the self-similar

ℓ	c_ℓ	$P_E^\ell(x)$	$P_K^\ell(x)$
$\frac{1}{2}$	$\frac{2}{\pi}$	2	-1
$\frac{3}{2}$	$\frac{1}{3\pi}$	$16x$	$-2(4x+1)$
$\frac{5}{2}$	$\frac{1}{15\pi}$	$4\left(32x^2-9\right)$	$-2\left(32x^2+8x-9\right)$
$\frac{7}{2}$	$\frac{1}{105\pi}$	$64x\left(24x^2-13\right)$	$2\left(-384x^3-96x^2+208x+25\right)$
$\frac{9}{2}$	$\frac{1}{315\pi}$	$8192x^4-6528x^2+588$	$-2\left(2048x^4+512x^3-1632x^2-264x+147\right)$

Table 7.4: Constants c_ℓ and polynomials $P_K^\ell(x)$ and $P_E^\ell(x)$ in the analytic expression (7.48) of the $1/2$-family of associate Legendre polynomials up to degree $\ell = 9/2$.

theory of dynamic cone formation developed in Section 6.4. Y. Zhou (2013) showed that the associate Legendre polynomial of $1/2$-order

$$P_{1/2}(x) = \frac{2}{\pi}\left[2E\left(\frac{1-x}{2}\right) - K\left(\frac{1-x}{2}\right)\right] \tag{7.45}$$

is directly related to complete elliptic integrals of the first and the second kind. Recall from the recurrence relation for associate Legendre polynomials of order ℓ (not necessarily interger),

$$(1+x^2)\frac{\mathrm{d}P_\ell(x)}{\mathrm{d}x} = (\ell+1)xP_\ell(x) - (\ell+1)P_{\ell+1}(x), \tag{7.46}$$

and the recurrence relations for the complete elliptic integrals,

$$\frac{\mathrm{d}K}{\mathrm{d}m} = \frac{E(m)}{2m(1-m)} - \frac{K(m)}{2m}, \quad \frac{\mathrm{d}E}{\mathrm{d}m} = \frac{E(m)-K(m)}{2m}, \tag{7.47}$$

we can symbolically bootstrap higher order members $P_\ell(x)$ of the entire $1/2$-family where

$$P_\ell(x) = c_\ell\left[P_E^\ell(x)E\left(\frac{1-x}{2}\right) + P_K^\ell(x)K\left(\frac{1-x}{2}\right)\right] \quad \text{for} \quad \ell = \frac{1}{2}, \frac{3}{2}, \ldots . \tag{7.48}$$

Coefficient constants c_ℓ and $(\ell-1/2)$-th degree polynomials, $P_K^\ell(x)$ and $P_E^\ell(x)$, are listed in table 7.4.

7.3 Discretization of Axisymmetric Boundary Integral Equation

In this section, we present the numerical algorithm for solving free-space Laplace equation in axisymmetric domains. Discretization and numerical integration of the boundary integral equation are treated properly with approximation techniques developed in the last section. In what follows, we restrict all variables (e.g., $\boldsymbol{\chi}$ and $\boldsymbol{\chi}'$) and operators (e.g., ∇ and ∇^2) to an axisymmetric plane parametrized either by spherical coordinates (r_s, θ) or cylindrical coordinates (r, z).

Boundary integral formulation

Let $\boldsymbol{\chi}'$ be a field point interior to the closed, simply connected region ω enclosed by the boundary γ and $\boldsymbol{\chi}$ be a source point on the boundary. The axisymmetric Green's function $g(\boldsymbol{\chi}';\boldsymbol{\chi})$ is the fundamental solution to the Poisson's equation

$$\nabla^2 g(\boldsymbol{\chi}';\boldsymbol{\chi}) = -\delta(\boldsymbol{\chi}',\boldsymbol{\chi}), \tag{7.49}$$

where $\delta(\boldsymbol{\chi}',\boldsymbol{\chi})$ is the axisymmetric Dirac delta function. Physically, $g(\boldsymbol{\chi}';\boldsymbol{\chi})$ is interpreted as the intensity of a harmonic field at field point $\boldsymbol{\chi}'$ due to a point (ring) source positioned at the source point $\boldsymbol{\chi}$. Analytic solution to the Poisson's equation (7.49) can be derived by integrating out azimuthal dependence in the full three-dimensional Green's function (Lennon, P. L.-F. Liu, and Liggett, 1979). In cylindrical coordinates $\boldsymbol{\chi} = (r, z)$, the expressions for $g(\boldsymbol{\chi}';\boldsymbol{\chi})$ and its directional derivative along vector $\boldsymbol{v} = (v_r, v_z)$, designated as $\partial g/\partial \boldsymbol{v} \equiv \boldsymbol{v}\cdot\nabla g$, are given by

$$g(\boldsymbol{\chi}';\boldsymbol{\chi}) = \frac{1}{\pi\sqrt{a+b}}K(m), \tag{7.50}$$

$$\frac{\partial g(\boldsymbol{\chi}';\boldsymbol{\chi})}{\partial \boldsymbol{v}} = \frac{1}{\pi\sqrt{a+b}}\left\{\left[\frac{v_r}{2r} + \frac{\boldsymbol{v}\cdot(\boldsymbol{\chi}'-\boldsymbol{\chi})}{\|\boldsymbol{\chi}'-\boldsymbol{\chi}\|^2}\right]E(m) - \frac{v_r}{2r}K(m)\right\}, \tag{7.51}$$

where $K(m)$ and $E(m)$ are the elliptic integrals (7.39) of the first and the second kind with auxiliary variables defined as

$$a = r'^2 + r^2 + (z'-z)^2, \quad b = 2r'r, \quad m = \frac{2b}{a+b}. \tag{7.52}$$

Note $\boldsymbol{\chi} \to \boldsymbol{\chi}'$ implies $m \to 1$ which precludes a logarithmic blow-up of the Green's function (recall from (7.43) that elliptic integral $E(m) \sim \ln(1-m)$ as $m \to 1$). Numerical integration across over logarithmic-singularities is the main source of difficulties in solving various kinds of boundary integral equation.

For notational convenience, let $\varphi(\boldsymbol{\chi}\in\gamma) \equiv \phi(\boldsymbol{\chi}\in\gamma)$ and $q(\boldsymbol{\chi}\in\gamma) \equiv \partial\phi(\boldsymbol{\chi}\in\gamma)/\partial\boldsymbol{n}$ be two boundary functions which coincide with the potential and flux evaluated on the boundary γ, respectively. If potential $\varphi(\boldsymbol{\chi})$ and flux $q(\boldsymbol{\chi})$ are known on the boundary, then Green's third identity allows us to compute field strength $\phi(\boldsymbol{\chi}')$ at an interior field point $\boldsymbol{\chi}'$ through an axisymmetric boundary integral (Jackson, 1999)

$$\int_\gamma \left\{g(\boldsymbol{\chi}';\boldsymbol{\chi})q(\boldsymbol{\chi}) - \varphi(\boldsymbol{\chi})\frac{\partial g(\boldsymbol{\chi}';\boldsymbol{\chi})}{\partial \boldsymbol{n}}\right\} r\,\mathrm{d}\gamma(\boldsymbol{\chi}) = \phi(\boldsymbol{\chi}') \quad \text{for} \quad \boldsymbol{\chi}' \text{ in } \omega. \tag{7.53}$$

Note the Green's third identity (7.53) doesn't apply if field point $\boldsymbol{\chi}\in\gamma$ is placed on the boundary γ. The actual solutions to the boundary potential $\varphi(\boldsymbol{\chi})$ and flux $q(\boldsymbol{\chi})$ correspond to the limit when the interior field point $\boldsymbol{\chi}'$ moves infinitesimally close to a point $\boldsymbol{\chi}$ on the boundary. Careful examination of such limit shows that boundary potential φ and flux q must satisfy an axisymmetric boundary integral equation posed

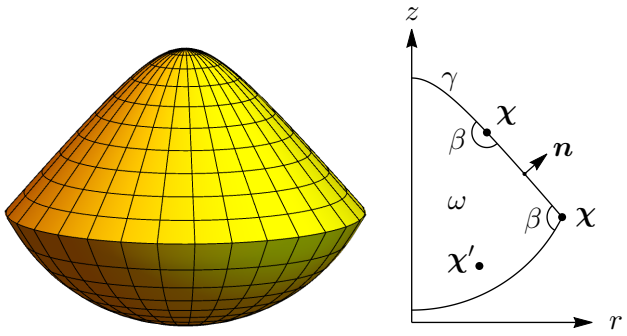

Figure 7.1: A surface of revolution (left) projected to an axisymmetric plane(right): $\boldsymbol{\chi}'$ is an interior field point, $\boldsymbol{\chi}$ is a source point on boundary γ (solid line), β is the interior angle at different boundary source points $\boldsymbol{\chi}$ and $\boldsymbol{n}$ is the boundary normal vector pointing from interior volume ω to exterior.

on γ (Wrobel, 2002),

$$\int_\gamma \left\{ g(\boldsymbol{\chi}';\boldsymbol{\chi}) q(\boldsymbol{\chi}) - \frac{\partial g(\boldsymbol{\chi}';\boldsymbol{\chi})}{\partial \boldsymbol{n}} \varphi(\boldsymbol{\chi}) \right\} r \, \mathrm{d}\gamma(\boldsymbol{\chi}) = \frac{\beta(\boldsymbol{\chi}')}{2\pi} \varphi(\boldsymbol{\chi}') \quad \text{for} \quad \boldsymbol{\chi}' \text{ on } \gamma, \quad (7.54)$$

where β is the interior angle at field point $\boldsymbol{\chi}'$ (see figure 7.1).

In many practical applications, the domain boundary γ is often divided into different segments so that either $\phi(\boldsymbol{\chi})$ or $\partial\phi/\partial\boldsymbol{n}$ is prescribed (but not both) on each portion of the boundary. The Dirichlet boundary condition refers to prescription of potential $\varphi(\boldsymbol{\chi})$ on a boundary segment and Neumann boundary condition means flux $q(\boldsymbol{\chi})$ is supplied instead. The mixed boundary condition, which is the type that we will use to compute to the self-similar solutions of dynamic cone formation, corresponds to the situation where instead of prescribing a single type of condition for the entire boundary, The Dirichlet condition is partially imposed on some boundary segments while the Neumann condition on the rest.

One of the major advantages of boundary integral method over other numerical techniques such as finite element and finite difference methods is the ability to recover field values of the harmonic potential and its higher order derivatives at arbitrary interior field points without being limited to the resolution of interior meshes. In practice, many physical observables of interest, e.g., velocity and electric fields, are not the field potential but rather the field gradient. Once the boundary potential $\varphi(\boldsymbol{\chi})$ and flux $q(\boldsymbol{\chi})$ are computed, we can readily evaluate field gradient at an arbitrary interior point $\boldsymbol{\chi}'$ in terms of boundary integrals by differentiating Green's identity (7.53) with respect to the field position $\boldsymbol{\chi}'$ as long as $\boldsymbol{\chi}'$ is strictly interior to the domain. In cylindrical

coordinates, the integral representations of $\partial\phi(\boldsymbol{\chi}')/\partial r'$ and $\partial\phi(\boldsymbol{\chi}')/\partial z'$ are given by

$$\left.\begin{aligned}\int_\gamma \left\{\frac{\partial g(\boldsymbol{\chi}';\boldsymbol{\chi})}{\partial r'}q(\boldsymbol{\chi}) - \frac{\partial^2 g(\boldsymbol{\chi}';\boldsymbol{\chi})}{\partial r'\partial \boldsymbol{n}}\varphi(\boldsymbol{\chi})\right\} r\,\mathrm{d}\gamma(\boldsymbol{\chi}) &= \frac{\partial\phi(\boldsymbol{\chi}')}{\partial r'},\\ \int_\gamma \left\{\frac{\partial g(\boldsymbol{\chi}';\boldsymbol{\chi})}{\partial z'}q(\boldsymbol{\chi}) - \frac{\partial^2 g(\boldsymbol{\chi}';\boldsymbol{\chi})}{\partial z'\partial \boldsymbol{n}}\varphi(\boldsymbol{\chi})\right\} r\,\mathrm{d}\gamma(\boldsymbol{\chi}) &= \frac{\partial\phi(\boldsymbol{\chi}')}{\partial z'},\end{aligned}\right\} \quad \text{for} \quad \boldsymbol{\chi}' \text{ in } \omega \tag{7.55}$$

where $\partial g(\boldsymbol{\chi}';\boldsymbol{\chi})/\partial r'$ and $\partial g(\boldsymbol{\chi}';\boldsymbol{\chi})/\partial z'$ can be derived by evaluating $\partial g(\boldsymbol{\chi}';\boldsymbol{\chi})/\partial \boldsymbol{v}$ in (7.51) with coordinate unit vectors $\boldsymbol{v} = (1,0)$ or $(0,1)$ followed by relabeling $(r,z) \leftrightarrow (r',z')$,

$$\left.\begin{aligned}\frac{\partial g(\boldsymbol{\chi}';\boldsymbol{\chi})}{\partial r'} &= \frac{1}{\pi\sqrt{a+b}}\left[\left(\frac{1}{2r'} + \frac{r-r'}{a-b}\right)E(m) - \frac{1}{2r'}K(m)\right],\\ \frac{\partial g(\boldsymbol{\chi}';\boldsymbol{\chi})}{\partial z'} &= \frac{1}{\pi\sqrt{a+b}}\frac{z-z'}{a-b}E(m).\end{aligned}\right\} \tag{7.56}$$

The expressions of $\partial^2 g(\boldsymbol{\chi}';\boldsymbol{\chi})/\partial r'\partial \boldsymbol{n}$ and $\partial^2 g(\boldsymbol{\chi}';\boldsymbol{\chi})/\partial z'\partial \boldsymbol{n}$ are more algebraically involved. Using a symbolic package, we manage to derive

$$\left.\begin{aligned}\frac{\partial^2 g(\boldsymbol{\chi}';\boldsymbol{\chi})}{\partial r'\partial \boldsymbol{n}} = \frac{1}{\pi\sqrt{a+b}}\Bigg\{ &+ \frac{\mathrm{d}E}{\mathrm{d}m}\frac{2\left(a-2r'^2\right)}{(a+b)^2}\frac{n_r\left(a-2r^2\right)+2n_z r(z'-z)}{a-b}\\ &+ E(m)\Bigg[-\frac{2(r'-r)}{a-b}\frac{n_r(r'-r)+n_z(z'-z)}{a-b} + \frac{n_r}{a-b}\\ &\qquad - \frac{r+r'}{a+b}\left(\frac{n_r(r'-r)+n_z(z'-z)}{a-b} + \frac{n_r}{2r}\right)\Bigg]\\ &- \frac{\mathrm{d}K}{\mathrm{d}m}\frac{2n_r\left(a-2r'^2\right)}{(a+b)^2} + K(m)\frac{n_r\left(b+2r'^2\right)}{2b(a+b)}\Bigg\},\\ \frac{\partial^2 g(\boldsymbol{\chi}';\boldsymbol{\chi})}{\partial z'\partial \boldsymbol{n}} = \frac{1}{\pi\sqrt{a+b}}\Bigg\{ &- \frac{\mathrm{d}E}{\mathrm{d}m}\frac{4b(z'-z)}{(a+b)^2}\left(\frac{n_r(r'-r)+n_z(z'-z)}{a-b} + \frac{n_r}{2r}\right)\\ &+ E(m)\Bigg[-\frac{2(z'-z)}{a-b}\frac{n_r(r'-r)+n_z(z'-z)}{a-b} + \frac{n_z}{a-b}\\ &\qquad - \frac{z'-z}{a+b}\left(\frac{n_r(r'-r)+n_z(z'-z)}{a-b} + \frac{n_r}{2r}\right)\Bigg]\\ &+ \frac{\mathrm{d}K}{\mathrm{d}m}\frac{4n_r r'(z'-z)}{(a+b)^2} + K(m)\frac{n_r(z'-z)}{2r(a+b)}\Bigg\},\end{aligned}\right\} \tag{7.57}$$

where derivatives of the complete elliptic integrals, $\mathrm{d}K/\mathrm{d}m$ and $\mathrm{d}E/\mathrm{d}m$, are evaluated through the closed-form recurrence relation (7.47).

To proceed with numerical evaluation of boundary integrals, the boundary γ is first discretized into a global quintic spline interpolation $\boldsymbol{\gamma}$ constructed from a set of knots $\boldsymbol{\chi}_j$. We then seek approximate solutions to boundary potential φ and flux q drawn from a finite-dimensional subspace such as the interpolation space of Lagrange polynomials by demanding boundary integral equation (7.54) to be satisfied at a finite number of collocation points. This is called the collocation method (Kress, 2014). Let $\boldsymbol{\gamma}^{(e)}$ be

a local spline of index e with $\xi^{(e)}$ being its local arc-length fraction. Then boundary potential φ and flux q can be approximated by the Lagrange interpolations along the arc-length of the global spline,

$$\varphi(\boldsymbol{\chi} \in \gamma) \approx \sum_e \sum_k \varphi_k^{(e)} \mathbb{N}_k(\xi^{(e)}), \quad q(\boldsymbol{\chi} \in \gamma) \approx \sum_e \sum_k q_k^{(e)} \mathbb{N}_k(\xi^{(e)}), \tag{7.58}$$

where $\varphi_k^{(e)}$ and $q_k^{(e)}$ are the nodal values of ϕ and $\partial\phi/\partial\boldsymbol{n}$ at the k-th local Lagrange node ξ_k of local spline $\gamma^{(e)}$ respectively. Here $\mathbb{N}_k$ is the k-th Lagrange interpolation polynomial such that $\mathbb{N}_k(\xi_j) = 1$ if $j = k$ and $= 0$ if $j \neq k$. The first order basis of Lagrange interpolation over the canonical interval $[0, 1]$ are linear polynomials,

$$\left.\begin{array}{ll} \mathbb{N}_0 = 1 - \xi, & \mathbb{N}_1 = \xi, \\ \xi_0 = 0, & \xi_1 = 1. \end{array}\right\} \text{ (first order)} \tag{7.59}$$

The second order basis are quadratic polynomials,

$$\left.\begin{array}{lll} \mathbb{N}_0 = (1-\xi)(1-2\xi), & \mathbb{N}_1 = 4\xi(1-\xi), & \mathbb{N}_2 = \xi(2\xi-1), \\ \xi_0 = 0, & \xi_1 = 1/2, & \xi_2 = 1. \end{array}\right\} \text{ (second order)} \tag{7.60}$$

For our purpose, the first and the second order basis over interval $[0, 1]$ provide sufficient accuracy. Note the Lagrange nodes ξ_k are constructed based on the arc-length fraction $\xi^{(e)}$ from (7.28) instead of the intrinsic coordinate t of the local spline $\boldsymbol{\gamma}^{(e)}(t)$ defined in (7.27). For numerical purposes, integrals are first parametrized in the intrinsic variable t and then integrated over the canonical interval $[0, 1]$ via appropriate quadrature rules. Therefore we must compute the corresponding intrinsic coordinates t_k of each Lagrange node ξ_k such that $\xi^{(e)}(t_k) = \xi_k$, which boils down to solving a few integral equations along each local spline $\boldsymbol{\gamma}^{(e)}$,

$$\xi_k = \frac{1}{\mathfrak{s}^{(e)}} \int_0^{t_k} |\dot{\boldsymbol{\gamma}}^{(e)}(t')| \, \mathrm{d}t'. \tag{7.61}$$

Integral equation (7.61) can be efficiently solved by standard Newton's methods. Given a reasonable initial guess (e.g., $t_k = \xi_k$), the iteration process typically converges within two or three steps up to machine-size errors.

Single-layer and double-layer boundary integrals

There are two types—single- and double-layer—of boundary integrals in equation (7.54). Convoluting boundary flux $q(\boldsymbol{\chi})$ with the Green's function $g(\boldsymbol{\chi}'; \boldsymbol{\chi})$ yields field intensity at a field point $\boldsymbol{\chi}'$ due to a single-layer integral

$$\mathcal{S}[q](\boldsymbol{\chi}') = \int_\gamma g(\boldsymbol{\chi}'; \boldsymbol{\chi}) q(\boldsymbol{\chi}) r \, \mathrm{d}\gamma(\boldsymbol{\chi}). \tag{7.62}$$

In electrostatic terms, the resulting potential $\mathcal{S}[q](\boldsymbol{\chi}')$ of a single-layer boundary integral is the sum of the potentials due to a distribution of surface charges with magnitude

$q(\boldsymbol{\chi})$ residing on the boundary γ. The single-layer integral (7.62) is approximated by the Lagrange interpolation introduced in equation (7.58). It is decomposed into a summation of integrals over the arc-length of each local spline $\gamma^{(e)}$,

$$\mathcal{s}[q](\boldsymbol{\chi}') \approx \sum_e \sum_k q_k^{(e)} \int_{\gamma^{(e)}} g(\boldsymbol{\chi}';\boldsymbol{\chi}) \mathbb{N}_k(\xi^{(e)}) r \,\mathrm{d}\gamma(\boldsymbol{\chi}) = \sum_e \sum_k q_k^{(e)} \mathcal{s}^{(e)}[\mathbb{N}_k](\boldsymbol{\chi}'), \quad (7.63)$$

where

$$\mathcal{s}^{(e)}[\mathbb{N}_k](\boldsymbol{\chi}') = \int_0^1 \frac{r\|\dot{\boldsymbol{\gamma}}\|}{\pi\sqrt{a+b}} \mathbb{N}_k(\xi^{(e)}) K(m) \,\mathrm{d}t \quad (7.64)$$

is the single-layer integral of a Lagrange basis function $\mathbb{N}_k$ restricted to a local spline $\boldsymbol{\gamma}^{(e)}$. Integral (7.64) is regular when field points $\boldsymbol{\chi}'$ do not overlap with a local spline $\boldsymbol{\gamma}^{(e)}$, in which case the standard Gauss-Legendre quadrature (7.35) is sufficient for numerical integration. However when field point $\boldsymbol{\chi}'$ coincides with an interior point $\boldsymbol{\gamma}^{(e)}(t')$ of the local spline, e.g., one of the Lagrange nodes $\boldsymbol{\gamma}^{(e)}(t_k)$, it becomes a source of logarithmic singularity in the integrand of (7.64) which can be handled the logarithmic-weighted quadrature rules (7.38) after some manipulations.

To analyze the singular behavior of single-layer integrals, we consider the limit of auxiliary variable $m(t)$ defined in equation (7.52) as $\boldsymbol{\chi} \to \boldsymbol{\chi}' = \boldsymbol{\gamma}^{(e)}(t')$ for some $t' \in [0,1]$,

$$m = \frac{4rr'}{(r'+r)^2+(z'-z)^2} = 1 - \frac{\dot{r}(t')^2+\dot{z}(t')^2}{4r'^2}(t'-t)^2 + O((t'-t)^3). \quad (7.65)$$

We see that $|1-m| \to 0$ quadratically in $|t'-t|$. It can thus be deduced from the Chebyshev approximation (7.43) of the complete elliptic integral $K(m)$ that the integrand of the single-layer integral (7.64) contains a logarithmic singularity $\sim \ln|t-t'|$ when field point $\boldsymbol{\chi}'$ is belongs to the local spline $\boldsymbol{\gamma}^{(e)}(t_k)$. Note the quadratic coefficient in front of $(t'-t)^2$ in (7.65) can never be zero since $\dot{r}(t)$ and $\dot{z}(t)$ are components of the tangential vector $\dot{\boldsymbol{\gamma}}^{(e)}$ which can not simultaneously vanish. This means we can first subtract off the logarithm $\ln|t'-t|$ from $\ln(1-m)$ and then add it back,

$$\ln(1-m) = \ln\frac{1-m}{|t'-t|^2} + 2\ln|t'-t|. \quad (7.66)$$

This technique is called singularity subtraction (Dommermuth and Yue, 1987; Oguz and Prosperetti, 1993; Padrino Inciarte, 2010). It follows that the single-layer integral (7.64) can be split into a regular integral and a logarithmic-singular one,

$$\mathcal{s}^{(e)}[\mathbb{N}_k](\boldsymbol{\chi}') \approx \int_0^1 \frac{r\|\dot{\boldsymbol{\gamma}}\|\mathbb{N}_k(\xi^{(e)})}{\pi\sqrt{a+b}} \Big[\underbrace{K_P(m) - K_Q(m)\ln\frac{1-m}{(t-t')^2}}_{\text{regular}} - \overbrace{2K_Q(m)\ln|t-t'|}^{\text{logarithmic-singular}} \Big] \mathrm{d}t. \quad (7.67)$$

To simplify notations, we introduce a few helper functions,

$$\left.\begin{aligned} \mathfrak{s}_K(t) &= \frac{r\|\dot{\boldsymbol{\gamma}}\|}{\pi\sqrt{a+b}}, \\ K_R(t';m) &= K_P(m) - K_Q(m)\ln\frac{1-m}{(t-t')^2}, \\ E_R(t';m) &= E_P(m) - E_Q(m)\ln\frac{1-m}{(t-t')^2}. \end{aligned}\right\} \tag{7.68}$$

We then lump various terms into integrands $I_{(\mathrm{o})}$, $I_{(\mathrm{i})}$ and $I_{(\mathrm{i})}^{\log}$ with subscripts $(\cdot)_{(\mathrm{i})}$ and $(\cdot)_{(\mathrm{o})}$ designated for source points $\boldsymbol{\chi}'$ inside and outside of a local spline $\boldsymbol{\gamma}^{(e)}$, respectively,

$$\left.\begin{aligned} I_{(\mathrm{o})}(t) &= \mathfrak{s}_K(t)K(m)\mathbb{N}_k(\xi^{(e)}), \\ I_{(\mathrm{i})}(t';t) &= \mathfrak{s}_K(t)K_R(t';m)\mathbb{N}_k(\xi^{(e)}), \\ I_{(\mathrm{i})}^{\log}(t) &= -2\mathfrak{s}_K(t)K_Q(m)\mathbb{N}_k(\xi^{(e)}), \end{aligned}\right\} \tag{7.69}$$

which will be used later.

Similar to the singular-layer integral (7.62), field intensity at field point $\boldsymbol{\chi}'$ due to a double-layer integral $\mathscr{d}[\varphi]$ is given by the convolution of boundary potential $\varphi(\boldsymbol{\chi})$ with the normal flux of the Green's function $g(\boldsymbol{\chi}';\boldsymbol{\chi})$,

$$\mathscr{d}[\varphi](\boldsymbol{\chi}') = \int_\gamma \frac{\partial g(\boldsymbol{\chi}';\boldsymbol{\chi})}{\partial \boldsymbol{n}}\varphi(\boldsymbol{\chi})r\,\mathrm{d}\gamma(\boldsymbol{\chi}). \tag{7.70}$$

Physically, the resulting potential of a double-layer boundary integral can be interpreted as the sum of potentials due to a distribution of surface electric dipole with strength $\varphi(\boldsymbol{\chi})$ covering the boundary. With the Lagrange interpolation (7.58), we reduce the double-layer integral $\mathscr{d}[\varphi]$ to a summation of integrals over each local spline $\boldsymbol{\gamma}^{(e)}$,

$$\mathscr{d}[\varphi](\boldsymbol{\chi}') \approx \sum_e\sum_k \varphi_k^{(e)}\int_{\gamma^{(e)}}\frac{\partial g(\boldsymbol{\chi}';\boldsymbol{\chi})}{\partial \boldsymbol{n}}\mathbb{N}_k(\xi^{(e)})r\,\mathrm{d}\gamma(\boldsymbol{\chi}) = \sum_e\sum_k \varphi_k^{(e)}\mathscr{d}^{(e)}[\mathbb{N}_k](\boldsymbol{\chi}') \tag{7.71}$$

where

$$\begin{aligned} \mathscr{d}^{(e)}[\mathbb{N}_k](\boldsymbol{\chi}') &= \int_0^1 \frac{\mathbb{N}_k(\xi^{(e)})\|\dot{\boldsymbol{\gamma}}\|}{\pi\sqrt{a+b}}\left\{\left[\frac{n_r}{2} + \frac{\boldsymbol{n}\cdot(\boldsymbol{x}'-\boldsymbol{x})}{\|\boldsymbol{x}'-\boldsymbol{x}\|^2}r\right]E(m) - \frac{n_r}{2}K(m)\right\}\mathrm{d}t \\ &= \int_0^1 \frac{\mathbb{N}_k(\xi^{(e)})}{\pi\sqrt{a+b}}\left\{\left[\frac{\dot{r}(z'-z)-\dot{z}(r'-r)}{(r'-r)^2+(z'-z)^2}r - \frac{\dot{z}}{2}\right]E(m) + \frac{\dot{z}}{2}K(m)\right\}\mathrm{d}t \end{aligned} \tag{7.72}$$

is the double-layer integral of a Lagrange basis function $\mathbb{N}_k$ restricted to a local spline $\boldsymbol{\gamma}^{(e)}$.

Analogous to the single-layer integral (7.64), the double-layer integral (7.72) is regular when field points $\boldsymbol{\chi}'$ locate outside of a local spline $\boldsymbol{\gamma}^{(e)}$. When a field point $\boldsymbol{\chi}' = \boldsymbol{\gamma}^{(e)}(t')$ moves to the interior, we come to the observation that the part of the integrand under

integral (7.72) that involves the complete elliptic integral of the second kind $E(m)$ is regular because $E(m) \to (1-m)\ln(1-m)$ as $t \to t'$ which is always finite for $m \in [0,1]$ and the second derivatives $\ddot{r}$ and $\ddot{z}$ are well defined for a smooth boundary shape. It suffices to employ the standard Gauss-Legendre quadrature rules. However, the rate at which the standard Gauss-Legendre quadrature rules converge scales with the overall magnitude of derivatives of the function being integrated. In our case, derivatives of the second kind elliptic integral $E(m)$ produce terms such as $\ln(1-m)$ which blows up at $t = t'$. Therefore we choose to treat both elliptic integrals $K(m)$ and $E(m)$ with logarithmic-weighted quadrature rules. For notation simplicity, we again introduce two helper functions for the double-layer integral,

$$\left.\begin{aligned} \mathscr{A}_E(t) &= \frac{1}{\pi\sqrt{a+b}}\left[\frac{\dot{r}(z'-z)-\dot{z}(r'-r)}{a-b}r - \frac{\dot{z}}{2}\right], \\ \mathscr{A}_K(t) &= \frac{1}{\pi\sqrt{a+b}}\frac{\dot{z}}{2}, \end{aligned}\right\} \tag{7.73}$$

as well as $I_{(\mathrm{o})}$, $I_{(\mathrm{o})}$ and $I^{\log}_{(\mathrm{i})}$,

$$\left.\begin{aligned} I_{(\mathrm{o})}(t) &= \left[\mathscr{A}_E(t)E(m) + \mathscr{A}_K(t)K(m)\right]\mathbb{N}_k(\xi^{(e)}), \\ I_{(\mathrm{i})}(t';t) &= \left[\mathscr{A}_E(t)E_R(t';m) + \mathscr{A}_K(t)K_R(t';m)\right]\mathbb{N}_k(\xi^{(e)}), \\ I^{\log}_{(\mathrm{i})}(t) &= -2\left[\mathscr{A}_E(t)E_Q(m) + \mathscr{A}_K(t)K_Q(m)\right]\mathbb{N}_k(\xi^{(e)}). \end{aligned}\right\} \tag{7.74}$$

With helper functions introduced in (7.69) and (7.74), given a local spline $\boldsymbol{\gamma}^{(e)}$ and a Lagrange basis function $\mathbb{N}_k$ we can compactly express the local integrals of both single- and double-layer types as the sum of a regular and a logarithmic-singular integral,

$$\mathscr{S}^{(e)} \text{ or } \mathscr{A}^{(e)}[\mathbb{N}_k](\boldsymbol{\chi}') = \begin{cases} \displaystyle\int_0^1 I_{(\mathrm{o})}(t)\,\mathrm{d}t & \text{for} \quad \boldsymbol{\chi}' \notin \boldsymbol{\gamma}^{(e)}, \\ \displaystyle\int_0^1 I_{(\mathrm{i})}(t';t)\,\mathrm{d}t + \int_0^1 I^{\log}_{(\mathrm{i})}(t)\ln|t'-t|\,\mathrm{d}t & \text{for} \quad \boldsymbol{\chi}' \in \boldsymbol{\gamma}^{(e)}, \end{cases} \tag{7.75}$$

where the logarithmic-singular integral can be efficiently treated with the logarithmic-weighted quadrature rules (7.38) developed in the last section.

Lastly we note that, when a field point $\boldsymbol{\chi}'$ is placed on the symmetry axis where $r' = 0$, the complete elliptic integrals can be evaluated to closed-form expressions which significantly simplify the single- and double-layer integrals. For a well-behaved surface of revolution, the technique of singularity subtraction is not needed. It suffices to use the standard Gauss-Legendre quadrature rules to treat the integrals,

$$\left.\begin{aligned} \mathscr{S}^{(e)}[\mathbb{N}_k](\boldsymbol{\chi}') &= \mathscr{S}^{(e)}[\mathbb{N}_k](z') = \int_0^1 \mathbb{N}_k(\xi^{(e)})r\frac{\|\dot{\boldsymbol{\gamma}}\|}{2\sqrt{r^2+(z-z')^2}}\,\mathrm{d}t, \\ \mathscr{A}^{(e)}[\mathbb{N}_k](\boldsymbol{\chi}') &= \mathscr{A}^{(e)}[\mathbb{N}_k](z') = \int_0^1 \mathbb{N}_k(\xi^{(e)})r\frac{\dot{z}r+\dot{r}(z'-z)}{2\left[r^2+(z'-z)^2\right]^{3/2}}\,\mathrm{d}t, \end{aligned}\right\} \tag{7.76}$$

assuming the integrands in (7.76) have well-defined limits as $\boldsymbol{\chi} \to \boldsymbol{\chi}' = (0, z')$. For instance, surface regularity demands that $\ddot{z}/\dot{r}$ must be finite at $r = 0$ (e.g., a generic conical tip aligned with symmetry axis is not allowed).

Matrix assembly for discretized boundary integrals

Let boundary γ be approximated by a collection of n local splines $\boldsymbol{\gamma}^{(e)}$. We use the ensemble of Lagrange nodes of each local splines as the collocation points at which boundary integral equation (7.54) must satisfy after discretization. These nodes serve as field points in evaluating the boundary integrals. For the second order Lagrange interpolation, we rearrange all field points into an ordered set

$$\begin{aligned}\{\boldsymbol{\chi}'_0, \boldsymbol{\chi}'_1, \cdots, \boldsymbol{\chi}'_N\} = \Big\{&\boldsymbol{\gamma}^{(0)}(t_0), \boldsymbol{\gamma}^{(0)}(t_1), \\ &\boldsymbol{\gamma}^{(1)}(t_0), \boldsymbol{\gamma}^{(1)}(t_1), \cdots, \boldsymbol{\gamma}^{(n-1)}(t_0), \boldsymbol{\gamma}^{(n-1)}(t_1), \boldsymbol{\gamma}^{(n-1)}(t_2)\Big\}\end{aligned} \tag{7.77}$$

with respect to the parametrization of the boundary curve γ. In what follows, we exclusively refer to index i as the global nodal index in the sense of (7.77). Note entries $\boldsymbol{\gamma}^{(e)}(t_2)$ do not explicitly appear in the nodal set (7.77) because adjacent local splines share one identical Lagrange node, i.e. $\boldsymbol{\gamma}^{(e)}(t_2) = \boldsymbol{\gamma}^{(e+1)}(t_0)$. Along the same lines, nodal values $\varphi_k^{(e)}$ of the boundary potential $\varphi(\boldsymbol{\chi})$ and $q_k^{(e)}$ of the flux $q(\boldsymbol{\chi})$ are sorted into ordered arrays, designated by boldface capital letters $\boldsymbol{\varphi}$ and $\boldsymbol{q}$,

$$\left.\begin{aligned}\boldsymbol{\varphi} &= [\varphi_0^{(0)}, \varphi_1^{(0)}, \varphi_0^{(1)}, \varphi_1^{(1)}, \cdots, \varphi_0^{(n-1)}, \varphi_1^{(n-1)}, \varphi_2^{(n-1)}]^\top, \\ \boldsymbol{q} &= [q_0^{(0)}, q_1^{(0)}, q_0^{(1)}, q_1^{(1)}, \cdots, q_0^{(n-1)}, q_1^{(n-1)}, q_2^{(n-1)}]^\top,\end{aligned}\right\} \tag{7.78}$$

where $\varphi_2^{(e)} = \varphi_0^{(e+1)}$ and $q_2^{(e)} = q_0^{(e+1)}$ are assumed to hold. The single- and double-layer integrals evaluated at field points $\boldsymbol{\chi}'_i$ can be identified with column vectors $\boldsymbol{s}_i$ and $\boldsymbol{d}_i$ such that

$$\left.\begin{aligned}\mathcal{S}[q](\boldsymbol{\chi}'_i) &\approx \sum_e \sum_k q_k^{(e)} \mathcal{J}^{(e)}[\mathbb{N}_k](\boldsymbol{\chi}'_i) = \boldsymbol{s}_i^\top \boldsymbol{q}, \\ \mathcal{D}[\varphi](\boldsymbol{\chi}'_i) &\approx \sum_e \sum_k \varphi_k^{(e)} \mathcal{J}^{(e)}[\mathbb{N}_k](\boldsymbol{\chi}'_i) = \boldsymbol{d}_i^\top \boldsymbol{\varphi}.\end{aligned}\right\} \tag{7.79}$$

Applying collocation procedure to the boundary integral equation (7.54) of a sufficiently continuous boundary γ yields a matrix equation

$$(\boldsymbol{b} + \boldsymbol{d})\boldsymbol{\varphi} = \boldsymbol{s}\boldsymbol{q}, \tag{7.80}$$

where $\boldsymbol{s}$ and $\boldsymbol{d}$ are fully populated dense matrices and $\boldsymbol{b}$ is a near-identity sparse matrix with interior angles β on its diagonal,

$$\boldsymbol{s} = \begin{bmatrix} \boldsymbol{s}_0^\top \\ \boldsymbol{s}_1^\top \\ \vdots \\ \boldsymbol{s}_{-1}^\top \end{bmatrix}, \quad \boldsymbol{d} = \begin{bmatrix} \boldsymbol{d}_0^\top \\ \boldsymbol{d}_1^\top \\ \vdots \\ \boldsymbol{d}_{-1}^\top \end{bmatrix}, \quad b_{ij} = \begin{cases} 0 & \text{if} \quad i \neq j, \\ \beta(\boldsymbol{\chi}'_i)/2\pi & \text{if} \quad i = j. \end{cases} \tag{7.81}$$

Description	Index	Range
Interpolation order	o	$o \geq 1$
Total number of splines	n	
Total number of nodes	N	$n \times o + 1$
Global nodal index of field point	i	$0 \leq i \leq n \times o$
Index of source spline	e	$0 \leq e \leq n - 1$
Index of spline knots	j	$0 \leq j \leq n$
Local nodal index of source point	k	$0 \leq k \leq o$
Global index of k-th local node in e-th spline	l	$l = e \times o + k$
Index set of splines which contain i-th node	$e\|i$	$\{\lfloor i/o \rfloor - 1,\ \lfloor i/o \rfloor\}$ if $i \,\%\, o = 0$
		$\{\lfloor i/o \rfloor - 1\}$ if $i \,\%\, o \neq 0$

Table 7.5: Indices used in the assembly procedure described by algorithm 2: operator $\lfloor \cdot \rfloor$ is the floor function and $\%$ is the modulo operation.

The matrix assembly procedure for $\boldsymbol{s}$ and $\boldsymbol{d}$ is summarized in algorithm 2, the loop indices of which are listed in table 7.5. For a C^1-continuous boundary γ (i.e. tangent vector is continuous), interior angle $\beta = \pi$ everywhere on the boundary which means $\boldsymbol{b} = \mathbb{I}/2$ behaves almost like an identity matrix.

Algorithm 2 Assembly procedure for matrices $\boldsymbol{s}$ and $\boldsymbol{d}$. Indices are defined in table 7.5.

procedure MATRIX ASSEMBLY
  for $0 \leq i \leq N$ **do** ▷ Parallel this loop
    $e|i$ = index set of splines which contain i-th node ▷ Check index bound
    for $0 \leq e \leq n$ **do**
      if $e \notin e|i$ **then**
        for $0 \leq k \leq o$ **do**
          $l = e \times o + k$
          $s_{il} = s_{il} + \mathcal{s}^{(e)}[\mathbb{N}_k](\boldsymbol{\chi}'_i)$ ▷ Gauss-Legendre quadrature
          $d_{il} = d_{il} + \mathcal{d}^{(e)}[\mathbb{N}_k](\boldsymbol{\chi}'_i)$
      else
        for $e \in e|i$ **do**
          for $0 \leq k \leq o$ **do**
            $l = e \times o + k$
            $s_{il} = s_{il} + \mathcal{s}^{(e)}[\mathbb{N}_k](\boldsymbol{\chi}'_i)$ ▷ Logarithmic-weighted quadrature
            $d_{il} = d_{il} + \mathcal{d}^{(e)}[\mathbb{N}_k](\boldsymbol{\chi}'_i)$

In a more complicated scenario where two adjacent boundaries γ_0 and γ_1 meet at a corner, e.g., the geometry shown in figure 7.2(a), we decompose the assembly process into four subroutines, for which source points $\boldsymbol{\chi}$ and field points $\boldsymbol{\chi}'$ may belong to different boundaries. Similar to the matrix equation (7.80), looping through all combinations of field and source points yields a block matrix equation,

$$\begin{bmatrix} \boldsymbol{b}_{00} & \boldsymbol{b}_{01} \\ \boldsymbol{b}_{10} & \boldsymbol{b}_{11} \end{bmatrix} \begin{bmatrix} \boldsymbol{\varphi}_0 \\ \boldsymbol{\varphi}_1 \end{bmatrix} + \begin{bmatrix} \boldsymbol{d}_{00} & \boldsymbol{d}_{01} \\ \boldsymbol{d}_{10} & \boldsymbol{d}_{11} \end{bmatrix} \begin{bmatrix} \boldsymbol{\varphi}_0 \\ \boldsymbol{\varphi}_1 \end{bmatrix} = \begin{bmatrix} \boldsymbol{s}_{00} & \boldsymbol{s}_{01} \\ \boldsymbol{s}_{10} & \boldsymbol{s}_{11} \end{bmatrix} \begin{bmatrix} \boldsymbol{q}_0 \\ \boldsymbol{q}_1 \end{bmatrix}, \tag{7.82}$$

where matrix subscript $(\cdot)_{ab}$ means the matrix entries are computed for field points $\boldsymbol{\chi}' \in \gamma_a$ and source points $\boldsymbol{\chi} \in \gamma_b$.

In our example of two smooth boundaries that join at a sharp corner, the last node of the first boundary γ_0 coincides with the first node of the second boundary γ_1. It is important to remember that, although the these two nodes are treated as two independent degrees of freedom in the matrix equation (7.82), they correspond to an identical position in the axisymmetric plane. We must be mindful about the choice of quadrature rules for the single- and double-layer integrals when field and source points coincide with these two nodes. Coefficients of $\boldsymbol{b}_{01}$ and $\boldsymbol{b}_{10}$ are identically zero whereas diagonals of $\boldsymbol{b}_{00}$ and $\boldsymbol{b}_{11}$ are everywhere $1/2$ except $[b_{00}]_{-1,-1} = [b_{11}]_{0,0} = \beta(\boldsymbol{\chi}_{\text{corner}})$ are determined by the interior angle at the corner discontinuity $\boldsymbol{\chi}_{\text{corner}}$ ($[\cdot]_{-i,-j}$ means the last i-th and j-th entry). After a close examination on the block matrix equation (7.82), we come to the observation that, there are two identical rows in $\boldsymbol{d}$ and $\boldsymbol{s}$ complemented by an extra constraint on the continuity of potential at the corner,

$$\left.\begin{aligned} \text{row}_{-1}(\boldsymbol{b}_{00}+\boldsymbol{d}_{00})\boldsymbol{\varphi}_0 + \text{row}_{-1}(\boldsymbol{b}_{01}+\boldsymbol{d}_{01})\boldsymbol{\varphi}_1 &= \text{row}_{-1}(\boldsymbol{s}_{00})\boldsymbol{q}_0 + \text{row}_{-1}(\boldsymbol{s}_{01})\boldsymbol{q}_1, \\ \text{row}_{0}(\boldsymbol{b}_{10}+\boldsymbol{d}_{10})\boldsymbol{\varphi}_0 + \text{row}_{0}(\boldsymbol{b}_{11}+\boldsymbol{d}_{11})\boldsymbol{\varphi}_1 &= \text{row}_{0}(\boldsymbol{s}_{10})\boldsymbol{q}_0 + \text{row}_{0}(\boldsymbol{s}_{11})\boldsymbol{q}_1, \\ (p_0)_{-1} - (p_1)_0 &= 0, \end{aligned}\right\} \tag{7.83}$$

where operator $\text{row}_0(\cdot)$ and $\text{row}_{-1}(\cdot)$ denotes the last and the first row vectors of the matrix. We choose to eliminate one of the identical rows by replacing it with the continuity condition,

$$\left.\begin{aligned} \text{row}_{-1}(\boldsymbol{b}_{00}+\boldsymbol{d}_{00}) = [0,\cdots,0,1], \quad \text{row}_{-1}(\boldsymbol{b}_{01}+\boldsymbol{d}_{01}) = [-1,0,\cdots,0], \\ \text{row}_{-1}(\boldsymbol{s}_{00}) = [0,\cdots,0,0], \qquad\qquad \text{row}_{-1}(\boldsymbol{s}_{01}) = [0,0,\cdots,0]. \end{aligned}\right\} \tag{7.84}$$

For a mixed-type boundary condition where potential φ (Dirichlet) is prescribed on boundary γ_0 and flux q (Neumann) on γ_1, the solutions to the unknown flux q on boundary γ_0 and unknown potential φ on boundary γ_1 (or the other way around) is given by a simple rearrangement of the block matrix equation,

$$\begin{bmatrix} \boldsymbol{b}_{00}+\boldsymbol{d}_{00} & -\boldsymbol{s}_{01} \\ \boldsymbol{b}_{10}+\boldsymbol{d}_{10} & -\boldsymbol{s}_{11} \end{bmatrix} \begin{bmatrix} \boldsymbol{\varphi}_0 \\ \boldsymbol{q}_1 \end{bmatrix} = \begin{bmatrix} \boldsymbol{s}_{00} & -\boldsymbol{b}_{01}-\boldsymbol{d}_{01} \\ \boldsymbol{s}_{10} & -\boldsymbol{b}_{11}-\boldsymbol{d}_{11} \end{bmatrix} \begin{bmatrix} \boldsymbol{q}_0 \\ \boldsymbol{\varphi}_1 \end{bmatrix}. \tag{7.85}$$

Elimination of identical rows from (7.84) still preserves continuity between the last nodal value of potential vector $\boldsymbol{\varphi}_0$ and the first nodal value of $\boldsymbol{\varphi}_1$ when we solve the rearranged block matrix equation (7.85). However, what cannot be achieved here is to prescribe identical potential values on from both sides of the corner discontinuity. In such an event, continuity of potential would no longer provide an extra equation which means the single-layer block matrix assemble from $\boldsymbol{s}_{00}$, $\boldsymbol{s}_{01}$, $\boldsymbol{s}_{10}$ and $\boldsymbol{s}_{11}$ is rank-deficient and hence may not yield a unique solution. A possible remedy for such problem is

to construct an extra constraint (Wrobel, 2002) based on some local approximation (e.g., finite difference approximation) near the corner which relates nodal values of the potential to flux value before and after the corner. To circumvent this issue, in this work we always consider a mixture of Direchlet and Neumann conditions before and after the discontinuity as described in Section 6.5 of Chapter 6.

Validation of boundary integral solver

To verify the accuracy of our boundary integral solver we formulate a test problem subject to mixed boundary conditions posed on a piecewise -smooth boundary $\gamma = \gamma_0 \cup \gamma_1$. As shown figure 7.2(a), boundary γ is divided into a sinusoidally deformed semi-circle γ_0 and a straight line γ_1 which join at a 90°-corner discontinuity. The explicit parametrizations of γ_0 and γ_1 are given by

$$\left.\begin{aligned} \boldsymbol{\gamma}_0(\theta) &= 2\Big(1+\frac{1}{4}\cos(8\theta-\pi)\Big)\begin{bmatrix}\cos\theta\\ \sin\theta\end{bmatrix} && \text{for} \quad \theta\in[0,\pi/2],\\ \boldsymbol{\gamma}_1(\theta) &= \begin{bmatrix}\theta\\ 0\end{bmatrix} && \text{for} \quad \theta\in[0,3/2]. \end{aligned}\right\} \tag{7.86}$$

We consider the following test problem for the interior axisymmetric volume enclosed by these two boundaries:

$$\text{given } \phi \text{ on } \gamma_0 \text{ and } \frac{\partial\phi}{\partial \boldsymbol{n}} \text{ on } \gamma_1, \quad \text{solve for } \frac{\partial\phi}{\partial \boldsymbol{n}} \text{ on } \gamma_0 \text{ and } \phi \text{ on } \gamma_1, \tag{7.87}$$

where $\boldsymbol{n}$ is the outward normal vector and $\phi = r_s^\ell P_\ell(\cos\theta)$ is an axisymmetric harmonic potential analytically constructed from the ℓ-th order Legendre polynomial P_ℓ. For $\ell = 2$, we have

$$\phi = -\frac{r^2}{2}+z^2, \quad \frac{\partial\phi}{\partial\boldsymbol{n}} = \boldsymbol{n}\cdot\begin{bmatrix}-r\\ 2z\end{bmatrix}. \tag{7.88}$$

The exact solution to the test problem (7.87) is readily deduced from the explicit parametrization (7.86) and potential (7.88). Discrepancy between numerical and analytic solutions can be then measured and quantified. In addition to the potential problem, we also verify the accuracy of our quintic spline interpolation. Recall from the curvature formula (7.30) of a planar curve $\boldsymbol{\gamma} = (r(\theta), z(\theta))$ in an axisymmetric plane that surface total curvature $2\hbar$ can be calculated through substitution of either quintic spline interpolation or the exact parametrization (7.86) into (7.30). The errors between numerical and analytic solutions are measured in l^∞-norm, i.e. the maximum point-wise absolute error over the set of all nodal points $\boldsymbol{\chi}_i$ on the boundary. The error of Dirichlet

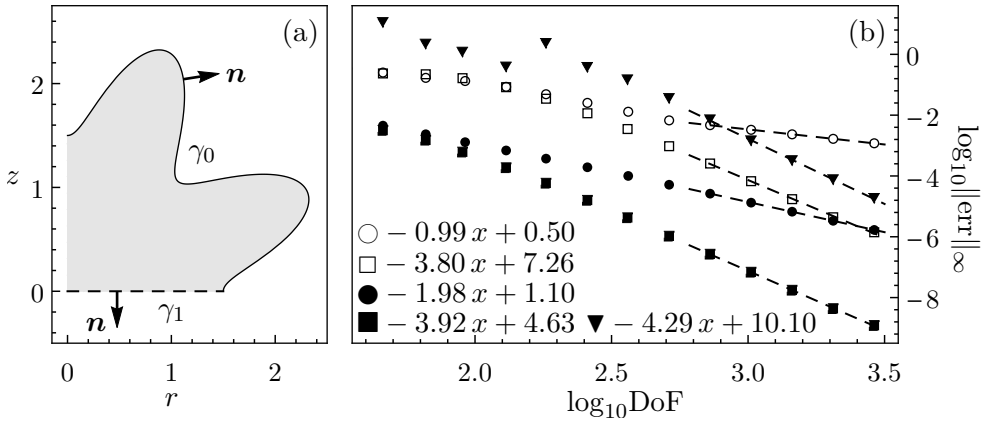

Figure 7.2: Convergence of errors between numerical and analytic solutions measured in l^∞-norm for the test problem (7.87): (a) Axisymmetric volume (shaded) enclosed by two boundaries γ_0 (solid) and γ_1 (dashed) parametrized by (7.86). Arrows represent direction of normal vector. (b) Log-log plot of curvature error (7.91) (▼) on γ_0, Neumann error (7.90) on γ_0 using linear (●) and quadratic (■) Lagrange basis functions and Dirichlet error (7.89) on γ_1 using linear (○) and quadratic (□) Lagrange basis functions against degrees of freedom (DoF) used by the solver. Inset: linear fits (dashed line) of the last five points of each type of error.

data $\mathrm{err_D}$, the error of Neumann data $\mathrm{err_N}$ and the error of curvature $\mathrm{err_C}$ are given by

$$\|\mathrm{err_D}\|_\infty = \max_{\boldsymbol{\chi}_i \in \gamma_1} |\varphi_i - \phi(\boldsymbol{x}_i)|, \tag{7.89}$$

$$\|\mathrm{err_N}\|_\infty = \max_{\boldsymbol{\chi}_i \in \gamma_0} |q_i - \partial\phi(\boldsymbol{\chi}_i)/\partial\boldsymbol{n}|, \tag{7.90}$$

$$\|\mathrm{err_C}\|_\infty = \max_{\boldsymbol{\chi}_i \in \gamma_0} |2\hbar_i - 2\hbar(\boldsymbol{\chi}_i)|, \tag{7.91}$$

where φ_i, q_i and $\hbar_i$ are the nodal values of boundary potential, flux and mean curvature produced by the boundary integral solver and quintic spline interpolation, respectively.

In figure 7.2(b), the Dirichlet error $\mathrm{err_D}$, the Neumann error $\mathrm{err_N}$ and curvature error $\mathrm{err_C}$ are plotted against the total degrees of freedom (DoF) employed by the solver, i.e. number of independent nodes. We observe robust power-law behaviors in asymptotic error convergence, which are expected for collocation methods based on interpolation functions (Kress, 2014). Solutions computed with quadratic Lagrange interpolation functions exhibit convergence rate at least as twice fast as the ones with linear ones.

7.4 Solutions to Self-Similar Cone Formation via Newton-Raphson Iteration

As discussed in Section 6.5, there are in total three boundary segments in the system of self-similar equations (6.20), (6.21) and (6.22), i.e. the dividing interface γ between vacuum and liquid phases, the upper spherical patch γ_{vac} for vacuum and the lower spherical patch γ_{liq} for liquid. These three curves join at the truncation point $\boldsymbol{\chi}_* =$

(r_*, z_*) and divide a spherical volume of radius $\chi_* = |\boldsymbol{\chi}_*|$ into a closed liquid domain $\omega_{\rm liq}$ bounded by γ and $\gamma_{\rm liq}$ and a closed vacuum domain $\omega_{\rm vac}$ bounded by γ and $\gamma_{\rm vac}$. In order to proceed with boundary integral formulation, all three boundary segments are approximated by quintic spline interpolation developed in Section 7.2. The analytic shapes of $\gamma_{\rm liq}$ and $\gamma_{\rm vac}$ are arcs which begin at $\boldsymbol{\chi}_*$ and end at south pole $(0, -\chi_*)$ for $\gamma_{\rm liq}$ and north pole $(0, \chi_*)$ for $\gamma_{\rm vac}$. The shape of interface γ is to be determined.

For γ to be an admissible solution to the self-similar Bernoulli system, it must satisfy a few constraints. Recall from the spline equations (7.13) that in addition to positions of the knots a quintic spline requires extra four boundary conditions. On the symmetry axis where $r = 0$, an odd condition must be supplied for the r-component of all three splines and an even condition for the z-component to enforce axial symmetry. At large axial distance where $r \gg 1$, the shape of liquid/vacuum interface γ is expected to converge to the far-field tail of asymptotic expansion (6.33), the higher order coefficients $c_2, c_3, \ldots$ of which are completely specified by any two of the three parameters a_0, c_1 and b_0. For numerical purposes, we use a_0 and c_1 as the two independent parameters of the solution family. By differentiating asymptotic height field $\eta_\infty(r)$ in (6.33), we arrive at three additional constraints relating the first two derivatives of interface $\boldsymbol{\gamma} = (r, z)$ at the truncation point $\boldsymbol{\chi}_*$,

$$\left.\begin{aligned} z &= \eta_\infty(r), \\ \dot{z} &= \frac{\mathrm{d}\eta_\infty}{\mathrm{d}r}\dot{r}, \\ \ddot{z} &= \frac{\ddot{r}\dot{z} + 2(\dot{r}^2 + \dot{z}^2)^{3/2}\hbar_\infty}{\dot{r}} - \frac{\dot{z}\,(\dot{r}^2 + \dot{z}^2)}{\dot{r}r}, \end{aligned}\right\} \text{ at } r = r_* \tag{7.92}$$

where $\hbar_\infty(r)$ is obtained by the curvature formula (7.30) applied to a shape parametrized by $(r, \eta_\infty(r))$.

Now if we introduce the residue of the Bernoulli's equation along a given interface γ,

$$\zeta(\boldsymbol{\chi}) = \frac{2}{3}\boldsymbol{\chi}\cdot\nabla\phi - \frac{1}{3}\phi + \frac{1}{2}|\nabla\phi|^2 - 2\hbar - \frac{1}{2}|\nabla\psi|^2 \quad \text{on} \quad \gamma, \tag{7.93}$$

then on an abstract level the problem of solving for possible liquid/vacuum interfaces γ constrained by the self-similar equations of the Bernoulli system is essentially equivalent to root-finding of the nonlinear integro-differential equation

$$\zeta(\gamma) = 0. \tag{7.94}$$

This argument can be made explicit if we transform residue (7.93) using boundary coordinate frame with unit tangent $\boldsymbol{s}$ and unit normal $\boldsymbol{n}$,

$$\zeta(\boldsymbol{\chi}) = \frac{1}{2}\left(\frac{\partial\phi}{\partial\boldsymbol{s}}\right)^2 + \frac{2}{3}(\boldsymbol{\chi}\cdot\boldsymbol{s})\frac{\partial\phi}{\partial\boldsymbol{s}} - \frac{\phi}{3} - \frac{2}{9}(\boldsymbol{n}\cdot\boldsymbol{\chi})^2 - 2\hbar - \frac{1}{2}\left(\frac{\partial\psi}{\partial\boldsymbol{n}}\right)^2. \tag{7.95}$$

Given asymptotic velocity potential ϕ_∞ from expansion (6.33) prescribed on the liquid patch γ_{liq} and kinematic boundary condition (6.21) imposed on γ, the boundary velocity potential $\phi(\gamma)$ is completely specified by the geometry of liquid/vacuum interface γ. Similar situation applies to the electric flux $\partial\psi/\partial\boldsymbol{n}(\gamma)$ when asymptotic electric field $\nabla\psi_\infty$ is prescribed on the vacuum patch γ_{vac} and equipotential condition on γ. We can compute interfacial quantities such as ϕ and $\partial\psi/\partial\boldsymbol{n}$ by solving boundary integral equations subject to mixed boundary condition as outlined in the last section. Curvature formula (7.30) applied to the quintic spline interpolation of interface γ yields a good approximation to $\hbar$. The only complication here is the surface gradient $\partial\phi/\partial\boldsymbol{s}$. Since boundary potential ϕ is expected to be sufficiently continuous with respect to the arc-length of interface γ, one way of approximating $\partial\phi/\partial\boldsymbol{s}$ at a knot $\boldsymbol{\chi}_j \in \gamma$ is to differentiate a third order polynomial interpolation through adjacent knots along arc-length, for example,

$$\Big\{(0,\phi(\boldsymbol{\chi}_j)),(\mathfrak{s}_j,\phi(\boldsymbol{\chi}_{j+1})),(\mathfrak{s}_j+\mathfrak{s}_{j+1},\phi(\boldsymbol{\chi}_{j+2})),(\mathfrak{s}_j+\mathfrak{s}_{j+1}+\mathfrak{s}_{j+2},\phi(\boldsymbol{\chi}_{j+3}))\Big\}, \tag{7.96}$$

where $\mathfrak{s}_k$ is the total arc-length (7.28) of a local spline $\boldsymbol{\gamma}^{(k)}$. The resulting local polynomial can be conveniently expressed in terms of the divided differences (Abramowitz and Stegun, 1965). By taking derivatives of this polynomial, we recover formulas of one-dimensional finite difference approximation on a nonuniform grid. Note there are multiple positions to evaluate the first derivative $\partial\phi/\partial\boldsymbol{s}$. Depending on the "wind" direction, i.e. the local sign of $\boldsymbol{\chi}\cdot\boldsymbol{s}$ in Bernoulli residue (7.95), either a backward or a forward finite difference must be chosen accordingly. Another possibility is to employ a global quintic spline interpolation through the entire set of points $(\sum_{k=0}^{j-1}\mathfrak{s}_k,\phi(\boldsymbol{\chi}_j))$ as suggested by Leppinen and Lister (2003).

In the Newton-Raphson-type iterative methods, the Jacobian matrix, i.e. first order derivatives with respect to knots of the quintic spline $\boldsymbol{\gamma}$, is required to improve solution at each iteration step. However aside from evident nonlinearity in velocity and electric fields, geometric nonlinearity of the Bernoulli residue $\zeta(\gamma)$ in (7.95) makes the exact calculation of Jacobian matrix very challenging due to the unknown interface shape γ. As we have already encountered in Chapter 5, perturbing boundaries of a domain where a harmonic potential is defined leads a number of extra complications. Analytically tracking shape perturbations can be difficult and error-prone. Therefore we choose to estimate the Jacobian matrix by a finite difference approximation such as the scheme mentioned in (3.80) for computing objective gradient, which is affordable for the one-dimensional problem we have here. A straightforward strategy for perturbing a global quintic spline $\boldsymbol{\gamma}$ at a knot $\boldsymbol{\chi}_j$ is to probe along its normal direction, i.e. $\boldsymbol{\chi}_j \to \boldsymbol{\chi}_j + \epsilon\boldsymbol{n}_j$ for some small number $\epsilon \ll 1$ where $\boldsymbol{n}_j$ is the unit normal vector of spline $\boldsymbol{\gamma}$ at knot $\boldsymbol{\chi}_j$. Recall from equation (7.92) that the truncation point $\boldsymbol{\chi}_*$ is specified by the asymptotic expansion $\eta_\infty(r_*)$, which would have sufficiently high accuracy if higher order terms are

retained in η_∞. Therefore we decide to clamp the interface position $\boldsymbol{\chi}$, the direction of local tangent $\boldsymbol{s}$ and mean curvature $\hbar$ of interface γ to fixed values at the truncation point $\boldsymbol{\chi}_*$. In this way, we avoid any boundary perturbation at $\boldsymbol{\chi}_*$, which would inevitably cause reconstruction of liquid and vacuum patches (hence the single- and double-layer dense matrices) with high computational costs. The overall iteration process of Newton-Raphson method is summarized in algorithm 3.

Algorithm 3 Newton-Raphson iteration for solving system of coupled nonlinear equations (6.20), (6.21) and (6.22).

procedure NEWTON ITERATION(c_1, b_0, r_*) ▷ Truncation distance r_*
  Compute $a_0, \dots, a_4$, $b_1, \dots, b_4$ and $c_3, \dots, c_4$. ▷ c_2 is always zero
  Initialize interface spline γ with guess ▷ Clamp r, z, $\dot{r}$, $\dot{z}$, $\ddot{r}$, $\ddot{z}$ at r_*
  Initialize liquid and vacuum splines, γ_{liq} and γ_{vac} ▷ Spherical patches
  Set asymptotic Dirichlet condition ϕ_∞ on γ_{liq}
  Set asymptotic Neumann condition $\partial\psi_\infty/\partial\boldsymbol{n}$ on γ_{vac}
  Compute Bernoulli residue $\boldsymbol{\zeta}$ ▷ $\zeta_i = \zeta(\boldsymbol{\chi}_i)$
  Allocate Jacobian matrix $\boldsymbol{J}$ ▷ $\dim(\boldsymbol{J}) = \#_{\mathrm{node}} \times (\#_{\mathrm{knot}} - 1)$
  while $\|\boldsymbol{\zeta}\|_\infty > \mathrm{tolerance}$ **do** ▷ L^∞-norm
    for all knots $\boldsymbol{\chi}_j$ of interface spline γ **do** ▷ Exclude ending knot
      Perturb $\boldsymbol{\chi}_j \to \boldsymbol{\chi}_j + \epsilon\,\boldsymbol{n}_j$ ▷ $\epsilon \sim 0.001 \ll 1$
      Compute derivatives $\dot{r}, \ddot{r}, \dot{z}, \ddot{z}$ at $r = r_*$
      Initialize perturbed interface spline $\tilde{\gamma}$
      Set kinematic condition on $\tilde{\gamma}$ for ϕ
      Set equipotential condition on $\tilde{\gamma}$ for ψ
      Compute solution ϕ on $\tilde{\gamma}$
      Compute solution $\partial\psi/\partial\tilde{\boldsymbol{n}}$ on $\tilde{\gamma}$
      Compute new residue $\tilde{\boldsymbol{\zeta}}$ after perturbation ▷ At knots only
      Update $\mathrm{col}_i(\boldsymbol{J}) = (\tilde{\boldsymbol{\zeta}} - \boldsymbol{\zeta})/\epsilon$ ▷ Finite difference
    Solve $\boldsymbol{J}\,\boldsymbol{\delta} = -\boldsymbol{\zeta}$ for $\boldsymbol{\delta}$ ▷ Matrix inverse (QR decomposition)
    Update $\boldsymbol{\chi}_i \to \boldsymbol{\chi}_i + \alpha\,\delta_i \boldsymbol{n}_i$ ▷ Damping rate $0 < \alpha \leq 1$
    Compute new residue vector $\boldsymbol{\zeta}$

Chapter 8

CONCLUDING PERSPECTIVE

A number of tools and models were developed in this thesis to investigate and quantify geometric nonlinearity in small-scale hydrodynamic systems driven by interfacial forces. This research represents a collection of problems bridging the gap between analytic linear theory and direct numerical simulation of interfacial flows with an emphasis on the full treatment of nonlinear effects beyond the linear regime.

In the first half of this dissertation, we have examined interfacial flows in the lubrication limit where the transverse dimensions of the liquid volume are significantly slender than the streamwise dimension. The total potential (free) energy of the liquid film is dissipated through internal viscous frictions quantified by the rate of shear deformation against the supporting substrate, and thus not transferred into kinetic energy. In this regime, velocity field and pressure field within the liquid film are entirely specified by surface forces acting on the liquid/gas interface. Fluid equations are then reduced to a single time-dependent, nonlinear, partial differential equation describing the evolution of local film thickness.

For nonlinear problems, it is customary to first perform a linear stability analysis about some trivial steady base state, such as a flat, static liquid film. While linear theory certainly provides insights into the emerging sinusoidal patterns at early times, it fails to capture strong interface distortions which typically occur at later stages beyond small amplitude deformations . It is especially the case for interfacial flows for which localized geometric singularities are more likely to develop under the action of strong surface forces. For example, the self-similar mechanism of spontaneous conic cusp formation in a viscous thin film when subject to extremely large thermocapillary shear stresses discovered in Chapter 2 cannot be properly resolved without recognizing the nonlinear amplification in thermocapillary stresses as the film apex approaches the top cold plate. In the same vein, linear or weakly nonlinear analysis (Cross and Greenside, 2009) alone with a small number of system parameters is not sufficient to achieve precision control over liquid shapes. As discussed in Chapter 3, when more effective means of control are available, such as the structured electrodes in Electrohydrodynamic Lithography used to pattern dielectric films, it is much more rewarding to solve the full nonlinear, spatiotemporally constrained optimization problem for the optimal electrode design rather than to proceed by trial and error. In more general scenarios where substrate supporting the liquid film is curved, nonlinear (i.e. non-Cartesian) effects of surface curvature can be quantified order by order through the use of appropriate curvilinear coordinate systems such as the ones introduced in Chapter 4. By retaining geometric nonlinearity of both

liquid volume and supporting surface, a novel nonlinear, nonflat, nonlocal model, describing the evolution of a thin dielectric liquid film coating a curved conductor driven by interfacial Maxwell stresses projected by an external electrode, can be derived.

In the second half of this thesis, we have investigated the strong interface distortions of a perfectly conductive liquid body under the nonlinear interplay between capillary and Maxwell stresses as well as inertia forces if inviscid motions of the liquid are considered. For a classical problem like this, the standard practice is to restrict calculations to small deformations of some trivial equilibrium shapes such as a sphere, cylinder and sheet which usually exist due to the rotational or translational invariance. In doing so, linearized calculations benefit greatly from the well-developed mathematical apparatuses (e.g. spherical harmonics) for particular geometries; however, these techniques tend to obscure geometric insights behind these already specialized quantities.

By evoking a nonlinear (convective Lagrangian) coordinate system without any preliminary approximations or restrictions to the liquid shape and its allowable deformations, in Chapter 5 we have obtained truly coordinate-free expressions of the first and second shape variations to the total potential energy for an arbitrary shaped liquid body. More importantly, placing geometric nonlinearity under scrutiny allows us to recover previously neglected contributions to the energy stability of a conductive liquid body in equilibrium when neither curvature nor charge distribution is constant along the liquid interface. By introducing nonlinearity of the convective acceleration in liquid into the picture, we unravel a large set of dynamic cone formations allowable in electrified inviscid liquids. The self-similar theory in Chapter 6, pioneered by Zubarev (2001), accounts for the dynamic balance between capillary, Maxwell and inertia forces due to strong distortion of liquid/vacuum interface. The self-similar transformation introduced by Zubarev preserves nonlinearity of the inviscid model, and hence is fundamentally different from standard linearized modal dynamics which is only suitable for weak disturbances about a hydrostatic Taylor cone. It is this nonlinearity that eventually leads to his key observation that pressure mismatch between interfacial Maxwell and capillary stresses can be possibly compensated by inertia forces such as self-similar suction of an asymptotic sink flow dominating in the far field away from the cone apex. We improve Zubarev's asymptotic analysis to show that in addition to self-similar suction, which is actually linear in velocity potential, liquid kinetic energy density (i.e. the squared norm of velocity field) is primarily responsible for the formation of localized conic cusps. Furthermore, despite his initial effort Zubarev never provided actual solutions to the self-similar theory. The numerical method developed by us in Chapter 7 for solving coupled nonlinear boundary integral equations posed on truncated semi-infinite domains has not only successfully produced accurate solutions of the self-similar dynamics but also revealed curious near-apex details of pressure field and velocity streamlines such as counter flows, stagnation points and interface oscillations not resolved by the asymptotic analysis.

BIBLIOGRAPHY

Abramowitz, M. and I. A. Stegun. *Handbook of Mathematical Functions: With Formulas, Graphs, and Mathematical Tables*. Applied mathematics series. Dover Publications, 1965.

Acome, E., S. K. Mitchell, T. G. Morrissey, M. B. Emmett, C. Benjamin, M. King, M. Radakovitz, and C. Keplinger. "Hydraulically amplified self-healing electrostatic actuators with muscle-like performance". *Science* **359** (6371) (Jan. 2018), pp. 61–65. DOI: 10.1126/science.aao6139.

Alessandri, F., M. Mongiardo, and R. Sorrentino. "New efficient full wave optimization of microwave circuits by the adjoint network method". *IEEE Microwave and Guided Wave Letters* **3** (11) (Nov. 1993), pp. 414–416. DOI: 10.1109/75.248517.

Aliabadi, M. H. *The Boundary Element Method, Volume 2: Applications in Solids and Structures*. The Boundary Element Method. Wiley, 2002.

Amiranashvili, Sh., U. Bandelow, and N. Akhmediev. "Dispersion of nonlinear group velocity determines shortest envelope solitons". *Physical Review A* **84** (4) (Oct. 2011), p. 043834. DOI: 10.1103/physreva.84.043834.

Anderson, T. G., R. Cimpeanu, D. T. Papageorgiou, and P. G. Petropoulos. "Electric field stabilization of viscous liquid layers coating the underside of a surface". *Physical Review Fluids* **2** (5) (May 2017). DOI: 10.1103/physrevfluids.2.054001.

Antil, H., R. Glowinski, R. H. W. Hoppe, C. Linsenmann, T.-W. Pan, and A. Wixforth. "Modeling, simulation, and optimaization of surface acoustic wave driven microfluidic biochips". *Journal of Computational Mathematics* **28** (2) (June 2010), pp. 149–169. DOI: 10.4208/jcm.2009.10-m1001.

Aris, R. *Vectors, Tensors and the Basic Equations of Fluid Mechanics*. Dover Books on Mathematics. Dover Publications, 1990.

Balestra, G., M. Badaoui, Y.-M. Ducimetière, and F. Gallaire. "Fingering instability on curved substrates: Optimal initial film and substrate perturbations". *Journal of Fluid Mechanics* **868** (Apr. 2019), pp. 726–761. DOI: 10.1017/jfm.2019.197.

Balestra, G., P.-T. Brun, and F. Gallaire. "Rayleigh-Taylor instability under curved substrates: An optimal transient growth analysis". *Physical Review Fluids* **1** (8) (Dec. 2016), p. 083902. DOI: 10.1103/physrevfluids.1.083902.

Bandle, C. and A. Wagner. "Second domain variation for problems with robin boundary conditions". *Journal of Optimization Theory and Applications* **167** (2) (Aug. 2015), pp. 430–463. DOI: 10.1007/s10957-015-0801-1.

Barker, A. T., T. Rees, and M. Stoll. "A fast solver for an H1 regularized PDE-constrained optimization problem". *Communications in Computational Physics* **19** (1) (Jan. 2016), pp. 143–167. DOI: 10.4208/cicp.190914.080415a.

Bartoli, C., H. von Rohden, S. P. Thompson, and J. Blommers. "A liquid caesium field ion source for space propulsion". *Journal of Physics D: Applied Physics* **17** (12) (Dec. 1984), pp. 2473–2483. DOI: 10.1088/0022-3727/17/12/014.

Baskin, L. M., A. V. Batrakov, S. A. Popov, and D. I. Proskurovsky. "Electrohydrodynamic phenomena on the explosive-emission liquid-metal cathode". *IEEE Transactions on Dielectrics and Electrical Insulation* **2** (2) (Apr. 1995), pp. 231–236. DOI: 10.1109/94.388245.

Batchelor, G. K. *An Introduction to Fluid Dynamics*. Cambridge University Press, 2000. DOI: 10.1017/cbo9780511800955.

Becker, J., G. Grun, M. Lenz, and M. Rumpf. "Numerical methods for fourth order nonlinear degenerate diffusion problems". *Applications of Mathematics* **47** (6) (Dec. 2002), pp. 517–543. DOI: 10.1023/b:apom.0000034537.55985.44.

Bellman, R. *Dynamic Programming*. 1st ed. Princeton, NJ, USA: Princeton University Press, 1957.

Bender, C. M. and S. A. Orszag. *Advanced Mathematical Methods for Scientists and Engineers I: Asymptotic Methods and Perturbation Theory*. Springer New York, 1999. DOI: 10.1007/978-1-4757-3069-2.

Berendsen, C. W. J., C. J. Kuijpers, J. C. H. Zeegers, and A. A. Darhuber. "Dielectrophoretic deformation of thin liquid films induced by surface charge patterns on dielectric substrates". *Soft Matter* **9** (19) (2013), p. 4900. DOI: 10.1039/c3sm27944h.

Bernoff, A. J., A. L. Bertozzi, and T. P. Witelski. "Axisymmetric surface diffusion: dynamics and stability of self-similar pinchoff". *Journal of Statistical Physics* **93** (3/4) (Nov. 1998), pp. 725–776. DOI: 10.1023/b:joss.0000033251.81126.af.

Bertozzi, A. L. and M. Bowen. "Thin film dynamics: theory and applications". *Modern Methods in Scientific Computing and Applications*. Springer Netherlands, 2002, pp. 31–79. DOI: 10.1007/978-94-010-0510-4_2.

Bertsekas, D. P. *Dynamic Programming & Optimal Control, Vol. I*. Athena Scientific, 2005.

Bestehorn, M., A. Pototsky, and U. Thiele. "3D Large scale Marangoni convection in liquid films". *The European Physical Journal B - Condensed Matter* **33** (4) (June 2003), pp. 457–467. DOI: 10.1140/epjb/e2003-00186-3.

Billingham, J. and A. C. King. "The interaction of a moving fluid/fluid interface with a flat plate". *Journal of Fluid Mechanics* **296** (Aug. 1995), pp. 325–351. DOI: 10.1017/s002211209500214x.

Bird, R. B. "Useful non-newtonian models". *Annual Review of Fluid Mechanics* **8** (1) (Jan. 1976), pp. 13–34. DOI: 10.1146/annurev.fl.08.010176.000305.

Blanchette, F. and W. W. Zhang. "Force balance at the transition from selective withdrawal to viscous entrainment". *Physical Review Letters* **102** (14) (Apr. 2009), p. 144501. DOI: 10.1103/physrevlett.102.144501.

Borrvall, T. and J. Petersson. "Topology optimization of fluids in stokes flow". *International Journal for Numerical Methods in Fluids* **41** (1) (2002), pp. 77–107. DOI: 10.1002/fld.426.

Boujo, E. and M. Sellier. "Pancake making and surface coating: Optimal control of a gravity-driven liquid film". *Physical Review Fluids* **4** (6) (June 2019), p. 064802. DOI: 10.1103/physrevfluids.4.064802.

Braun, R. J., R. Usha, G. B. McFadden, T. A. Driscoll, L. P. Cook, and P. E. King-Smith. "Thin film dynamics on a prolate spheroid with application to the cornea". *Journal of Engineering Mathematics* **73** (1) (June 2011), pp. 121–138. DOI: 10.1007/s10665-011-9482-4.

Burelbach, J. P., S. G. Bankoff, and S. H. Davis. "Nonlinear stability of evaporating/condensing liquid films". *Journal of Fluid Mechanics* **195** (-1) (Oct. 1988), p. 463. DOI: 10.1017/s0022112088002484.

Burton, J. C. and P. Taborek. "Two-dimensional inviscid pinch-off: An example of self-similarity of the second kind". *Physics of Fluids* **19** (10) (Oct. 2007), p. 102109. DOI: 10.1063/1.2800387.

– "Simulations of coulombic fission of charged inviscid drops". *Physical Review Letters* **106** (14) (Apr. 2011), p. 144501. DOI: 10.1103/physrevlett.106.144501.

Byerly, W. E. *An Elementary Treatise on Fourier's Series: and Spherical, Cylindrical, and Ellipsoidal Harmonics, with Applications to Problems in Mathematical Physics*. Dover Books on Mathematics. Ginn & Company, 1895.

Capovilla, R. and J. Guven. "Second variation of the Helfrich-Canham Hamiltonian and reparametrization invariance". *Journal of Physics A: Mathematical and General* **37** (23) (May 2004), pp. 5983–6001. DOI: 10.1088/0305-4470/37/23/003.

Chang, C., K. Limkrailassiri, and L. Lin. "Continuous near-field electrospinning for large area deposition of orderly nanofiber patterns". *Applied Physics Letters* **93** (12) (Sept. 2008), p. 123111. DOI: 10.1063/1.2975834.

Chang, T. H. P. "Proximity effect in electron-beam lithography". *Journal of Vacuum Science and Technology* **12** (6) (Nov. 1975), pp. 1271–1275. DOI: 10.1116/1.568515.

Chapman, S. J., P. H. Trinh, and T. P. Witelski. "Exponential asymptotics for thin film rupture". *SIAM Journal on Applied Mathematics* **73** (1) (Jan. 2013), pp. 232–253. DOI: 10.1137/120872012.

Cheng, K. J. and J. B. Chaddock. "Deformation and stability of drops and bubbles in an electric field". *Physics Letters A* **106** (1-2) (Nov. 1984), pp. 51–53. DOI: 10.1016/0375-9601(84)90491-2.

– "Maximum size of bubbles during nucleate boiling in an electric field". *International Journal of Heat and Fluid Flow* **7** (4) (Dec. 1986), pp. 278–282. DOI: 10.1016/0142-727x(86)90005-6.

Cheng, Y., J. Cao, Y. Zhang, and Q. Hao. "Review of state-of-the-art artificial compound eye imaging systems". *Bioinspiration & Biomimetics* **14** (3) (Feb. 2019), p. 031002. DOI: 10.1088/1748-3190/aaffb5.

Cherney, L. T. "Structure of Taylor cone-jets: limit of low flow rates". *Journal of Fluid Mechanics* **378** (Jan. 1999), pp. 167–196. DOI: 10.1017/s002211209800319x.

Choo, R. T. C. and J. M. Toguri. "The electrodynamic behavior of metal and metal sulphide droplets in slags". *Canadian Metallurgical Quarterly* **31** (2) (Apr. 1992), pp. 113–126. DOI: 10.1179/cmq.1992.31.2.113.

Chou, S. Y. and L. Zhuang. "Lithographically induced self-assembly of periodic polymer micropillar arrays". *Journal of Vacuum Science & Technology B: Microelectronics and Nanometer Structures* **17** (6) (1999), p. 3197. DOI: 10.1116/1.590979.

Chou, S. Y., L. Zhuang, and L. Guo. "Lithographically induced self-construction of polymer microstructures for resistless patterning". *Applied Physics Letters* **75** (7) (Aug. 1999), pp. 1004–1006. DOI: 10.1063/1.124579.

Chung, M. S., P. H. Cutler, T. E. Feuchtwang, E. Kazes, and N. M. Miskovsky. "Use of variational equations to analyze equilibrium and stability of an electrostatically stressed conducting fluid: Application to a cuspidal model of a LMIS". *Le Journal de Physique Colloques* **45** (C9) (Dec. 1984), pp. 153–159. DOI: 10.1051/jphyscol:1984926.

Chung, M. S., P. H. Cutler, and N. M. Miskovsky. "A first-order Navier-Stokes treatment of the shape and instability of liquid metal ion sources". *Journal of Applied Physics* **66** (12) (Dec. 1989), pp. 6065–6072. DOI: 10.1063/1.343586.

Ciarlet, P. G. *The Finite Element Method for Elliptic Problems*. Society for Industrial and Applied Mathematics, Jan. 2002. DOI: 10.1137/1.9780898719208.

Çlabuk, H. and V. Modi. "Optimum plane diffusers in laminar flow". *Journal of Fluid Mechanics* **237** (Apr. 1992), pp. 373–393. DOI: 10.1017/s0022112092003458.

Cobb, N. B. and A. Zakhor. "Fast, low-complexity mask design". *Optical/Laser Microlithography VIII*. Ed. by Timothy A. Brunner. SPIE, May 1995. DOI: 10.1117/12.209263.

Cody, W. J. "Chebyshev approximations for the complete elliptic integrals K and E". *Mathematics of Computation* **19** (89) (Jan. 1965), pp. 105–105. DOI: 10.1090/s0025-5718-1965-0171370-4.

Cohen, I. and S. R. Nagel. "Scaling at the selective withdrawal transition through a tube suspended above the fluid surface". *Physical Review Letters* **88** (7) (Feb. 2002), p. 074501. DOI: 10.1103/physrevlett.88.074501.

Collins, R. T., J. J. Jones, M. T. Harris, and O. A. Basaran. "Electrohydrodynamic tip streaming and emission of charged drops from liquid cones". *Nature Physics* **4** (2) (Dec. 2007), pp. 149–154. DOI: 10.1038/nphys807.

Collins, R. T., K. Sambath, M. T. Harris, and O. A. Basaran. "Universal scaling laws for the disintegration of electrified drops". *Proceedings of the National Academy of Sciences* **110** (13) (Mar. 2013), pp. 4905–4910. DOI: 10.1073/pnas.1213708110.

COMSOL Multiphysics, Inc. V5.3. Burlington, MA, USA, 2017.

Cook, R. D., D. S. Malkus, M. E Plesha, and R. J. Witt. *Concepts and Applications of Finite Element Analysis*. USA: John Wiley & Sons, Inc., 2007.

Corson, L. T., N. J. Mottram, B. R. Duffy, S. K. Wilson, C. Tsakonas, and C. V. Brown. "Dynamic response of a thin sessile drop of conductive liquid to an abruptly applied or removed electric field". *Physical Review E* **94** (4) (Oct. 2016). DOI: 10.1103/physreve.94.043112.

Craster, R. V. and O. K. Matar. "Electrically induced pattern formation in thin leaky dielectric films". *Physics of Fluids* **17** (3) (Mar. 2005), p. 032104. DOI: 10.1063/1.1852459.

Craster, R. V. and O. K. Matar. "Dynamics and stability of thin liquid films". *Reviews of Modern Physics* **81** (3) (Aug. 2009), pp. 1131–1198. DOI: 10.1103/revmodphys.81.1131.

Cross, M. and H. Greenside. *Pattern Formation and Dynamics in Nonequilibrium Systems*. Cambridge University Press, 2009. DOI: 10.1017/cbo9780511627200.

Crouzeix, M. and F. J. Lisbona. "The convergence of variable-stepsize, variable-formula, multistep methods". *SIAM Journal on Numerical Analysis* **21** (3) (June 1984), pp. 512–534. DOI: 10.1137/0721037.

Day, R. F., E. J. Hinch, and J. R. Lister. "Self-similar capillary pinchoff of an inviscid fluid". *Physical Review Letters* **80** (4) (Jan. 1998), pp. 704–707. DOI: 10.1103/physrevlett.80.704.

del Campo, A. and E. Arzt. "Fabrication approaches for generating complex micro- and nanopatterns on polymeric surfaces". *Chemical Reviews* **108** (3) (Mar. 2008), pp. 911–945. DOI: 10.1021/cr050018y.

Deserno, M. "Rayleigh instability of charged droplets in the presence of counterions". *The European Physical Journal E* **6** (2) (Oct. 2001), pp. 163–168. DOI: 10.1007/s101890170018.

– *Notes on differential geometry with special emphasis on surfaces in* $\mathbb{R}^3$. Accessed: 08-15-2019. 2004. URL: https://www.cmu.edu/biolphys/deserno/pdf/diff_geom.pdf.

Dietzel, M. and S. M. Troian. "Thermocapillary patterning of nanoscale polymer films". *Materials Systems and Processes for Three Dimensional Micro- and Nanoscale Fabrication and Lithography*. Ed. by S. M. Kuebler and V. T. Milam. Vol. 1179. Materials Research Society. Cambridge University Press, 2009, 1179-BB08–02. DOI: 10.1557/proc-1179-bb08-02.

– "Formation of nanopillar arrays in ultrathin viscous films: The critical role of thermocapillary stresses". *Physical Review Letters* **103** (7) (Aug. 2009), p. 074501. DOI: 10.1103/physrevlett.103.074501.

– "Mechanism for spontaneous growth of nanopillar arrays in ultrathin films subject to a thermal gradient". *Journal of Applied Physics* **108** (7) (Oct. 2010), p. 074308. DOI: 10.1063/1.3475516.

Dommermuth, D. G. and D. K. P. Yue. "Numerical simulations of nonlinear axisymmetric flows with a free surface". *Journal of Fluid Mechanics* **178** (May 1987), pp. 195–219. DOI: 10.1017/s0022112087001186.

Doyle, A., D. R. Moffett, and B. Vonnegut. "Behavior of evaporating electrically charged droplets". *Journal of Colloid Science* **19** (2) (Feb. 1964), pp. 136–143. DOI: 10.1016/0095-8522(64)90024-8.

Driesel, W. and Ch. Dietzsch. "In situ HVTEM observation of the tip shape of tin liquid metal ion sources". *Applied Surface Science* **93** (2) (Feb. 1996), pp. 179–190. DOI: 10.1016/0169-4332(95)00326-6.

Driesel, W., Ch. Dietzsch, and R. Mühle. "In situ observation of the tip shape of AuGe liquid alloy ion sources using a high voltage transmission electron microscope". *Journal of Vacuum Science & Technology B: Microelectronics and Nanometer Structures* **14** (5) (Sept. 1996), p. 3367. DOI: 10.1116/1.588537.

Duft, D., T. Achtzehn, R. Müller, B. A. Huber, and T. Leisner. "Rayleigh jets from levitated microdroplets". *Nature* **421** (6919) (Jan. 2003), pp. 128–128. DOI: 10.1038/421128a.

Durán-Olivencia, M. A., R. S. Gvalani, S. Kalliadasis, and G. A. Pavliotis. "Instability, rupture and fluctuations in thin liquid films: theory and computations". *Journal of Statistical Physics* **174** (3) (Jan. 2019), pp. 579–604. DOI: 10.1007/s10955-018-2200-0.

Ea, C. S. and A. D. Brown. "Incorporating a corner correction scheme into enhanced pattern area density proximity effect correction". *Journal of Vacuum Science & Technology B: Microelectronics and Nanometer Structures* **19** (5) (2001), p. 1985. DOI: 10.1116/1.1396642.

Eggers, J. "Universal pinching of 3D axisymmetric free-surface flow". *Physical Review Letters* **71** (21) (Nov. 1993), pp. 3458–3460. DOI: 10.1103/physrevlett.71.3458.

– "Air entrainment through free-surface cusps". *Physical Review Letters* **86** (19) (19 May 2001), pp. 4290–4293. DOI: 10.1103/physrevlett.86.4290.

Eggers, J. and M. A. Fontelos. *Singularities: Formation, Structure, and Propagation*. Cambridge University Press, 2015. DOI: 10.1017/cbo9781316161692.

Elele, E. O., Y. Shen, D. R. Pettit, and B. Khusid. "Detection of a dynamic cone-shaped meniscus on the surface of fluids in electric fields". *Physical Review Letters* **114** (5) (Feb. 2015), p. 054501. DOI: 10.1103/physrevlett.114.054501.

Ern, A. and J.-L. Guermond. *Theory and Practice of Finite Elements*. Springer New York, 2004. DOI: 10.1007/978-1-4757-4355-5.

Feng, J. Q. "Electrically charged conducting drops revisited". *Quarterly of Applied Mathematics* **55** (3) (Sept. 1997), pp. 525–536. DOI: 10.1090/qam/1466146.

Fenn, J. B. "Ion formation from charged droplets: Roles of geometry, energy, and time". *Journal of the American Society for Mass Spectrometry* **4** (7) (July 1993), pp. 524–535. DOI: 10.1016/1044-0305(93)85014-o.

Fernández de la Mora, J. "The effect of charge emission from electrified liquid cones". *Journal of Fluid Mechanics* **243** (-1) (Oct. 1992), p. 561. DOI: 10.1017/s0022112092002829.

– "The fluid dynamics of Taylor cones". *Annual Review of Fluid Mechanics* **39** (1) (Jan. 2007), pp. 217–243. DOI: 10.1146/annurev.fluid.39.050905.110159.

Ferrera, C., J. M. López-Herrera, M. A. Herrada, J. M. Montanero, and A. J. Acero. "Dynamical behavior of electrified pendant drops". *Physics of Fluids* **25** (1) (Jan. 2013), p. 012104. DOI: 10.1063/1.4776238.

Fiedler, K. R., E. McLeod, and S. M. Troian. "Differential colorimetry measurements of fluctuation growth in nanofilms exposed to large surface thermal gradients". *Journal of Applied Physics* **125** (6) (Feb. 2019), p. 065303. DOI: 10.1063/1.5051456.

Fiedler, K. R. and S. M. Troian. "Early time instability in nanofilms exposed to a large transverse thermal gradient: Improved image and thermal analysis". *Journal of Applied Physics* **120** (20) (Nov. 2016), p. 205303. DOI: 10.1063/1.4968575.

Frankel, T. *The Geometry of Physics: An Introduction*. 3rd ed. Cambridge University Press, 2011. DOI: 10.1017/cbo9781139061377.

Fujarewicz, K. and K. Łakomiec. "Adjoint sensitivity analysis of a tumor growth model and its application to spatiotemporal radiotherapy optimization". *Mathematical Biosciences and Engineering* **13** (6) (Aug. 2016), pp. 1131–1142. DOI: 10.3934/mbe.2016034.

Gañán-Calvo, A. M. "Cone-jet analytical extension of Taylor's electrostatic solution and the asymptotic universal scaling laws in electrospraying". *Physical Review Letters* **79** (2) (July 1997), pp. 217–220. DOI: 10.1103/physrevlett.79.217.

Gañán-Calvo, A. M., J. M. López-Herrera, M. A. Herrada, A. Ramos, and J. M. Montanero. "Review on the physics of electrospray: From electrokinetics to the operating conditions of single and coaxial Taylor cone-jets, and AC electrospray". *Journal of Aerosol Science* **125** (Nov. 2018), pp. 32–56. DOI: 10.1016/j.jaerosci.2018.05.002.

Gañán-Calvo, A. M., J. M. López-Herrera, N. Rebollo-Muñoz, and J. M. Montanero. "The onset of electrospray: the universal scaling laws of the first ejection". *Scientific Reports* **6** (1) (Sept. 2016). DOI: 10.1038/srep32357.

Garnier, N., R. O. Grigoriev, and M. F. Schatz. "Optical manipulation of microscale fluid flow". *Physical Review Letters* **91** (5) (July 2003), p. 054501. DOI: 10.1103/physrevlett.91.054501.

Gennes, P. G. de. "Wetting: statics and dynamics". *Reviews of Modern Physics* **57** (3) (July 1985), pp. 827–863. DOI: 10.1103/revmodphys.57.827.

Giacomelli, L. and F. Otto. "Rigorous lubrication approximation". *Interfaces and Free Boundaries* **5** (2003), pp. 483–529. DOI: 10.4171/ifb/88.

Giglio, E., B. Gervais, J. Rangama, B. Manil, B. A. Huber, D. Duft, R. Müller, T. Leisner, and C. Guet. "Shape deformations of surface-charged microdroplets". *Physical Review E* **77** (3) (Mar. 2008). DOI: 10.1103/physreve.77.036319.

Gilbert, W. *De Magnete*. Dover Classics of Science and Mathematics. Republished in 1958. Dover Publications, 1600.

Giles, M. B. and N. A. Pierce. "An introduction to the adjoint approach to design". *Flow, Turbulence and Combustion* **65** (3/4) (Apr. 2000), pp. 393–415. DOI: 10.1023/a:1011430410075.

Girault, V. and P.-A. Raviart. *Finite Element Methods for Navier-Stokes Equations: Theory and Algorithms*. 1st ed. Springer Berlin Heidelberg, 1986. DOI: 10.1007/978-3-642-61623-5.

Goldberg-Oppenheimer, P., P. Kohn, R. M. Langford, and U. Steiner. "Patterning of crystalline organic materials by electro-hydrodynamic lithography". *Small* **8** (16) (June 2012), pp. 2595–2601. DOI: 10.1002/smll.201200194.

Goldberg-Oppenheimer, P. and U. Steiner. "Rapid electrohydrodynamic lithography using low-viscosity polymers". *Small* **6** (11) (May 2010), pp. 1248–1254. DOI: 10.1002/smll.201000060.

Goldman, M., M. Novaga, and B. Ruffini. "Existence and stability for a non-local isoperimetric model of charged liquid drops". *Archive for Rational Mechanics and Analysis* **217** (1) (Dec. 2014), pp. 1–36. DOI: 10.1007/s00205-014-0827-9.

Goldman, M. and B. Ruffini. "Equilibrium shapes of charged droplets and related problems: (mostly) a review" (2017). arXiv: http://arxiv.org/abs/1709.04660v1 [math.AP].

Golub, G. H. and C. F. Van Loan. *Matrix Computations*. 4th ed. Johns Hopkins University Press, Jan. 7, 2013. URL: https://www.ebook.de/de/product/20241149/gene_h_golub_matrix_computations.html.

Golub, G. H. and J. H. Welsch. "Calculation of gauss quadrature rules". *Mathematics of Computation* **23** (106) (May 1969), pp. 221–221. DOI: 10.1090/s0025-5718-69-99647-1.

Gonzalez, R. C. and R. E. Woods. *Digital Image Processing*. 4th ed. Pearson, 2017.

Granik, Y. "Solving inverse problems of optical microlithography". *Optical Microlithography XVIII*. SPIE, May 2005. DOI: 10.1117/12.600141.

Grigoriev, R. O. and T. Qin. "The effect of phase change on stability of convective flow in a layer of volatile liquid driven by a horizontal temperature gradient". *Journal of Fluid Mechanics* **838** (Jan. 2018), pp. 248–283. DOI: 10.1017/jfm.2017.918.

Grün, G., K. Mecke, and M. Rauscher. "Thin-film flow influenced by thermal noise". *Journal of Statistical Physics* **122** (6) (Mar. 2006), pp. 1261–1291. DOI: 10.1007/s10955-006-9028-8.

Guennebaud, Gaël, Benoît Jacob, et al. *Eigen v3*. http://eigen.tuxfamily.org. 2010.

Guerrero, I., R. Bocanegra, F. J. Higuera, and J. Fernández de la Mora. "Ion evaporation from Taylor cones of propylene carbonate mixed with ionic liquids". *Journal of Fluid Mechanics* **591** (Oct. 2007), pp. 437–459. DOI: 10.1017/s0022112007008348.

Gurtin, M. E. "The linear theory of elasticity". *Linear Theories of Elasticity and Thermoelasticity*. Ed. by C. Truesdell. Mechanics of solids. Springer Berlin Heidelberg, 1973, pp. 1–295. DOI: 10.1007/978-3-662-39776-3_1.

Hadamard, J. "Mémoire sur le problème d'analyse relatif à l'équilibre des plaques élastiques encastrées." French. *Mém. Sav. étrang.* **33** (2) (1908).

Haynes, W. M., ed. *CRC Handbook of Chemistry and Physics*. 92nd. CRC Handbook of Chemistry and Physics. CRC Press, 2011.

Heinkenschloss, Matthias. "Formulation and analysis of a sequential quadratic programming method for the optimal dirichlet boundary control of Navier-Stokes flow". *Applied Optimization*. Boston, MA: Springer US, 1998, pp. 178–203. DOI: 10.1007/978-1-4757-6095-8_9.

Helfrich, W. "Elastic properties of lipid bilayers: Theory and possible experiments". *Zeitschrift für Naturforschung C* **28** (11-12) (Dec. 1973), pp. 693–703. DOI: 10.1515/znc-1973-11-1209.

Hendricks, C. D. and J. M. Schneider. "Stability of a conducting droplet under the influence of surface tension and electrostatic forces". *American Journal of Physics* **31** (6) (June 1963), pp. 450–453. DOI: 10.1119/1.1969579.

Henrot, A. and M. Pierre. *Variation et Optimisation de Formes: Une Analyse Géométrique*. Mathématiques et Applications. Springer Berlin Heidelberg, 2005. DOI: 10.1007/3-540-37689-5.

Herminghaus, S. "Dynamical instability of thin liquid films between conducting media". *Physical Review Letters* **83** (12) (Sept. 1999), pp. 2359–2361. DOI: 10.1103/physrevlett.83.2359.

Hinze, M., R. Pinnau, M. Ulbrich, and S. Ulbrich. *Optimization with PDE Constraints*. 1st ed. Vol. 23. Mathematical Modelling: Theory and Applications. Springer Netherlands, 2009. DOI: 10.1007/978-1-4020-8839-1.

Hocking, L. M. *Optimal Control: An Introduction to the Theory with Applications*. Oxford: Clarendon press, 1991. 272 pp. URL: https://www.ebook.de/de/product/3596665/leslie_m_hocking_optimal_control.html.

Hoepffner, J. and G. Paré. "Recoil of a liquid filament: escape from pinch-off through creation of a vortex ring". *Journal of Fluid Mechanics* **734** (Oct. 2013), pp. 183–197. DOI: 10.1017/jfm.2013.472.

Hohman, M. M., M. Shin, G. Rutledge, and M. P. Brenner. "Electrospinning and electrically forced jets. I. Stability theory". *Physics of Fluids* **13** (8) (Aug. 2001), pp. 2201–2220. DOI: 10.1063/1.1383791.

– "Electrospinning and electrically forced jets. II. Applications". *Physics of Fluids* **13** (8) (Aug. 2001), pp. 2221–2236. DOI: 10.1063/1.1384013.

Horn, B. K. P. "The curve of least energy". *ACM Transactions on Mathematical Software* **9** (4) (Dec. 1983), pp. 441–460. DOI: 10.1145/356056.356061.

Hou, T. Y., J. S. Lowengrub, and M. J. Shelley. "Boundary integral methods for multicomponent fluids and multiphase materials". *Journal of Computational Physics* **169** (2) (May 2001), pp. 302–362. DOI: 10.1006/jcph.2000.6626.

Howell, P. D. "Surface-tension-driven flow on a moving curved surface". *Journal of Engineering Mathematics* **45** (3/4) (Apr. 2003), pp. 283–308. DOI: 10.1023/a:1022685018867.

Hu, H., H. Tian, J. Shao, Y. Ding, C. Jiang, and H. Liu. "Fabrication of bifocal microlens arrays based on controlled electrohydrodynamic reflowing of pre-patterned polymer". *Journal of Micromechanics and Microengineering* **24** (9) (Aug. 2014), p. 095027. DOI: 10.1088/0960-1317/24/9/095027.

Huang, Y., N. Bu, Y. Duan, Y. Pan, H. Liu, Z. Yin, and Y. Xiong. "Electrohydrodynamic direct-writing". *Nanoscale* **5** (24 2013), pp. 12007–12017. DOI: 10.1039/C3NR04329K.

Huppert, H. E. "Flow and instability of a viscous current down a slope". *Nature* **300** (5891) (Dec. 1982), pp. 427–429. DOI: 10.1038/300427a0.

Isakov, V. *Inverse Problems for Partial Differential Equations*. 2nd ed. Vol. 127. Applied Mathematical Sciences. Springer-Verlag New York, 2006. DOI: 10.1007/0-387-32183-7.

Ito, T. and S. Okazaki. "Pushing the limits of lithography". *Nature* **406** (6799) (Aug. 2000), pp. 1027–1031. DOI: 10.1038/35023233.

Jackson, J. D. *Classical Electrodynamics*. 3rd ed. New York, NY: John Wiley & Sons, Inc., 1999.

Jameson, A. "Aerodynamic design via control theory". *Journal of Scientific Computing* **3** (3) (Sept. 1988), pp. 233–260. DOI: 10.1007/bf01061285.

Jaworek, A. "Electrospray droplet sources for thin film deposition". *Journal of Materials Science* **42** (1) (Nov. 2006), pp. 266–297. DOI: 10.1007/s10853-006-0842-9.

Jensen, J. S. and O. Sigmund. "Topology optimization for nano-photonics". *Laser & Photonics Reviews* **5** (2) (Dec. 2010), pp. 308–321. DOI: 10.1002/lpor.201000014.

Jensen, O. E. and J. B. Grotberg. "The spreading of heat or soluble surfactant along a thin liquid film". *Physics of Fluids A: Fluid Dynamics* **5** (1) (Jan. 1993), pp. 58–68. DOI: 10.1063/1.858789.

Johnson, S. G. *Notes on adjoint methods*. https://math.mit.edu/~stevenj/18.336/adjoint.pdf. Accessed: 2019-06-25. 2012.

Joseph, D. D. "Parameter and domain dependence of eigenvalues of elliptic partial differential equations". *Archive for Rational Mechanics and Analysis* **24** (5) (Jan. 1967), pp. 325–351. DOI: 10.1007/bf00253151.

– "Domain perturbations: The higher order theory of infinitesimal water waves". *Archive for Rational Mechanics and Analysis* **51** (4) (Jan. 1973), pp. 295–303. DOI: 10.1007/bf00250536.

Karpitschka, S., J. Eggers, A. Pandey, and J. H. Snoeijer. "Cusp-shaped elastic creases and furrows". *Physical Review Letters* **119** (19) (Nov. 2017), p. 198001. DOI: 10.1103/physrevlett.119.198001.

Kasumba, H. and K. Kunisch. "On computation of the shape hessian of the cost functional without shape sensitivity of the state variable". *Journal of Optimization Theory and Applications* **162** (3) (Sept. 2014), pp. 779–804. DOI: 10.1007/s10957-013-0520-4.

Keller, J. B. and M. J. Miksis. "Surface tension driven flows". *SIAM Journal on Applied Mathematics* **43** (2) (Apr. 1983), pp. 268–277. DOI: 10.1137/0143018.

Kelly, P. *Mechanics Lecture Notes: An introduction to Solid Mechanics*. Accessed: 08-15-2019. 2013. URL: http://homepages.engineering.auckland.ac.nz/~pkel015/SolidMechanicsBooks/index.html.

Kirk, D. E. *Optimal Control Theory: An Introduction (Dover Books on Electrical Engineering)*. Dover Publications, 2004.

Kolmogorov, A. N. "The local structure of turbulence in incompressible viscous fluid for very large reynolds numbers". *Proceedings of the Royal Society A: Mathematical, Physical and Engineering Sciences* **434** (1890) (July 1991), pp. 9–13. DOI: 10.1098/rspa.1991.0075.

Kolvin, I., G. Cohen, and J. Fineberg. "Crack front dynamics: The interplay of singular geometry and crack instabilities". *Physical Review Letters* **114** (17) (May 2015), p. 175501. DOI: 10.1103/physrevlett.114.175501.

Kondic, L. "Instabilities in gravity driven flow of thin fluid films". *SIAM Review* **45** (1) (Jan. 2003), pp. 95–115. DOI: 10.1137/s003614450240135.

Krechetnikov, R. "On application of lubrication approximations to nonunidirectional coating flows with clean and surfactant interfaces". *Physics of Fluids* **22** (9) (Sept. 2010), p. 092102. DOI: 10.1063/1.3484276.

– "Structure of marangoni-driven singularities". *Physics of Fluids* **24** (2) (Feb. 2012), p. 022111. DOI: 10.1063/1.3685831.

– "Cusps and cuspidal edges at fluid interfaces: Existence and application". *Physical Review E* **91** (4) (Apr. 2015), p. 043019. DOI: 10.1103/physreve.91.043019.

Kress, R. *Linear Integral Equations*. Springer New York, 2014. DOI: 10.1007/978-1-4614-9593-2.

Kreyszig, E. *Differential Geometry*. Differential Geometry. Dover Publications, 1991.

Krpoun, R. and H. R. Shea. "A method to determine the onset voltage of single and arrays of electrospray emitters". *Journal of Applied Physics* **104** (6) (Sept. 2008), p. 064511. DOI: 10.1063/1.2981077.

Lalau-Keraly, C. M., S. Bhargava, O. D. Miller, and E. Yablonovitch. "Adjoint shape optimization applied to electromagnetic design". *Optics Express* **21** (18) (Sept. 2013), p. 21693. DOI: 10.1364/oe.21.021693.

Laugesen, R. S. and M. C. Pugh. "Energy levels of steady states for thin-film-type equations". *Journal of Differential Equations* **182** (2) (July 2002), pp. 377–415. DOI: 10.1006/jdeq.2001.4108.

Leal, L. G. *Advanced Transport Phenomena: Fluid Mechanics and Convective Transport Processes*. Cambridge Series in Chemical Engineering. Cambridge University Press, 2007. DOI: 10.1017/cbo9780511800245.

Lee, J. and C.-J. Kim. "Surface-tension-driven microactuation based on continuous electrowetting". *Journal of Microelectromechanical Systems* **9** (2) (June 2000), pp. 171–180. DOI: 10.1109/84.846697.

Lee, S., S. H. Jung, D. J. Kang, and J. Lee. "Fabrication of a nano-scale pattern with various functional materials using electrohydrodynamic lithography and functionalization". *RSC Advances* **6** (7) (2016), pp. 5944–5948. DOI: 10.1039/c5ra24493e.

Lennon, G. P., P. L.-F. Liu, and J. A. Liggett. "Boundary integral equation solution to axisymmetric potential flows: 1. Basic formulation". *Water Resources Research* **15** (5) (Oct. 1979), pp. 1102–1106. DOI: 10.1029/wr015i005p01102.

Lenz, P. and R. Lipowsky. "Stability of droplets and channels on homogeneous and structured surfaces". *The European Physical Journal E* **1** (2) (Feb. 2000), p. 249. DOI: 10.1007/s101890050027.

Leppinen, D. and J. R. Lister. "Capillary pinch-off in inviscid fluids". *Physics of Fluids* **15** (2) (Feb. 2003), pp. 568–578. DOI: 10.1063/1.1537237.

Li, H., W. Yu, Y. Wang, H. Bu, Z. Liu, E. Abraham, and M. P. Y. Desmulliez. "Simulation of the electrohydrodynamic instability process used in the fabrication of hierarchic and hollow micro/nanostructures". *RSC Advances* **4** (27) (2014), p. 13774. DOI: 10.1039/c3ra48046a.

Lin, Z., T. Kerle, S. M. Baker, D. A. Hoagland, E. Schäffer, U. Steiner, and T. P. Russell. "Electric field induced instabilities at liquid/liquid interfaces". *The Journal of Chemical Physics* **114** (5) (Feb. 2001), pp. 2377–2381. DOI: 10.1063/1.1338125.

Ljepojevic, N. N. and R. G. Forbes. "Variational thermodynamic derivation of the formula for pressure difference across a charged conducting liquid surface and its relation to the thermodynamics of electrical capacitance". *Proceedings of the Royal Society A: Mathematical, Physical and Engineering Sciences* **450** (1938) (July 1995), pp. 177–192. DOI: 10.1098/rspa.1995.0078.

Marin, A. G., O. R. Enriquez, P. Brunet, P. Colinet, and J. H. Snoeijer. "Universality of tip singularity formation in freezing water drops". *Physical Review Letters* **113** (5) (July 2014), p. 054301. DOI: 10.1103/physrevlett.113.054301.

Marsden, J. E. and T. J. R. Hughes. *Mathematical Foundations of Elasticity*. Dover Civil and Mechanical Engineering Series. Dover Publications, Inc., 1994.

Matar, O. K. and S. M. Troian. "Spreading of a surfactant monolayer on a thin liquid film: Onset and evolution of digitated structures". *Chaos: An Interdisciplinary Journal of Nonlinear Science* **9** (1) (Mar. 1999), pp. 141–153. DOI: 10.1063/1.166385.

McLeod, E., Y. Liu, and S. M. Troian. "Experimental verification of the formation mechanism for pillar arrays in nanofilms subject to large thermal gradients". *Physical Review Letters* **106** (17) (Apr. 2011), p. 175501. DOI: 10.1103/physrevlett.106.175501.

McLeod, E. and S. M. Troian. "One step non-contact fabrication of polymer microlens arrays by thermocapillary lithography". *CLEO:2011 - Laser Applications to Photonic Applications*. OSA Technical Digest. Optical Society of America. OSA, 2011, p. CM.3. DOI: 10.1364/cleo_si.2011.cml3.

McNamara, A., A. Treuille, Z. Popović, and J. Stam. "Fluid control using the adjoint method". *ACM SIGGRAPH 2004 Papers on - SIGGRAPH '04*. Vol. 23. 3. ACM Press, Aug. 2004. DOI: 10.1145/1186562.1015744.

Melcher, J. R. and C. V. Smith. "Electrohydrodynamic charge relaxation and interfacial perpendicular-field instability". *Physics of Fluids* **12** (4) (1969), p. 778. DOI: 10.1063/1.1692556.

Melcher, J. R. and G. I. Taylor. "Electrohydrodynamics: a review of the role of interfacial shear stresses". *Annual Review of Fluid Mechanics* **1** (1) (Jan. 1969), pp. 111–146. DOI: 10.1146/annurev.fl.01.010169.000551.

Minka, T. *Old and new matrix algebra useful for statistics*. https://tminka.github.io/papers/matrix/minka-matrix.pdf. Accessed: 2019-08-14. Sept. 1997.

Miskovsky, N. M., J. He, P. H. Cutler, and M. Chung. "Electrohydrodynamical study of the instability of a thin liquid metal film: Application to planar liquid metal ion sources". *Journal of Applied Physics* **69** (4) (Feb. 1991), pp. 1956–1961. DOI: 10.1063/1.348767.

Mitlin, V. S. "Dewetting of Solid Surface: Analogy with Spinodal Decomposition". *Journal of Colloid and Interface Science* **156** (2) (Mar. 1993), pp. 491–497. DOI: 10.1006/jcis.1993.1142.

Moroshkin, P., P. Leiderer, Th. B. Möller, and K. Kono. "Taylor cone and electrospraying at a free surface of superfluid helium charged from below". *Physical Review E* **95** (5) (May 2017), p. 053110. DOI: 10.1103/physreve.95.053110.

Morrison, C. A., R. P. Leavitt, and D. E. Wortman. "The extended Rayleigh theory of the oscillation of liquid droplets". *Journal of Fluid Mechanics* **104** (Mar. 1981), pp. 295–309. DOI: 10.1017/s0022112081002929.

Mullins, W. W. "Theory of Thermal Grooving". *Journal of Applied Physics* **28** (3) (Mar. 1957), pp. 333–339. DOI: 10.1063/1.1722742.

Mund, E. H., P. Hallet, and J. P. Hennart. "An algorithm for the interpolation of functions using quintic splines". *Journal of Computational and Applied Mathematics* **1** (4) (Dec. 1975), pp. 279–288. DOI: 10.1016/0771-050x(75)90020-0.

Muratov, C. B., M. Novaga, and B. Ruffini. "On equilibrium shape of charged flat drops". *Communications on Pure and Applied Mathematics* **71** (6) (Jan. 2018), pp. 1049–1073. DOI: 10.1002/cpa.21739.

Myers, T. G. "Thin films with high surface tension". *SIAM Review* **40** (3) (Jan. 1998), pp. 441–462. DOI: 10.1137/s003614459529284x.

Natarajan, R. and R. A. Brown. "The role of three-dimensional shapes in the break-up of charged drops". *Proceedings of the Royal Society A: Mathematical, Physical and Engineering Sciences* **410** (1838) (Mar. 1987), pp. 209–227. DOI: 10.1098/rspa.1987.0035.

Naughton, J. W. and M. Sheplak. "Modern developments in shear-stress measurement". *Progress in Aerospace Sciences* **38** (6-7) (Aug. 2002), pp. 515–570. DOI: 10.1016/s0376-0421(02)00031-3.

Nazaripoor, H., C. R. Koch, M. Sadrzadeh, and S. Bhattacharjee. "Compact micro/nano electrohydrodynamic patterning: using a thin conductive film and a patterned template". *Soft Matter* **12** (4) (2016), pp. 1074–1084. DOI: 10.1039/c5sm02258d.

Nie, Q. and G. Baker. "Application of adaptive quadrature to axi-symmetric vortex sheet motion". *Journal of Computational Physics* **143** (1) (June 1998), pp. 49–69. DOI: 10.1006/jcph.1998.5972.

Nocedal, J. and S. J. Wright. *Numerical Optimization*. 2nd ed. New York, NY, USA: Springer New York, 2006. DOI: 10.1007/978-0-387-40065-5.

Nowlin, K. and D. R. LaJeunesse. "Fabrication of hierarchical biomimetic polymeric nanostructured surfaces". *Molecular Systems Design & Engineering* **2** (3) (2017), pp. 201–213. DOI: 10.1039/c7me00009j.

O'Brien, S. and L. Schwartz. "Theory and modeling of thin film flows". *Encyclopedia of Surface and Colloid Science* (Jan. 2002), pp. 5283–5297.

Oguz, H. N. and A. Prosperetti. "Dynamics of bubble growth and detachment from a needle". *Journal of Fluid Mechanics* **257** (-1) (Dec. 1993), p. 111. DOI: 10.1017/s0022112093003015.

Oh, M. I., A. Malevanets, M. Paliy, D. Frenkel, and S. Consta. "When droplets become stars: charged dielectric droplets beyond the Rayleigh limit". *Soft Matter* **13** (46) (2017), pp. 8781–8795. DOI: 10.1039/c7sm02017a.

Orloff, J. *Handbook of Charged Particle Optics*. Ed. by J. Orloff. CRC Press, Dec. 2017. DOI: 10.1201/9781420045550.

Orloff, J., M. Utlaut, and L. Swanson. "Physics of liquid metal ion sources". *High Resolution Focused Ion Beams: FIB and its Applications*. Springer US, 2003, pp. 21–77. DOI: 10.1007/978-1-4615-0765-9_3.

Oron, A., S. H. Davis, and S. G. Bankoff. "Long-scale evolution of thin liquid films". *Reviews of Modern Physics* **69** (3) (July 1997), pp. 931–980. DOI: 10.1103/revmodphys.69.931.

Oron, A. and P. Rosenau. "On a nonlinear thermocapillary effect in thin liquid layers". *Journal of Fluid Mechanics* **273** (Aug. 1994), pp. 361–374. DOI: 10.1017/s0022112094001977.

Otto, F. "The geometry of dissipative evolution equations: The porous medium equation". *Communications in Partial Differential Equations* **26** (1-2) (Jan. 2001), pp. 101–174. DOI: 10.1081/pde-100002243.

Otto, O. W., J. G. Garofalo, K. K. Low, C.-M. Yuan, R. C. Henderson, C. Pierrat, R. L. Kostelak, S. Vaidya, and P. K. Vasudev. "Automated optical proximity correction: a rules-based approach". *Optical/Laser Microlithography VII*. Ed. by Timothy A. Brunner. SPIE, May 1994. DOI: 10.1117/12.175422.

Padrino Inciarte, J. C. "Topics in Viscous Potential Flow of Two-phase Systems". PhD thesis. University of Minnesota, 2010. URL: https://conservancy.umn.edu/handle/11299/59751.

Padrino, J. C. and D. D. Joseph. "Viscous irrotational analysis of the deformation and break-up time of a bubble or drop in uniaxial straining flow". *Journal of Fluid Mechanics* **688** (Nov. 2011), pp. 390–421. DOI: 10.1017/jfm.2011.381.

Papageorgiou, D. T. "Film flows in the presence of electric fields". *Annual Review of Fluid Mechanics* **51** (1) (Jan. 2019), pp. 155–187. DOI: 10.1146/annurev-fluid-122316-044531.

Papageorgiou, D. T., P. G. Petropoulos, and J.-M. Vanden-Broeck. "Gravity capillary waves in fluid layers under normal electric fields". *Physical Review E* **72** (5) (Nov. 2005). DOI: 10.1103/physreve.72.051601.

Pease, L. F. and W. B. Russel. "Linear stability analysis of thin leaky dielectric films subjected to electric fields". *Journal of Non-Newtonian Fluid Mechanics* **102** (2) (Feb. 2002), pp. 233–250. DOI: 10.1016/s0377-0257(01)00180-x.

– "Electrostatically induced submicron patterning of thin perfect and leaky dielectric films: A generalized linear stability analysis". *The Journal of Chemical Physics* **118** (8) (Feb. 2003), pp. 3790–3803. DOI: 10.1063/1.1529686.

– "Limitations on length scales for electrostatically induced submicrometer pillars and holes". *Langmuir* **20** (3) (Feb. 2004), pp. 795–804. DOI: 10.1021/la035022o.

Peralta-Martinez, M. V. and W. A. Wakeham. "Thermal conductivity of liquid tin and indium". *International Journal of Thermophysics* **22** (2) (2001), pp. 395–403. DOI: 10.1023/a:1010714612865.

Peters, I., J. H. Snoeijer, A. Daerr, and L. Limat. "Coexistence of two singularities in dewetting flows: Regularizing the corner tip". *Physical Review Letters* **103** (11) (Sept. 2009), p. 114501. DOI: 10.1103/physrevlett.103.114501.

Piggott, A. Y., J. Petykiewicz, L. Su, and J. Vučković. "Fabrication-constrained nanophotonic inverse design". *Scientific Reports* **7** (1) (May 2017). DOI: 10.1038/s41598-017-01939-2.

Pillai, R., J. D. Berry, D. J. E. Harvie, and M. R. Davidson. "Electrokinetics of isolated electrified drops". *Soft Matter* **12** (14) (2016), pp. 3310–3325. DOI: 10.1039/c6sm00047a.

Pironneau, O. "On optimum design in fluid mechanics". *Journal of Fluid Mechanics* **64** (1) (June 1974), pp. 97–110. DOI: 10.1017/s0022112074002023.

Plateau, J. *Statique expérimentale et théorique des liquides sommis aux seules forces moléculaires.* French. Gand, Clemm. Paris, Gauthier-Villars. 1873.

Pont, S. Courrech du and J. Eggers. "Sink flow deforms the interface between a viscous liquid and air into a tip singularity". *Physical Review Letters* **96** (3) (Jan. 2006), p. 034501. DOI: 10.1103/physrevlett.96.034501.

Poonawala, A. and P. Milanfar. "Mask design for optical microlithography: an inverse imaging problem". *IEEE Transactions on Image Processing* **16** (3) (Mar. 2007), pp. 774–788. DOI: 10.1109/tip.2006.891332.

Pozrikidis, C. "Interfacial dynamics for Stokes flow". *Journal of Computational Physics* **169** (2) (May 2001), pp. 250–301. DOI: 10.1006/jcph.2000.6582.

Press, W. H., S. A. Teukolsky, W. T. Vetterling, and B. P. Flannery. *Numerical Recipes: The Art of Scientific Computing*. 3rd ed. New York, NY, USA: Cambridge University Press, 2007.

Qi, C., K. A. Gallivan, and P.-A. Absil. "Riemannian BFGS algorithm with applications". *Recent Advances in Optimization and its Applications in Engineering*. Springer Berlin Heidelberg, 2010, pp. 183–192. DOI: 10.1007/978-3-642-12598-0_16.

Quake, S. R. and A. Scherer. "From micro- to nanofabrication with soft materials". *Science* **290** (5496) (Nov. 2000), pp. 1536–1540. DOI: 10.1126/science.290.5496.1536.

Ramkrishnan, A. and S. Kumar. "Electrohydrodynamic deformation of thin liquid films near surfaces with topography". *Physics of Fluids* **26** (12) (Dec. 2014), p. 122110. DOI: 10.1063/1.4904204.

Rayleigh, Lord. "XX. On the equilibrium of liquid conducting masses charged with electricity". *The London, Edinburgh, and Dublin Philosophical Magazine and Journal of Science* **14** (87) (Sept. 1882), pp. 184–186. DOI: 10.1080/14786448208628425.

Reynolds, O. "IV. On the theory of lubrication and its application to Mr. Beauchamp tower's experiments, including an experimental determination of the viscosity of olive oil". *Philosophical Transactions of the Royal Society of London* **177** (Jan. 1886), pp. 157–234. DOI: 10.1098/rstl.1886.0005.

Roberts, S. A. and S. Kumar. "AC electrohydrodynamic instabilities in thin liquid films". *Journal of Fluid Mechanics* **631** (July 2009), pp. 255–279. DOI: 10.1017/s0022112009006843.

Roy, R. V., A. J. Roberts, and M. E. Simpson. "A lubrication model of coating flows over a curved substrate in space". *Journal of Fluid Mechanics* **454** (Mar. 2002), pp. 235–261. DOI: 10.1017/s0022112001007133.

Rüdenauer, F. G. "Field emission devices for space applications". *Surface and Interface Analysis* **39** (2-3) (2007), pp. 116–122. DOI: 10.1002/sia.2472.

Rumpf, M. and O. Vantzos. "Numerical gradient flow discretization of viscous thin films on curved geometries". *Mathematical Models and Methods in Applied Sciences* **23** (05) (Feb. 2013), pp. 917–947. DOI: 10.1142/s0218202512500649.

Saad, Y. *Iterative Methods for Sparse Linear Systems*. 2nd ed. Society for Industrial and Applied Mathematics, Jan. 2003. DOI: 10.1137/1.9780898718003.

Sakai, K. and Y. Yamamoto. "Electric field tweezers for characterization of liquid surface". *Applied Physics Letters* **89** (21) (Nov. 2006), p. 211911. DOI: 10.1063/1.2387864.

Saville, D. A. "ELECTROHYDRODYNAMICS:The Taylor-Melcher leaky dielectric model". *Annual Review of Fluid Mechanics* **29** (1) (Jan. 1997), pp. 27–64. DOI: 10.1146/annurev.fluid.29.1.27.

Schäffer, E., T. Thurn-Albrecht, T. P. Russell, and U. Steiner. "Electrically induced structure formation and pattern transfer". *Nature* **403** (6772) (6772 Feb. 2000), pp. 874–877. DOI: 10.1038/35002540.

– "Electrohydrodynamic instabilities in polymer films". *Europhysics Letters (EPL)* **53** (4) (Feb. 2001), pp. 518–524. DOI: 10.1209/epl/i2001-00183-2.

Schwabe, M., M. Rubin-Zuzic, S. Zhdanov, A. V. Ivlev, H. M. Thomas, and G. E. Morfill. "Formation of bubbles, blobs, and surface cusps in complex plasmas". *Physical Review Letters* **102** (25) (June 2009), p. 114501. DOI: 10.1103/physrevlett.102.255005.

Schwartz, L. W. and D. E. Weidner. "Modeling of coating flows on curved surfaces". *Journal of Engineering Mathematics* **29** (1) (Jan. 1995), pp. 91–103. DOI: 10.1007/bf00046385.

Sethian, J. A. *Level Set Methods and Fast Marching Methods: Evolving Interfaces in Computational Geometry, Fluid Mechanics, Computer Vision, and Materials Science*. Cambridge Monographs on Applied and Computational Mathematics. Cambridge University Press, 1999.

Shankar, V. and A. Sharma. "Instability of the interface between thin fluid films subjected to electric fields". *Journal of Colloid and Interface Science* **274** (1) (June 2004), pp. 294–308. DOI: 10.1016/j.jcis.2003.12.024.

Shrimpton, J. S. "Dielectric charged drop breakyup at sub-rayleigh limit conditions". *IEEE Transactions on Dielectrics and Electrical Insulation* **12** (3) (June 2005), pp. 573–578. DOI: 10.1109/tdei.2005.1453462.

Sierou, A. and J. R. Lister. "Self-similar recoil of inviscid drops". *Physics of Fluids* **16** (5) (May 2004), pp. 1379–1394. DOI: 10.1063/1.1689031.

Sigmund, O. and J. S. Jensen. "Systematic design of phononic band–gap materials and structures by topology optimization". *Philosophical Transactions of the Royal Society of London. Series A: Mathematical, Physical and Engineering Sciences* **361** (1806) (Mar. 2003). Ed. by Roger T. Bonnecaze and Gregory J. Rodin, pp. 1001–1019. DOI: 10.1098/rsta.2003.1177.

Sokolowski, J. and J.-P. Zolesio. *Introduction to Shape Optimization*. Springer Series in Computational Mathematics. Springer Berlin Heidelberg, 1992. DOI: 10.1007/978-3-642-58106-9.

Southwell, W. H. "Pyramid-array surface-relief structures producing antireflection index matching on optical surfaces". *Journal of the Optical Society of America A* **8** (3) (Mar. 1991), p. 549. DOI: 10.1364/josaa.8.000549.

Sternberg, S. *Curvature in Mathematics and Physics*. Dover books on mathematics. Dover Publications, 2012.

Stocker, R. and A. E. Hosoi. "Lubrication in a corner". *Journal of Fluid Mechanics* **544** (-1) (Nov. 2005), p. 353. DOI: 10.1017/s0022112005006725.

Stoker, J. J. *Differential Geometry*. Wiley Classics Library. John Wiley & Sons, Inc., Dec. 1988. DOI: 10.1002/9781118165461.

Stokes, G. G. "On the theory of oscillatory waves". *Mathematical and Physical Papers vol.1*. Vol. 8. Cambridge University Press, 1847, pp. 197–229. DOI: 10.1017/cbo9780511702242.013.

Stoll, M. and A. Wathen. "All-at-once solution of time-dependent Stokes control". *Journal of Computational Physics* **232** (1) (Jan. 2013), pp. 498–515. DOI: 10.1016/j.jcp.2012.08.039.

Storti, M., J. D'Elía, and L. Battaglia. "Tensorial equations for three-dimensional laminar boundary layer flows". *Latin American Applied Research* **41** (Jan. 2011), pp. 31–41.

Subbotin, A. V. and A. N. Semenov. "Electrohydrodynamics of stationary cone-jet streaming". *Proceedings of the Royal Society A: Mathematical, Physical and Engineering Sciences* **471** (2182) (Oct. 2015), p. 20150290. DOI: 10.1098/rspa.2015.0290.

Sujatha, N., P. H. Cutler, E. Kazes, J. P. Rogers, and N. M. Miskovsky. "Variational formulation for the equilibrium condition of a conducting fluid in an electric field". *Applied Physics A Solids and Surfaces* **32** (2) (Oct. 1983), pp. 55–61. DOI: 10.1007/bf00617829.

Suvorov, V. G. and N. M. Zubarev. "Formation of the Taylor cone on the surface of liquid metal in the presence of an electric field". *Journal of Physics D: Applied Physics* **37** (2) (Jan. 2004), pp. 289–297. DOI: 10.1088/0022-3727/37/2/019.

Taflin, D. C., T. L. Ward, and E. J. Davis. "Electrified droplet fission and the Rayleigh limit". *Langmuir* **5** (2) (Mar. 1989), pp. 376–384. DOI: 10.1021/la00086a016.

Tajmar, M., C. Scharlemann, A. Genovese, N. Buldrini, W. Steiger, and I. Vasiljevich. "Liquid-metal-ion source development for space propulsion at ARC". *Ultramicroscopy* **109** (5) (Apr. 2009), pp. 442–446. DOI: 10.1016/j.ultramic.2008.10.009.

Takagi, D. and H. E. Huppert. "Flow and instability of thin films on a cylinder and sphere". *Journal of Fluid Mechanics* **647** (Mar. 2010), pp. 221–238. DOI: 10.1017/s0022112009993818.

Taylor, G. I. "Disintegration of water drops in an electric field". *Proceedings of the Royal Society of London. Series A. Mathematical and Physical Sciences* **280** (1382) (July 1964), pp. 383–397. DOI: 10.1098/rspa.1964.0151.

Taylor, G. I. and A. D. McEwan. "The stability of a horizontal fluid interface in a vertical electric field". *Journal of Fluid Mechanics* **22** (01) (May 1965), p. 1. DOI: 10.1017/s0022112065000538.

Taylor, J. E. and J. W. Cahn. "Linking anisotropic sharp and diffuse surface motion laws via gradient flows". *Journal of Statistical Physics* **77** (1-2) (Oct. 1994), pp. 183–197. DOI: 10.1007/bf02186838.

Thete, S. S., C. Anthony, O. A. Basaran, and P. Doshi. "Self-similar rupture of thin free films of power-law fluids". *Physical Review E* **92** (2) (Aug. 2015), p. 023014. DOI: 10.1103/physreve.92.023014.

Thomée, V. *Galerkin Finite Element Methods for Parabolic Problems*. Springer Series in Computational Mathematics. Springer Berlin Heidelberg, 2006. DOI: 10.1007/3-540-33122-0.

Tian, H., J. Shao, Y. Ding, X. Li, and H. Hu. "Electrohydrodynamic micro-/nanostructuring processes based on prepatterned polymer and prepatterned template". *Macromolecules* **47** (4) (Feb. 2014), pp. 1433–1438. DOI: 10.1021/ma402456u.

Tian, H., J. Shao, Y. Ding, X. Li, X. Li, and H. Liu. "Influence of distorted electric field distribution on microstructure formation in the electrohydrodynamic patterning process". *Journal of Vacuum Science & Technology B, Nanotechnology and Microelectronics: Materials, Processing, Measurement, and Phenomena* **29** (4) (July 2011), p. 041606. DOI: 10.1116/1.3609808.

Trinh, P. H., H. Kim, N. Hammoud, P. D. Howell, S. J. Chapman, and H. A. Stone. "Curvature suppresses the Rayleigh-Taylor instability". *Physics of Fluids* **26** (5) (May 2014), p. 051704. DOI: 10.1063/1.4876476.

Troian, S. M., E. Herbolzheimer, S. A. Safran, and J. F. Joanny. "Fingering instabilities of driven spreading films". *Europhysics Letters (EPL)* **10** (1) (Sept. 1989), pp. 25–30. DOI: 10.1209/0295-5075/10/1/005.

Tröltzsch, F. *Optimal Control of Partial Differential Equations*. Vol. 112. Graduate Studies in Mathematics. American Mathematical Society, 2010.

Tseluiko, D., M. G. Blyth, D. T. Papageorgiou, and J.-M. Vanden-Broeck. "Electrified falling-film flow over topography in the presence of a finite electrode". *Journal of Engineering Mathematics* **68** (3-4) (May 2010), pp. 339–353. DOI: 10.1007/s10665-010-9377-9.

Tseluiko, D., M. G. Blyth, D. T. Papageorgiou, and J.-M. Vanden-broeck. "Electrified viscous thin film flow over topography". *Journal of Fluid Mechanics* **597** (Feb. 2008), pp. 449–475. DOI: 10.1017/s002211200700986x.

Tseluiko, D. and D. T. Papageorgiou. "Nonlinear dynamics of electrified thin liquid films". *SIAM Journal on Applied Mathematics* **67** (5) (Jan. 2007), pp. 1310–1329. DOI: 10.1137/060663532.

Vanhook, S. J., M. F. Schatz, J. B. Swift, W. D. Mccormick, and H. L. Swinney. "Long-wavelength surface-tension-driven Bénard convection: experiment and theory". *Journal of Fluid Mechanics* **345** (Aug. 1997), pp. 45–78. DOI: 10.1017/s0022112097006101.

Verma, R., A. Sharma, K. Kargupta, and J. Bhaumik. "Electric field induced instability and pattern formation in thin liquid films". *Langmuir* **21** (8) (Apr. 2005), pp. 3710–3721. DOI: 10.1021/la0472100.

Veronis, G., R. W. Dutton, and S. Fan. "Method for sensitivity analysis of photonic crystal devices". *Optics Letters* **29** (19) (Oct. 2004), p. 2288. DOI: 10.1364/ol.29.002288.

Villermaux, E. and C. Almarcha. "Node dynamics and cusps size distribution at the border of liquid sheets". *Physical Review Fluids* **1** (4) (Aug. 2016), 041902(R). DOI: 10.1103/physrevfluids.1.041902.

Vogel, C. R. *Computational Methods for Inverse Problems*. Society for Industrial and Applied Mathematics, Jan. 2002. DOI: 10.1137/1.9780898717570.

Voicu, N. E., M. S. M. Saifullah, K. R. V. Subramanian, M. E. Welland, and U. Steiner. "TiO_2 patterning using electro-hydrodynamic lithography". *Soft Matter* **3** (5) (5 2007), p. 554. DOI: 10.1039/b616538a.

von Helmholtz, H. "Zur theorie der stationären ströme in reibenden flüssigkeiten". *Wissenschaftliche Abhandlungen* **1** (1868), pp. 223–230.

Wang, H., L. Liu, and D. Liu. "Equilibrium shapes of a heterogeneous bubble in an electric field: a variational formulation and numerical verifications". *Proceedings of the Royal Society A: Mathematical, Physical and Engineering Sciences* **473** (2199) (Mar. 2017), p. 20160494. DOI: 10.1098/rspa.2016.0494.

Wang, L. and J. Liu. "Liquid metal folding patterns induced by electric capillary force". *Applied Physics Letters* **108** (16) (Apr. 2016), p. 161602. DOI: 10.1063/1.4947440.

Warner, M. R. E., R. V. Craster, and O. K. Matar. "Fingering phenomena associated with insoluble surfactant spreading on thin liquid films". *Journal of Fluid Mechanics* **510** (July 2004), pp. 169–200. DOI: 10.1017/s0022112004009437.

Washizu, K. *Variational Methods in Elasticity and Plasticity*. 3rd ed. Elsevier Science Limited, 1982.

Weatherburn, C. E. *Differential Geometry of Three Dimensions*. reprint. Cambridge University Press, 2016.

Weiblen, R. J., C. R. Menyuk, L. E. Busse, L. B. Shaw, J. S. Sanghera, and I. D. Aggarwal. "Optimized moth-eye anti-reflective structures for As_2S_3 chalcogenide optical fibers". *Optics Express* **24** (10) (May 2016), p. 10172. DOI: 10.1364/oe.24.010172.

Weile, D. S., D. A. Hopkins, G. A. Gazonas, and B. M. Powers. *A convective coordinate approach to continuum mechanics with application to electrodynamics*. Tech. rep. Army Research Laboratory, 2013.

White, F. M. *Viscous Fluid Flow*. 3rd ed. McGraw-Hill, 2006.

Williams, M. B. and S. H. Davis. "Nonlinear theory of film rupture". *Journal of Colloid and Interface Science* **90** (1) (Nov. 1982), pp. 220–228. DOI: 10.1016/0021-9797(82)90415-5.

Wisdom, K. M., J. A. Watson, X. Qu, F. Liu, G. S. Watson, and C.-H. Chen. "Self-cleaning of superhydrophobic surfaces by self-propelled jumping condensate". *Proceedings of the National Academy of Sciences* **110** (20) (Apr. 2013), pp. 7992–7997. DOI: 10.1073/pnas.1210770110.

Wit, A. De, D. Gallez, and C. I. Christov. "Nonlinear evolution equations for thin liquid films with insoluble surfactants". *Physics of Fluids* **6** (10) (Oct. 1994), pp. 3256–3266. DOI: 10.1063/1.868058.

Witelski, T. P. and A. J. Bernoff. "Stability of self-similar solutions for van der Waals driven thin film rupture". *Physics of Fluids* **11** (9) (Sept. 1999), pp. 2443–2445. DOI: 10.1063/1.870138.

– "Dynamics of three-dimensional thin film rupture". *Physica D: Nonlinear Phenomena* **147** (1-2) (Dec. 2000), pp. 155–176. DOI: 10.1016/s0167-2789(00)00165-2.

Wolfram Research, Inc. *Mathematica, Version 12.0*. Champaign, IL, 2019. 2019.

Wong, A. K. *Resolution Enhancement Techniques in Optical Lithography*. SPIE, Mar. 2001. DOI: 10.1117/3.401208.

Wray, A. W., D. T. Papageorgiou, and O. K. Matar. "Electrostatically controlled large-amplitude, non-axisymmetric waves in thin film flows down a cylinder". *Journal of Fluid Mechanics* **736** (Nov. 2013). DOI: 10.1017/jfm.2013.543.

Wriggers, P. *Nonlinear Finite Element Methods*. Springer Berlin Heidelberg, 2008. DOI: 10.1007/978-3-540-71001-1.

Wrobel, L. C. *The Boundary Element Method, Volume 1: Applications in Thermo-Fluids and Acoustics*. The Boundary Element Method. Wiley, 2002.

Wu, N., L. F. Pease, and W. B. Russel. "Electric-field-induced patterns in thin polymer films: Weakly nonlinear and fully nonlinear evolution". *Langmuir* **21** (26) (Dec. 2005), pp. 12290–12302. DOI: 10.1021/la052099z.

Wu, N. and W. B. Russel. "Dynamics of the formation of polymeric microstructures induced by electrohydrodynamic instability". *Applied Physics Letters* **86** (24) (June 2005), p. 241912. DOI: 10.1063/1.1949288.

Xiao, Z., J. Zhang, A. T. Sornborger, and L. Tao. "Cusps enable line attractors for neural computation". *Physical Review E* **96** (5) (Nov. 2017), p. 052308. DOI: 10.1103/physreve.96.052308.

Yang, Q., B. Q. Li, and Y. Ding. "A numerical study of nanoscale electrohydrodynamic patterning in a liquid film". *Soft Matter* **9** (12) (2013), p. 3412. DOI: 10.1039/c3sm27239g.

Yang, Z.-H., N. T. Maitra, and K. Burke. "Effect of cusps in time-dependent quantum mechanics". *Physical Review Letters* **108** (6) (Feb. 2012), p. 063003. DOI: 10.1103/physrevlett.108.063003.

Zeff, B. W., B. Kleber, J. Fineberg, and D. P. Lathrop. "Singularity dynamics in curvature collapse and jet eruption on a fluid surface". *Nature* **403** (6768) (Jan. 2000), pp. 401–404. DOI: 10.1038/35000151.

Zhang, W. W. "Viscous entrainment from a nozzle: singular liquid spouts". *Physical Review Letters* **93** (18) (Oct. 2004), p. 184502. DOI: 10.1103/physrevlett.93.184502.

Zhang, W. W. and J. R. Lister. "Similarity solutions for van der Waals rupture of a thin film on a solid substrate". *Physics of Fluids* **11** (9) (Sept. 1999), pp. 2454–2462. DOI: 10.1063/1.870110.

Zhong-can, O.-Y. and W. Helfrich. "Bending energy of vesicle membranes: General expressions for the first, second, and third variation of the shape energy and applications to spheres and cylinders". *Physical Review A* **39** (10) (May 1989), pp. 5280–5288. DOI: 10.1103/physreva.39.5280.

Zhou, C. and S. M. Troian. "Self-similar cuspidal formation by runaway thermocapillary forces in thin liquid films". *New Journal of Physics* **21** (1) (Jan. 2019), p. 013018. DOI: 10.1088/1367-2630/aaf51d.

Zhou, Y. "Legendre functions, spherical rotations, and multiple elliptic integrals". *The Ramanujan Journal* **34** (3) (Oct. 2013), pp. 373–428. DOI: 10.1007/s11139-013-9502-2.

Zienkiewicz, O. C., R. L. Taylor, and J. Z. Zhu. *The Finite Element Method: its Basis and Fundamentals*. Elsevier, 2013. DOI: 10.1016/c2009-0-24909-9.

Zubarev, N. M. "Formation of conic cusps at the surface of liquid metal in electric field". *Journal of Experimental and Theoretical Physics Letters* **73** (10) (May 2001), pp. 544–548. DOI: 10.1134/1.1387524.